UNIVERSITY OF SALERNO
Department of Civil Engineering

PhD Course
in
Risk and Sustainability in Civil Engineering, Architecture
and Environmental Engineering Systems
CYCLE XXXV (2019-2022)

Seismic behaviour of Seismic-Resilient Steel Moment-Resisting Frames equipped with Damage-Free Self-Centring Column Bases

Elena Elettore

Supervisor
Prof. Gianvittorio Rizzano (UNISA)

PhD Coordinator
Prof. Fernando Fraternali (UNISA)

Co-Supervisors
Prof. Massimo Latour (UNISA)
Prof. Fabio Freddi (UCL)

Declaration of authorship

I, Elena Elettore confirm that the work presented in this thesis is my own. Where information has been derived from other sources, I confirm that this has been indicated in the thesis.

Abstract

Recent destructive seismic events have underlined the need for increasing research efforts devoted to the development of innovative seismic-resilient structures able to reduce seismic-induced direct and indirect losses. For steel Moment Resisting Frames (MRFs), the inclusion of Friction Devices (FDs) in Beam-to-column Joints (BCJs) has been widely investigated as a viable solution to provide both high local ductility and energy dissipation capacity. However, it has been demonstrated that, although using FDs efficiently protects the BCJs' components from local damage, global damage can still be observed in significant post-earthquake residual drifts. This issue has been tackled by several research works, introducing elastic restoring forces able to regulate the structure's Self-Centring (SC) capability, having the main advantage of ensuring both the energy dissipation capacity and the SC behaviour of the structure. However, although considerable attention has been given to define innovative technologies for BCJs, further research is still needed to define innovative configurations for Column Bases (CBs), which play a fundamental role in the seismic performance of steel MRFs, and their protection is paramount for the achievement of the structural resilience. In this context, an innovative Damage-Free Self-Centring Column Base (SC-CB) has been recently experimentally developed at the University of Salerno. It consists of a rocking column splice joint where a combination of FDs and PT bars with disk springs dissipates the seismic energy and promotes the connection's SC behaviour. Component tests of an isolated SC-CB specimen showed a good and stable flag-shaped hysteretic behaviour, demonstrating the advantages of this technology in terms of improved SC and energy dissipation capabilities.

The present Thesis investigates the seismic behaviour of seismic-resilient steel MRFs equipped with SC-CBs through different methodologies. Firstly, the thesis proposes a robust design methodology of the SC-CB based on analytical formulations, discussing its assumptions and limitations. Then, an experimental study of a SC-CB prototype is reviewed, and two modelling strategies (*i.e.,* simplified and advanced) are developed and validated against the experimental results. Successively, a Finite Element (FE) parametric analysis is conducted in ABAQUS to investigate the relevant parameters affecting the global and local behaviour of the joints while providing additional recommendations to improve the design methodology. Besides, extensive numerical simulations are conducted in OPENSEES to investigate the seismic performances of several case-study perimeter MRFs equipped with the SC-CB connections through Incremental Dynamic Analyses (IDAs) and fragility curves. Lastly, an experimental campaign on a large-scale two-storey steel structure equipped with BCJs endowed with FDs and the proposed SC-CBs is carried out by adopting the Pseudo-Dynamic (PsD) procedure. In addition, a simple repairing methodology, consisting of loosening and re-tightening all the high-strength pre-loadable bolts of the FDs, is proposed and analysed to evaluate the effectiveness in terms of residual drift reduction during repair. The results of this thesis highlight the effectiveness of the SC-CBs in drastically reducing the residual drifts of steel MRFs below the acceptable drift limits while not affecting the peak response and in protecting the first-storey columns from damage. In addition, the outcomes of the thesis provide a large set of data for the validation process of simplified and advanced models, giving insights into the use of the adopted SC-CB connections while defining the boundaries of the investigated parameters for their application. Finally, results also demonstrate the repairing methodology's considerable benefits in terms of repairability, functional recovery, and seismic resilience.

Impact statement

The present thesis addresses multiple aspects related to the seismic assessment of steel Moment-Resisting Frames (MRFs) equipped with innovative Damage-Free Self-Centring Column Base (SC-CB) connections. The primary objective is to define design strategies for steel MRFs equipped with SC-CBs and to show the benefits related to the use of these technologies in mitigating the impact of earthquakes on steel MRFs. The reported findings on the SC-CB connections can significantly impact the increase in popularity of these devices. In addition to being cheaper than many other seismic-resilient systems, steel MRFs with SC-CBs are characterised by feasibility and practicality (*i.e.,* the technology is easily applied in practice) and, based on the observations highlighted in this document, are capable of withstanding multiple strong earthquakes with almost no damage. In fact, introducing the proposed SC-CB improves the self-centring behaviour of the whole system and protects the columns, which are difficult to repair or substitute, from damage.

This work will have both scientific and practical impact. Scientific implications relate to develop and validate new design criteria and modelling strategies for steel MRFs with SC-CB connections. These will also strongly impact the evolution of the next generation of Eurocodes. In addition, the work aims to develop standardised and feasible solutions that can be immediately applied in the industry. In fact, the proposed SC-CBs are easy to implement from a technological point of view and can be introduced with a negligible increase in the overall cost of the structure. Moreover, the experimental work reported in this thesis can be used as a benchmark case study structure to evaluate the performance of other steel MRFs equipped with other innovative CB connections, validate numerical models, and evaluate the existing ones.

At this stage, the work presented in this thesis has already impacted the existing literature with the following publications:

- **Elettore E**, Freddi F, Latour M, Rizzano G. Design and analysis of a seismic resilient steel moment-resisting frame equipped with damage-free self-centring CBs. ***Journal of Constructional Steel Research***. 2021; 179:106543. https://doi.org/10.1016/j.jcsr.2021.106543
- **Elettore E**, Lettieri A, Freddi F, Latour M, Rizzano G. Performance-based assessment of seismic-resilient steel moment resisting frames equipped with innovative column base connections. ***Structures***. 2021; 32:1646-1664. https://doi.org/10.1016/j.istruc.2021.03.07
- Lettieri A, **Elettore E**, Pieroni L, Freddi F, Latour M, Rizzano G. Parametric analysis of steel MRFs with self-centring column bases. ***Steel Construction***. 2022;5(2):91–99. https://doi.org/10.1002/stco.202100050
- **Elettore E**, Freddi F, Latour M, Rizzano G. Parametric Finite Element Analysis of Self-centring Column Bases with different Structural Properties. ***Journal of Constructional Steel Research***. 2022; 199:107628. https://doi.org/10.1016/j.jcsr.2022.107628

Also, a journal article is currently Under Review for publication in ***Earthquake Engineering & Structural Dynamics*** in 2023, entitled "Pseudo-Dynamic Testing, Repairability, and Resilience Assessment of a Large-Scale Steel Structure Equipped with Self-centring Column Bases" by **Elettore**

E, Freddi F, Latour M, Piluso V, Rizzano G. Moreover, most of the work here presented has been included in multiple conference proceedings, including the SECED 2019 (Award for the Best Paper by a young author), the CTA 2019 (Award for the Best Thesis), ANIDIS 2019, the EUROSTEEL 2020/21 (Nomination for the Best Paper), the WCEE17 2020/21, the STESSA 2022, the ANIDIS 2022 and the COMPDYN 2023. In Addition, this work will also be included in the EUROSTEEL 2023, WCEE18 2024 and in STESSA 2024 Conference Proceedings.

Additionally, it is also worth highlighting that the outcomes of this work have also been included in the project entitled "SC-RESTEEL: Self-Centring seismic-RESilient sTEEL structures", which has been recently funded within the framework of ERIES: Engineering Research Infrastructures for European Synergies call (2023). The project will investigate the structural response, repairability, resilience, and performance recovery of steel low-damage SC MRFs with FDs and PT bars with disk springs at both CBs and SC-CBs. To this end, shaking table tests will be carried out on large-scale 3D three-storey steel MRFs with the proposed joints considering different properties and placements of SC connections. Experimental results will help validate new modelling strategies and design criteria for MRFs with SC joints.

Acknowledgements

This work is part of a joint research project between the Department of Civil Engineering (DICIV, UNISA, Salerno) and the Department of Civil, Environmental and Geomatic Engineering (CEGE, UCL, London) started in 2018.

I sincerely want to express my highest gratitude and appreciation to my supervisors involved in this project: Prof. Gianvittorio Rizzano (UNISA), Prof. Massimo Latour (UNISA) and Prof. Fabio Freddi (UCL), who made this collaboration possible. They introduced me to the world of research, providing outstanding research supervision and encouraging, supporting and motivating me over the past years. They represent my highest academic inspiration as mentors and role models of professionalism, hard work, integrity and humanity. I will always be grateful to them for their extraordinary support and motivation during these years.

Also, I would like to acknowledge the continuous support provided by Prof. Fabio Freddi (UCL). I feel extremely lucky to have formed part of his talented research group for the extraordinary exchange of knowledge and experiences as a Visiting Master's Thesis Student in 2018 and a Visiting PhD student in 2022 at UCL. Working with him in these years has been an honour and privilege, and I look forward to working with him again after my PhD.

Thanks to my family, who encouraged and supported me in every decision I made in these academic years. Finally, special thanks to my dad, my highest inspiration of strength and courage, a concrete and constant guide in my life.

Contents

List of Figures

List of Tables

Chapter 1 Introduction

1.1 Background and motivations

Earthquakes are among the deadliest and costliest catastrophic events worldwide. According to the traditional 'capacity design' philosophy, suggested by most seismic design codes and guidelines, structures must remain elastic or only slightly damaged in case of frequent (*i.e.,* low intensity) seismic events (*i.e.,* Damage Limit State). Conversely, in case of rare (*i.e.,* high intensity) seismic events (*i.e.,* Ultimate Limit State), structures are typically designed to concentrate the seismic damage into dissipative fuses, which are usually detailed to sustain cyclic inelastic demands. At the same time, the other members of the frame are conceived to remain in the elastic range. Therefore, the seismic energy dissipation capacity and ductility are adequately provided by the development of a high number of dissipative fuses, referred to as plastic hinges, typically located at the beam ends and at the first-storey columns.

Steel Moment Resisting Frames (MRFs) represent widely used seismic-resisting systems in building structures, thanks to their ductile properties and 'good' seismic performance. The traditional design strategy for these structures results in over-strengthened columns and connections, leading to structures characterised by weak beams, strong columns and full-strength joints. This approach, if on one hand allows the fulfilment of life safety requirements, on the other hand, it implicitly leads to the development of significant structural damage in the structural members and significant permanent structural displacements in the aftermath of strong earthquakes, which can significantly compromise the building's reparability. Residual drifts and inelastic damage to nonreplaceable structural components are often complex and costly to reinstate, so the structure may be demolished rather than repaired, even though the collapse risk is remote. This leads to high direct (*i.e.,* causalities, repair costs) and indirect (*i.e.,* business interruption, downtime) losses, which, in many cases, are often unacceptable from both social and economic perspectives. Furthermore, the inelastic response of the structural components can lead to permanent structural displacements (*i.e.,* residual deformations), which compromise the buildings' reparability. As evidence of this, the 1994 Northridge (USA) and 1995 Kobe (Japan) earthquakes caused extensive damage to thousands of steel MRFs, impairing their reparability and leading, in several cases, to their demolition.

This situation strongly affects communities subjected to extreme seismic events, mainly when damaged structures include strategic facilities that must remain operational after a damaging earthquake. In this direction, the field of earthquake engineering is directing a growing research effort to provide innovative structural systems that are durable, efficient, cost-effective, and capable of sustaining the design earthquake intensity with limited socio-economic losses towards the so-called 'seismic resilience. Seismic resilience is defined as the capability of a structure to return to functionality (*i.e.*, 100% quality) within an acceptable short, if not immediate, time, to minimise the repair time and loss of service during the lifespan of a structural system. In this direction, many recent research studies focused on the development of advanced and more performing structural solutions that aim to minimise both seismic damage and repair time, allowing a functional recovery after severe earthquakes. Significant advances in seismic engineering have been developed, with further refinements of performance-based seismic design philosophies and the definition of corresponding compliance criteria. Some examples are

represented by seismic isolation systems or supplemental damping devices, which are currently implemented in international design codes and used in practice in many earthquake-prone regions.

For steel MRFs, the inclusion of Friction Devices (FDs) in Beam-to-column Joints (BCJs) has been widely investigated as a promising strategy to provide both high local ductility and energy dissipation capacity with only minor yielding and wearing within replaceable elements. Noteworthy examples of Damage-Free Beam-to-Column Joints (DF-BCJs) are the Sliding Hinge Joint, developed at the University of Auckland, and the FREEDAM joint, proposed at the University of Salerno. However, although using FDs efficiently protects the BCJs' components from local damage, global damage can still be observed in the form of significant post-earthquake residual drifts. In fact, it has been demonstrated that the reduction of structural damage does not automatically entail repairability because of possible post-earthquake residual drifts, exceeding the commonly accepted limits (*i.e.,* 0.5% for buildings' repairability or 0.2% for structural realignment according to FEMA P58-1).

This issue has been tackled by several research works, introducing elastic restoring forces able to regulate the structure's Self-Centring (SC) capability, which is defined as the ability to return to the undamaged, fully functional condition in a short time. For steel MRFs, beams are usually clamped to the columns through high strength Post-Tensioned (PT) steel bars/ strands parallel to the beams and anchored outside the connection, allowing the control of gap-opening mechanisms (*i.e.,* rocking) at BCJs. The seismic energy dissipation is provided by replaceable/repairable dissipative devices (*e.g.,* yielding set angles or FDs) included in the SC connection. These systems showed excellent post-earthquake repairability due to their inherent ability to return to upright after strong earthquakes and promoted several subsequent studies in this direction.

However, although significant attention has been given to the definition of innovative technologies for BCJs that have been conceived, studied, and experimentally tested, additional research is required to define innovative solutions for Column Bases (CBs). In fact, it has been demonstrated that CBs play a fundamental role in the seismic performance of steel MRFs, and their protection is paramount to achieve structural resilience. According to modern seismic design strategies, CBs can be designed as full- or partial-strength. Conventional full-strength steel CBs may suffer from residual rotations, large plastic deformations and axial shortening phenomena, which impair the structure returning to the initial condition after severe earthquakes. Conversely, the design of partial-strength CBs needs the knowledge of the hysteretic behaviour of the column base under cyclic loadings, which is difficult to predict, and hence this strategy is rarely followed. To overcome the drawbacks of conventional CBs, in the last two decades, several research studies have proposed novel CB configurations having the advantages of being damage-free and characterised by an easy-to-predict hysteretic behaviour under cyclic loadings. Several strategies focused on replacing the conventional full-strength CB connections with dissipative partial-strength joints equipped with yielding or FDs. Furthermore, additional configurations have been developed by combining energy dissipation devices and PT bars or strands, showing the advantages of these systems in terms of improved SC and energy dissipation capabilities.

Within this context, an innovative Damage-Free Self-Centring Column Base (SC-CB) has been recently proposed and experimentally tested at the University of Salerno. It consists of a rocking column splice

joint where a combination of FDs and PT bars with disk springs dissipates the seismic energy and promotes the connection's self-centring behaviour. Component tests of an isolated SC-CB specimen subjected to cyclic loads demonstrated a good and stable flag-shaped hysteretic behaviour, with negligible residual deformations, highlighting the promising behaviour of the system in terms of SC and energy dissipation capabilities. Concerning past innovative CBs configurations previously proposed, this connection is characterised by several advantages such as: *1)* feasible and economically comparable with conventional joints; *2)* self-centring capability obtained with elements (*i.e.,* PT bars and disk springs) that have a size comparable to the size of the joint (*i.e.,* no need for long PT bars); *3)* the moment-rotation hysteretic behaviour of the components can be easily calibrated. Previous experimental tests only focused on the response of an isolated SC-CB under cyclic loads, demonstrating the advantages of this technology. However, there is a significant need for advanced studies to promote the application of this innovative joint typology in practice towards the definition of pre-qualified design rules.

1.2 Research objectives

The present thesis investigates the seismic behaviour of steel seismic-resilient steel MRFs equipped with Damage-Free Self-Centring Column Base (SC-CBs) through different methodologies. In this regard, the thesis describes the concept, the main features and the moment-rotation behaviour of the SC-CB and proposes a robust design methodology based on analytical formulations, highlighting and discussing its assumptions and limitations. Then, an experimental study of a SC-CB prototype is reviewed and two modelling strategies (*i.e.,* simplified and advanced) are developed and validated against the experimental results. Successively, a Finite Element (FE) parametric analysis is conducted in ABAQUS [1] on three selected case-study SC-CBs to investigate the relevant parameters affecting the global and local behaviour of the joints. Besides, a performance-based assessment is carried out to investigate the seismic performance of several case-study perimeter steel MRFs equipped with the proposed SC-CB connections through extensive numerical simulations conducted in OPENSEES [2]. In addition, a parametric analysis is conducted to evaluate the influence of some design parameters (*i.e.,* the frame layout and the seismic mass) on the SC capability of the case-study MRFs. For the numerical simulations, Incremental Dynamic Analyses (IDAs) are performed with 30 ground motion records to derive the samples of the demand for both global and storey-level Engineering Demand Parameters (EPDs) while accounting for the record-to-record variability. Fragility curves are successively derived to evaluate the SC capability of the analysed structures.

Lastly, an experimental campaign on a large-scale two-storey steel structure equipped with Damage-Free BCJs (DF-BCJs) endowed with FDs and with the proposed SC-CBs is carried out by adopting the Pseudo-Dynamic (PsD) procedure, giving valuable insights into the overall structural performance of the structure, collecting data for the validation process while also providing further investigations regarding the structure's repairability and resilience. In addition, a simple repairing methodology, consisting of loosening and re-tightening all the high-strength pre-loadable bolts of the FDs, is proposed and analysed to study the effectiveness in terms of residual drift reduction during repair.

The main findings of this work are expected to finalize the seismic design recommendations for standardized and feasible solutions that can be immediately applied in the industry. To fulfil this aim, the following objectives can be summarised as follows:

- **Obj1** To derive a step-by-step design methodology for the SC-CB using analytical formulations;
- **Obj2** To investigate and focus on the relevant design parameters affecting the global and local behaviour of the SC-CBs to provide design recommendations for specific performance objectives;
- **Obj3** To investigate the effectiveness of the use of SC-CBs within steel MRFs in terms of damage-free behaviour and residual drift reduction within steel MRFs;
- **Obj4** To investigate the seismic performances of several case-study perimeter steel MRFs with SC-CBs while also evaluating the influence of some design parameters (*i.e.,* frame layout and the seismic mass) over the self-centring capability;
- **Obj5** To provide experimental evidence into the use of the SC-CB connection through pseudo-dynamic testing;
- **Obj6** To assess a large-scale steel structure's repairability, resilience, and performance recovery;
- **Obj7** To investigate the effectiveness of simple repairing methodologies for these structures;
- **Obj8** To validate simplified and advanced previously developed FE modelling strategies for the SC-CB and steel MRFs with SC-CBs based on a wide range of experimental results;
- **Obj9** To support adoption into engineering practice and demonstrate the feasibility and advantages of the SC-CB;
- **Obj10** To contribute towards the development of the new generation of anti-seismic codes.

1.3 Thesis outline and methodology

The core of the present research work is divided into four categories: concept development and analytical studies, FE parametric analyses, numerical simulations and experimental programs. Table 1 summarizes the contents of the thesis, highlighting the main sections and evidencing the contribution of the Author to the work. The structure of the present work is outlined as follows:

- **Chapter 2:** covers the Literature Review in the fields of interest made by the Author, mainly focusing on those topics used as a base for the subsequent parts of the thesis. The literature review covers background topics related to traditional and innovative structural solutions for steel MRFs, focusing on friction and self-centring BCJs and CBs. Attention is paid to the innovative configurations of damage-free and self-centring CBs proposed within the current literature. In addition, the numerical modelling strategies existing in current literature and adopted for the structural modelling of this thesis are presented and discussed.

- **Chapter 3:** describes the SC-CB considered within this thesis. The concept, the expected forces in the joint, the moment-rotation behaviour and the analytical formulations are described, highlighting the assumptions and limitations of the design methodology. Then, an experimental

study of an isolated SC-CB prototype is reviewed, and two FE modelling strategies (*i.e.,* simplified in OPENSEES [2] and advanced in ABAQUS [1]) are developed and validated against the experimental results. The validation process allows the prediction of both global and local responses of the SC-CBs, while assessing the validity of design assumptions.

- **Chapter 4:** presents the Parametric FE Analysis of SC-CBs with different structural properties. Three case-study steel MRFs equipped with the SC-CBs, extracted from reference prototype buildings, are designed following Eurocode 8 [3], while the SC-CBs are designed by following the design procedure proposed in Chapter 3. Then, three case-study SC-CBs are selected, and a matrix of sixteen different configurations is considered for each SC-CB, obtained by varying three design properties of the joints. A parametric FE analysis is conducted in ABAQUS [1] to fulfil the following objectives: *i)* to investigate the scale effect on different geometrical configurations; *ii)* to provide insights into the local behaviour of SC-CBs under cyclic loading; *iii)* to identify the parameters that mainly affect the local behaviour of SC-CBs in view of obtaining specific performance objectives (*i.e.,* minimal yielding of the joint components and self-centring capacity); *iv)* to provide insights and design guidelines for this joint typology.

- **Chapter 5:** performs a Performance-Based Assessment of case-study MRFs equipped with SC-CBs. Several case-study steel MRFs are extracted from prototype structures and designed following the Eurocode 8 provisions. Numerical models are developed in OPENSEES [2] for the MRFs with traditional full-strength CBs and for the equivalent MRFs equipped with the proposed SC-CB connections. IDAs are carried out to assess and compare the seismic performances of the two structures while accounting for the record-to-record variability. Fragility curves are derived, based on the IDA results, to evaluate the probability of exceedance of the value of residual interstorey drift limit of 0.5%, which, for building frames, is conventionally associated to the building's reparability. Moreover, several performance levels are considered by monitoring both global and local EDPs and hence deriving both system and components-level fragility curves to provide information about the hierarchy of activation of the different mechanisms within the structure. Additionally, a parametric numerical analysis is performed in OPENSEES [2] to investigate the frame layout's influence and the seismic mass on the self-centring capability of the considered MRFs. Therefore, additional case-study MRFs are selected, and their seismic behaviour is investigated through IDAs and fragility curves.

- **Chapter 6:** presents the PsD experimental campaign performed on a large-scale two-storey steel structure equipped with DF-BCJs endowed with FDs and SC-CB connections. The tests have been performed at the STRENGTH Laboratory of the University of Salerno. The large-scale steel tested specimen is first described, including a presentation of the characterization tests conducted to investigate the material properties of the specimen. Then, the experimental set-up and the instrumentations are shown, with a description of the applied test matrix and procedure. A sequence of six ground motion records, scaled to several intensities, has been defined and applied. Moreover, two additional tests have been carried out considering additional structural configurations. In addition, a simple repairing methodology, consisting of loosening and re-

tightening all the high-strength pre-loadable bolts of the FDs of both DF-BCJs and SC-CBs, is proposed and analysed to study the effectiveness in terms of residual drift reduction during repair. Further insights concerning resilience and reparability are provided.

- **Chapter 7:** draws the main conclusions and findings obtained in the previous chapters and provides an integrated view of these findings, along with some of the limitations of the current work and suggests future work paths in this field.

Table 1. Contribution to the thesis.

Section or topic	Contribution
• **Chapter 1 Introduction**	Introduction
• **Chapter 2 Literature Review**	Bibliographic studies
• **Chapter 3 Damage-Free Self-Centring Column Base (SC-CB)**	
Concept and Design Procedure	Results of previous research projects
Experimental tests on an isolated SC-CB	Results of previous research projects
Modelling strategies and validation	Personal contribution
• **Chapter 4 Parametric FE Analysis of SC-CBs with different structural properties**	
Design of the case-study MRFs with SC-CBs FE Modelling Parametric FE Analysis Design recommendations	Personal contribution
• **Chapter 5 Performance-Based Assessment of case-study MRFs equipped with SC-CBs**	
Design of the case-study MRFs Numerical Modelling Incremental Dynamic Analysis Fragility Curves Parametric Analysis	Personal contribution
• **Chapter 6 Pseudo-dynamic Testing**	
Design of the SC-CB as part of a large-scale steel structure Set-up and instrumentation Pseudo-dynamic Tests Numerical Modelling and validation Reparability and resilience assessment	Personal contribution

1.4 References

1 ABAQUS/Standard and ABAQUS/Explicit – Version 2017. ABAQUS Theory Manual, Dassault Systems, 2016. http://130.149.89.49:2080/v6.14/books/usb/default.htm

2 S. Mazzoni, F. McKenna, M.H. Scott, G.L. Fenves OpenSEES: Open System for earthquake engineering simulation, Pacific Earthquake Engineering Research Centre (PEER), 2009, Univ. of California, Berkley, CA

3 EN 1998-1, Eurocode 8: Design of structures for earthquake resistance – Part 1: General rules, seismic actions and rules for buildings, European Committee for Standardization, Brussels.

Chapter 2 Literature Review

2.1 Seismic behaviour of traditional Steel Moment Resisting Frames

Steel Moment Resisting Frames (MRFs) represent widely used seismic resisting systems in building structures, thanks to their architectural flexibility and 'good' seismic performance [*e.g.,* 1-4] (Figure 2.1). They have been adopted worldwide for low-rise industrial buildings and multi-storey low, medium and high-rise buildings. Steel MRFs are conventionally designed to withstand relevant seismic actions by bending their structural members (*i.e.,* beams, columns, and connections). Their primary source of stiffness and lateral strength is given by the flexural resistance of members and connections, and the seismic energy dissipation capacity and ductility are provided by the formation of a high number of dissipative zones, which can be located in beams, columns or joints strictly depending on the applied design philosophy. In a perimetral layout, MRFs are usually located along the building edges, while the internal part is generally designed to sustain only gravity loads with pinned connections. Consequently, in the hypothesis of rigid floors and during a seismic event, the equivalent horizontal actions induced by the global mass of the building can be considered ideally distributed only among the MRFs.

a) b)

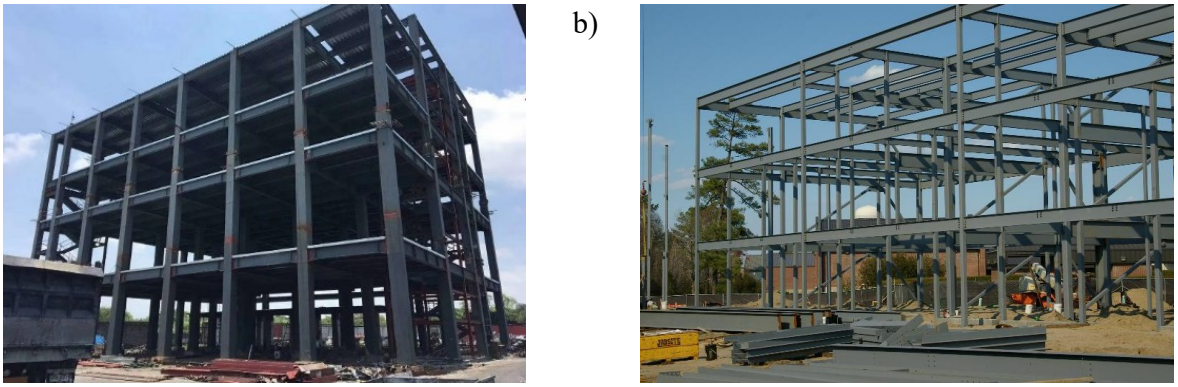

Figure 2.1. Steel Moment Resisting Frames (MRFs) [1-4].

Alternative solutions such as Eccentrically Braced Frames (EBFs) [*e.g.,* 5-7], Concentrically Braced Frames (CBFs) [*e.g.,* 8] or shear walls are also widely adopted (Figure 2.2). These systems require gravity frames to carry vertical loads while the energy dissipation capacity is assigned to the bracing system. In the case of CBFs, the energy dissipation capacity is provided by the plasticization of diagonals in tension. In the case of EBFs, the hysteretic dissipation relies on the participation of predetermined regions of the beams, individuated by the bracing system, which is subjected to high bending and/or shear. Nevertheless, although the aforementioned systems generally allow more rigid configurations, resulting in structures less prone to second-order effects and compliant with the serviceability limit states more easily compared to MRFs, bracings and walls could represent limits from both the architectural and functional points of view. Steel MRFs can provide large open spaces without the obstruction usually caused by bracings or shear walls. In addition, thanks to their flexibility and relatively long periods of vibration, MRFs usually attract smaller seismic forces than CBFs or EBFs.

Steel MRFs can be designed to exhibit fully elastic or dissipative behaviour. In the first case, the structural members of the frame are designed consistently with the maximum design actions. This strategy is able to preserve human life and the serviceability limit states, but it generates a relevant oversizing of the structural elements. Conversely, the dissipative strategy assumes that the structure can

withstand the earthquake effects by dissipating the seismic input energy by activating a high number of well-defined dissipative fuses that strictly depend on the assumed design philosophy.

a) b)

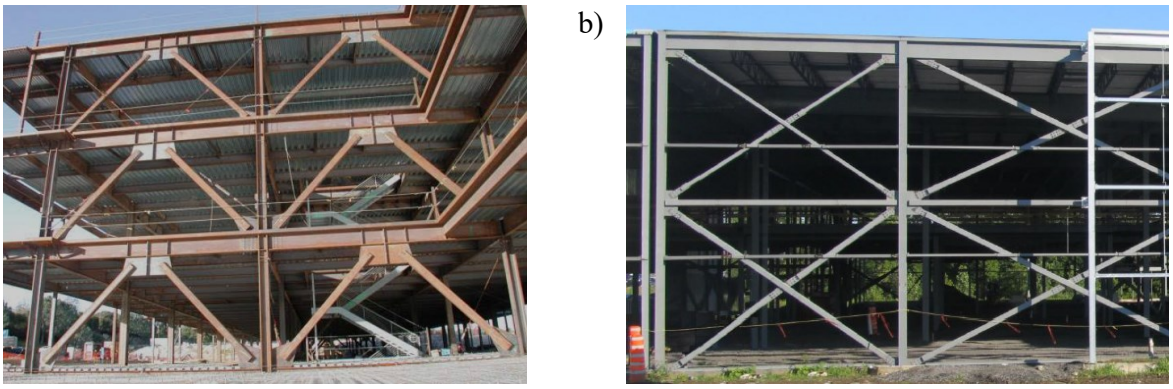

Figure 2.2. Steel structural typologies: a) Eccentrically Braced Frames (EBFs) [5-7]; b) Concentrically Braced Frames (CBFs) [8].

The traditional 'capacity design' philosophy of the 'strong-column strong-joint weak-beam' [9] (Figure 2.3(a)) implemented in current seismic design codes [*e.g.,* 10-13] ensures that steel MRFs remain elastic or only slightly damaged in case of frequent (*i.e.,* low intensity) seismic events (*i.e.,* Damage Limit State DLS). Conversely, extensive damage is generally accepted in rare (*i.e.,* high intensity) seismic events (i.e., Ultimate Limit State ULS). The damage is assured to occur in the ductile parts of the structures where dissipative zones are located, which are usually detailed to sustain cyclic inelastic rotation demands. The seismic energy dissipation capacity and ductility are adequately provided by the formation of a high number of dissipative zones, while the other parts must remain in the elastic range. This design strategy results in strong columns, weak beams and full-strength joints, enforcing the development of plastic hinges beams' end to promote a global failure mechanism if first-storey columns base sections are involved in the plastic range. In this way, the maximum global ductility of the structure is guaranteed, and undesired collapse mechanisms are avoided. This approach inevitably leads to significant structural damage in the structural members, thus implying structural damage with associated repair costs and business downtime. Figure 2.3 (b) shows the expected damage in steel MRFs.

a) b)

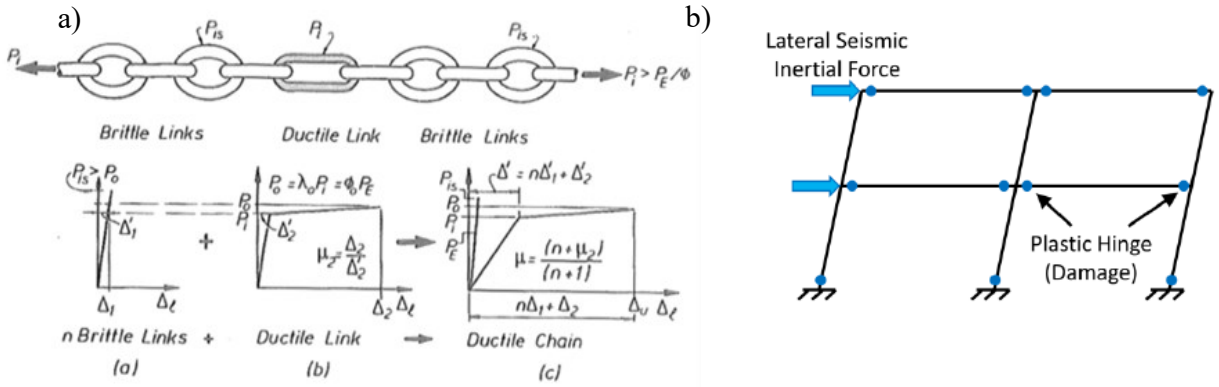

Figure 2.3. Conventional design for seismic-resisting systems: a) Basic concept of capacity design philosophy (Paulay and Priestley, 1992) [9]; b) Expected damage in conventional Steel MRFs.

These drawbacks have been highlighted by several post-earthquake inspections after severe seismic events, which revealed unsatisfactory performances on structures employing perimeter MRFs, and the lessons learned from the field survey have been shown in several studies to date [*e.g.,* 14-20]. For example, the Northridge (California, USA, 1994) [14-15], Kobe (Japan, 1995) [16], and Tohoku (Japan, 2011) [17-18] earthquakes caused devastating losses and resulted in significant damage to buildings, reinforcing the crucial importance of implementing measures for the reduction of the seismic damage. In fact, after the Northridge earthquake, a survey of 2066 steel buildings showed that 70% of them experienced connection damage [15]; after the Kobe earthquake [16], 4530 steel buildings suffered damage, among which 1067 were unable to recover and needed to be fully or partially demolished. Figure 2.4 (a) and (b) show a three-storey and a two-storey building from the 2011 Tohoku earthquake in Japan [17-18]. Although these structures did not collapse, they still had to be demolished due to excessive residual deformations after the seismic event.

a) b)

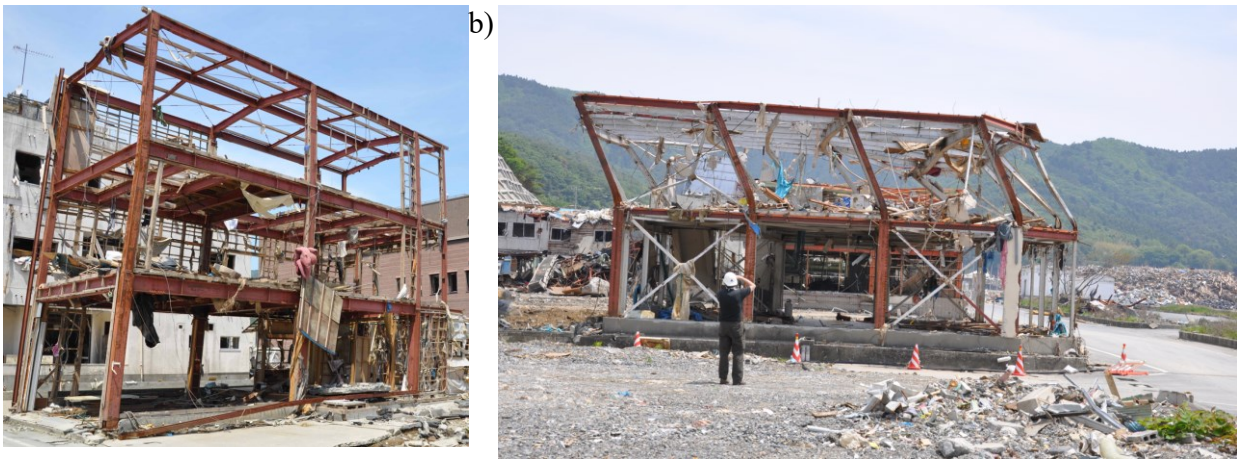

Figure 2.4. Post-earthquake effects on steel MRFs: Tohoku Earthquake, Japan, 2011 [17-18].

Alternatively, it is possible to apply another approach based on the 'strong-column weak-joint strong-beam' philosophy. This strategy assumes partial-strength connections and allows energy dissipation through the plastic engagement of well-defined joint components while the column and the beam end behave elastically. In this latter case, the dissipation of the seismic input energy is provided by the plastic engagement of dissipative joint components.

2.1.1 Frame classification

According to Astaneh *et al.,* 1995 [1], several steel MRF typologies can be individuated in practice according to the following classification:

- *i)* the spatial distribution of the frames within the whole building (*i.e.,* space frame, perimeter frames, planar frames);
- *ii)* the ductility class (*i.e.,* Low, Medium, High);
- *iii)* the beam-column connections' typology (*i.e.,* riveted, bolted, welded);
- *iv)* the stiffness of the joints (*i.e.,* pinned, semi-rigid or rigid);

v) the relative flexural resistance and rotational supply of the structural members and the connections.

According to Eurocode 3 [21], a classification of frames is provided according to the following characteristics:

i) the sensitivity of the structural system to second-order effects;

ii) the presence of a bracing system. According to the susceptibility to second-order effects, framed structures are classified as non-sway or sway frames. The term non-sway frames is used when the in-plane lateral stiffness is sufficient to allow geometrical second-order effects to be neglected. Conversely, a sway frame is affected by relevant internal actions induced by its high lateral deformability. A frame can be non-sway if the following relationships are satisfied:

- $\boldsymbol{\alpha_{cr} = \frac{F_{cr}}{F_{Ed}} > 10}$ for elastic analysis;
- $\boldsymbol{\alpha_{cr} = \frac{F_{cr}}{F_{Ed}} > 15}$ for plastic analysis.

where α_{cr} is the multiplier of the design loading to cause global elastic instability, F_{cr} is the elastic critical buckling load for global instability on the initial elastic stiffness and F_{Ed} is the design load. Another classification involves the braced and unbraced frames, which differ in the presence or absence of specific stiffening elements that can reduce lateral displacements by at least 80%.

2.1.1.1 Spatial distribution

According to the spatial distribution, MRFs can be classified into the following categories:

i) space frames;
ii) perimeter frames;
iii) perimeter frames with only a few MRFs;
iv) planar frames and hybrid systems.

Figure 2.5 (a) shows a typical structure with space frames, in which all the frames withstand both the vertical and horizontal loads, resulting in structures that need the adoption of expensive rigid full-strength joints and, therefore, are not cost/effective. Figure 2.5 (b) shows a perimeter-framed building characterised by MRFs located only along the perimeter. At the same time, the inner part has a pendular behaviour and sustains only the gravity loads. Such a solution is preferred, as it is more effective and cheaper than the previous one, primarily because the number of rigid connections is reduced. For this reason, the adoption of perimeter MRFs has been widely applied in the last two decades. Later, the concept of perimeter MRFs was extended in the perimeter MRFs with only a few rigid bays, further reducing the number of continuous joints and the cost and structural redundancy. Figure 2.5 (c) shows a perimeter-framed building characterized by a few MRFs, which are called to withstand seismic actions, while the other parts of the structure carry the vertical loads only. Moreover, different seismic-resistant strategies can be adopted along with the main directions of the building. For example, this

happens in the case of planar frames (*i.e.,* different systems in two directions) illustrated in Figure 2.5 (d) and hybrid systems (*i.e.,* a combination of two systems in the same direction), where the solution with MRFs can be coupled with other strategies (*e.g.,* EBFs, CBFs).

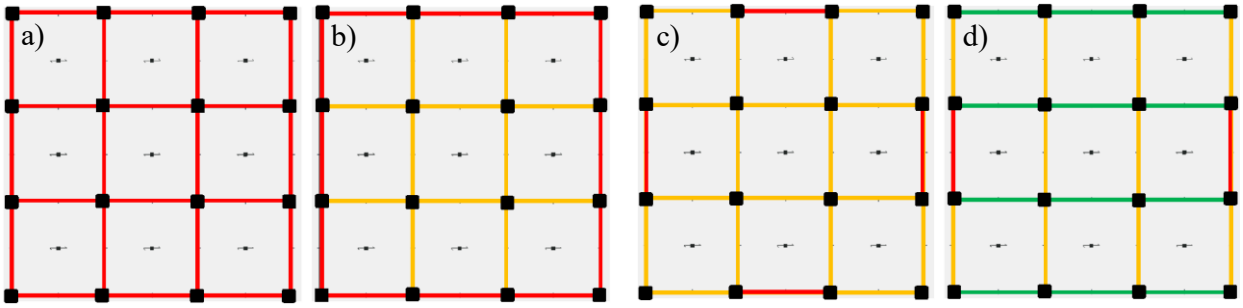

Figure 2.5. MRFs typologies: (a) Space MRFs; (b) Perimeter MRFs; (c) Perimeter frames with a few MRFs; (d) Planar frames. The MRFs are highlighted in red, the pendular frames are highlighted in yellow, and other structural systems are in green.

2.1.1.2 The connection typology

Another classification of MRFs is according to the connection typology. The Beam-to-Column Joints (BCJs) can be classified as riveted, welded and bolted, as illustrated in Figure 2.6. In practice, before the 1920s, steel structures were built exclusively by assembling beams and columns employing riveted joints (Figure 2.6 (a)), enabling the connections to withstand shear and tension loads. Afterwards, the introduction of high-strength bolts represented a significant innovation and an excellent alternative to the riveted connections thanks to the friction mechanism developed between the two clamped surfaces. High-strength bolts allowed to fasten of plates through high contact pressures, leading to the development of the so-called slip-resistant joints. The adoption of these connections allowed relevant time-savings thanks to the ease of installation due to threads and washers (Figure 2.6 (b)).

Figure 2.6. Beam-to-column connection typologies: (a) Riveted; (b) Bolted; (c) Welded.

Besides, starting from the 1920s and becoming more popular in the 1950s, the welding technique started being developed due to the introduction of more advanced techniques (Figure 2.6 (c)). Since the 1960s, with the refinement of the welding procedures and the reduction of the cost of the welding process, such a technique has also been applied to steel structures. This technique allowed the connection of beams and columns by melting the two parts and adding filler material. The first applications were limited to shear connections, but the welding technique was also applied in the case of full-strength BCJs.

Nevertheless, during the unfortunately famous earthquakes of Northridge (California, 1994) [14-15], Kobe (Japan, 1995) [16] and Tohoku (Japan, 2011) [17], many welded BCJs belonging to MRFs exhibited unexpected brittle fractures, causing irreparable damage to the MRFs. Such unsatisfactory behaviour, which occurred both in several perimeter MRFs, typically used in the USA, and in space MRFs typically adopted in Japan, was found in the welding techniques used at the time, which was inadequate and characterised by low ductility [22]. Therefore, the role of welded joints has been reevaluated, and the significant advantages provided by adopting welded connections have been discussed. Therefore, the costly but reliable bolted connections have been reconsidered as an effective alternative to the low ductile and brittle "Pre-Northridge" field welded BCJs. Additional considerations regarding traditional BCJs are discussed in Section 2.1.2 of this thesis.

2.1.1.3 The ductility classes

A further classification of steel MRFs is based on the Ductility Class (*i.e.,* DC) (*i.e.,* Low, Medium, High). As a result of the importance of the current approach to the ductility supply, current seismic international codes [*e.g.,* 10-13] provide a classification of structures regarding the inelastic capacities of the dissipative zones. According to the Eurocode 8 [10] requirements, three DCs have been defined, differentiating for the rotational capacity of the connections (Table 2) according to the three following categories:

- EC8: Ductility Class Low (DCL);
- EC8: Ductility Class Medium (DCM);
- EC8: Ductility Class High (DCH);

In the case of DCL, the MRFs are expected to exhibit a low dissipative behaviour, and connections are not required to possess a specific plastic rotation supply. In the case of DCM and DCH, the structural system is designed to behave in a ductile manner when subjected to a severe seismic event. Thus, brittle mechanisms and buckling are avoided, and dissipation is reached through the inelastic behaviour of the plastic hinges. Connections are required to sustain a minimum rotational capacity equal to 25 and 35 mrad for DCM and DCH, respectively.

Table 2. Required ductility of connections according to Eurocode 8 DC [10]

Ductility Cass	**Minimum Rotational Capacity**
[-]	**[mrad]**
Ductility Class Low (DCL)	[-]
Ductility Class Medium (DCM)	25
Ductility Class High (DCH)	35

Regarding the definition of dissipative and non-dissipative mechanisms, it is highlighted that inelasticity in steel structures can occur from different mechanisms, such as the bending of beams/connections, the shear plasticization of PZs or the friction due to the slippage of plates. Conversely, some examples of non-dissipative mechanisms are the local buckling of members and/or of plates and the yielding of low ductile materials, such as the plastic engagement of welds, which have been discovered to possess low

dissipation capacities. To obtain ductile structures, non-dissipative mechanisms must be avoided, and the brittle elements must be over-strengthened concerning the maximum actions associated with developing the inelastic mechanisms.

In steel MRFs designed for DCM or DCH, the earthquake input energy is dissipated through the plastic engagement of some specific zones (*i.e.,* plastic hinges) located at the beams' ends, in connections, PZs or columns' ends accordingly to the adopted design approach. Following the classical design strategy, dissipative zones are located at the beams' ends and the bottom sections of the first-storey columns, thus providing a collapse mechanism of global type. The other structural parts (*i.e.,* the connections, the PZs and the columns) are designed to possess adequate overstrength compared to the maximum actions transferred by the fully developed plastic hinges. In particular, connections and PZs are required to possess a flexural strength greater than the maximum bending resistance of the fully yielded and strain-hardened beams' ends. The columns must be designed to satisfy the so-called strong-column weak-beam requirements.

2.1.1.4 The stiffness and strength of the joints

The joints' stiffness, strength and rotational capacity strongly influence the overall structural response and the dynamic structural behaviour of steel MRFs. Therefore, the classifications of the frames and joints are strictly related. Several configurations of connections range from quasi-perfectly rigid to flexible configurations, representing the two opposite extremal configurations. In the first case, no relative rotations among the connected members are allowed, whereas in the second case, the joint allows relative rotations among the members converging in the node. It is highlighted that, unlike concrete structures, where the connections can be considered so rigid that no relative rotations among the connected members are allowed, this solution represents an extreme behaviour of the joints in the case of steel structures. Depending on the BCJ typology, it can be assumed that all the ends of the members converging in the joint are subjected to the same rotation and the same displacements or that the joints can permit free rotations. The first case leads to continuous frames, while the second one leads to pinned frames.
In the case of elastic design, MRFs can be classified into the following categories according to the rotational stiffness of the joints as follows (Figure 2.7):

i) Simple (*i.e.,* nominally pinned) connections that are able to transfer only shear and axial force since they allow the relative rotation among the members converging in the node without the development of bending moments; as a consequence, the initial stiffness is negligible. The obtained structural system is pendular, and joints can be modelled using hinges.

ii) Continuous (*i.e.,* rigid connections) that are able to transfer not only shear and axial actions but also bending moments since the relative rotation among the members of the joint is significantly limited. Connections can be modelled employing clamps.

iii) Semi-continuous (*i.e.,* semi-rigid connections) that exhibit an intermediate behaviour between the two previously described solutions. Joints are intermediate between the external

situation of pinned and rigid-full strength. Their structural behaviour must be properly accounted for through accurate models representing the actual moment-rotation curve.

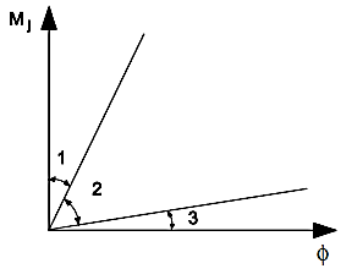

Zone 1: rigid, if $S_{j,ini} \geq k_b EI_b / L_b$

where
$k_b = 8$ for frames where the bracing system reduces the horizontal displacement by at least 80 %
$k_b = 25$ for other frames, provided that in every storey $K_b/K_c \geq 0{,}1$ *)

Zone 2: semi-rigid

All joints in zone 2 should be classified as semi-rigid. Joints in zones 1 or 3 may optionally also be treated as semi-rigid.

Zone 3: nominally pinned, if $S_{j,ini} \leq 0{,}5\, EI_b / L_b$

*) For frames where $K_b/K_c < 0{,}1$ the joints should be classified as semi-rigid.

Key:

K_b is the mean value of I_b/L_b for all the beams at the top of that storey;
K_c is the mean value of I_c/L_c for all the columns in that storey;
I_b is the second moment of area of a beam;
I_c is the second moment of area of a column;
L_b is the span of a beam (centre-to-centre of columns);
L_c is the storey height of a column.

Figure 2.7. Classification of the joint according to the rotational stiffness (Eurocode 3 part 1-8 [30]).

In the case of rigid-plastic design, the classification criterion is based on the flexural strength of the connections. According to Eurocode 3 [21], joints can be classified into the following categories (Figure 2.8):

i) Full-strength joints which are designed to have higher resistance than the connected members ($M_{beam,pl,Rd} > M_{joint,Rd}$) so that plastic hinges can develop only at the beam or the column ends;

ii) Partial-strength joints, which are designed to have lower resistance than the connected members ($0.25M_{beam,pl,Rd} < M_{joint,Rd} < M_{beam,pl,Rd}$) and for this reason, they are characterized by dissipative components that are damaged or activated during a seismic event;

iii) Nominally pinned joints, whose design resistance is much lower than the ones of the connected members ($M_{joint,Rd} < 0.25M_{beam,pl,Rd}$).

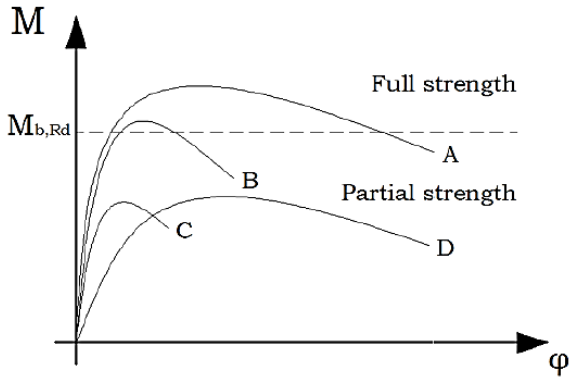

Figure 2.8. Classification of the joint according to the flexural resistance (Eurocode 3 part 1-8 [30]).

Finally, the third classification criterion is based on the plastic rotation supply of the joints, according to which it is possible to define two categories:

i) Full-ductility connections, whose plastic rotation supply is equal to or higher of the connected members;
ii) Partial-ductility connections, whose plastic rotation supply is lower than the connected members.

According to this classification, in the case of elastic analyses, only the rotational stiffness can affect the overall structural behaviour, and the connections can be considered pinned, semi-rigid or rigid. Instead, the stiffness and flexural strength must be considered if an elastic-plastic analysis is performed. Finally, in the case of a rigid-plastic analysis, only the bending resistance plays a relevant role in the overall response. Consequently, the joints can be classified as full-strength, partial-strength or pinned. A summary of the joint classification is reported in Table 3.

Table 3. Joint classification

Method	**Classification Of The Joint**		
Elastic	Nominally Pinned	Rigid	Semi-Rigid Semi-Rigid And Partial-Strength
Elastic-Plastic	Nominally Pinned	Rigid And Full-Strength	Semi-Rigid And Full-Strength Rigid And Partial-Strength
Rigid-Plastic	Nominally Pinned	Full-Strength	Partial-Strength
Type Of Joint Model	**Simple**	**Continuous**	**Semi-Continuous**

2.1.2 Beam-to-column joints (BCJs)

The best strategy to design seismic-resistant steel structures is to increase their energy dissipation capacity by developing a relevant number of dissipative fuses characterized by wide and stable hysteresis loops adequately designed according to the 'Capacity Design' principles [9] (*i.e.,* hierarchy criteria of the strong-column strong-connection weak-beam philosophy), according to which, the energy dissipation capacity is provided by the development of a relevant number of dissipative fuses, characterized by wide and stable hysteresis loops, which are usually detailed to experience significant inelastic deformations under moderate-to-strong earthquakes.

According to the first principle of the 'Capacity Design', the dissipative zones are adequately designed from the maximum actions deriving from the design phase. Instead, according to the second principle of the capacity design, the non-dissipative zones must remain within the elastic range. Consequently, they are designed considering the maximum actions that the yielded and strain-hardened dissipative fuses are able to transfer. These principles assure, in most cases, the prevention of both brittle crises and the development of storey mechanisms.

This strategy is traditionally applied by over-strengthening columns and connections, enforcing the development of plastic hinges at the end of beams to promote a global failure mechanism if first-storey column base sections are involved in the plastic range. In this way, the maximum global ductility of the structure is guaranteed, and undesired collapse mechanisms (*i.e.,* storey mechanisms) are consequently avoided. These mechanisms represent the worst approach through which the structure withstands a seismic event as they induce the plastic engagement of the top and base ends of the columns belonging to the same storey, whose plastic hinges are characterized by low ductility and energy dissipation capacity due to the significant axial loads sustained by vertical elements. Within this context, it is clear that the BCJs play a relevant role in the overall structural behaviour of steel MRFs.

2.1.2.1 The component method approach

The component method approach consists of modelling the monotonic moment-rotation law of connections, starting from the characterization of individual joint components in terms of stiffness and resistance [23-29]. This approach has mainly been exploited to investigate connections between double-tee section profiles, assessing the response of partial-strength and/or semi-rigid connections, often referred to as semi-continuous joints. Different joint components have been experimentally, numerically and analytically investigated. For instance, to model welded and bolted joints, many works focused on the study of the PZ [24-25], the end-plates [25] and the T-stubs [27]. After these studies, the component method was first reported in the European Norm Voluntary version of EC3 (into annexe J) [21] and, subsequently, in Eurocode 3 part 1-8 [30]. Moreover, the Eurocode 3 provides many design formulations to assess the strength and stiffness of the following components: column web panel in shear; column web panel in transverse tension; column web in transverse compression; column flange in bending; end-plate in bending; flange cleat in bending; beam flange and web in compression; beam web in tension; bolts in shear; bolts in tension; plates in bearing; welds; haunched beam. For instance, in Figure 2.9, the main components of a welded connection with double-tee profiles as beam and column are reported:

i) the column web in shear (*cws*);
ii) the column web in compression (*cwc*);
iii) the column web in tension (*cwt*);
iv) the column flange in bending (*cfb*);
v) the web and the flange of the beam in compression (*bfc*).

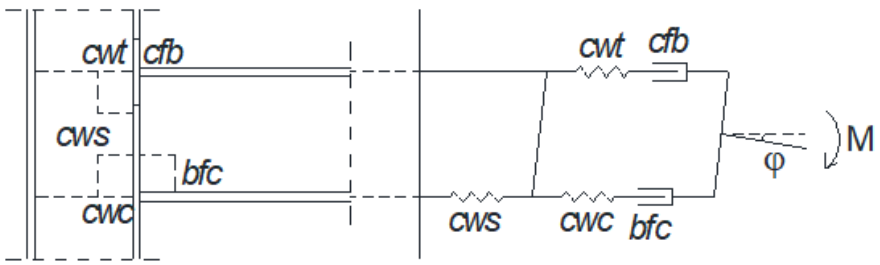

Figure 2.9. Components belonging to the connection.

In particular, the column web in shear, compression and tension represent elements that directly affect the rotational stiffness and strength. Instead, the column flange in bending and the web and the flange of the beam in compression can affect only the flexural strength of the joint. Since the component method approach requires defining a force-displacement law for each joint component, an elastic-plastic relationship is assumed for *cws*, *cwc*, *cwt*, while a rigid-plastic behaviour is assigned *cfb* and *bfc*, as illustrated in Figure 2.10:

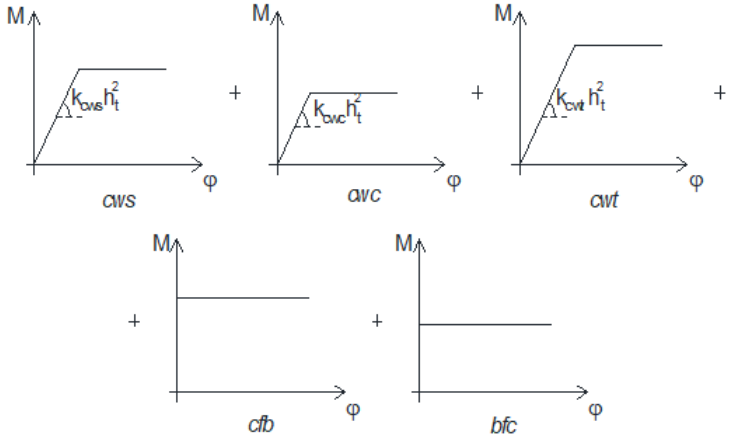

Figure 2.10. Constitutive laws of the connections.

According to the above schematization, the rotational stiffness of the connection is assessed as:

$$k_{\varphi} = E\frac{h_t^2}{\frac{1}{k_{cws}} + \frac{1}{k_{cwc}} + \frac{1}{k_{cwt}}} \tag{2.1}$$

where E is the modulus of elasticity, h_t is the distance between the flanges of the beam, while k_{cws}, k_{cwc} and k_{cwt} represent the stiffness of the components *cws*, *cwc* and *cwt*. Instead, the flexural strength of the joint is related to the weakest among the abovementioned components:

$$M_{j,Rd} = min\{F_{cws}; F_{cwc}; F_{cwt}; F_{cfb}; F_{bfc}\} \cdot h_t \tag{2.2}$$

Further and detailed formulations for the above application and more complex cases (*e.g.* bolted connections with end-plates or angle flange cleats) are provided in the Eurocode 3 Part 1-8 [30].

2.1.2.2 Full-and Partial-Strength Beam-to-column connections

The traditional design approach for the BCJ is represented by the full-strength welded or bolted joints, which have been widely adopted solutions within steel MRFs. Eurocode 8 [10] requires that the joint design resistance ($M_{j,Rd}$) should be higher than the plastic moment of the connected beam ($M_{b,Rd}$) amplified by the coefficient 1.1 to account for the effects of the material strain-hardening and the overstrength coefficient γ_{ov} to consider the random variability of the steel yield strength (*i.e.,* the recommended value γ_{ov} = 1.25):

$$M_{j,Rd} > 1.1 \cdot \gamma_{ov} \cdot M_{b,Rd} \quad (2.3)$$

For many decades, there has been deep exploitation of full-strength welded or bolted BCJs. Although this design approach should avoid damage to the non-dissipative structural elements, during the unfortunately famous earthquakes of Northridge (California, 1994) [14-15] Kobe (Japan, 1995) [16] and Tohoku (Japan, 2011) [17] many welded BCJs belonging to MRFs exhibited unexpected brittle fractures, causing irreparable damage to the MRFs Figure 2.11. For example, the connection shown in Figure 2.11 (b) exhibited the failure of the fillet welding at the beam's end. The reasons for such unsatisfactory behaviour were found in the welding techniques used at the time, which were demonstrated to be inadequate and characterized by low ductility [22] but also because the adopted design criteria did not ensure the right overstrength to the complete development of the beam's plastic rotation capacity.

Figure 2.11. Damaged welded connections after the seismic event of a) Northridge 1994 [14-15]; b) Kobe 1995 [16]; c) Tohoku 2011 [17].

To solve the issues of conventional BCJs, two strategies were proposed. The first one was based on strengthening the welding details. The second one was based on weakening the beam ends into areas located sufficiently far from the column. The weakening approach called Reduced Beam Section (RBS) or dog-bone [31-32] (Figure 2.12 (a)), allows the concentration of the damage in well-defined regions sufficiently far from the columns. to reduce the welds' stresses, thus enhancing the overall seismic performance. Such an improvement is mainly related to reducing the stress concentrations in the welds while increasing the local ductility. This connection typology has been widely studied, and its design rules are also part of the AISC provisions [33]. Recently, due to the rising interest in the cyclic behaviour of this joint, experimental, numerical and analytical activities have been carried out at the University of Salerno to investigate the response of RBS connections [34-35]. Partial-strength BCJs represent an alternative to this design philosophy. These joints can lead to a high ductility and energy dissipation capacity, provided that their geometry is designed by applying capacity design principles at the level of the single components [26-29]. The weakest joint component can be initially selected and designed to provide the required ductility and energy dissipation supply within this framework. In contrast, all the other joint components, including the beam end, must be designed with appropriate over-strength to account for the strain hardening and random material variability exhibited by the weakest joint component. This approach has been applied in the last decades in many experimental activities worldwide, showing that traditional connections (*e.g.,* extended end-plate [44-28], double split-tee [36-

40]) can assure high ductility supply when properly designed. The double-split T-stub BCJ [36-40] represents an excellent example of such a strategy (Figure 2.12 (b)). This connection typology is characterized by a couple of T-stubs to connect the beam flanges to the column. The T-stubs, if properly designed, act as seismic dampers with levels of ductility and energy dissipation capacity, which can be easily calibrated within the design phase. In such a way, according to the component method approach, the bending moment at the beam end can be ideally schematized as opposite horizontal forces, respectively stressing the T-stubs in tension and compression. Many studies have been carried out on the classic T-stub BCJ. Among these, it has been demonstrated that the free deformation of the stem can be increased by adequately designing a hole or a reduced section in the stem [39]. There are also other proposed solutions based on weakening the flange of the T-element [40-41]. For example, Latour and Rizzano [41] have proposed another connection characterized by X-shaped T-stubs. This connection typology differs from the traditional one because the flange of the T-element is properly cut thanks to an hourglass shape similar to the bending moment that arises in the plate part between the stem and the bolts, thus ensuring a uniform yielding of this part.

Besides, another widely used BCJ typology within steel MRFs is represented by the unstiffened end-plate bolted joint (Figure 2.12 (c)) or the Extended stiffened end-plate bolted (ESEPB) joints [42-48]. This type of bolted joint can guarantee satisfactory energy dissipation capacity without appreciable degradation of strength and stiffness. In Europe (EU), the current versions of the Eurocodes (*i.e.,* Eurocode 3 Part 1-8 [30] and Eurocode 8 [10]) provide neither specific requirements nor codified prequalification procedures for seismic-resistant ESEPBjoints. However, prequalification criteria for different types of bolted joints have been developed in Europe within the framework of the EQUALJOINTS (*i.e.,* European pre-QUALified steel JOINTS) research project [46-48]. Both AISC 358-16 [45] and EQUALJOINTS [46-48] provided design procedures for full-strength BCJs. This purpose is differently achieved, and the main differences concern the configuration of the connection (*i.e.* distribution of bolts and requirements on rib stiffeners), the calculation assumptions (*i.e.* capacity design rules, the position of the centre of compression, active bolt rows, yield line pattern), and some ductility criteria (*i.e.* limitations on the thickness of end-plate compared to the diameter of bolts).

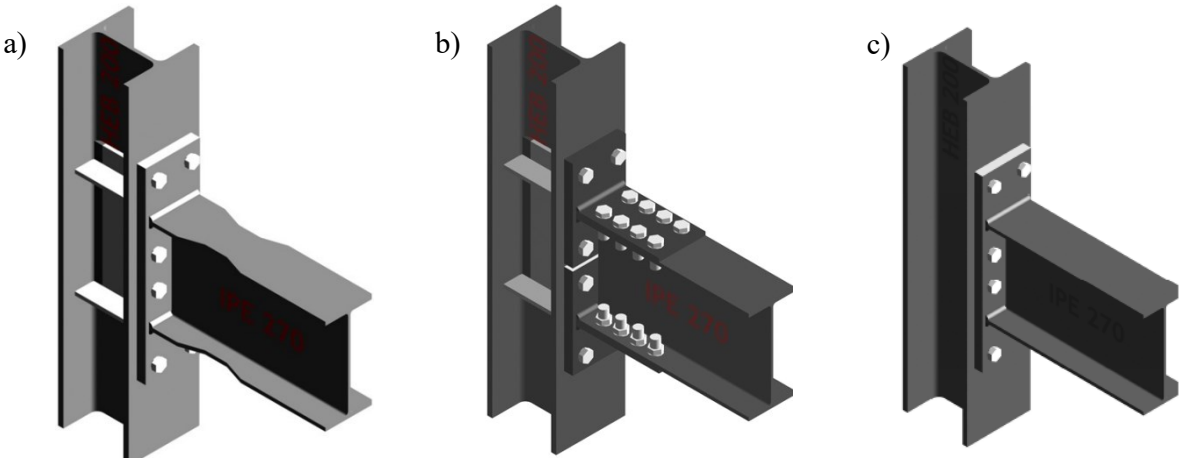

Figure 2.12. Different connection typologies for BCJs: a) Reduced-Beam Section (RBS) connection; b) Double split T-stub joint; c) Extended-end plate connection.

2.1.3 Column Base (CB) Connections

Every structure has to transfer gravity, wind, seismic actions, etc., from the vertical elements to the foundation. Typically, between the steel columns and the footing, it is necessary to insert an intermediate element to spread the stresses along a smooth loading path. The Column Base (CB) joint represents the intermediate element between the steel column and the concrete footing. Generally, a CB connection may be constituted by steel plates, stiffeners and anchor bolts employed to transfer bi-directional bending, axial forces and bi-directional shear. In some cases, only shear and axial forces may be transferred through the CB, such as in the case of braced frames.

As suggested by Grauvilardell *et al.,* 2005 [49], several Configurations of CB connections exist and are usually classified based on their interaction with the reinforced concrete foundation. They can be classified into two macro-categories:

i) Exposed CB plate joints: in which, except for the anchor bolts, the connection elements are all out from the concrete foundation [*e.g.,* 49-54];
ii) Embedded CB plate joints: in which at least part of the connection and the column are inside the concrete foundation [*e.g.,* 55-58];

However, other configurations of CB connections exist, such as concrete-encased [*e.g.,* 59] or shallowly embedded type [*e.g.,* 60]. The exposed CB plate joint (Figure 2.13) is typically realised with a steel plate welded at the column's end, bolted to the concrete foundation through high-strength or mild-steel anchors. This connection typology may be conceived to transfer bending moments, axial forces and shear or to only transfer axial forces and shear. The capacity of an exposed CB joint to transfer significant bending moments depends on the position of the anchor bolts that, when located outside the column flanges, such as into an extended end-plate joint configuration, can provide high stiffness and flexural resistance due to the high value of the lever arm. Conversely, when the anchors are placed only inside the column flanges or even at the centre of the column base, such as for a flush end-plate connection, the joint provides a behaviour intermediate between the semi-rigid and the perfectly pinned.

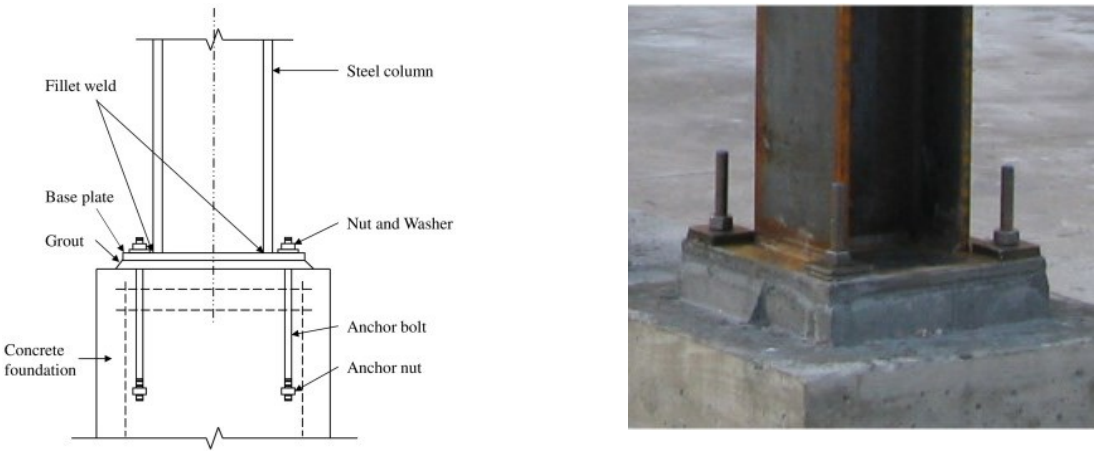

Figure 2.13. Typical Exposed Column Base joint [*e.g.,* 49-54].

Exposed base plates have been particularly popular for industrial buildings. Historically, two anchor rods providing only a limited capacity to resist bending moments have been used in many constructions. When couples of anchor rods were used, the traditional design assumption was provided to neglect the rotational stiffness of the connection, which was modelled as a pin. However, this assumption is not realistic as the bending moment capacity of the connection may be relevant both in the low and high eccentricity ranges. This wide range of responses has recently led to failures due to unexpected behaviour. Several studies (e.g., Astaneh *et al.,* 1995 [1]; Lee and Goel, 2001 [50]; Latour *et al.,* 2015 [52]) have confirmed that most CBs exhibited a semi-rigid response. Therefore, when assumed as fully fixed in the structural analysis, without a specific assessment of the rigidity, they may be able to resist the required loads only after significant deformations, which are not considered in the design phase. Not accounting for the base plate's real fixity may result in larger values of the expected storey drifts, large deformations, and, in critical cases, structural collapses [14-16].

As an alternative to the configuration with exposed base plates, columns may also be embedded in the reinforced concrete foundation (Figure 2.14). Embedded base plates have been used more in building applications than in lightweight industrial buildings. Typically, embedded base plate arrangements may provide different responses based on the embedment length. In fact, for deep embedment length, the objective is to provide the connection a full fixity resulting from the capacity of the joint to transfer to the forces by contact with concrete. In this case, the base plate's function is different because it simply helps to increase the axial resistance of the connection, while most of the bending and shear actions are transferred directly by the column (Figure 2.15).

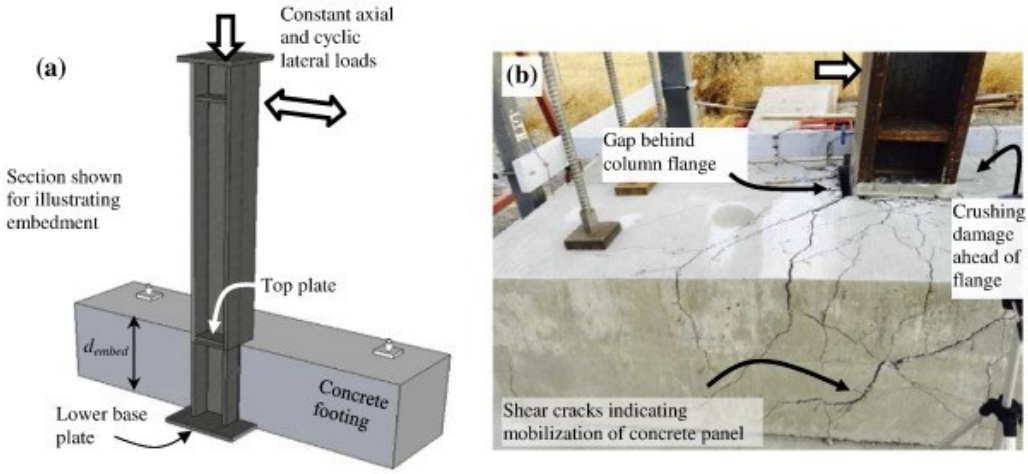

Figure 2.14. Typical Embedded Column Base joint (Grilli et al., 2017 [56]).

Besides, exposed base plates with shallowly embedded beams, welded at the bottom surface of the plate, have the objective of providing mainly an additional shear resistance to the joint, which, normally, would transfer the shear load through the anchor rods. In the intermediate cases, as the behaviour will be mixed and ranging from long embedment to shallow embedment, the behaviour will range smoothly from fully fixed and, based on the transfer by bearing with concrete, to that of a traditional exposed base plate joint (Figure 2.16). A disadvantage of the embedded CB is the higher complexity during

construction. In fact, steel profiles must be placed before concrete pouring, providing a series of issues related to the accuracy of positioning, which sometimes cannot be easily solved.

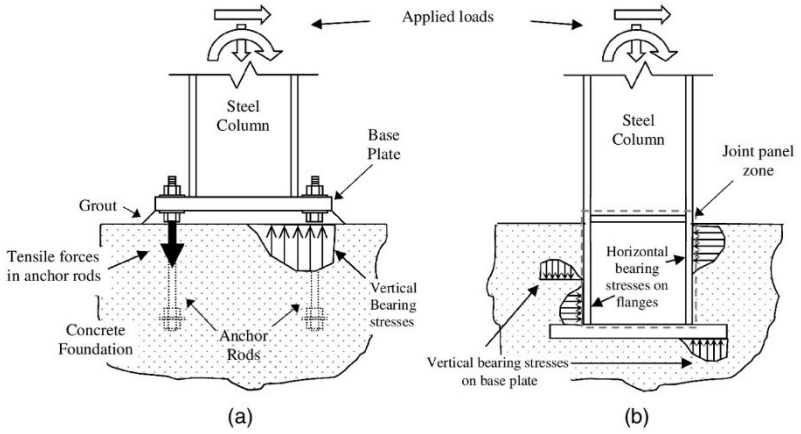

Figure 2.15. Force transfer in the embedded configurations (Torres-Rodas *et al.,* 2018 [57]).

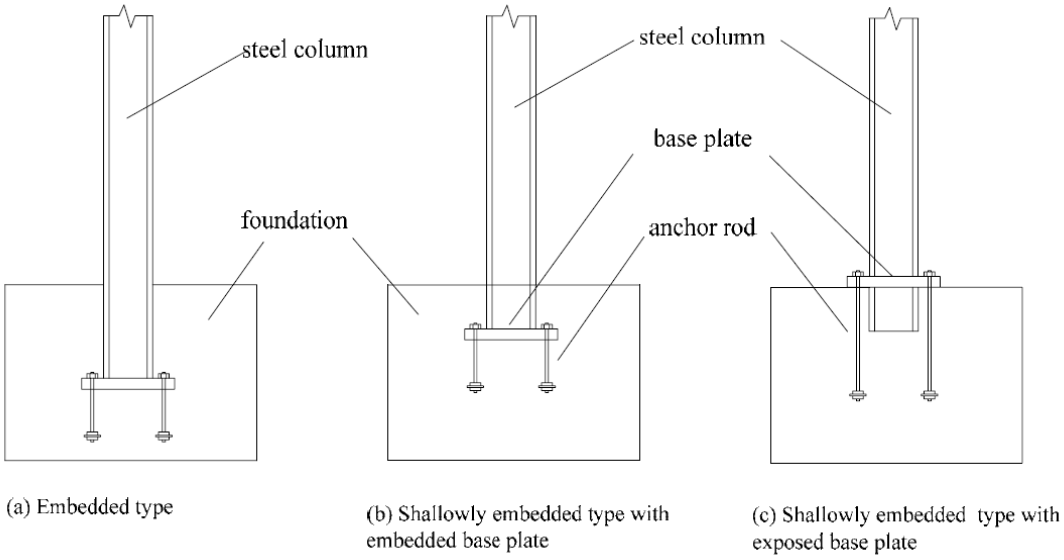

Figure 2.16. Different levels of embedment [55-58, 60]

However, independently from the CB typology, according to Grauvilardell *et al.,* 2005 [49], CBs can be divided based on a phenomenological classification according to:

i) The base plate behaviour;
ii) the failure mode of the steel elements;
iii) the failure mode of concrete;
iv) the type of frame.

Astaneh *et al.,* 1995 [1] proposed a classification according to the base plate thickness (Figure 2.17), indicating three failure modes referred to as mechanism-1, mechanism-2 or mechanism-3 in the classical

T-stub theory. CB connections having thick base plates are expected to be the strongest and most rigid of the three types summarized in this classification. However, these are typologies most likely to present a non-ductile behaviour due to fracture of anchor rods, which are often the weakest link in the design, or the development of crushing and spalling failure of the grout for large rotations (*i.e.,* larger than 0.03 rad.). Conversely, CB connections having thin base plates are characterized by flexible, ductile behaviour, in which the inelasticity is concentrated in the base plate itself. Yield lines are formed along the flanges; if the base plate is thin enough, 45º yield lines can form at the corners of the base plate. The rest of the components (*e.g.,* anchor rods and concrete foundation) remain in the elastic range.

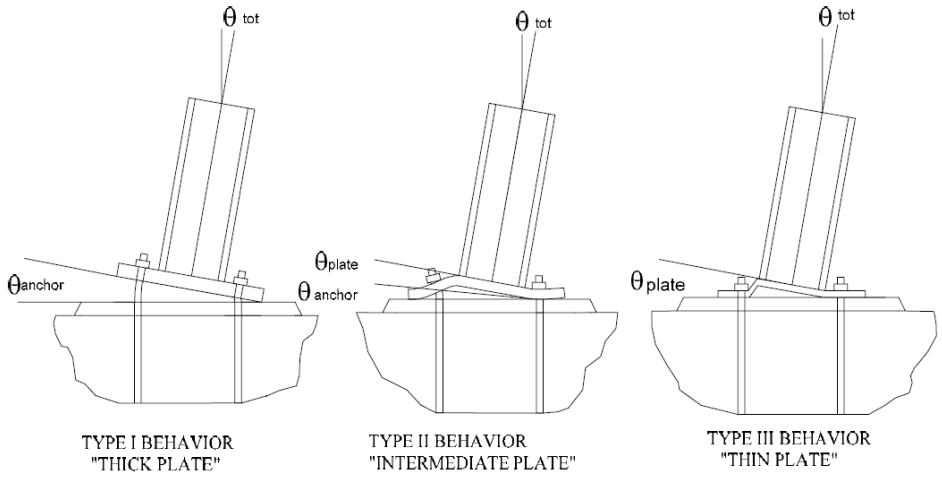

Figure 2.17. Failure modes according to Astaneh *et al.* (1995) [1].

The CB joint can also be classified according to the weak steel element. Three cases can be individuated: *1)* weak column, *2)* weak connection, *3)* intermediate behaviour. In the first case, the formation of a plastic hinge at the base of the steel column occurs, and the rest of the connection elements remain elastic or exhibit only incipient yielding. With this behaviour, the post-yield deformation reaches maximum values with high strengths and the failure, after local buckling phenomena (Figure 2.18), may also be due to the welds' premature fracture at the CB. Welds are essential in CBs with strong connections/weak columns and must be checked and realized carefully. Conversely, strong column/weak connection details are characterized by the inelastic deformation of one or more components of the CB assemblage, and potential brittle failures are more likely to occur (*e.g.,* concrete crushing and anchor rod fracture). The intermediate behaviour consists of a balanced column and base plate resistance design, leading to simultaneous yielding. In this case, not only one component is subjected to extreme deformations, but all the elements of the base plate undergo inelastic behaviour (Figure 2.19).

According to Stamatopoulos and Ermopoulos, 1997 [53] (Figure 2.20), the CB behaviour can be divided into three failure modes according to the level of bearing concrete stresses that develop under the base plate. For low axial loads (pattern 1), the bearing capacity of the concrete is never reached, and the collapse occurs either when anchor rods yield or when the plastic mechanism forms in the base plate. In the case of medium axial loads (pattern 2), the behaviour is characterized by the anchor rod reaching yielding and the concrete attaining its bearing strength. The failure mode for high axial loads (pattern

3) is identified because only the concrete bearing capacity is reached at collapse. In this last case, failure occurs mainly in the low eccentricity range with no tension in the anchor bolts.

Figure 2.18. Failure of the column due to the onset of local buckling phenomena.

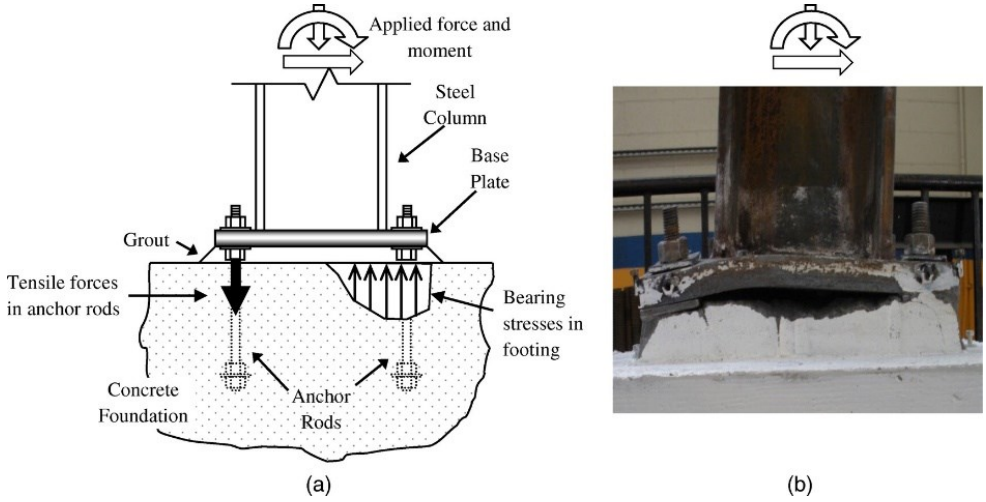

Figure 2.19. Failure of the base plate due to the formation of a plastic hinge in the plate and concrete spalling (Torres-Rodas *et al.,* 2016 [54]).

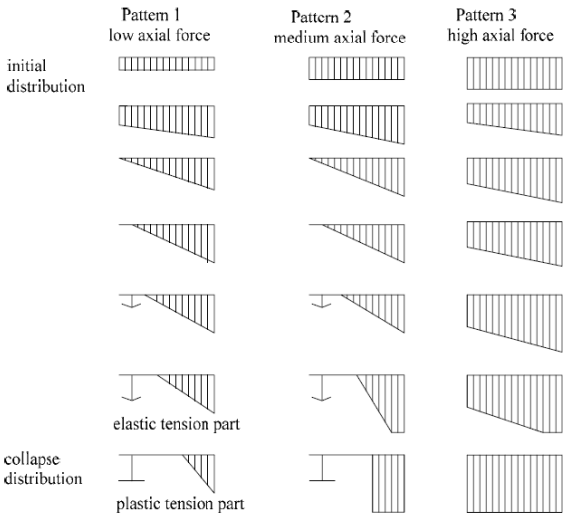

Figure 2.20. Bearing stress distributions in concrete (Stamatopoulos and Ermopoulos, 1997 [53]).

However, the overall behaviour of the exposed base plates and the nature of the forces acting on the CB will vary depending on the type of structure. When CBs are inserted in MRFs, they will be subjected to the action of moments, axial forces, and shear. When gravity loads at the sides of the frames are low and the lateral forces are important, this load combination may be the most demanding for this CB typology.

2.1.3.1 The component method approach

Exposed CB joints are ruled under Eurocode 3 part 1-8 [30], where the component method is applied to predict their flexural response. In this code, CB joints are characterized in terms of stiffness and resistance, but only the case of CBs under major axis bending with a single row of anchor bolts in tension is explicitly addressed. For all the other cases, reference to literature models has to be made, or extensions of the component method could be accepted for the case of more bolt lines. The models for CB joints were developed during the '90s and are now being further developed for improved implementation in the structural Eurocodes. Besides, the design of embedded CBs indications can be found in AISC or ACI codes [*e.g.,* 11-12].

The prediction of stiffness and resistance of CB plate joints can be carried out through the component method [61]. Within this framework, the elementary components are in part similar to those already introduced for bolted joints but, in some other part, have to be added to consider the response of concrete in bearing, which, in these connections, represents one of the main sources of resistance, especially in the low eccentricity range. The approach to model the connection through the component method is similar to that used for the BCJs, and, therefore, the joint components are first identified, then modelled individually and finally assembled into a mechanical model representative of the connection's physical response. In the case of extended end-plate joints, some components contribute in terms of both resistance and stiffness (elastic-plastic components) and others only in terms of resistance (rigid-plastic components).

The active components in the case of an exposed CB joint are:

i) **The column flange under local compression (*cfc*);**
ii) **The base plate in bending (*epb*);**
iii) **The column web in tension (*cwt*);**
iv) The anchor bolts in tension (*at*);
v) The concrete in compression, including grout (*cc*);

where three of the active components (*i.e.,* highlighted in bold) have already been fully or partially characterized with reference to welded and bolted BCJs in Section 2.1.2. Conversely, the remaining two are those typical of CB joints, and they are mainly introduced to consider the response of the concrete in compression and bedding grout (*cc*) and the anchor bolts in tension (at), whose behaviour is similar to bolts. Still, there are some specific aspects which need to be addressed. Similarly, the base plate's behaviour in bending needs to be specified to account for some issues arising due to the higher deformability of the anchor bolts. All the listed components govern the joint's strength and stiffness

except for the column flange in compression (*cfc*), which, at most, can limit the connection resistance. For the response of the base plate joint, the geometry of the plates and the position of the anchors play a primary role because they affect more than the other components the stiffness and resistance of the connection. The evaluation of the flexural strength and the rotational stiffness of the joint requires the definition of the strength and stiffness of each component and the lever arm. In the case of base-plate joints with a single row of anchors in tension, according to Eurocode 3 part 1-8 [30], the lever arm depends on the sign of the axial force (*i.e.,* compression/tension) and the eccentricity. Eurocode 3 part 1-8 [30] model represents the CB joint through four springs (Figure 2.21). Two hook springs (*i.e.,* only active in tension), which are assumed aligned with the anchors, model the anchor bolts in tension and the base plate in bending. Two gap springs (*i.e.,* only active in compression), placed below the column flanges, model the behaviour of the concrete in compression (*cc*), including grout. Therefore, for low levels of eccentricity and relatively large compression axial forces, the mechanical model includes only the compression springs because the combination of bending and axial forces is balanced only through compression forces. Conversely, for low eccentricity levels and relatively high tensile axial forces, the actions are only carried by the tensile springs. Lastly, in the high eccentricity range, namely, when one side of the connection is in compression, and the other side is in tension (*i.e.,* high eccentricity), the lever arm is given by the distance between the compression column flange and the farthest line of anchors ($z = z_c + z_t$).

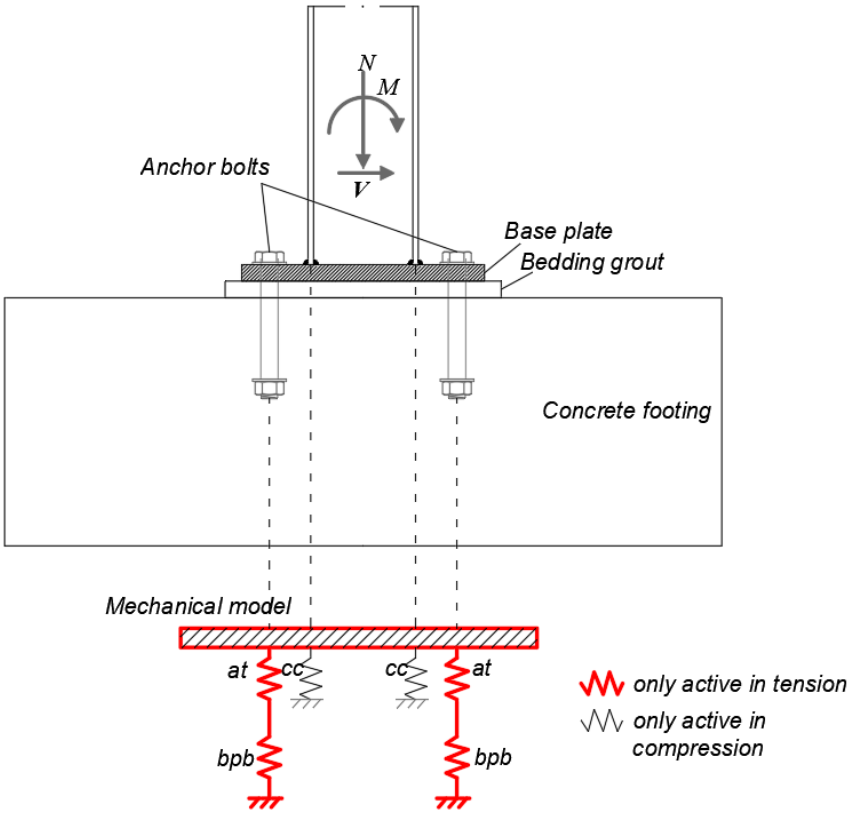

Figure 2.21. Active components of a bolted end-plate CB joint and mechanical model according to to Eurocode 3 part 1-8 [30].

The modelling of base plate joints is more complex than BCJs because both the equipment needed to perform experimental tests and the difficulties related to interpreting the experimental response of this typology is influenced by a set of additional parameters. This higher complication is mainly due to a set of further variables with respect to BCJs, which assess the response more complex:

i) the influence of the axial force;
ii) the dependence of the response on the load path (*e.g.,* constant axial load or constant eccentricity);
iii) the influence of long bolts and the typological variation of anchors and embedment technologies;
iv) the distribution of prying forces underneath the plate due to the complex plate/concrete interaction;
v) the influence of the resistance of the bedding grout;
vi) the random variation of the concrete mechanical properties;
vii) the influence of the shear force on the behaviour of the anchors.

Since the base plate joint's response is influenced by the axial force sign and the eccentricity that changes the configuration of active springs, different cases may be individuated in practice. As aforementioned, in the case of symmetric CBs, basically, three cases can be individuated:

i) Axial force of compression, low eccentricity;
ii) Axial force of tension, low eccentricity;
iii) Combined axial force and bending moment, high eccentricity.

In the first case, the active springs only represent the compression elements, namely the concrete in compression, including grout and the column flange in compression (rigid-plastic component). In the second case, the active springs only represent the behaviour of the tension elements, namely the base plated in bending and anchor bolts in tension. In the third case, the compression springs are active on one side of the connection, and the tension springs are active on the other. These three cases must be treated separately to characterise the CB's stiffness and resistance. The connection response can be characterized by writing translational and rotational equilibria and assessing the settlement or elongation of the joint components to calculate the base plate joint rotation for a unitary value of the bending moment. As it will be seen, the base plate joint's properties depend upon the eccentricity's value. Therefore, from the practical point of view, the value of the eccentricity and the sign of the axial force must be fixed to define the connection stiffness and strength. It is worth noting that this aspect provides a significant complication because of the correlation between the actions deriving from the structural analysis and the stiffness of the connections.

To evaluate the accuracy of the component approach for predicting the rotational behaviour of CB connections, Latour *et al.,* 2013 [62-63] and Latour *et al.,* 2014 [64] developed a mechanical model to predict the rotational behaviour of base plate connections under cyclic loads. The accuracy of the component method in predicting the rotational stiffness, flexural resistance and the overall moment–rotation curve of CB connections was validated against experimental tests. A refinement of the approach

for predicting the connection rotational stiffness was suggested, considering the definition of an effective width to be explicitly applied for stiffness calculation.

2.1.3.2 Full-and Partial-Strength Column Base connection

According to modern seismic design strategies, like those implemented within current international building codes [*e.g.,* 10], CBs can be conventionally designed as full- or partial-strength. However, most typically, the seismic design of steel MRFs is carried out by adopting full-strength CB joints. Both full- or partial-strength approaches are characterised by significant drawbacks. The first one usually leads to the development of plastic hinges in the bottom end of the first-storey columns, thus causing significant structural damage and residual drifts after a severe seismic event. Conventional full-strength steel CBs may suffer from residual rotations, large plastic deformations [*e.g.,* 62, 54], and axial shortening phenomena [*e.g.,* 65-68], which impair the structure returning to the initial condition after severe earthquakes. In fact, post-earthquake inspections after the 1994 Northridge, 1995 Kobe, and 2011 Tohoku earthquakes [*e.g.,* 14-19] revealed unsatisfactory performances, confirming the susceptibility of CBs to difficult-to-repair damage and residual deformations due to several effects, such as anchor rods elongation, base plate yielding, weld fracture, and concrete crushing. Figure 2.22 illustrates some CB connections' most typical damaged configurations after the Tohoku earthquake in 2011 [17]. Most investigated buildings were low- to mid-rise, where exposed CB connections were more commonly used than embedded or encased CB connections. The damage to exposed base plates pointed out that, unless the anchor bolts fractured, residual storey drift and structural damage to the building was minimal. On the other hand, evidence suggested that the anchor bolt's fracture led to the column's dislocation and severe residual storey drift.

Figure 2.22. Damaged welded connections after Tohoku, 2011 [17] for a) elongation of anchor bolts; b) fracture of anchor bolts; c) spalling of concrete.

In the second approach, partial-strength CBs are designed to dissipate energy through inelastic deformations in their main components (*i.e.,* base plate anchor rods) [*e.g.,* 10]. The design of partial-strength joints allows better control of the dimensions of the CBs, but it requires the knowledge of its complex hysteretic behaviour under cyclic loading, which is difficult to predict and is affected by strength and stiffness degradation as demonstrated in Rodas *et al.,* 2016 [54] and Latour and Rizzano, 2013 [64]. Hence, this strategy is rarely followed.

From the design point of view, the design assumptions for the CBs may significantly affect the seismic response of the structure. CBs can be designed as fully fixed, pinned, and other intermediate stiffness conditions (*i.e.,* rigid, flexible, semi-rigid). However, the stiffness and cyclic response of conventional CBs are difficult to predict, as they are strongly affected by the base plate flexibility (Figure 2.23 [69]) and the magnitude of the axial force [*e.g.,* 63]. Some studies in this direction demonstrated that the assumptions made on the CBs' flexibility influence internal force distribution, deformations, and seismic reliability of steel MRFs. Therefore, assumptions on the CBs' stiffness might underestimate or overestimate the height-wise distribution of steel MRFs' drift demands and the internal force distribution, thus leading to uneconomical or unconservative designs [*e.g.,* 69-70]. Zareian and Kanvinde, 2013 [69] designed and analysed the seismic responses of four categories of MRFs (*i.e.,* 2-, 4-, 8- and 12-storey) through static pushover simulations and sophisticated nonlinear response-history simulations, including collapse simulations. A range of base fixities was investigated for each frame, including realistic values calculated from the designed connections. The base stiffness was estimated based on the response modes illustrated in Figure 2.23, schematically showing the various contributions to connection flexibility. Results demonstrated that a reduction in base fixity alters the force distribution and the plastic mechanism, significantly reducing ductility capacity, strength, and collapse resilience while increasing member forces.

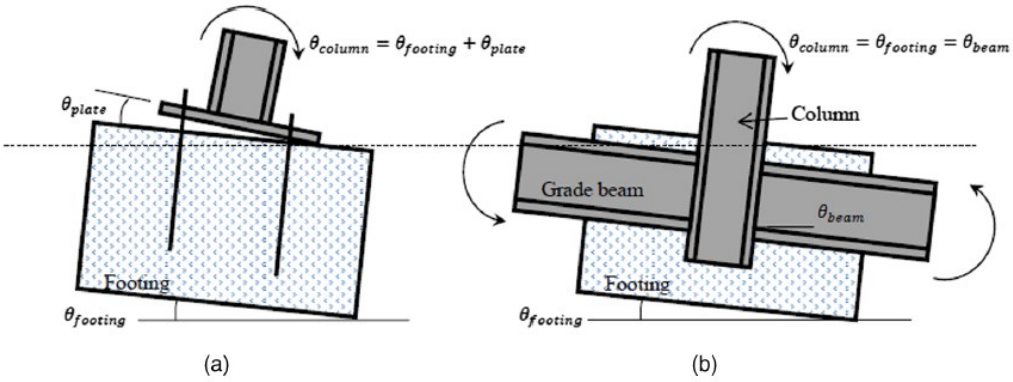

Figure 2.23. (a) Exposed base plate connection in low-rise buildings and (b) embedded-type connection with grade beams in mid- and high-rise buildings, indicating rotation components (from Zareian and Kanvinde [69]).

2.2 Friction Connections

2.2.1 Generality

Friction connections are partial-strength joints equipped with friction dampers that are able to provide dissipation of the seismic input energy by means of relative sliding between two surfaces in opposite directions [*e.g.,* 71-86]. These connections can provide high local ductility and energy dissipation capacity, provided that the damper stroke is selected and the damper components are designed by applying capacity design principles at the global and local levels. Based on Coulomb's Law of friction, the slippage force between surfaces directly depends on two parameters, as follows:

$$F = \mu \cdot N \tag{2.4}$$

where μ is the friction coefficient of the contacting materials, and N is the normal force exerted by each surface on the other. The friction coefficient depends on different factors, such as adhesion and ploughing in friction surfaces, caused by asperities. The hardness properties are also important since when one of the surfaces is much stronger than the other, the softer one suffers 'scratches and cuts', enhancing referred phenomena and shear stresses (Latour *et al.,* 2014 [78]).

The Friction Devices (FDs) currently proposed for BCJs can be divided into two categories:

i) dampers based on Symmetric Friction Connections (SFC);
ii) dampers based on Asymmetric Friction Connections (AFC).

The SFC is typically constituted by two external plates bolted with regular holes to an internal plate with long slotted holes in the direction of the applied force. Moreover, friction pads are between the external and internal plates (Figure 2.24 (a)). The friction pads can be constituted by a plate of a selected friction material or by properly coated steel plates. The friction material needs to be accurately selected to provide adequate friction coefficient values, aiming at assuring stable hysteresis loops. The normal washers are usually substituted by means of Belleville washers, *i.e.* disk springs, to reduce the bolts' preloading losses. The theoretical force-displacement behaviour of a SFC corresponds to the ideal rigid-perfectly plastic model (Figure 2.24 (b)) where the plateau is actually due to the slip resistance of the connection, which can be calculated as:

$$N_{\text{slip}} = n_b n_s \mu N_b \tag{2.5}$$

where n_b is the number of bolts, n_s is the number of contact surfaces, μ is the friction coefficient and N_b is the bolt preloading.

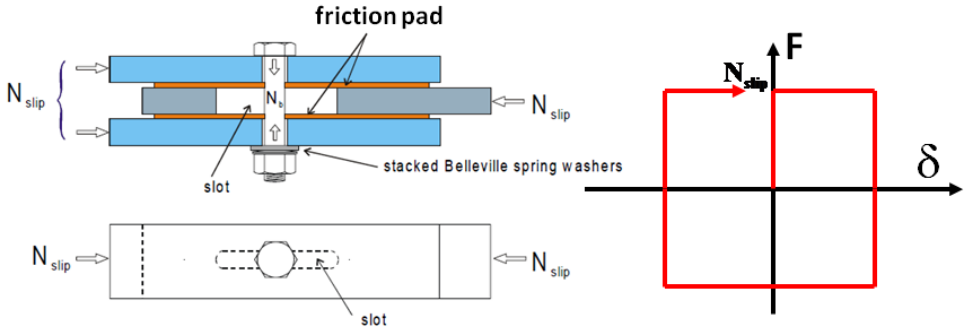

Figure 2.24. SFC concept and theoretical force-displacement behaviour.

The Asymmetric Friction Connection (AFC) (Figure 2.25 (a)) is constituted by two external plates that are bolted with regular holes to an internal plate with long slotted holes in the direction of the applied force, but the force is transmitted to the device by only one external plate. The second external plate,

the so-called 'cap plate', is not subjected to external forces. Moreover, two shims or friction pads are located between the external plates and the internal plate.

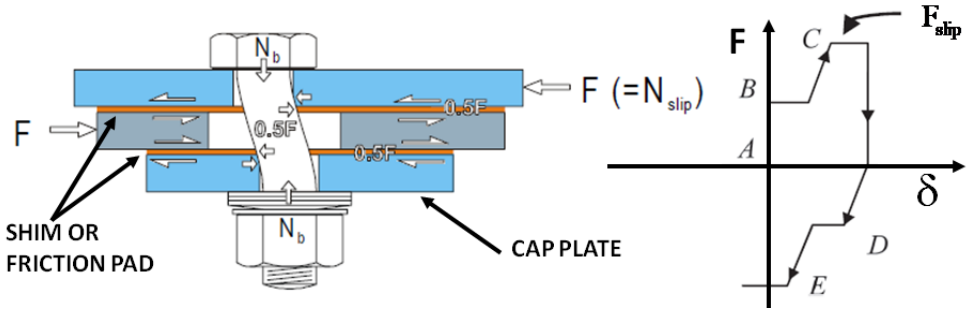

Figure 2.25. AFC concept and theoretical force-displacement behaviour.

The AFC has two sliding surfaces: the interface between the upper shim and the external plate transmitting the applied force and the interface between the lower shim and the internal plate. The idealised force-displacement behaviour of AFCs is characterised by two slip resistance levels (Figure 2.25 (b)). It is demonstrated that the slip resistance due to a single bolt is evaluated as:

$$F_{\text{slip}} = 2\mu N \tag{2.6}$$

It is useful to note that the main disadvantage of AFCs compared to SFCs is due to M-N-V interaction in the bolt shank, which, given the coefficient of friction and the bolt diameter, leads to a reduction of the force transmitted by friction. In fact, the value of N corresponding to the bolt-yielding condition is less than N_b so that AFCs are able to transmit a lower force compared to SFCs.

2.2.2 Friction Beam-to-column Connections

Connections equipped with FDs have been increasingly proposed in earthquake-resisting systems since they represent effective solutions that can improve steel MRFs' performance in dissipating the seismic input energy, improving large dissipation capacity and limiting damage under severe conditions. Several types of FDs have been developed to improve the seismic response of structures. The type of friction mechanism, which can be either asymmetric or symmetric, influences the non-linear response of these connections. Grigorian *et al.,* 1993 [71] pioneered the first FDs to be applied within BCJ for steel MRFs. Successively, many theoretical and experimental works, as well as practical applications, were carried out. The research activity on this innovative connection typology received a strong impact in New Zealand [72-75], where the AFC concept has been applied within BCJs in the Sliding Hinge Joints 'SHJ', proposed by the research group of the University of Auckland [72-74] and the first applications to real buildings have been also made in the '*Te Puni Village Buildings*' [75] (Figure 2.26).

The SHJ (Figure 2.27) is an AFC BCJ representing a particular type of supplemental energy dissipation system designed to prevent column/beam yielding. In this design approach, the top flange is connected to the column flange using a cover plate welded to the column and bolted to the beam. The end of the

cover plate, welded to the column, fixes the Centre Of Rotation (COR) location. The location of the COR minimizes slab damage. The top web bolts carry the shear force in the beam. Horizontally slotted holes are designed in the bottom flange plate and the bottom holes of the column web plate to accommodate the expected rotation demands under severe seismic events. Below the bottom flange plate, the bottom flange cap plate is located. This is a floating plate, as it has no physical connection to the rest of the joint except through the bolts. A web cap plate is similarly placed on the outside of the web plate. On all surfaces where sliding may occur, shims are placed. These shims may be manufactured of steel, brass or other materials. These have standard-sized holes, such that sliding is expected to occur on the side of the shim in contact with the bottom flange plate or web plate.

Figure 2.26. SHJ adopted in new buildings in New Zealand (*Te Puni Village Buildings*) [72-75]

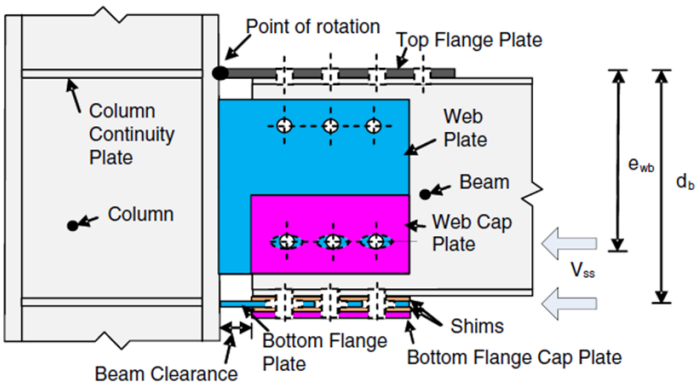

Figure 2.27. SHJ with AFC BCJ [36, 43].

Another significant example of such connections is represented by the 'FREE from DAMage' (FREEDAM) joint, developed within the framework of the European RFCS Research Project FREEDAM [76] and further progressed in the RFCS Research Project FREEDAM+ [77]. In this context, a comprehensive experimental analysis of different configurations of BCJs equipped with symmetric FDs has been carried out at the University of Salerno, aiming to validate the design procedure and assess the proposed system in terms of energy dissipation and prevention of connection damage. Two configurations have been designed, namely the Horizontal Friction Configuration (HFC), where the haunch is parallel to the beam flange, and the Vertical Friction Configuration (VFC), where the haunch is orthogonal to the beam's flange and parallel to the beam's web (Figure 2.28 and Figure 2.29

[79]). The connection is conceived to allow the use of a friction damper completely prefabricated and assembled on the shop to assure the maximum control of the tightening of the bolts and, consequently, of the bolt preloading level governing the slip resistance of the friction damper. Therefore, the prefabricated and pre-assembled friction damper is successively bolted on-site to the column and beam flange. In addition, the prefabricated friction damper increases the lever arm, thus increasing the slippage bending moment of the connection.

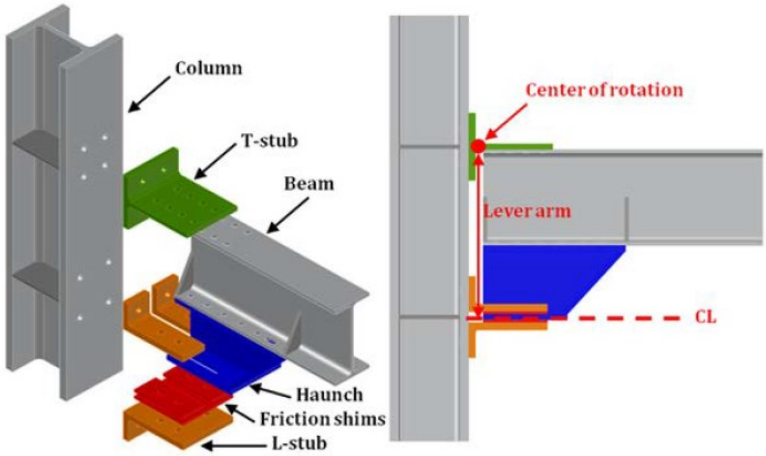

Figure 2.28. FREEDAM Configuration with damper plane parallel to the beam flange (HFC Configuration) [79].

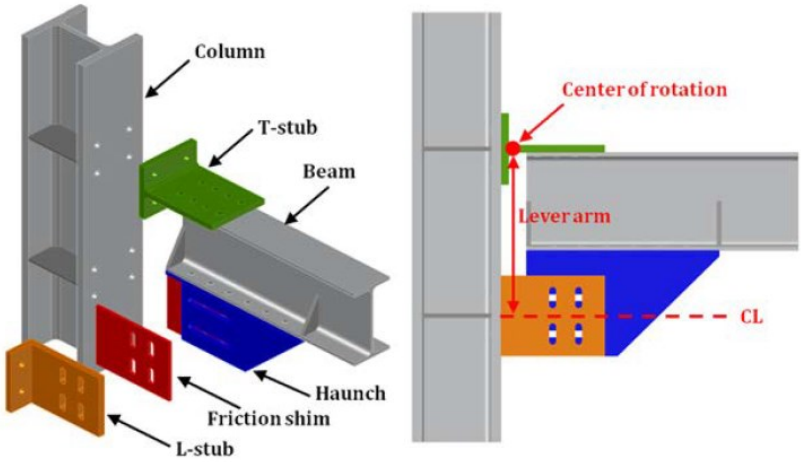

Figure 2.29. FREEDAM Configuration with damper plane parallel to the beam web (VFC Configuration) [79].

In both configurations, the FD employs an additional haunch bolted at the beam's bottom flange, pre-stressed with pre-loadable high-strength bolts. The joint resistance is controlled by properly regulating the tightening torque of pre-loadable high-strength bolts while properly designed slotted holes adjust the ductility. Beyond that, the main features of these connections are represented by the possibility of uncoupling the stiffness of the connection from its resistance and the negligible post-elastic strain-

hardening. The main advantage of this practice is that, in case of rare seismic events, the connections exhibit wide and stable hysteretic cycles, yet concentrating damage in FDs, which can be easily replaced with low additional cost.

During the FREEDAM European project [76], many experimental tests were carried out to choose and characterise the best friction material constituting the dampers (Cavallaro *et al.,* 2017 [80]; Cavallaro *et al.,* 2018 [81] and Latour *et al.,* 2018 [82]). The experimental program consisted of specimens with eight different materials (*i.e.,* from M1 to M8) to define the static and dynamic friction coefficients (Figure 2.30). Many parameters were monitored during the tests. These data allowed the definition of an 'effective' and an 'actual' value of the friction coefficient. The effective value is calculated as the ratio between the slippage force and the sum of the nominal values of the pre-loading forces. Conversely, the actual value was determined as the ratio between the slippage force and the sum of the values of the bolts' forces directly read from the load cells during the test. The present work's aim does not consist of discussing all these results. For this reason, only the main outcomes are reported.

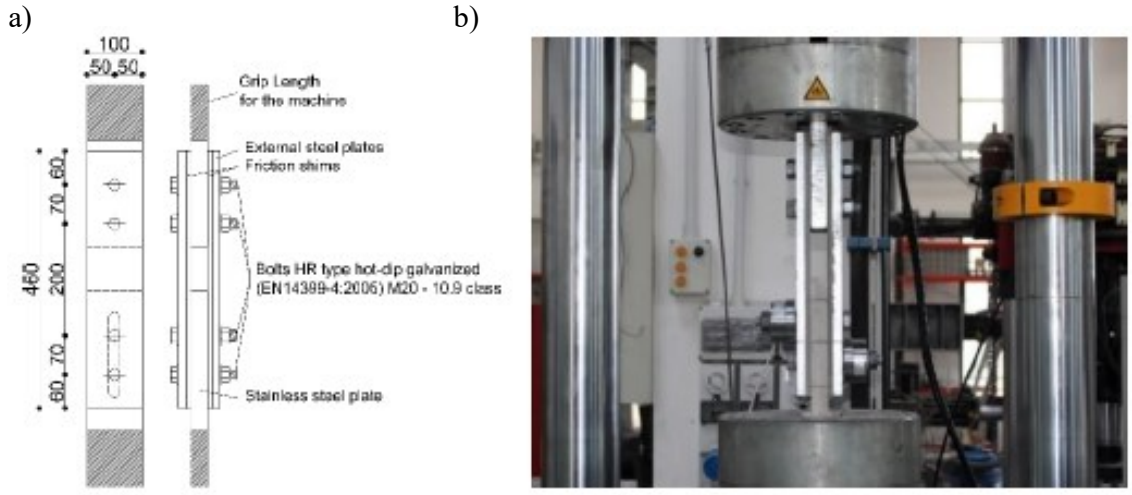

Figure 2.30. Characterisation of the friction material: a) Typical layout of a specimen; b) Set-up [80-82].

Considering the materials M1, M4 and M8, it was observed that a force-slippage behaviour characterised the tests with high initial stiffness until the achievement of the static friction coefficient, which was higher than the dynamic friction coefficient obtained in the first stabilized cycle. In addition, high energy dissipation and rectangular hysteresis loops were observed (Figure 2.31 (a)). The initial value of the friction coefficient for material M1 was between 0.67 and 0.75, for material M4 from 0.71 to 0.94, and for material M6 from 0.62 to 0.65. A clear correlation between the friction coefficient and the bolts' force was not observed. Instead, it was noticed that the reduction of the preloading force resulted in a lower loss of the bolt's preload and lower energy degradation. The conclusion was that the stick and slip phenomenon and the minimum requirements for effective damping degradation suggested limiting the preload to 60% of the proof load reported by Eurocode 3 part 1-8 [30] (Figure 2.31 (b)). According to the abovementioned considerations, the material M4 was chosen as the best solution for the FREEDAM BCJ.

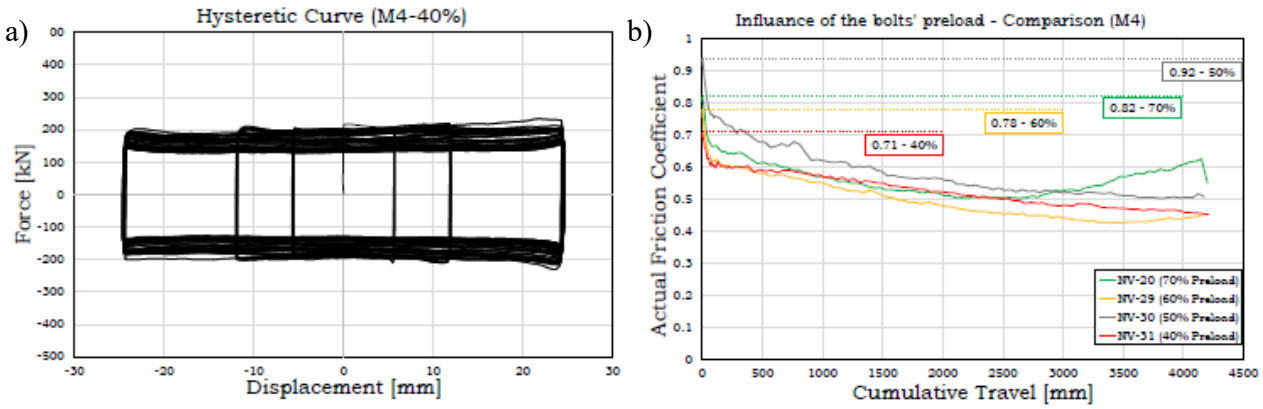

Figure 2.31. Characterisation of the friction material: a) Force-displacement hysteretic response (M4); b) Influence of the bolts' preload over the actual friction coefficient [80-82].

Several FREEDAM BCJs have been tested in the experimental campaign, considering different element sizes and different friction dampers configurations. The tests have been executed for each damper using different configurations of disc springs or simple flat washers for the bolts' assemblies [83]. For example, the testing of a BCJ equipped with the friction damper in the HFC is shown in Figure 2.32. The profiles were IPE 270 for the beam and HE 220M for the column. The cyclic behaviour is presented in terms of bending moment, evaluated at the column flange, *vs.* connection rotation. The shape of the hysteresis loops is due to the bending of the stem of the fixed T-stub and to the bending of the angles due to the connection rotation, which leads to a pressure distribution on the friction pads (*i.e.,* cockpit effect) different from the characterisation of the FDs alone. Besides, some minor yielding is limited to the T-stub stem and the angles' stems for the cockpit effect.

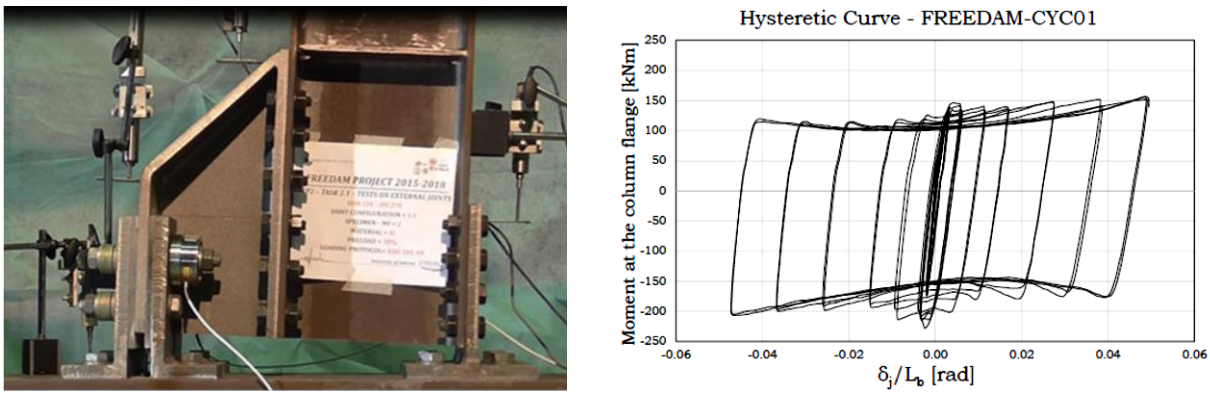

Figure 2.32. Testing of a FREEDAM BCJ equipped with the friction damper in the HFC [79, 83].

The BCJ equipped with the friction damper in the VFC has been conceived to avoid the cockpit effect and, as a consequence, to improve the shape of the hysteresis loops (Figure 2.33). The shape of the hysteresis loops is very close to the ideal rectangular shape, with excellent stability and no stiffness or strength degradation. In addition, only minor degradation of the slip resistance is due to the wearing of the contact surfaces of the friction pads. In addition, minor yielding is limited to the stem of the fixed T-stub, subjected to the bending due to the connection rotation, used to locate the COR. The COR is

located at the top flange supporting the concrete slab. Such a choice aims to prevent concrete slab damage in building structures.

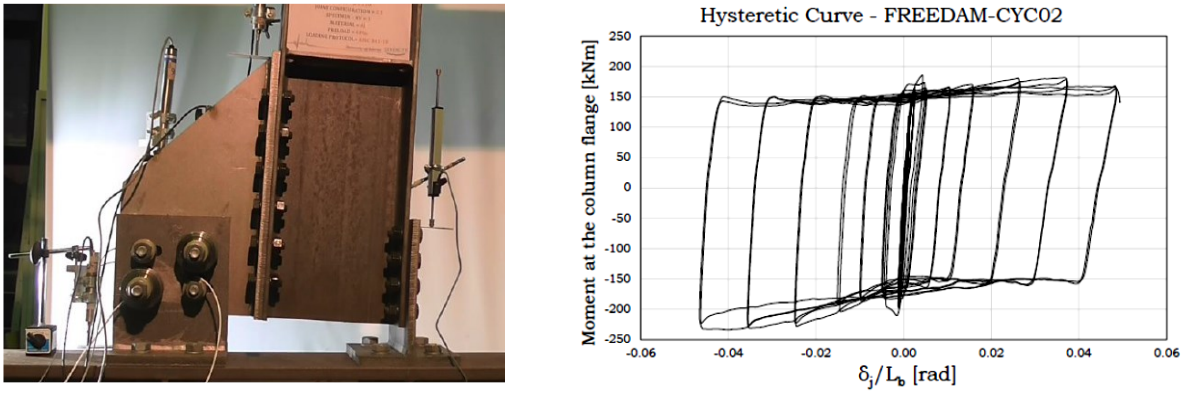

Figure 2.33. Testing of a FREEDAM BCJ equipped with the friction damper in the VFC [79, 83].

In addition, it is also worth mentioning that the FREEDAM BCJ has been extensively investigated by further experimental works, which have addressed significant aspects, such as the response of the FDs under different loading rates in Santos *et al.,* 2020 [84] and the behaviour of the pre-loadable bolts at installation and over their service-life by analysing the short- and long- term loss of preloading in D'Antimo *et al.,* 2020 [85]. Besides, a wide range of numerical and FE analyses have been conducted by Tartaglia *et al.,* 2021 [86].

2.2.3 Friction Column Base (CB) Connections

Steel MRFs with damage-free BCJs have been largely studied during the past decades. However, more recently, innovative low-damage or damage-free systems have been proposed in CB connections to overcome the shortcomings of conventional CBs. The idea of developing the dissipation of the input seismic energy within CBs comes from the observation of the effects of past strong earthquake events (*e.g.,* Northridge (1994) [15], Kobe (1995) [16] and Tohuku (2011) [17]) where severe damage involving plates and anchor bolts was observed.

Among the first attempts to develop minimal-damage CBs, Kelly and Tsztoo, 1977 [87] proposed and experimentally investigated a partial isolation system associated with an energy-absorbing device that could be easily replaced after an earthquake. This study demonstrated the advantages of damage-free structural systems and promoted many successive studies in this direction. Alternatively, based on the concept originally pioneered by Grigorian *et al.,* 1993 [71], other authors further extended this idea to CBs. MacRae *et al.,* 2009 [88] and Borzouie *et al.,* 2015 [89] developed two different configurations of column base where the moment resistance and the energy dissipation were provided by friction resistance activated by the relative movement of the column flanges with respect to foundation flange plates with slotted holes.

Based on the SHJ concept, originally developed for steel BCJs [72], MacRae *et al.,* 2009 [88] proposed two typologies of Double Friction (DF) low-damage CB connections (Figure 2.34) where the prevention

of the column's yielding due to the introduction of the FDs, is identified as an effective solution to mitigate the axial shortening. The first configuration is illustrated in Figure 2.34 (a), where the axial and the shear forces are transferred directly from the column to the pin at the centre of the column to the foundation. Slotted holes in the foundation flange plate allow the achievement of large deformations. A floating plate on the outside of the foundation flange plate is connected only by bolts to the column flange through the foundation flange plate slotted holes. As the column flange moves relative to the foundation flange plate, it also drags the floating plate, creating friction on two surfaces on each flange. The second configuration is illustrated in Figure 2.34 (b), and it represents an alternative DF concept, where the column sits on top of the foundation without a direct connection, except through the bolts to the foundation flange plates and web plate. The flange plates are detailed as the first solution. The column axial compression force goes directly from the column into the foundation. Conversely, the shear force is carried by the web bolts. This detail is more feasible than the first one, but one side of the column has to move up to allow flexural deformation. This changes the height of the centre of the column. In addition, after a severe earthquake, the column may not have returned to its initial position, so the bolts may need to be loosened and re-tightened. These CB configurations allowed superior behaviour under loading in the column strong-axis direction. At the same time, damage and stiffness degradation were observed under loading of the column in the weak-axis direction. In addition, the long-term durability of the sliding surfaces for different environments could significantly affect the energy dissipation capacity of the CB.

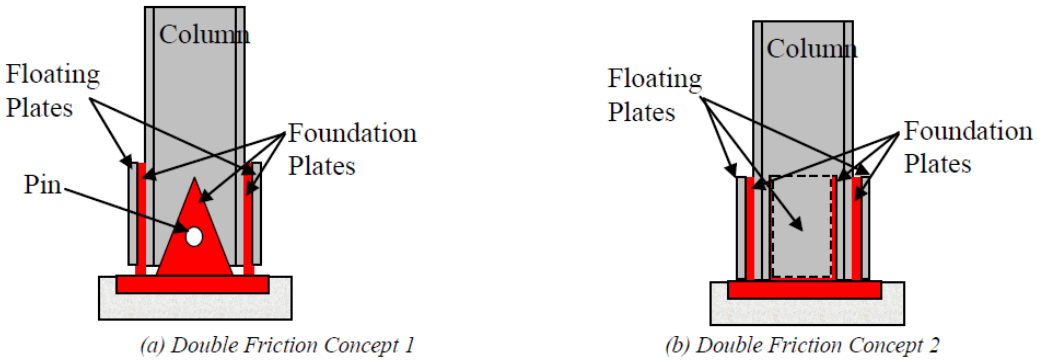

Figure 2.34. DF Low-Damage CB connections (MacRae *et al.,* 2009 [88]).

Borzouie *et al.,* 2016 [89] implemented several experimental works on different low-damage steel connections to prove the efficiency of seismic energy dissipation through CB solutions (Figure 2.35). The work assesses a series of low-damage connections, and the traditional exposed CB connections are reviewed in terms of low-damage concept, low cost, and feasibility. Two designs are remarkable: the Weak-axis aligned Asymmetric Friction Connection (WAFC) ((Figure 2.35 (a)), where friction surfaces are parallel to the web, and the Strong-axis aligned Asymmetric Friction Connection (SAFC) ((Figure 2.35 (b)), where the friction surfaces are parallel to the flanges. Both the CB connections experience rocking, and energy is dissipated through the relative sliding of surfaces. Results showed that the base plate connections with yielding angles and AFC are suitable for replaceability, permanent deformation, cost and low damage to the column. However, although an efficient behaviour can be seen in the

column's strong axis direction, damage and stiffness degradation were observed under loading in the column's weak axis direction.

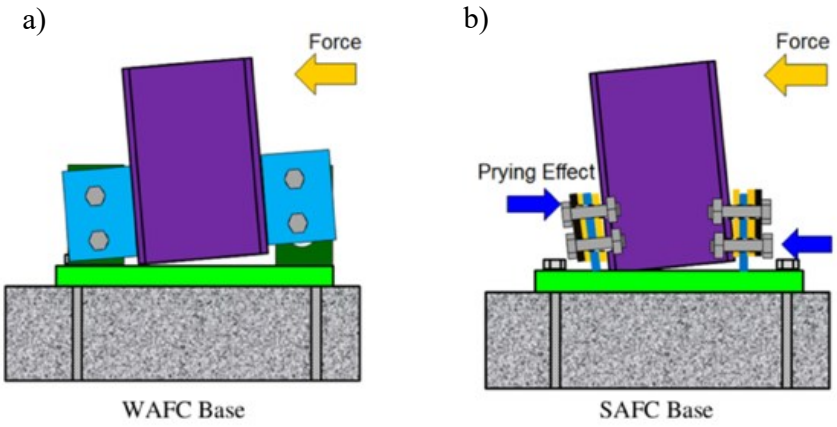

Figure 2.35. Low-Damage CBs with AFCs: a) Weak-axis aligned Asymmetric Friction Connection (WAFC); b) Strong-axis aligned Asymmetric Friction Connection (SAFC) (Borzouie *et al.,* [89]).

2.3 Self-Centring Systems

2.3.1 Generality

In the previous sections, it has been extensively shown that using FDs within both BCJs and CB connections significantly improves the seismic performance of steel MRFs, thus representing a viable and effective solution to protect the frame components from local damage. Nevertheless, it has been demonstrated that global damage can still be observed in large residual drifts, jeopardizing both the operativity and repairability of such structures. In this direction, new structural systems have been conceived to fulfil the urgent need for structural systems to limit residual deformations while minimizing repair costs and business downtime. McCormick *et al.,* 2008 [90] suggested a threshold of 0.5% as a permissible residual drift to ensure the building's repairability. Conversely, FEMA P58-1 [91] recommends a limit value of 0.2% to ensure that no structural realignment is necessary.

Several research studies have discussed possible solutions to this issue, focusing on new seismic lateral resisting systems able to return to the initial upright position after the seismic event [*e.g.,* 92-112]. This is generally provided by the introduction of elastic restoring forces provided by the inclusion of Post-Tensioned (PT) bars or strands able to regulate the self-centring capability of the structures. Several self-centring systems have been conceived, theoretically studied and experimentally tested to date, demonstrating excellent post-earthquake repairability under moderate-to-strong earthquakes. In these structural systems, the structural damage is reduced or prevented by softening the structural response through elastic gap opening mechanisms at different locations (*e.g.,* at the base, at the BCJ level or between telescoping concentric tubes and anchorage plates) instead of yielding in primary structural elements. Generally, the restoring force component allows the control of the gap-opening (*i.e.,* rocking) mechanism, and it is generally combined with energy-dissipating elements to produce flag-shaped hysteretic behaviour. The shape of the hysteretic behaviour can be tuned by proportioning the restoring

forces and the energy dissipation components. Self-centring systems are capable of fully self-centre when the lateral forces are removed, thus eliminating residual drift. It has been demonstrated that full self-centring behaviour is usually achieved using a nonlinear elastic restoring force, such as the bilinear elastic restoring force shown in Figure 2.36 [96].

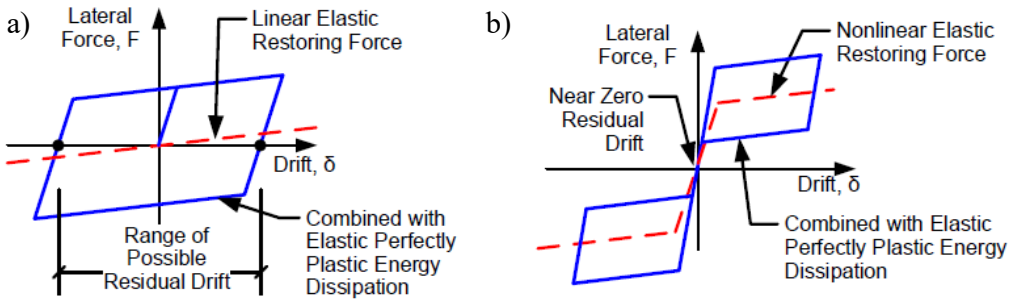

Figure 2.36. Nonlinear elastic restoring force to create full self-centring behaviour: a) Added restoring force, but not full self-centring; (b) Full self-centring obtained by nonlinear elastic restoring force (Chancellor *et al.,* 2014 [96]).

The most common approach to creating a bilinear elastic restoring force requires gap-opening mechanisms generally developed between two surfaces initially pre-compressed together. As shown in Figure 2.37 (b) [96], the seismic lateral force resisting system behaves elastically at low levels of lateral force. Successively, once the lateral force becomes large enough to overcome the precompression force provided by the PT elements, the joint decompresses, and a gap opens. At the decompression level, the lateral force-resisting system significantly reduces stiffness. This effect is desirable as it lengthens the structure's period and helps limit the forces that can develop in the lateral force-resisting system (*i.e.,* softening occurs without structural damage). When the lateral forces are removed, the PT bars pull the structure back to a vertical condition, closing the gap. The system's stiffness after gap opening is primarily controlled by axial stiffness and the location of the PT bars. If the PT bar is subjected to strains greater than the elastic limit, yielding or fracture may occur.

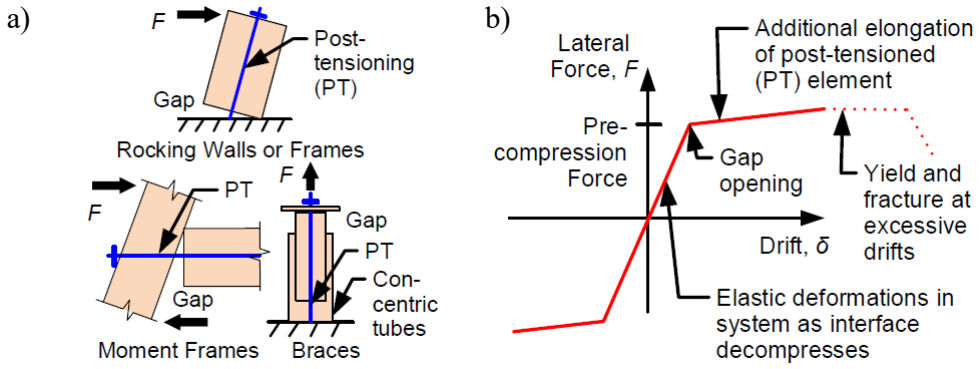

Figure 2.37. Methods for creating bilinear elastic restoring force using gap opening: a) Gap-opening mechanisms; b) Restoring force associated with gap openings. (Chancellor *et al.,* 2014 [96])

The gap opening behaviour and the forces in the PT bars provide the bilinear elastic self-centring behaviour shown in Figure 2.38 [92] but do not provide energy dissipation to the structure. Therefore, specific dissipative elements are also introduced to produce sufficient energy dissipation capacity. The dissipative and re-centring mechanism of hybrid systems is described by a peculiar 'flag-shape' hysteresis behaviour, whose properties and shape can be modified by the designer by varying the moment contributions between the self-centring and the dissipation components. For example, a 50-50 flag shape (*i.e.,* λ=1) would generate maximum energy dissipation while maintaining fully self-centring capability.

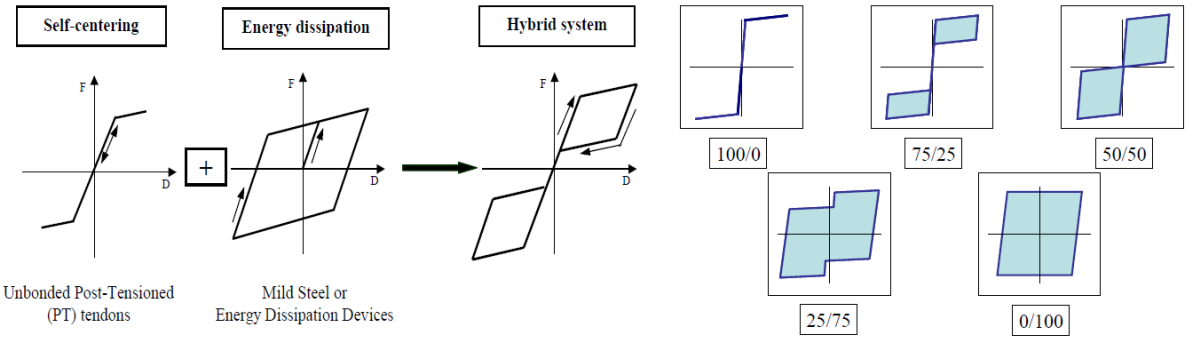

Figure 2.38. Flag-shape hysteresis loop for a hybrid system. Effects of varying the ratio between Self-Centring *vs* dissipative contributions to the Flag-Shape Hysteresis loop (Pampanin *et al.,* 2012 [92]).

The sum of the resistances characterizes the capacity of the self-centring seismic system to resist lateral loads due to the restoring forces (*i.e.,* PT force, gravity loads) and the force in the energy dissipation elements [96]. The height of the hysteresis loop (as defined by β or βE in Figure 2.39 (a) [96]) for a self-centring system is a function of the strength and location of the energy dissipation elements, assumed with a static force capacity (*e.g.,* FDs). The flag-shaped hysteresis demonstrates the self-centring ability as the displacement returns to negligible values when removing lateral forces [96]. For the system to fully self-center, $\beta \leq 1.0$.

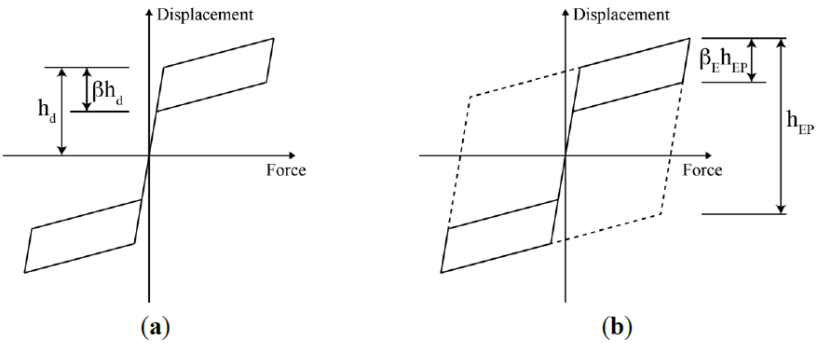

Figure 2.39. Self-centring criteria for SC systems: (a) $\beta \leq 1.0$ (adapted from [92]. Copyright 2002 John Wiley & Sons, Ltd.); (b) $\beta E \leq 0.5$ (adapted from [93]. Copyright 2005 ACI).

Alternatively, another parameter that has been used to quantify self-centring capability in the literature is defined based on the relative area contained (*i.e.,* energy dissipated) in the self-centring hysteresis loops with respect to the area of a comparable bilinear elastoplastic hysteresis loop. If the hysteretic behaviour is assumed to be a perfect flag shape, the ratio of energies is equal to the ratio of heights, βE, as shown in Figure 2.39 (b) [96]. For the system to fully self-center, $\beta E \leq 0.5$. Therefore, the self-centring capacity is adjusted by tuning the relative magnitudes of the initial PT force (which sets the capacity at decompression when elastic behaviour softens due to gap opening) and the capacity of the energy dissipation elements (which controls the height of the hysteresis loop). A typical 'hybrid' system is illustrated in Figure 2.40 [94], which combines unbonded PT bars or tendons and non-prestressed mild steel. However, similarly, additional external dissipation devices could be adopted to allow replacement after severe earthquakes. Several energy-dissipating elements exist, and they can be divided into the following categories: *1)* hysteretic damping elements; *2)* viscous damping elements; *3)* frictional damping elements or other advanced materials (*e.g.,* Shape Memory Alloys (SMA), visco-elastic systems). The mechanism acts as a fuse or 'internal isolation system' with negligible or no damage in the primary structural elements, which remain in the elastic range without needing repairing intervention.

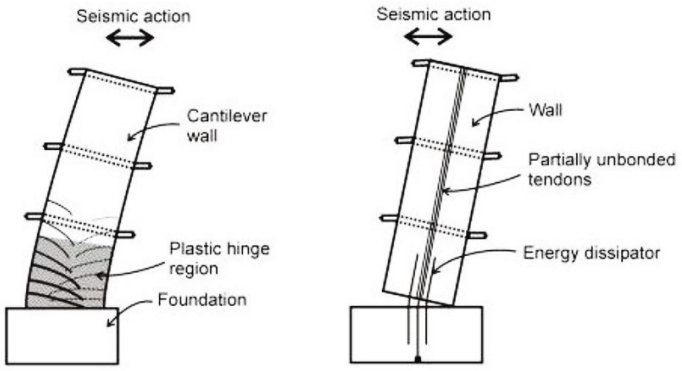

Figure 2.40. Comparative response of a traditional monolithic system (damage in the plastic hinge and residual deformations) and a jointed precast ('hybrid') solution (rocking mechanism with negligible damage and negligible residual deformations (from Pampanin *et al.,* 2012 [94]).

This strategy represents a clear example of the use of modern technology based on our ancient heritage. In fact, it is possible to recognise the lessons and inspiration from the long-lasting earthquake-resisting solutions used since the ancient Greek and Roman temples, consisting of segmental construction with marble blocks 'rocking' on each other under the lateral sway. The weight of the blocks themselves and the heavy roof beams provided the required "clamping" and self-centring vertical force (Figure 2.41) [94].

One of the earliest self-centring systems was introduced in the late 1990s as the main outcome of the U.S. PRESSS (*i.e.,* PREcast Structural Seismic System) program [99-101] coordinated by the University of California, San Diego on the seismic design and performance of precast concrete structural systems. This project culminated with the pseudo-dynamic test of a large-scale Five Storey Test Building [101], shown in Figure 2.42. The new construction system, based on dry jointed ductile connections, was conceived and developed for precast concrete buildings (*i.e.,* frames and walls) in

seismic regions to create an alternative approach to the traditional connections characterised by the cast-in-place approach.

Precast elements are joined in the PRESSS frame or wall systems through unbonded PT tendons/strands or bars, creating moment-resisting connections (Figure 2.43). Within the PRESSS program framework, several seismic tests of precast external and internal BCJ sub-assemblages with unbonded tendons have been tested under cyclic loads (Figure 2.44). Satisfactory seismic performances were observed, with significant energy absorption of the hysteretic response and negligible residual displacements. Results of the PRESS program demonstrated the viability of precast concrete design for high-seismicity regions, emphasized the advantages of using such systems, developed design guidelines in zones of high and moderate seismicity for incorporation into building codes and promoted many successive studies in this direction.

a) b)

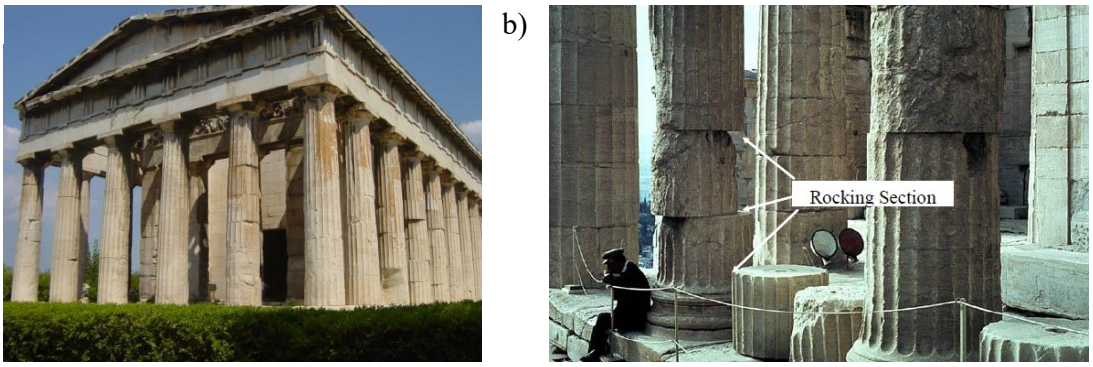

Figure 2.41. Examples of earlier implementation of rocking systems, self-centring and limited damage response under earthquake loading: a) Dionysus temple in Athens, ancient agora; b) Rocking segments of marble columns (Acropolis, Athens). (from Pampanin *et al.,* 2012 [94]).

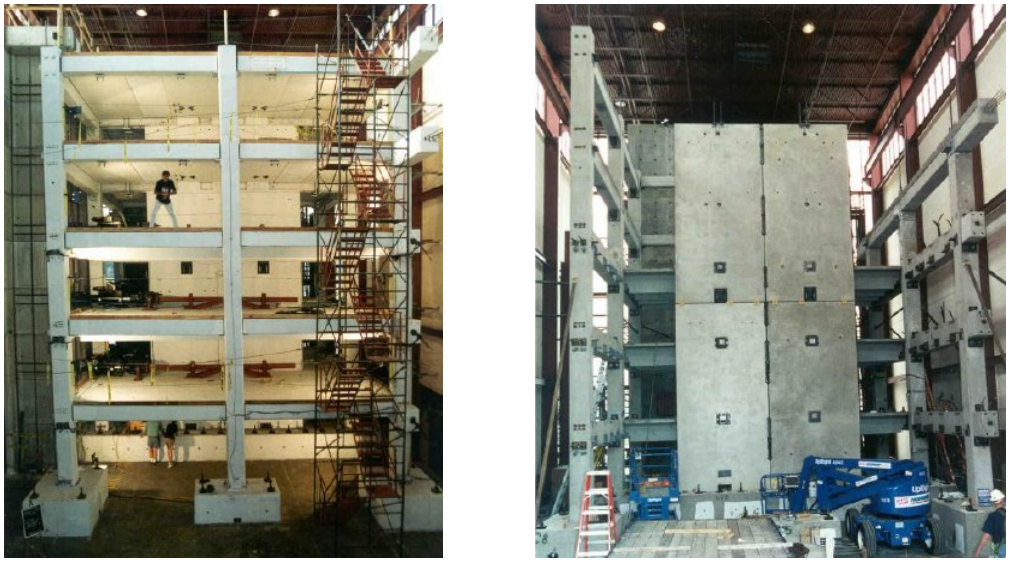

Figure 2.42. Five-Storey PRESSS Building tested at the University of California, San Diego (Priestley *et al.,* 1999 [101])

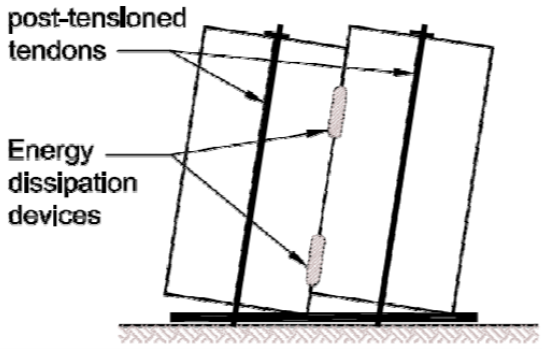

Figure 2.43. PREES project, basic concept (Priestley *et al.,* 1999 [99-101])

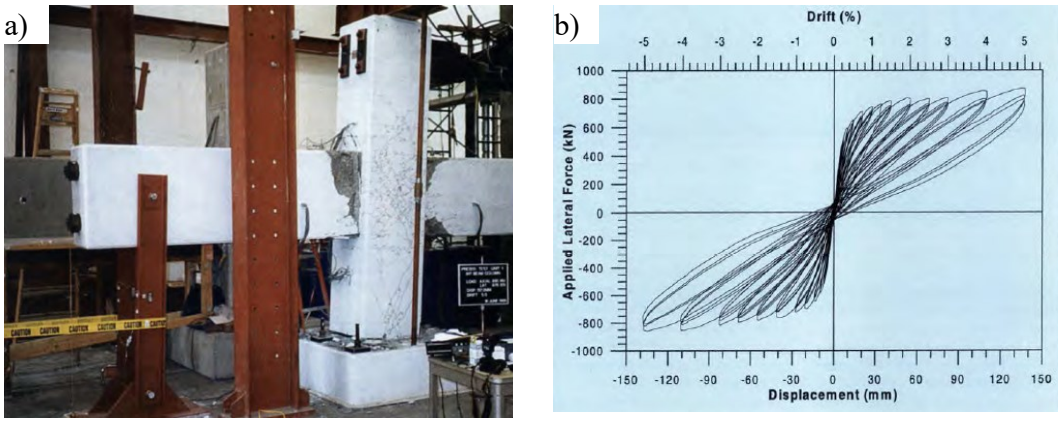

Figure 2.44. Interior precast BCJ with unbonded tendons: a) General view; b) Force-displacement response. (Priestley *et al.,* 1999 [100])

According to Chancellor *et al.,* 2014 [96], three categories of restoring force mechanisms can be individuated. The first category uses a gap at the foundation when subjected to a prescribed overturning moment and includes rocking precast concrete walls (*e.g.,* [102-103]), precast concrete columns (*e.g.,* [104]) and steel Self-Centring CBFs (SC-CBFs) (*e.g.,* [106-107]). The second restoring force mechanism category includes precast coupled concrete shear walls (*e.g.,* [113]), concrete Self-Centering MRFs (*i.e.,* SC-MRFs) (*e.g.,* [114]) or steel SC-MRFs (*e.g.,* [115-129]), which allow gap opening between beam and column (or wall) joints when subjected to a prescribed moment. The third restoring force mechanism category includes self-centring bracing systems, in which a gap forms between telescoping concentric tubes and anchorage plates when subjected to a prescribed axial force (*e.g.,* [130-133]).

Self-Centring CBFs (SC-CBFs)

In the first category, Roke *et al.,* 2010 [106] (Figure 2.45) proposed and investigated a type of steel SC-CBFs. At high levels of lateral load, the fundamental lateral load behaviour of the SC-CBF system is represented by rocking at the base of the compression column, which occurs when the column under tension from the overturning moment decompresses and uplifts at the foundation. To control the uplift, high-strength PT bars, oriented vertically over the SC-CBF's height, were used for prestressing the frame to the foundation.

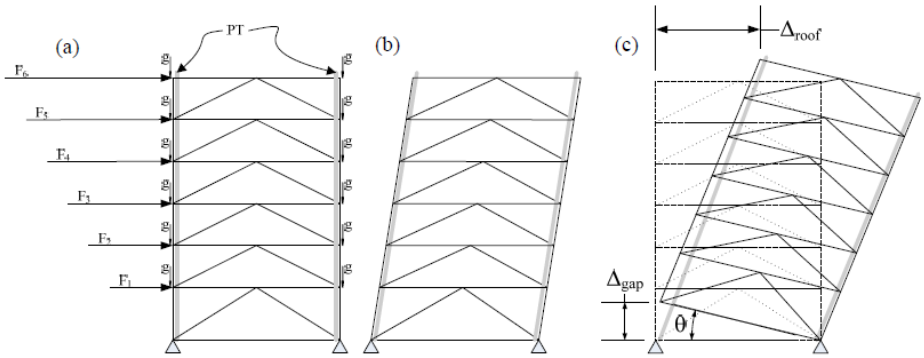

Figure 2.45. SC-CBFs System: (a) schematic of members and lateral forces; (b) elastic response before column uplift; (c) rigid-body rotation after column uplift (Roke *et al.,* 2010 [106]).

Similarly, Eatherton *et al.,* 2010 [107] (Figure 2.46) investigated a controlled rocking braced-frame system for steel-framed buildings consisting of three main components: *1)* Steel frames that remain essentially elastic and are allowed to rock at the CBs; *2)* Vertical PT tendons providing active self-centring forces; *3)* Replaceable energy-dissipating elements act as structural fuses that yield, limiting the forces imposed on the rest of the structure. Results from large-scale static experimental tests provided the efficiency of these systems in concentrating the structural damage in the replaceable energy dissipation fuses and promoting a uniform distribution of the height-wise inter-storey drift, thus preventing soft-storey that may occur in a traditional seismic force-resisting system.

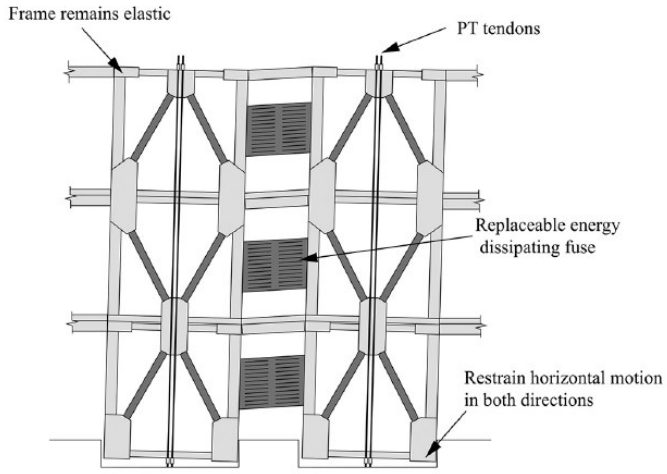

Figure 2.46. Controlled rocking system (Eatherton *et al.,* 2010 [107], adapted by Fang *et al.,* 2022 [98]).

However, some new issues arise with the introduction of the rocking mechanism. Firstly, the local members at the base of the rocking frame could yield or be damaged as the CBs are expected to experience large concentrated vertical force caused by pounding. In addition, rocking systems could have non-constant CORs during earthquake events, and consequently, additional axial tensile force demands may be generated in the columns. Therefore, from a practical application point of view, implementing the PT technology at some construction sites may be challenging. To address these issues,

Hu *et al.,* 2020 [108] and 2021 [109] recently proposed three novel self-centring energy-absorbing rocking core (SERC) systems, shown in Figure 2.47. Compared to many of the existing rocking technologies/systems, the new SERC systems provided friction spring dampers, which did not introduce extra demands on frame members, and undesirable column uplifting did not occur.

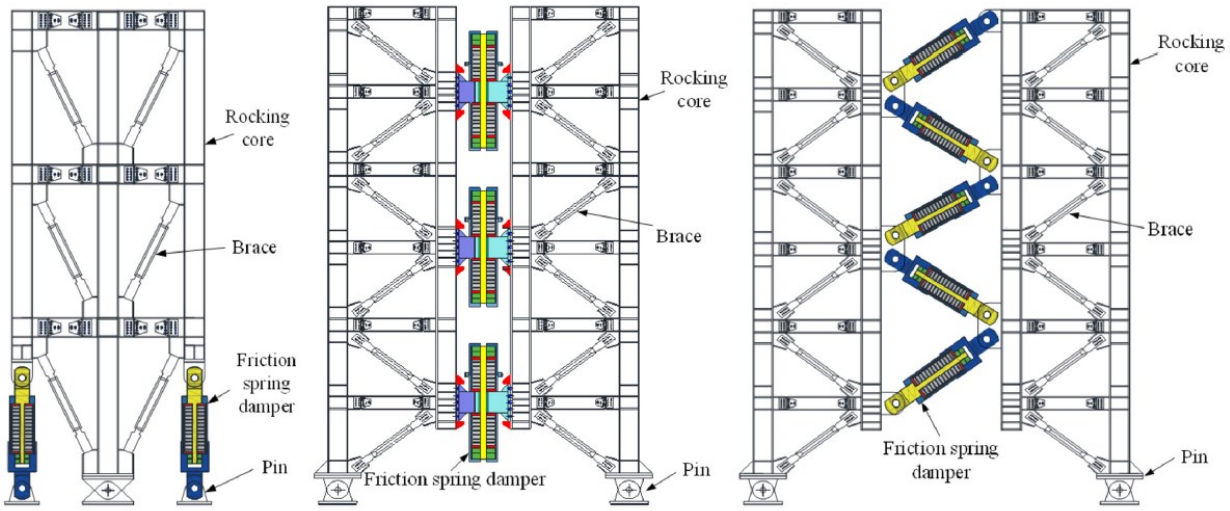

Figure 2.47. SERC systems with friction spring devices (Hu *et al.,* [108-109]).

Self-Centring MRFs (SC-MRFs)

According to Chancellor *et al.,* 2014 [96], the second category includes steel SC-MRFs, in which beams are PT to the columns by high-strength PT strands parallel to the beams and anchored outside the connection so that a gap can open at the beam-column interface. Energy dissipation devices (*e.g.,* yielding seat angles [115], short axial yielding devices similar in behaviour to buckling restrained braces (BRBs) [116], FDs [118-121, 111-129] or yielding web hourglass pins (WHPs) [123]) are included in the SC-MRFs to dissipate the seismic input energy. Additional information will be given in detail regarding steel SC-MRFs in Section 2.3.2 of this thesis.

Self-Centring Bracing Systems

The third restoring force mechanism category includes self-centring bracing systems, in which a gap opening is generated between telescoping concentric tubes and anchorage plates when subjected to a prescribed axial force (*e.g.,* [130-133]). In this case, self-centring braces return to their original length after undergoing significant axial elongation or shortening. Although these systems allow gap opening at different locations, the restoring force mechanisms function identically. For example, Christopoulos *et al.,* 2008 [130] proposed and experimentally tested a new self-centring energy dissipative (SCED) bracing system that uses a restoring force mechanism consisting of two concentric tubes pre-compressed by aramid fibre PT strands and an energy dissipation mechanism using friction pads (Figure 2.48). Results demonstrated that the proposed SCED represented a viable alternative to current braced frame systems because of its attractive self-centring property and simplicity, allowing it to be scaled to any desired strength level. Eatherton *et al.,* 2014 [133] developed and experimentally validated a self-centring buckling-restrained brace (SC-BRB) that employs a restoring mechanism created using

concentric tubes held flush with PT SMA rods in conjunction with a BRB that dissipates seismic energy. Figure 2.49 schematically shows the configuration of telescoping concentric tubes and PT elements for the restoring force mechanism. The SC-BRB dissipated sufficient energy even with large self-centring ratios because the SMA can also dissipate significant seismic energy.

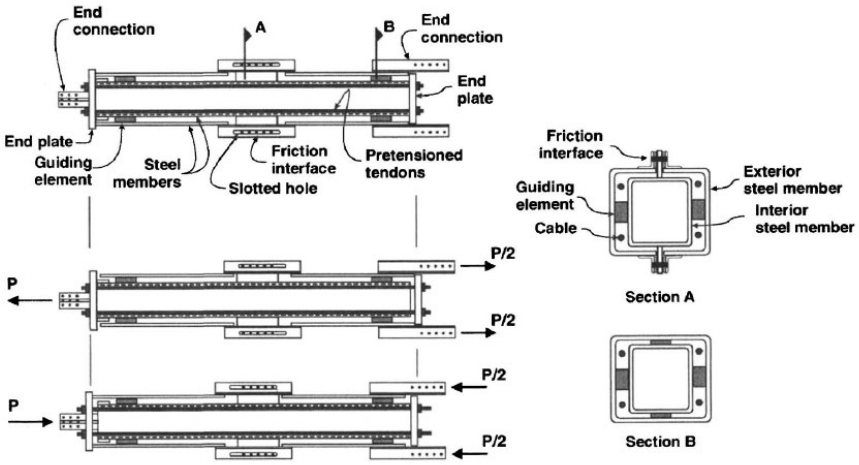

Figure 2.48. SCED system (Christopoulos et al., 2008 [130]).

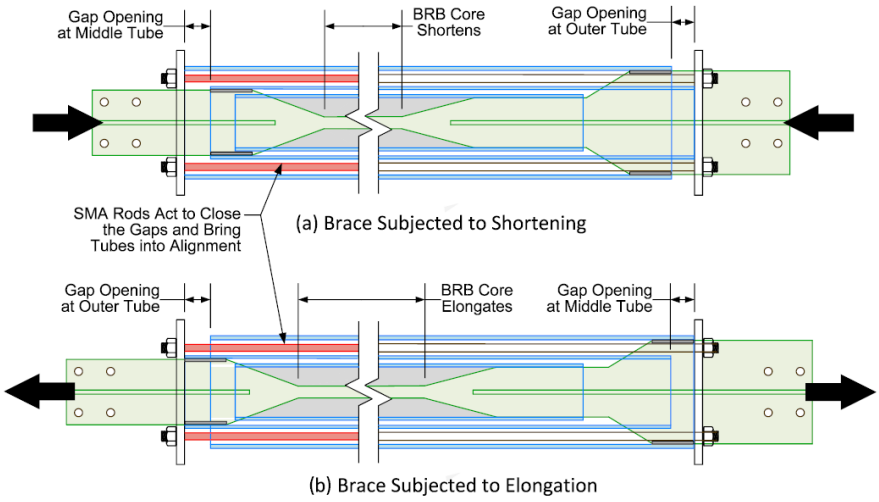

Figure 2.49. Self-centring BRB behaviour subjected to shortening and elongation. (Eatherton et al., 2014 [133], [106]): a) Brace subjected to shortening; b) Brace subjected to elongation.

Besides the concentric self-centring braces, self-centring EBFs have also been proposed [134-137]. For example, Tong *et al.,* 2019 [134] employed a PT-based strategy similar to that of MRFs with PT connections, as shown in Figure 2.50 (a). This type of EBF still suffered from the detrimental frame expansion effect and local slab damage. A modified self-centring EBF, namely, Y-type EBF [135], was proposed to address the problem, as shown in Figure 2.50 (b). Another strategy to eliminate frame expansion is prefabricated self-centring modular panels [136].

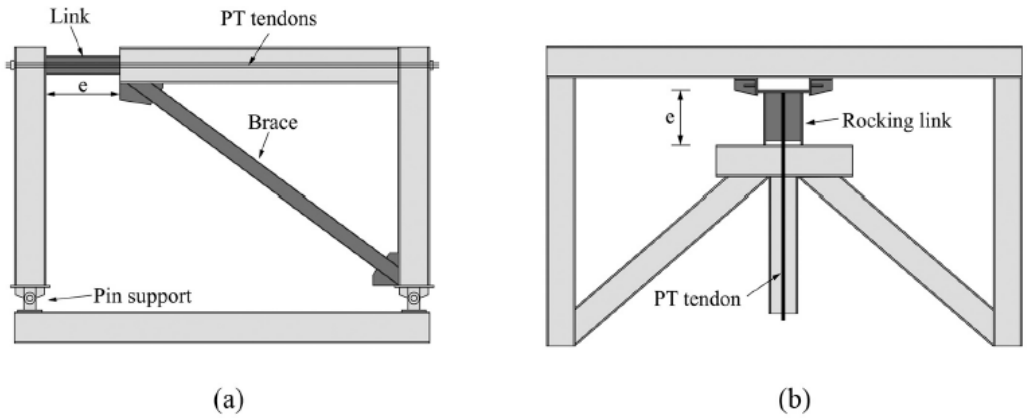

Figure 2.50. Alternative PT-based self-centring frames: a) EBF with a horizontal link, b) EBF with a vertical link [134-135] (adapted from Fang et al., 2022 [98])

2.3.2 Self-Centring Beam-to-column Connections

For steel MRFs, this technology is based on including self-centring and damage-free devices at the BCJ level. Figure 2.51 (a) shows the concept of the PT BCJ technology, which consists of prestressing/post-tensioning prefabricated beams to the column interface. During large lateral deformations, expected from severe seismic events, a gap opens between the end of the beam and the column face, as illustrated in Figure 2.51 (b). As the gap opens, the PT tendon extends, providing additional force to close the gap. Additionally, specific energy dissipative elements may be placed over the gap to dissipate the seismic input energy, whose strength should be small enough to let the tendons pull the structure towards its initial position. This is demonstrated by the displacement at zero force, which is nearly zero, as shown in the hysteresis loop of Figure 2.51 (c). Even though the self-centring devices proposed by different researchers are mainly equipped with hysteretic or friction dampers, the dissipative elements can generally be represented by any typology of passive seismic dampers. Tests of beam/column subassemblies with one column and without slabs have shown excellent behaviour with no permanent displacements or significant damage after the earthquake. However, additional effects may result in damage when the beam supports a slab and/or is part of a frame with more than one column.

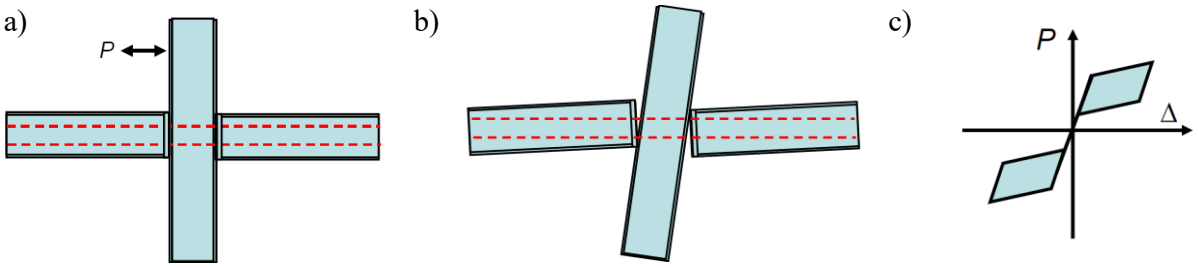

Figure 2.51. Concept of PT BCJs: a) Joint; b) Deformed shape; c) Hysteretic Behaviour (MacRae and Clifton 2013).

PT BCJs were one of the earliest attempts to achieve self-centring capability for steel frames [115-129]. Ricles *et al.* 2001 [115] pioneered the first innovative lateral resisting system (Figure 2.52-Figure 2.53),

where beams were post-tensioned to the columns by high-strength PT strands parallel to the beams and anchored outside the connection, reinforced by steel angles. Results from numerical simulations highlighted the huge advantages of this connection typology. The beams and columns remained essentially elastic, while inelastic deformation (and damage) was confined to the angles of the connection. Additionally, results demonstrated the feasibility of the connection from the practical point of view, as field welding was not required, and the connection was made with conventional materials.

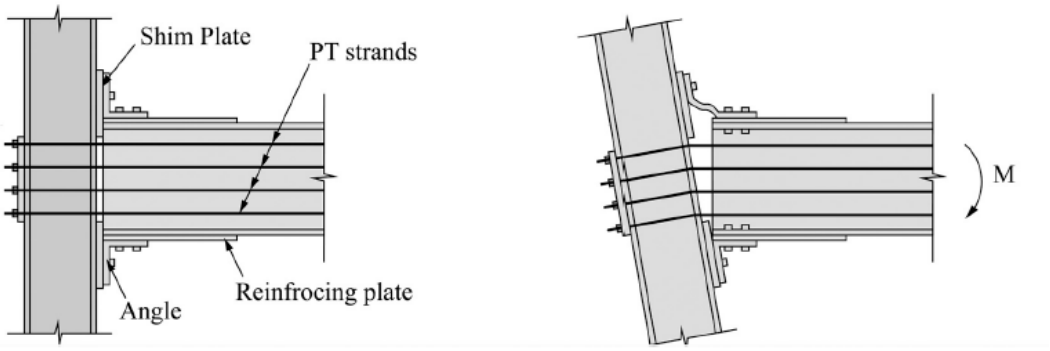

Figure 2.52. Concept of the first-generation PT-based self-centring steel BCJs (after Fang *et al.,* 2022 [98]).

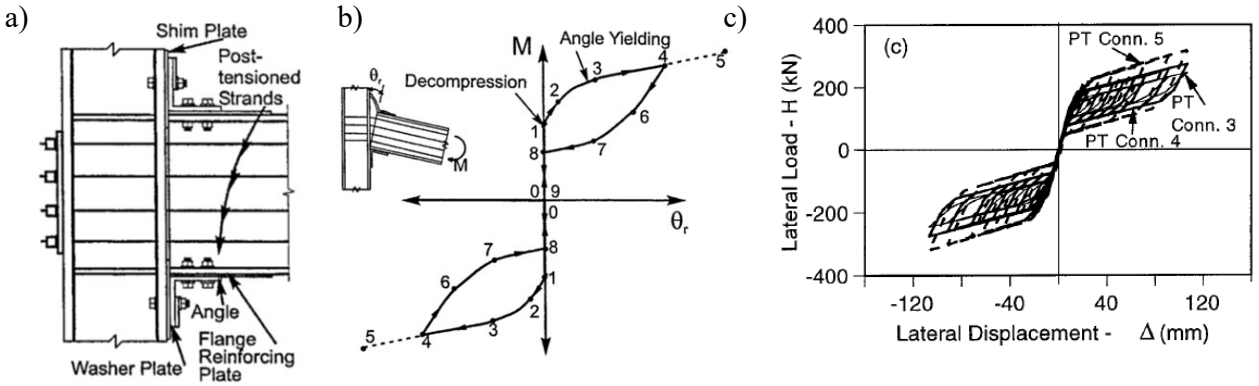

Figure 2.53. Ricles et al., 2001 [115] a) Concept of PT connections; b) Theoretical Moment-Rotation Behaviour, c) Force-Displacement Behaviour.

Also, experimental investigations were carried out to study the experimental response of these connections. One of the earliest examples is provided by Garlock *et al.,* 2005 [117] (Figure 2.54), who experimentally tested six full-scale interior connection subassemblies of PT wide flange BCJs, originally proposed in Ricles *et al.,* 2001 [115]. The connections have been subjected to inelastic cyclic loading up to 4% storey drift. The experimental results demonstrated that the PT connection has good energy dissipation and ductility. Under drift levels of 4%, the beams and columns remained elastic, while only the top and seat angles were damaged and dissipated energy. Predictive equations were presented to estimate the decompression moment, maximum connection moment, and maximum strand force. The equations were found to produce results that were in good agreement with the experimental results.

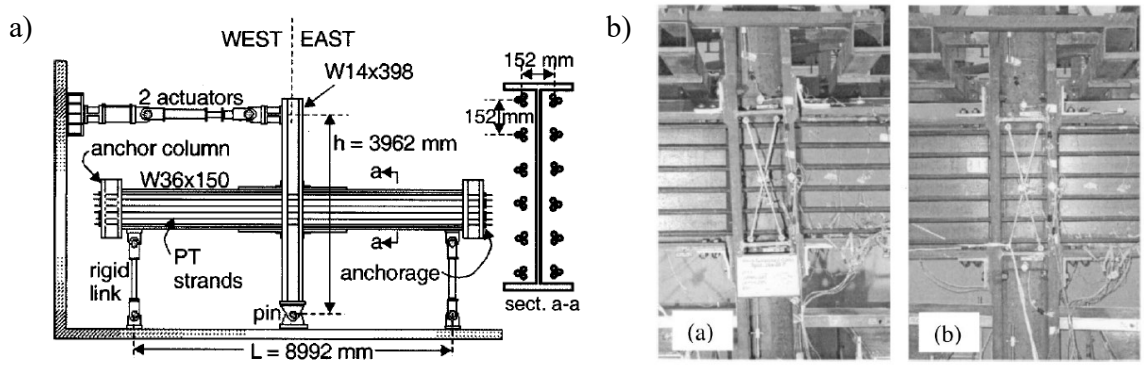

Figure 2.54. Garlock et al. [117] PT connections: a) Experimental test setup; b) specimen at 4% rotation and at the end of the test.

Apart from using seat angles as energy-dissipating devices, FDs were also used within self-centring BCJs. Rojas *et al.,* 2005 [118] investigated the seismic performance of a PT friction-damped connection (PFDC), including FDs, as depicted in Figure 2.55. The beam flanges were compressed against the column flanges because of the initial PT force applied to the strands. To prevent premature yielding or buckling of the beam flanges due to excessive compression under the combined action of axial force due to post-tensioning and bending, reinforcing plates were welded on the outside faces of the beam flanges. Shim plates were placed between the column flange and the beam flanges so that only the beam flanges and reinforcing plates were in contact with the column. This enabled good contact between the beam flanges and column face while protecting the beam web from yielding under bearing. Results demonstrated that the connection minimized inelastic deformation to the components of the connection as well as the beams and columns and required no field welding. Nevertheless, yielding developed at the first-storey columns.

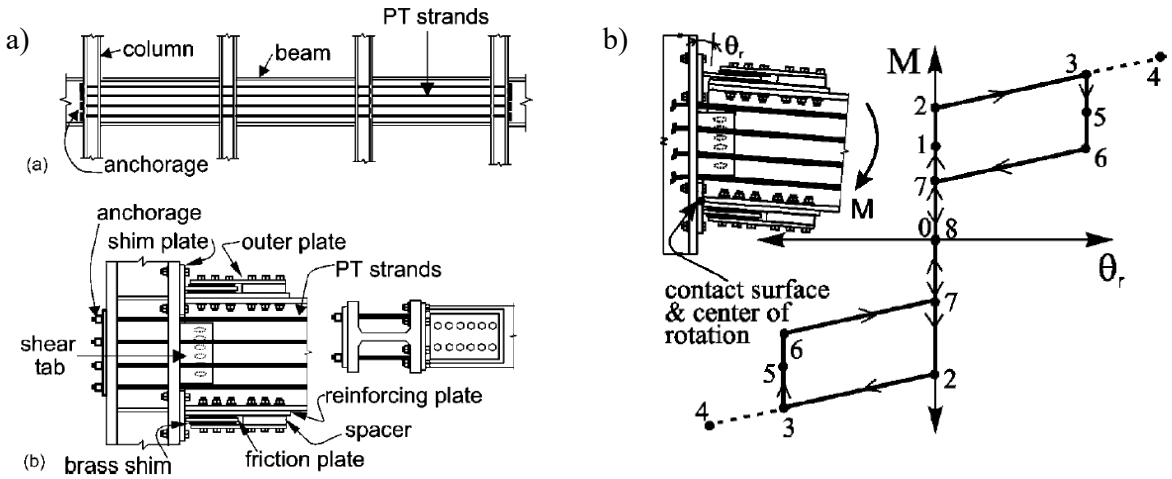

Figure 2.55. Rojas et al., [118] PFCD: a) Components; b) cyclic response

Kim and Christopoulos, 2008 [120-121] (Figure 2.56) proposed and numerically tested a step-by-step seismic design procedure for PT self-centring friction-damped (SCFR) connections, demonstrating their

superior seismic performance. Time-history analyses showed that the maximum interstorey drifts and maximum floor accelerations of the SCFR frame were similar to those of the special steel welded MRFs but with almost zero residual drifts. In addition, the proposed seismic design procedure resulted in structures that achieved the desired performance levels under different seismic loading. However, the SCFR frame almost eliminated residual deformations except for the first-storey columns. Hence, additional studies were required to solve these issues. In this direction, the proposed CB proposed in this thesis represents an efficient solution to mitigate this effect.

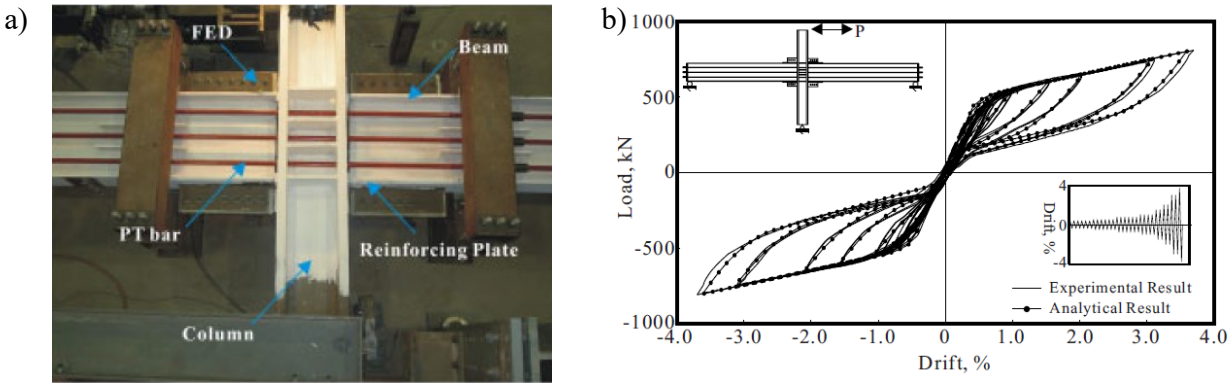

Figure 2.56. Kim and Christopoulos, 2008 [120-121] SCFR: a) Test Set-up; b) Load-drift relationship

However, the appeal of such PT connections gradually faded away as people realized that gap opening causes undesirable frame expansion (also known as beam growth), leading to deformation incompatibility between the gravity frames and the lateral force-resisting frame, which can cause extensive floor damage. Therefore, further studies were required to define and validate the restraining effects of the frame expansion and concrete slabs under simulated strong ground motion. Some new flooring systems, *e.g.,* sliding slabs with discontinuous metal decks, have been proposed to mitigate the frame expansion effect, as discussed in Chou *et al.,* 2011 [122]. A promising strategy is to shift the rotation centre to the top flange of the beam.

Vasdravellis *et al.,* 2012 [123] proposed and experimentally validated a new self-centring BCJ consisting of PT high-strength steel bars and carefully designed energy-dissipation (ED) elements that consist of steel cylindrical hourglass shape pins (WHPs) (Figure 2.57). In addition, repeated tests on a connection specimen and replacing damaged ED elements were conducted. These tests showed that the proposed ED elements could be easily replaced without welding or bolting. Hence, after a significant earthquake, the proposed connection can be repaired with minimal disturbance to building use or occupation. Nonlinear FE models were constructed in ABAQUS [124] (Figure 2.58) to trace the inelastic behaviour of the connection up the ultimate local failure modes both of the individual WHPs and the connection when subjected to either monotonic or cyclic loading. In addition, local web buckling at the connection region after the beam flange reinforcing plates was avoided by using web stiffeners. However, this detailing resulted in excessive local yielding at the beam-column interface due to high bearing forces.

Figure 2.57. Vasdravellis *et al.,* 2012 [123] self-centring BCJ with WHPs: a) Overview of the specimen SC-WHP1; b) Detail of the WHP; c) Gap opening at 6% drift of specimen SC-WHP1

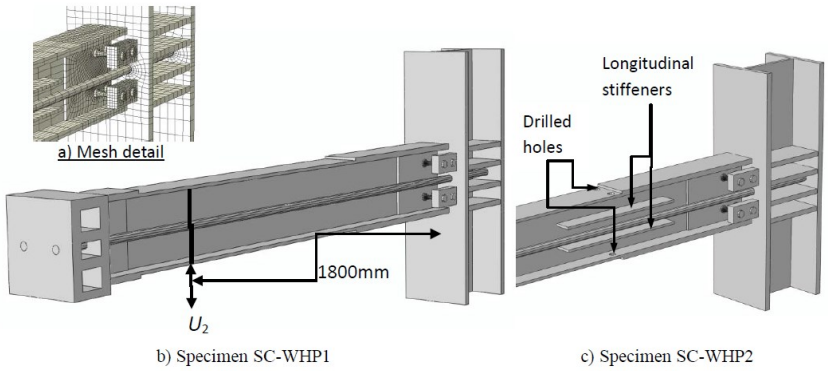

Figure 2.58. Vasdravellis *et al.,* 2012 [123] FE modelling of the connections

Furthermore, other studies investigated the collapse behaviour of such systems. For example, Ahmadi *et al.,* 2018 [125] (Figure 2.59) investigated the collapse resistance of self-centring MRFs to determine the collapse margin ratio of a prototype low-rise steel building with perimeter SC-MRFs. The structural model for the SC-MRF included finite shell elements to enable important limit states, including local buckling in the beams, to be included in the analyses. Results showed that the seismic collapse of an SC-MRF under extreme ground motions is mainly governed by the development of inelastic local buckling and significant axial shortening in the beams that lead to a decrease in PT strand force, with subsequent loss of stiffness and strength of the self-centring BCJs and reduction in the SC-MRFs lateral resistance.

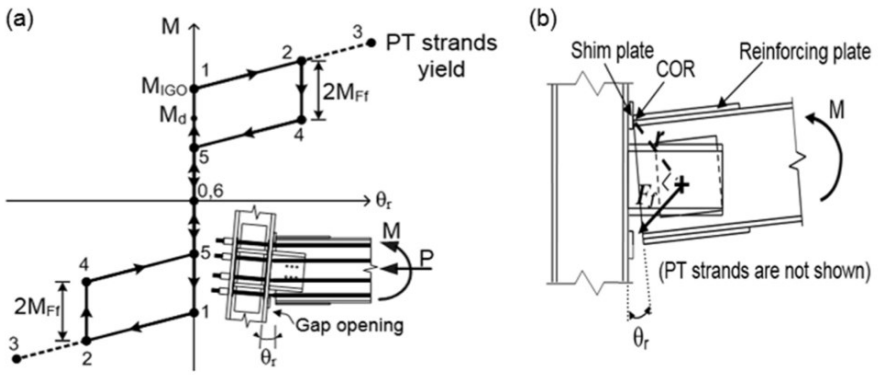

Figure 2.59. Ahmadi *et al.,* 2018 [125] Self-centring-connection: a) conceptual moment-relative rotation behaviour; and b) illustration of BCJ rotation.

Also, recent studies focused on the progressive collapse resistance of steel self-centring MRFs. Dimopoulos *et al.,* 2020 [126] (Figure 2.60) assessed the robustness of a seismic-resistant building using SC-MRFs under a sudden column loss scenario. A FE model was built in ABAQUS [124] and validated against experimental results. Results allowed for identifying all possible failure modes and quantifying the composite floor's contribution to the frame's robustness. Based on the outcomes of this research, it can be expected that steel buildings with PT connections designed to accommodate seismic events with PGA larger than 0.35 g and typical Type B soil conditions according to Eurocode 8 will be robust enough to survive in the case of an internal column removal of the SC-MRF.

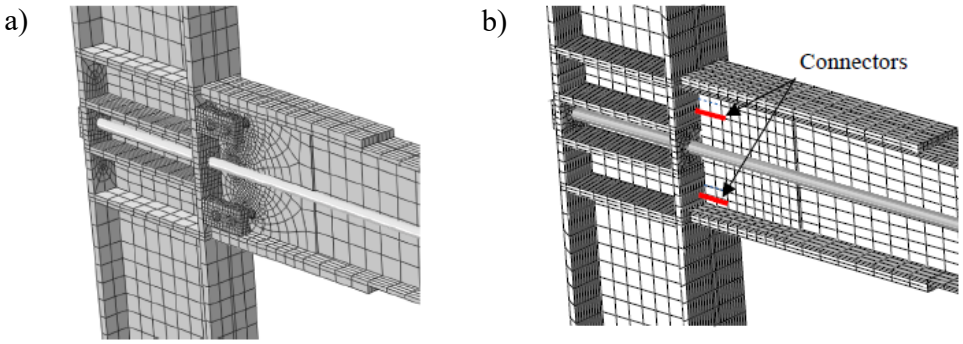

Figure 2.60. Dimopoulos *et al.,* 2020 [126] Self-centring BCJs: Finite Element model with (a) and without connectors (b)

More recently, Huang *et al.,* 2022 [127] (Figure 2.61) proposed the concept of resilient friction beams (RFBs) and investigated how RFBs can be economically implemented in steel MRFs to improve seismic performance. The RFBs mainly consist of two T-shaped beams and four cap plates, resulting in a cost-effective configuration that employs less steel than previous self-centring beam designs. A set of steel-framed buildings with different heights was designed and computationally subjected to two seismic levels of ground motions. The results suggest that residual interstorey drift, peak base shears and peak absolute accelerations can be effectively limited by providing RFBs at the lower storeys.

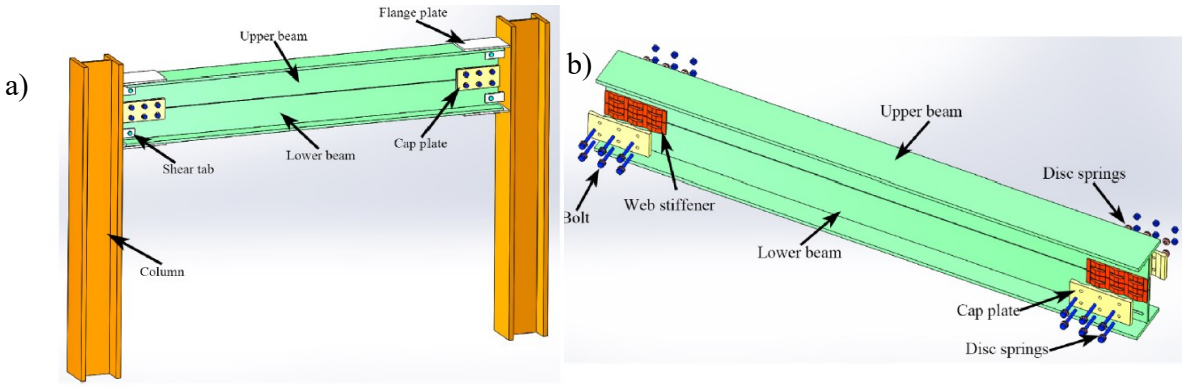

Figure 2.61. Huang *et al.,* 2022 [127] RFBs: a) Configuration of a prototype frame; b) Structural details

Most past studies on this topic [*e.g.,* 115-123, 125] demonstrated the beneficial effects gained in damage and residual drift reduction by including self-centring devices at all BCJs. However, this solution may represent a limit to the practical application due to increased structural complexity. To address this issue,

Pieroni *et al.,* 2022 [128-129] numerically investigated the influence of Self-Centring BCJs (SC-BCJs) placement within an 8-storey case-study steel MRF. Several configurations with different locations of SCDF joints were analysed and compared. Results demonstrated that significant advantages could be obtained by considering the effective placement of a limited number of SC-BCJs, representing the optimum compromise between structural complexity and seismic performance. Figure 2.62 (a) shows some of the considered configurations, while Figure 2.62 (b) shows the regression curve for residual drifts obtained from stripe analysis with 30 ground motions at the design intensity, considering an increasing number of levels with SC-BCJs. The results show that including SC-BCJs only at 2 levels leads to approximately 50% residual drifts.

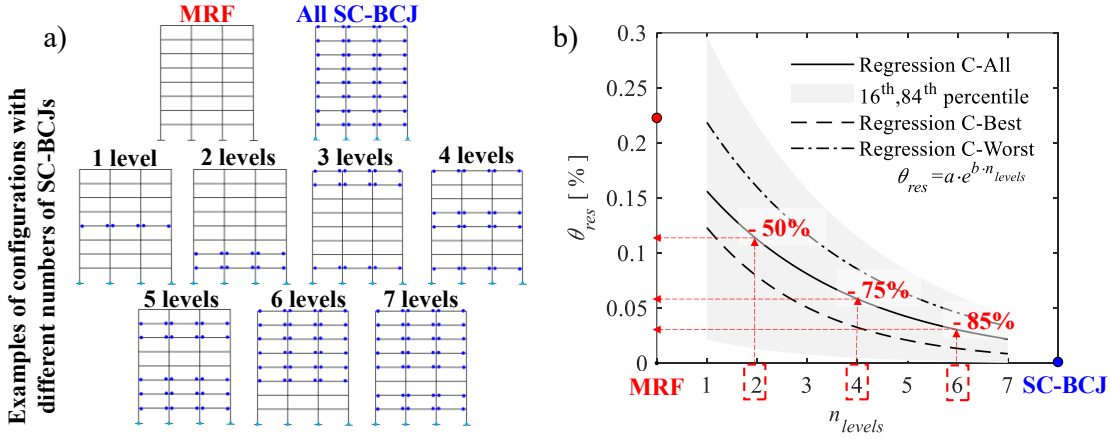

Figure 2.62. Pieroni *et al.,* 2022 [128-129]. Effective placement of SC-BCJs: a) Some examples of different placement of a limited number of SC-BCJs; b) Regressions for residual drift ratios

2.3.3 Self-Centring Column Base Connections

The first generation of PT and self-centring systems adopted for steel MRFs demonstrated excellent seismic performance, with small residual deformations, through gap opening and closing responses at the BCJ interfaces. However, although the experimental and analytical studies demonstrated the superior seismic performance of the SC-MRFs compared to the conventional MRFs, the introduction of self-centring devices eliminated residual deformations within steel MRFs, except for the first floor. In addition, it has already been explained that conventional CB may suffer from residual rotations, large plastic deformations [*e.g.,* 62, 54], and axial shortening phenomena [*e.g.,* 65-68], which impair the structure returning to the initial condition after severe earthquakes. Therefore, CBs play a fundamental role in the self-centring capacity of steel MRFs.

To overcome these downsides, several research efforts have proposed alternative solutions. In Section 2.2.3 of this thesis, some solutions based on dissipative partial-strength joints equipped with yielding or FDs have already been presented. However, even though using FDs may be an efficient solution to mitigate damage within CBs, additional studies have been developed on innovative self-centring CBs capable of minimizing the structural residual drifts in the aftermath of strong seismic events. In this direction, several research efforts have proposed alternative solutions by combining self-centring systems and energy dissipation devices (*e.g.,* yielding or FDs) designed for easy inspection and replacement after strong seismic events [*e.g.,* 138-156]. Some of these research works [*e.g.,* 139-156]

have focused on using rocking column bases where PT bars or rods, or yielding bolts, were used to control rocking behaviour and provide the self-centring capability. Dedicated devices were used to dissipate seismic energy (*e.g.,* FDs [*e.g.,* 144, 145] or metallic energy dissipating devices [*e.g.,* 146, 147]). In addition, some studies also focused on achieving self-centring behaviour using advanced materials (*i.e.,* SMA) [*e.g.,* 149-151]). Different configurations were investigated considering different column sections, lengths, and positions of the PT bars. While in some cases, the results showed the system's advantages in terms of improved self-centring behaviour of the CBs, several drawbacks were also highlighted, including undesirable column axial shortening, loss of PT force and inelastic deformations.

In this context, Mackinven *et al.,* 2007 [139] proposed a low-damage steel CB equipped with unbounded steel rods specifically detailed with nuts above and below the end plate (Figure 2.63). The unbonded length of the rods was specifically designed to allow elastic extension and to control the self-centring behaviour during rocking. This CB was characterized by the absence of yielding in the column, resulting in the elimination of inelastic axial shortening. However, some drawbacks were highlighted. In fact, the CB lacked energy dissipation and experienced moderate pinching under large cyclic drifts and significant stress concentration due to rocking.

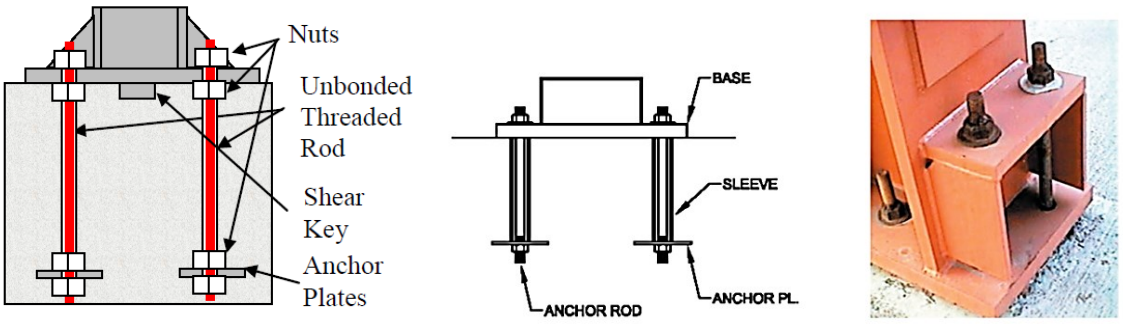

Figure 2.63. Machkiven *et al.,* 2007 [139] Base connection with anchor rods with sleeves and detail of the CB with stools

Chou and Chen, 2011 [140] investigated the seismic response of a self-centring frame with PT CB connections through shake table tests and cyclic tests (Figure 2.64). An analytical model based on the rotational spring model approach for predicting the seismic performance of the frame subassembly was proposed and analysed, and the results were compared with the experimental data. Results demonstrated that the first-storey residual drift could be significantly minimized by using the PT CBs. However, the maximum interstorey drift in the self-centring frame increased with the decreasing fixity at the CB connection level.

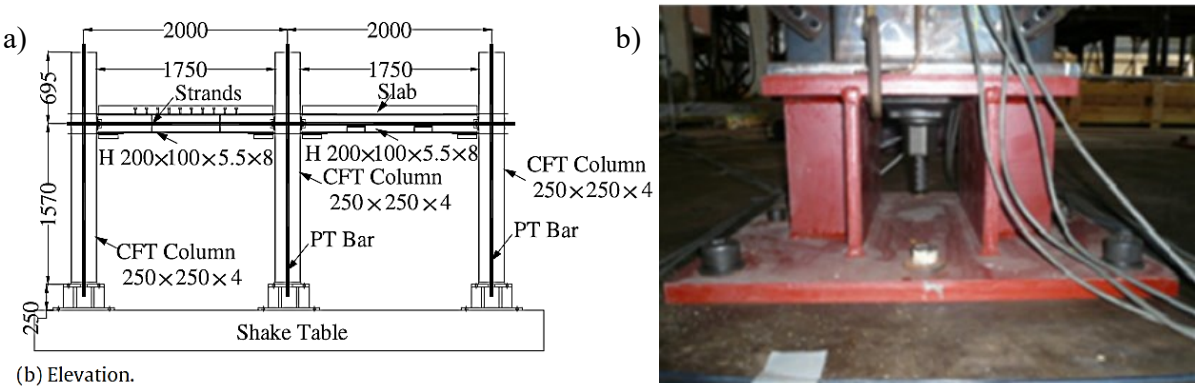

Figure 2.64. Chou and Chen [140] a) Tested prototype building; b) Detail of the PT CB connection.

Chi and Liu, 2012 [141] studied the cyclic response of a CB connection in which the column is connected to the base plate by PT bars, anchored at the mid-storey height and at the bottom of a grade steel beam using BRS plates as energy dissipation, while additional shear resistance is provided by bolted keeper plates (Figure 2.65). A series of PT column base connection subassemblies were subjected to axial load and cyclic lateral displacements. Test parameters included initial PT force, initial axial force in column (constant or varying), column size and loading history. The test results demonstrated that adequately designed CB connections could undergo lateral displacement up to 4% interstorey drift while the columns and grade beams remained elastic. Also, the BRS plates showed good energy dissipation capacity by yielding in tension and compression without fracture. Nevertheless, this CB provided energy dissipation only in one loading direction, so further investigations were needed to provide insights regarding its behaviour under biaxial loading.

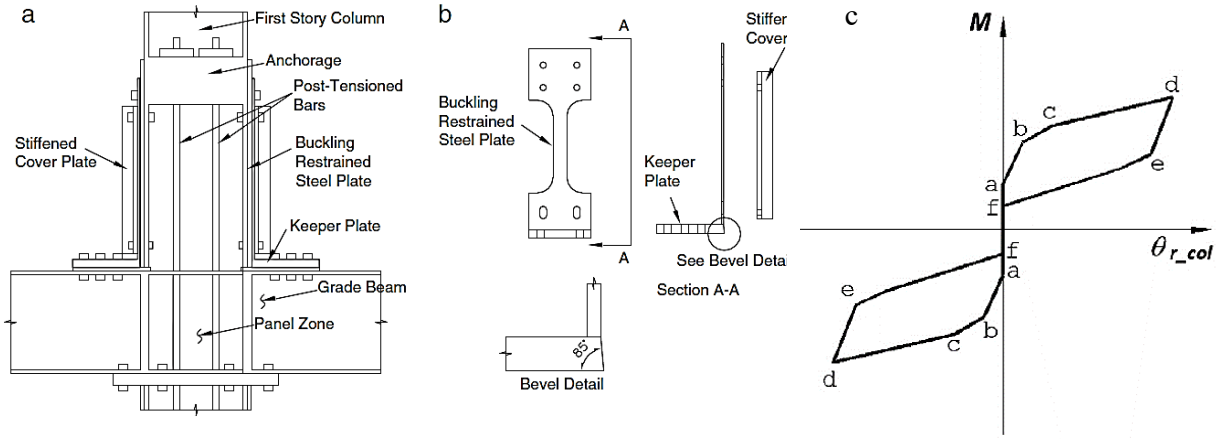

Figure 2.65. Chi and Liu, 2012 [141]: a) Configuration of PT CB connection; b) BRS and keeper plates; c) Moment-rotation behaviour of the connections in two configurations

Yamanishi *et al.,* 2012 [142] proposed an anchor-bolt-yield-type exposed CB with rotational rigidity control function and repair performance (Figure 2.66). The CB was equipped with yield bolts anchored on a strong plate welded on the column and connected to the anchor bolts through couplers. The yield bolts were the only components that experienced damage and could be easily replaced. The proposed CB was validated through experiments and detailed analyses using cyclically applied rotations.

Theoretical equations to predict the elastic rotational stiffness were also proposed, and they appear to correlate well with both experimental and analytical results. This CB showed a semi-rigid behaviour caused by anchor-bolt elongation and base plate bending deformation out of plane. However, this connection's main downside was the absence of self-centring capability and the pinching behaviour during unloading.

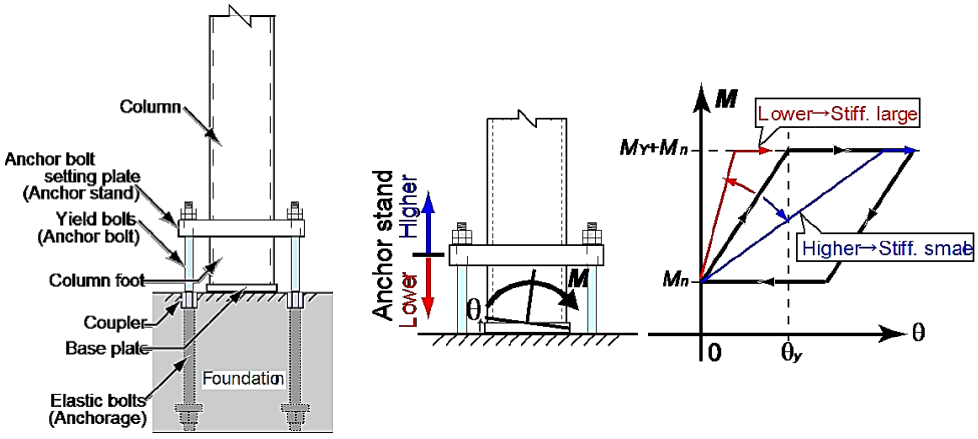

Figure 2.66. Yamanishi et al., 2012 [142] Anchor-bolt-yield-type exposed CB.

However, all the configurations investigated and described so far did not prevent high-stress concentration and damage at the onset of rocking. In addition, they did not provide solutions to control the response of the CB in different plan directions except the principal direction of the column cross-section. Some other studies were developed to overcome these issues. Freddi *et al.,* 2017 [144] presented a rocking damage-free steel CB equipped with FDs and high-strength steel PT bars (Figure 2.67).

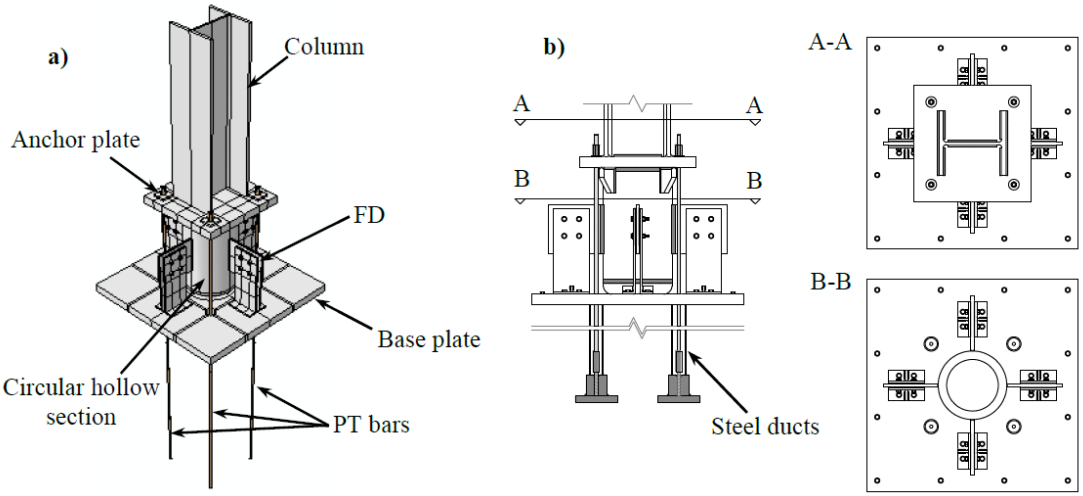

Figure 2.67. Freddi et. al., 2017 [144] Rocking damage-free steel CB: a) 3D view; b) Lateral and sections views.

Amongst others, the main advances, with respect to other studies, were related to using a circular steel plate with rounded edges as a rocking base. The rounded edges prevented stress concentration and

damage to the contact surfaces during the rocking, while the circular shape allowed rocking towards all plane directions. Contrary to conventional steel CBs, the proposed solution exhibited monotonic and cyclic moment–rotation behaviour that was easily described by analytical equations, allowing the definition of a step-by-step design procedure, which ensured damage-free behaviour, self-centring capability, and energy dissipation capacity for a target design base rotation. Non-linear dynamic analyses showed the CB's potential to prevent the first-floor column yielding and eliminate the first-storey residual drift without any peak interstorey drift in steel MRFs.

Successively, Freddi *et al.,* 2019 [145] experimentally investigated this connection with monotonic and cyclic tests (Figure 2.68). The experimental tests were conducted on a 3/5 scaled specimen under monotonic and cyclic quasi-static lateral loading protocols while simulating an about constant axial force. The results agreed with the expected behaviour from analytical equations, which validated the design procedure. Results demonstrated the damage-free behaviour up to the target design rotation and the ability to limit the damage only to a few easily replaceable components under large rotations. This demonstrated the high potential of the innovative rocking CB to be used in earthquake-resilient steel structures. The experimental results were also used to calibrate refined 3D numerical models in ABAQUS [124] that allowed further investigations.

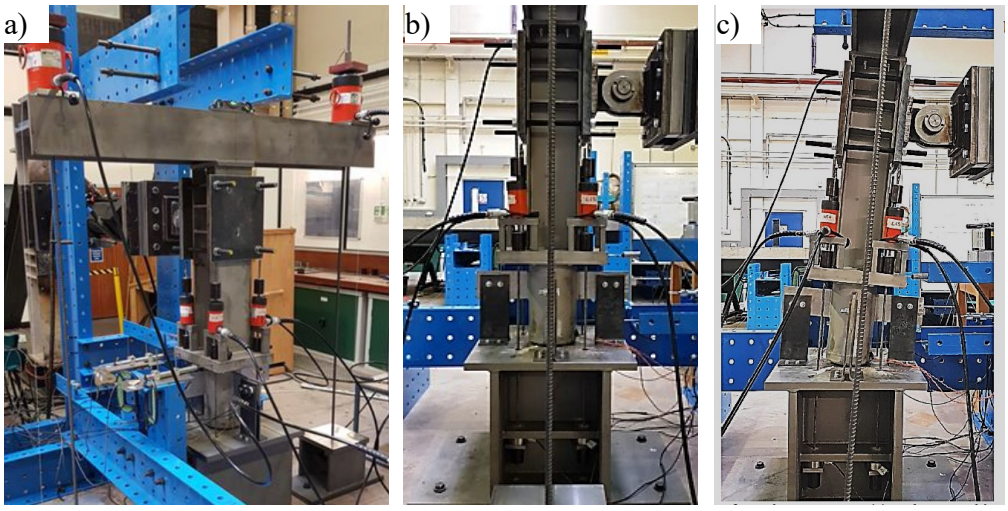

Figure 2.68. Freddi et al., 2019 [145] Rocking damage-free steel column base. a) Full-test setup; b) Specimen; c) Rocking during the cyclic tests.

Similarly, Kamperidis *et al.,* 2018 [146] proposed a partial strength low-damage self-centring steel CB equipped with PT strands and WHPs to dissipate seismic energy (Figure 2.69). Unlike the other solutions, the CB was composed of a concrete-filled square steel section and used external PT strands to control the rocking behaviour. An analytical model that predicted the stiffness, strength, and hysteretic behaviour of the CB was presented, and nonlinear dynamic analyses were carried out on a prototype steel SC-MRF. Results showed the efficiency of the CBs in protecting the first-storey columns from yielding and drastically reducing the first-storey residual drifts under the considered earthquake intensities. Successively, Kamperidis *et al.,* 2020 [147] also performed a parametric by varying the

initial, post-yield, and strength of the proposed self-centring CBs. Results revealed that these properties are relevant in affecting the seismic response and the collapse capacity of steel SC-MRFs.

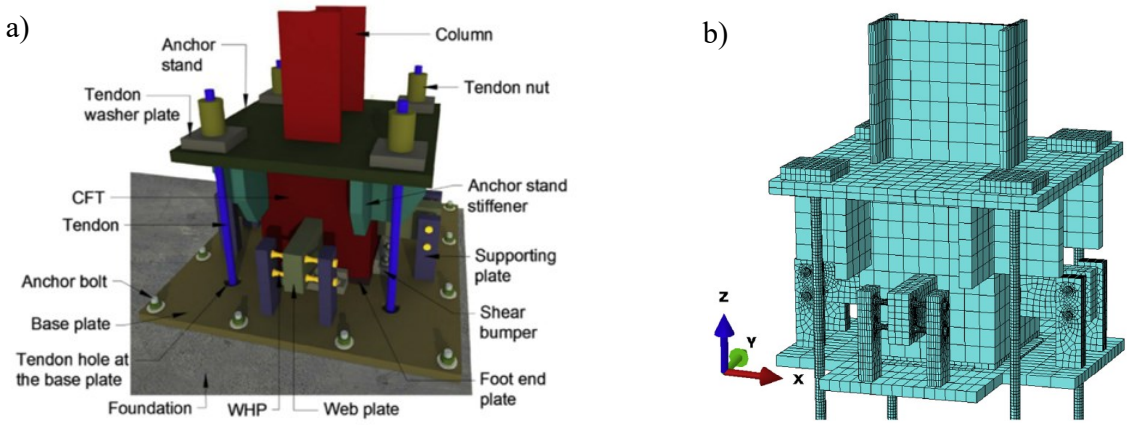

Figure 2.69. Kamperidis *et al.,* 2018 [146] Partial strength low-damage self-centring steel CB: a) 3D representation of the CB; b) FE [124] model.

A similar approach was also followed by Wang *et al.,* 2019 [148] while considering three different Concrete-Filled Square steel Tubular (CFST) CB connections with PT strands and sandwiched energy dissipaters in the two orthogonal directions (Figure 2.70). The analytical model was developed to predict the moment-relative rotation relationship of the self-centring CFST CB connection, and a good correlation with the experimental data was obtained. All of the connections demonstrated the typical flag-shape self-centring behaviour, with stable energy dissipation, while the best-performing one showed very low residual drifts (0.15%) even at significant drifts (4%).

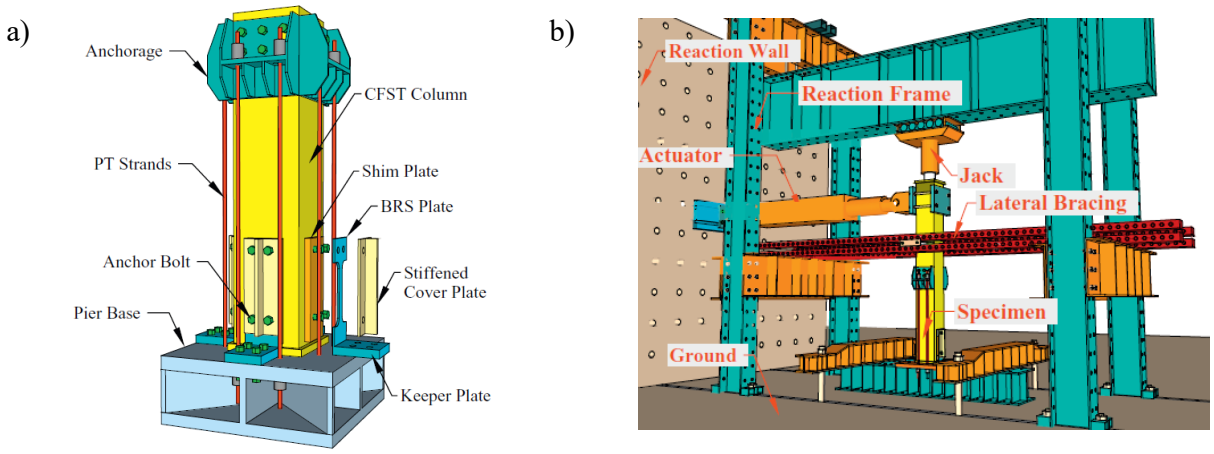

Figure 2.70. Wang *et al.,* 2019 [148] Concrete-Filled Square steel Tubular (CFST) CB connections: a) 3D view; b) Testing set-up.

In addition, some studies also focused on achieving self-centring behaviour using advanced materials. For example, Wang *et al.,* 2019 [149-150] investigated a novel type of steel column equipped with SMA bolts to study its potential for achieving earthquake resilience (Figure 2.71). Structural details of the CB

and mechanical properties of the SMA bolts were described, and an analytical model of the self-centring column for different limit states and the corresponding design procedure was presented. The seismic behaviours of two steel column specimens were experimentally tested to investigate the effects of the initial pre-strain in the SMA bolts and the axial compressive force in the column under cyclic loading. Results showed that the steel columns with SMA bolts exhibited satisfactory and stable flag-shaped hysteresis loops with excellent self-centring but moderate energy dissipation capabilities.

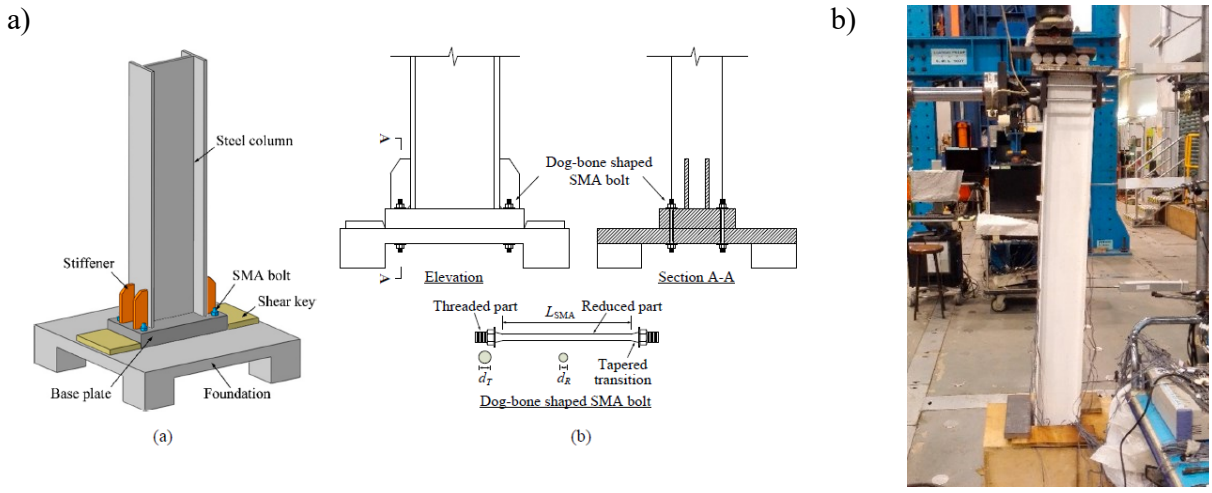

Figure 2.71. Wang *et al.,* 2019 [149-150] Steel columns equipped with SMA bolts; a) 3D view and sections; b) Testing set-up.

More recently, few research studies are currently focusing on simple repairing methodologies for the structural performance recovery of buildings using innovative CB connections. For example, Zhang *et al.,* 2022 [152] recently investigated the low-damage performance of a novel steel rocking CB joint equipped with an AFC (Figure 2.72). Cyclic tests with and without axial forces were carried out along the strong axis of the column, including initial, aftershock and repair cases. In this study, the resilience of the joint was also investigated by re-tightening the bolts of the FDs, and the results demonstrated that the seismic performance of the joint was restored without loss of strength and stiffness.

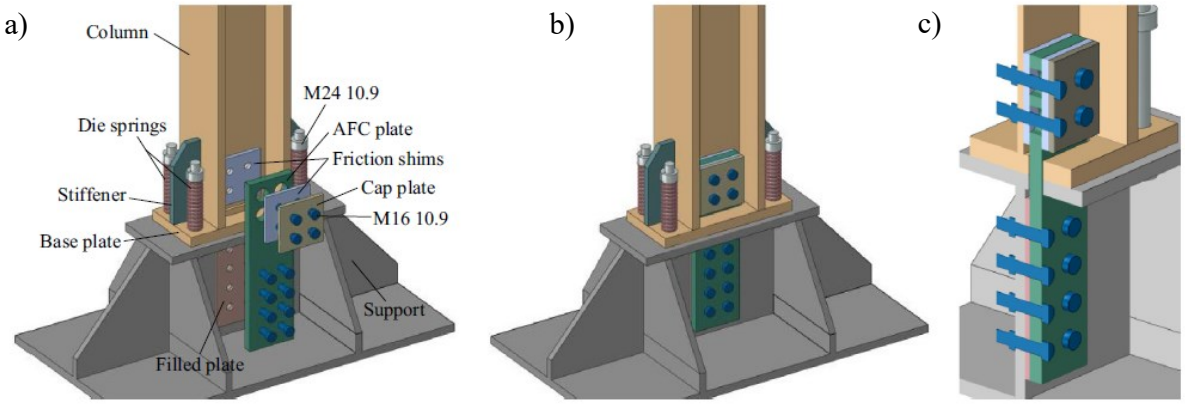

Figure 2.72. Zhang *et al.,* 2022 [152] Schematic diagram of CB: a) Exploded view; b) Assembly view; c) Cutaway view.

In this direction, Sun *et al.,* 2022 [154] investigated an innovative performance-recoverable self-centring CB with replaceable stiffener angle steels (Figure 2.73) to achieve the restoration of structural functionality after severe earthquakes. In the experimental campaign, the ability to resist aftershocks, the effects of replacing stiffener angle steels, and the re-tensioning PT strands after the earthquake on the seismic performance recovery under different axial compression ratios for this CB were also investigated. Results demonstrated that replacing stiffener angle steels could significantly recover the seismic performance with a fast and low-cost post-earthquake repair methodology. Further investigations about this topic are provided in Chapter 6 of this thesis.

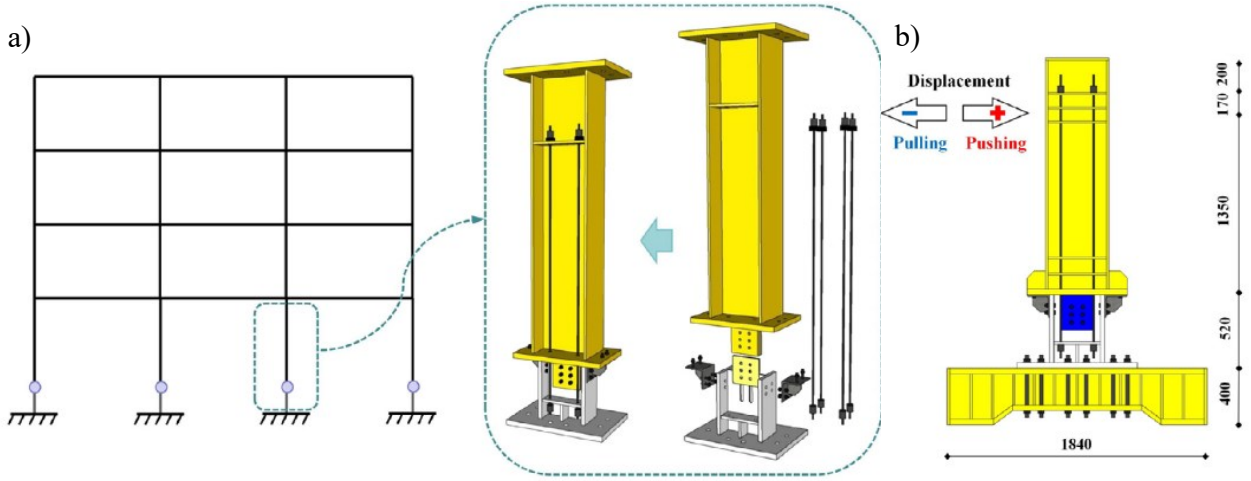

Figure 2.73. Sun *et al.,* 2022 [154] Self-centring CB with replaceable stiffener angle: a) Location and assembly; b) Front view of the tested specimen.

These studies demonstrated the effectiveness of the proposed connections in providing both self-centring capabilities and damage-free behaviour. However, their complexity and the need for long PT bars could lead to high costs, thus limiting the application to some special structures. In addition, it is noteworthy that most past studies [*e.g.,* 112-120, 122, 141] have focused on using self-centring devices in all BCJs and CBs, demonstrating the advantages of self-centring capabilities and damage-free behaviour. Nevertheless, a drawback of these solutions could be represented by the complexity of the structural details. If, on the one hand, the use of self-centring devices in all the joints is expected to produce a fully damage-free and self-centring response, on the other hand, it may represent a limit to the practical application due to the increase of structural complexity. In this regard, two fundamental aspects have been further investigated to promote the use in the practice of such systems: *1)* the definition of self-centring connections that can be easily fabricated and installed; *2)* a limited number of self-centring connections within the structure.

Within this context, Latour *et al.,* 2019 [156] recently proposed and experimentally tested an innovative damage-free Self-Centring Column Base (SC-CB) consisting of a rocking column splice joint where a combination of FDs and PT bars with disk springs are respectively used to dissipate the seismic energy and to promote the self-centring behaviour of the connection. Results from the experimental tests [156] showed a satisfactory and stable flag-shaped hysteretic behaviour of the SC-CB, with negligible residual deformations in the column. They also highlighted the influence of some design parameters over the

joint response, such as the assumed design value of the axial load and the key role of the initial pre-load of the PT bars on the self-centring response of the device. Considering this connection typology, it has been recently investigated the effectiveness of these joints in terms of residual drift reduction within steel MRFs [157-158]. This thesis will discuss these aspects in detail through numerical simulations, FE analysis, parametric studies and experimental testing.

2.4 Numerical modelling for Moment Resisting Frames (MRFs)

2.4.1 Distributed plasticity *vs.* concentrated plasticity

In the traditional seismic design of structures, the plastic deformation capacity of the structural elements is considered while using linear elastic models to perform the analyses. Although this approach may be adequate for regular small and medium structures, it quickly becomes unfeasible for other structures as its conservativism often results in over-expensive, hence inefficient structures. Although a detailed nonlinear analysis would typically require higher computational and professional capabilities, the cheapening of computational power has enabled even small engineering firms to use simple (or even complex) nonlinear analysis methods for designing and assessing structures against seismic loads. Therefore, with the advancements in software and hardware capabilities, the accessibility to highly detailed FE modelling tools has increased. However, regardless of the feasibility, the computational time spent on running a highly detailed analysis may not be necessarily justified by the accuracy gained, as the use of significantly simpler models may be helpful to represent the structural elements to a satisfactory level while reducing the analysis time and modelling complexity.

Different inelastic structural models can be differentiated by how plasticity is distributed through the member cross sections and along its length. Figure 2.74 illustrates a comparison of five idealized model types for nonlinear elements. The choice of the optimal model typically involves a balance between reliability, practicality and computational efficiency, and it has to consider the structural system and materials, the expected amount of non-linearity and the level of detail for the input and output data. The main difference among the models relies on how plasticity is distributed along the length of the element and through its cross sections. The first difference can be explained between concentrated and distributed plasticity elements. The models for nonlinear analysis can range from the simplest models with uniaxial spring or hinge models to fibre-type models to much more sophisticated models characterized by detailed continuum finite element models. The type of analysis, the expected behaviour, the assumptions, and the approximations inherent to the proposed model type influence the choice. The NEHRP Seismic Design Technical Brief No. 4 [161] highlights this issue and classifies unidimensional nonlinear elements into five categories depending on their plasticity distribution.

Figure 2.74 (a) illustrates the simplest model, in which the inelastic deformations are concentrated in a rigid-plastic hinge at the ends of the element. This model has the advantage of being computationally efficient, modelling non-linear effects in the localized regions of the structure. The non-linear behaviour is governed by a simple moment-rotation relationship, leading to more efficiency in terms of computational effort and formulation of the problem.

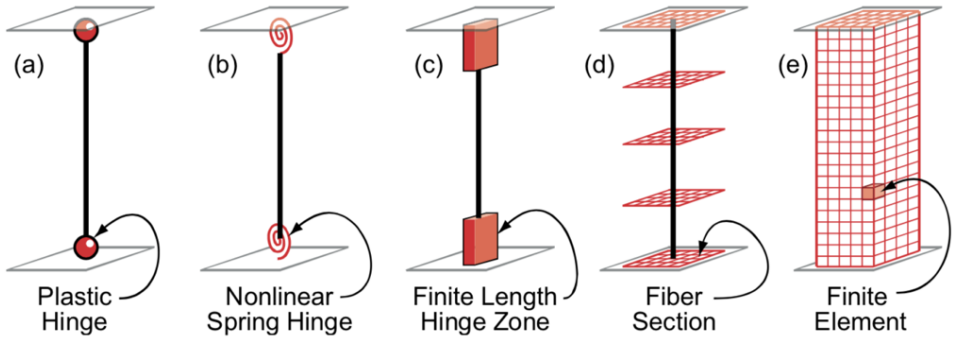

Figure 2.74. Plasticity models of unidimensional nonlinear elements, as classified by Deierlein *et al.,* 2010 [161]

Figure 2.74 (b) shows a similar model, although in this case, the hinges at the ends are represented by nonlinear springs with hysteretic properties. The formulation is significantly condensed in both models by concentrating the plasticity in simple end elements. However, although these modelling approaches can reach appropriate accuracy levels, they cannot represent simultaneous load effects, such as the interaction between bending and axial, which restricts their use in elements in which the interaction of these simultaneous loads must be considered.

Figure 2.74 (c) shows a distributed plasticity model in which the plastic hinges are expected to develop and are modelled as fibre-based. Cross sections in the inelastic hinge zones are described by non-linear moment-curvature relationships or by explicit fibre-section integrations. This model is used because the finite length hinge zone can better capture the effective spread of inelasticity within the member, thus efficiently concentrating the inelastic demands in smaller detailed regions. In contrast, the finite length of the zone leads to a less time-consuming analysis.

Figure 2.74 (d) shows a fibre model that distributes plasticity by numerical integrations through the member length. The models do not report plastic hinge rotations but report strains in the steel cross-section fibres. In particular, uniaxial material fibres, which can capture the non-linear hysteretic behaviour, are numerically integrated over the cross-section to derive the corresponding stress-strain characteristics. Then, the cross-section parameters are integrated at discrete sections along the member length, alternatively using a displacement or force-based formulation. This model allows capturing the interaction of axial and bending loads. On the other hand, this modelling approach fails to allow the shear and torsion interaction with the fibres. It assumes that each integration layer (*i.e.,* at each fibre length) keeps its plane undeformed as if a very stiff plate were located at different heights of the element.

Figure 2.74 (e) shows the refined finite element approach representing the most complex. It is a continuum model that discretizes the member along the member length and through the cross-section into small microfinite elements with nonlinear hysteretic constitutive properties. It represents the behaviour at the most fundamental level and is able to model three-dimensional behaviour, including complex geometries and stress-strain states. Despite not having all the limitations mentioned in other modelling approaches, its use is restricted due to its higher computational demands. This approach is often used in small structures or sub-structures that require high fidelity or resolution. In addition, it

should also be remarked that while more sophisticated models like distributed plasticity models may capture more effectively the realistic behaviour of structures, concentrated plasticity models are commonly used and generally preferred to distributed ones since they are more efficient and less time-consuming.

2.4.2 Lignos and Krawinkler deterioration model

Lignos and Krawinkler, 2011 [162] proposed a beam's plastic hinges deterioration model based on the deterioration model referred to as Ibarra-Krawinkler (IK) model [163] with the modifications based on regressions on an extensive database of experimental data obtained by several tests conducted beams with and without RBS. The modified IK model is based on a monotonic backbone curve, as the IK model, taking into account asymmetric component hysteretic behaviour with a new branch, which allows the simulation of complete loss of strength incorporating an ultimate rotation θ_u at which the strength of a component drops to zero (Figure 2.75 (a)). A set of rules define the characteristics of the hysteretic behaviour, illustrated in Figure 2.75 (b). The modified IK model is implemented in OPENSEES [164].

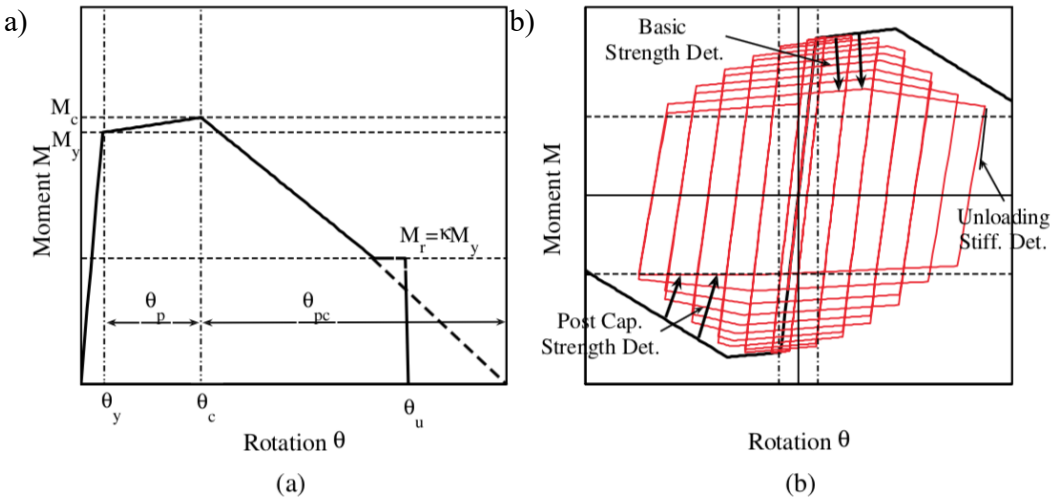

Figure 2.75. Modified IK deterioration model: (a) monotonic curve; (b) basic modes of cyclic deterioration and associated definitions (Lignos and Krawinkler, 2011) [162]

The model is defined in terms of moment-rotation behaviour (Figure 2.76) rather than force-deformation (as in the original version) since the model is usually applied to concentrated flexural plastic hinges, as in Section 4 of this thesis. Three strength parameters define the curve:

- M_y: effective yield moment;
- M_c: capping moment strength (or post-yield strength ratio M_c/M_y);
- $M_r = k \cdot M_y$: residual moment;

and by four deformation parameters:

- ϑ_y, yielding rotation;
- ϑ_p , pre-capping plastic rotation for monotonic loading (*i.e.,* the difference between yield rotation and rotation at the maximum moment);
- $\vartheta_{p,c}$, post-capping plastic rotation (*i.e.,* the difference between rotation at the maximum moment and rotation at a complete loss of strength);
- ϑ_u, ultimate rotation capacity.

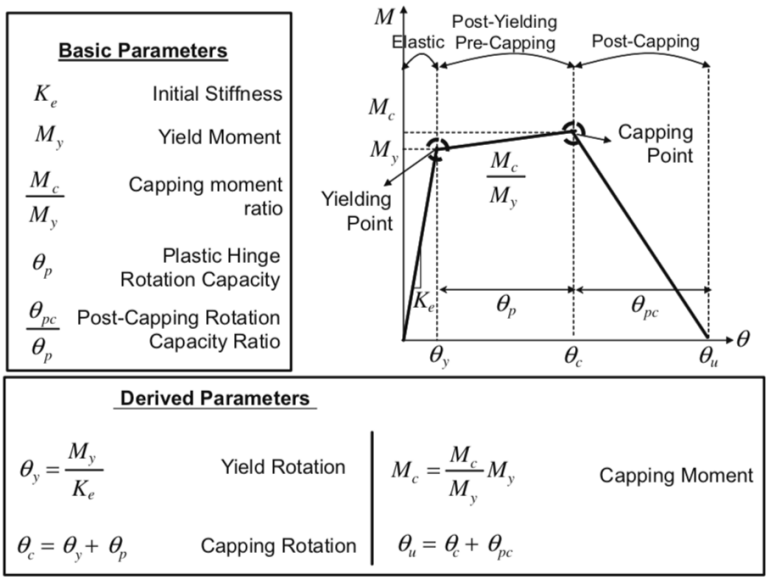

Figure 2.76. Component backbone curve and parameters (Lignos and Krawinkler, 2011) [162]

Yielding Moment M_y

The modified IK deterioration model does not account for cyclic hardening, but the effect of isotropic hardening is indirectly incorporated by increasing the yielding moment (computed as the yield strength f_y times the plastic modulus W_{pl}) to an effective value M_y that accounts for isotropic hardening on average. The coefficient M_c/M_y is variable from 1.06 for beams with RBS to 1.17 for other sections, while a coefficient equal to 1.1 can be used independently for all sections.

Yielding Rotation ϑ_y

The yielding rotation is defined as the ratio between M_y and the initial stiffness K, does not coincide with the elastic stiffness of the element since a concentrated plasticity model with Rayleigh damping is used in the analysis, as indicated by Zareian and Medina [165]. In fact, concerning an element where plasticity is fully concentrated in beam end springs and the central portion is kept elastically, the rotational stiffness K of the end spring must be related to the rotational stiffness K_{el} of the ordinary beam element through the coefficient n, as follows:

$$K = \frac{n+1}{1} K_{el}$$

In the absence of transverse load, it is also possible to assume that the point of contra flexure is located at the mid-span of the element, hence:

$$K_{el} = \frac{6EI}{L}$$

Where E, I and L represent the modulus of elasticity, the moment of inertia and the clear length $(L - d_c)$ of the element respectively. As for the coefficient n, Zareian and Medina [165] proposed to assume a value equal to 10 to avoid numerical instability problems.

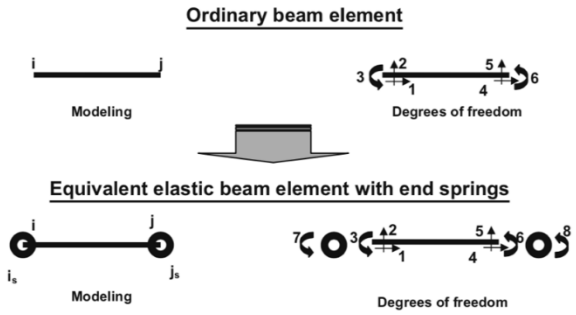

Figure 2.77. Beam element and equivalent model that consists of an elastic beam element with springs at both ends (after Zareian and Medina, 2009 [165])

This assumption can be illustrated in the following figure, where it is possible to note the variation of the two coefficients. S_{ii} and S_{ij} with the coefficient n. The two coefficients were originally proposed by Zareian and Medina [165] to relate the stiffness matrix $[K]$ of the element between the two nodes i and j to its geometric and material properties. Figure shows that S_{ii} and S_{ij} asymptotically reach 4.0 and 2.0 for very large values n. However, the values corresponding to the recommended value of n =10 are very close to the asymptotic ones, ensuring that the response of the equivalent beam with end springs is identical to the elastic response of its equivalent prismatic beam.

Post yield Strength Ratio M_c/M_y

Medina and Krawinkler [166] reported the post-yield strength M_c/M_y and ϑ_c/ϑ_y ratios as parameters which define the strain-hardening stiffness of the backbone curve. This stiffness is important because it plays a key role in the P-Δ stability of a structural system, and as a result of, this parameter should never be neglected in steel structures. Lignos and Krawinkler [162] reported a mean value of the capping strength to the effective yield strength M_c/M_y equal to 1.09 for beams with RBS to 1.11 beams with no-RBS connections. However, a coefficient equal to 1.1 can be used independently for all types of sections.

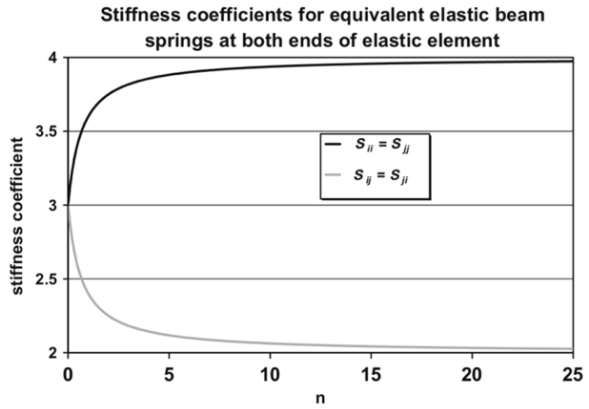

Figure 2.78. Variation of stiffness coefficient S_{ii} and S_{ij} with n for equivalent elastic beam element (after Zareian and Medina, 2009 [165])

Residual Strength Ratio k

Steel elements, whose hysteretic behaviour deteriorates due to local instabilities, approach stabilization of the hysteretic response at very large deformations. (Lignos and Krawinkler [162]). For this reason, the rate of deterioration can be neglected and a constant residual moment $M_r = kM_y$ can be assumed up to ϑ_u. A value of k equal to 0.4 can be assumed, consistently with international guidelines for steel modelling (PEER/ATC 72-1 Report).

Empirical relationships were obtained for modelling of pre-capping plastic rotation (θ_p), post-capping plastic rotation (θ_{pc}) and the cumulative plastic rotation Λ (*i.e.,* cyclic deterioration parameter) for beams with and without RBS. The regression parameters are shown in the following equations:

Pre-capping Plastic Rotation ϑ_p

$$\theta_p = 0.0865\left(\frac{h}{t_w}\right)^{-0.365}\left(\frac{b_f}{2t_f}\right)^{-0.140}\left(\frac{L}{d}\right)^{0.340}\left(\frac{c_{unit}^1 d}{533}\right)^{-0.721}\left(\frac{c_{unit}^2 f_y}{355}\right)^{-0.230}$$

Post-capping Plastic Rotation ϑ_{pc}

$$\theta_{pc} = 5.63\left(\frac{h}{t_w}\right)^{-0.565}\left(\frac{b_f}{2t_f}\right)^{-0.800}\left(\frac{L}{d}\right)^{0.340}\left(\frac{c_{unit}^1 d}{533}\right)^{-0.280}\left(\frac{c_{unit}^2 f_y}{355}\right)^{-0.430}$$

Cumulative Plastic Rotation Λ

$$\Lambda = 495\left(\frac{h}{t_w}\right)^{-1.34}\left(\frac{b_f}{2t_f}\right)^{-0.595}\left(\frac{L}{d}\right)^{0.340}\left(\frac{c_{unit}^2 f_y}{355}\right)^{-0.360}$$

where h is the web depth, t_w is the thickness of the web, b_f is the flange width, t_f is the flange thickness, L is the length of the beam (equal to half of the length of the element), d depth of the steel section, f_y is the yield strength of the steel and c_{unit}^1, c_{unit}^2 are coefficients for unit conversion (*i.e.,* equal to 1.0 if millimetres and MPa are used).

Ultimate Rotation Capacity ϑ_u

The modified IK deterioration model captures the effects of the failure mode due to very large inelastic rotations through the parameter ϑ_u. Lignos and Krawinkler [162] recommended a value for ϑ_u equal to 0.06 rad for beams without RBS and 0.07 for beams with RBS. As a result, a more realistic value equal to 0.4 rad is generally recommended (Eads, 2013 [167]), which also contributes to avoid numerical convergence problems.

Rates of cyclic deterioration

The rates of cyclic deterioration are controlled by Rahnama [168], assuming that every component has a reference hysteretic energy dissipation capacity E_t, which is an inherent property of the components, regardless of the loading history applied to the component. The reference hysteretic energy dissipation capacity is expressed for steel structures as follows:

$$E_t = \lambda \cdot \vartheta_p \cdot M_y = \Lambda \cdot M_y$$

where $\Lambda = \lambda \cdot \vartheta_p$ is the reference cumulative rotation capacity. Other parameters must also be defined to complete the characterization of the modified IK model implemented in OPENSEES [163] with a bilinear hysteretic response. In particular, the coefficients c_s, c_c, c_a and c_k associated with the rate of strength, post-capping strength, accelerated reloading and unloading stiffness deterioration, respectively, can be generally assumed to be equal to 1 (Eads, 2013 [167]). Finally, if a symmetric hysteretic behaviour is considered between positive and negative loading directions, the coefficients D^+ and D^- which define the rate of cyclic deterioration in the two directions can be set equal to 1. Lignos and Krawinkler [162] also provided the necessary relationships that associate the parameters of the deterioration models described so far with geometric and material properties and detailing criteria that control deterioration in actual structural elements. The interested reader is referred to the original literature (Lignos et al. 2011 [162]) for further information regarding the experimental campaign and the statistical treatment of the results carried out by the authors.

2.4.3 Kinematics of the Panel zone

The behaviour of the Panel Zone (PZ) of MRFs has commonly represented the subject of both experimental and analytical tests to understand the complex interaction between column and beam components. The sources of deformation in the PZ can be divided into three different contributions (*i.e.,* axial, flexural and shear. Although the first two are usually negligible, the shear deformation may be significant and enable a node relative rotation mechanism (*i.e.,* beams rotating with respect to columns). Many numerical models have been proposed to represent the PZ mechanism, typically based on simple mechanical analogies consisting of rigid links and rotational spring assemblages. Among the proposed models, there is the 'Krawinkler model' initially proposed by Krawinkler *et al.,* 1971 [169] and Krawinkler *et al.,* 1978 [170], refined in 1987 [171] and published in its final version by Gupta *et al.* in 1999 [173]. This thesis focuses on the 'Krawinkler' model [169] and the 'Scissor model' [170]. It will be shown that the 'Scissors' model, referred to as the simplest mechanical model, can provide results

comparable to those obtained from the more complex mechanical models. In particular, results obtained from the 'Scissors' and the 'Krawinkler' models are identical, even though the kinematics of the Krawinkler model are significantly different. The following part will provide a complete description of the two models.

2.4.4 The 'Krawinkler' model

The model, as illustrated in Figure 2.79, consists of a rectangular assembly of rigid pin-ended elastic elements connected by rotational springs, modelled as zero-length rotational springs at the corners. The rotational springs at the upper right and lower left corners have no stiffness. Hence, they act as real hinges. The springs at the upper left and the lower right corner represent the PZ shear resistance and the column flange bending resistance. The two flexural and shear resistances of the column flange and panel are assumed to act in parallel.

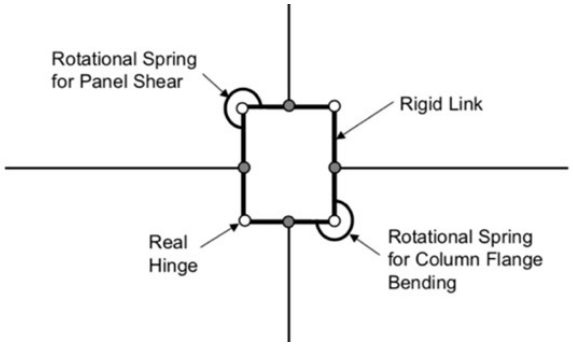

Figure 2.79. Krawinkler model for PZs in MRFs (after Charney and Downs, 2004 [174])

According to Krawinkler, the total response of the beam-column joint is equal to the sum of the response of the contribution of the panel and the column flange. The δ_γ represents the shear strain corresponding to the yielding of the PZ, while the flange contributes in remaining elastic up to an overall strain equal to $4\delta_\gamma$. The total trilinear relationship can be determined by adding the contribution of both components' strain hardening. The assumed force-displacement behaviour of the beam-column joint is illustrated in Figure 2.80. It is important to note that, to compute the properties of the equivalent zero-length springs, the V- δ relationships must be converted into the equivalent M- θ relationships.

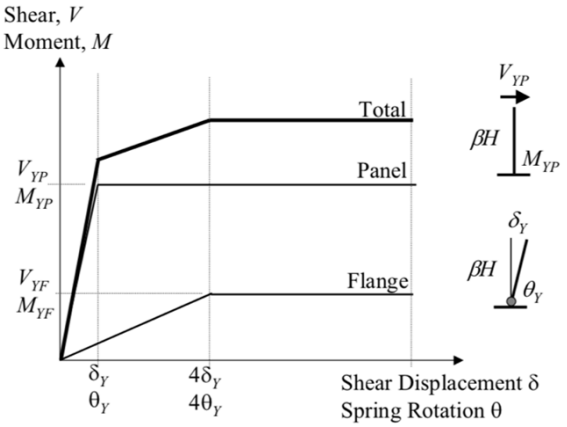

Figure 2.80. Force-displacement for beam-column joint (after Charney and Downs, 2004 [174])

2.4.4.1 Derivation of the properties of the panel zone

Elastic stiffness properties of the panel zone

To calculate the shear force in the panel V_p, the force transferred from the beam flanges $F_{Flange,G}$ to the PZ is preliminarily determined. A typical interior beam-column sub-assemblage of a MRF is shown in Figure 2.81. The sub-assemblage is considered in equilibrium with the shear force V_C, if the moments at the mid-span of the beams and mid-height of the column are equal to zero.

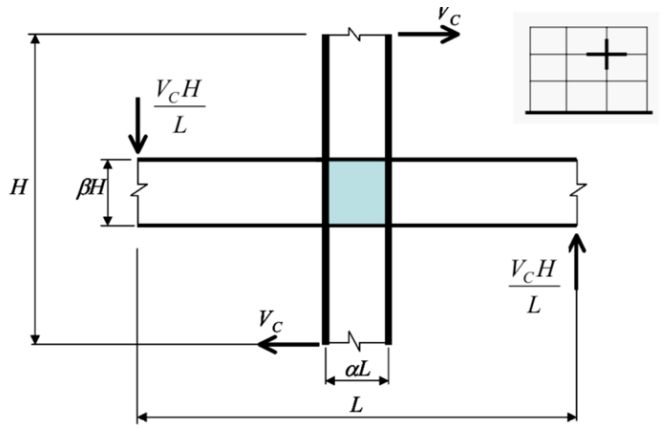

Figure 2.81. Cruciform subassembly in the PZ of MRFs (after Charney and Downs, 2004 [174])

L and H represent the length of the beam span and the column's height, and α and β account for the effective depths of the column and beam, as follows:

$$\alpha = \frac{d_c - t_{fc}}{L}$$

$$\beta = \frac{d_b - t_{fb}}{H}$$

where d_c, d_b are the column and the beam depth and t_{fc}, t_{fb} the thickness of the column and beam flanges. The beams are welded to the column flanges and doubler plates may be used to reinforce the PZ.

With simple static equilibrium, it is possible to calculate the moment at the midpoint of column flanges and girder flanges:

$$M_{Girder} = \frac{V_C H}{L}\left(\frac{L - \alpha L}{2}\right) = \frac{V_C H}{2}(1 - \alpha)$$

Subsequently, the equivalent force couple $F_{Flange,G}$ acting on the flange of the girder (considering the adequate depth of the girder itself) is equal to:

$$F_{Flange,G} = \frac{M_{Girder}}{\beta H} = \frac{V_C}{2\beta}(1-\alpha)$$

Considering Figure 2.82, the shear force acting on the panel web (V_{Panel}) is then calculated by summing the forces:

$$V_{Panel} = V_C - 2F_{Flange,G} = -\frac{V_C(1-\alpha-\beta)}{\beta}$$

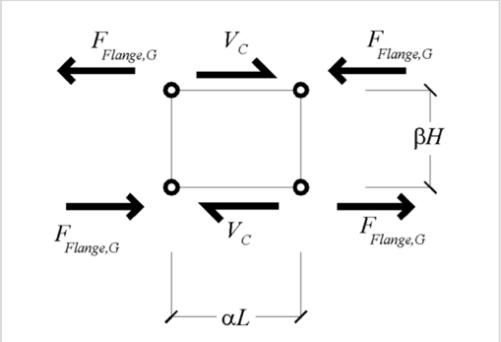

Figure 2.82. Krawinkler model PZ shear forces (after Charney and Downs, 2004 [174])

Subsequently, by applying the virtual work theorem, as shown in Figure 2.83, it is also possible to verify that the displacement $\delta_{Shear,P}$ induced by the shear force V_{Panel} is equal to:

$$\delta_{Shear,P} = \frac{V_{Panel}\beta H}{G t_p \alpha L}$$

where G is the steel shear modulus and t_p is the panel web's thickness, including any additional reinforcing doubler plate.

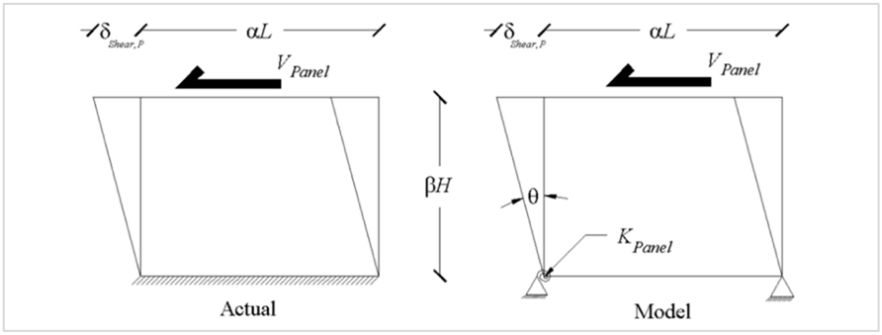

Figure 2.83. Application of virtual work to the "Krawinkler" model PZ (after Charney and Downs, 2004 [174])

Considering that the model requires a M - θ relationship, the moment in the model spring due to V_{Panel} is:

$$M_{Panel} = V_{Panel}\beta H = K_{Panel}\theta$$

The rotation angle θ_{Panel} can be approximated by using small displacement theory:

$$\theta_{Panel} = \frac{\delta_{Shear,P}}{\beta H}$$

Substituting and rewriting this equation in terms of stiffness and setting it equal to the stiffness determined using the $V - \delta$ relationship, the required stiffness K_{Panel} of the zero-length spring for the PZ is based on the model $M - \theta$ relationship is equal to:

$$K_{Panel} = \frac{M_{Panel}}{\theta} = \frac{V_{Panel}\beta^2 H^2}{\delta_{Shear,P}} = \frac{V_{Panel}\beta^2 H^2 G t_p \alpha L}{V_{Panel}\beta H} = G t_p \alpha L \beta H$$

Finally, the required stiffness K_{Panel} of the zero-length spring for the PZ is:

$$K_{Panel} = G t_p \alpha L \beta H$$

Inelastic strength properties of the panel zone

Assuming Von Mises's yield criterium (*i.e.,* $f_y/\sqrt{3} \cong 0{,}6 f_y$), the maximum shear force ($V_{Y,Panel}$) can be obtained as follows:

$$V_{Y,Panel} = 0{,}6 f_y d_c t_p = 0{,}6 f_y \alpha L t_p$$

where f_y is the yielding strength of the steel.

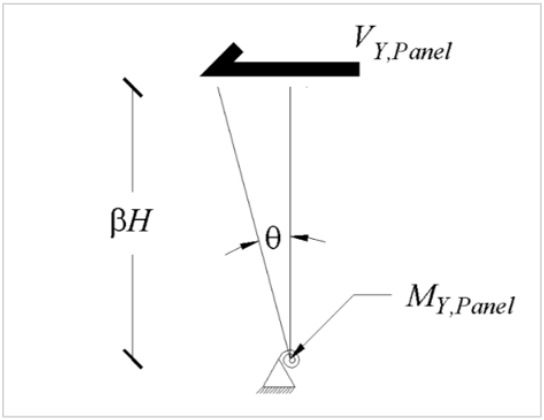

Figure 2.84. Krawinkler yield moment in the PZ (after Charney and Downs, 2004 [174])

The moment (Figure 2.84) is equal to:

$$M_{Y,Panel} = V_{Y,Panel}\beta H = 0{,}6 f_y \alpha L t_p \beta H$$

Inelastic strength properties of the column flanges

The flexural resistance of the column flanges is based on Krawinkler's assumption that the column flanges yield a deformation that is four times larger than the yield deformation (θ_y) of the panel. At this level of deformation, the flanges are assumed to develop plastic hinges and the plastic moment M_p developed at each plastic hinge is equal to:

$$M_p = f_y W_{pl} = f_y \frac{b_{cf} t_{cf}^2}{4}$$

where b_{cf} and t_{cf}^2 are the width and thickness of the column flange, respectively.

Considering Figure 2.85 and using the principle of virtual work:

$$V_{Flange}\delta_{shear,P} = 4M_p\theta$$

And substituting

$$\delta_{Shear,P} = \beta H\theta$$

$$V_{Flange} = f_Y \frac{b_{cf} t_{cf}^2}{\beta H}\theta$$

The yield moment of the flanges is equal to:

$$M_{Y,Flange} = 1.8 V_{Flange}\beta H = 1{,}8 f_Y b_{cf} t_{cf}^2$$

where the coefficient 1.8 is a correcting factor introduced by Krawinkler 1978 [XX], to fit experimental data.

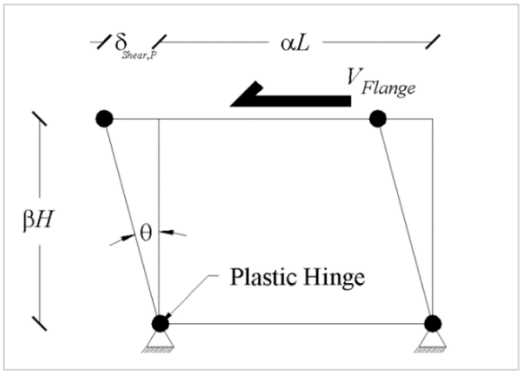

Figure 2.85. Application of virtual work to the "Krawinkler" model column flanges (after Charney and Downs, 2004 [174])

Elastic stiffness properties of the column flanges

From the previous equations, it has been shown that the yield rotation of the spring representing the panel component is:

$$\theta_Y = \frac{M_{Y,Panel}}{K_{Panel}} = \frac{0{,}6 f_y}{G}$$

According to the Krawinkler assumption 1971 [169]:

$$K_{Flange} = \frac{M_{Y,Flange}}{4\theta_{y,P}} = 0{,}75 G b_{cf} t_{cf}^2$$

2.4.5 The 'Scissors' model

The "Krawinkler" model represents one of the most accurate approaches for modelling the PZs of MRFs joints, even though it is characterized by computational complexity. Therefore, the "Scissors" model (Krawinkler *et al.* 1987 [171] Kim *et al.* 1995 [172]) can be conveniently adopted. The scissors model requires two nodes if rigid end zones are used for the column and beam regions inside the PZ, for 4 degrees of freedom, with a single hinge in the centre. As for the 'Krawinkler model', two rotational springs represent the shear and flange bending components. The properties of these springs keep the same formulation of the 'Krawinkler model', scaled by a factor equal to $(1-\alpha-\beta)^2$ and $(1-\alpha-\beta)$ as shown by the following relationships:

$$\boldsymbol{K_{Scissors} = \frac{K_{Krawinkler}}{(1-\alpha-\beta)^2}}$$

$$\boldsymbol{M_{Y,Scissors} = \frac{M_{Y,Krawinkler}}{(1-\alpha-\beta)}}$$

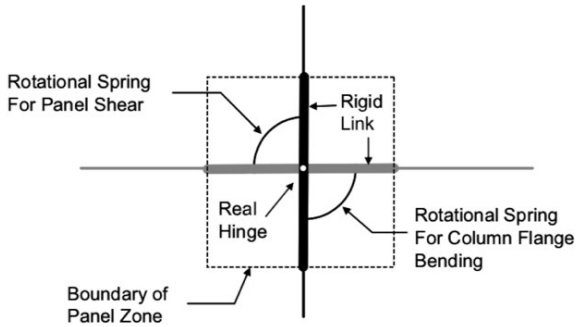

Figure 2.86. The "Scissor model" (after Charney and Downs, 2004 [174])

For the sake of brevity, the calculations for the "Scissors" model are omitted since they follow a consistent procedure with the one of the 'Krawinkler model', discussed before. Hereinafter, the main

formulations for the definition of the parameters belonging to the rotational springs for the panel shear and the column flange bending are reported:

$$K_{Panel} = \frac{Gt_p\alpha\beta HL}{(1-\alpha-\beta)^2}$$

$$\boldsymbol{M_{Y,Panel} = \frac{0,6f_y\alpha Lt_p\beta H}{(1-\alpha-\beta)}}$$

$$\boldsymbol{K_{Flange} = \frac{0,75 \cdot G \cdot b_{cf} \cdot t_{cf}^2}{(1-\alpha-\beta)^2}}$$

$$\boldsymbol{M_{Y,Flange} = \frac{1,8 \cdot f_Y b_{cf} \cdot t_{cf}^2}{(1-\alpha-\beta)}}$$

It is worth highlighting that, as noted by Charney and Downs, 2004 [174], adopting the Scissors should be limited only to frames with equal bay widths and storey heights. In these cases, the "Scissors" model proved to be generally as effective as the "Krawinkler" one. Conversely, in the presence of irregular structures, the more refined "Krawinkler" approach should be preferred (Castro *et al.,* 2008 [175]). When the 'Krawinkler model' progresses through its motion, its configuration is able to maintain the PZ boundaries, causing an offset to develop between the column and the girder centerlines. Conversely, in the "Scissors" model, the right angles between the PZ boundaries and the adjacent beams and columns cannot be maintained, resulting in approximated deflections (Gupta *et al.,* 1999 [173]). As shown in Figure 2.87, the "Scissors" model (on the right) cannot capture, in the deformed shape, the offset of the centerlines of the columns and girders, as done by the "Krawinkler" model (on the left).

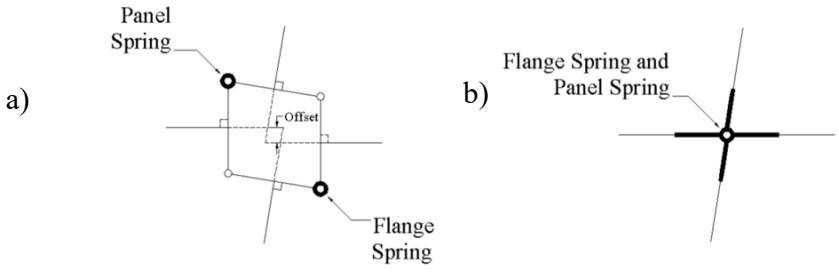

Figure 2.87. Kinematics of 'Krawinkler model' a) and 'Scissors' model b) (after Charney and Downs, 2004 [174])

2.5 Personal contribution

Chapter 2 covers the Literature Review in the fields of interest, comprising bibliographic studies to frame the present work in a more general research field. The section introduces innovative structural solutions for steel MRFs, focusing on friction connections and self-centring systems. The attention is paid to the innovative configurations of column bases proposed within the current literature, equipped with damage-free and self-centring systems. Consequently, no author contribution is provided.

2.6 References

1 Astaneh-Asl A. Seismic Design of Bolted Steel Moment-Resisting Frames, University of California, Berkley, USA, 1995

2 F.M. Mazzolani, V. Piluso, Theory and Design of Seismic Resistant Steel Frames. London, UK, 1996.

3 Bruneau, M., Uang, C. M., Whittaker, A., 1998. Ductile Design of Steel Structures. McGraw-Hill, New York, 1998.

4 C. Faella, V. Piluso, G. Rizzano, Structural steel semirigid connections. CRC Press, Boca Raton (FL), 2000.

5 Roeder C.W., Popov E.P., Inelastic behaviour of eccentrically braced steel frames under cyclic loading, Berkeley Earthquake Engineering Research Center. University of California, Report No. UCB/EERC-77/18, Berkeley, CA, USA, 1977.

6 Hielmstad D.K., Popov E.P., Characteristics of eccentrically braced frames, Journal of Structural Engineering, 110(2), 340-353, 1984.

7 Okazaki T., Arce G., Ryu H.-C., Engelhardt M.D. Experimental study of local buckling, overstrength, and fracture of links in eccentrically braced frames. Journal of Structural Engineering, 131(10): 1526 - 1535, 2005.

8 Costanzo S., D'Aniello M., Landolfo R., Seismic design rules for ductile Eurocode-compliant two-storey X concentrically braced frames, *Steel and Composite Structures*, 36, 273-291, 2020.

9 Paulay, T. and Priestley, M.J.N. (1992). Seismic Design of Reinforced Concrete and Masonry Buildings. John Wiley & Sons, Chichester, UK.

10 EN 1998-1, Eurocode 8: Design of structures for earthquake resistance – Part 1: General rules, seismic actions and rules for buildings, European Committee for Standardization, Brussels.

11 ANSI/AISC 360-10 Specification for Structural Steel Buildings. *American Institute of Steel Construction*, Chicago, USA, 2010.

12 ANSI/AISC 341-16 Seismic provisions for structural steel buildings American Institute of Steel Construction, Chicago, USA, 2016.

13 ASCE/SEI 7–16, Minimum Design Loads and Associated Criteria for Buildings and Other Structures, American Society of Civil Engineers, USA, 2017.

14 R. Tremblay, P. Timler, M. Bruneau, A. Filiatrault, Performance of steel structures during the 1994 Northridge earthquake. J. Civil. Eng. 22(2) (1995) 338−60.

15 Duane K. Miller, Lessons learned from the Northridge earthquake, Engineering Structures, Volume 20, Issues 4–6, 1998, 249-260

16 M. Nakashima, K. Inoue, M. Tada, Classification of damage to steel buildings observed in the 1995 Hyogoken-Nanbu earthquake. Eng. Struct. 20(4–6) (1998) 271–81.

17 M. Midorikawa, I. Nishiyama, M. Tada, T. Terada, Earthquake and tsunami damage on steel buildings caused by the 2011 Tohoku Japan earthquake. Proceedings of the International Symposium on Engineering Lessons Learned From the 2011 Great East Japan Earthquake. Japan Association for Earthquake Engineering, Tokyo, Japan, 2012.

18 Okazaki T, Lignos DG, Midorikawa M, Ricles JM, Love J. Damage to steel buildings observed after the 2011 Tohoku-oki earthquake. Earthquake Spectra 2013; 29(SUPPL.1): 219–243. https://doi: 10.1193/1.4000124

19 FEMA-355 E- State of the Art Report on Past Performance of Steel Moment-Frame Buildings in Earthquakes
20 F. Freddi, V. Novelli, R. Gentile, E. Veliu, A. Andonov, S. Andreev, F. Greco, E. Zhuleku, Observations from the 26th November 2019 Albania Earthquake: the Earthquake Engineering Field Investigation Team (EEFIT) mission. Bull. Earth. Eng., 19 (2021) 2013-2044.
21 EN 1993-1-1, Eurocode 3: Design of steel structures, Part 1-1: Design of steel structures: Design of joints, 2005, European Committee for Standardization, Brussels.
22 SAC, 2000b, "Recommended Seismic Evaluation and Upgrade Criteria for Existing Welded Steel Moment-Frame Buildings", prepared by the SAC Joint Venture for the Federal Emergency Management Agency, Report No. FEMA-351, Washington, D. C.
23 Steenhuis, M., Jaspart, J. P., Gomes, F., Leino, T., Application of the component method to steel joints, Proceeding of the Control of the Semi-Rigid Behaviour of Civil Engineering Structural Connections Conference, 1998.
24 Augusto, H., Simões da Silva, L., Rebelo, C., and Castro, J. M., Cyclic behaviour characterization of web panel components in bolted end-plate steel joints, J. Constr. Steel Res., vol. 133, pp. 310–333, Jun. 2017.
25 Girão Coelho, A. M., Bijlaard, F. S. K., da Silva, L. S., Experimental assessment of the ductility of extended end plate connections, Eng. Struct., 2004.
26 Iannone, F., Latour, M., Piluso, V. and Rizzano, G., Experimental Analysis of Bolted Steel Beam-to-column Connections: Component Identification, J. Earthq. Eng., vol. 15, no. 2, pp. 214–244, 2011.
27 Swanson, J., Leon, R.T., Bolted Steel Connections: Tests on T-stub Components, ASCE, Journal of Structural Engineering, Vol.126, No.1, pp.50-56, 2000.
28 Francavilla, A.B., Latour, M., Piluso, V., Rizzano, G., "Design of full-strength full-ductility extended end-plate beam-to-column joints", Journal of Constructional Steel Research, 148, pp. 77-96, 2018.
29 Latour, M., Piluso, V. and Rizzano, G., Cyclic modelling of bolted beam-to-column connections: Component approach, J. Earthq. Eng., vol. 15, no. 4, 2011.
30 CEN [2005]: EN 1993-1-8 Eurocode 3: Design of Steel Structures. Part 1-8: Design of Joints, CEN, European Committee for Standardization, 2005.
31 Iwankiw, R. N. and Carter, C. J., "The Dogbone: A New Idea to Chew On", Modern Steel Construct., Vol. 36. No.4, pp. 18-23, AISC, Chicago IL, 1996.
32 Chen, S. J., Yeh, C. H. and Chu, J. M., "Ductile Steel Beam-Column Connections for Seismic Resistance", J. Struct. Engrg., Vol. 122, No. 11, pp. 1292-1299, ASCE, 1996.
33 ANSI/AISC, "Prequalified Connections for Special and Intermediate Steel Moment Frames for Seismic Applications", 2016.
34 Latour, M., Analisi teorico-sperimentale di collegamenti dissipativi a parziale ripristino di resistenza in strutture intelaiate in acciaio, Ph. D. Thesis, University of Salerno, 2010.
35 Di Benedetto S, Francavilla AB, Latour M, Piluso V, Rizzano G. Pseudo-dynamic testing of a full-scale two-storey steel building with RBS connections, *Eng. Struct.* 2020; 110494
36 Francavilla, A.B., Latour, M., Piluso, V., Rizzano, G., Bolted T-stubs: A refined model for flange and bolt fracture modes, Steel and Composite Structures, 20 (2), pp. 267-293, 2016.
37 Bravo, M. A., Herrera, R. A., Performance under cyclic load of built-up T-stubs for Double T

moment connections, Journal of Constructional Steel Research, Volume 103, Pages 117-130, ISSN 0143-974X

38 Wang, P., Sun, L., Xia, C., Gu, H., Liu, Y., Liu, M., Liu, F., Cyclic behaviour of T-stub connection to hollow section steel column using TSOBs, Journal of Constructional Steel Research, Volume 185, 106874, ISSN 0143-974X, https://doi.org/10.1016/j.jcsr.2021.106874., 2021

39 Irvani, M., Ezati, H., Khafajeh, R., Kalat Jaari, V. R., Numerically study on the seismic response of partially restrained moment connection with structural fuse T-stub for European sections, Structures, Volume 35, Pages 82-105, ISSN 2352-0124

40 Bayat, K., Shekastehband, B., Seismic performance of beam to column connections with T-shaped slit dampers, Thin-Walled Structures, Volume 141, Pages 28-46, ISSN 0263-8231, https://doi.org/10.1016/j.tws.2019.04.010, 2019.

41 Latour, M., Rizzano, G., Design of X-shaped double split tee joints accounting for moment–shear interaction, Journal of Constructional Steel Research. 104. 10.1016/j.jcsr.2014.10.015, 2015.

42 Murray TM. AISC design guide 4. Extended end-plate moment connections Chicago, IL: AISC (American Institute of Steel Construction); 1990.

43 Sumner EA, Murray TM. Behaviour of extended end-plate moment connections subject to cyclic loading. J Struct Eng-ASCE 2002;128(4):501–8.

44 Da Silva, L. S., Rebelo L., Mota, C., "Extension of the component method to end-plate beam-to-column steel joints subjected to seismic loading," Trends Civ. Struct. Eng. Comput. Comput. Sci., vol. 22, pp. 149–167, 2009.

45 AISC (American Institute of Steel Construction). Prequalified connections for special and intermediate steel moment frames for seismic applications. ANSI/AISC 358-16, Chicago, IL; 2016.

46 R. Tartaglia, M. D'Aniello, G.A. Rassati, J.A. Swanson, R. Landolfo, Full strength extended stiffened end-plate joints: AISC vs recent European design criteria, Eng. Struct. 159 (2018) 155–71

47 R. Tartaglia, M. D'Aniello, G.A. Rassati, Proposal of AISC-compliant seismic design criteria for ductile partially restrained endplate bolted joints. J. Constr. Steel Res. 159 (2019) 364-383

48 M. D'Aniello, R. Tartaglia, S. Costanzo, R. Landolfo, Seismic design of extended stiffened end-plate joints in the framework of Eurocodes, J. Constr. Steel Res. 128 (2017) 512–527.

49 J.E. Grauvilardell, D. Lee, J. F. Hajjar, R.J. Dexter, Synthesis of Design, Testing And Analysis Research on Steel Column Base Plate Connections In High-Seismic Zones, 2005, Structural Engineering Report No. ST-04-02, University of Minnesota

50 Lee, Soon-Sik and Goel, S. C. "Performance-Based Design of Steel Moment Frames Using Target Drift and Yield Mechanism." Report No. UMCEE 01-17, Department of Civ. & Env. Engrg., University of Michigan, Ann Arbor, MI, USA, 2001.

51 T. Takamatsu, H. Tamai Non-slip-type restoring force characteristics of an exposed-type CB. J. Constr. Steel Res. 61(7) (2005) 942–961.

52 M. Latour, V. Piluso, G. Rizzano, Rotational behaviour of column base plate connections: Experimental analysis and modelling, Engineering Structures, Volume 68, 2014, Pages 14-23, ISSN 0141-0296

53 G.N. Stamatopoulos, J.Ch. Ermopoulos, Interaction curves for column base-plate connections, Journal of Constructional Steel Research, Volume 44, Issues 1–2, 1997, Pages 69-89, ISSN 0143-974X

54 P. Torre-Rodas, F. Zareian, A. Kanvinde, Hysteretic model for exposed column-base connections,

J. Struct. Eng.; 142(12) (2016) 1–14.
55 H. Inamasu, A. M. Kanvinde, D.G. Lignos, Seismic Stability of Wide-Flange Steel Columns Interacting with Embedded Column Base Connections, J. Struc. Eng., 145(12), 2019
56 D.A. Grilli, A.M. Kanvinde, Embedded column base connections subjected to seismic loads: Strength model, Journal of Constructional Steel Research, Volume 129, 2017, Pages 240-249, ISSN 0143-974X
57 Torres-Rodas P, Zareian F, Kanvinde A. Seismic Demands in Column Base Connections of Steel Moment Frames. Earthquake Spectra. 2018;34(3):1383-1403.
58 H. Inamasu, A. M. Kanvinde, D.G. Lignos, Seismic design of non-dissipative embedded column base connections, J. Const. Steel Res. 177, 106417, 2021
59 Y. Cui, M. Nakashima, Hysteretic behaviour and strength capacity of shallowly embedded steel column bases with SFRCC slab, Earth. Eng. Struct. Dyn, 40(13), 1495-1513, 2011
60 A. Yu-Feng, H. Lin-Hai, Behaviour of concrete-encased CFST columns under combined compression and bending, J. Const. Steel Res. 101, 314-330, 2014
61 Wald, F., Gresnigt, A. M., Weynand, K., Jaspart, J. P., Application of the component method to column bases, Proceeding of the Control of the Semi-Rigid Behaviour of Civil Engineering Structural Connections Conference, 1998.
62 M. Latour, G. Rizzano, Full strength design of column base connections accounting for random material variability, Eng. Struct. 48 (2013) 458–71.
63 M. Latour, G. Rizzano, A theoretical model for predicting the rotational capacity of steel base joints, Eng. Struct. 91 (2013) 89–99.
64 M. Latour, V. Piluso, G. Rizzano, Rotational behaviour of column base plate connections: Experimental analysis and modelling, Eng. Struct. 68 (2014) 14–23.
65 A. Elkady, D.G. Lignos. Full-scale testing of deep wide-flange steel columns under multiaxis cyclic loading: loading sequence, boundary effects, and lateral stability bracing force demands. J. Struc. Eng., 144(2), 2018
66 A. Elkady, G. Guell, D.G. Lignos, Proposed methodology for building-specific earthquake loss assessment including column residual axial shortening, Earthq. Eng. Struct. Dyn. 49 (2020) 339–355.
67 H. Inamasu, A. de Castro e Sousa, G. Guell, D.G. Lignos: Anchor-yield exposed column bases for minimizing residual deformations in seismic-resistant steel moment frames, Earth. Eng. Struc. Dyn. 50 (2021)1083–1100.
68 H. Inamasu, D.G. Lignos. Seismic performance of steel columns interacting with embedded column bases while exhibiting inelastic deformations, Eng. Struct. 251, Part A (2022) 113381
69 F. Zareian, A. Kanvinde, Effect of column-base flexibility on the seismic response and safety of steel moment-resisting frames, Earth. Spectra 29 (2013) 1537–1559
70 F. Zareian, A. Kanvinde, P. Torre-Rodas, F. Flores, F. Zareian, Seismic response of steel moment frame considering gravity system and column base flexibility, Proc. 11th US Natl. Conf. Earthq. Eng., June 25–29, Los Angeles, USA, 2018.
71 Grigorian CE, Yang TS, Popov EP. Slotted bolted connection energy dissipators, Earthq. Spectra 1993; 9(3): 491–504.
72 MacRae GA, Clifton GC, Mackinven H, Mago N, Butterworth JW, Pampanin S. The Sliding Hinge Joint Moment connection, Bulletin of The New Zealand Society for Earthq. Eng. 2010; 43(3): 202–

212.
73 MacRae G., Clifton G.C.: “New Technology Applications, Recent Developments and Research Directions for Seismic Steel Structures in New Zealand”, Asian Conference on Earthquake Engineering, Bangkok, Thailand, December, 2010
74 H.H. Khoo, C. Clifton, J. Butterworth, G. MacRae, S. Gledhill, G. Sidwell, Development of the self-centring sliding hinge joint with friction ring springs, J. Constr. Steel Res. 78 (2012) 201–211.
75 MacRae G., Clifton G.C.: “Low Damage Design of Steel Structures”, Steel Innovations 2013, Workshop, 21-22 February 2013, Christchurch
76 RFCS FREEDAM: FREE from DAMage steel connections, 2015-2018. Fund for Coal and Steel Grant Agreement No. RFSR-CT-2015-00022.
77 RFCS FREEDAM PLUS Valorisation of knowledge for FREE from DAMage steel connections, Seismic Design of Steel Structures with FREE from DAMage joints, Part I: Informative Documents, 2020
78 Latour M., Piluso V., Rizzano G.: “Experimental analysis on friction materials for supplemental damping devices”, Construction and Building Materials 65, pp. 159-176, 2014.
79 A.B. Francavilla, M. Latour, V. Piluso, G. Rizzano, Design criteria for beam-to-column connections equipped with friction devices. J. Constr. Steel Res. 172 (2020)106240.
80 G.F. Cavallaro, A. Francavilla, M. Latour, V. Piluso, G. Rizzano, Experimental behaviour of innovative thermal spray coating materials for FREEDAM joint. Composites Part B 115 (2017) 289-299
81 G.F. Cavallaro, A. Francavilla, M. Latour, V. Piluso, G. Rizzano, Cyclic behaviour of friction materials for low yielding connections. Soil Dyn. Earthq. Eng. 114 (2018) 404–423.
82 Latour M, Piluso V, Rizzano G. Experimental analysis of beam-to-column joints equipped with sprayed aluminium friction dampers, J. Constr. Steel Res. 2018; 146: 33–48.
83 M. Latour, M. D’Aniello, M. Zimbru, G. Rizzano, V. Piluso, R. Landolfo, Removable friction dampers for low-damage steel beam-to-column joints, Soil Dyn. Earthq. Eng. 115 (2018) 66–81.
84 A.F. Santos, A. Santiago, M. Latour, G. Rizzano, L.S. da Silva, Response of friction joints under different velocity rates. J. Const. Steel Res. 168 (2020)
85 M. D’Antimo, M. Latour, G.F. Cavallaro, J-P. Jaspart, S. Ramhormozian, J-F. Demonceau, Short- and long- term loss of preloading in slotted bolted connections, J. Constr. Steel Res. 167 (2020) 105956
86 Tartaglia R, D'Aniello M, Campiche A, Latour M, Symmetric friction dampers in beam-to-column joints for low-damage steel MRFs, J. Constr. Steel Res. 2021;184:106791. https://doi.org/10.1016/j.jcsr.2021.106791
87 Kelly, J.M., Tsztoo, D.F. (1977). “Earthquake simulation testing of a stepping frame with energy-absorbing devices. 666 NZ Soc. Earthquake Eng. Bull.; 10(4): 196-207.
88 G.A. MacRae, C.R. Urmson, W.R. Walpole, P. Moss, K. Hyde, G.C. Clifton, Axial Shortening of Steel Columns in Buildings Subjected to Earthquakes, Bulletin of The New Zealand Society for Earthq. Eng. 42(4) (2009) 275–287.
89 J. Borzouie, G.A. MacRae, J.G. Chase, G.W. Rodgers, G.C. Clifton. Experimental studies on cyclic performance of CB strong axis – aligned asymmetric friction connections. J. Struct. Eng. (ASCE), 142(1) (2016) 1–10.
90 J. McCormick, H. Aburano, M. Nakashima, Permissible residual deformation levels for building

structures considering both safety and human elements, 14th World Conf. Earthq. Eng. 12-17 Oct 2008, Beijing, China.

91 FEMA P58-1. Seismic performance assessment of buildings. Volume 1-Methodology. Applied Technology Council, Redwood City, CA, 2012.

92 Christopoulos, C.; Filiatrault, A.; Folz, B. Seismic response of self-centring hysteretic SDOF systems. Earthq. Eng. Struct. Dyn. 2002, 31, 1131–1150.

93 Seo, C.Y.; Sause, R. Ductility demands on self-centring systems under earthquake loading. ACI Struct. J. 2005, 102, 275.

94 S. Pampanin, Reality-Check and renewed challenges in Earthquake Engineering: implementing low-damage systems from theory to practice. Bull New Zealand Society Earthq Eng. 45(4) (2012) 137-160.

95 G. MacRae, G.C. Clifton, Low Damage Design of Steel Structures, Steel Innovations 2013 Workshop, Christchurch, 21-22 Feb. 2013, New Zealand.

96 N.B. Chancellor, M.R. Eatherton, D.A. Roke, T. Akbas, Self-centring Seismic Lateral Force Resisting Systems: High Performance Structures for the City of Tomorrow, Buildings 4 (2014) 520–548.

97 F. Freddi, C. Galasso, G. Cremen, A. Dall'Asta, L. Di Sarno, A. Giaralis, L.F. Gutiérrez-Urzúa, C. Málaga-Chuquitaype, S. Mitoulis, C. Petrone, A. Sextos, L. Sousa, K. Tarbali, E. Tubaldi, J. Wardman, G. Woo, Innovations in Earthquake Risk Reduction for Resilience: Recent Advances and Challenges, International Journal of Disaster Risk Reduction, 60 (2021) 102267.

98 C. Fang, W. Wang, C. Qiu, S. Hu, G.A. MacRae, M.R. Eatherton, Seismic resilient steel structures: A review of research, practice, challenges and opportunities. J. Constr. Steel Res. 191 (2022) 107172.

99 Priestley, M.J.N. (1991). Overview of the PRESSS Research Programme, PCI Journal, Vol.36, No.4, pp.50 57.

100 Priestley MJN and MacRae GA, 1996. Seismic Tests of Precast Beam-to-column Joint Subassemblage with Unbonded Tendons, PCI Journal, January-February; 64-80.

101 Priestley, M.J.N., Sritharan, S., Conley, J.R. and Pampanin, S. (1999). "Preliminary results and conclusions from the PRESSS five-storey precast concrete test building." PCI Journal, 44(6), 42-67.

102 Holden, T.; Restrepo, J.; Mander, J.B. Seismic performance of precast reinforced and prestressed concrete walls. *J. Struct. Eng.* 2003, *129*, 286–296.

103 Kurama, Y.; Pessiki, S.; Sause, R.; Lu, L.W. Seismic behaviour and design of unbonded *PT* precast concrete walls. *PCI J.* 1999, *44*, 72–89.

104 Palermo, A.; Pampanin, S.; Marriott, D. Design, modeling, and experimental response of seismic resistant bridge piers with posttensioned dissipating connections. J. Struct. Eng. 2007, 133, 1648–1661.

105 Pollino, M.; Bruneau, M. Seismic testing of a bridge steel truss pier designed for controlled rocking. J. Struct. Eng. 2010, 136, 1523–1532

106 Roke, D.; Sause, R.; Ricles, J.M.; Chancellor, N.B. Damage-Free Seismic-Resistant Self-centring Concentrically-Braced Frames; ATLSS Report 10–09; Lehigh University: Bethlehem, PA, USA, 2010.

107 Eatherton, M.; Hajjar, J.; Ma, X.; Krawinkler, H.; Deierlein, G. Seismic Design and Behaviour of

Steel Frames with Controlled Rocking—Part I: Concepts and Quasi-Static Subassembly Testing. In Proceedings of the ASCE Structures Congress, Orlando, FL, USA, 12–15 May 2010.
108 S. Hu, W. Wang, B. Qu, Alam M. Shahria, Self-centring energy-absorbing rocking core system with friction spring damper: experiments, modeling and design, Eng. Struct. 225 (2020), 111338.
109 S. Hu, W. Wang, B. Qu, Self-centring companion spines with friction spring dampers: validation test and direct displacement-based design, Eng. Struct. 238 (2021), 112191.
110 Y. Shen, F. Freddi, J. Li, Experimental and numerical investigations on seismic behaviour of socket connections and hybrid connections for PCFT bridge columns. Eng. Stru. 253 (2022) 113833.
111 S. Hu, W. Wang, B. Qu, Self-centring companion spines with friction spring dampers: Validation test and direct displacement-based design, Eng. Struct. 238 (2021), 112191,
112 S. Hu, S. Zhu, W. Wang, M. S. Alam, Structural and nonstructural damage assessment of steel buildings equipped with self-centring energy-absorbing rocking core systems: A comparative study, J. Constr. Steel Res., 198 (2022), 107559
113 Kurama, Y.C.; Weldon, B.D.; Shen, Q. Experimental evaluation of posttensioned hybrid coupled wall subassemblages. *J. Struct. Eng.* 2006, *132*, 1017–1029.
114 Rahman, M.A.; Sritharan, S. Performance-based seismic evaluation of two five-storey precast concrete hybrid frame buildings. *J. Struct. Eng.* 2007, *133*, 1489–1500.
115 J. Ricles, R. Sause, M. Garlock, C. Zhao, Posttensioned Seismic-Resistant Connections for Steel Frames, J. Struct. Eng. 127(2) (2001) 113–121.
116 C. Christopoulos, A. Filiatrault, C-M. Uang, B. Folz, Posttensioned energy dissipating connections for moment-resisting steel frames, J. Struct. Eng. 128(9) (2002) 1111–20.
117 Garlock, M.M.; Ricles, J.M.; Sause, R. Experimental studies of full-scale posttensioned steel connections. *J. Struct. Eng.* 2005, *131*, 438–448.
118 Rojas P., Suárez D.C., Ricles J.M., Sause R.: "Seismic Performance of PT Steel Moment Resisting Frames With Friction Devices", J. Struct. Eng., 2005, 131(4): 529-540
119 Wolski, M.; Ricles, J.M.; Sause, R. Seismic Resistant Self-centring Steel Moment Resisting Frames with Bottom Flange Friction Devices. In *Behaviour of Steel Structures in Seismic Areas: 5th International Conference on Behaviour of Steel Structures in Seismic Areas*; Taylor & Francis: London, UK, 2006.
120 H.J. Kim, C. Christopoulos, Friction damped posttensioned self-centring steel moment-resisting frames, J. Struct. Eng. 134(11) (2008) 1768–79.
121 Kim H-J, Christopoulos C. Seismic design procedure and seismic response of PT self-centring steel frames. Earthq Eng Struct Dyn. 2009;38:355–376.
122 C. Chou, J. Chen, Development of floor slab for steel post-tensioned self-centring moment frames, J. Constr. Steel Res. 67 (10) (2011) 1621–1635.
123 G. Vasdravellis, T.L. Karavasilis, B. Uy, Large-scale experimental validation of steel posttensioned connections with web hourglass pins. J. Struct. Eng. 139 (2012) 1033–1042.
124 ABAQUS/Standard and ABAQUS/Explicit – Version 2017. ABAQUS Theory Manual, Dassault Systems, 2016. http://130.149.89.49:2080/v6.14/books/usb/default.htm
125 Ahmadi O., Ricles, JM, Sause R., Modeling and seismic collapse resistance study of a steel SC-MRF, Soil Dynamics and Earthquake Engineering, 113 (2018), 324-338
126 Dimopoulos C, Freddi F, Karavasilis TL, Vasdravellis G. Progressive collapse of Self-centring moment resisting frames. Eng Struct. 2020; 208:109923

127 X. Huang, X. Zhou, Y. Wang, R. Zhu, Development of resilient friction beams and application to moment-resisting frames. J. Build. Eng. 45 (2022) 103494

128 L. Pieroni, F. Freddi, M. Latour, Effective placement of Self-centring Damage-Free Connections for Seismic-Resilient Steel Moment Resisting Frames, Earth. Eng. Stru. Dyn. 51(5) (2022) 1292–1316.

129 L. Pieroni, S. Di Benedetto, F. Freddi, M. Latour, Genetic Algorithm for the optimal placement of Self-centring Damage-Free joints in steel MRFs, J. Constr. Steel Res., 197 (2022)

130 Christopoulos, C.; Tremblay, R.; Kim, H.J.; Lacerte, M. Self-centring energy dissipative bracing system for the seismic resistance of structures: Development and validation. J. Struct. Eng. 2008, 134, 96–107.

131 Tremblay, R.; Poirier, L.P.; Bouaanani, N.; Leclerc, M.; Rene, V.; Fronteddu, L.; Rivest, S. Innovative Viscously Damped Rocking Braced Steel Frames. In Proceedings of the 14th World Conference on Earthquake Engineering, Beijing, China, 12–17 October 2008.

132 Miller, D.J.; Fahnestock, L.A.; Eatherton, M.R. Development and experimental validation of a nickel–titanium shape memory alloy self-centring buckling-restrained brace. *Eng. Struct.* **2012**, *40*, 288–298.

133 Eatherton, M.R.; Fahnestock, L.A.; Miller, D. Computational study on the behaviour of self-centring buckling restrained braces. Earthq. Eng. Struct. Dyn. 2014, doi:10.1002/eqe.2428.

134 L. Tong, Y. Zhang, X. Zhou, A. Keivan, R. Li, Experimental and analytical investigation of D-type self-centring steel eccentrically braced frames with replaceable hysteretic damping devices, J. Struct. Eng. 145 (1) (2019), 04018229.

135 A. Keivan, Y. Zhang, Nonlinear seismic performance of Y-type self-centring steel eccentrically braced frame buildings, Eng. Struct. 179 (2019) 448–459.

136 W. Wang, J. Kong, Y. Zhang, G. Chu, Y. Chen, Seismic behaviour of self-centring modular panel with slit steel plate shear walls: experimental testing, J. Struct. Eng. 144 (1) (2018), 04017179.

137 A Lettieri, A de la Peña, F Freddi, M Latour, Damage-free self-centring links for eccentrically braced frames: development and numerical study, Journal of Constructional Steel Research, Volume 201, 2023, 107727, ISSN 0143-974X.

138 M. Ikenaga, T. Nagae, M. Nakashima, K. Suita, Development of CBs having self-centring and damping capability. 5th Int. Conf. on Behaviour of Steel Struct. in Seismic Areas 2006, Yokohama, Japan.

139 H. Mackinven, G.A. MacRae, S. Pampanin, G.C. Clifton, J. Butterworth, Generation four steel moment frame joints. 8th Pacific Conf. on Earthq. Eng. 2007, Singapore.

140 C. Chou, J.H. Chen, Analytical model validation and influence of CBs for seismic responses of steel PT self-centring MRF systems. Eng. Struct. 33(9) (2011) 2628–2643.

141 H. Chi, J. Liu, Seismic behaviour of PT CB for steel self-centring moment resisting frame, J. Constr. Steel Res. 78 (2012) 117–130.

142 T. Yamanishi, K. Kasai, T. Takamatsu, H. Tamai, Innovative column-base details capable of tuning rigidity and strength for low to medium-rise steel structures. 15th World Conf. on Earthq. Eng. 2012, Lisbon, Portugal.

143 Chen C-C, Lin H-W, Tsai R-S, Self-Centring and energy dissipation of a PT steel column base, (2014), Second European conference on earthquake engineering and seismology, Istanbul

144 F. Freddi, C.A. Dimopoulos, T.L. Karavasilis, Rocking damage-free steel CB with Friction Devices:

design procedure and numerical evaluation, Earthq. Eng. Struct. Dyn. 46 (2017) 2281–2300.
145 F. Freddi, C.A. Dimopoulos, T.L. Karavasilis, Experimental evaluation of a rocking damage-free steel CB with friction devices, J. Struct. Eng. 146(10) (2020) 04020217
146 V. Kamperidis, T.L. Karavasilis, G. Vasdravellis, Self-centring steel CB with metallic energy dissipation devices, J. Constr. Steel Res. 149 (2018) 14–30.
147 Kamperidis VC, Papavasileiou GS, Kamaris GS, Vasdravellis G. Seismic collapse of self-centring steel MRFs with different column base structural properties, J. Constr. Steel Res. 2020; 175: 106364.
148 X.T. Wang, C.D. Xie, L.H. Lin, J. Li, Seismic behaviour of self-centring concrete-filled square steel tubular (CFST) CB. J. Constr. Steel Res. 156 (2019) 75–85.
149 B. Wang, S. Zhu, C-X Qui, H. Jin, High-performance self-centring steel columns with shape memory alloy bolts: Design procedure and experimental evaluation. Eng. Struc. 182 (2019) 446-458
150 B. Wang, H. Jiang, J. Wang, Numerical simulation and behaviour insights of steel columns with SMA bolts towards earthquake resilience. J. Constr. Steel Res. 161 (2021) 285-295
151 Goshtaei S.M., Moradi S., Khandaker M., Hossain A., Sensitivity analysis of self-centring column base connections with shape memory alloy bolts, Structures, 38, 2022, 1050-1065
152 R. Zhang, J.-Y. Xie, K. E. Chouery, J. Liu, L.-J. Jia, P. Xiang, X. Zhao, G. A. Macrae, G. C. Clifton, R. P. Dhakal, S. Ramhormozian, Z. Yan, Strong axis low-damage performance of rocking column-base joints with asymmetric friction connections, Journ Constr Steel Res, 191, 2022, 107175
153 George S. Kamaris, Georgios S. Papavasileiou, Vasileios C. Kamperidis, George Vasdravellis, Residual drift risk of self-centring steel MRFs with novel steel column bases in near-fault regions, Soil Dynamics and Earthquake Engineering, Volume 162, 2022, 107391, ISSN 0267-7261
154 Dongde Sun, Yong Yang, Yinke Ma, Yicong Xue, Yunlong Yu, Shiqiang Feng, Seismic behaviour of self-centring column base with replaceable stiffener angle steels, Thin-Walled Structures, Volume 181, 2022, 110113, ISSN 0263-8231
155 Z. Yan, S. Ramhormozian, G. Charles Clifton, R. Zhang, P. Xiang, L.-J. Jia, G. A. MacRae, X. Zhao, Numerical studies on the seismic response of a three-storey low-damage steel framed structure incorporating seismic friction connections, Resilient Cities and Structures, 2(1), 2023, 91-102.
156 M. Latour, G. Rizzano, A. Santiago, L. Da Silva, Experimental response of a low-yielding, self-centring, rocking CB joint with friction dampers, Soil Dyn. Earthq. Eng. 116 (2019) 580–592.
157 E. Elettore, F. Freddi, M. Latour, G. Rizzano, Design and analysis of a seismic resilient steel moment-resisting frame equipped with damage-free self-centring column bases. J Constr Steel Res. 179 (2021)106543.
158 E. Elettore, A. Lettieri, F. Freddi, M. Latour, G. Rizzano, Performance-based assessment of seismic-resilient steel moment resisting frames equipped with innovative column base connections. Structures 32 (2021)1646-1664.
159 Lettieri A, Elettore E, Pieroni L, Freddi F, Latour M, Rizzano G. Parametric analysis of steel MRFs with self-centring column bases. Steel Construction. 2022;5(2):91–99. https://doi.org/10.1002/stco.202100050
160 Elettore E, Freddi F, Latour M, Rizzano G. Parametric Finite Element Analysis of Self-centring Column Bases with different Structural Properties. J Constr Steel Res. 2022;199:107628.
161 Deierlein GG, Reinhorn AM, Willford MR. NEHRP Seismic Design Technical Brief No. 4.

Nonlinear structural analysis for seismic design. NIST GCR 10-917-5 2010(4): 36.

162 Lignos DG, Krawinkler H. Deterioration modeling of steel components in support of collapse prediction of steel moment frames under earthquake loading. *Journal of Structural Engineering* 2011; 137(11): 1291–1302.

163 Ibarra LF, Medina RA, Krawinkler H. Hysteretic models that incorporate strength and stiffness deterioration. *Earthquake Engineering and Structural Dynamics* 2005; 34(12): 1489–1511. DOI: 10.1002/eqe.495.

164 S. Mazzoni, F. McKenna, M.H. Scott, G.L. Fenves OpenSEES: Open System for earthquake engineering simulation, Pacific Earthquake Engineering Research Centre (PEER), 2009, Univ. of California, Berkley, CA

165 Zareian, F., Medina, R. A. (2009). A practical method for proper modelling of structural damping in inelastic plane structural systems. Computer and Structures.

166 Medina, R., Krawinkler, H. (2003). Seismic demands for non-deteriorating frame structures and their dependence on ground motions. Report. No. TB 144, The John A. Blume Earthquake Engineering Centre, Stanford University, Stanford, CA.

167 Eads, L. (2013). Seismic collapse risk assessment of buildings: effects of intensity measure selection and computational approach. PhD dissertation, Stanford University, Stanford, CA.

168 Rahnama, M., Krawinkler, H. (1993). Effects of soft soil and hysteresis model on seismic demands. Report No. 108, The John A. Blume Earthquake Engineering Centre, Stanford University, Stanford, CA.

169 Krawinkler, H., Bertero, V. V., Popov, E. P. (1971). Inelastic behaviour of steel beam-to-column subassemblages". Report No. UCB/EERC-71/07, Earthquake Engineering Research Centre (EERC), University of California at Berkeley.

170 Krawinkler, H. (1978). Shear design of steel frame joints. Engineering Journal, 15, 3.

171 Krawinkler, K., Mohasseb, S. (1987). Effects of PZ deformations on seismic response. Journal of Constructional Steel Research, 8

172 Kim, K., Engelhardt, M. D. (1995). Development of analytical models for earthquake analysis of steel moment frames. Report No. PMFSEL 95-2, Department of Civil Engineering, University of Texas at Austin.

173 Gupta A, Krawinkler H. Seismic Demands for Performance Evaluation of Steel Moment Resisting Frame Structures. 1999.

174 Charney F, Downs W. Modelling procedures for PZ deformations in moment resisting frames. Connections in Steel Struct. V 2004. ESSC/AISC Workshop, Amsterdam.

175 Castro, J. M., Davila-Arbona, F. J., Elghazouli, A. Y. (2008). Seismic Design Approaches for PZs in Steel Moment Frames. Journal of Earthquake Engineering, 12, 34-51.

Chapter 3 Damage-Free Self-Centring Column Base

3.1 Concept

The Damage-Free Self-Centring (SC-CB) connection is shown in Figure 3.1. It consists of a column composed of two parts connected by a combination of FDs, which dissipate the seismic input energy through the alternate slippage of the surfaces in contact, and a self-centring system which, together with the gap opening mechanism, controls the self-centring behaviour of the connection. The FDs consist of properly coated steel friction shims and steel cover plates clamped with pre-loadable bolts. The FDs are characterised by a rigid-plastic hysteretic model, which depends on the clamping force and the friction coefficient μ of the contact interfaces. It is worth highlighting that the FD typology used within this connection has been extensively investigated by previous experimental works, which have addressed significant aspects, such as the response of the FDs under cyclic loading histories [2-6], the behaviour of the pre-loadable bolts at installation and over their service-life [7] and under different loading rates [8]. The self-centring system is composed of PT bars symmetrically placed with respect to the column's depth and arranged in series with a system of disk springs. The disk springs are arranged in series and parallel, acting as a macro-spring system, ensuring an adaptable stiffness-resistance combination to the self-centring system. It is worth mentioning that the overall dimension of the connection is similar to the size of a traditional column splice, and it is characterised by the absence of interaction with the concrete foundation. The self-centring system is connected to anchorage plates welded to the column to increase the axial force and to control the SC-CB rocking behaviour by providing restoring forces in the joint, returning towards the initial straight position at the end of the seismic event. An exploded 3D view of the SC-CB connections is illustrated in Figure 3.2. In addition, oversized web holes and flange slots are designed on the column's web and flanges to accommodate the design rotation (θ_t) during the gap opening phase, as illustrated in Figure 3.3.

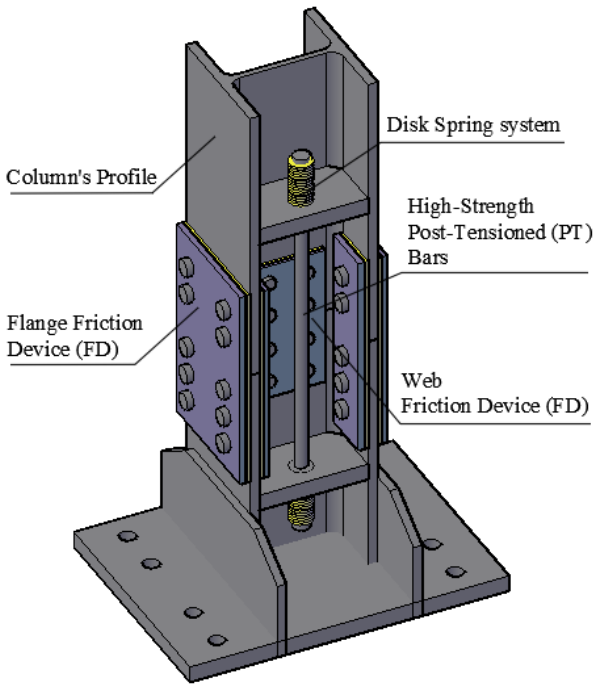

Figure 3.1: 3D view of the Damage-Free Self-Centring Column Base (SC-CB) [1]

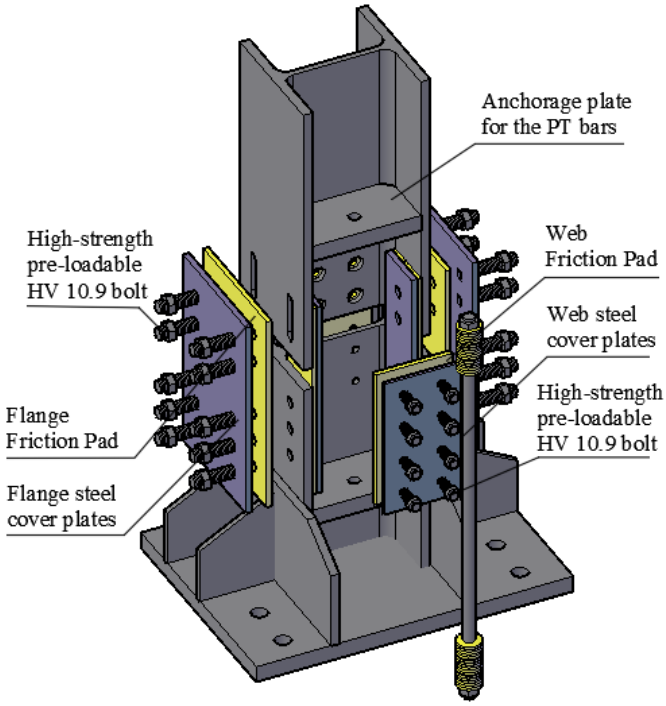

Figure 3.2: 3D exploded view of the Damage-Free Self-Centring Column Base (SC-CB) [1]

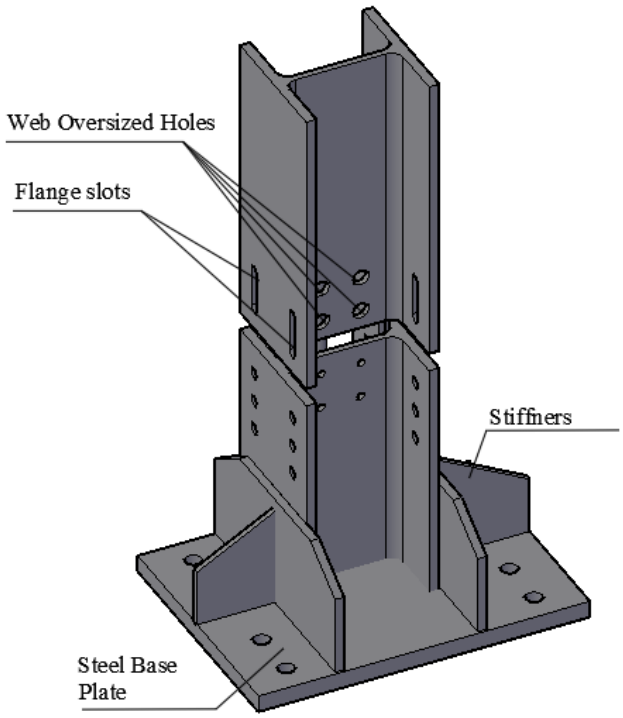

Figure 3.3: 3D exploded view of the column [1]

3.2 Main features and advantages

Concerning the configurations previously described, this connection is characterised by several advantages, which can be summarised as follows:

i) the self-centring capability is obtained with elements (*i.e.,* PT bars and disk springs) that have a size comparable to the overall size of the column (*e.g.,* long PT bars can be avoided);
ii) the moment-rotation hysteretic behaviour of the components can be easily calibrated;
iii) the overall dimension of the connection is similar to the size of a traditional column splice;
iv) the connection elements are moved far from the concrete foundation, avoiding interaction. Consequently, the design of the joint is independent of that of the base plate connection; therefore, all common configurations for CB connections (*i.e.,* embedded, concrete encased or shallowly embedded) could be adopted.

It is worth mentioning that the SC-CB connection was originally proposed and experimentally tested by Latour *et al.,* 2019 [1] on an isolated specimen. The review of the experimental campaign and the main results are summarised in Section 3.7. Results from the experimental tests [1] showed a satisfactory and stable flag-shaped hysteretic behaviour of the SC-CB, with negligible residual deformations in the column. In this direction, it has been recently demonstrated through extensive numerical simulations and parametric FE analysis [9-12] that the SC-CBs provide considerable benefits when introduced within steel MRFs in terms of *1)* residual drift reduction and self-centring capability even under high seismic intensities; *2)* protection of the first storey column from yielding*; 3)* damage-free behaviour of the structural components; *4)* significant advantages in terms of repairability and hence resilience of the structure. This thesis will discuss these aspects in detail through numerical simulations, FE analysis, parametric studies and experimental testing.

3.3 Expected Forces

The main geometrical dimensions of the SC-CB joint are illustrated in Figure 3.4 (a). The design of the SC-CB joint is based on the knowledge of the forces developed during the gap-opening phase, as illustrated in Figure 3.4 (b). It is worth mentioning that some assumptions are required to define the design formulations of the SC-CB joint. Some of these have been verified through experimental tests [1], and others through simplified numerical models [9] or advanced FE models [12]. The analytical formulations for the behaviour of the FDs are based on the following simplifying assumptions:

i) stable friction coefficient [1-3];
ii) constant clamping force of the bolts;
iii) negligible bending stiffness of the flanges' plates of the FDs. Based on these assumptions, the FDs exhibit a rigid-plastic behaviour that depends on the clamping force and the friction coefficient of the interfaces in contact.

The forces in the FDs of the web (F_w) and flanges (F_f) are defined as follows:

$$F_w = F_{slip,w} = \mu \cdot n_s \cdot n_{b,w} \cdot F_{p,w} \tag{3.1}$$

$$F_f = F_{slip,f} = \mu \cdot n_s \cdot n_{b,f} \cdot F_{p,f} \tag{3.2}$$

where μ is the design value of the friction coefficient; n_s is the number of friction interfaces (*i.e.,* equal to 2 in the considered Configuration); $n_{b,w}$ and $n_{b,f}$ are the numbers of bolts, respectively in the web and the flanges; $F_{p,w}$ and $F_{p,f}$ are the pre-loading forces of each web and flange bolt, respectively. In addition, F_c is the compression force at the Centre of Rotation (COR).

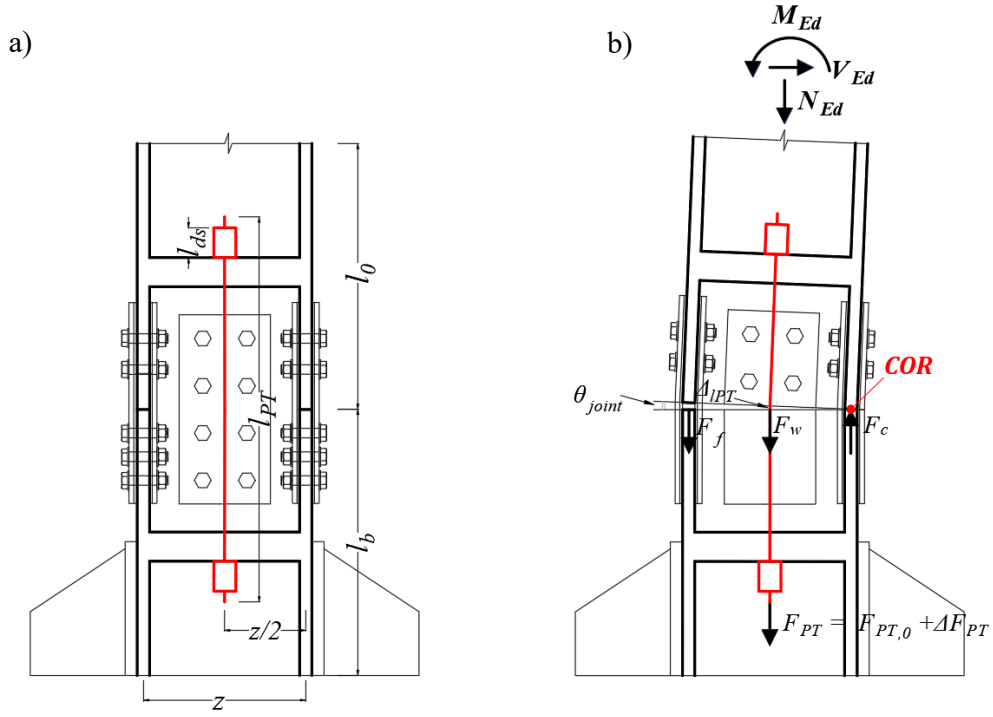

Figure 3.4: SC-CB (a) Geometrical dimensions; (b) Schematic representation during the gap-opening.

One or more PT bars with disk springs are symmetrically placed to control the self-centring behaviour of the joint. The force acting in the self-centring system (F_{PT}) (*i.e.,* PT bars and disk springs) is defined as follows:

$$F_{PT} = F_{PT,0} + \Delta F_{PT} \tag{3.3}$$

$$F_{PT,0} = n_{PT} \cdot F_{p,PT} \tag{3.4}$$

$$\Delta F_{PT} = K_{eq} \cdot \Delta l_{avg,PT} \tag{3.5}$$

where $F_{PT,0}$ is the initial bars pre-load; ΔF_{PT} is the extra force occurring in the system during the gap-opening phase; n_{PT} is the total number of PT bars employed in the connection; $F_{p,PT}$ is the initial pre-load force on each PT bar; K_{eq} is the stiffness of the self-centring system. The average elongation of the PT bars corresponding to the target rotation (θ_t) of the joint and considering that the PT bars are

symmetrically placed with respect to the centre of the section, is $\Delta l_{avg,PT}$, evaluated considering θ_t equal to 40 mrad, which is the benchmark rotation established by AISC 341-16 [13] for Special MRFs. It can be calculated as follows:

$$\Delta l_{avg,PT} = \theta_t \cdot (z/2) \tag{3.6}$$

where z is the internal lever arm of the connection, corresponding to $z = h_c - t_{fc}$, with h_c and t_{fc} being respectively the height and the flange's thickness of the column's cross-section.

3.4 Stiffness of the Self-Centring system

The equivalent stiffness of the self-centring system (K_{eq}) is a function of the stiffness of the single components (*i.e.,* PT bars and disk springs) (see Figure 3.5 (a)) and is defined as follows:

$$K_{eq} = n_{PT} \frac{K_{PT,1} K_{DS}}{K_{PT,1} + K_{DS}} \tag{3.7}$$

$$K_{PT,1} = \frac{E_{PT} A_{s,res,PT}}{l_{PT}} \tag{3.8}$$

$$K_{DS} = \frac{n_{ds,par}}{n_{ds,ser}} K_{ds,1} \tag{3.9}$$

where $K_{PT,1}$ is the stiffness of a single PT bar; K_{DS} is the stiffness of a set of disk springs arranged both in series and in parallel; E_{PT} is the elastic modulus of the PT bars; $A_{s,res,PT}$ is the resistance area of one PT bar; l_{PT} is the length of the PT bar, including the length of the disk springs; $K_{ds,1}$ is the stiffness of one disk spring. The number of disk springs arranged in parallel and in series are indicated with $n_{ds,par}$ and $n_{ds,ser}$ respectively, and a possible arrangement is illustrated in Figure 3.5 (b).

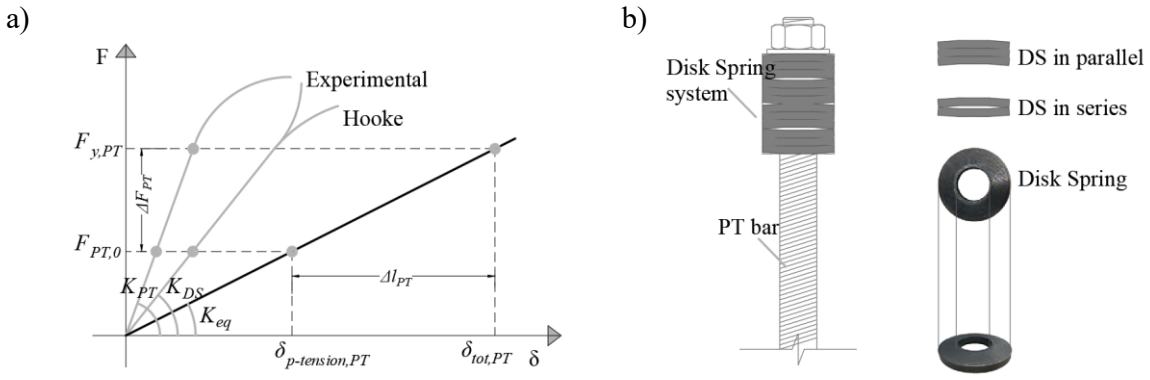

Figure 3.5: Self-centring system: (a) Stiffness of the self-centring components; (b) Details.

3.5 Moment-Rotation Behaviour

The SC-CB is characterised by a flag-shape moment-rotation behaviour characterised by two phases, as shown in Figure 3.6 (a). In the closed phase, the forces in the FDs are assumed to be completely developed, and thus, their contributions are assumed to remain constant during the gap-opening phase. In addition, the contribution of the initial pre-load force of the PT bars is assumed constant, while the contribution due to the extra forces in the self-centring system occurring in the gap-opening phase is assumed to be linearly proportional to the joint's rotation. The moments' contributions are illustrated in Figure 3.6 (b), and they are a function of the forces developed by each component during the gap-opening phase and can be calculated, with respect to the COR, as follows:

$$M_D = M_N + M_{PT,0} \tag{3.10}$$

$$M_N = N_{Ed} \cdot (z/2) \tag{3.11}$$

$$M_{PT,0} = F_{PT,0} \cdot (z/2) \tag{3.12}$$

$$M_{FD} = M_{FD,w} + M_{FD,f} = F_w \cdot (z/2) + F_f \cdot z \tag{3.13}$$

$$\Delta M_{PT} = \Delta F_{PT} \cdot (z/2) \tag{3.14}$$

where M_D is the decompression moment; M_N is the moment contribution related to the axial load (*i.e.*, N_{Ed}) directly applied on the joint; $M_{PT,0}$ is the moment provided by the PT bars at zero rotation; M_{FD} is the moment provided by the web and flanges FDs; ΔM_{PT} is the moment developed by the additional forces in the self-centring system, and z is the lever arm of the connection. It is worth highlighting that N_{Ed} is assumed to remain in the original position of the column centre.

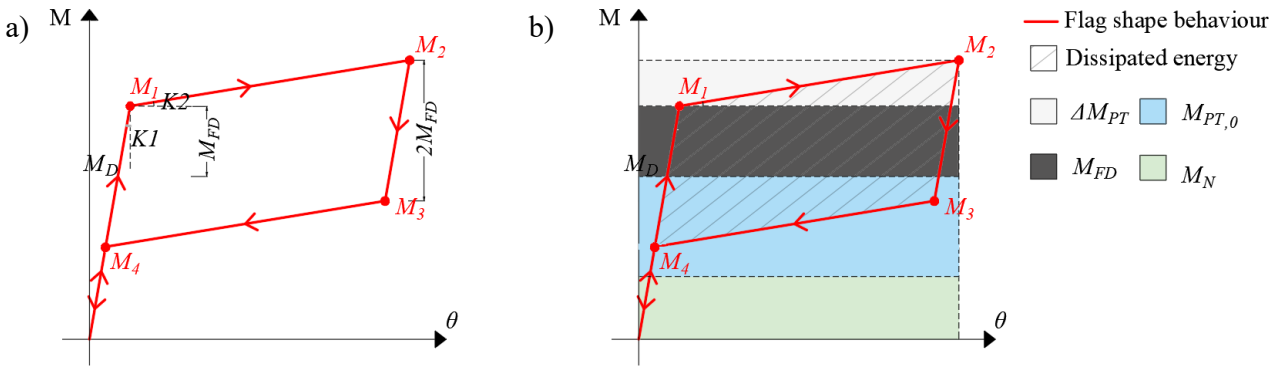

Figure 3.6: Flag-shape hysteretic behaviour: (a) Fundamental moments; (b) Moment Contributions.

The four fundamental moments defining the entire cyclic moment-rotation behaviour (*i.e.*, M_1 ,M_2, M_3 and M_4) are reported in Figure 3.6, where M_1 is the moment at the onset of rocking, while M_2 is the maximum moment achieved at the target rotation θ_t. It is worth highlighting that from M_2 to M_3 there

is a moment reduction equal to $2M_{FD}$ for a constant rotation value because of the rigid behaviour of the FDs and the change in the CB rotation direction.

$$M_1 = M_N + M_{PT,0} + M_{FD} \tag{3.15}$$

$$M_2 = M_1 + \Delta M_{PT} \tag{3.16}$$

$$M_3 = M_2 - 2M_{FD} \tag{3.17}$$

$$M_4 = M_1 - 2M_{FD} \tag{3.18}$$

The first branch (K_1) of the moment-rotation curve is characterised by an infinite stiffness of the connection and, therefore, the stiffness of the whole system is equal to the flexural stiffness of the cantilever column, calculated as follows:

$$K_1 = K_{col} = \frac{E_s I_{col}}{h_0^3} \tag{3.19}$$

where E_s is the steel modulus of elasticity, h_0 is the length of the column above the splice section and I_{col} is the column's moment of Inertia. The second branch (K_2) is controlled by the equivalent stiffness of the self-centring system (K_{eq}) and it is defined as follows:

$$K_2 = \frac{1}{\left(\frac{1}{K_{col}} + \frac{1}{K_{eq} \cdot (z/2)^2}\right)} \tag{3.20}$$

It is worth reminding that the flexural resistance of the flanges' cover plates and friction shims is assumed to be negligible; thus, their bending contribution to the moment-rotation behaviour is neglected.

3.6 Design Procedure

The design of the SC-CB is based on a step-by-step procedure consisting of the definition of the design input parameters (*i.e.,* geometry and design forces in the column), the design of the components (*i.e.,* FDs and Self-centring system) and the design of the structural details of the joint (*i.e.,* plates of the FDs, holes and slots). The design methodology is affected by the assumptions previously discussed. Additionally, some design choices are required, such as:

i) the design axial force is assumed to be constant considering two limit conditions;
ii) the design shear force is assumed to be assigned to the web FDs;
iii) no yielding of the joint components.

In addition, further recommendations that allow for identifying the optimal design condition in terms of self-centring behaviour and minimal yielding of the components are provided in this thesis. Further considerations on the design assumptions and limitations are reported in the subsequent sections.

3.6.1 Step 1: Design input parameters

The design procedure of the SC-CB requires as input parameters:

i) the geometrical properties of the column (*i.e.,* cross-section properties and the splice position above the foundation (l_b)) (see Figure 3.4 (a));
ii) the design forces in the column (*i.e.,* the maximum/minimum expected axial forces ($N_{Ed,max}$;$N_{Ed,min}$) and the design bending moment (M_{Ed})) derived through the procedure suggested by Eurocode 8 [14], namely considering a proper overstrength of the dissipative zones.

The design shear force in the CB joint is estimated as follows:

$$V_{Ed} = M_{Ed}/l_0 \tag{3.21}$$

where $l_0 = l_s - l_b$, where l_s and l_b are respectively defined as the column shear length and the distance between the splice and the base. Once the input parameters are selected, the SC-CB connection design can be addressed by first designing the bolts of the web FD and, consequently, designing the PT bars and the bolts of the flange FDs. The objective of the design procedure is to satisfy at the same time three main conditions:

i) no yielding of the column;
ii) self-centring behaviour;
iii) bending moment corresponding to the gap opening higher than the one defined by Eurocode 8 [14] for the seismic design combination according to the ULS (*i.e.,* Ultimate Limit State).

These conditions are summarised in the following system of inequalities:

$$\begin{cases} M_2 < M_{y,c} \\ M_D \geq M_{FD} \\ M_1 > M_{Ed} \end{cases} \tag{3.22}$$

where $M_{y,c}$ is the column's yielding bending moment.

3.6.2 Step 2: Design of the components

Web Friction Device (Web FD)

The required pre-load force for each web bolt ($F_{p,w}$) is easily determined by imposing that the slippage force of the web FD (F_w) (see Eq. (3.1) must be larger or equal to the required value of the design shear force (V_{Ed}) (see Eq. (3.21)), as follows:

$$F_w = \mu \cdot n_s \cdot n_{b,w} \cdot F_{p,w} \geq V_{Ed} \quad \rightarrow \quad F_{p,w} \geq \frac{V_{Ed}}{\mu \cdot n_s \cdot n_{b,w}} \tag{3.23}$$

PT Bars

The post-tensioning force of the PT bars ($F_{PT,0}$) is defined by imposing the system of equations for the self-centring condition of Eq. (3.22) and the equilibrium between the internal and external bending moment in the SC-CB, as follows:

$$\begin{cases} F_{PT,0} \geq 2F_f + F_w - N_{Ed} \\ F_{PT,0} \cdot (z/2) + F_f\,(z) = M_{Ed} - (F_w + N_{Ed})(z/2) \end{cases} \quad \rightarrow \quad F_{PT,0} \geq \frac{M_{Ed}}{z} - N_{Ed} \tag{3.24}$$

where $F_{PT,0}$ is the minimum PT force to be applied to the PT bars. It can be increased to satisfy the other design conditions.

Flange Friction Device (Flange FD)

In addition, the minimum pre-load force for each flange bolt ($F_{p,f}$) is provided by addressing the contribution of the PT bars' force and the web FD's force. The slippage force of the flange FDs (F_f) (see Eq. (3.1)) can be obtained by Eq. (3.24) as indicated by the following expressions:

$$F_f = \frac{M_{Ed}}{z} - \frac{1}{2}\left(F_w + N_{Ed} + F_{PT,0}\right) \quad \rightarrow \quad F_{p,f} = \frac{F_f}{\mu \cdot n_s \cdot n_{b,f}} \tag{3.25}$$

Disk Spring system

The disk springs, also called “Belleville Washers”, are arranged in series and in parallel, as shown in Figure 3.7.

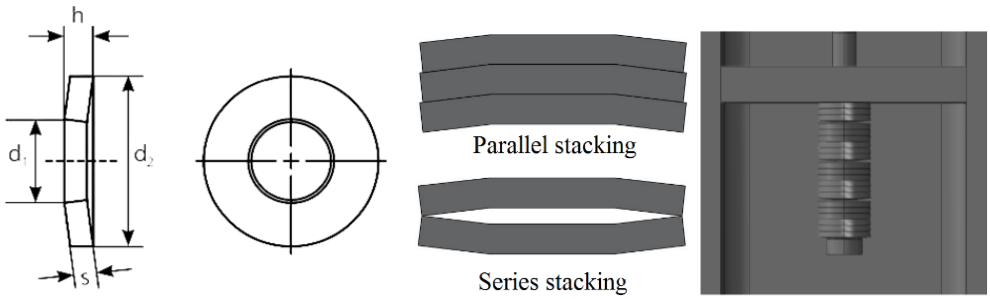

Figure 3.7. Disk springs in series and in parallel.

The disk springs system is designed to be over-strength with respect to the PT bars by calculating the number of disk springs in parallel ($n_{ds,par}$) as follows:

$$F_{y,DS} \geq F_{y,PT} \qquad \rightarrow \quad n_{ds,par} = \frac{A_{s,res,PT} \cdot f_y}{F_{y,DS,1}} \tag{3.26}$$

where $A_{s,res,PT}$ and f_y are the net area and the yield stress of the PT bar, respectively, and $F_{y,DS,1}$ is the yield strength of the single disk spring.

The number of disk springs in series ($n_{ds,ser}$) controls the stiffness of the self-centring system (*i.e.,* K_{eq}) by providing sufficient deformability to the system, and it is calculated assuming that:

$$\frac{(f_y \cdot A_{s,res,PT} - F_{p,PT})}{\delta_{PT}} = K_{eq,1} \geq K_{eq} \qquad \rightarrow n_{ds,ser} \geq n_{ds,par} K_{ds,1} \left(\frac{K_{PT} - K_{eq,1}}{K_{eq,1} K_{PT}} \right) \tag{3.27}$$

where $\delta_{PT} = \theta_t \cdot d_{PT}$ is the maximum elongation of the farther bar from the COR and d_{PT} is the distance of the PT bar with respect to the COR. It is worth noting that Eq. (3.21) provides the minimum number of disk springs in series ($n_{ds,ser}$) and it can be increased to reduce K_{eq} (see Eqn.s (3.6, 3.7, 3.8)). Additionally, a tensile resistance check of the PT bars is carried out, considering their individual elongation. This check ensures that both the PT bars and the disk springs remain elastic.

3.6.3 Step 3: Design of the structural details

Anchorage plates for the PT bars are placed symmetrically along with the column's depth and welded to the column, as shown in Figure 3.8 (a). The dimensions of the plates are known (*i.e.,* b_p and l_p), except for the thickness (t_p), which is designed and checked to resist the total force of the PT bars (F_{PT}). To design the right thickness of the anchorage plates, the Grashof method is used by imposing the congruence of the deflections of two limit schemes, together with the congruence of the concentrated forces (*i.e.,* the total force of the PT bar).

$$\begin{cases} F_1 + F_2 = F_{PT,0} + \Delta F_{PT} \\ \delta_1 = \delta_2 \end{cases} \tag{3.28}$$

where F_1 and F_2 are the concentrated load respectively acting on the cantilever and the bi-fixed-end schemes, and δ_1 and δ_2 are the two deflections. Considering that the bending moments of the two schemes are equal to:

$$M_1 = \frac{(F_1/2) \cdot l_2}{2} \qquad M_2 = \frac{(F_2/2) \cdot l_1}{8} \tag{3.29}$$

$$M_{el,p} = W_{el,p} f_{yd} \geq max(M_1, M_2) \tag{3.30}$$

where $W_{el,p}$ is the elastic modulus of the rectangular section and f_{yd} is the yielding strength of the adopted steel. From the Eqn.s. (3.29-3.30), it is possible to design the minimum thickness of the plate. The fillet weld for the anchorage plates is determined using both the simplified and directional methods following the Eurocode 3 part 1-8 [15]. According to the simplified method, the design resistance of a

fillet weld may be assumed to be adequate if, at every point along its length, the resultant of all the forces per unit transmitted by the weld satisfies the following criterion:

$$F_{weld} < F_{w,Rd} \tag{3.31}$$

where F_{weld} is the design value of the weld force per unit length and $F_{w,Rd}$ is the design resistance per unit length, calculated as follows:

$$F_{w,Rd} = f_{vw,d}a = \frac{\frac{f_u}{\sqrt{3}}}{\beta_w \cdot \gamma_{M2}}a \tag{3.32}$$

where $f_{vw,d}$ is the design shear strength of the weld, β_w is a correlation factor for angle welding and f_u is defined as the ultimate tension resistance of the weakest linked material. The β_w factor is the correlation factor for angle welds indicated in the Eurocode 3 part 1-8 [15], f_u is the ultimate strength, as indicated in the Eurocode 3 part 1-1 [16] and γ_{M2} is the partial safety factor equal to 1.25. Considering the scheme in Figure 3.8 (b):

$$M_{weld} = (F_{PT,0} + \Delta F_{PT})l_1/8$$

Therefore, it is possible to design the minimum thickness considering the following relationship:

$$t_{p,min} \geq \frac{M_{weld}}{F_{weld}}$$

According to the Directional method, the design resistance of the fillet weld will be sufficient if the following are both satisfied:

$$\sqrt{\left({\sigma_{perp}}^2 + 3(\tau_{perp}^2 + \tau_{par}^2)\right)} \leq \frac{f_u}{\beta_\omega \gamma_{M2}} \qquad \sigma_{perp} \leq \frac{0.9 f_u}{\gamma_{M2}} \tag{3.33}$$

where σ_{perp} is the normal stress perpendicular to the throat, τ_{perp} is the is the shear stress (in the plane of the throat) perpendicular to the axis of the weld, τ_{perp} is the is the shear stress (in the plane of the throat) parallel to the axis of the weld and f_u , β_w and γ_{M2} have already been defined.

Web oversized holes (d_h) and flange slots (l_{slot}) are designed to accommodate the design rotation (θ_t) during the gap-opening phase, as illustrated in Figure 3.9. The adopted design criteria are assumed as follows:

$$\delta = \sqrt{\delta_h^2 + \delta_v^2} \tag{3.34}$$

where $\delta_h = \theta_t x_i$ and $\delta_v = \theta_t y_i$ are the displacements in the *x*- and *y*- direction of the hole "i", with x_i and y_i represent the distances in the x and y direction of the centroid of the hole "i" with respect to the COR position. The diameter of the oversized hole is assumed to be equal to

$$d_h \geq d_{bolt} + 2\delta \tag{3.35}$$

The same procedure has been used for each row. For the sake of simplicity, the dimension of the web oversized holes has been fixed equal among all the holes (equal to the distance of the farther web bolt). Regarding the flange slots, the bolt is assumed to translate a distance equal to half a diameter in the vertical position.

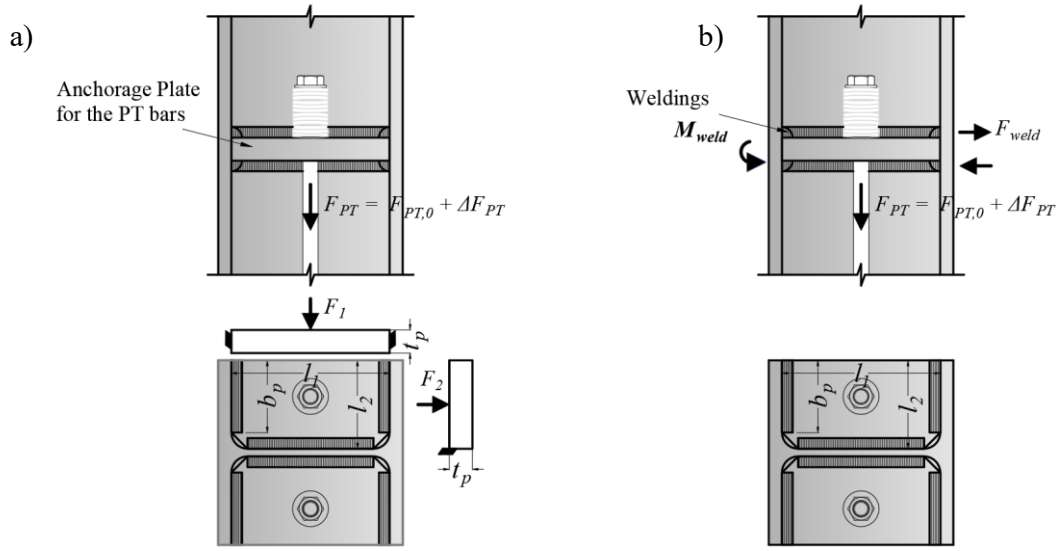

Figure 3.8. Design of the anchorage plates of the PT bars.

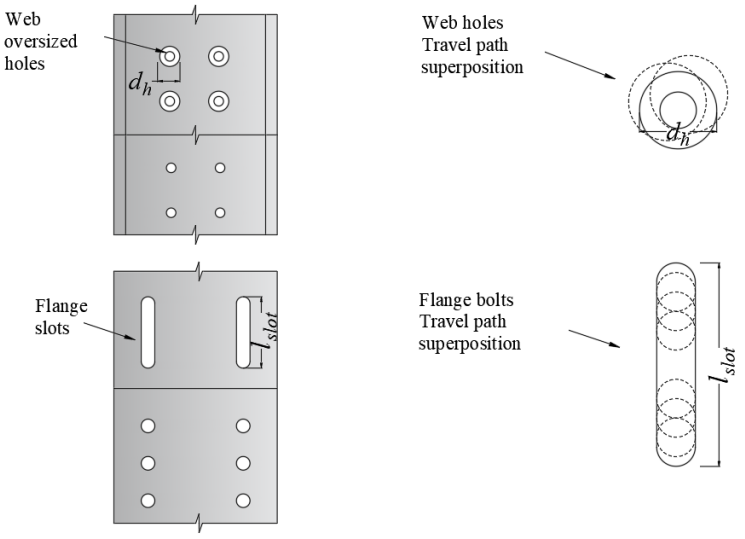

Figure 3.9: Design of the oversized web holes and flange slots.

The cover plates of the flange FDs are designed and verified to resist the tensile force provided by the design actions (*i.e.,* the contribution of M_{Ed}, N_{Ed}, F_w and F_{PT}). In addition, the flanges' plate thickness is checked to avoid local buckling. The holes' positions are designed to comply with the edge distances and spacing of bolts suggested by Eurocode 3 Part 1-8 [15] (Figure 3.10). Finally, the design resistance of the lower part of the connection is calculated and checked, considering the failure modes (*i.e.,* shear resistance, bearing resistance, punching shear resistance, combined shear and tension) as indicated in the Eurocode 3 Part 1-8 [15]. The design method aims at avoiding the possible failure modes up to the target rotation. After that, possible failure modes could be represented by the yielding of the PT bars or the bolts reaching the end of their travel paths.

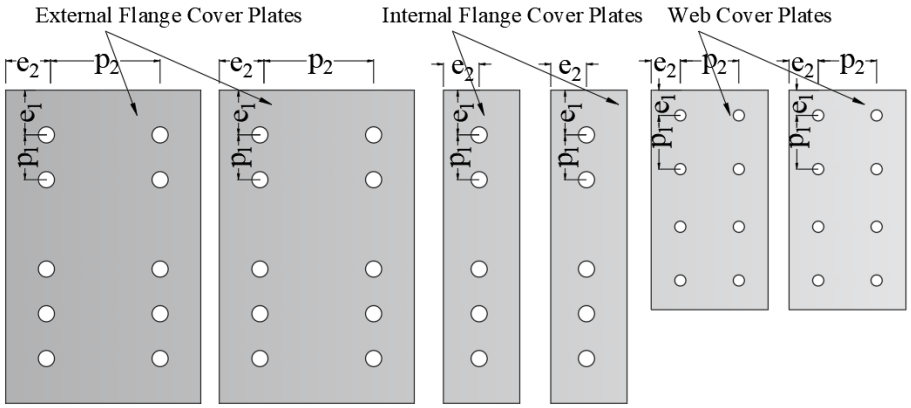

Figure 3.10: Design of the cover plates.

3.6.4 Assumption and Limitations of the design procedure

The design procedure is based on some design assumptions, as already pointed out. These assumptions can be summarized as follows and will be discussed in detail in Chapter 4:

i) The contribution in bending of the flanges' plates is negligible;
ii) The design shear force (V_{Ed}) is assigned to the web FD;
iii) The design axial force is considered within a range between the maximum compressive ($N_{Ed.max}$) and the minimum compressive (or maximum tensile) ($N_{Ed,min}$) axial forces;

Firstly, the contribution in bending of the flange plates: the contribution of the friction pads to the tensile resistance of the FDs is neglected, as well as the flexural resistance of the flange cover plates and friction pads. However, in the parametric analysis in Chapter 4, this is studied by varying the thickness of the flanges' plates, considering several configurations with different thicknesses of the flanges' plates for each SC-CB.

The web FDs are assumed to carry alone the design shear load, as proposed by the original design procedure proposed by Latour *et al.,* 2019 [1]. This assumption is used to validate the FE model against the experimental results in Section 3.8. However, in the parametric analysis in Chapter 4, several

distributions of the design shear load are considered. Therefore, the web FD is designed to carry a percentage (*i.e.,* 100%, 75%, 50%, 0%) of the design shear force (V_{Ed}) to provide information on how this design choice affects both the global and local behaviour of the SC-CB connection, as well as on the shear redistribution among the components. Additional information and details regarding this design assumption are further investigated in Chapter 4 of this thesis.

Regarding the design axial force (N_{Ed}), it is worth highlighting that the use of a constant axial force does not represent the real load condition of all columns of a MRF due to large axial force fluctuations that happen during the earthquake. Generally, the axial force in the columns of a MRF varies according to *i)* the distribution of the gravity loads and *ii)* the force fluctuations during the earthquake loading. In fact, especially the external columns usually experience significant transient axial load demands due to the dynamic overturning effects of the earthquake. Conversely, the internal columns typically undergo lower axial load fluctuations during the seismic event. Therefore, in order to properly account for the variability of the axial force within the design procedure, the maximum compressive ($N_{Ed.max}$) and the minimum compressive (or maximum tensile) ($N_{Ed,min}$) axial forces are considered. Therefore, the initial sizing of the SC-CB is performed considering the maximum axial force, which represents the worst condition for the no-yielding requirement (*i.e.,* first check condition of Eq. (3.22)), and the design is successively verified considering the minimum axial force, which is the worst condition for the self-centring requirement (*i.e.,* second check condition of Eq. (3.22)). Nevertheless, designing with the min compressive axial force may represent an over-conservative design assumption, which may lead to an overestimation/oversizing of the necessary components of the self-centring system. Further explanations and considerations on the validity of these assumptions are reported in Chapter 4 of this thesis.

3.7 Experimental campaign

The experimental campaign was performed on an isolated full-scale column with the SC-CB connection and consisted of several quasi-static cyclic tests [1]. The key characteristics of the test and the main results are briefly summarised herein to investigate the validation process. Figure 3.11 shows the specimen considered within the experimental campaign. The specimen consists of a HE 240B column of S275 steel class, where the FDs were made of 8 mm coated friction shims and cover plates of 5 mm and 8 mm for the web and the flanges, respectively. All the plates were S275 steel class, and the bolts were high-strength pre-loadable HV 10.9 class. According to previous experimental studies, the friction interface was characterised by a friction coefficient (μ) equal to 0.53 [3]. Besides, the self-centring system was composed of two threaded high-strength M20 PT bars of 10.9 class, and the disk springs system consisted of Belleville Disk Springs DIN 6796 arranged with three parallel disks and seven series disks. The anchorage plates were made of 40 mm S275 steel plates welded to the inner parts of the column. An overview of the tested specimen, containing the dimensions of the spare components, is illustrated in Figure 3.12.

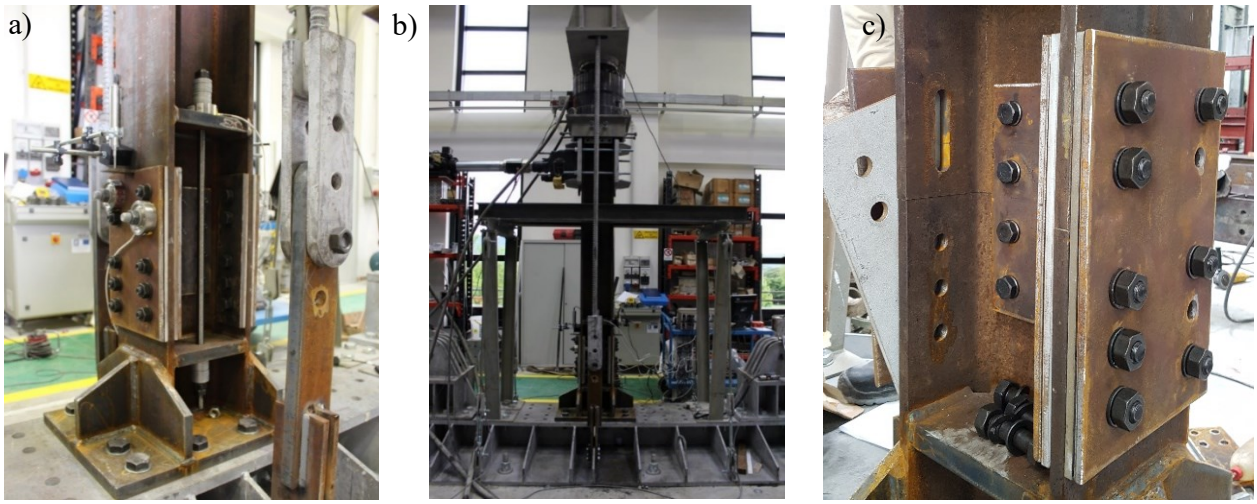

Figure 3.11: Experimental test of the SC-CB: a) Specimen; b) Testing Set-up; c) Details [1].

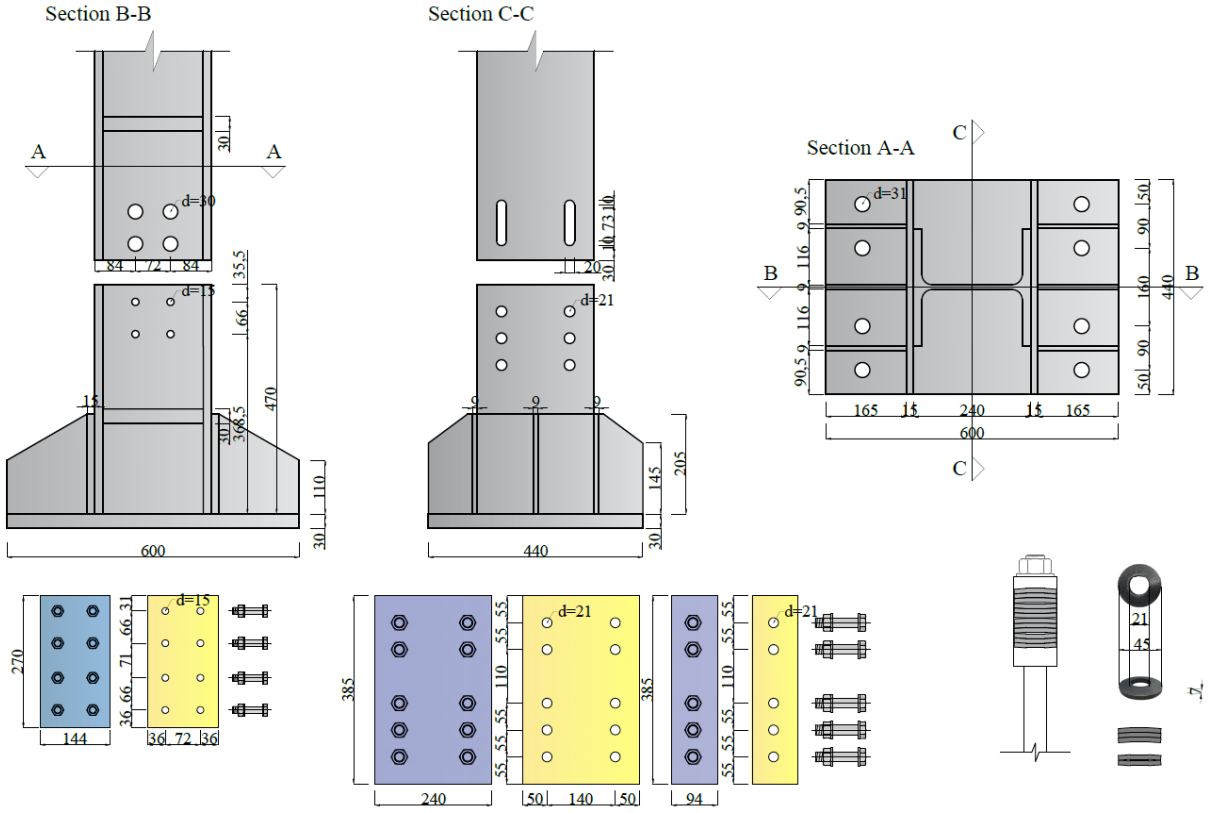

Figure 3.12: Geometry of the tested specimen SC-CB (dimensions in mm) [1].

The main material properties of the joint components are summarised in Table 4, where E, fy and fu are the Young's modulus, the yield strength and the ultimate tensile strength of the materials, respectively. The other proprieties of the adopted structural steel (*i.e.,* the shear modulus, the Poisson's ratio and the coefficient of linear thermal expansion) are based on Eurocode 3 Part 1-1 [16]. The interested reader can find additional information in Latour *et al.,* 2019 [1].

Table 4. Material properties of the tested SC-CB [1].

Elements	Class [-]	E [GPa]	f_y [MPa]	f_u [MPa]	Number [-]	Diameter [-]
Column and plates	S275	210	275	430	-	-
Web Bolts	HV 10.9	210	900	1000	4	M14
Flange Bolts	HV 10.9	210	900	1000	4	M20
PT bars	10.9	205	900	1000	2	M20

The testing equipment is shown in Figure 3.13. The loads in the quasi-static tests have been applied through two hydraulic actuators. The vertical actuator is used to apply the axial force, which is kept constant during the test, while the horizontal actuator is used to impose the horizontal cyclic displacement history. It is important to underline that although adopting a constant axial force is not fully representative of a real situation in a steel MRF, this assumption allowed an easier interpretation of the experimental results.

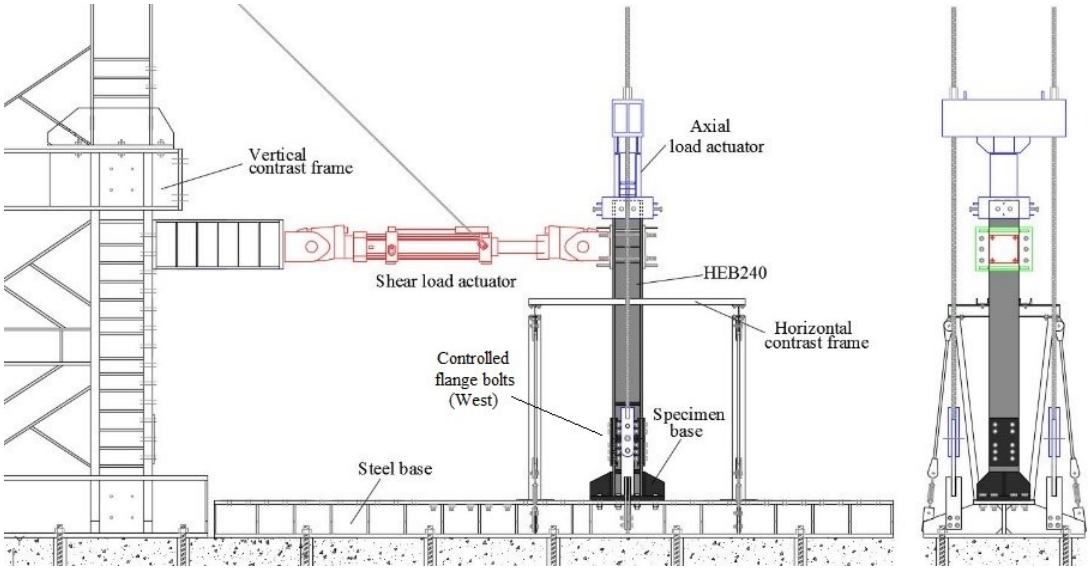

Figure 3.13: Experimental Layout of the SC-CB: Test Set-Up [1].

a) b) c)

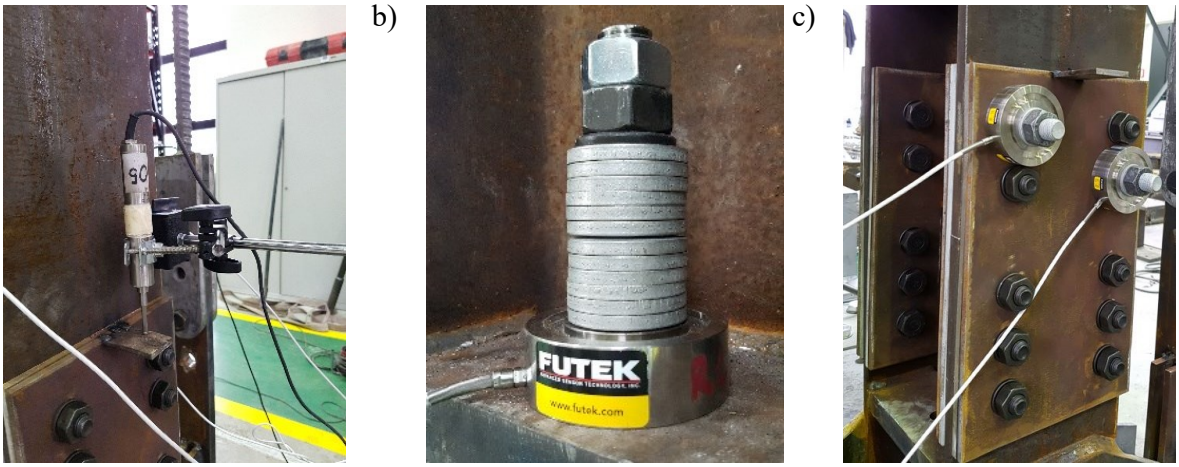

Figure 3.14: Instrumentations and measurement devices: a) Displacement transducers; b) Load cells for the PT bars; c) Load cells for the bolts of the flange FDs [1].

The pre-loading forces of the bolts and the bars were applied with a calibrated torque wrench, while four FUTEK load cells were installed in the connection to monitor the tensile forces of the PT bars and in two bolts of the flange FDs, as shown in Figure 3.14. In addition, LVDT displacement transducers have been adopted to measure the vertical displacements in both column sides. Regarding the bolt tightening procedure, it is worth mentioning that the initial pre-load of the bolts, according to EN 1090-2 [17] specifications, was increased by 10% to account for random variability of the bolt tightening and initial installation loss. Several full-scale cyclic tests on the proposed SC-CB were performed at the STRENGTH Laboratory of the University of Salerno. The loading protocol is shown in Figure 3.15, characterized by an increasing amplitude at each step, consistent with the loading protocol suggested by AISC 360-10 [18]. The tests have been performed varying some design parameters (*i.e.,* the axial load in the column, the pre-loading force in the bolts of the FDs, and the pre-loading force in the PT bars) to evaluate their influence on the overall experimental response of the joint. The tests have also been performed, including or not including the contribution of the PT bars. It is noteworthy that axial load ratios equal to 25% (*i.e.,* 728 kN) and 12.5% (*i.e.,* 350 kN) have been selected in a reasonable range of variation, considering the typical size of MRFs designed according to Eurocode 8 [14]. The test matrix is shown in Table 5, and the behaviour of the SC-CB during one of the tests is illustrated in Figure 3.16.

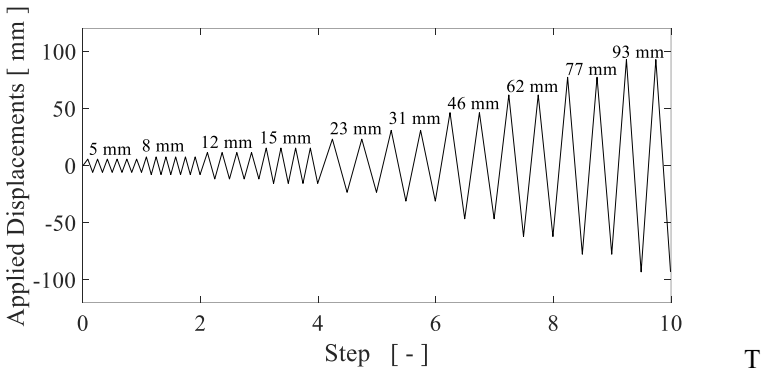

Figure 3.15: Experimental cyclic displacement loading history [1].

a)

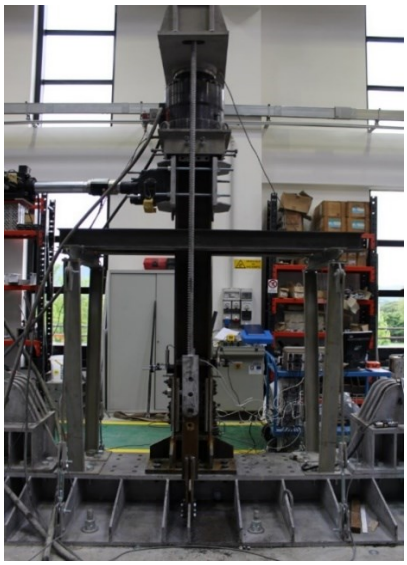

b)

Figure 3.16: Experimental test: (a) Before testing; (b) During testing [1].

Table 5. Test matrix of the experimental campaign [1].

Test	Typology	Column axial load [kN]	Pre-load in the PT bars [kN]	Ratio between the applied load in the PT bars and the minimum of Eq. (24)	Pre-load of each web bolt [kN]	Pre-load of each flange bolt [kN]	Residual rotation at the end of the test [mrad]
1	Cyclic	728 (25% N_p)	200	2.03	32	62	2.1
2	Cyclic	728 (25% N_p)	-	-	32	100	4.1
3	Cyclic	365 (12.5% N_p)	-	-	32	100	49.7
4	Cyclic	365 (12.5% N_p)	280	0.48	35	65	31.0

It is worth mentioning that the experimental campaign included several quasi-static cyclic and pseudo-dynamic tests. However, this work has not considered the pseudo-dynamic tests to validate the modelling strategies. In this work, four cyclic tests are selected and used to validate both the simplified and the advanced FE models, as explained in the following section. The main results of this experimental campaign are summarized hereinafter.

3.8 Finite Element Modelling (FEM) and Validation

Two modelling strategies are proposed and validated against the experimental results of Latour *et al.* (2019) [1]. The simplified modelling strategy is developed in OPENSEES [19], and it is preliminarily used to investigate the main parameters affecting the moment-rotation hysteretic behaviour of the SC-CB connection. Conversely, the advanced modelling approach is developed in the ABAQUS [20] to better investigate the influence of some design parameters. The results are compared and used to assess the effectiveness of the analytical equations and the design procedure presented in Section 3.6.

3.8.1 Simplified FEM (OPENSEES)

3.8.1.1 Modelling strategy

The OPENSEES model of the SC-CB connection is shown in Figure 3.17. It consists of a 2D non-linear advanced FE model where the column is modelled with '*nonlinear beam-column elements*' fibre elements associated with the '*Steel01*' material [19] for 275 MPa yield strength and 0.02 post-yield stiffness ratio. The rocking interface is modelled with 8 rigid '*elastic beam-column elements*' [19] with very high flexural stiffness. These elements are used to connect the lower and the upper part of the column through non-linear springs.

Modelling of the web and flanges FDs

The FDs are modelled with 4 translational springs represented by four '*zero-length elements*' [19]. They are defined by the bilinear elasto-plastic '*Steel01*' material [19] considering a rigid initial behaviour and a very low strain-hardening ratio to simulate the rigid plastic behaviour and a yield strength equal to the slippage forces in web and flanges FDs obtained from the design procedure. They are symmetrically placed with respect to the column's depth to account for their proper location with respect to the COR.

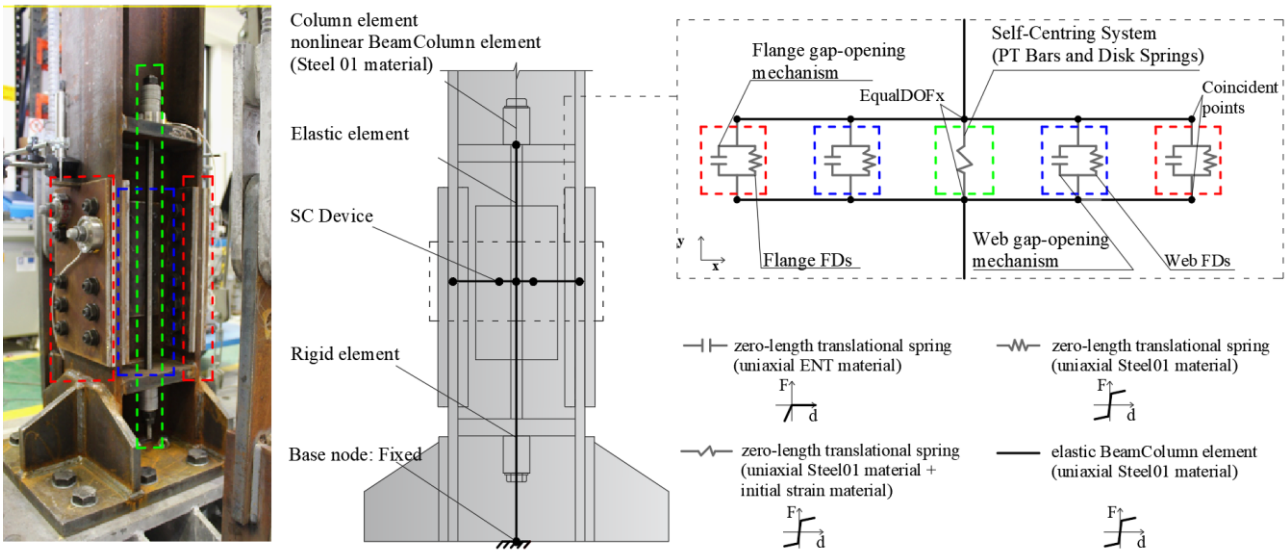

Figure 3.17: 2D OPENSEES [19] FE model for the SC-CB.

Modelling of the contacts

The contact behaviour is modelled with 4 translational springs ('*element zeroLength*' [19]) defined by the '*Compression-no-tension (ENT)*' material [19] which exhibits an elastic compression-no tension force-displacement behaviour. The compression stiffness of the contact spring is assumed as a very high value in order to model the contact behaviour.

Modelling of the Self-centring system

The self-centring system is modelled with a single translational spring represented by a central single '*zero-length element*' [19] with bilinear elastic-plastic behaviour having the characteristics of the whole system and placed in the center of the joint to simulate the system in a simplified way. It is defined by the '*Steel01*' material [19], with an elastic stiffness equal to the equivalent stiffness of the self-centring system and a yield strength equal to the yield strength of the PT bars obtained from the design procedure. The initial PT force is modelled by imposing an initial strain using the '*Initial strain material*' [19]. The '*equalDOF*x' option is used. Furthermore, it is worth mentioning that the P-delta effects are not included in the simulations of these tests to capture the distribution of the forces according to the test setup.

Properties of the springs

The Force-displacement relationships and the properties of the springs used to model all the components are illustrated in Figure 3.18 and defined in Table 6. The yielding force of the springs modelling the FDs is determined though the analytical equations, while the initial stiffness and the slope of the hardening branch have been calibrated on the experimental data, finding the optimized values reported in Table 6. Conversely, the stiffness of the self-centring system has been calculated as previously reported in the analytical equations (*i.e.,* K_{eq}). The post-elastic stiffness of the self-centring system has been calibrated starting from the experimental data.

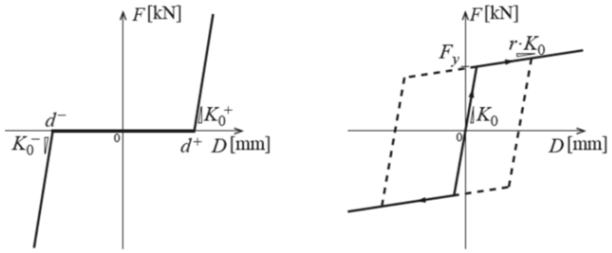

Figure 3.18: F-d relationships for the springs used for the OPENSEES [19] model: (a) Contact; (b) FDs.

Table 6. Properties of the springs used for the OPENSEES [19] model.

Test Number	Properties	Web FD	Flange FD	PT Bars and DS
1	K_0 [kN/m]	450000	450000	45150
	F_y [kN]	64	248	490
	b [-]	0.0001		0.01
	Initial strain	-		0.00354
2	K_0 [kN/m]	450000	450000	45150
	F_y [kN]	64	400	490
	b [-]	0.0001		0.01
	Initial strain	-		-
3	K_0 [kN/m]	450000	450000	45150
	F_y [kN]	64	400	490
	b [-]	0.0001		0.01
	Initial strain	-		-
4	K_0 [kN/m]	450000	450000	45150
	F_y [kN]	70	260	490
	b [-]	0.0001		0.01
	Initial strain	-		0.00620

Figure 3.19 shows the Force- displacement behaviour of the springs of the SC-CB components (*i.e.,* contact elements, FDs, self-centring system). As it can be seen from the results, the contact elements show an elastic compression F- δ behaviour, while the FDs' behaviour is bilinear with a very low post-elastic stiffness. All PT bars are modelled to remain in the elastic range.

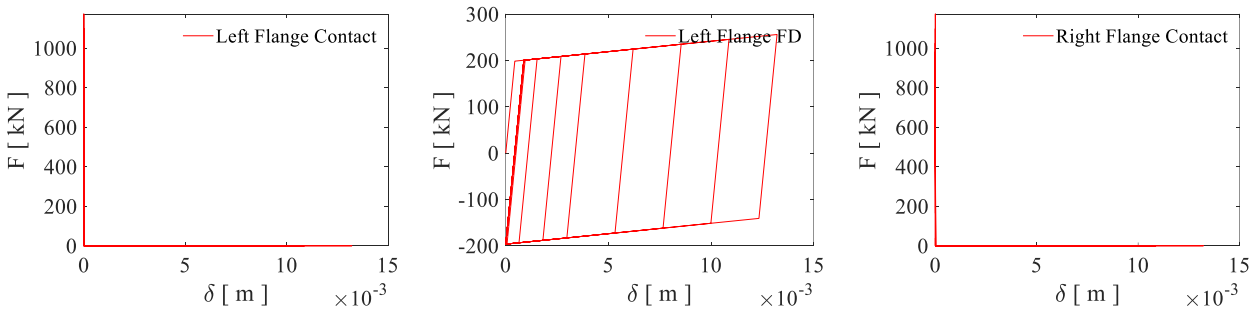

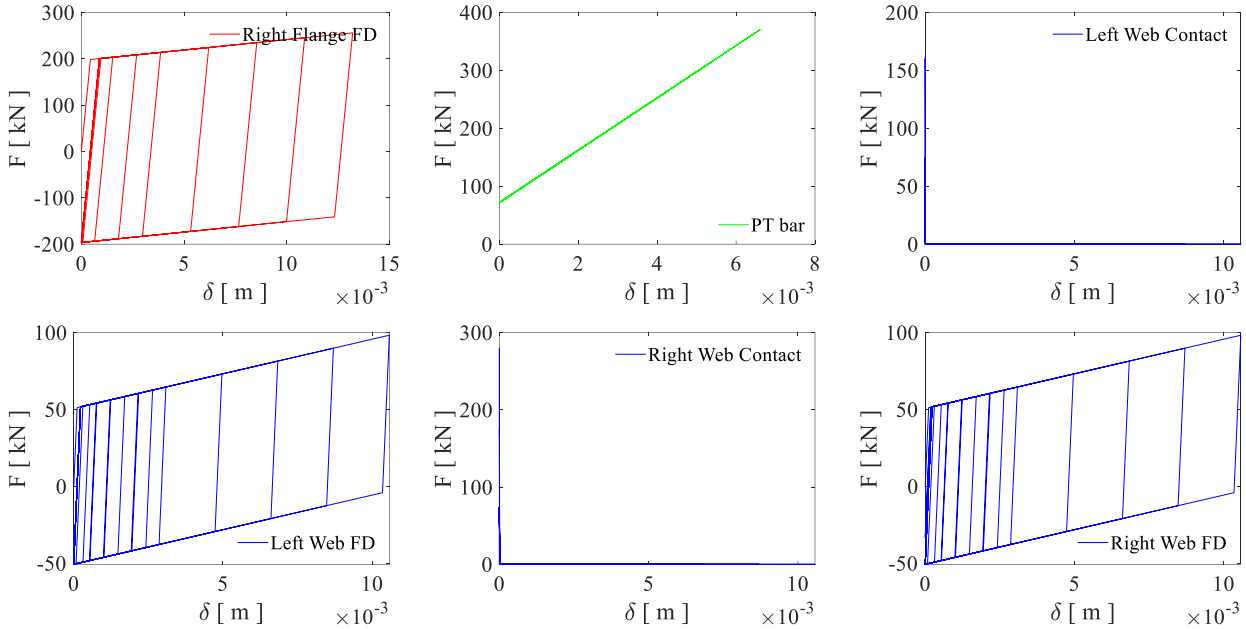

Figure 3.19: OPENSEES [19] Model. Force-displacement behaviour of the springs.

3.8.1.2 Validation

The modelling strategy has been validated by comparing the numerical FE models in OPENSEES [19] against the experimental results [1]. The validation process allowed the investigation of the main parameters affecting the moment-rotation hysteretic behaviour of the SC-CB and, consequently, on each element of the connection. The validation has been performed with four cyclic tests with different design parameters (*i.e.,* the axial load in the column, the pre-loading force in the bolts of the FDs, and the pre-loading force in the PT bars), as reported in Table 7.

Table 7. Experimental input data [1] for the validation.

Test Number	Axial load [kN]	Pre-load of each web bolt [kN]	Pre-load of each flange bolt [kN]	Contribution of the PT bars	Pre-load in each PT bar [kN]
1	728	32	62	with	100
2	728	32	100	without	-
3	350	32	100	without	-
4	350	35	65	with	140

Hence, 4 FE models have been built in OPENSEES [19] according to the modelling strategy previously described. Static cyclic analyses have been performed by applying the loading protocol shown in Figure 3.15. To account for the bolts' pre-loading loss during the experimental test [1] the web and flange bolts' pre-loading forces are reduced by 20% with respect to the experimental values. The results in terms of moment-rotation hysteretic curves are reported in Figure 3.20. The OPENSEES [19] numerical results are shown by red lines, while the experimental data are reported by blue lines. Also, the analytical moment-rotation relationships are reported with dotted black lines. The comparison shows a good agreement, demonstrating the effectiveness of the OPENSEES [19] model and of the analytical formulation in predicting the experimental response with high accuracy.

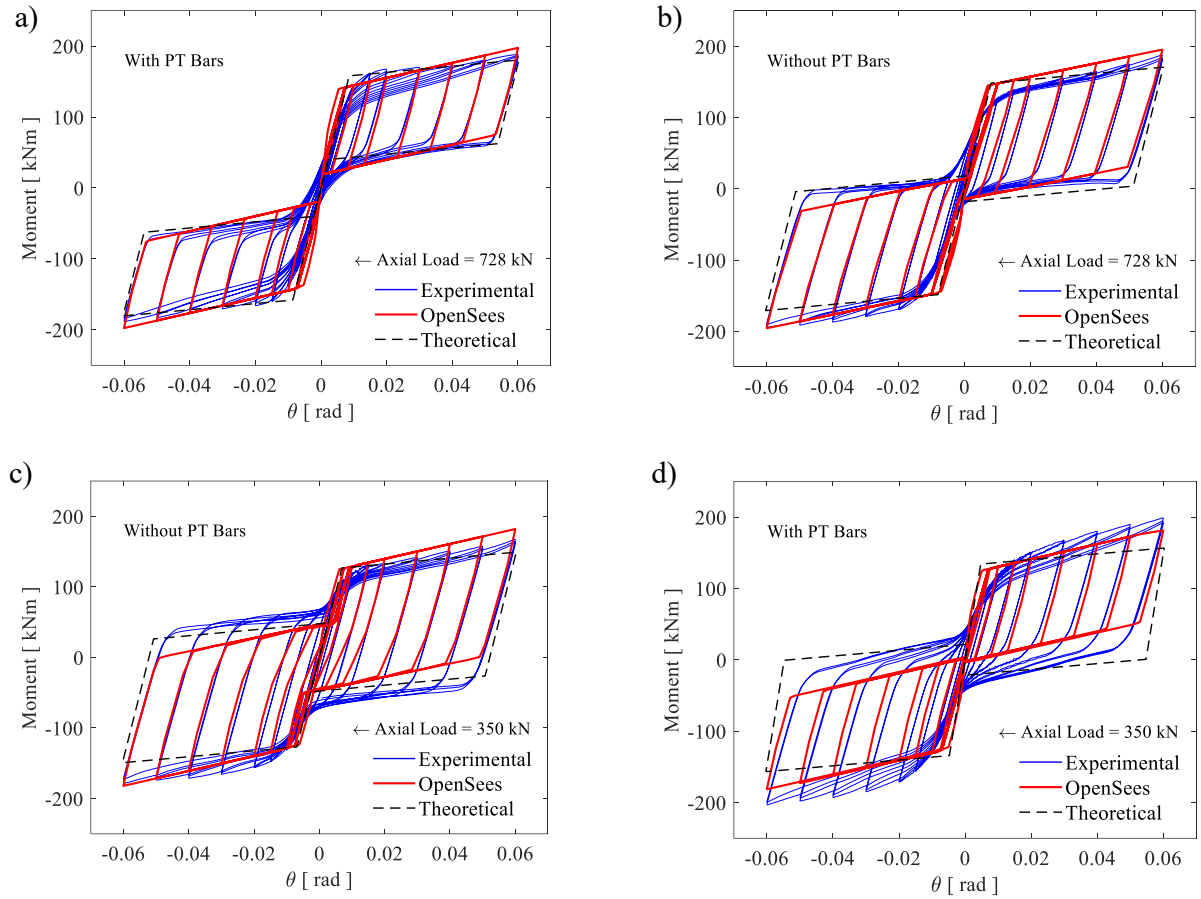

Figure 3.20: Comparison between OPENSEES [19] and experimental data [1]. Moment-Rotation hysteretic behaviour for the: (a) Test 1; (b) Test 2; (c) Test 3; (d) Test 4.

Figure 3.20 (a) (*i.e.,* Test 1 - high axial force and PT bars) shows a full self-centring behaviour with a very low residual rotation (*i.e.,* 2.1 mrad), Figure 3.20 (b) (*i.e.,* Test 2 - high axial force and no PT bars) shows a reduced self-centring capacity with a low residual rotation (*i.e.,* 4.1 mrad), while Figure 3.20 (c) (*i.e.,* Test 3 - low axial force and no PT bars) shows a significant residual rotation (*i.e.,* 49 mrad). Figure 3.20 (d) (*i.e.,* Test 4- low axial force and with PT bars) shows a reduced self-centring capacity since the initial tension in the bars was not enough to achieve the self-centring condition. The test 3 and 4 were carried out mainly to highlight the role of the PT bars, even though in these cases, to obtain a full self-centring, as already evidenced, higher capacity self-centring systems should have been employed. These results highlight the influence of the axial force and the key role of the pre-load of the PT bars in controlling the moment-rotation behaviour of the SC-CB and demonstrate the ability of the numerical and analytical models to capture these effects. However, some limitations of the numerical and analytical models can be observed. Among others, the numerical model neglects the flange plates' bending contribution and the fluctuation of the bolts' forces, as well as the PT bars' force loss, leading to some differences between the numerical and the experimental results. However, these effects will be explained in detail in the subsequent section.

3.8.2 Advanced FEM (ABAQUS)

3.8.2.1 Modelling strategy

Boundary Conditions

The model is a detailed 3D non-linear FE model where the bottom surface of the base is fully fixed using boundary conditions type '*encastre*' [20], while the lateral load of the horizontal actuator is simulated by a controlled horizontal displacement using boundary conditions type '*displacement*' (*i.e.,* U1=0, U2=1, UR3=0, corresponding to *x*, *y* and *z* axes). Additionally, the axial force is simulated by a uniform pressure applied at the upper surface of the column's cross-section. Figure 3.21 (a) shows the boundary conditions of the model.

Geometry and meshing

The geometry has been defined by extruding the cross-section along the longitudinal direction, while the '*cut-extrusion*' command has been used to generate the holes for all the components. The bolts and the PT bars have been generated through a 360° revolution of their half section. All the elements have been adequately partitioned to ensure the correct contact between all the members. All the components are modelled using the eight-node linear brick element (*i.e.,* C3D8R) available in the ABAQUS library [20]. Elements C3D8R rely on '*reduced integration*' [20] and '*hourglass control*' [20]. Meshing is carried out by selecting local seeds with a mesh size of 8 mm in the areas with contact interaction to monitor the complex stress distributions during the cyclic loading. Conversely, a mesh size of 20 mm is used in the areas where the expected stresses are relatively insignificant (*i.e.,* the base and the upper part of the column). The *'curvature control'* is chosen with a maximum deviation factor of 0.1, while the minimum size control is specified as equal to 0.1. This option is used to avoid the problem of inadequate seeding around small-curved features [20]. Both geometrical and mechanical nonlinearities are considered. An overview of the mesh details is illustrated in Figure 3.21 (b), while the material properties adopted for the FE model are reported in Table 8.

Material properties

The material true stress-strain law of the steel S355 adopted for the FE model is consistent with the multilinear law with the multilinear curve proposed by Faella *et al.* 2000 [21], shown in Figure 3.22. The strain corresponding to the beginning of the hardening (ε_h) is assumed equal to 1.5%. Conversely, the ultimate strain (ε_u) is assumed equal to 76%, and it can be evaluated by means of the following relationship:

$$\varepsilon_u = \ln\frac{A_o}{A_f} \tag{3.36}$$

where A_o is the original cross-sectional area of the test specimen and A_f is the minimum cross-sectional area after fracture. Instead, a trilinear model has been applied to the bolts. To simplify the modelling strategy, the FE model does not include a detailed model of the disk springs. Conversely, the properties of the PT bars (*i.e.,* stiffness and strength) are adjusted to represent the mechanical properties of the whole self-centring system composed of PT bars and disk springs.

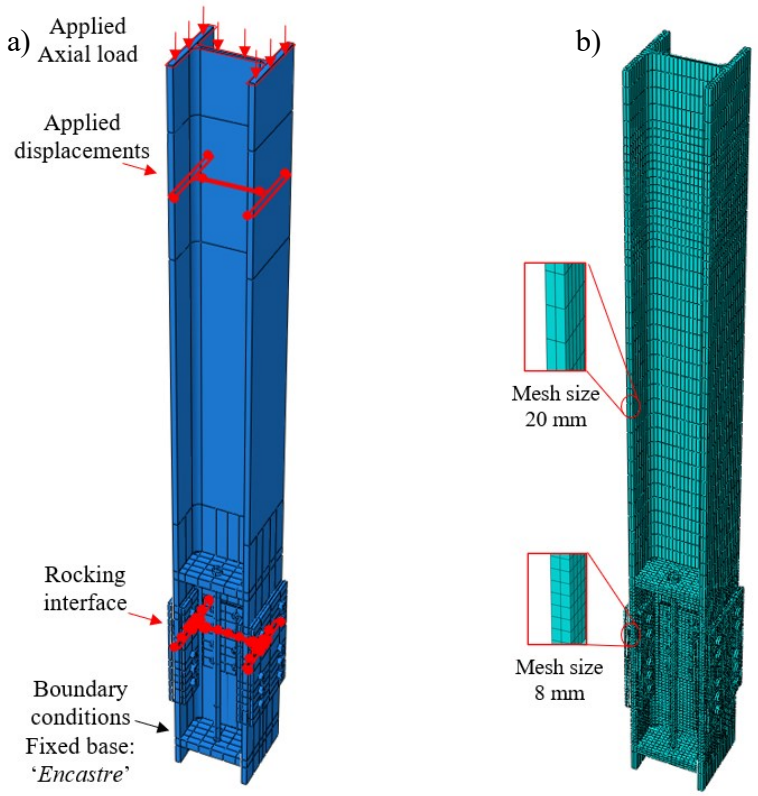

Figure 3.21: ABAQUS [20] FE model: (a) Boundary conditions, (b) Geometry and meshing.

a)

Steel	f_y (N/mm^2)	f_u (N/mm^2)	$\frac{\varepsilon_h}{\varepsilon_y}$	$\frac{E}{E_h}$	$\frac{E}{E_u}$	$\frac{\varepsilon_u}{\varepsilon_y}$	ε_u (%)
Fe360	235	360	12.3	37.5	523.2	≥ 357	≥ 40
Fe430	275	430	11.0	42.8	447.6	≥ 425	≥ 56
Fe510	355	510	9.8	48.2	381.7	≥ 479	≥ 81

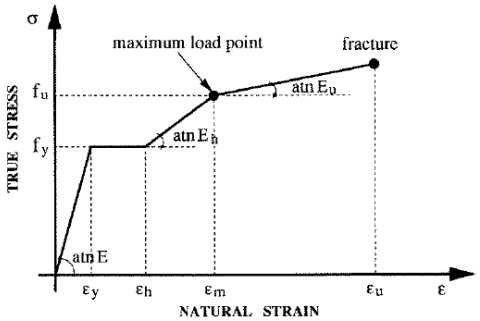

b)

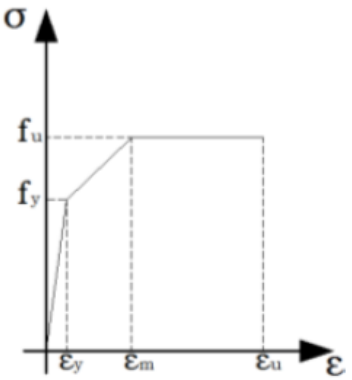

Figure 3.22: Materials constitutive laws: (a) SC-CB components; b) bolts/PT bars.

Applied loads

The option '*bolt load*' [20] is used to model the initial pre-load force in the web and flange bolts and the initial PT force in the PT bars. The '*apply force*' option [20] is used for bolts to keep the force constant throughout the analysis. Conversely, the '*adjust length*' option [20] is used to allow correctly capturing the force variation of the PT bars (*i.e.,* elongation or shortening during the rocking behaviour). It is important to highlight that the self-centring system is modelled by including the PT bars with mechanical properties modified to also account for the deformability of the disk springs. The '*von Mises*

yield criterion' coupled with '*isotropic hardening*' [20] is used to model plasticity. Figure 3.23 (a) illustrates the applied loads on the bolts and PT bars.

Table 8. Material properties for the ABAQUS [20] model.

Steel S275		
Elastic	Young's Modulus	Poisson's Ratio
	210000	0.3
Plastic	Yield Stress	Plastic Strain
	306.57	0
	306.57	0.0146
	341.76	0.0218
	593.6	0.5585
Bolts		
Elastic	Young's Modulus	Poisson's Ratio
	210000	0.3
Plastic	Yield Stress	Plastic Strain
	900	0
	900	0.09
	1000	0.654
PT bar		
Elastic	Young's Modulus	Poisson's Ratio
	22575	0.3
Plastic	Yield Stress	Plastic Strain
	900	0
	900	0.09
	1000	0.654

Interactions properties

The interaction properties among the parts are modelled with the '*surface-to-surface*' contact interaction [20]. This is implemented using the '*hard*' contact property to describe the behaviour in the normal direction. In contrast, the '*penalty*' option is used for the tangential response with friction coefficient values equal to 0.30 for interfaces among steel parts (*i.e.,* plates, bolts, PT bars, and the column). This value is assumed to model the friction coefficient for all the interfaces of the steel components, consistently with EN 1090-2 [17]. Conversely, the friction coefficient 0.53 is used for the shims-steel interfaces of the FDs (*i.e.,* equivalent to the 5% dynamic percentile of the friction coefficient [5]). The '*TIE*' constraint [20] is used to simulate full penetration welds (*i.e.,* monolithic connection) between the PT bars' anchorage plates and the column's internal part. Figure 3.23(b) illustrates a detail of the contact interactions of the connection.

Analyses

The analyses (Figure 3.24) are performed considering three loading steps with the following sequence:

i) axial load (*i.e.,* the axial load is applied as a uniform pressure on the column's top section);
ii) pre-loading of the bolts and the PT bars (*i.e.,* the pre-loading forces are applied with the '*apply force*' and '*adjust length*' options for bolts and PT bars respectively;
iii) displacement history (*i.e.,* the displacement history is applied to the column's top section).

The displacement-controlled protocol is consistent with the test procedure [1] for displacements up to 93 mm (*i.e.,* joint rotation of 0.06 rad). The non-linear equilibrium equations are solved using the '*static general*' analysis procedure. The standard '*full Newton*' solution technique is adopted with an automatic incrementation scheme to apply the load. The initial increment size is 0.001 mm, with minimum and maximum values equal to 10^{-15} mm and 1 mm, respectively. The '*automatic stabilization*' (*i.e.,* viscous damping is applied between contact pairs [20]) with '*specify dissipated energy fraction*' (*i.e.,* calculates the damping factor from a specific value of dissipated energy fraction [20]) and with '*specify damping factor*' (*i.e.,* assigns the damping factor [20]) are adopted to overcome convergence problems during the analysis. Geometrical imperfections are not considered in the model.

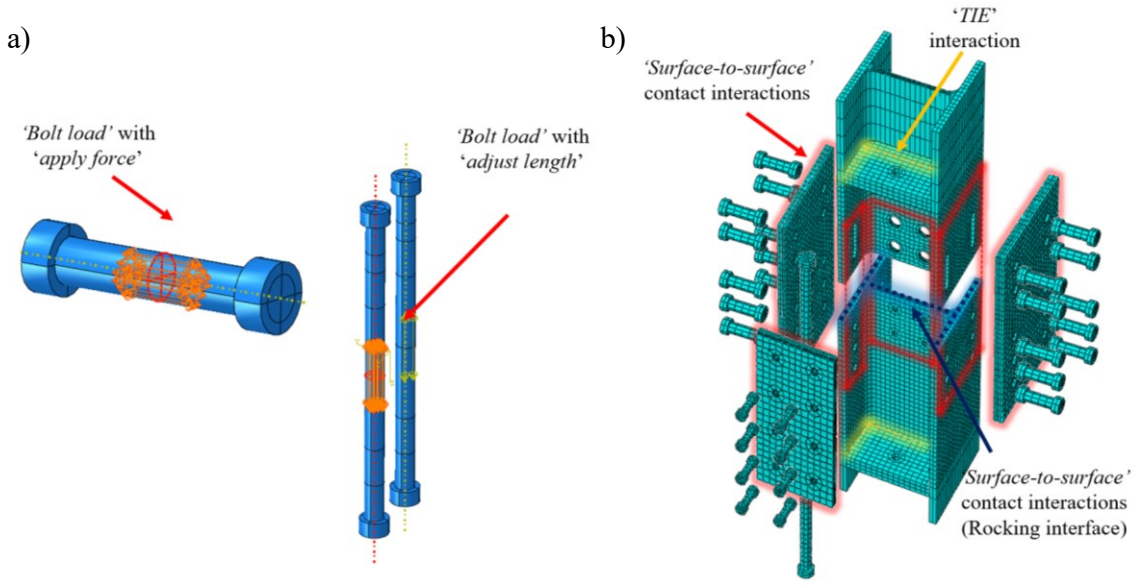

Figure 3.23: ABAQUS [20] FE model: a) Applied loads, b) Interaction properties.

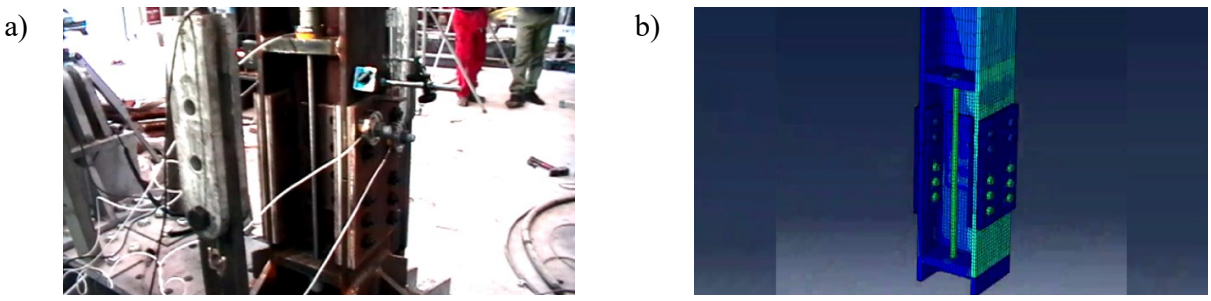

Figure 3.24: SC-CB: a) Experimental Tests; b) Validation of the FE model in ABAQUS [20]

3.8.2.2 Validation

As for the numerical model developed in the previous section, the FE modelling strategy in ABAQUS [20] is validated against the experimental results [1] for three cyclic tests whose main design parameters are reported in Table 7. Tests 1 and 2 are characterised by the higher value of the axial load (*i.e.,* 728 kN) and are performed respectively with and without PT bars. Test 3 is carried out considering the lower value of the axial load ratio (*i.e.,* 350 kN), and it is characterised by the absence of the PT bars. Figure 3.25 shows the comparison between the FE model and the experimental results in terms of moment-rotation (*Moment- θ*) behaviour of the joints for rotation up to 0.06rads.

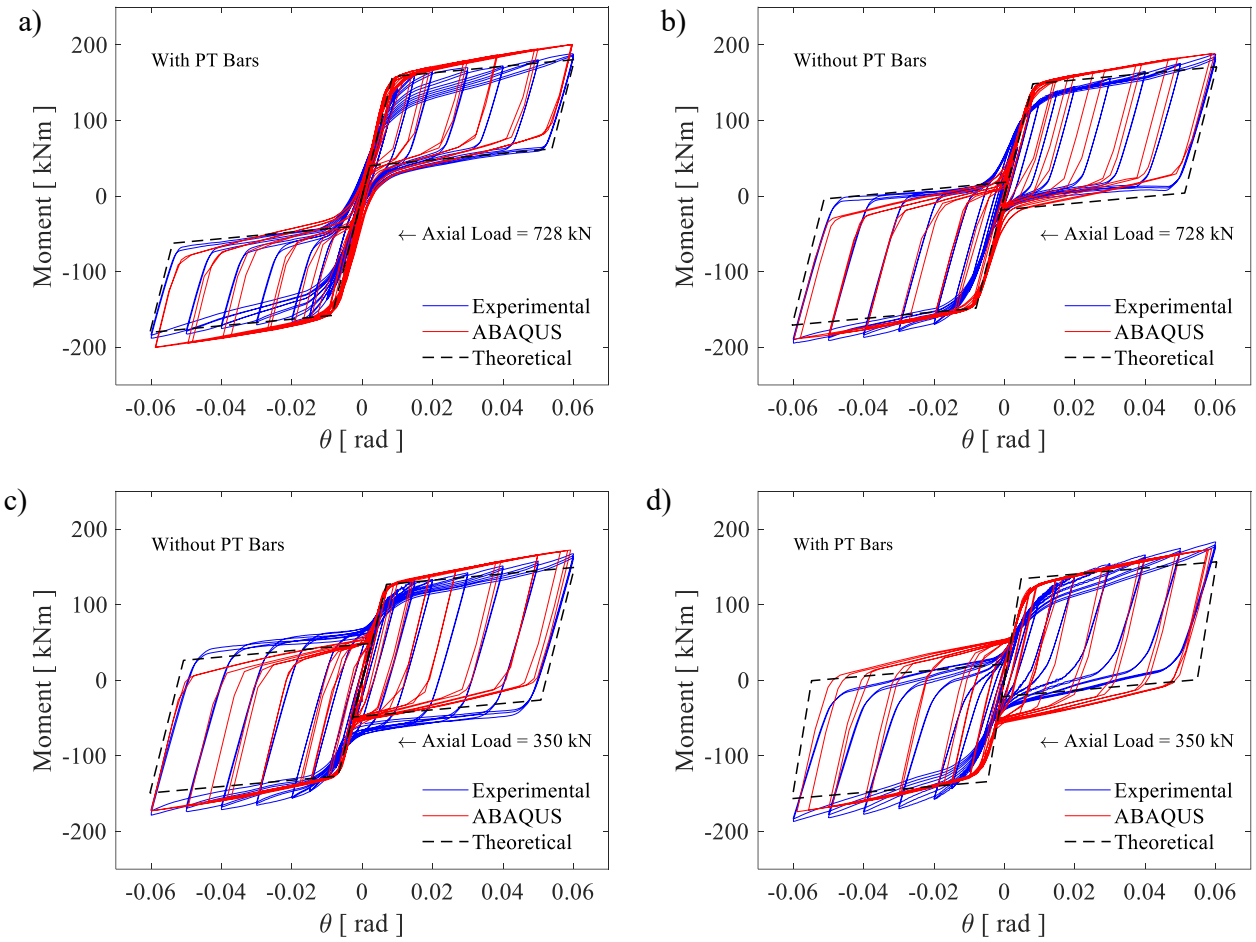

Figure 3.25: Comparison between ABAQUS [20] model and experimental data [1]. Moment-Rotation hysteretic behaviour for the: (a) Test 1; (b) Test 2; (c) Test 3; (d) Test 4.

The ABAQUS results are shown in red lines, while the experimental data are reported in blue lines. Also, the analytical moment-rotation relationships are reported with dotted black lines. The comparison shows a good agreement, demonstrating the effectiveness of the FE model and of the analytical formulation in predicting the experimental response. Figure 3.25 (a) (*i.e.,* Test 1 - high axial force and PT bars) shows a full self-centring behaviour with a very low residual rotation (*i.e.,* 2.1 mrad), Figure 3.25 (b) (*i.e.,* Test 2 - high axial force and no PT bars) shows a reduced self-centring capacity, while Figure 3.25 (c) (*i.e.,* Test 3 - low axial force and no PT bars) shows a significant residual rotation. Figure

3.25 (d) (*i.e.,* Test 4- low axial force and with PT bars) shows a reduced self-centring capacity since the initial tension in the bars was not enough to achieve the self-centring condition. These results highlight the influence of the axial force (N_{Ed}) and of the pre-load of the PT bars in controlling the moment-rotation behaviour of the SC-CB and demonstrate the ability of the numerical and analytical models to capture these effects.

However, some limitations of the FE and analytical models can be observed. Among others, as previously discussed, the analytical model neglects the flange plates' bending contribution, and the effect of this assumption is reflected in the analytical model's slightly lower strain hardening behaviour with respect to both experimental results. In addition, with respect to the OPENSEES [19] simplified model, smoother curves are obtained from ABAQUS [20] due to the modelling of the flexibility of all the SC-CB components. In addition, the contribution of the flange plates' in bending is considered in ABAQUS [20]. Moreover, the experimental results showed a loss of the pre-loading force in the bolts of the FDs during the cyclic loading history. Figure 3.26 (a) and (b) show, respectively, the forces of two flange bolts and of the two PT bars along with Test 1.

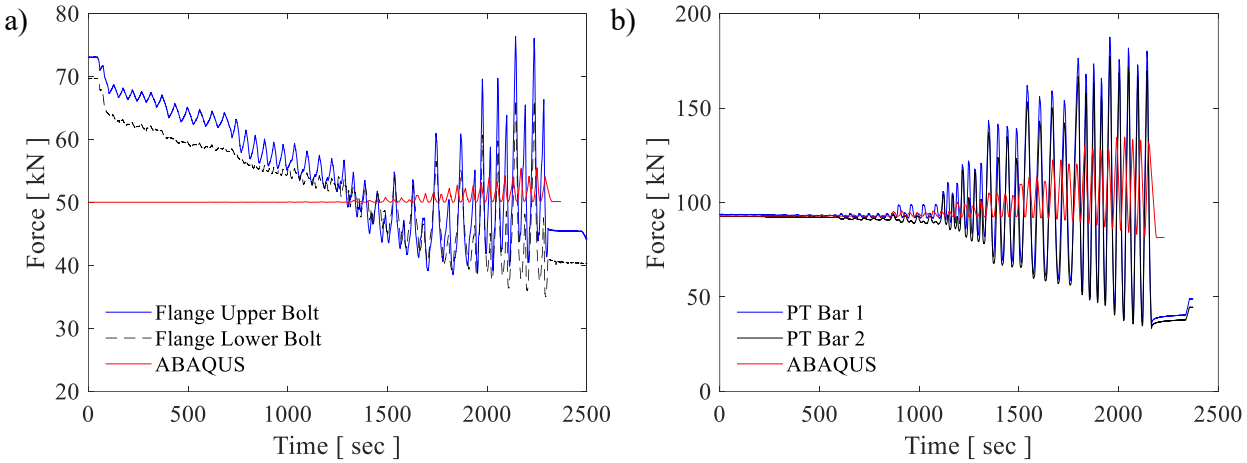

Figure 3.26: Comparison between ABAQUS [20] model and experimental data [1] for Test 1: a) Force fluctuation of the bolts of the flange FDs; b) Force fluctuation of the PT bars

In particular, as it is possible to observe in Figure 3.26 (a), it has been noted that the flange bolts, which were initially tightened to reach the proof load, were characterised by a loss of 7-10% of the initial pre-load after the first cycle of the loading history. Afterwards, they uniformly reached a total loss of about 20%. Also, the deterioration of the coating may represent a possible explanation for this loss. For these reasons, the web and flange bolts' pre-loading forces in the ABAQUS [20] model were reduced by 20% with respect to the pre-loading experimental values. However, the time history of the bolts' force loss is not simulated in the FE model, leading to some small differences between numerical and experimental results.

Figure 3.27 shows the Von Mises stress distributions obtained from the ABAQUS results, corresponding to a lateral displacement of 93 mm (*i.e.,* SC-CB rotation of 0.06 rad). It can be observed that, as expected,

all regions of the SC-CB connection are characterised by stresses lower than yielding, with only some stress concentrations nearby the spliced section and in the PT bars during their elongation.

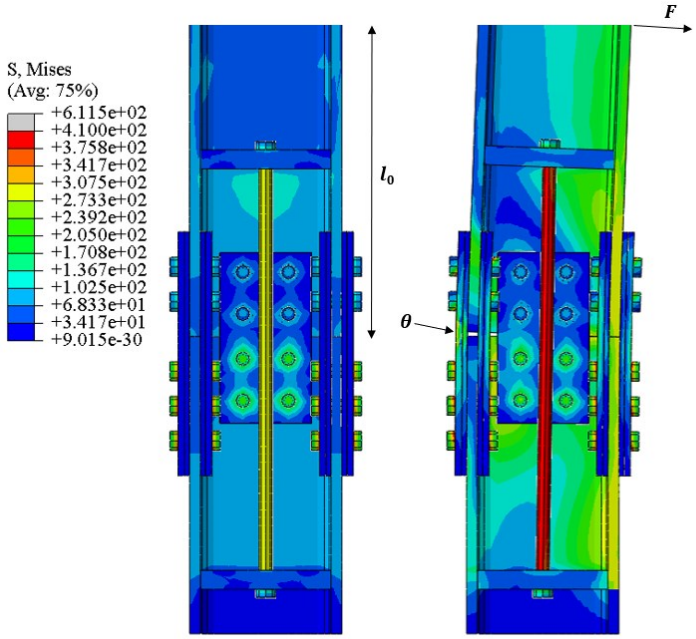

Figure 3.27: ABAQUS [20] results: Von Mises stresses corresponding to a lateral displacement of 62 mm (*i.e.,* SC-CB rotation of 0.06 rad)

In addition, it has already been pointed out that no evident damage was observed in the steel elements during the experimental campaign. However, the numerical analyses show some concentrations of slight plastic deformations, depicted in Figure 3.28 in terms of equivalent plastic strain (PEEQ) evaluated at 0.06rads (*i.e.,* the maximum rotation reached during the experimental tests). In the legend, the PEEQ limit has been assumed to be equal to 0.0146, which is the plastic strain of the material (highlighted in red), while the $PEEQ_{Max}$ is highlighted in blue. It is observed that the plastic damage on the column is concentrated near the spliced section (*i.e.,* where the COR is located), close to the oversized web holes and the flanges' slots. Conversely, no relevant plastic damage is observed in the cover plates, the friction shims of the web FD, and the web bolts. Furthermore, slight plastic deformations can be observed in the cover plates and friction shims of the flange FDs and in the bolts' shanks of the flange FDs, not shown due to space constraints. In addition, the PT bars do not exhibit plastic strain, as they remain in the elastic range, as expected. Additional considerations and investigations about the distribution of the plastic strains on the column are provided in Chapter 4.

3.9 Personal contribution

Chapter 3 focuses on the Damage-Free Self-Centring (SC-CB) connection. For this typology, theoretical formulation, experimental, and numerical activities have been presented and discussed. However, the original design procedure and the experimental investigations related to an isolated SC-CB are part of previous studies carried out at the University of Salerno; instead, the two FE modelling strategies (*i.e.,* simplified and advanced) and the validation against the experimental results represent the novelty of the

work and the main author's contribution. Consequently, the results from the validation process provide a more comprehensive view into the assumptions and limitations of the design methodology.

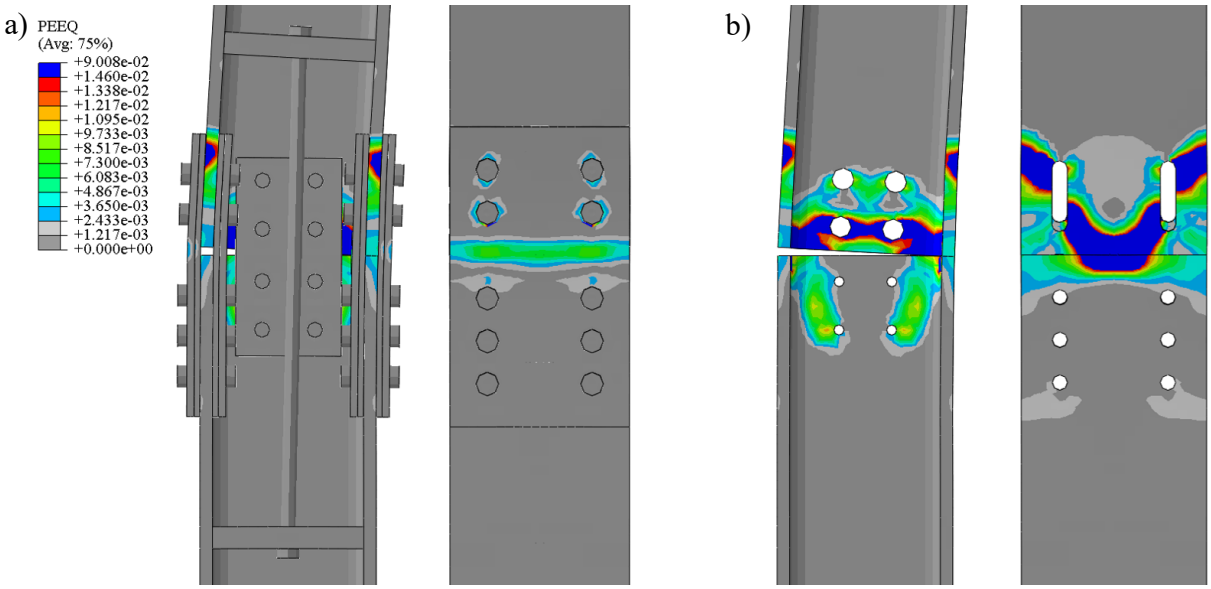

Figure 3.28: ABAQUS [20] results: equivalent plastic damage (PEEQ) at 0.06rads for the Cyclic Test 1: a) Assembly; b) Web and Flanges of the column's profile

3.10 References

1 M. Latour, G. Rizzano, A. Santiago, L. Da Silva, Experimental response of a low-yielding, self-centring, rocking CB joint with friction dampers, Soil Dyn. Earthq. Eng. 116 (2019) 580–592

2 G.F. Cavallaro, A. Francavilla, M. Latour, V. Piluso, G. Rizzano, Experimental behaviour of innovative thermal spray coating materials for FREEDAM joint. Composites Part B 115 (2017) 289-299

3 G.F. Cavallaro, A. Francavilla, M. Latour, V. Piluso, G. Rizzano, Cyclic behaviour of friction materials for low yielding connections. Soil Dyn. Earthq. Eng. 114 (2018) 404–423.

4 Latour M, Piluso V, Rizzano G. Experimental analysis of beam-to-column joints equipped with sprayed aluminium friction dampers, J. Constr. Steel Res. 2018; 146: 33–48.

5 M. Latour, M. D'Aniello, M. Zimbru, G. Rizzano, V. Piluso, R. Landolfo, Removable friction dampers for low-damage steel beam-to-column joints, Soil Dyn. Earthq. Eng. 115 (2018) 66–81.

6 A.B. Francavilla, M. Latour, V. Piluso, G. Rizzano, Design criteria for beam-to-column connections equipped with friction devices. J. Constr. Steel Res. 172 (2020)106240.

7 M. D'Antimo, M. Latour, G.F. Cavallaro, J-P. Jaspart, S. Ramhormozian, J-F. Demonceau, Short- and long- term loss of preloading in slotted bolted connections, J. Constr. Steel Res. 167 (2020) 105956

8 A.F. Santos, A. Santiago, M. Latour, G. Rizzano, L.S. da Silva, Response of friction joints under different velocity rates. J. Const. Steel Res. 168 (2020)

9 Elettore E, Freddi F, Latour M, Rizzano G. Design and analysis of a seismic resilient steel moment-resisting frame equipped with damage-free self-centring CBs. J Constr Steel Res. 2021;179:106543. https://doi.org/10.1016/j.jcsr.2021.106543

10 Elettore E, Lettieri A, Freddi F, Latour M, Rizzano G. Performance-based assessment of seismic-resilient steel moment resisting frames equipped with innovative column base connections. Structures 2021; 32:1646-1664. https://doi.org/10.1016/j.istruc.2021.03.072
11 Lettieri A, Elettore E, Pieroni L, Freddi F, Latour M, Rizzano G. Parametric analysis of steel MRFs with self-centring column bases. Steel Construction. 2022; 5(2), 91–99. https://doi.org/10.1002/stco.202100050
12 Elettore E, Freddi F, Latour M, Rizzano G. Parametric Finite Element Analysis of Self-centring Column Bases with different Structural Properties. J Constr Steel Res. 2022; 199, 107628. https://doi.org/10.1016/j.jcsr.2022.107628
13 ANSI/AISC 341-16 Seismic provisions for structural steel buildings. American Institute of Steel Construction, Chicago, USA, 2016.
14 EN 1998-1, Eurocode 8: Design of structures for earthquake resistance – Part 1: General rules, seismic actions and rules for buildings, European Committee for Standardization, Brussels
15 EN 1993-1-8, Eurocode 3: Design of steel structures, Part 1-8: Design of steel structure: General rules and rules for buildings, 2005, European Committee for Standardization, Brussels
16 EN 1993-1-1, Eurocode 3: Design of steel structures, Part 1-1: Design of steel structures: Design of joints, 2005, European Committee for Standardization, Brussels.
17 EN 1090-2. Execution of steel structure and aluminium structure: technical requirements for steel structures
18 ANSI/AISC 360-10 Specification for Structural Steel Buildings. *American Institute of Steel Construction*, Chicago, USA, 2010.
19 S. Mazzoni, F. McKenna, M.H. Scott, G.L. Fenves OpenSEES: Open System for earthquake engineering simulation, Pacific Earthquake Engineering Research Centre (PEER), 2009, Univ. of California, Berkley, CA
20 ABAQUS/Standard and ABAQUS/Explicit – Version 2017. ABAQUS Theory Manual, Dassault Systems, 2016. http://130.149.89.49:2080/v6.14/books/usb/default.htm
21 C. Faella, V. Piluso, G. Rizzano, Structural steel semirigid connections. CRC Press, Boca Raton (FL), 2000.

Chapter 4 Parametric Finite Element Analysis of SC-CBs with different structural properties

4.1 Introduction

In the previous Chapter, the design methodology for the SC-CB has been proposed, and two FE modelling strategies (*i.e.,* simplified and advanced) have been developed and validated against experimental results. The results of the FE validation showed that both models correctly predicted the global response observed during the experimental tests, also providing useful insights into the characterisation of both the global and local behaviour of the SC-CB connection. However, the parameters investigated in the experimental campaign were limited, and further research and additional information are still required for the definition of a more detailed view into the influence of the relevant design parameters affecting the local behaviour of the connection toward the following objectives:

i) to investigate the scale effect on different geometrical configurations;
ii) to provide insights into the local behaviour of SC-CBs under cyclic loading;
iii) to identify the parameters that mainly affect the local behaviour of SC-CBs given specific performance objectives (*i.e.,* minimal yielding of the joint components and self-centring capacity);
iv) to provide insights about the adopted design procedure for the development of design guidelines and design recommendations for this joint typology.

A parametric FE analysis was conducted in ABAQUS [1] to fulfil these objectives. Three case-study perimeter steel MRFs are selected, equipped with the SC-CBs, extracted from reference prototype buildings. The design for the case-study MRFs follows the Eurocode 8 provisions [2], while the design for the SC-CBs follows the design procedure proposed in Chapter 3. Then, three SC-CBs are selected, and a matrix of sixteen different Configurations is considered for each SC-CB, obtained by varying three design properties of the joints. The parametric FE analysis focuses on three crucial aspects deriving from the design assumptions, which can be summarised as follows:

i) the bending contribution of the flanges' plates of the FDs over the global and local behaviour of the SC-CB;
ii) the distribution of the shear forces among the joint components (*i.e.,* the web FDs, the flange FDs, the PT bars and the sliding mechanisms of the friction at the rocking interface;
iii) the effect of the variability of the axial force over the self-centring capacity of the SC-CB. The SC-CBs are modelled in ABAQUS [1] by following the validated modelling strategy presented in Chapter 3.

Global and local parameters are monitored and critically compared for each SC-CB, considering all the Configurations, to identify the best design solution for improved self-centring capacity of the joint and minimal yielding of the components. The global response of the joints is evaluated in terms of hysteretic moment-rotation behaviour. Conversely, the local responses are evaluated by monitoring the equivalent plastic strain distributions and the column's plastic dissipated energy and components. The results from the FE parametric analysis provide a more comprehensive view of the design methodology's assumptions and limitations, suggesting additional recommendations to improve the design requirements.

4.2 Design of the case-study MRFs

The selected case-study MRFs are extracted from three prototype structures whose plan and elevation views are shown in Figure 4.1. Seismic-resistant perimeter MRFs are located in the *x*- and *y*- directions, while the interior part comprises gravity frames (*i.e.,* with pinned BCJs and pinned CBs). The first prototype structure (*i.e.,* MRF1) is characterised by four MRFs in each direction. Conversely, the second and the third prototype structures (*i.e.,* MRF2 and MRF3) are equipped with two perimeter MRFs in each direction. It is worth highlighting that the MRF1 is the large-scale representation of the reference building, and additional details are provided in Chapter 6. Concerning the MRF2 and the MRF3, the layout has interstorey heights of 3.20 m except for the first level, whose height is equal to 3.50 m, while all the bays have spans of 6 m. The present study focuses on the MRFs located in the *x*-direction, and the design is performed following the Eurocode 8 provisions [2].

The steel-concrete composite floor system comprises steel beams and HI BOND A55/P600 type composite floor connected through shear connectors to a concrete slab. The slab is supposed to be disconnected from the BCJs by adopting crushable material. The gravity and the live loads are assumed to be uniformly distributed, and the masses have been assessed considering the tributary areas and evaluated based on the seismic combination of Eurocode 8 [2]. The gravity and live loads are assumed to be uniformly distributed with values listed in Table 9. A uniform load for cladding of 2.0 kN/m is considered only for the external beams at the intermediate storeys. The total mass of the building is equal to 38 and 28.4 tons for the intermediate storey and the roof, respectively, for the MRF1. The total mass of the building is equal to 156.1 and 154.4 tons for the intermediate storey and the roof, respectively, for the MRF2 and MRF3. The indications of the masses are listed in Table 9 for all the case-study MRFs.

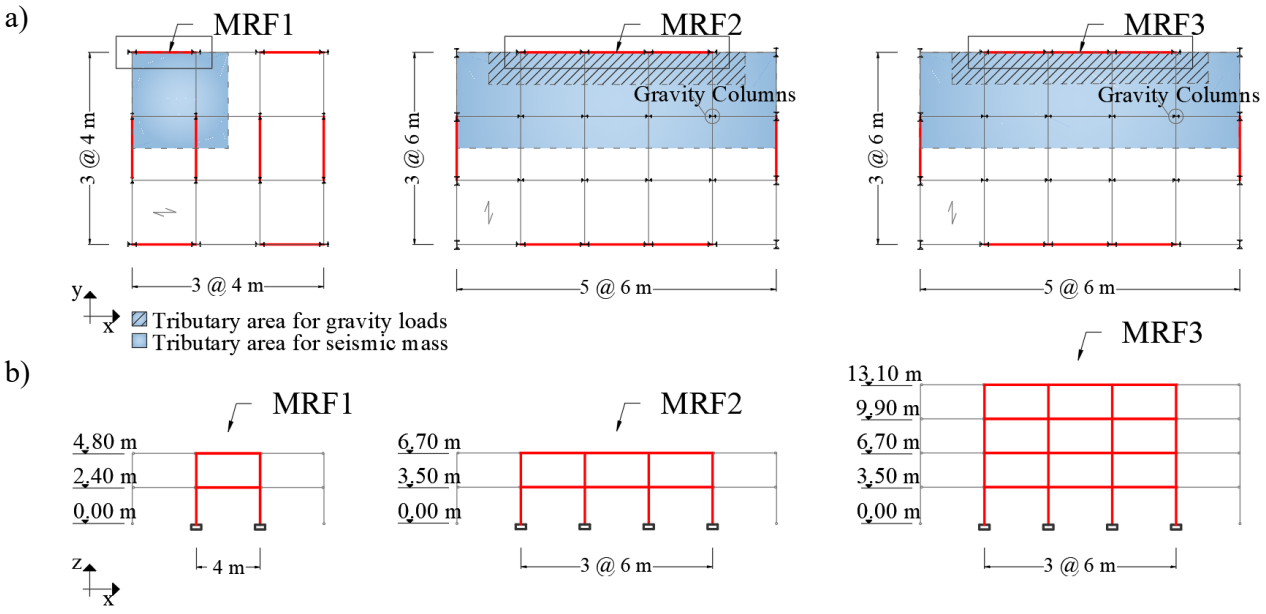

Figure 4.1: Case-study buildings: (a) Plan views; (b) Elevation views.

Table 9. Loads and masses of the case-study MRFs.

	MRF1		MRF2		MRF3	
Loads and masses	i-level	roof	i-level	roof*	i-level	roof*
Gk [kN/m^2]	3.90	3.60	4.50	4.50	4.50	4.50
qk [kN/m^2]	3.00	0.50	2.00	0.50	2.00	0.50
Mass [tons]	38	28.4	156.1	154.4	156.1	154.4

*Note: roof no claddings

The ULS (*i.e.,* Ultimate Limit State, probability of exceedance of 10% in 50 years) is defined considering the Type 1 elastic response spectrum with a 2% damping factor ξ, a Peak Ground Acceleration (PGA) equal to 0.35g and soil type C. The CLS (*i.e.,* Collapse Limit State, probability of exceedance of 5% in 50 years) is assumed to have an intensity equal to 150% of the ULS. The behaviour factor is evaluated according to the requirements of Eurocode 8 [2] for MRFs in Ductility Class High (DCH) and hence assumed as q = 6.5. The design and elastic spectra are illustrated in Figure 4.2. It is important to mention that other methodologies for a more consistent selection of q in DCH exist (*i.e.,* the Improved Force-Based Design (IFBD) methodology by Macedo *et al.*, [3-4]) and aim at exhibiting a more uniform inelastic demand over the building height, compatible with the design assumptions. These studies evaluated the expected direct economic seismic losses in steel MRFs designed in DCH. However, these methodologies are not considered in the present thesis, as the objective is to assess the influence of the proposed SC-CB on the seismic response of steel MRFs.

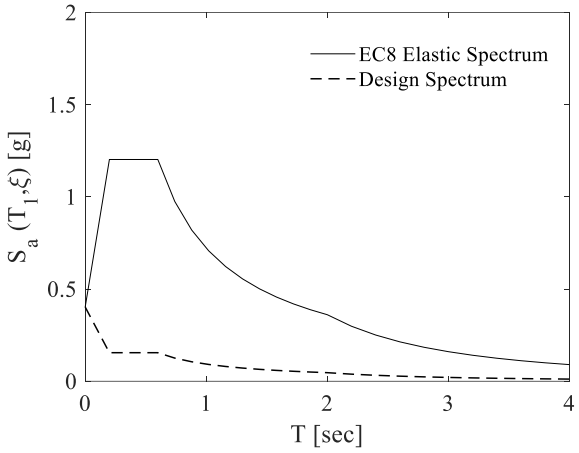

Figure 4.2: Eurocode 8 [2] Elastic and Design Spectra for the case-study MRF2 and MRF3.

The structures have non-structural elements fixed so as not to interfere with structural deformations. Therefore, the interstorey drift limit for DLS (*i.e.,* Damage Limit State, probability of exceedance of 10% in 10 years) is assumed as 1%, accordingly to Eurocode 8 [2] recommendations. The indications of the beams' and columns' cross sections are reported in Table 10 for each of the designed case-study frames. Two steel grades are used for the beams and the columns: the steel yield strength is equal to 355 MPa for columns and 275 MPa for beams. The frames are optimally designed to distribute a uniform ductility demand for all the storeys. In all cases, the BCJs are conventional full-strength welded joints. The PZs are stiffened with doubler plates with a thickness equal to one of the column's web. This is essential to ensure adequate stiffness to the joints and promote the plastic engagement of the beams.

The fundamental periods of vibration are respectively equal to T_1 = 0.42, 0.56 and 0.74 sec for the MRF1, MRF2 and MRF3.

Table 10. Profiles' cross-sections.

MRF1			MRF2			MRF3		
Floor	Beams	Columns	Floor	Beams	Columns	Floor	Beams	Columns
						1	IPE 550	HE 600B
1	IPE 270	HE 220B	1	IPE 450	HE 400B	2	IPE 550	HE 600B
2	IPE 270	HE 220B	2	IPE 450	HE 400B	3	IPE 500	HE 500B
						4	IPE 500	HE 500B

Table 11 reports the fundamental periods of vibrations and the spectral accelerations corresponding to the DBE ($S_{a,\,DBE}$) and MCE ($S_{a,\,MCE}$). It is underlined that DBE (*i.e.,* Design Based Earthquake), MCE (*i.e.,* Maximum Credible Earthquake) and FOE (*i.e.,* Frequently Occurred Earthquake) correspond to the ULS, CLS and DLS, respectively, according to the USA definition [5] and will be used in this work to identify the selected seismic intensities of interest. It is essential to highlight that the stiffness requirement related to the DSL is the one that controls the sizing of beams and columns and that the design of the frames has been performed by considering code prescriptions and technological requirements consistently such that it allows assessing the influence of the design strategy on the seismic response of the different case studies The P-delta effects are not considered since the interstorey drift sensitivity coefficient θ is less than 0.1, at all the storeys of all the case-study frames, where θ is calculated following Eurocode 8 requirements [2].

Table 11. Fundamental Period (T_1) and spectral acceleration ($Sa(T_1,\xi)$) for DBE and MCE.

MRF1			MRF2			MRF3		
T_1 [sec]	$S_{a,\,DBE}$ [g]	$S_{a,\,MCE}$ [g]	T_1 [sec]	$S_{a,\,DBE}$ [g]	$S_{a,\,MCE}$ [g]	T_1 [sec]	$S_{a,\,DBE}$ [g]	$S_{a,\,MCE}$ [g]
0.42	1.05	1.58	0.74	1.00	1.50	1.27	0.57	0.85

4.3 Design of the SC-CB

Once the frame design is finalised with rigid full-strength CBs, the damage-free SC-CB connections are designed according to the procedure presented in Chapter 3. The cross-section profiles of the first storey external columns are HE 200B, HE 400B, and HE 600B of S355 steel class. The columns are designed by following Eurocode 3 [6] and Eurocode 8 [2] requirements (*e.g.,* resistance and buckling checks).
The geometrical configurations of the SC-CBs are indicated in Table 12, including the position of the splice and the internal lever arm for each connection, corresponding to $z = h_c - t_{fc}$ with h_c and t_{fc} being respectively the height and the flange's thickness of the cross-section of the column. The three considered SC-CBs are hereinafter referred to as SC-CB1, SC-CB2 and SC-CB3. The design input actions are reported in Table 13, where "-" stands for tension and "+" for compression. It is worth mentioning that these columns' actions are defined by considering the proper location of the splices. With the design actions, FDs, PT bars and the disk spring system are designed accordingly. The material properties are summarised in Table 14, where *E,* f_y and f_u are the nominal values of the Young's

modulus, the yield strength and the ultimate tensile strength of the materials, respectively. The other proprieties of the adopted structural steel (*i.e.,* the shear modulus, the Poisson's ratio) are based on the Eurocode 3. The FDs comprise 8 mm coated friction pads of S355 steel class, clamped with HV 10.9 class bolts and S355 steel cover plates for both web and flanges. The friction coefficient (μ) is assumed to be equal to 0.53, consistent with previous studies on friction interfaces [7]. The geometry and the structural details of the web and flanges FDs are reported in Table 15 and Table 16, respectively.

Table 12. SC-CBs geometrical configurations.

Specimen	Column [-]	Splice (l_b) [mm]	Internal lever arm (z) [mm]
SC-CB1	HE 200B	500	185
SC-CB2	HE 400B	700	376
SC-CB3	HE 600B	850	570

Table 13. SC-CBs Design input actions.

Specimen	N_{Ed} [kN]	M_{Ed} [kNm]	V_{Ed} [kN]
SC-CB1	+138, -127	127	115
SC-CB2	+372, -183	683	427
SC-CB3	+1248, -848	1430	765

Note: negative values are for tension; positive values are for compression.

Table 14. SC-CBs Material properties.

Elements	Class [-]	E [GPa]	f_y [MPa]	f_u [MPa]
Column and plates	S275	210	355	510
Web Bolts	HV 10.9	210	900	1000
Flange Bolts	HV 10.9	210	900	1000
PT bars	10.9	205	900	1000

Table 15. Web FDs geometry and structural properties

Specimen	b_{wp} [mm]	h_{wp} [mm]	t_{wp} [mm]	e1 [mm]	p1 [mm]	e2 [mm]	p2 [mm]	d_h [mm]	$z/2$ [mm]	Bolts [-]	$n_{b,w}$ [-]	$F_{p,w}$ [kN]
SC-CB1	130	300	8	30	70	30	70	30	93	M14	4	28
SC-CB2	290	600	12	80	140	75	140	60	187	M27	4	100
SC-CB3	390	800	15	120	180	90	200	75	258	M30	4	181

Table 16. Flange FDs geometry and structural properties

Specimen	b_{fp} [mm]	h_{fp} [mm]	t_{fp} [mm]	e1 [mm]	p1 [mm]	e2 [mm]	p2 [mm]	l_{slot} [mm]	z [mm]	Bolts [-]	$n_{b,f}$ [-]	$F_{p,f}$ [kN]
SC-CB1	200	300	8	50	50	39	122	30	185	M14	4	34
SC-CB2	400	600	12	80	70	60	184	60	374	M27	6	44
SC-CB3	600	800	15	100	100	65	170	75	570	M27	6	68

The self-centring system includes high-strength PT bars 10.9 class and disk springs special washers DIN 6796 where each disk spring's resistance and stiffness ($K_{ds,1}$) are 200 kN and 100 kN/mm, respectively.

The properties of the PT bars and the disk spring system are indicated in Table 17. Figure 4.3 illustrates the plan and the elevation view of the SC-CBs.

Table 17. Self-centring system geometry and structural properties

Specimen	t_p [mm]	Bars [-]	n_{PT} [-]	$F_{p,PT}$ [kN]	n_{par} [-]	n_{ser} [-]	K_{PT} [kN/mm]	K_{DS} [kN/mm]	K_{eq} [kN/mm]	$\Delta l_{avg,PT}$ [mm]
SC-CB1	40	M30	2	366	3	7	162	39	63	4
SC-CB2	85	M36	4	514	4	18	112	21	69	13
SC-CB3	100	M36	6	514	4	26	84	14	72	18

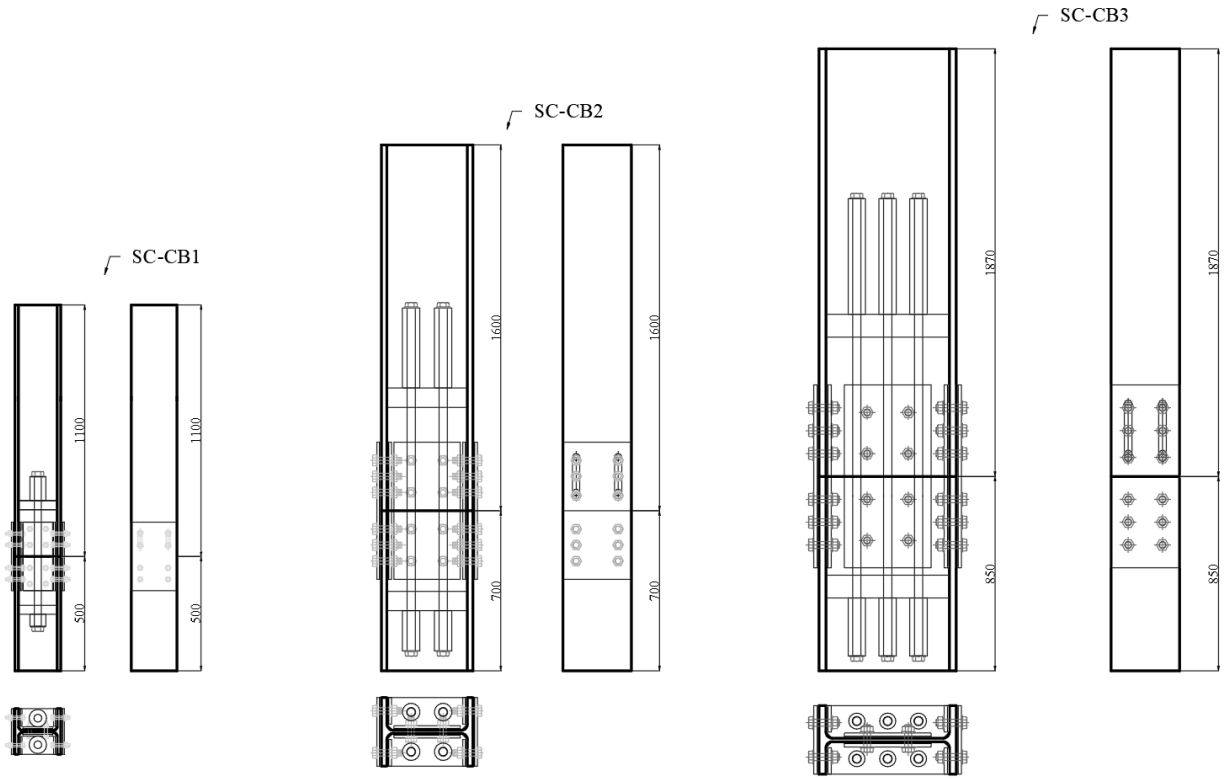

Figure 4.3: Plan and elevation view of the case-study SC-CBs.

4.4 Investigated structural properties

A parametric FE analysis is carried out on three SC-CBs belonging to three different MRFs. The SC-CBs are designed following the design procedure proposed in Chapter 2 and successively developed in ABAQUS [1] following the modelling strategy discussed in Chapter 3. The objectives of the FE parametric analysis are *i)* to investigate the scale effect on different geometrical Configurations of the SC-CB joint and *ii)* to focus the attention on three crucial aspects deriving from the design assumptions in view of obtaining specific performance objectives (*i.e.,* minimal yielding of the joint components and self-centring capacity). The parametric FE analysis focuses on three crucial aspects deriving from the design assumptions, which can be summarised as follows:

Influence of the thickness of the flanges' plates
The bending contribution of the flanges' plates of the FDs (Section 4.6): this is studied by varying the thickness of the flanges' plates, considering two limit Configurations for each SC-CB. The first corresponds to the design thickness (*i.e.,* obtained as the lower limit with respect to the axial force transmitted by the flange plates), while the second one refers to a value two times larger;

Influence of the design shear load
The distribution of the shear forces among the components (Section 4.7): this design aspect is analysed by considering the percentage of the design shear force assigned to the web FDs in the design phase. This value is assumed to be varied in a range of cases (*i.e.,* 100%, 75%, 50%, 0% of the design shear force (V_{Ed}) to provide information on how this design choice affects both the global and local behaviour of the SC-CB while evaluating the corresponding mechanism of the shear redistribution among the joint components (*i.e.,* the web FDs, the flange FDs, the PT bars and the sliding mechanisms of the friction at the rocking interface). These configurations are hereinafter referred to as 100%, 75%, 50% and 0%WFD, where 50%WFD indicates that 50% of the design shear force is assigned to the web FDs;

Influence of the design axial load
The effect of the variability of the axial force over the self-centring capacity of the SC-CB (Section 4.8): each Configuration is analysed under the maximum and minimum axial load conditions to evaluate the influence of the axial load over the global and local response of the joint. In addition, to verify the validity of the design assumptions concerning the axial design load described in Chapter 2, an additional Configuration of the SC-CB is designed and analysed, obtained by assuming the axial gravity load for the joint design. The self-centring requirements are checked for this additional axial load condition;

A matrix of sixteen design Configurations is considered for each SC-CB, obtained by varying the design parameters as indicated in Table 18.

Table 18. Matrix parameters for each SC-CB.

Model	Flanges' Plates Thickness	Shear Load % Web FDs	Axial Load
Configuration 1	t_{fp}	100	Max (+) - Min (-)
Configuration 2	2 t_{fp}	100	Max (+) - Min (-)
Configuration 3	t_{fp}	75	Max (+) - Min (-)
Configuration 4	t_{fp}	50	Max (+) - Min (-)
Configuration 5	t_{fp}	0	Max (+) - Min (-)
Configuration 6	2 t_{fp}	75	Max (+) - Min (-)
Configuration 7	2 t_{fp}	50	Max (+) - Min (-)
Configuration 8	2 t_{fp}	0	Max (+) - Min (-)

4.5 Methodology of the Parametric FE Analysis

The three SC-CBs FE models are developed in ABAQUS [1] by following the validated methodology defined in Chapter 2. An overview of the three FE models is shown in Figure 4.4. It is worth underlining that the length of the upper part of the columns above the splice differs for each case (*i.e.,* 1100 mm,

1500 mm and 1875 mm for the SC-CB1, SC-CB2 and the SC-CB3, respectively). Therefore, considering a target rotation (θ_t) equal to 0.04 rads, the target displacements are equal to 44 mm, 64 mm and 75 mm for the SC-CB1, SC-CB2 and SC-CB3, respectively. It is worth mentioning that the present work only considers the quasi-static cyclic response of the SC-CB. Additional studies are required to evaluate the seismic performance by explicitly considering the dynamic effects.

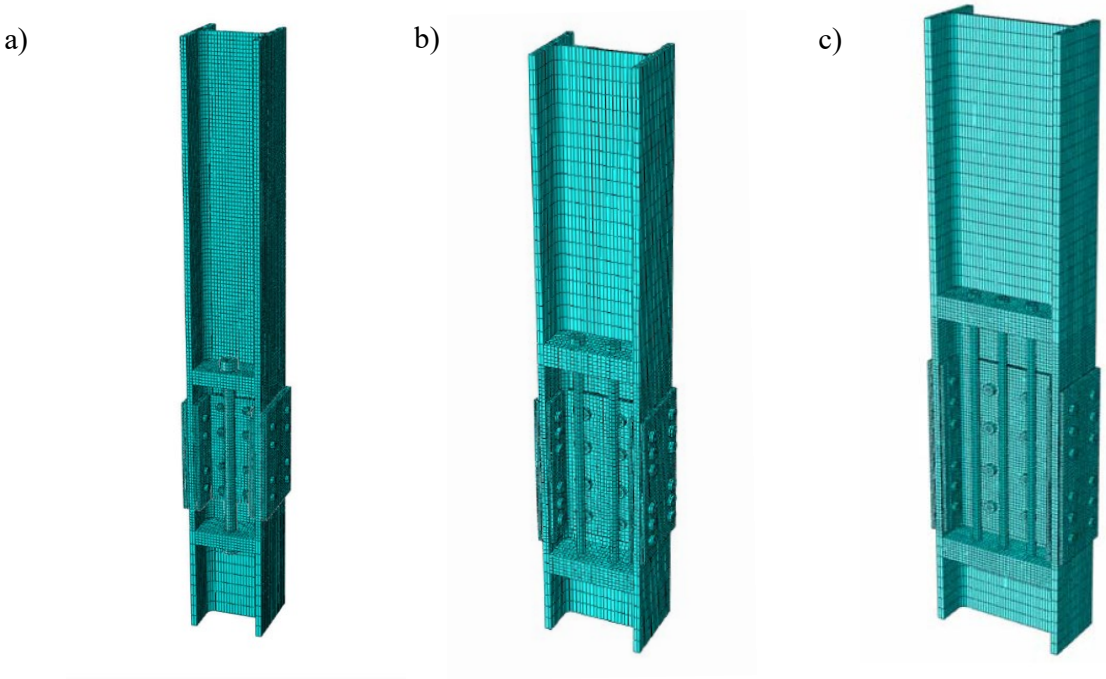

Figure 4.4: FE models developed in ABAQUS [1]: (a) SC-CB1; (b) SC-CB2; (c) SC-CB3.

Global and local responses are monitored to assess how the selected parameters affect the behaviour of each SC-CB. The responses for each SC-CB are compared to identify the best design solution in terms of improved self-centring capacity and minimal damage (*i.e.,* minimal yielding of the components). The global response of the joints is evaluated in terms of hysteretic moment-rotation behaviour. Conversely, the local responses are evaluated by monitoring the equivalent plastic strain distributions and the column's plastic dissipated energy and components.

The equivalent plastic strain is defined in ABAQUS [1] as PEEQ, which is a scalar variable representing the material's inelastic deformation, providing a yes/no flag telling if the material is currently yielding or not. The PEEQ is defined as follows:

$$\bar{\varepsilon}^{pl}|_0 + \int_0^t \dot{\bar{\varepsilon}}^{pl} dt \tag{4.1}$$

where $\bar{\varepsilon}^{pl}|_0$ is the initial equivalent plastic strain and $\dot{\bar{\varepsilon}}^{pl}$depends on the material model [1]. Conversely, the plastic dissipated energy is defined in ABAQUS [1] as ALLPD, representing the amount of the plastic energy dissipated by the whole connection during the analysis. Additionally, the distributions of the shear forces are illustrated to provide insights into the magnitude of the shear transferred by each

component of the SC-CB. For the sake of brevity, only the global and local responses of SC-CB1 and SC-CB2 are illustrated, considering the maximum (N_{Max}) and minimum compressive axial loads (N_{Min}). Results are not shown for SC-CB3. However, they exhibit a consistent trend with the results shown herein, and the following considerations can be extended to all cases.

4.6 Influence of the thickness of the flanges' plates

4.6.1 Global behaviour

Figure 4.5 and Figure 4.6 show the moment-rotation hysteretic curves for SC-CB1 and the SC-CB2 for the Configuration with N_{Max} and N_{min}. For all the SC-CBs, the figures compare the results of Configurations 1 and 2 (*i.e.,* t_{fp} - continuous blue lines; $2t_{fp}$ - dotted red lines), considering the maximum and minimum compressive axial load condition (*i.e.,* N_{Max} and N_{min}). These two Configurations are equipped with flange plates having a thickness of 8 - 16 mm for the SC-CB1, 12 - 24 mm for the SC-CB2 and 15 – 30 mm for the SC-CB3. In addition, the analytical models are also shown with continuous black lines. The results show that the global response of the connections is not significantly affected by the thickness of the flanges' plates, as expected. A quite similar hysteretic behaviour is observed between the two Configurations for all the SC-CBs. Nevertheless, it is noteworthy that the hysteretic curves of the Configurations equipped with the thicker plates show a slightly increased hardening, confirming the larger bending contribution with respect to the Configurations equipped with the thinner plates. However, these results suggest that neglecting the bending contribution of the flanges' plates in the design phase is possible. Consistent results are observed by considering the other axial load condition (N_{Min}).

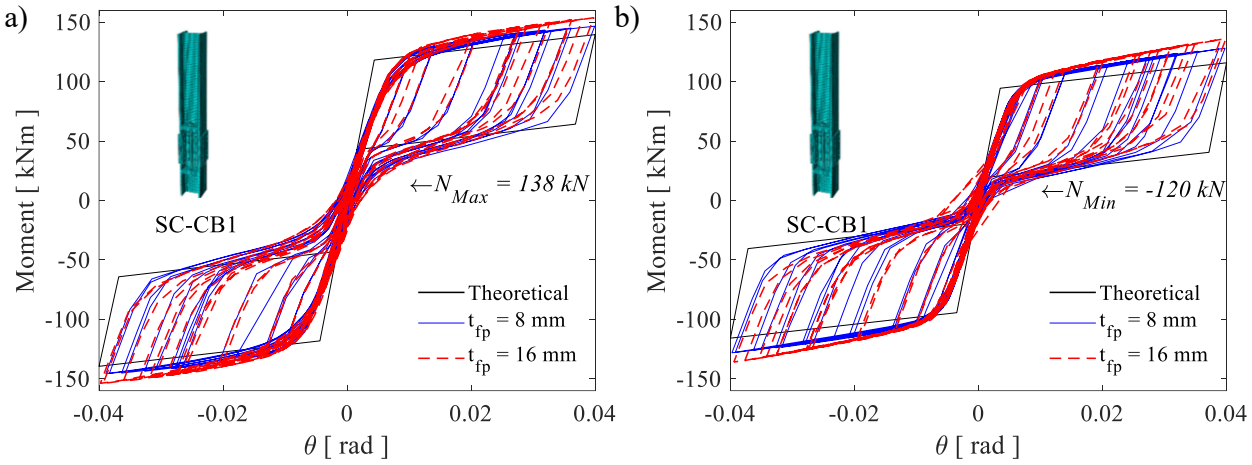

Figure 4.5: Influence of flanges' plate thickness. Moment-rotation behaviour of the SC-CB1 for the Configurations with: (a) N_{Max} and (b) N_{Min}

It is also worth highlighting that intermediate dimensions of the thickness of the flanges' plates have been investigated; however, for the sake of brevity, they have not been included, as they show a consistent trend with the results reported hereinafter. For example, results are shown for one case-study (*i.e.,* SC-CB1) in Figure 4.7. In this specific case, the thickness of the flanges plates has been varied

among 8 mm (*i.e.,* the lower limit value), 16 mm (*i.e.,* the two-times larger value) and 12 mm (*i.e.,* the intermediate case), considering the max axial load condition. Both the global and local responses have been analysed and compared; however, the intermediate case shows a consistent trend in agreement with the results already reported in this work. Therefore, it has been possible to derive a general tendency by comparing the results corresponding to the most significant cases, *i.e.,* the lower and the upper limits. Regarding the moment-rotation behaviour, negligible differences have been observed in the global responses of the three cases.

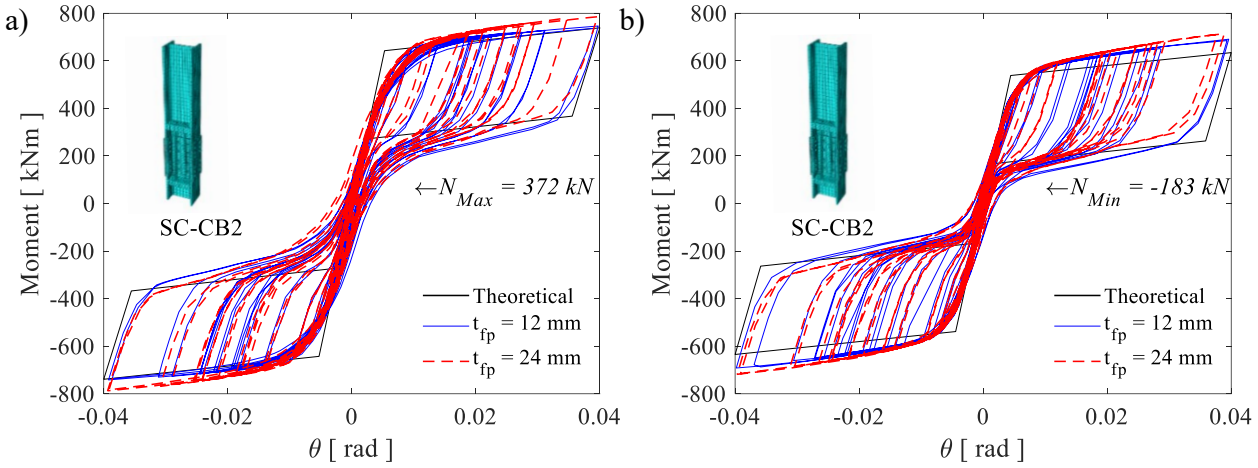

Figure 4.6: Influence of flanges' plate thickness. Moment-rotation behaviour of the SC-CB2 for the Configurations with (a) N_{Max} and (b) N_{Min}

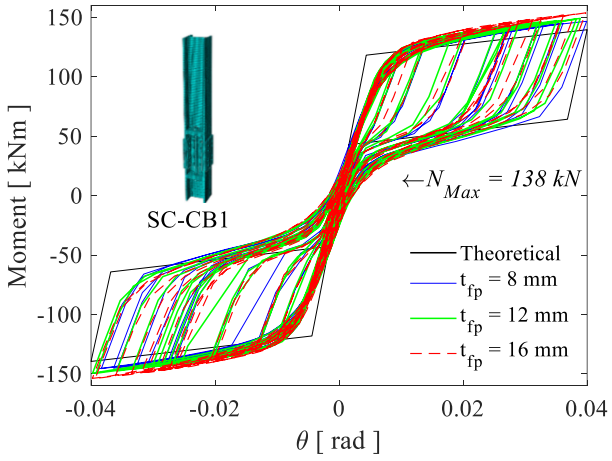

Figure 4.7: Influence of flanges' plate thickness, intermediate dimensions. Moment-rotation behaviour of the SC-CB1 for N_{Max}

4.6.2 Local behaviour

Figure 4.8 and Figure 4.9 show the local results in terms of PEEQ (*i.e.,* equivalent plastic strain) distributions for the SC-CB1 and the SC-CB2 in Configuration 1 and 2, respectively (*i.e.,* t_{fp} equal to 8

mm and 16 mm and t_{fp} equal to 12 mm and 24 mm). The results show the front and side views (*i.e.,* web and flanges) of the column at the end of the cyclic analysis, considering the maximum compressive axial load (N_{Max}). It is worth highlighting that the limit in the PEEQ legend is assumed equal to the strain corresponding to the beginning of the hardening (ε_h) of the material. Besides, the values exceeding the limit in the PEEQ legend (*i.e., $PEEQ_{max}$*) are depicted in blue within the legend, and their values are indicated by the arrows. Consistent results have been observed for the other configurations, which are not shown here for the sake of brevity. Some general considerations can be made regarding the location of the plastic strains for both Configurations. Some concentrations of slight plastic deformations are located nearby the splice, close to the oversized web holes and flanges' slots. In addition, slight plastic deformations can be observed in the cover plates and friction shims and in the bolts' shanks of the flange FDs, not shown herein due to space constraints. Conversely, as expected, the PT bars do not exhibit any plastic strain. These results are consistent with what is enforced by the design methodology described in Chapter 2. Additionally, comparing the PEEQ distribution between the two limit Configurations shows that the use of thicker flanges' plates leads to an increment of the strains' concentrations on the column's web and flanges. This effect is mainly due to their more significant stiffness.

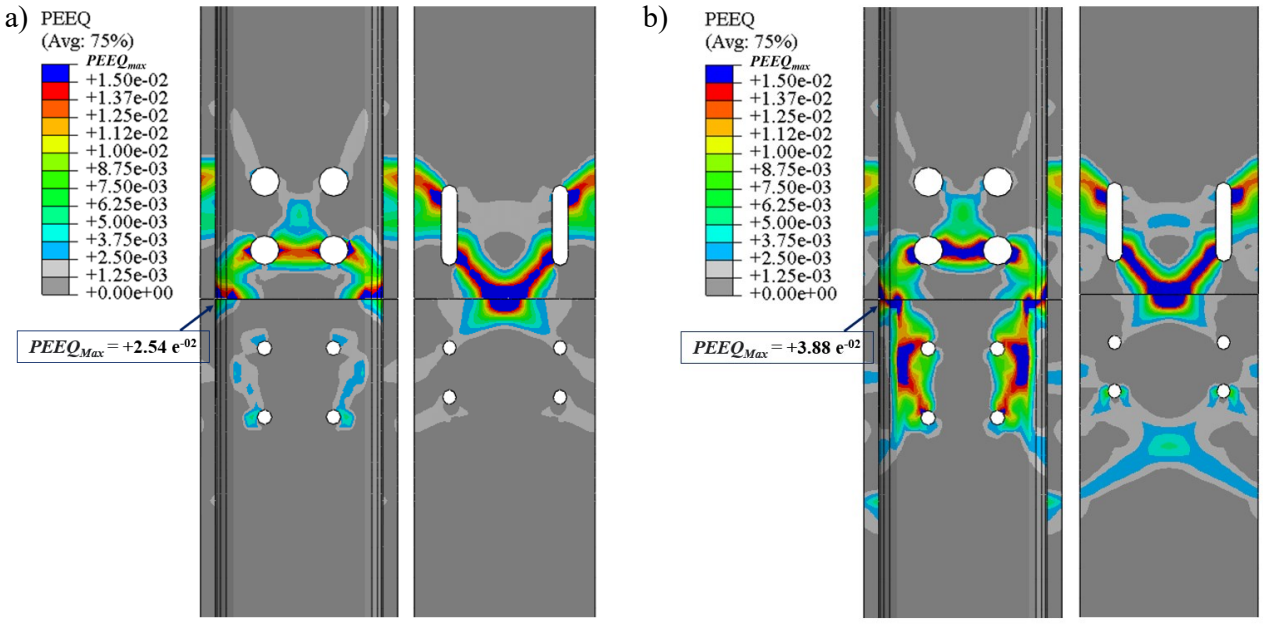

Figure 4.8: Influence of flanges' plate thickness. PEEQ Distribution at the end of the cyclic analysis for the SC-CB1: (a) t_{fp} = 8 mm; (b) t_{fp} = 16 mm

It is also worth highlighting that in addition to the previous considerations, the comparison of the PEEQ distributions of the front view of the column at the end of the cyclic analysis demonstrates that the use of 12 mm plates (*i.e.,* the intermediate case) leads to an increment of the strain concentrations on the column with respect to the 8 mm plates (*i.e.,* the lower limit case), as shown in Figure 4.10. Consistent results have been obtained for the other case study SC-CBs. This trend is also confirmed by observing the comparison of the ALLPD (*i.e.,* Dissipated Plastic Energy) shown in Figure 4.11 (a). The ALLPD informs on the amount and evolution of damage along with the time of the FE simulation. It is important to stress that although a larger energy dissipation is generally beneficial, this parameter corresponds to

the energy dissipated by components expected to remain elastic. Thus, a smaller plastic energy dissipation represents an advantage for the SC-CB connection.

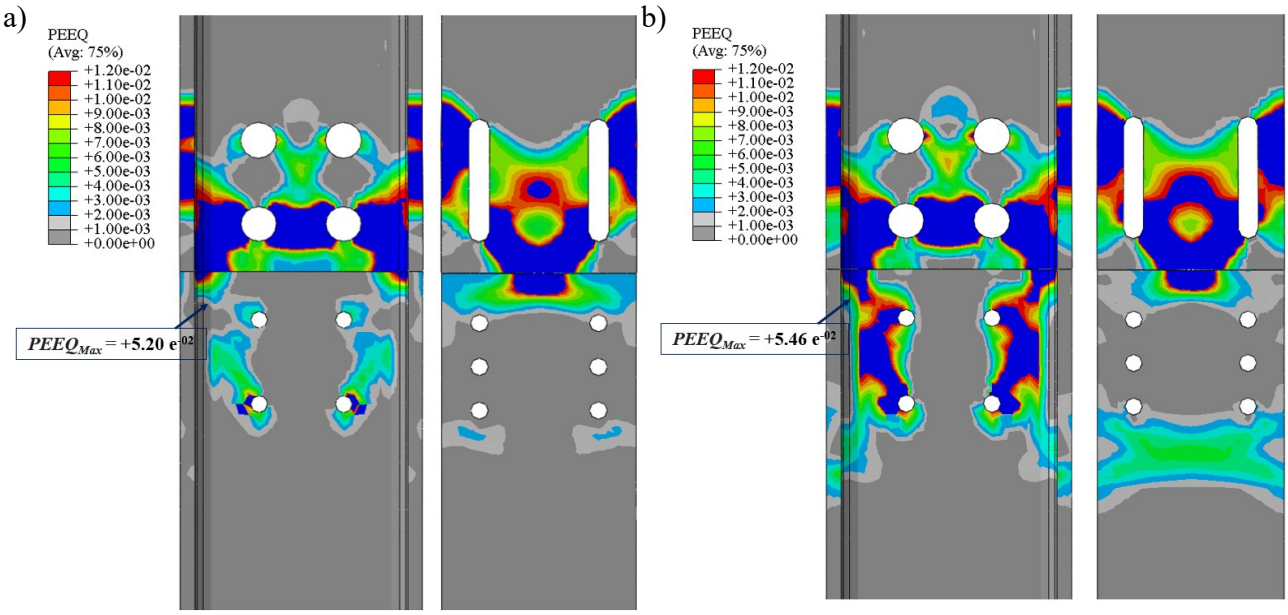

Figure 4.9: Influence of flanges' plate thickness. PEEQ Distribution at the end of the cyclic analysis for the SC-CB2: (a) t_{fp} = 12 mm; (b) t_{fp} = 24 mm

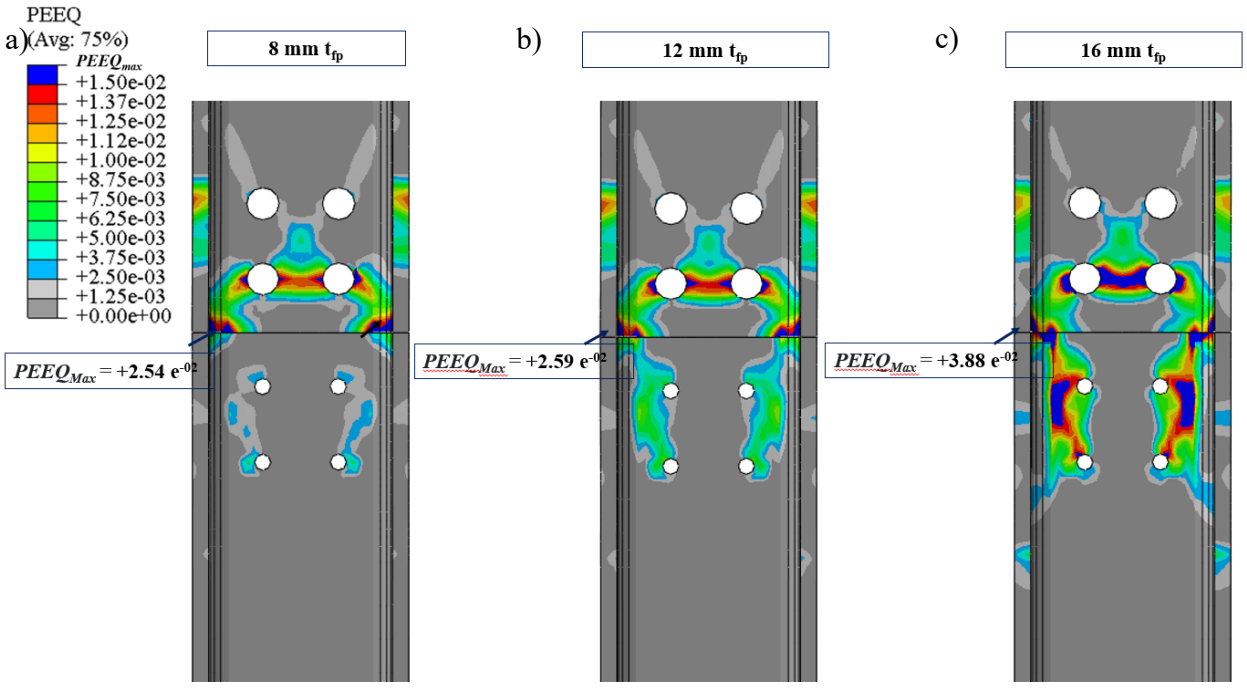

Figure 4.10: Influence of flanges' plate thickness, intermediate dimensions. PEEQ Distribution at the end of the cyclic analysis for the SC-CB1: (a) t_{fp} = 8 mm; (b) t_{fp} = 12 mm ; (c) t_{fp} = 16 mm

Results are shown for the SC-CB1 in Configurations 1 and 2 under the maximum (N_{Max}) and minimum (N_{Min}) design axial load. Figure 4.11 (a) shows that thinner flange plates allow a reduction of the dissipated plastic energy. Figure 4.11 (b) shows the $PEEQ_{max}$ normalised with respect to the ultimate strain of the material (ε_u) for the SC-CB1. The results shows that a larger flanges' plate thickness produces an increase of the $PEEQ_{max}$ and, consequently, an increment of damage on the column. This trend is consistent under both axial load conditions. Similarly, Figure 4.12 shows the same results for the SC-CB2, confirming what was previously observed. In addition, the ALLPD of the intermediate values of the flanges' plate thickness is analysed and compared in Figure 4.13 for the SC-CB1, with the results corresponding to the upper (*i.e.,* t_{fp}) and lower limits (*i.e.,* $2t_{fp}$). Results demonstrate that the use of 12 mm plates (*i.e.,* the intermediate case) leads to an increment of the strain concentrations on the column with respect to the 8 mm plates (*i.e.,* the lower limit case). These results agree with the results previously shown in the PEEQ distributions.

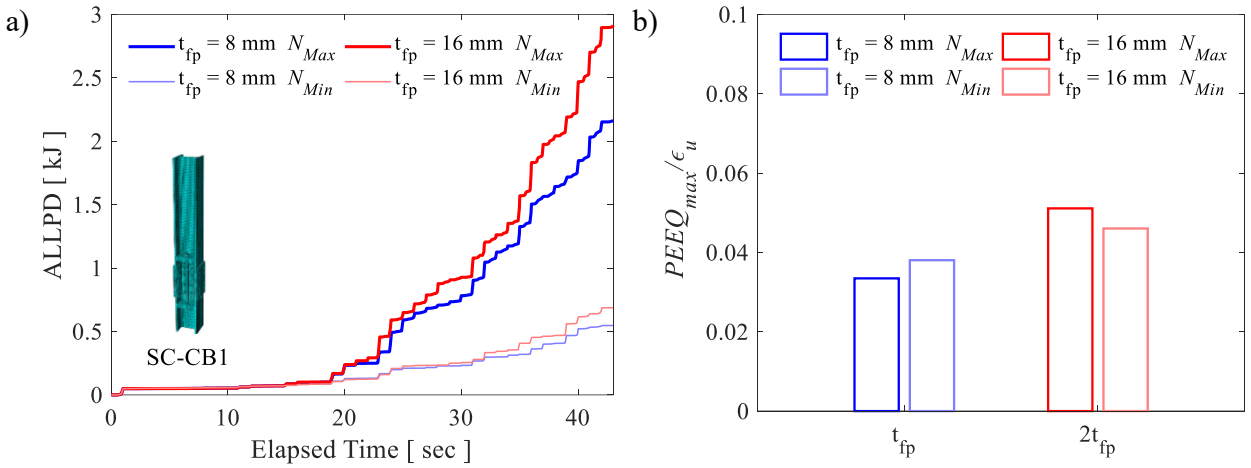

Figure 4.11: Influence of flanges' plate thickness. (a) Plastic Dissipated Energy (ALLPD); (b) Maximum local strains.

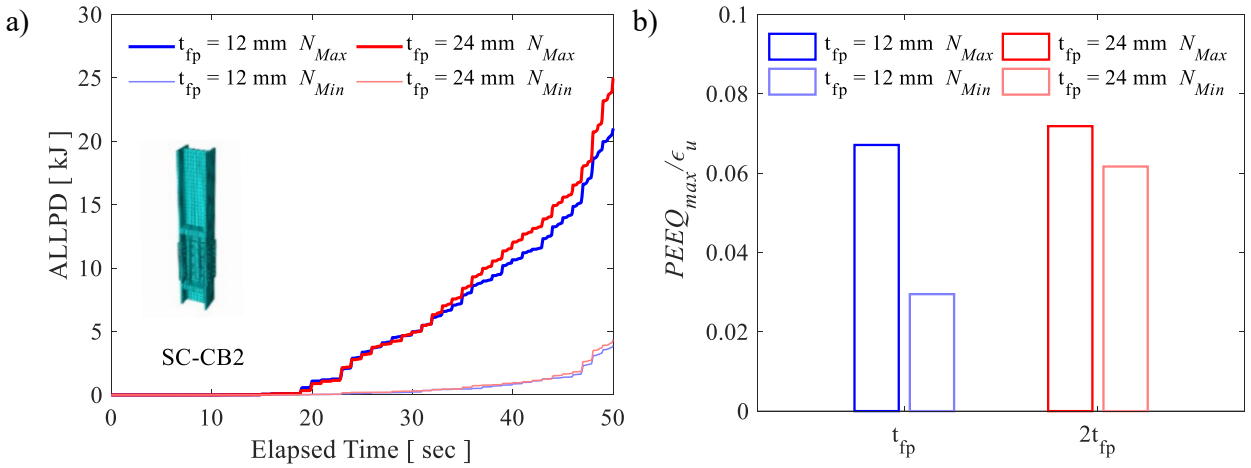

Figure 4.12: Influence of flanges' plate thickness. (a) Plastic Dissipated Energy (ALLPD); (b) Maximum local strains.

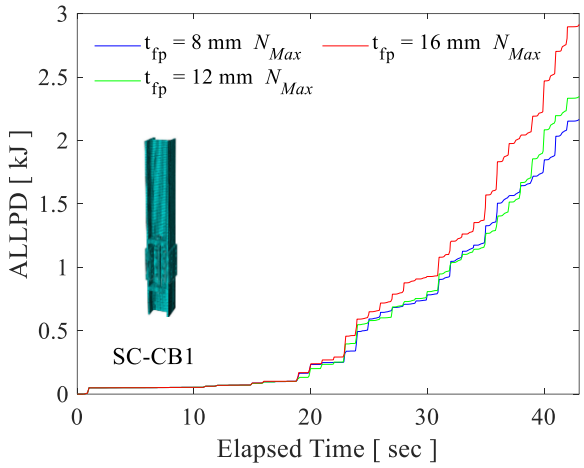

Figure 4.13: Influence of flanges' plate thickness, intermediate dimensions. ALLPD for the SC-CB1

Further considerations can be made to provide information about the transfer mechanism of the shear force among the components, which cannot be predicted in the design procedure. Figure 4.14 shows the distributions of the shear forces among the components for the SC-CB1 in the three analysed configurations. The shear force has been evaluated at the sections represented with the dash-dotted lines. The shear force has been calculated using the '*View cut*' option of ABAQUS [1], creating a cut along the z-axis and choosing the '*Free body plot*' option of ABAQUS [1]. The comparison of the shear distributions among the three cases highlights that the ticker flanges plates transfer larger shear forces due to the larger stiffness of the plates. In fact, there are stress peaks as the thickness of the flanges' plates increases. Therefore, by comparing the distributions, it is evidenced that the use of thinner flanges' plates represents a benefit in terms of shear distribution, confirming the previous observations.

a) t_{fp} = 8 mm

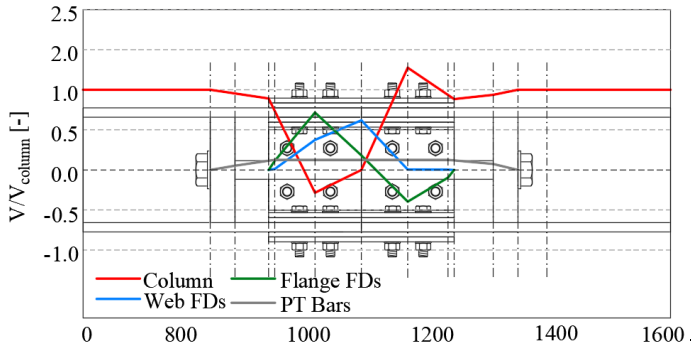

b) t_{fp} = 12 mm

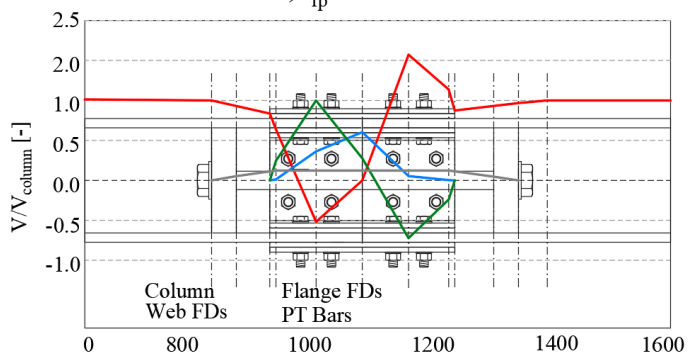

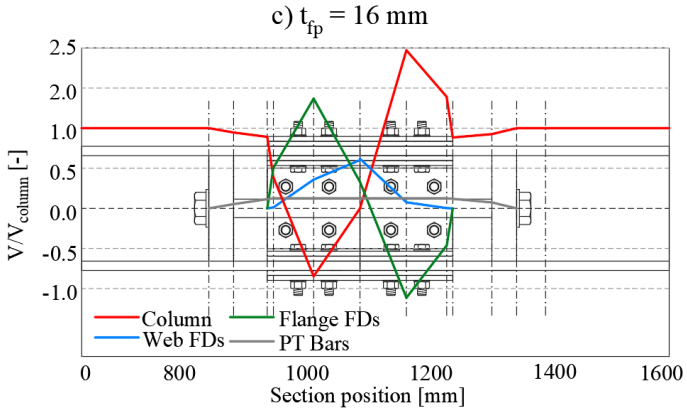

Figure 4.14: Distribution of shear of the SC-CB1 at 0.04 rad rotation:
a) t_{fp} = 8 mm; b) t_{fp} = 12 mm ; c) t_{fp} = 16 mm

4.7 Influence of the design shear load

4.7.1 Global behaviour

Figure 4.15 and Figure 4.16 show the moment-rotation hysteretic curves for SC-CB1 and SC-CB2, respectively, for both axial load conditions (*i.e.,* maximum and minimum compressive). For both SC-CBs, the figures compare the results of Configurations 1, 3, 4 and 5 (*i.e.,* 100%, 75%, 50% and 0% of V_{ED} assigned to the web FDs, respectively). In addition, the analytical model is also shown with continuous black lines. The results show that similar hysteretic responses are observed for all considered Configurations for both SC-CB1 and SC-CB2. These considerations demonstrate that, similarly to what was previously observed, this parameter does not alter the global hysteretic behaviour of the SC-CBs. Consistent results have been observed by considering the SC-CB3, not shown here for brevity.

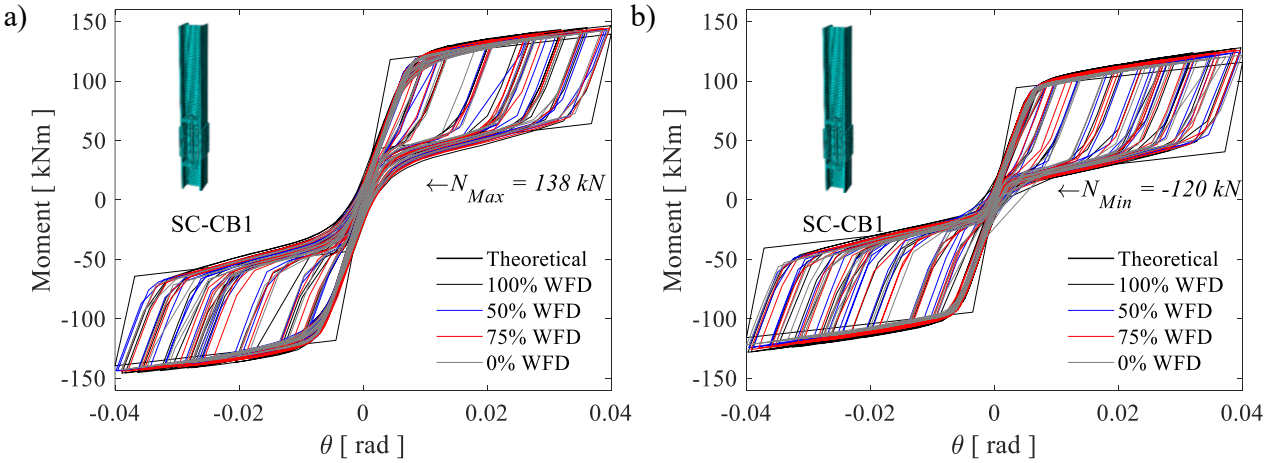

Figure 4.15: Influence of the design shear load. Moment-rotation behaviour for the SC-CB1 (a) N_{Max}; (b) N_{Min}

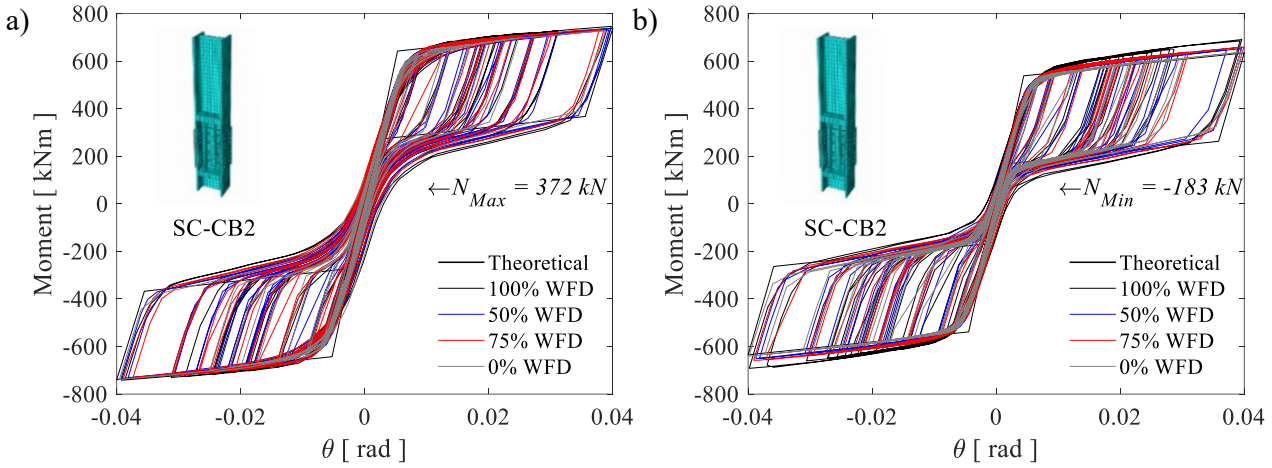

Figure 4.16: Influence of the design shear load. Moment-rotation behaviour for the SC-CB2 (a) N_{Max}; (b) N_{Min}

4.7.2 Local behaviour

The local results corresponding to Figure 4.15 (a) and Figure 4.16 (a) are illustrated in Figure 4.17 and Figure 4.18 in terms of PEEQ distribution on the column's web. Results are evaluated at the end of the FE analysis (*i.e.,* zero rotation). The $PEEQ_{max}$ are depicted in blue within the legend, and the arrows indicate their values. By comparing the PEEQ distributions, it is observed an evident influence of the considered design parameter over the strain distributions. The damage extension is higher in Configuration 1 (*i.e.,* 100% WFD) and proportionally reduces with the other Configurations (*i.e.,* 75%, 50% and 0% WFDs).

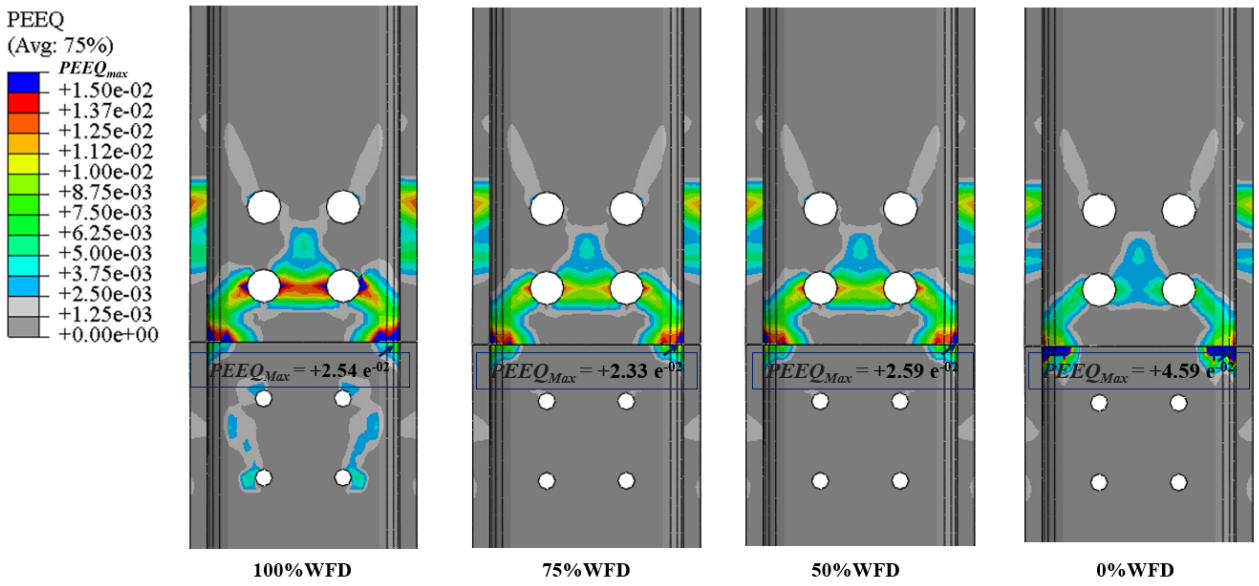

Figure 4.17: Influence of the design shear load. PEEQ Distribution at the end of the cyclic analysis for the SC-CB1

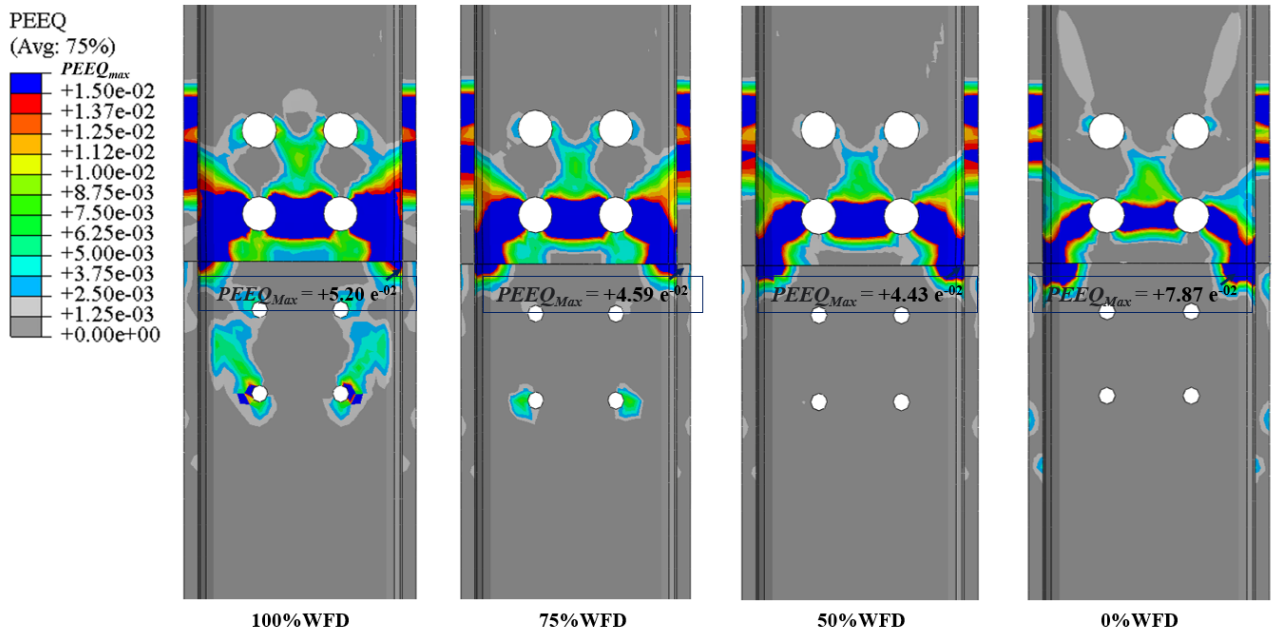

Figure 4.18: Influence of the design shear load. PEEQ Distribution at the end of the cyclic analysis for the SC-CB2

This trend is also confirmed by observing the comparison of the ALLPD shown in Figure 4.19 (a). Results highlight that assigning to the web FDs a percentage of the design shear load allows a reduction of the amount of the dissipated plastic energy. Similarly, Figure 4.19 (b) shows the $PEEQ_{max}$ normalised with respect to the ultimate strain of the material (ε_u). It is observed that the maximum local strain assumes the lowest value in Configuration 4 (*i.e.,* 50% WFD). Conversely, the highest value of the maximum local strain occurs in Configuration 5 (*i.e.,* 0% WFD). This trend is consistent for both the design axial load conditions. Consequently, these results suggest that the design choice of assigning 50% of the design shear load to the web FDs represents the optimal design Configuration in terms of local damage reduction on the column.

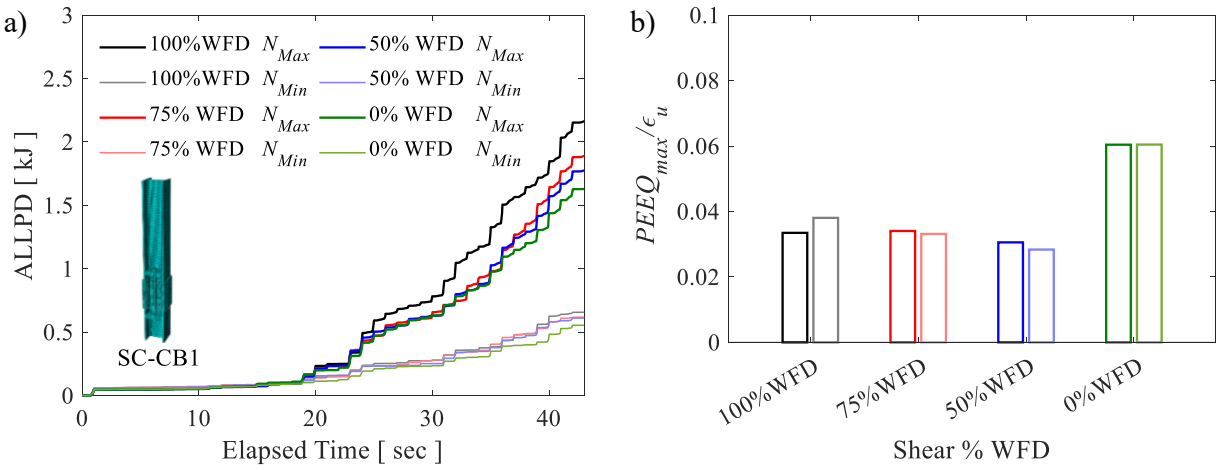

Figure 4.19: Influence of the design shear load (SC-CB1). (a) Plastic Dissipated Energy (ALLPD); (b) Maximum local strains.

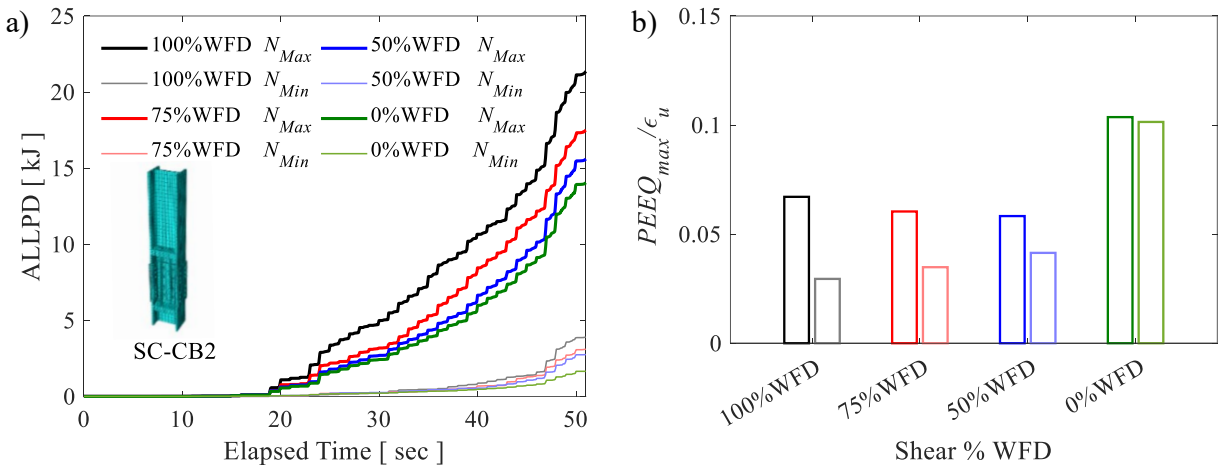

Figure 4.20: Influence of the design shear load (SC-CB2). (a) Plastic Dissipated Energy (ALLPD); (b) Maximum local strains.

Further considerations are made to provide information about the transfer mechanism of the shear force among the joint components while offering insights into the magnitude of the shear transferred by each component, which cannot be predicted in the design procedure. Figure 4.21 (a) and (b) show the distributions of the shear forces among the components for the SC-CB1 in Configuration 1 (*i.e.,* 100% WFD) and in Configuration 4 (*i.e.,* 50% WFD), respectively. The SC-CB1 in Configuration 1 is characterised by levels of maximum shear forces transferred by the web FDs of about 50% of the total shear, while the flange FDs reach values close to 80% of the total shear. This result highlights a significant contribution of the flange FDs, mainly due to the larger stiffness provided by the flanges' plates, which transfer larger shear forces than those transferred by the web plates. Conversely, the distribution of the shear forces of the SC-CB1 in Configuration 4 exhibits different behaviour. In particular, the web FDs carry less than 50% of the design shear force. At the same time, there is a higher shear contribution of the flange FDs with respect to Configuration 1 and consequently, a smoother transfer of the shear forces on the column is observed. By comparing the two distributions, it is evidenced that designing the web FD to carry 50% of the design shear load represents a benefit in terms of shear redistribution among the components, confirming the previous observations.

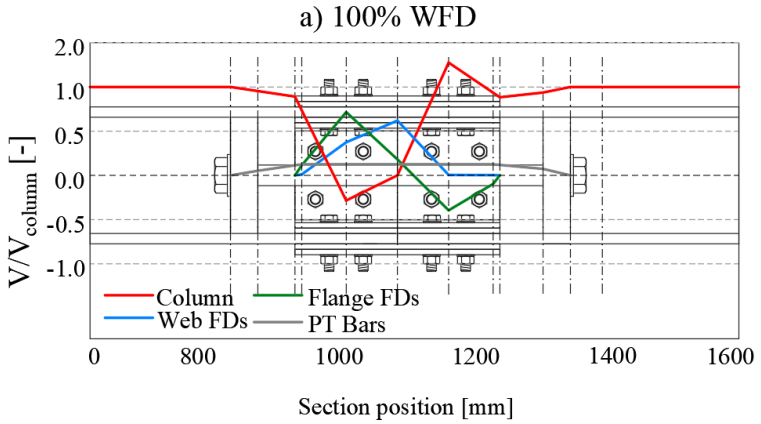

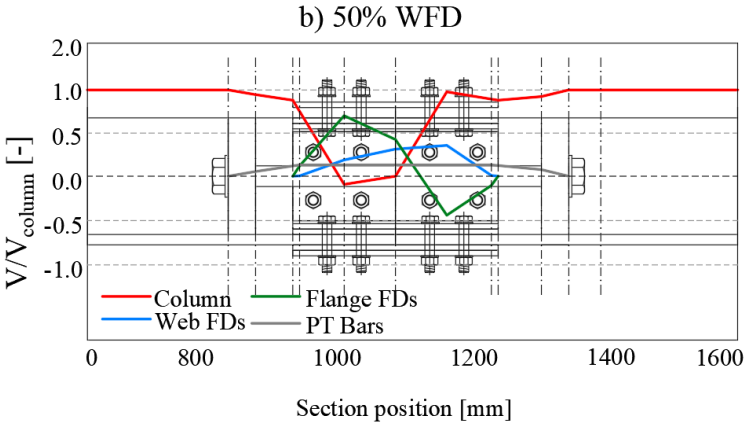

Figure 4.21: Distribution of shear of the SC-CB1 at 0.04 rad rotation: (a) 100%WFD; (b) 50%WFD.

Finally, Figure 4.22 shows a summary of the results in terms of the $PEEQ_{max}$ normalised with respect to the ultimate strain of the material (ε_u) in all the analysed Configurations (*i.e.,* sixteen Configurations for each case-study) for all the SC-CBs. Results demonstrate that, as already stated, the use of thinner flange plates represents a benefit in terms of reduction of the local plastic damage on the column; therefore, the Configurations with t_{fp} = 8mm, 12mm and 16mm are preferred for the SC-CB1, SC-CB2 and SC-CB3 respectively. In addition, assigning 50% of the design shear load to the web FD represents the most efficient design solution for local plastic damage reduction on the column while also allowing a benefit in terms of shear redistribution among the components. These considerations are consistent with the maximum and the minimum axial load conditions.

4.8 Influence of the design axial load

The design procedure is based on axial forces of the SC-CB assumed to be constant, considering two limit conditions (*i.e.,* $N_{Ed,\,Max}$ and $N_{Ed,\,Min}$). However, it has been highlighted how the moment-rotation behaviour of the SC-CB is strongly affected by the axial force. Therefore, two main issues have been discussed and analysed in Chapter 2. Firstly, the assumption of the adoption of a constant axial force is clearly not reproducing the real load situation of all columns of a MRF due to large axial force fluctuations during the seismic event. Therefore, to properly account for the variability of the axial force within the design procedure, the maximum compressive and the minimum compressive (*i.e.,* maximum tensile) axial forces are considered. Consequently, the initial sizing of the SC-CB is performed considering the maximum axial force, which represents the worst condition for the no-yielding requirement and the design is successively verified considering the minimum axial force, which is the worst condition for the self-centring requirement.

Successively, it has been evidenced that this assumption (*i.e.,* the adoption of the min compressive axial force (*i.e.,* $N_{Ed,Min}$) as the design axial load for the SC-CB) may represent an over-conservative design approach for the self-centring requirement, which may lead to an overestimation/oversizing of the necessary components of the self-centring system. Hence, this part aims to provide some indications to

clarify this design aspect by considering the axial load due to the gravity loads as the axial design load and to evaluate the self-centring capacity when the SC-CB is subjected to a variable axial load input.

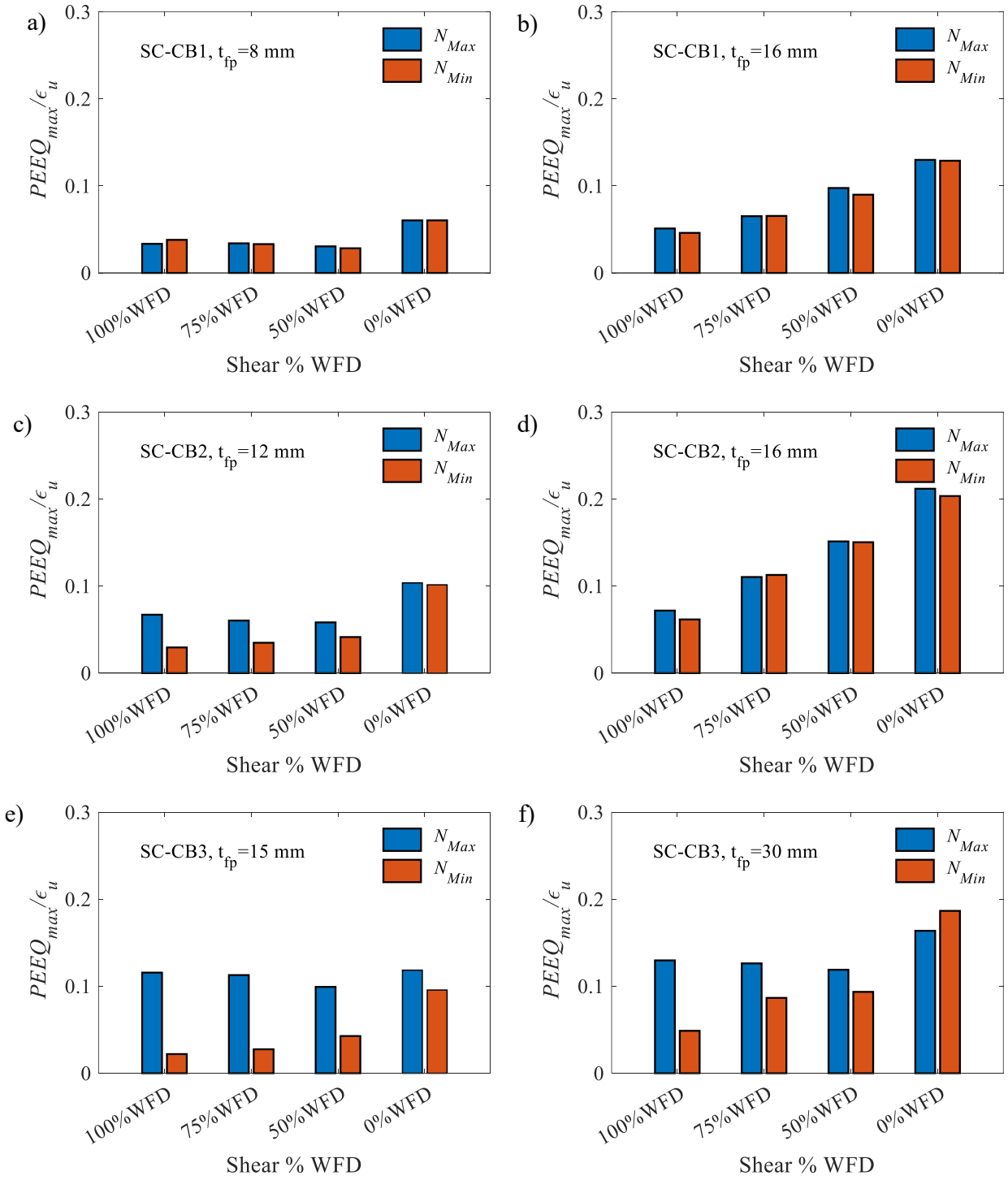

Figure 4.22: Summary of the 16 analysed configurations in terms of $PEEQ_{max}/\varepsilon_u$ for the: a) SC-CB1 with tfp; b) SC-CB1 with 2tfp; c) SC-CB2 with tfp; d) SC-CB2 with 2tfp; e) SC-CB3 with tfp; f) SC-CB3 with 2tfp

Therefore, an additional design Configuration of the SC-CB is analysed, obtained by assuming the axial gravity load for the design (Chapter 2) to verify the self-centring requirement when the SC-CB is subjected to a variable axial load input. Considering the MRFs designed in Section 4.2, Table 19 indicates the maximum (*i.e.,* $N_{Ed,Max}$), the minimum (*i.e.,* $N_{Ed,Min}$) and the axial gravity forces for the external (*i.e.,* $N_{g,ext}$) and the internal (*i.e.,* $N_{g,int}$) columns of each case-study MRF. In addition, the axial loads' ratios referred to each external column (*i.e.,* $N_{g,ext}/N_{Pl}$) are also reported, where N_{Pl} is the column's plastic axial load.

Table 19: Axial loads

Specimen	$N_{Ed,Max}$ [kN]	$N_{Ed,Min}$ [kN]	$N_{g,ext}$ [kN]	$N_{g,int}$ [kN]	$N_{g,ext}/N_{Pl}$ [-]
SC-CB1	+138	-127	+15	+15	0.0054
SC-CB2	+372	-183	+95	+198	0.0135
SC-CB3	+1248	-848	+201	+405	0.0209

Note: negative values are for tension; positive values are for compression.

A numerical FE model of the MRF1 equipped with the SC-CB1 connections designed in Section 4.2 is implemented in OPENSEES [8], adopting a modelling strategy illustrated in Chapter 2. Non-Linear Time History Analyses (NLTHAs) are successively performed by considering two ground motion records. Successively, the response of one column extracted from the MRF1 is assumed as an input parameter for an additional FE analysis. Consequently, a static analysis is performed in ABAQUS [1], applying simultaneously the selected column's axial load time history and the selected column's displacement history evaluated at the splice. For a single ground motion record, the results of the NLTHA performed in OPENSEES [8] are shown in Figure 4.23 (a) in terms of axial load time history of the first storey column of the MRF1. The values corresponding to the axial gravity force (*i.e.,* N_g) as well as the maximum (*i.e.,* N_{Max}) and minimum (*i.e.,* N_{Min}) axial force are highlighted. It is worth reminding that the other results obtained by the NLTHAs are not shown for brevity. The axial load time history (N History) represents the input of the static analysis performed in ABAQUS. Figure 4.23 (b) shows the ABAQUS [1] hysteretic curve of the SC-CB1 (*i.e.,* continuous red line) designed with the axial gravity load (*i.e.,* $N_{g,ext}$) and subjected to the variable axial load history (*i.e.,* N_{Var}) of Figure 4.23 (a). In addition, the backbone curves of the moment-rotation behaviour of the SC-CB1 obtained considering the maximum (*i.e.,* $N_{Ed,Max}$), the minimum (*i.e.,* $N_{Ed,Min}$) compressive and the axial gravity force (*i.e.,* $N_{g,ext}$) are depicted in black, grey and blue dotted lines, respectively. Similarly, Figure 4.24 (a) and (b) show the same results for another ground motion record.

Results show that the moment-rotation behaviour of the SC-CB1 designed with the axial gravity load and subjected to a variable axial load history shows a self-centring behaviour with a very low residual rotation, included within the backbone curves corresponding to the gravity and the minimum axial forces. Therefore, for the examined case, the self-centring requirement is satisfied. Consistent results have been obtained for another ground motion record, whose results are shown in Figure 4.24. These results suggest that it may be possible to consider the gravity axial force as the design axial load for the SC-CB. Therefore, the design methodology could be improved. Nevertheless, the validity of this

assumption should be verified by considering additional case-study structures to provide general recommendations on this design aspect.

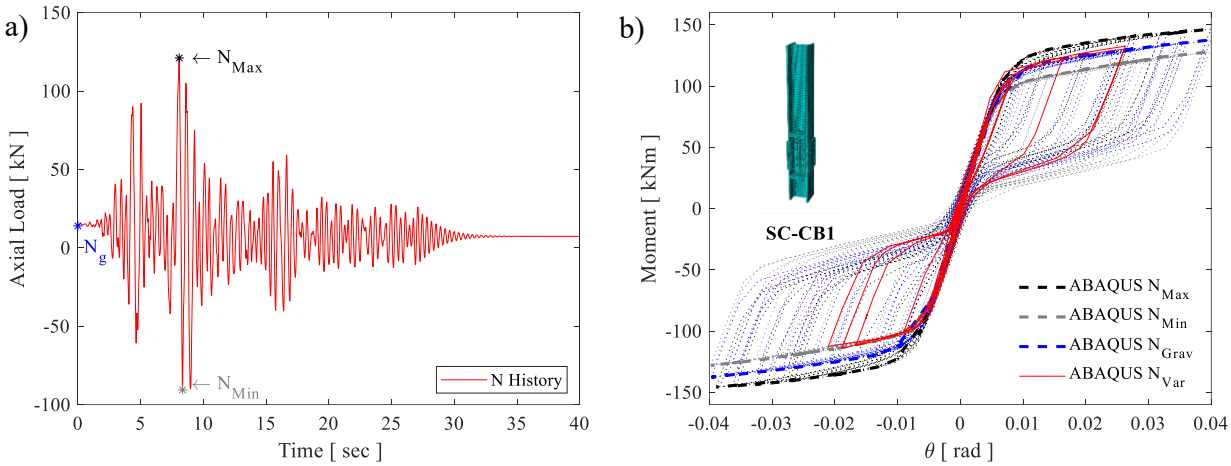

Figure 4.23: Influence of the axial load variability, ground motion #1: a) Axial load history (input); b) Moment-rotation behaviour

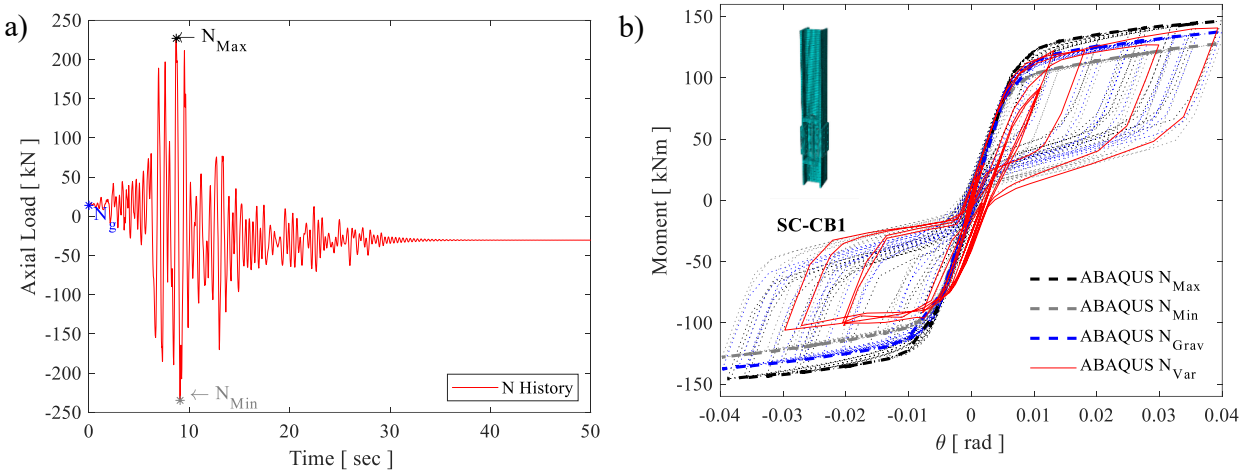

Figure 4.24: Influence of the axial load variability, ground motion #2: a) Axial load history; b) Moment-rotation behaviour

4.9 Conclusive remarks

The present chapter investigates the SC-CB through a parametric FE analysis to provide insight into the global and local behaviour under cyclic loading while proposing improvements to the existing design procedure. Three SC-CBs belonging to different case-study MRFs are selected and modelled in ABAQUS by following the modelling strategy proposed and validated in Chapter 2. A matrix of sixteen different configurations is considered for each SC-CB, obtained by varying three design properties of the joints (*i.e.,* the thickness of the flanges' plates, the design shear load, and the axial design load). For each configuration, global and local parameters are monitored to investigate the influence of these parameters on the global and local behaviour of the SC-CB connections. The results are compared for all the configurations to identify the best design solution in terms of improved self-centring capacity of

the joint and minimal yielding of the components. Results from the FE parametric analysis provide a more comprehensive view of the assumptions and limitations of the design methodology, highlighting the crucial aspects of the design procedure and suggesting additional recommendations to improve the design requirements.

Based on the obtained outcomes, the following remarks can be drawn: *i)* the moment-rotation behaviour of the connection is not affected by the considered design parameters, while the local behaviour is significantly influenced; *ii)* the use of thinner flange plates represents a benefit in terms of reduction of the local plastic damage on the column while also allowing a reduction of the amount of the dissipated plastic energy; *iii)* assigning to the web FD the 50% of the design shear load represents an efficient design solution in reducing both local plastic damage on the column while also allowing a benefit in terms of shear redistribution among the components; *iv)* the optimal design Configuration in terms of damage reduction is represented by the connection equipped with the thinner flanges' plates and assigning to the web FDs the 50% percentage of the design shear load; *v)* the moment-rotation behaviour of the SC-CB is strongly affected by the axial load. The self-centring requirement is satisfied for the examined SC-CB subjected to the variable axial load history. This result suggests that it may be possible to consider the gravity axial force as the design axial load for the SC-CB. Nevertheless, additional research is required to provide more general recommendations on this design aspect.

4.10 Personal contribution

Chapter 4 represents one of the novelties of the present work and performs a parametric FE analysis on several case-study SC-CBs with the objectives of providing insight into the global and local behaviour of the SC-CBs under cyclic loading while proposing additional recommendations to the existing design procedure described in Chapter 2.

4.11 References

1 ABAQUS/Standard and ABAQUS/Explicit – Version 2017. ABAQUS Theory Manual, Dassault Systems, 2016. http://130.149.89.49:2080/v6.14/books/usb/default.htm
2 EN 1998-1, Eurocode 8: Design of structures for earthquake resistance – Part 1: General rules, seismic actions and rules for buildings, European Committee for Standardization, Brussels
3 L. Macedo, J.M. Castro, Earthquake loss assessment of steel moment-resisting frames designed according to EC8, EUROSTEEL 2017, September 13–15, 2017, Copenhagen, Denmark
4 L. Macedo, A. Silva, J.M. Castro, A more rational selection of the behaviour factor for seismic design according to Eurocode 8, Engineering Structures, 188, 2019, 69-86, ISSN 0141-0296
5 ASCE/SEI 7–16, Minimum Design Loads and Associated Criteria for Buildings and Other Structures, American Society of Civil Engineers, USA, 2017
6 EN 1993-1-8, Eurocode 3: Design of steel structures, Part 1-8: Design of steel structure: General rules and rules for buildings, 2005, European Committee for Standardization, Brussels
7 M. Latour, M. D'Aniello, M. Zimbru, G. Rizzano, V. Piluso, R. Landolfo, Removable friction dampers for low-damage steel beam-to-column joints, Soil Dyn. Earthq. Eng. 115 (2018) 66–81
8 S. Mazzoni, F. McKenna, M.H. Scott, G.L. Fenves OpenSEES: Open System for earthquake

engineering simulation, Pacific Earthquake Engineering Research Centre (PEER), 2009, Univ. of California, Berkley, CA, Available at: http://opensees.berkeley.edu.

Chapter 5 Performance-Based Assessment of Case-Study MRFs equipped with SC-CBs

5.1 Introduction

The present chapter evaluates the benefits related to the introduction of innovative SC-CB joints within steel MRFs in terms of residual drift reduction, self-centring capabilities and damage-free behaviour. To fulfil this objective, the seismic performance of several case-study perimeter steel MRFs equipped with innovative SC-CB connections and the equivalent conventional steel MRFs with full-strength CB connections are numerically investigated and compared. The design of the case-study MRFs follows Eurocode 8 [1] provisions, while the design of the SC-CBs follows the methodology shown in Chapter 4. In both cases, the BCJs are conventional full-strength welded joints.

Successively, a parametric numerical analysis is performed to investigate two critical aspects of the design of the MRFs equipped with the SC-CBs and their influence on the self-centring behaviour:

i) the frame layout (*i.e.,* storeys and bays number);
ii) the seismic mass.

The first parameter is investigated through nine case-studies MRFs with a different number of storeys (*i.e.,* 4, 6 and 8) and bays (*i.e.,* 3, 5 and 8) designed according to the Eurocode 8 [1]. Moreover, an additional parameter is investigated (*i.e.,* the combination of the seismic mass and acceleration) with three additional 5-bay steel MRFs with 4, 6 and 8 storeys considered as case-study structures, and two different values of the seismic masses (*i.e.,* M1 and M2). The seismic responses of the case-study MRFs with SC-CBs are compared with the equivalent conventional MRF in each configuration.

Numerical models are developed in OPENSEES [4] for the frames with and without the investigated SC-CB connections, and Incremental Dynamic Analyses (IDA) [5] are carried out on a set of 30 ground motion records for each case-study MRF to account for the influence of the uncertainty related to the earthquake input (*i.e.,* the record-to-record variability). The effects of model parameter uncertainty and epistemic uncertainty are less notable than the effects of record-to-record variability [7], and hence, they are not considered in this study. The spectral acceleration corresponding to the fundamental period of vibration is used as Intensity Measure (IM), and global Engineering Demand Parameters (EDPs) are monitored.

Fragility curves [8] are successively derived based on IDA results, providing the probability of exceeding a specified performance level, corresponding to the value of residual interstorey drift limit of 0.5%, which, for building frames, is conventionally associated with building reparability [9]. Additionally, several performance levels are considered by monitoring both global and local EDPs and hence deriving both system and components-level fragility curves [8]. It is worth highlighting that in this Chapter, the results are presented and discussed in detail for a single case-study MRF (*i.e.,* the 3-bay 4-storey frame in both configurations), while for the other case-study MRFs, the maximum quantities of the selected global EDPs monitored by the IDAs are illustrated.

5.2 Case-study MRFs

Figure 5.1 shows the plan and elevation views of the case-study steel MRFs extracted from prototype buildings with different storeys (*i.e.,* 4, 6 and 8). The nine case-study buildings have 5, 7 and 10 bays in the *x*-direction and 3 bays in the *y*-direction. Seismic-resistant perimeter MRFs are located in the -*x*-direction and the *y*-direction, while the interior part comprises gravity frames (*i.e.,* with 'pinned' BCJs and 'pinned' CBs). The study focuses on the seismic assessment of the MRFs in the *x*-direction having 3,5 and 8 bays, respectively and 4,6 and 8 storeys. Two configurations are analysed and compared for each case-study MRF: the first is a MRF with full strength BCJs and conventional CBs (MRF); the second is an equivalent seismic resilient frame equipped with the innovative CB connections (MRF-CB) designed according to the procedure presented in Chapter 3. In both cases, the BCJs are conventional full-strength welded joints.

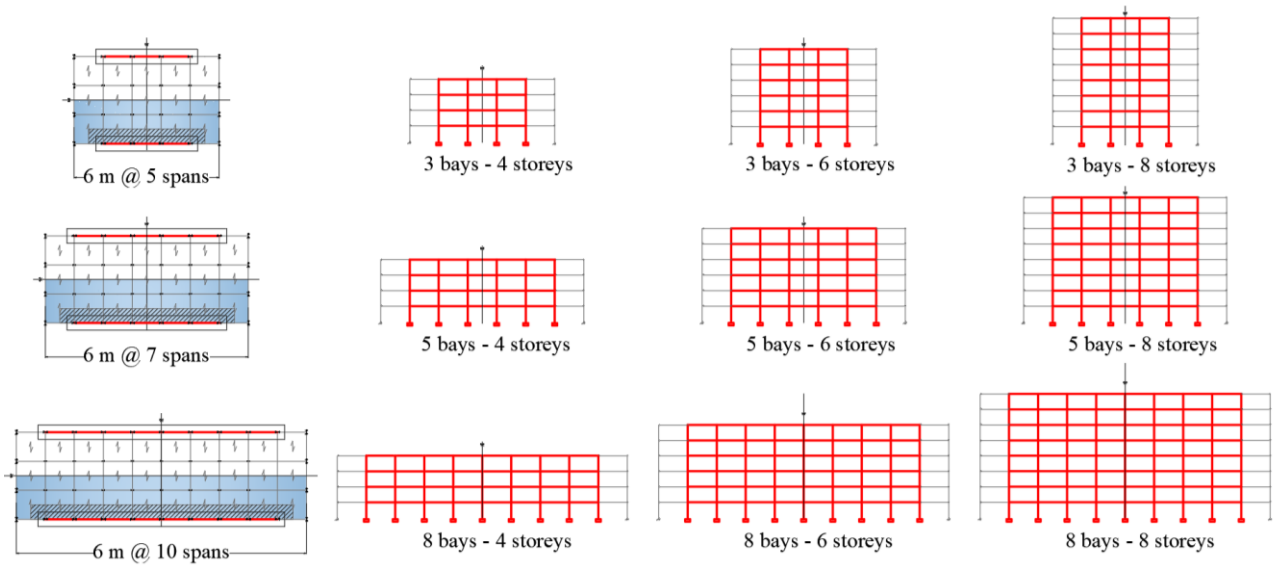

Figure 5.1. Case-study buildings: (a) Plan views; (b) Elevation views.

The design is performed by following Eurocode 8 [1] provisions adopting the procedure suggested in Chapter 4. The main features of the case-study MRFs are summarised for the sake of brevity in this section. For further information regarding the geometrical characteristics, the loads and masses, the adopted floor system and the design methodology, see Chapter 4. The elastic and design response spectra are illustrated in Figure 5.2, with the indications of the periods of the frame, while Table 20 reports the profiles' cross-section for each of the designed case-study MRFs. Table 21 lists the fundamental periods (T_1) and the spectral acceleration ($S_a(T_1,\xi)$) for the DBE ($S_{a,\,DBE}$) and MCE ($S_{a,\,MCE}$), which represent the two seismic intensities of interest for the study. Table 22 reports the distribution of the interstorey drifts evaluated at the DSL and the minimum overstrength factors (Ω_{min}), defined according to Eurocode 8 [1] provisions.

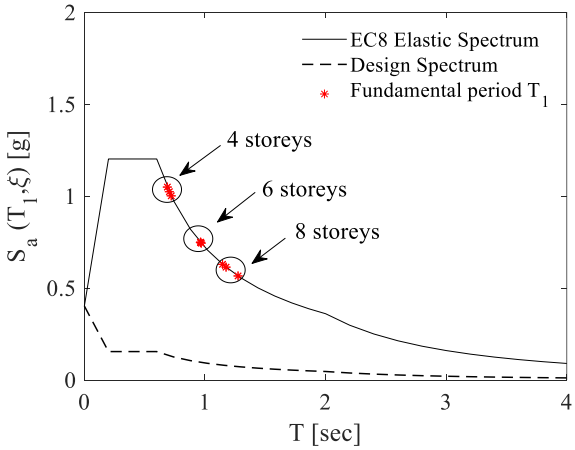

Figure 5.2. EC 8 Elastic and Design Spectra with indications of the periods of the frames.

Table 20. Profiles' cross-sections.

MRF 3-4			MRF 3-6			MRF 3-8		
Floor	Beams	Columns	Floor	Beams	Columns	Floor	Beams	Columns
						1	IPE 600	HE 650M
			1	IPE 600	HE 600M	2	IPE 600	HE 650M
1	IPE 550	HE 550M	2	IPE 600	HE 600M	3	IPE 600	HE 600M
2	IPE 550	HE 550M	3	IPE 600	HE 500M	4	IPE 600	HE 600M
3	IPE 550	HE 450M	4	IPE 600	HE 500M	5	IPE 550	HE 600M
4	IPE 550	HE 450M	5	IPE 550	HE 400M	6	IPE 550	HE 500M
			6	IPE 550	HE 400M	7	IPE 500	HE 500M
						8	IPE 500	HE 500M
MRF 5-4			MRF 5-6			MRF 5-8		
Floor	Beams	Columns	Floor	Beams	Columns	Floor	Beams	Columns
						1	IPE 600	HE 650M
			1	IPE 600	HE 500M	2	IPE 600	HE 650M
1	IPE 550	HE 450M	2	IPE 600	HE 500M	3	IPE 600	HE 600M
2	IPE 550	HE 450M	3	IPE 600	HE 400M	4	IPE 600	HE 600M
3	IPE 550	HE 360M	4	IPE 600	HE 400M	5	IPE 550	HE 600M
4	IPE 550	HE 360M	5	IPE 550	HE 340M	6	IPE 550	HE 500M
			6	IPE 550	HE 340M	7	IPE 500	HE 500M
						8	IPE 500	HE 500M
MRF 8-4			MRF 8-6			MRF 8-8		
Floor	Beams	Columns	Floor	Beams	Columns	Floor	Beams	Columns
						1	IPE 600	HE 600M
			1	IPE 600	HE 450M	2	IPE 600	HE 600M
1	IPE 550	HE 450M	2	IPE 600	HE 450M	3	IPE 600	HE 550M
2	IPE 550	HE 450M	3	IPE 600	HE 360M	4	IPE 600	HE 550M
3	IPE 550	HE 360M	4	IPE 600	HE 360M	5	IPE 550	HE 550M
4	IPE 550	HE 360M	5	IPE 550	HE 320M	6	IPE 550	HE 500M
			6	IPE 550	HE 320M	7	IPE 500	HE 500M
						8	IPE 500	HE 500M

Table 21. Fundamental Period (T_1) and spectral acceleration ($S_a(T_1,\xi)$) for DBE and MCE.

MRF 3-4			MRF 3-6			MRF 3-8		
T_1 [sec]	$S_{a,\,DBE}$ [g]	$S_{a,\,MCE}$ [g]	T_1 [sec]	$S_{a,\,DBE}$ [g]	$S_{a,\,MCE}$ [g]	T_1 [sec]	$S_{a,\,DBE}$ [g]	$S_{a,\,MCE}$ [g]
0.70	1.02	1.54	0.96	0.75	1.12	1.27	0.57	0.85

MRF 5-4			MRF 5-6			MRF 5-8		
T_1 [sec]	$S_{a,\,DBE}$ [g]	$S_{a,\,MCE}$ [g]	T_1 [sec]	$S_{a,\,DBE}$ [g]	$S_{a,\,MCE}$ [g]	T_1 [sec]	$S_{a,\,DBE}$ [g]	$S_{a,\,MCE}$ [g]
0.72	1.00	1.50	0.97	0.74	1.12	1.17	0.61	0.92
MRF 8-4			MRF 8-6			MRF 8-8		
T_1 [sec]	$S_{a,\,DBE}$ [g]	$S_{a,\,MCE}$ [g]	T_1 [sec]	$S_{a,\,DBE}$ [g]	$S_{a,\,MCE}$ [g]	T_1 [sec]	$S_{a,\,DBE}$ [g]	$S_{a,\,MCE}$ [g]
0.69	1.05	1.57	0.96	0.75	1.13	1.15	0.63	0.94

Table 22. Damage State Limitation (DSL) check and Ωmin.

MRF 3-4	MRF 3-6	MRF 3-8
$\Omega_{min} = 2.16$	$\Omega_{min} = 2.14$	$\Omega_{min} = 2.10$
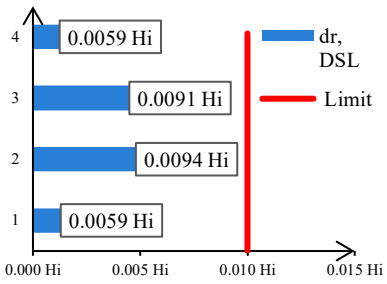	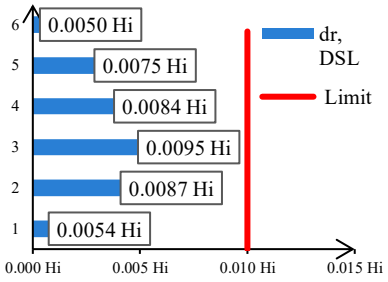	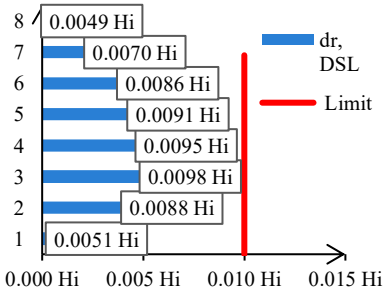
MRF 5-4	MRF 5-6	MRF 5-8
$\Omega_{min} = 2.18$	$\Omega_{min} = 2.08$	$\Omega_{min} = 2.03$
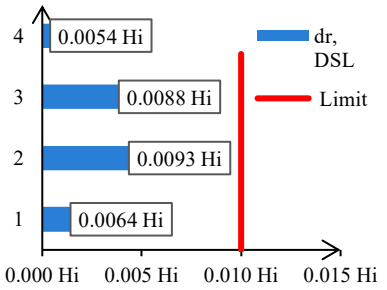	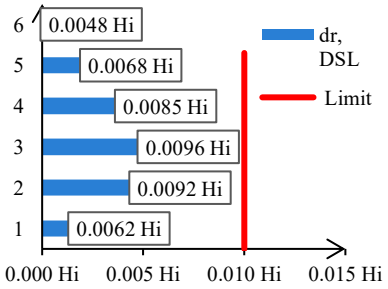	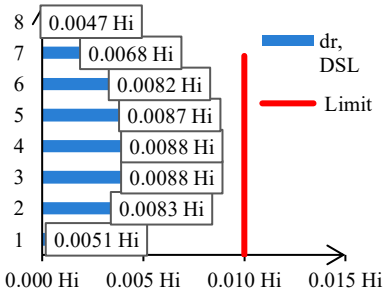
MRF 8-4	MRF 8-6	MRF 8-8
$\Omega_{min} = 2.25$	$\Omega_{min} = 2.13$	$\Omega_{min} = 2.12$
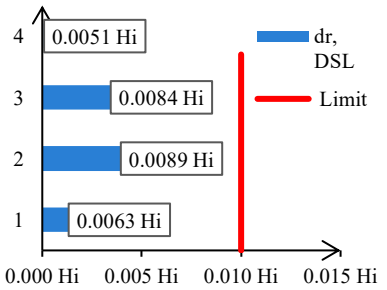	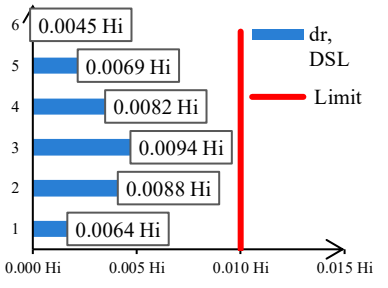	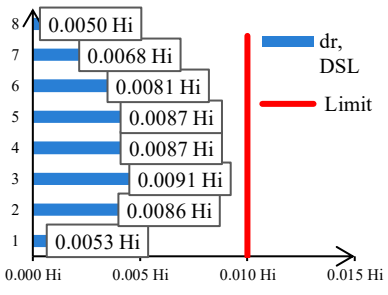

5.2.1 SC-CBs

The SC-CB connections are designed according to the procedure presented in Chapter 4, considering the design recommendations provided by the parametric analysis (*i.e.,* minimum thickness of the flanges' plates). Concerning the design shear load, the web Friction Device (FD) is assumed to carry

alone the design shear load, as proposed by the original design procedure proposed by Latour *et al.,* 2019 [2] as this assumption is used to validate the numerical model against the experimental results in Section 3.8. In addition, to properly account for the variability of the axial force within the design procedure, as discussed in Chapter 4, the maximum compressive and the minimum compressive (*i.e.,* maximum tensile) axial forces are considered. The design actions are derived based on the seismic analysis of the equivalent frame with rigid full-strength CBs and are defined considering the proper location of the column splices. The values of the design axial forces for the inner and outer columns are reported in Table 23. Successively, the FDs, the PT bars and the disk spring system are designed. The properties of the components (*i.e.,* number and pre-load forces of the web and flanges FDs and number and pre-load of the PT bars) are summarized in Table 24.

Table 23. SC-CBs design axial forces.

MRF 3-4		MRF 3-6		MRF 3-8	
N_{Ed} [kN]		N_{Ed} [kN]		N_{Ed} [kN]	
Outer column	Inner column	Outer column	Inner column	Outer column	Inner column
+719	-451	+1318	-667	+1721	-812
MRF 5-4		MRF 5-6		MRF 5-8	
N_{Ed} [kN]		N_{Ed} [kN]		N_{Ed} [kN]	
Outer column	Inner column	Outer column	Inner column	Outer column	Inner column
+623	-550	+1133	-815	+1434	-933
MRF 8-4		MRF 8-6		MRF 8-8	
N_{Ed} [kN]		N_{Ed} [kN]		N_{Ed} [kN]	
Outer column	Inner column	Outer column	Inner column	Outer column	Inner column
+707	-574	+1023	-805	+1397	-952

Note: negative values are for compression; positive values are for tension.

Table 24. SC-CBs Properties of the components.

		MRF 3-4		MRF 3-6		MRF 3-8	
		Outer column	Inner column	Outer column	Inner column	Outer column	Inner column
PT bars	N [-]	8	6	8	6	8	4
Web bolts	N [-]	4	4	4	4	4	4
	Pre-load [kN]	135	155	140	175	140	170
Flange bolts	Number [-]	8	8	8	8	8	8
	Pre-load [kN]	110	130	135	105	75	100
		MRF 5-4		MRF 5-6		MRF 5-8	
		Outer column	Inner column	Outer column	Inner column	Outer column	Inner column
PT bars	N [-]	8	6	8	6	8	6
Web bolts	N [-]	4	4	4	4	4	4
	Pre-load [kN]	120	125	130	165	135	170
Flange bolts	N [-]	8	8	8	8	8	8
	Pre-load [kN]	105	120	120	100	135	80
		MRF 8-4		MRF 8-6		MRF 8-8	
		Outer column	Inner column	Outer column	Inner column	Outer column	Inner column
PT bars	N [-]	8	6	8	6	8	6
Web bolts	N [-]	4	4	4	4	4	4
	Pre-load [kN]	135	165	130	160	140	170
Flange bolts	N [-]	8	8	8	8	8	8
	Pre-load [kN]	150	155	120	100	140	130

The material properties of the CB connections obtained by the design for the inner and outer columns are summarised in Table 25, where E, f_y and f_u are the nominal values of Young's modulus, the yield strength and the ultimate tensile strength of the materials, respectively. The other proprieties of the adopted structural steel (*i.e.,* the shear modulus, the Poisson's ratio and the coefficient of linear thermal expansion) are based on the Eurocode 3 [3]. The main moment contributions of the moment-rotation behaviour are listed in Table 26.

Table 25. SC-CBs Material properties of the column base connections.

Elements	Class [-]	E [GPa]	f_y [MPa]	f_u [MPa]
Column and plates	S355	210	355	510
PT bars	10.9	205	900	1000
Web Bolts	10.9	210	900	1000
Flange Bolts	10.9	210	900	1000

Table 26. Parameters of the moment-rotation behaviour.

	MRF 3-4		MRF 3-6		MRF 3-8	
	Outer column	Inner column	Outer column	Inner column	Outer column	Inner column
M_N [kNm]	(-)206	129	(-)409	207	(-)575	271
M_D [kNm]	1101	1109	1007	1269	951	1034
M_1 [kNm]	1779	1895	1883	2020	1557	1811
M_2 [kNm]	2120	2150	2104	2320	1852	2043
	MRF 5-4		MRF 5-6		MRF 5-8	
	Outer column	Inner column	Outer column	Inner column	Outer column	Inner column
M_N [kNm]	(-)149	131	(-)409	207	(-)479	311
M_D [kNm]	943	950	1007	1269	1047	1456
M_1 [kNm]	1472	1536	1883	2020	1980	2123
M_2 [kNm]	1650	1714	2104	2320	2275	2471
	MRF 8-4		MRF 8-6		MRF 8-8	
	Outer column	Inner column	Outer column	Inner column	Outer column	Inner column
M_N [kNm]	(-)169	137	(-)297	213	(-)433	295
M_D [kNm]	923	956	900	1111	983	1357
M_1 [kNm]	1642	1716	1557	1711	1879	2229
M_2 [kNm]	1859	1894	1771	1872	2133	2454

Note: the moments are calculated with the values of the axial design forces reported in Table 4. Consequently, for the columns in tensions, M_N is opposite with respect to M_{PT}.

5.3 Selected case-study (*i.e.,* MRF3)

In the following part of the thesis, a case study MRF is selected, modelled, and numerically investigated to evaluate the proposed SC-CB's influence on the structure's seismic response. Results are discussed in detail for the selected case-study MRF, and successively, a parametric numerical analysis is performed by considering several case-study MRFs. Figure 5.3 shows the plan and the elevation view of the selected case-study structure, which is the MRF3 of Figure 4.1.
Table 27 lists the profiles' cross-sections of the selected MRF.

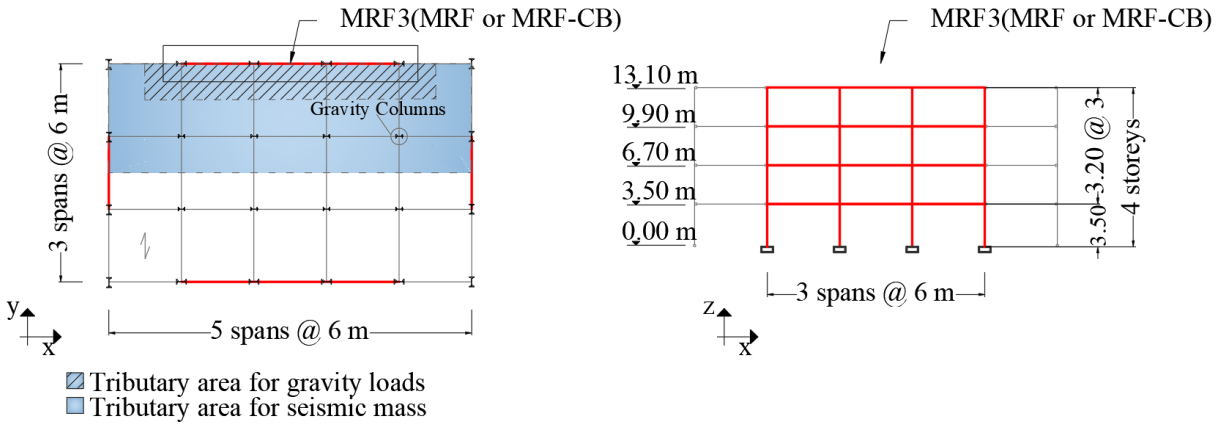

Figure 5.3: Case study building (*i.e.,* MRF3 of Figure 4.1): (a) Plan view; (b) Elevation view.

Table 27. Profiles' cross-sections (*i.e.,* MRF3 of Figure 4.1).

Storey	Columns	Beams
1	HE 600B	IPE 550
2	HE 600B	IPE 550
3	HE 500B	IPE 500
4	HE 500B	IPE 500

5.3.1 SC-CB (*i.e.*, HE 600B)

The design actions are derived based on the seismic analysis of the equivalent frame with rigid full-strength CBs and are defined considering the proper location of the column splices. The maximum axial compressive force for the inner columns is equal to 460 kN, and its variation due to the seismic action is limited. The axial tensile and compressive forces in the outer columns equal 807 kN and 1240 kN, respectively. In this case, the tensile axial force is used for the design, while the CB is successively verified also with the max compressive force. The values of the design actions for the inner and outer columns are reported in Table 28.

Table 28. Design input for the SC-CB (HE600B)

Design Actions	Inner columns	Outer columns
Axial Load N_{Ed} [kN]	-460	+807 and -1240
Bending Moment M_{Ed} [kNm]	1985	1633
Shear Load V_{Ed} [kN]	894	605

*Note: negative values are for compression; positive values are for tension.

Consequently, the FDs, the PT bars and the disk spring system are designed according to the procedure presented in Chapter 4. The friction pads comprise 8 mm of thermally sprayed friction metal steel shims. The flange cover plates are designed considering the minimum design thickness, equal to 15 mm. The friction coefficient is assumed to equal $\mu = 0.53$, consistent with the results of previous tests on the same friction material [17]. Considering four HV M30 10.9 class bolts for the web FD, the necessary pre-load

for each bolt is 210 kN and 140 kN for the inner and outer columns, respectively. Six M36 PT bars, having a maximum capacity of pre-loading of 570 kN each, are introduced to control the self-centring behaviour. Considering eight HV M30 10.9 class bolts for the flange FD, the necessary pre-load for each bolt is 110 kN and 60 kN, respectively for the inner and outer columns. The resistance of each disk spring is 200 kN, while the stiffness (K_{ds1}) is of 100 kN/mm. The overstrength of the disk spring with respect to the PT bars is satisfied by using a system of 3 disks in parallel. The maximum displacement of the farther PT bar with respect to the COR is equal to 17.4 mm (0.04 × 435 mm), where 0.04 rad is assumed as the target rotation. Hence, a system of 18 disks in series is required to obtain the optimal stiffness of the equivalent system (K_{eq}). The properties of the CB connections obtained by the design for the inner and outer columns are summarised in Table 29. Figure 5.4 shows a 3D and exploded views of the proposed SC-CB.

Table 29. Material properties for the SC-CB (HE 600B)

	Material properties				Outer column		Inner column	
Elements	Class	E	f_y	f_u	Number	Pre-load	Number	Pre-load
	[-]	[GPa]	[MPa]	[MPa]	[-]	[kN]	[-]	[kN]
Column and plates	S355	210	355	510	-	-	-	-
PT bars	10.9	205	900	1000	8	570	6	570
Web Bolts	10.9	210	900	1000	4	140	4	210
Flange Bolts	10.9	210	900	1000	8	60	8	110

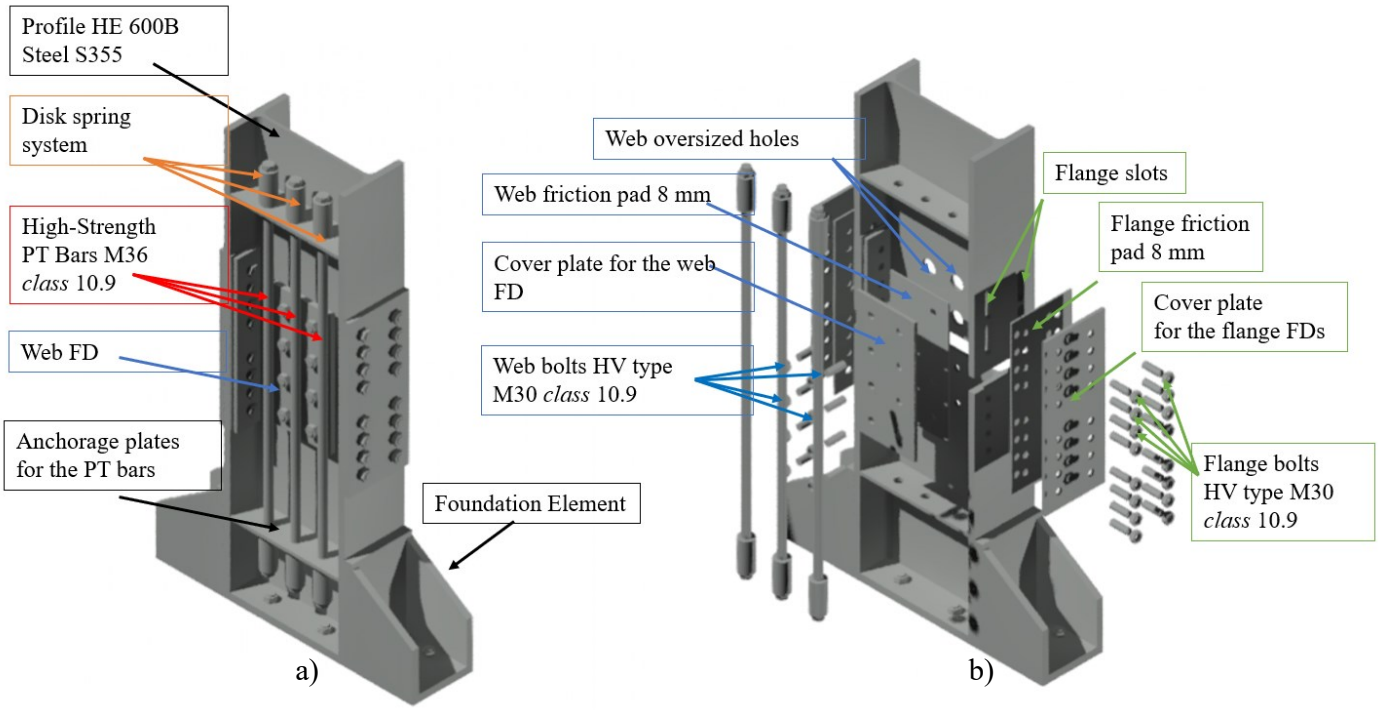

Figure 5.4: SC-CB connection for the MRF3: (a) 3D view; (b) Exploded 3D view

5.4 Numerical Modelling

Two-dimensional FE models of the frames with and without the SC-CB connections are developed in OPENSEES [4]. The structural models are able to describe the non-linear response of the system by detailed modelling of the components.

Beams

Beams are modelled by a lumped plasticity approach where the internal part of the beams is modelled with '*elastic BeamColumn elements'* in OPENSEES [4], while the plastic hinges are modelled by non-linear rotational springs at beams' ends represented by '*zero-length elements'* in OPENSEES [4] (Figure 5.6). The rotational behaviour of these non-linear springs follows the hysteretic behaviour based on the modified Ibarra-Krawinkler deterioration rule implemented by Lignos and Krawinkler (2011) [10], already discussed in Chapter 2.

Table 30 shows the parameters used to model the plastic hinges according to Lignos and Krawinkler model [10] (Figure 5.5). For the sake of simplicity, assuming a symmetric behaviour, the Lignos parameters (*i.e.,* the same terminology adopted in the literature review in Chapter 2) are shown for the positive direction of loading only. It is important to stress that the coefficient $n = 10$ is relatively modest on the initial elastic stiffness, while strength properties are extremely dependent on the size of the beam. The average pre-capping rotation is consistent with the value 0.035 rad, recommended by Eurocode 8 [1].

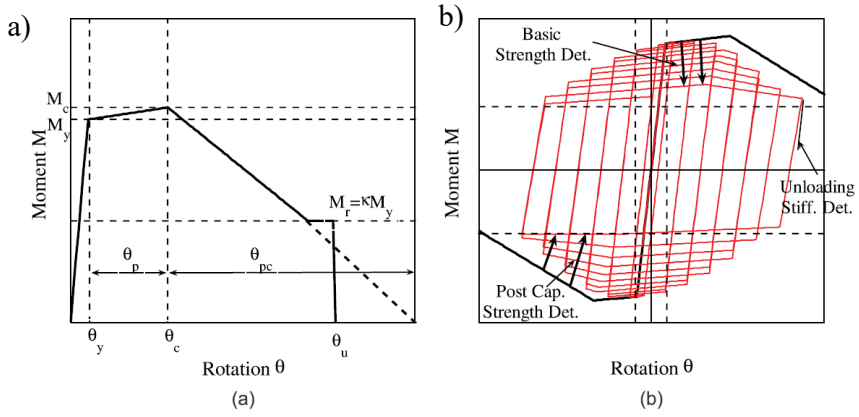

Figure 5.5: Lignos and Krawinkler deterioration model [10]: a) monotonic curve and associated definitions; and b) basic modes of cyclic deterioration and associated definitions

Table 30. Plastic hinges parameters according to Lignos and Krawinkler model [10]

Storey	K	M_c/M_y	My	Λ	c	ϑ_p	ϑ_{pc}	k	ϑ_u	D
[-]	[kNm]	[-]	[kNm]	[-]	[-]	[rad]	[rad]	[-]	[rad]	[-]
1	1722747	1.1	843	1.23	1	0.031	0.177	0.4	0.4	1
2	1722747	1.1	843	1.23	1	0.031	0.177	0.4	0.4	1
3	1214640	1.1	664	1.23	1	0.034	0.179	0.4	0.4	1
4	1214640	1.1	664	1.23	1	0.034	0.179	0.4	0.4	1

Columns

Since lumped plasticity cannot explicitly capture axial force-bending moment interaction, a different strategy has been adopted for column modelling. Columns are modelled by a distributed plasticity approach (see Figure 5.6) using '*nonlinear BeamColumn elements*' in OPENSEES [4] with four integration points, and each section is discretised into eight fibres along with the depth and four along each flange. To properly account for the shear stiffness of the column, the plastic shear capacity of the section ($V_R = A_v f_y$ where A_v stands for the shear area of the section, computed according to EC 3 [3]) is included in the properties of the section by using the section '*aggregator*' function in OPENSEES [4].

Panel zone

Considering the symmetry and regularity of the structure (*i.e.,* constant span length and inter-storey height), PZs are modelled using the "Scissors" model [12-12], where two rotational springs represent the shear behaviour of the PZ and bending behaviour of the column flange, respectively (see Figure 5.6). PZs are represented by two orthogonal rigid elements, defined as '*elastic BeamColumn elements'* in OPENSEES [4], combined with two '*zero-length*' [4] rotational springs, modelling the panel and flange contributions. Doubler plates stiffen the PZ with a thickness equal to the one of the column's web (*i.e., t*=2t_w) to ensure adequate stiffness to the joints and promote only the plastic engagement of the beams. The parameters are reported in Table 31.

Table 31. Parameters for the "Scissor" [12] springs for the PZ

Storey	M_{Flange}	K_{Flange}	M_{Panel}	K_{Panel}
[-]	[kNm]	[kN/m]	[kNm]	[kN/m]
1	229,193077	28863,134	2663,895855	1341897,110000
2	233,622207	29989,466	2715,375339	139426,226100
3	195,164333	24025,246	1832,429342	902307,601000
4	195,164333	24025,246	1832,429342	902307,601000

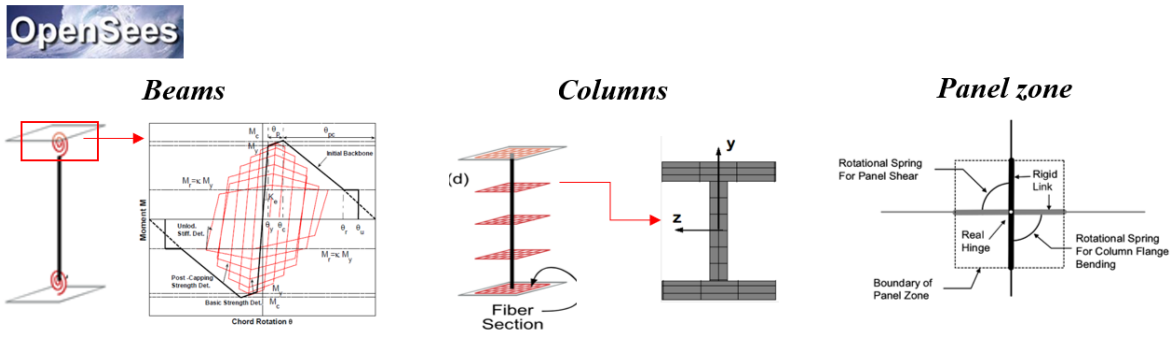

Figure 5.6: Modelling strategy adopted in OPENSEES [4].

Leaning column

To consider the P-delta effects related to the displacements and the axial forces in the gravity columns, an additional leaning column [13-15] is included in the numerical model (see Figure 5.7). The leaning column, comprised of '*elastic beam-column elements'* [4] with second-order effects, must represent all the gravity columns belonging to the tributary area of the structure. This column is pinned at the base and continuous along the height of the building, and it is connected to the MRF using rigid '*truss elements*' of OPENSEES [4]. The flexural and axial stiffness of the leaning column is equal to the sum of the flexural and axial stiffness of the gravity columns it represents.

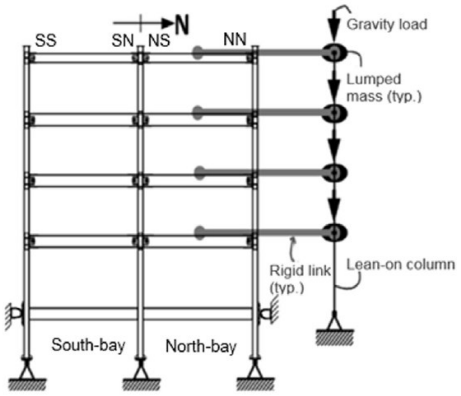

Figure 5.7: Leaning column (from Ahmadi *et al.* 2018 [15]).

Floor, Materials, Damping

The rigid-floor diaphragm is modelled by assigning a high value to the axial stiffness of the beams. Gravity loads are applied on the beams by considering the seismic combination of the Eurocode 8 [1], while the masses are concentrated at the BCJs. The *'Steel01'* material of OPENSEES [4] for 355 MPa yield strength and 275 MPa yield strength and 0.2% post-yield stiffness ratio is employed for columns and beams, respectively. Geometric non-linearities are considered in the elements of the MRF. Damping sources other than the hysteretic energy dissipation are modelled through the Rayleigh damping matrix, where the values of the mass-related and stiffness-related damping coefficients are considered for a damping factor of 2% for the first two vibration modes.

5.5 Non-linear static analysis

Non-linear static analyses with a distribution of lateral forces defined according to the first mode are performed on the MRF with conventional CBs and the same MRF, including the proposed SC-CBs. The results of these analyses are shown in Figure 5.8 (a) and (b), which illustrate the storey shear *vs* the interstorey drift for each storey of the two structures. It is worth stressing that, thanks to the design procedure, the structures are characterised by a homogeneous inelastic demand at all storeys. However, pushover results show that the first-storey columns of the MRF with conventional CBs experience damage and plastic deformations, while all the columns are fully protected from yielding in the MRF with the innovative SC-CBs. It is also observed that beams develop a similar level of damage in the two structures.

Based on the results of the pushover analyses, structure-specific damage state thresholds, defined in terms of maximum interstorey drift, are mapped against local EDPs, as reported in Table 32. The use of global EDPs has several advantages, and, amongst others, it synthetically describes the structural response containing the computational effort involved in the analysis of complex models. In this paper, the maximum interstorey drift ($\theta_{s\text{-}max}$) is defined to describe the damage conditions at the local level considering specific member-level performances for both the structures (*i.e.,* linear elastic limits of the components, yielding of the components, several inelastic deformation levels and ultimate chord rotation of the beams) and also including the behaviour of the CBs components (*i.e.,* the sliding force of the FDs, ultimate chord rotation of the CB connections, yielding of the PT bars).

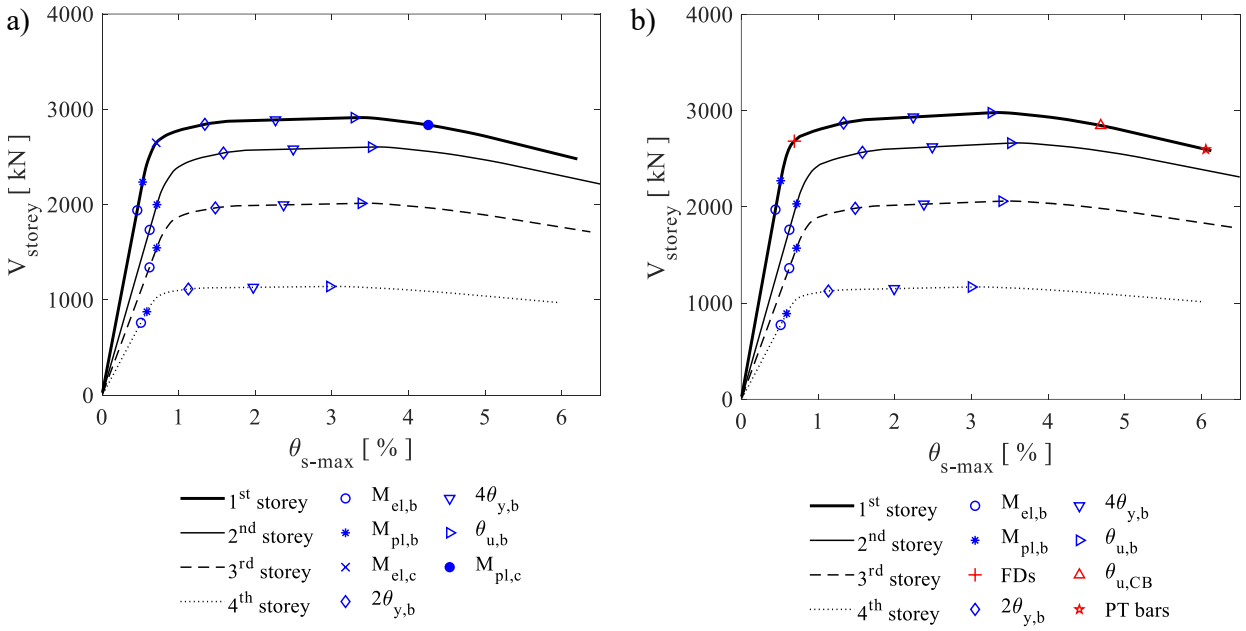

Figure 5.8: Storey shear *vs* interstorey drift for: a) the MRF; b) the MRF-CB.

Table 32. Maximum interstorey drifts thresholds mapping.

EDPs	Performance levels	MRF	MRF-CB
$M_{el,b}$	Limit of elastic behaviour in one beam	4.6 ‰	4.6 ‰
$M_{pl,b}$	Plastic moment in one beam	5.3 ‰	5.3 ‰
FDs	Sliding force of the friction devices	-	6.8 ‰
$M_{el,c}$	Limit of elastic behaviour of one column	7.0 ‰	-
$2\theta_{y,b}$	Beams performance levels	1.3 %	1.3 %
$4\theta_{y,b}$	measured as a multiplier of the chord rotation at yielding	2.7 %	2.7 %
$\theta_{u,b}$	Ultimate chord rotation in one beam	3.2 %	3.2 %
$M_{pl,c}$	Plastic moment in one column	4.2 %	-
$\theta_{u,CB}$	Ultimate chord rotation $\theta_{u,CB}$ of the CB	-	4.7 %
PT bars	Yielding of the PT bar	-	6.1 %

For the beams, the inelastic deformation levels are expressed in terms of the plastic rotation as a multiple of the chord rotation at yielding ($\theta_{y,b}$). It is worth mentioning that these plastic rotation levels are considered only to compare the results of the two frames and do not correlate with conventional standardised damage levels. For the sake of brevity, the interstorey drift limits corresponding to the member-level criteria are reported only for the first storey. However, the same performance level for local EDPs is reached for very similar values of interstorey drifts at the other storeys, as expected from the design. Figure 5.8 (a) and (b) show the pushover analyses' results regarding storey shear *vs.* interstorey drifts for the two structures, including the specific damage state thresholds.

5.6 Incremental Dynamic Analysis

The Incremental Dynamic Analyses (IDA) [5] approach is a comprehensive method for evaluating the conditional distribution of the structural response [6]. IDA is a parametric analysis method utilised to estimate structural systems' seismic performance. This is done by subjecting a structural model to non-linear time history analysis under a suite of ground motion accelerograms scaled to increasing levels of the Intensity Measure (IM), covering the whole range from elastic to non-linear seismic response of the frame up to collapse [6]. The IDA curve relates a selected IM of the selected ground motion set with Engineering Demand Parameters (EDPs) of the structural system (*e.g.,* peak interstorey drifts or peak floor accelerations, storey drift ratio or absolute acceleration), given the IM for any number of IM levels, from elasticity to global collapse. In an IDA, the intensity of the ground motion is incremented and applied to the structural model and the structural response is recorded at each step. In this way, the IDA approach is able to provide insights about the structural response even under rare, high-intensity ground shakings, for which only a few or no recordings are available [6]. There are various ways to scale a ground motion. A 'traditional' IM that may be used is the spectral acceleration at the fundamental period of the building $S_a(T_1)$. The output of IDA is a set of discrete points (*i.e.,* obtained by scaling each of the selected ground motions) of the IM *vs.* the demand parameter of interest, for instance, the first mode spectral acceleration, $S_a(T_1)$ and the maximum interstorey drift (see Figure 5.9).

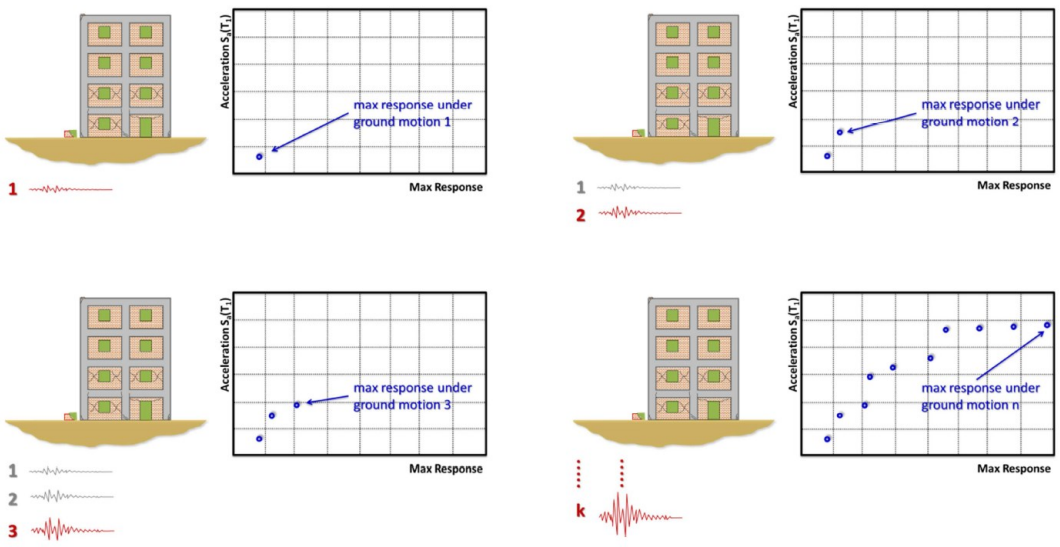

Figure 5.9: Steps of IDA [5] using ground motion scaling (from D'Ayala *et al.* 2015 [6])

In this thesis, IDAs [5] are performed to investigate how the proposed SC-CB's introduction influences the MRFs' seismic response while also considering the influence of record-to-record variability. Non-linear time history analyses for the MRF and MRF-CB are performed by considering a suite of ground motion records scaled to increasing levels of the IM. The spectral acceleration corresponding to the first vibration mode ($S_a(T_1)$) is used as IM. Residual interstorey drifts $\theta_{s\text{-}res}$ and peak interstorey drifts $\theta_{s\text{-}max}$ are selected as global EDPs, allowing the comparison of the seismic performance of the two systems. Figure 5.10 illustrates an overview of the IDA [5] methodology adopted in this work.

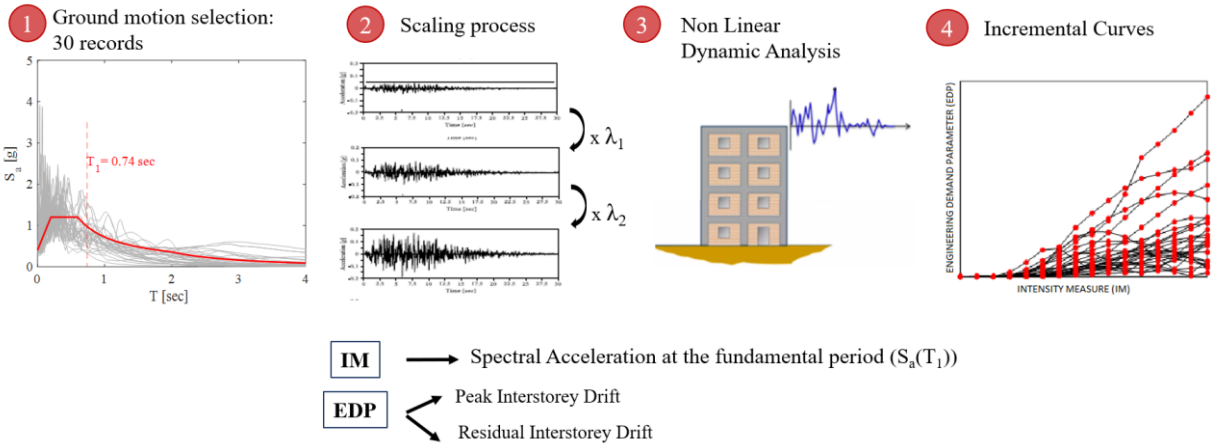

Figure 5.10: IDA [5] Methodology

5.6.1 Ground motion records selection

A set of 30 natural ground motion records is selected from the SIMBAD Database [16] with the following parameters: moment magnitude (M_w) ranging from 6 to 7, epicentral distance R ≤ 30 km and spectrum-compatibility in the range of periods between $0.2T_1$ and $2T_1$. The mean elastic spectrum of the records set is kept between 75% and 130% of the corresponding Eurocode-based elastic response spectrum [1] expected at the site, as indicated in Figure 5.11.

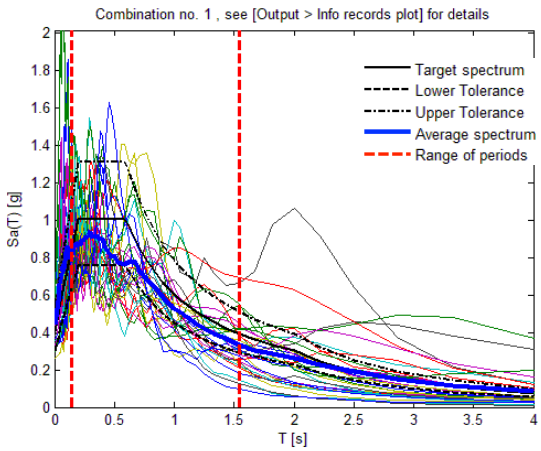

Figure 5.11: Selected ground motion records from the SIMBAD Database [16].

Table 33. Selected ground motion records from the SIMBAD Database [16].

Earthquake	Date	Fault	M_w	Station	PGA [g]
Name		Mechanism		Country	
Imperial Valley	1979_October_15	strike-slip	6.5	California, USA	0.49
Loma Prieta	1989_October_18	oblique	6.9	California, USA	0.59
Olfus	2008_May_29	strike-slip	6.3	Iceland	0.54
Erzincan	1992_March_13	strike-slip	6.6	Turkey	0.52
L'Aquila mainshock	2009_April_06	normal	6.3	Italy	0.66
Olfus	2008_May_29	strike-slip	6.3	Iceland	0.51
Loma Prieta	1989_October_18	oblique	6.9	California, USA	0.64
Imperial Valley	1979_October_15	strike-slip	6.5	California, USA	0.52
Imperial Valley	1979_October_15	strike-slip	6.5	California, USA	0.52
Imperial Valley	1979_October_15	strike-slip	6.5	California, USA	0.44
Loma Prieta	1989_October_18	oblique	6.9	California, USA	0.53
Noto Peninsula	2007_March_25	reverse	6.7	Japan	0.79
Olfus	2008_May_29	strike-slip	6.3	Iceland	0.67
Niigata	2007_July_16	reverse	6.6	Japan	0.68
South Iceland	2000_June_17	strike-slip	6.5	Iceland	0.47
Dinar	1995_October_01	normal	6.4	Turkey	0.33
Loma Prieta	1989_October_18	oblique	6.9	California, USA	0.37
L'Aquila mainshock	2009_April_06	normal	6.3	Italy	0.49
South Iceland	2000_June_17	strike-slip	6.5	Iceland	0.35
Loma Prieta	1989_October_18	oblique	6.9	California, USA	0.51
Northridge	1994_January_17	reverse	6.7	California, USA	0.34
Loma Prieta	1989_October_18	oblique	6.9	California, USA	0.37
EMILIA_Pianura_Padana	2012_May_29	reverse	6	Italy	0.29
Erzincan	1992_March_13	strike-slip	6.6	Turkey	0.52
Northridge	1994_January_17	reverse	6.7	California, USA	0.36
Imperial Valley	1979_October_15	strike-slip	6.5	California, USA	0.44
EMILIA_Pianura_Padana	2012_May_20	reverse	6.1	Italy	0.26
L'Aquila mainshock	2009_April_06	normal	6.3	Italy	0.49
Gazli	1976_May_17	reverse	6.7	Uzbekistan	0.72
Friuli 1st shock	1976_May_06	reverse	6.4	Italy	0.35

It is noteworthy that a large number of zero acceleration points (*i.e.,* 40 s) have been added at the end of each record to allow the free vibrations to stop and correctly capture the residual deformations. The selected ground motions are listed in Table 33 with the indications of the date, fault mechanism, M_w, station and PGA. The fundamental period of vibration is $T_1 = 0.74$ sec for both structures. The spectral acceleration corresponding to the first vibration mode ($S_a(T_1)$) is equal to 0.98g and 1.46g, respectively, for the DBE and MCE, representing the two seismic intensities of interest. The accelerograms have been homogeneously scaled using a normalization based on the first period of vibration of the structure, as illustrated in Figure 5.12. The spectra of the scaled ground motions are illustrated in Figure 5.13 (a) and (b) for the DBE and MCE, respectively.

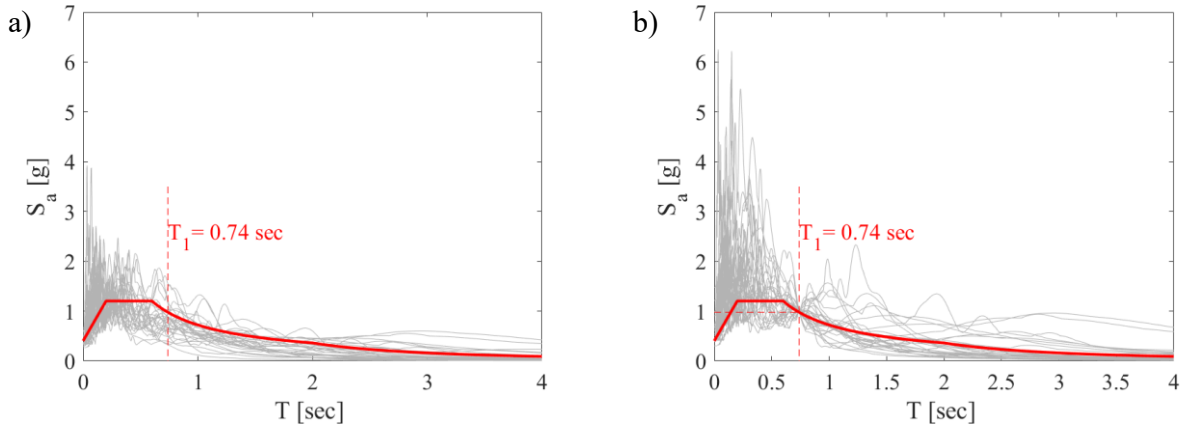

Figure 5.12: Selected ground motion records from the SIMBAD Database [16]: a) Spectra; b) Normalization

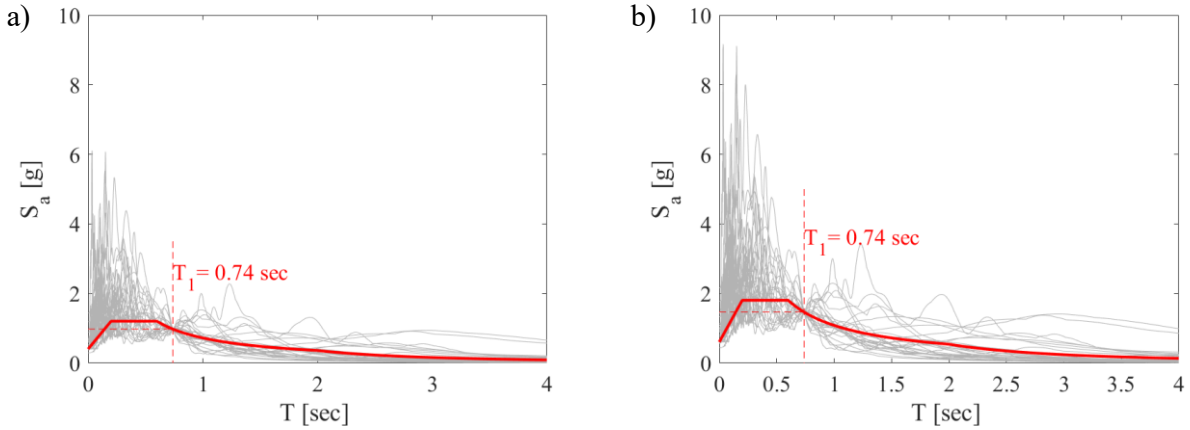

Figure 5.13: Spectra of the scaled ground motions: a) DBE and b) MCE.

5.6.2 Global EDPs

Figure 5.14 (a) (b), (c) and (d) show the samples of the demand for the peak interstorey drifts ($\theta_{s\text{-}max}$) *vs.* the IM for the first, the second, the third and the fourth storeys, respectively. It is noteworthy to observe that the introduction of the proposed SC-CBs does not affect the maximum response parameters of the structure. In fact, the two structures experience similar values of the maximum interstorey drifts at all the storeys. Moreover, it is also highlighted that the two structures achieve peak interstorey drifts $\theta_{s\text{-}max}$ lower than the Limit of 1% under the FOE, as expected from the design [1]. Under this latter intensity, the higher values occur at the intermediate floors, where the peak interstorey drifts are close to the 1% limit.

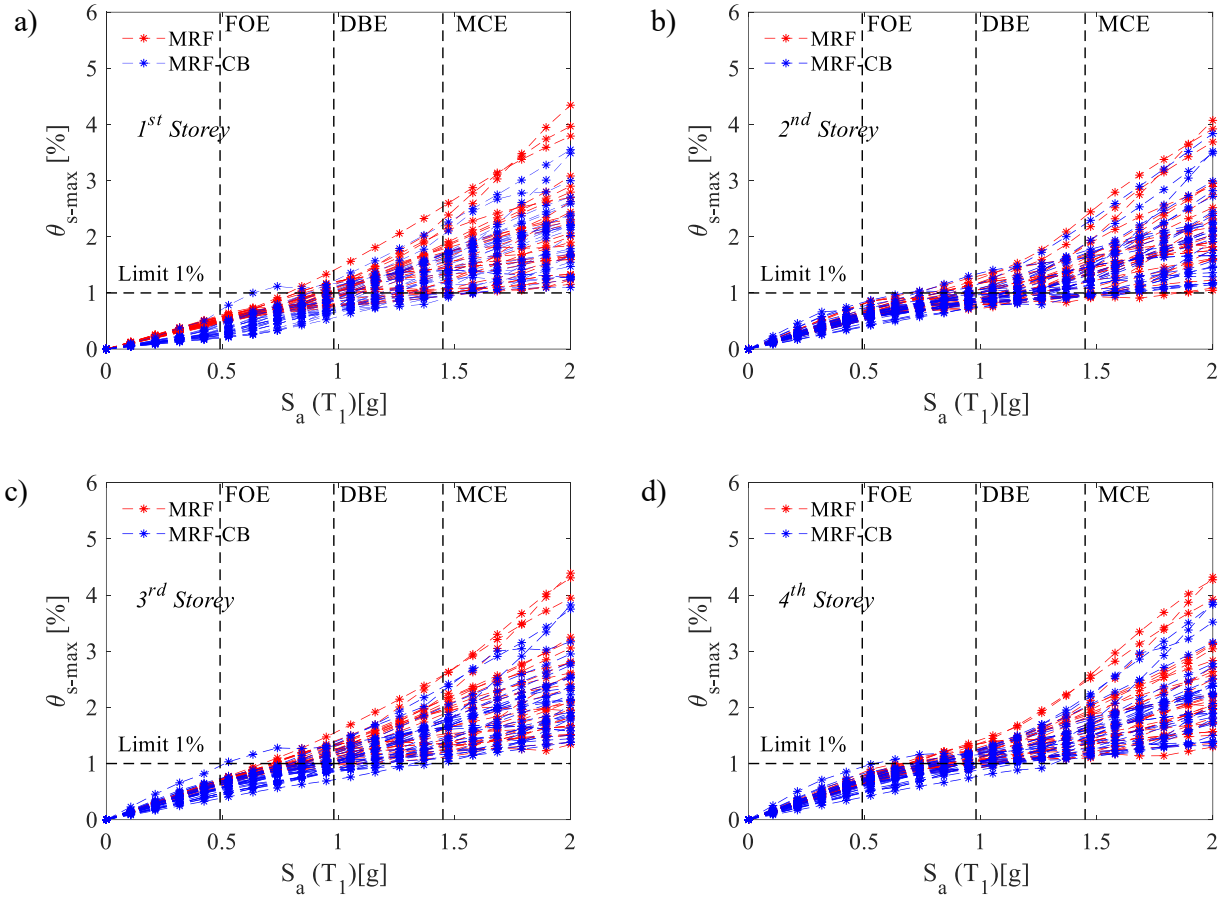

Figure 5.14: Comparison of peak interstorey drifts of the: a) first, b) second, c) third and d) fourth storeys.

Figure 5.15 (a), (b), (c) and (d) illustrate the sample of the demand for the residual interstorey drifts ($\theta_{s\text{-}res}$) *vs.* the IM for the first, the second, the third and the fourth storeys, respectively. It is worth highlighting that the introduction of the proposed CB allows a significant reduction of the residual interstorey drifts for both the reported intensities (*i.e.,* DBE and MCE). In particular, the MRF-CB experiences residual interstorey lower than the Limit of 0.5% [9], even for the MCE. Conversely, this limit is not satisfied at the MCE for the structure with full-strength CBs, which experience plastic deformations and damage.

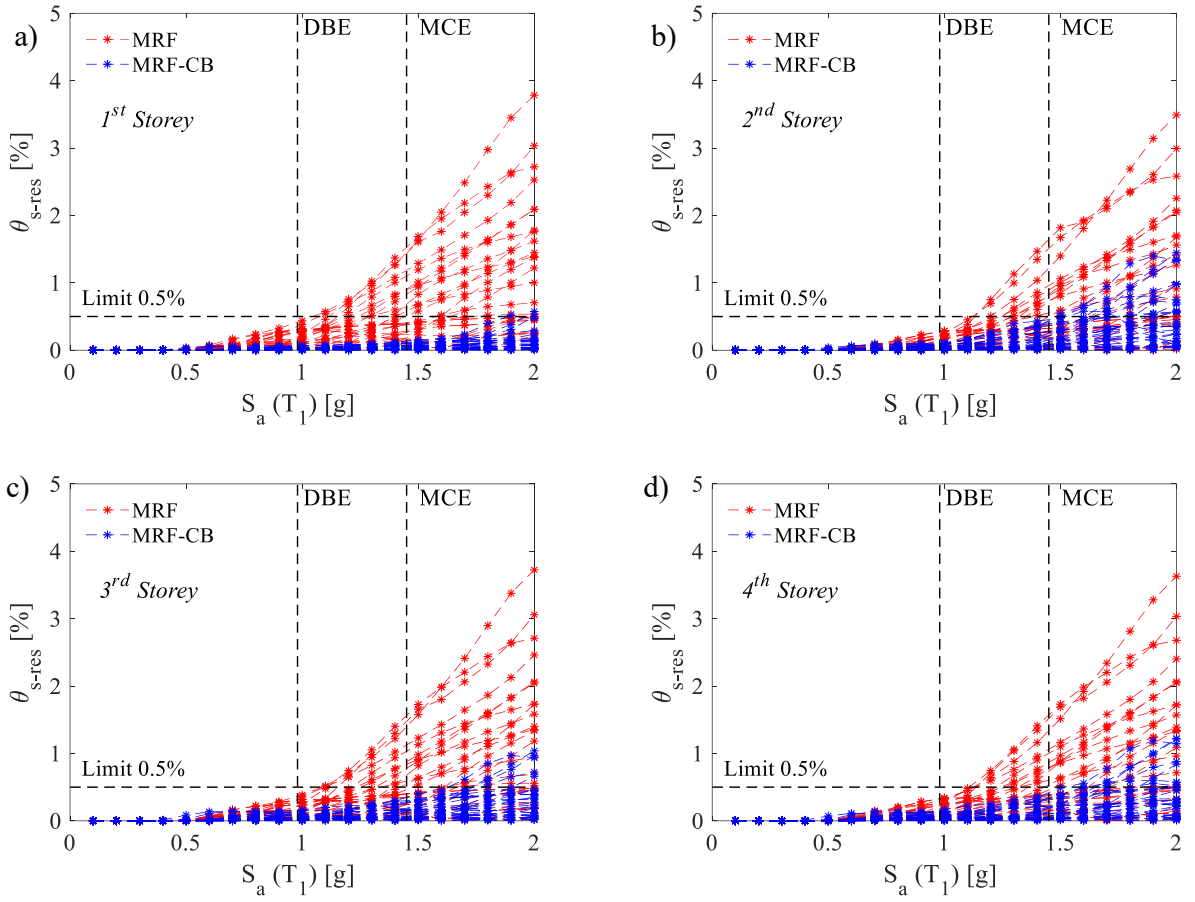

Figure 5.15: Comparison of the residual interstorey drifts of the: a) first, b) second, c) third and d) fourth storeys.

For a single ground motion record and the two intensities of interest, Figure 5.16 compares the first-storey displacements of the two frames. It is highlighted how the proposed SC-CB minimises the residual first-storey drifts of the MRF-CB for both DBE and MCE. The comparison of these displacement histories further highlights how the peak response is similar for the two structures.

Besides, the distribution of the residual interstorey drifts ($\theta_{s\text{-}res}$) at all the storeys is illustrated in Figure 5.17 (a) and (b), respectively, for the DBE and MCE intensities. Dotted lines represent the response of the single ground motions, while the mean values are shown with solid lines. It can be observed that, although the self-centring system is introduced only at the first storey, this also allows a reduction of the residual drifts at the higher storeys, with an efficiency that decreases along the height. This trend can be observed for both the seismic intensities of interest. Similarly, the distribution of peak interstorey drifts at all storeys is illustrated in Figure 5.18 for the two seismic intensities of interest. The results show that the maximum response parameters of the structure are not affected by the introduction of the CBs at any storey.

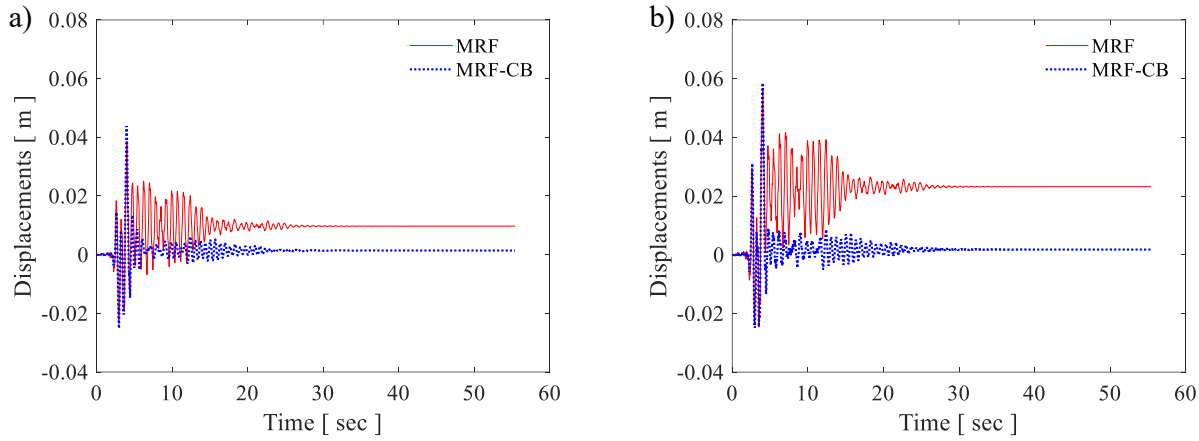

Figure 5.16: Comparison of the first storey displacement time history for a single ground motion record for: (a) DBE and (b) MCE intensities.

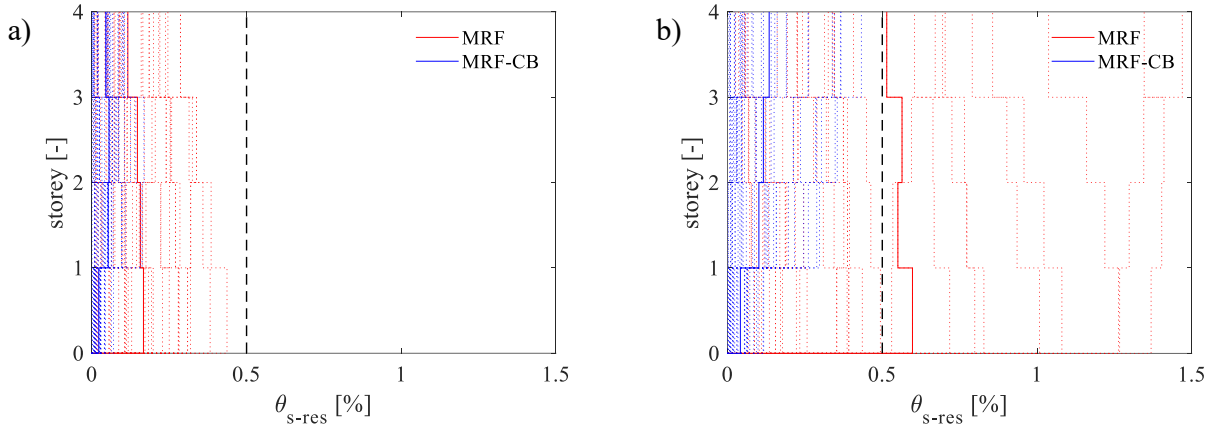

Figure 5.17: Comparison of the residual interstorey drifts distribution at all the storeys for the: (a) DBE and (b) MCE intensities.

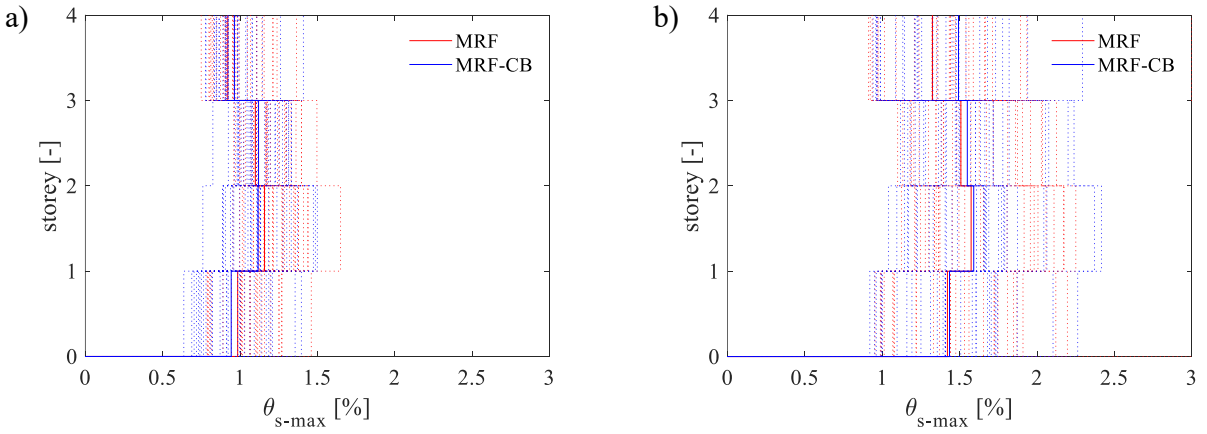

Figure 5.18: Comparison of the peak interstorey drift distribution at all the storeys for the: (a) DBE and (b) MCE intensities.

5.6.3 Local EDPs

Figure 5.19 compares the moment-curvature hysteretic behaviour of the two structures' bottom sections of the first-storey columns for a single ground motion record. Figure 5.19 (a) shows how the MRF with conventional CBs experiences large plastic deformations and damage, thus leading to the need for repair measures after strong earthquakes. Figure 5.19 (b) refers to the MRF-CB, where the first storey columns experience a linear elastic behaviour and are fully protected from yielding under the DBE and MCE. This is expected due to the limitation imposed on the moment capacity of the connection during the design. Moreover, Figure 5.20 shows similar representations for the beams' end where plastic hinges are developed. It can be observed that beams undergo similar plastic deformation and damage in both frames. This was expected based on the similar values of the peak interstorey drifts shown in Figure 5.18. Moreover, columns at higher storeys remain elastic for both structures due to the capacity design rule enforced during the design, and PZs remain within the elastic range, thanks to the introduction of the doubler plates.

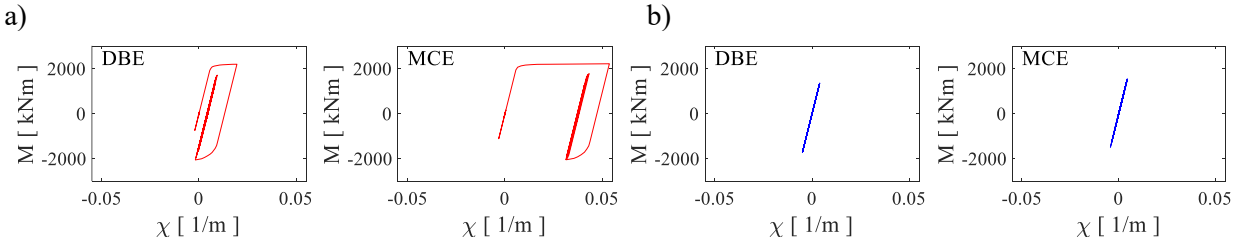

Figure 5.19: Moment-curvature relationship in the bottom section of one of the first storey columns of the: (a) MRF and (b) MRF-CB for a single ground motion record scaled at DBE and MCE.

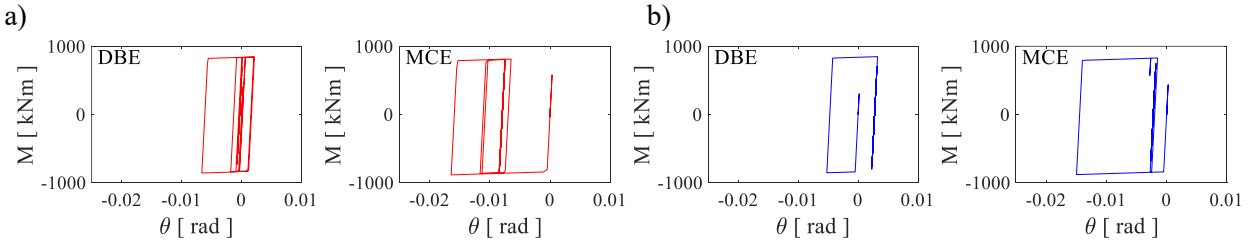

Figure 5.20: Moment-rotation relationship in the beam end of one of the first storey beams of the: (a) MRF and (b) MRF-CB for a single ground motion record scaled at DBE and MCE.

5.7 Fragility curves

The performances of the two structures are presented in terms of fragility curves derived from the results of the IDAs and successively fitted by analytical lognormal curves through least-square minimisation. The assumption of lognormality simplifies the analysis of the results and allows the synthetic description of the fragility of the systems using the two characteristic parameters describing the lognormal distribution. Fragility curves permit to quantify of the probability that the structural demand exceeds a specific value, defined as the characteristic threshold for a limit state, conditional to the seismic intensity defined by properly selected intensity measure [8] as follows:

$$F_{LS}(IM) = P[EDP > EDPc\,|IM] \tag{5.1}$$

In this study, the demand is derived from the results of the IDAs, and the associated capacity threshold is assumed as the Limit of 0.5% [9]. Figure 5.21 illustrates the methodology to derive the fragility curves in this work.

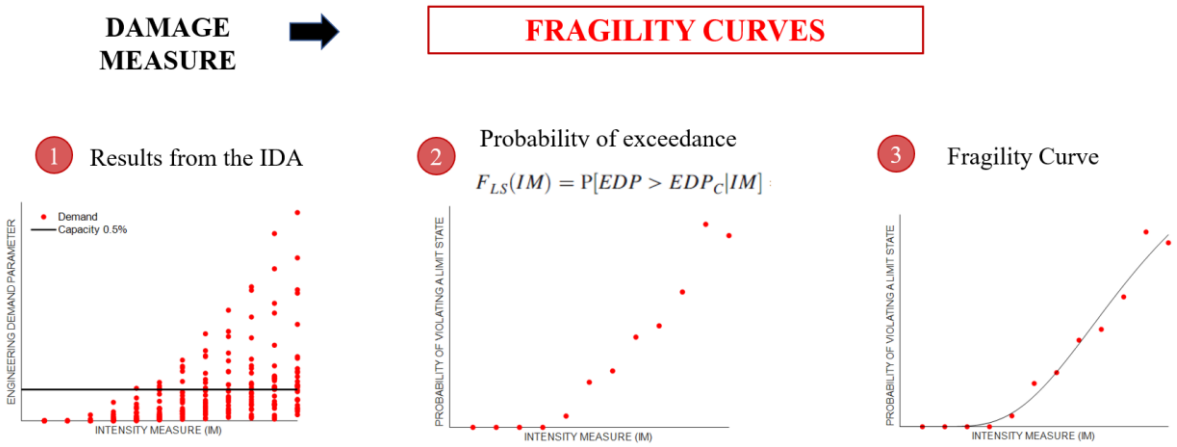

Figure 5.21: Comparison of global fragility curves for repairability.

Figure 5.22 shows the fragility curves related to the building repairability based on residual interstorey drifts. The samples of the demand for these EDPs are represented by the maximum residual interstorey drifts and are derived by the IDAs. The associated capacity threshold is assumed to be 0.5% [9]. Results show how the introduction of the SC-CBs significantly contributes to the reduction of the residual interstorey drifts for both DBE and MCE seismic intensities.

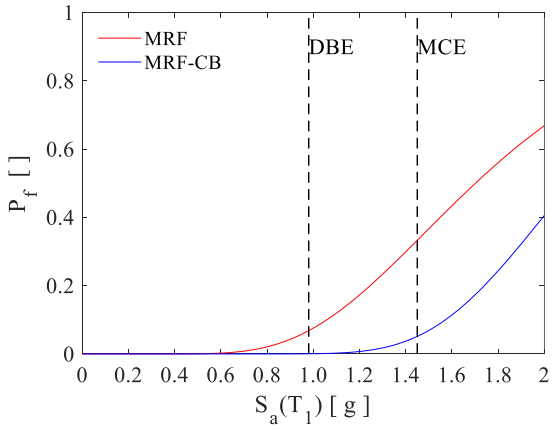

Figure 5.22: Comparison of global fragility curves for repairability.

In addition, the comparison of the fragility curves is carried out for each storey of the two structures (Figure 5.23), demonstrating how the introduction of the SC-CBs fully contributes to the reduction of the probability of failure at the first storey, while the effect decreases along the height, as it is highlighted

in Table 34. This result suggests that the use of a self-centring system localised only in the column bases of the building is particularly effective for low-rise buildings. Conversely, its effectiveness for medium- and high-rise buildings should be verified by enlarging the range of investigated structures. Therefore, it is expected that the effect due to the use of self-centring column base joints may disappear after a certain number of storeys.

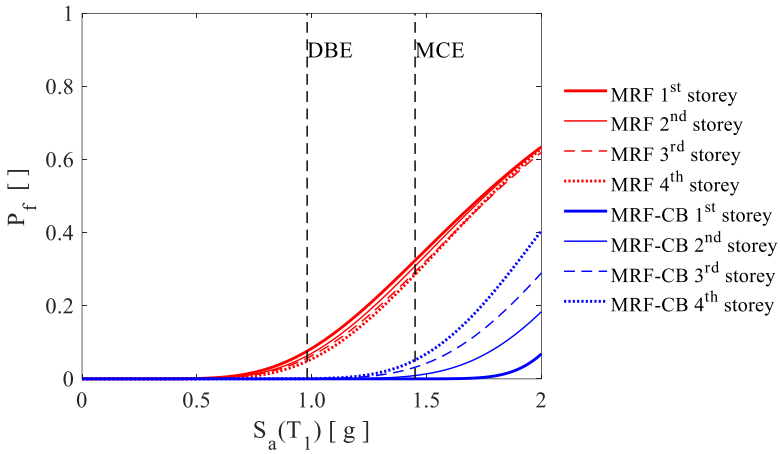

Figure 5.23: Comparison of storey-level fragility curves for repairability.

Table 34. Probability of failure for the repairability based on residual interstorey drifts.

	P_f	DBE	MCE
MRF	1st storey	7.6 %	32 %
	2nd storey	6.3 %	31 %
	3rd storey	5.6 %	29 %
	4th storey	4.8 %	28 %
MRF-CB	1st storey	0 %	0 %
	2nd storey	0 %	1.0 %
	3rd storey	0.2 ‰	3.0 %
	4th storey	0.4 ‰	5.0 %

Finally, component fragility curves are derived based on the maximum interstorey drift thresholds identified in Section 5.5. The fragility curves for the different components and performance levels are shown in Figure 5.24 (a) and (b) for the MRF and MRF-CB, respectively. From the results, it is possible to observe how the introduction of the CBs does not produce any detrimental effect on the components and the sequence of activation of the different mechanisms within the structure. The beams are the first to reach their elastic limit ($M_{el,b}$) and plastic ($M_{pl,b}$) limits in both structures. This highlights that the introduction of the CBs does not protect the beams from yielding, as expected from the design. Following the yielding of the beams, the friction devices in the CBs are successively activated. For the beams of both structures, two inelastic deformation levels are expressed in terms of the plastic rotation as a multiple of the chord rotation at yielding ($\theta_{y,b}$). Then, the ultimate chord rotation is reached in the beams of both structures ($\theta_{u,b}$). Additionally, the yielding of the columns of the first storey is reached ($M_{pl,c}$) for the MRF, as expected from the design, while the columns of the first storey of the MRF-CB

do not undergo any damage due to the presence of the CBs which fully protect the columns from yielding and the PT bars which do not experience yielding (PT_{bars}).

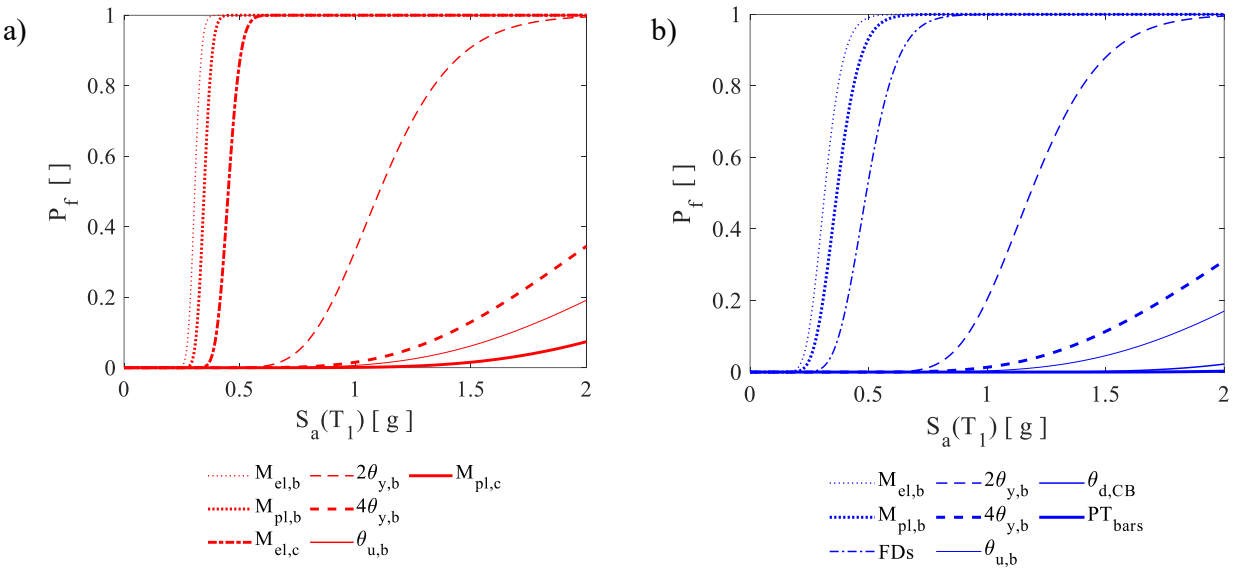

Figure 5.24: Components-level fragility curves for (a) MRF and (b) MRF-CB.

5.8 Influence of the frame layout

In this section, a parametric numerical analysis is performed to investigate the influence of the frame layout (*i.e.,* storeys and bay numbers) on the self-centring behaviour of the case-study MRFs illustrated in Section 5.2. This parameter is investigated through nine case-studies MRFs with a different number of storeys (*i.e.,* 4, 6 and 8) and bays (*i.e.,* 3, 5 and 8) designed according to the Eurocode 8 [1]. The nine case studies MRFs equipped with SC-CBs are designed and modelled by following the procedure shown in Section 5.4. Their seismic performance is assessed through IDAs [5] and fragility curves [8], following a consistent methodology with the procedure shown for the single case-study MRF.

5.8.1 Incremental Dynamic Analysis

A set of 30 natural ground motion records is selected from the SIMBAD Database [16] for each case-study MRF with the following parameters: moment magnitude (M_w) ranging from 6 to 7, the epicentral distance $R \leq 30$ km and spectrum-compatibility in the range of periods between $0.2T_1$ and $2T_1$. The mean elastic spectrum of the records set is kept between 75% and 130% of the corresponding Eurocode-based elastic response spectrum [1] expected at the site, as indicated in Figure 5.25. It is noteworthy that a large number of zero acceleration points (*i.e.,* 40 s) have been added at the end of each record to allow the free vibrations to stop and correctly capture the residual deformations. The ground motion records are scaled to increasing IM values within the IDA procedure with a constant step of 0.1g until 'collapse'. The spectral acceleration corresponding to the first vibration mode ($S_a(T_1,\xi)$) is used as IM. It is important to highlight that the vibration periods, and consequently the IM values, are the same for the two 'equivalent' structures with and without the SC-CBs, allowing the comparison of fragility curves.

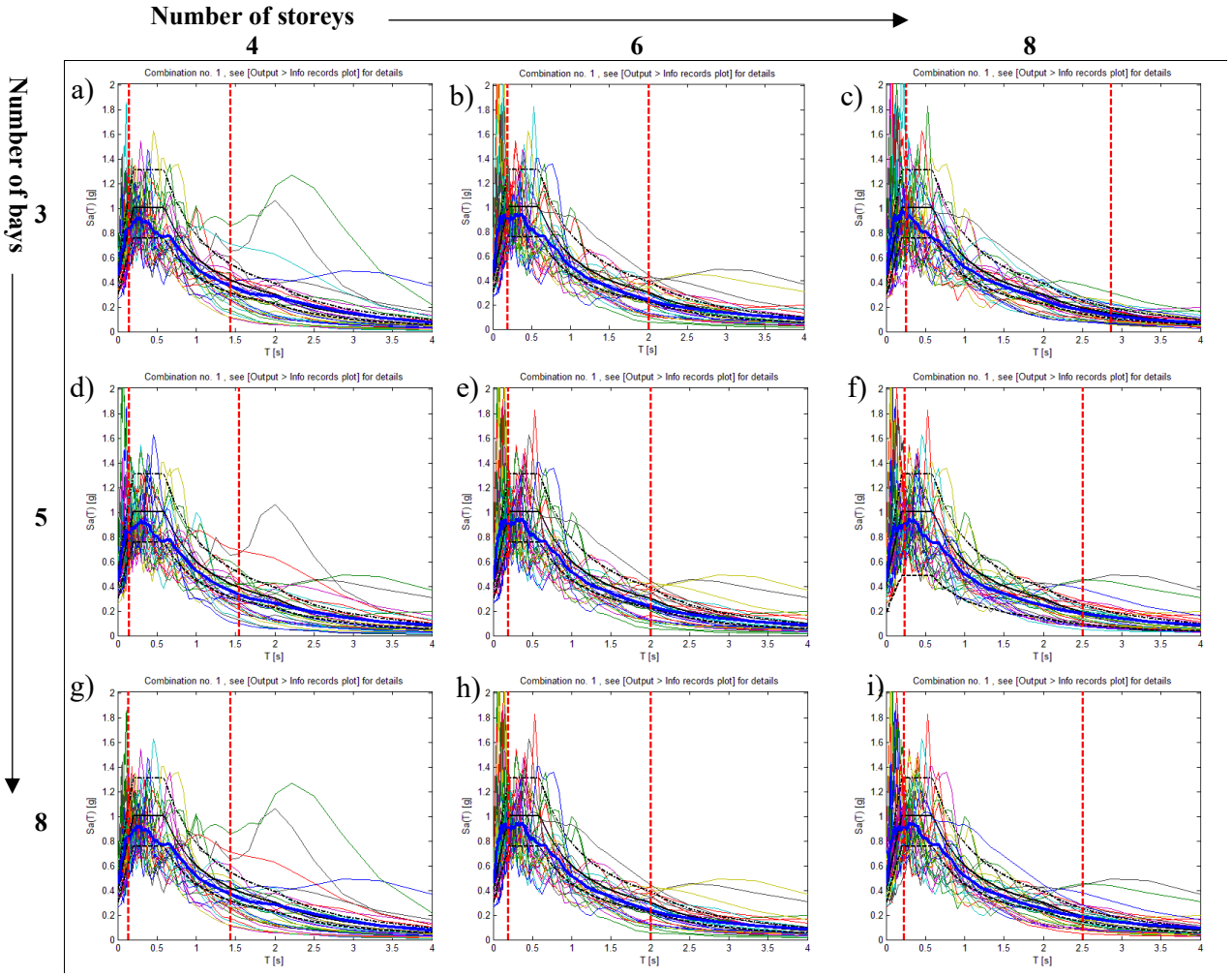

Figure 5.25: Selected ground motion records from the SIMBAD Database [16].

Global and storey-level EDPs are monitored to investigate the frame layout's influence on the self-centring capability provided by the SC-CBs. For these case studies, peak and residual interstorey drifts are considered storey-level EDPs, while the maximum values of these quantities among all the storeys are used as global EDPs (*i.e.,* the maximum (among all the storeys) peak interstorey drifts ($\theta_{\text{max-peak}}$) and the maximum (among all the storeys) residual interstorey drifts ($\theta_{\text{max-res}}$)). The effectiveness of the SC-CBs in reducing the residual interstorey drifts is evaluated by comparing the 'equivalent' MRF with conventional full-strength CBs and the MRF with SC-CB connections (MRF-CB). The assessment is performed by comparing the 16%, 50%, and 84% fractiles among all ground motions to synthesise the demand values for $\theta_{\text{max-peak}}$ and $\theta_{\text{max-res}}$.

Results are illustrated in Figure 5.26 only for a single case-study (*i.e.,* the 5-bay 6-storey frame in both configurations) to show the selected global EDPs monitored by the IDAs. Figure 5.26 (a) and (b) show the IDA curves for the $\theta_{\text{max-peak}}$ case-study frames with 5 bays and 6 storeys in both configurations. Similarly, Figure 5.26 (c) and (d) show the IDA curves for the maximum (among all the storeys) residual interstorey drifts ($\theta_{\text{max-res}}$). Highlighted in the figures are the 16%, 50%, and 84% fractiles among all

ground motions, while the single IDA curves are shown in grey. The selected fractiles' values are reported for both seismic intensities of interest, DBE and MCE. The results in terms of $\theta_{max\text{-}peak}$ and $\theta_{max\text{-}res}$ for the other case-studies are shown in ANNEX A.

The comparison of Figure 5.26 (a) and (b) shows that the introduction of SC-CBs does not alter the structures' maximum response. The selected fractiles of the maximum peak interstorey drift for the two configurations show similar values along with the whole range of IM intensities. Conversely, the comparison of Figure 5.26 (c) and (d) shows that the use of the SC-CBs allows a significant reduction of the maximum residual interstorey drifts. In particular, Figure 5.26 (d) shows that considering the median results (50% fractile curve) among all ground motions, the introduction of the SC-CB allows a reduction of the residual interstorey drifts, which is lower than the limit of 0.5% [9], for both the DBE and the MCE. Conversely, this limit is not satisfied for the MRF with conventional column bases at the MCE intensity.

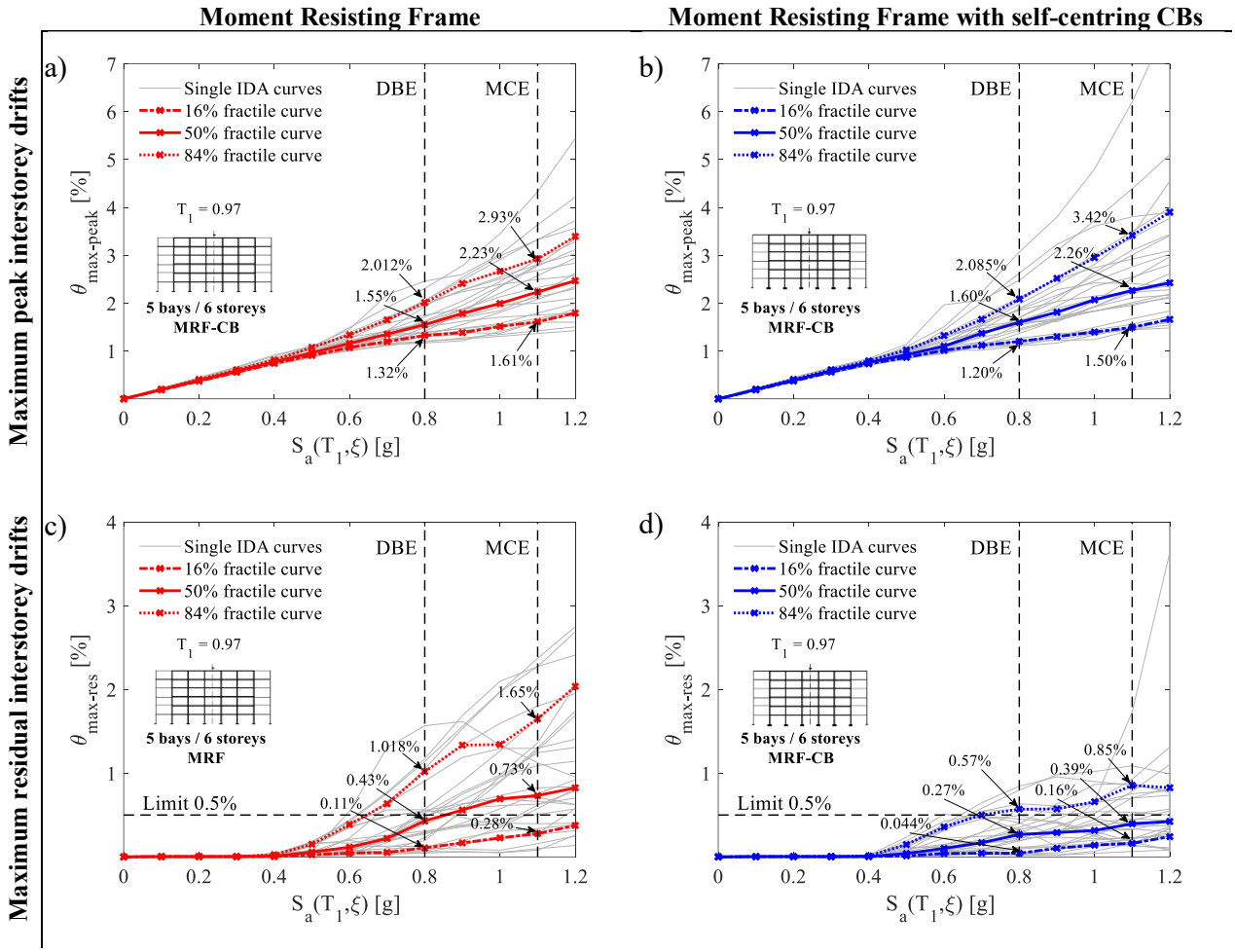

Figure 5.26: IDA Results: Maximum peak interstorey drifts: (a) MRF 5-6; (b) MRF-CB 5-6; Maximum residual interstorey drifts: (c) MRF 5-6; (d) MRF-CB 5-6

Figure 5.27 compares the maximum residual interstorey drifts, synthesized by the median values ($\theta_{max\text{-}res,50\%}$), for all the considered structures (*i.e.,* with and without SC-CBs). The median values correspond

to the 50% fractiles previously illustrated for the single case-study in Figure 5.26. The percentage reduction (Δ) is also reported for the two seismic intensities of interest. The figure highlights that the use of the SC-CBs allows for a significant reduction of the maximum residual interstorey drifts for all structures for both the DBE and the MCE. The only exception is the 8-storey frames, where the percentage reduction is limited at the DBE (*i.e.,* from 0% to 13%). However, it is noteworthy that all the structures equipped with the SC-CBs experience values lower than the Limit of 0.5%, also when the 'equivalent' conventional MRFs overcome it. The comparison of these reduction values provides an understanding of the frame layout's influence on the effectiveness of the proposed SC-CBs in terms of residual drift reduction.

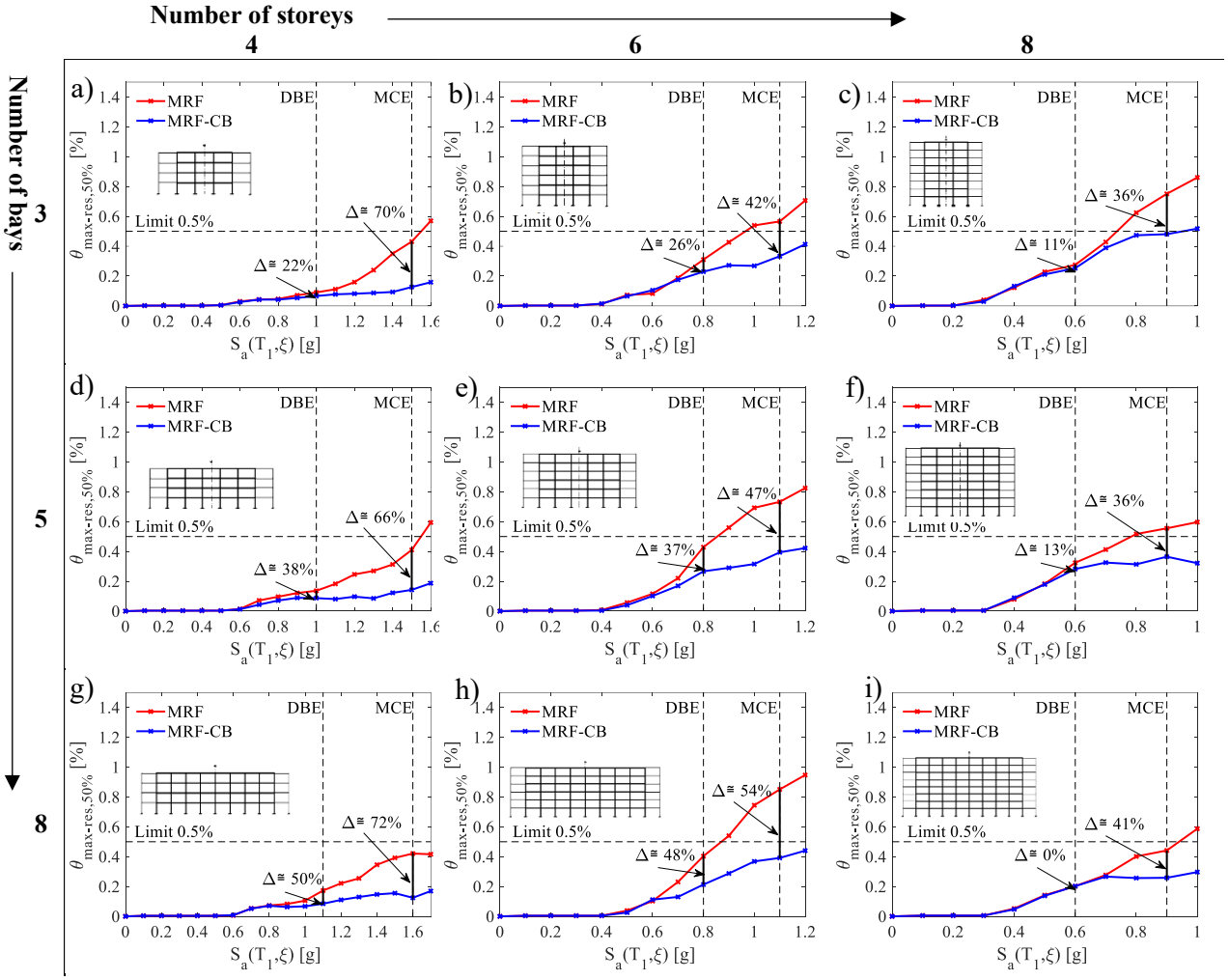

Figure 5.27: IDA Results: Comparison of the maximum residual interstorey drifts in terms of median values (50% fractile) among all ground motions: (a) 3-4; (b) 3-6; (c) 3-8; (d) 5-4; (e) 5-6; (f) 5-8; (g) 8-4; (h) 8-6; (i) 8-8.

In particular, the results show a high sensitivity of the self-centring response to the number of storeys of the structures. This is evidenced by the percentage reductions Δ observed in Figure 5.27 (a), (b) and (c) of the 3-bays 4-storey, 3-bays 6-storey and 3-bays 8-storey frames, which assume decreasing values at the MCE (*i.e.,* from 70% to 36%). A similar trend can be seen for the 5-bays (*i.e.,* from 66% to 36%) and the 8-bay frames (*i.e.,* from 72% to 41%), at the same intensity, as shown in Figure 5.27 (d), (e) and

(f) and Figure 5.27 (g), (h) and (i), respectively. It is highlighted that these results are particularly relevant at the MCE due to the high plastic engagement of the plastic hinges of the structures. Conversely, with respect to the number of bays, the frames' response does not show a clear tendency. In fact, it is not possible to observe a significant influence of the number of bays in reducing the efficiency of the SC-CBs, as evidenced in Figure 5.27 (a), (d) and (g) by the values of the percentage reductions Δ of the 3-bays 4-storey, 5-bays 4-storey and 8-bays 4-storey frames, which experience similar values at the MCE (*i.e.,* from 66% to 72%). Similarly, this also occurs for the 6-storey (*i.e.,* from 42% to 54%) and the 8-storey frames (*i.e.,* from 36% to 41%) at the same intensity, as shown in Figure 5.27 (b), (e) and (h) and Figure 5.27 (c), (f) and (i), respectively. Moreover, it is not possible to see a consistent trend at the DBE intensity. Figure 5.29 and Figure 5.29 show the height-wise peak interstorey drift distributions synthesized by the median value ($\theta_{peak,50\%}$) for both structures, at the DBE and at the MCE, to provide additional information about the trends of the selected EDPs at all the storeys of the case-studies in both configurations.

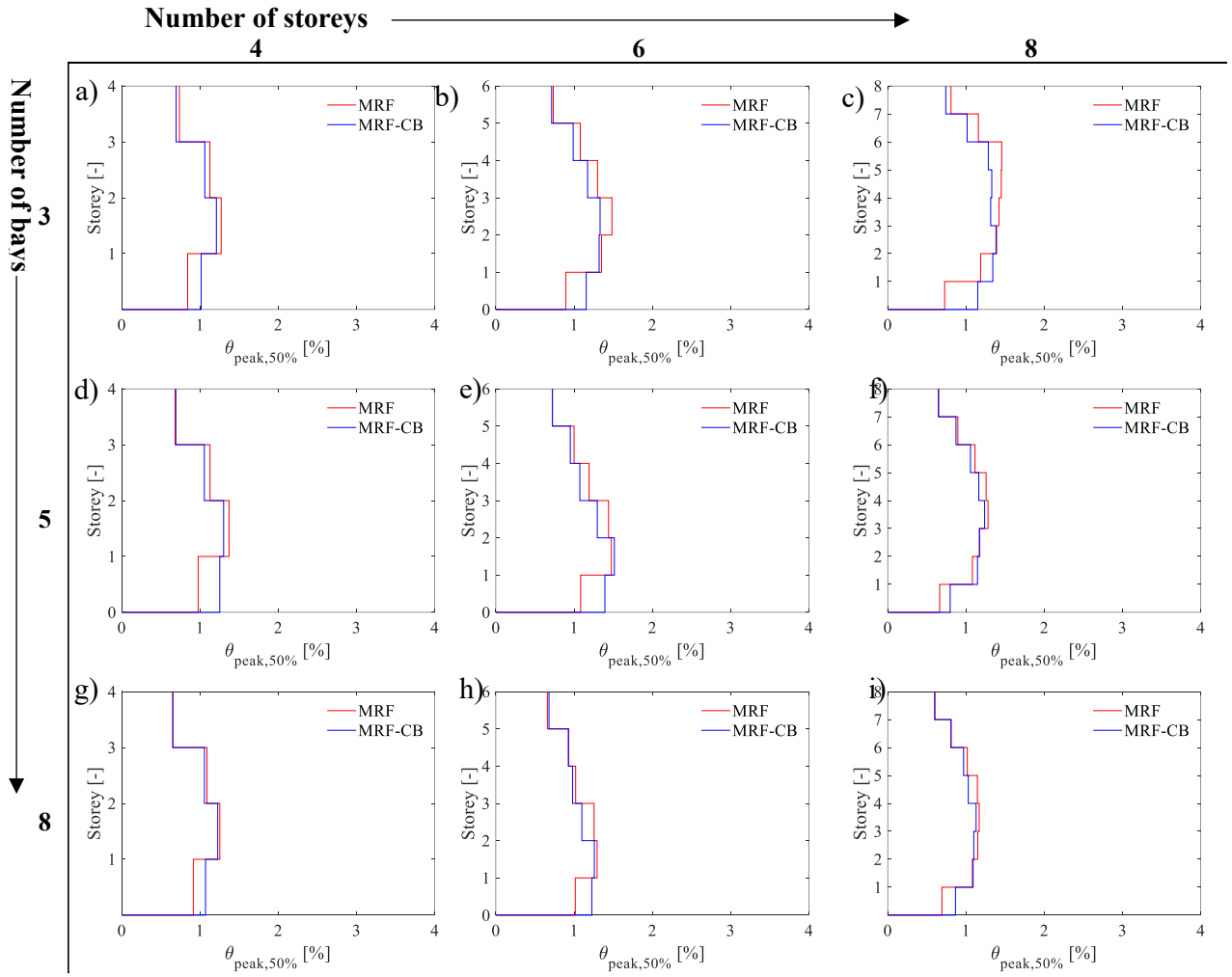

Figure 5.28: IDA Results: Comparison of the distribution of the peak storey drifts of the case-study frames for DBE: (a) 3-4; (b) 3-6; (c) 3-8; (d) 5-4; (e) 5-6; (f) 5-8; (g) 8-4; (h) 8-6; (i) 8-8.

In particular, Figure 5.29 illustrates the comparison of the peak interstorey drifts' distributions, synthesized by the median value ($\theta_{peak,50\%}$) at the MCE. As expected, the 'equivalent' structures (*i.e.,* MRF and MRF-CB) are characterized by similar values and distribution for the peak interstorey drifts. The only exception is related to the first storeys, where the structures equipped with SC-CBs show a slight increase in the peak interstorey drifts. This is expected and related to the lower effective (*i.e.,* tangent) stiffness of the SC-CB connection. It is worth mentioning that for the 8-storey frames, the maximum values of the peak interstorey drifts tend to concentrate at intermediate storeys. This highlights the influence of the higher modes in the response of these structures. Conversely, for the 4- and 6-storey frames, $\theta_{peak\ 50\%}$ assumes its maximum value at the lower storeys.

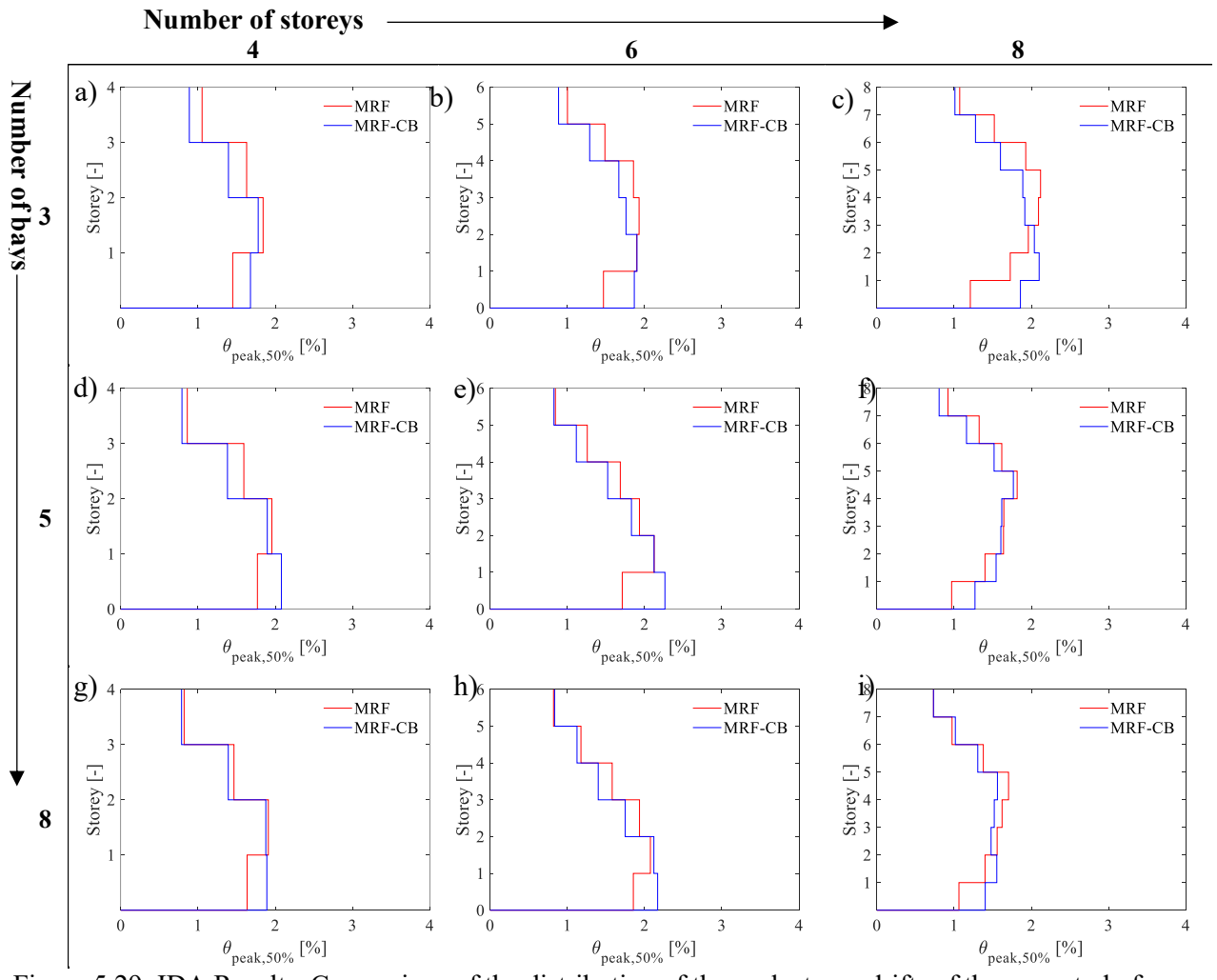

Figure 5.29: IDA Results: Comparison of the distribution of the peak storey drifts of the case-study frames for MCE: (a) 3-4; (b) 3-6; (c) 3-8; (d) 5-4; (e) 5-6; (f) 5-8; (g) 8-4; (h) 8-6; (i) 8-8.

Figure 5.30 and Figure 5.31 show the height-wise residual interstorey drift distributions synthesized by the median value ($\theta_{res,50\%}$) for all the structures with and without the SC-CBs at the DBE and the MCE, respectively. The distribution patterns of the $\theta_{res,50\%}$ for the MRFs with conventional CBs, are similar to the height-wise peak interstorey drift distributions previously shown. In fact, the 4- and 6-storey conventional MRFs experience the maximum values of residual interstorey drifts at the first storeys,

with a distribution pattern proportionally decreasing with the height. Conversely, for 8-storey frames, the highest values of residual interstorey drifts occur at the intermediate storeys. Differently, for the structures with SC-CBs, a significant reduction of the residual interstorey drifts in the lower storeys can be observed. In comparison, its effectiveness reduces and tends to disappear at higher storeys. For example, for the 5-bay 6-storey frames, the value of $\theta_{res,50\%}$ is reduced by 83% (*i.e.,* from 0.71% to 0.12%) at the first storey by 55% (*i.e.,* from 0.55% to 0.25%) at the third storey and by 41% (*i.e.,* from 0.083% to 0.049%) at the sixth storey. Similar trends can be seen in the other case studies.

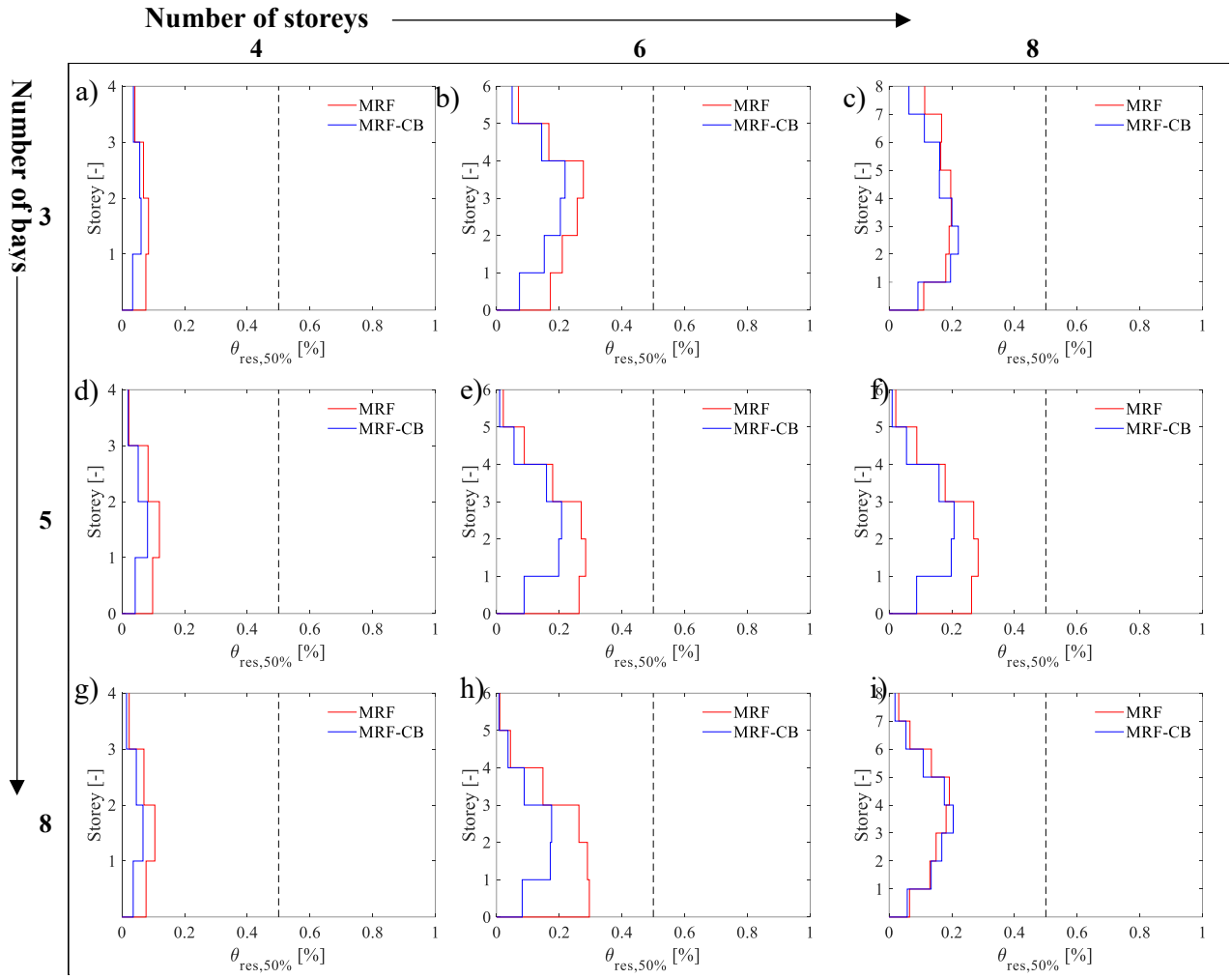

Figure 5.30: IDA Results: Comparison of the distribution of the residual storey drifts in terms of median values (50% fractile) among all ground motions of the case-study frames for DBE: (a) 3-4; (b) 3-6; (c) 3-8; (d) 5-4; (e) 5-6; (f) 5-8; (g) 8-4; (h) 8-6; (i) 8-8

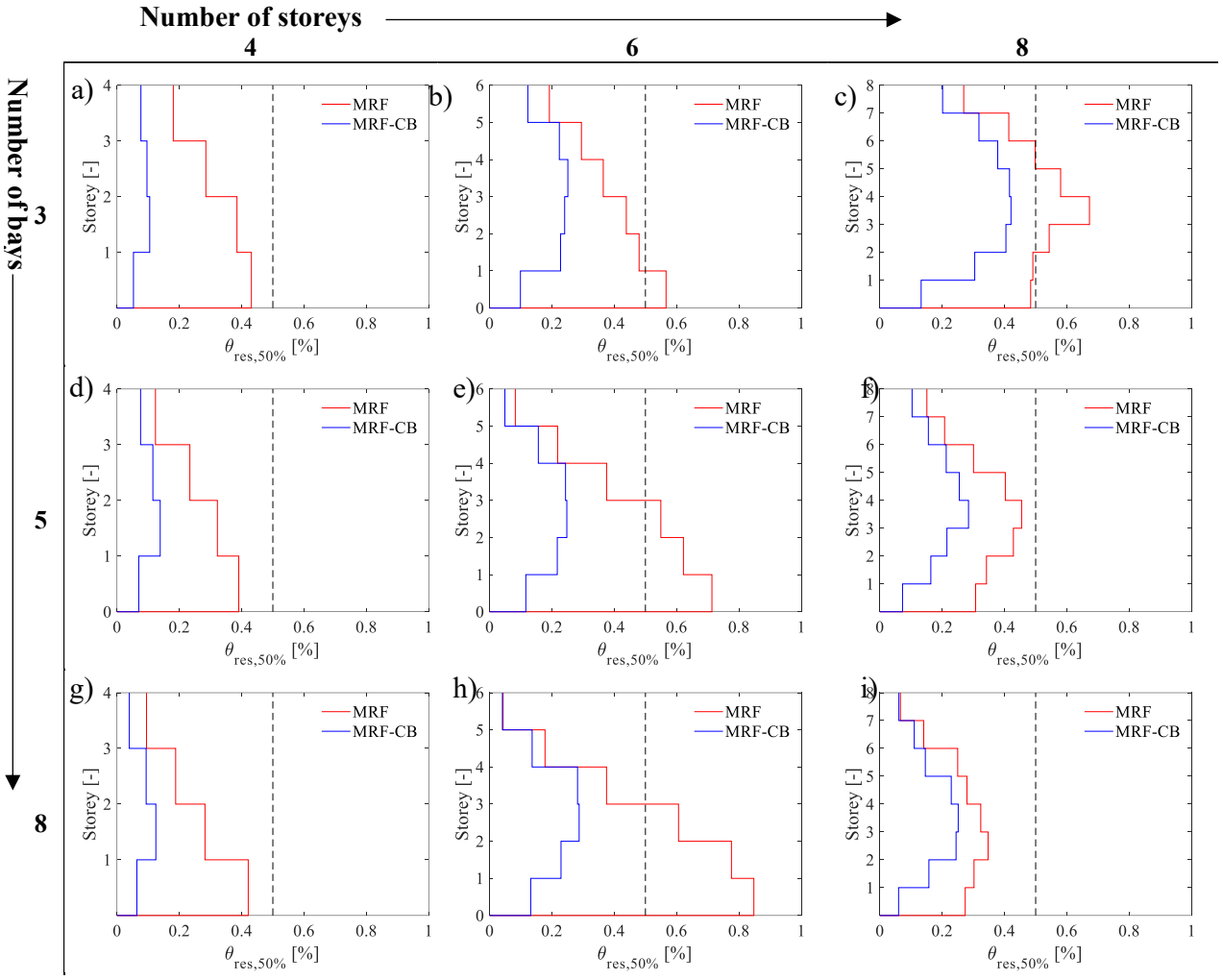

Figure 5.31: IDA Results: Comparison of the distribution of the residual storey drifts in terms of median values (50% fractile) among all ground motions of the case-study frames for MCE: (a) 3-4; (b) 3-6; (c) 3-8; (d) 5-4; (e) 5-6; (f) 5-8; (g) 8-4; (h) 8-6; (i) 8-8

5.8.2 Fragility Curves

Based on the IDA results, fragility curves are derived to quantify the probability of the seismic demand exceeding the associated capacity threshold of 0.5% [9]. The spectral acceleration corresponding to the first vibration period (*i.e.,* $S_a(T_1,\xi)$) is assumed as IM. Global and storey-level residual response parameters (*i.e.,* the maximum residual interstorey drifts and the storey-level residual interstorey drifts) are considered EDPs to investigate the structure's self-centring capability. These values are compared with the associated capacity of 0.5% [9]. Numerical fragility curves are initially derived based on EDPs-IMs pairs obtained by the IDAs and successively fitted by analytical lognormal curves trough least-square minimization. Such fragility curves provide the probability of exceeding the assumed residual interstorey drifts capacity value (*i.e.,* probability of failure P_f) *vs*. the seismic IM values, giving insights into the self-centring capability and the structures' reparability. It is noteworthy that the fragilities provide a probabilistic interpretation of the results and the sensitivity of the seismic response concerning the frame layout. This study derives storey-level (i.e., residual interstorey drifts as EDPs) and global

fragility curves (i.e., maximum residual interstorey drifts among all the storeys as EDPs). The global fragility curves are compared in Figure 5.32 for all the case-studies for the two configurations (*i.e.,* with and without the SC-CBs). The maximum (among all the storeys) residual interstorey drifts ($\theta_{max\text{-}res}$) are used as EDPs. The percentage reductions of the probability of exceeding the limit value (*i.e.,* ΔP_f) are also reported for the two seismic intensities of interest (*i.e.,* DBE and MCE).

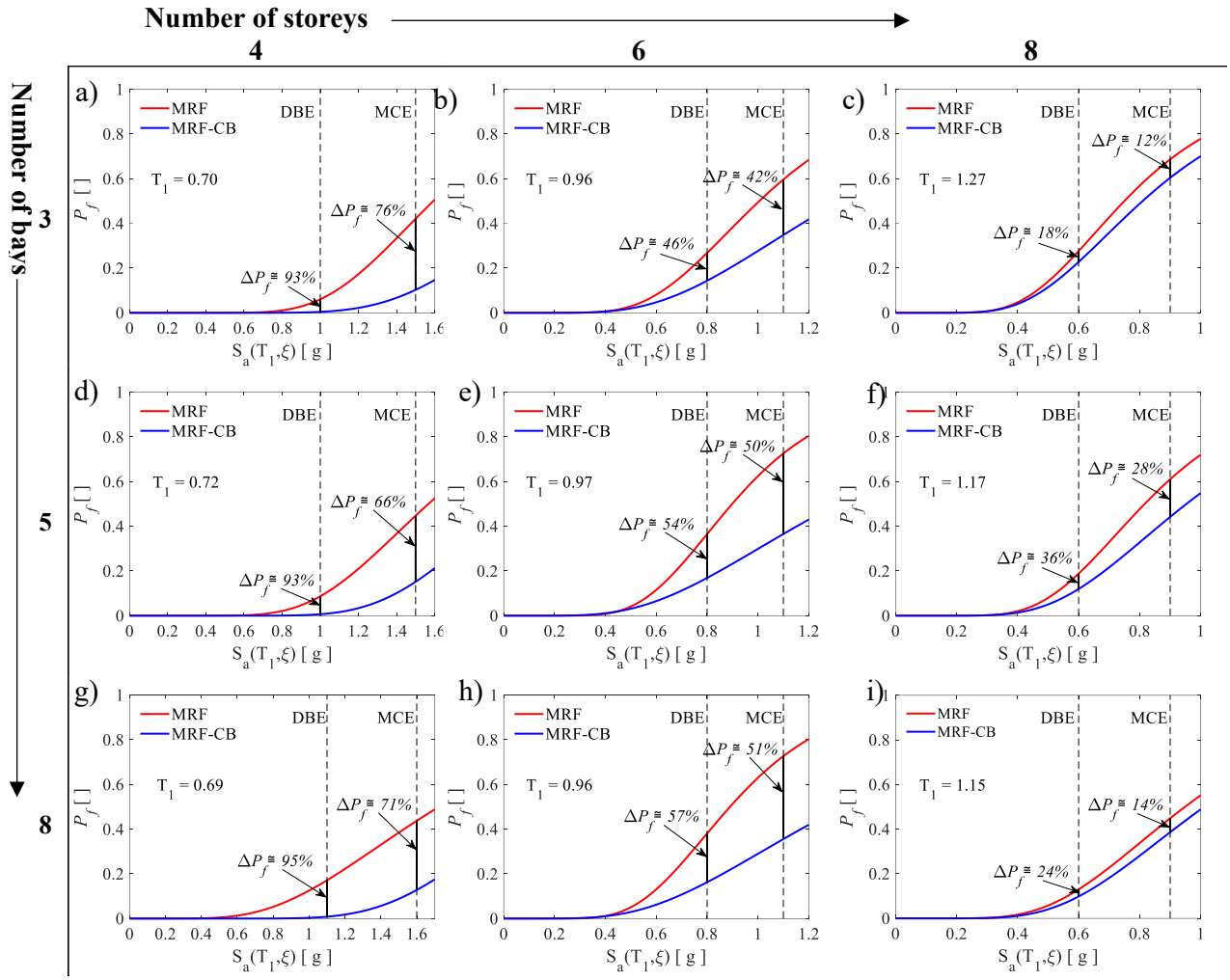

Figure 5.32: Comparison of the global fragility curves for the maximum residual interstorey drifts with respect to the threshold limit of 0.5% for the case study frames: (a) 3-4; (b) 3-6; (c) 3-8; (d) 5-4; (e) 5-6; (f) 5-8; (g) 8-4; (h) 8-6; (i) 8-8.

Figure 5.32 provides, in a probabilistic framework, the results of the IDAs previously shown. A clear correlation between P_f and the increasing number of storeys for both the DBE and the MCE is pointed out. This is evidenced by the percentage reductions ΔP_f reported in Figure 5.32 (a) (b) and (c) of the 3-bays 4-storey, 3-bays 6-storey and 3-bays 8-storey frames, which assume decreasing values at the DBE (*i.e.,* from 93% to 18%) and at the MCE (*i.e.,* from 76% to 12%). Similar behaviour is observed for the 5-bay and 8-bay frames. These results show that the ΔP_f decreases along with the height. On the other hand, it is not possible to observe a significant sensitivity to the variation of the number of bays on the ΔP_f in all the structures in Figure 5.32 (a) (d) and (g) by the ΔP_f of the 3-bays 4-storey, 5-bays 4-storey

and 8-bays 4-storey frames, which experience similar values at the DBE (*i.e.,* from 93% to 95%) and at the MCE (*i.e.,* from 66% to 76%). A similar trend can be seen for the 5-storey and the 8-storey frames. Furthermore, storey-level fragility curves are carried out to evaluate the probability of exceeding the threshold limit of 0.5% at each storey for each case-study. Figure 5.33 compares the fragility curves for each storey of all the case-study frames. The residual interstorey drifts are used as storey-level EDPs. The colour-filled areas represent the interval between the most and the least fragile storeys (*i.e.,* red for the frames with conventional CBs and blue for the frames equipped with the SC-CBs). In Figure 5.33, it is possible to observe a correlation with the height-wise distributions previously shown in probabilistic terms. Figure 5.33 shows that, for all the structures equipped with conventional CBs, P_f is maximum at the 1st storey. The only exceptions are related to the 8-storey frames, where P_f is higher at the intermediate storeys (*i.e.,* 3rd – 4th storey) due to the influence of the higher modes. Conversely, P_f assumes the minimum values at the upper storeys. This behaviour highlights that the higher storeys of the structures experience minor post-elastic deformations due to the technological and design criteria adopted.

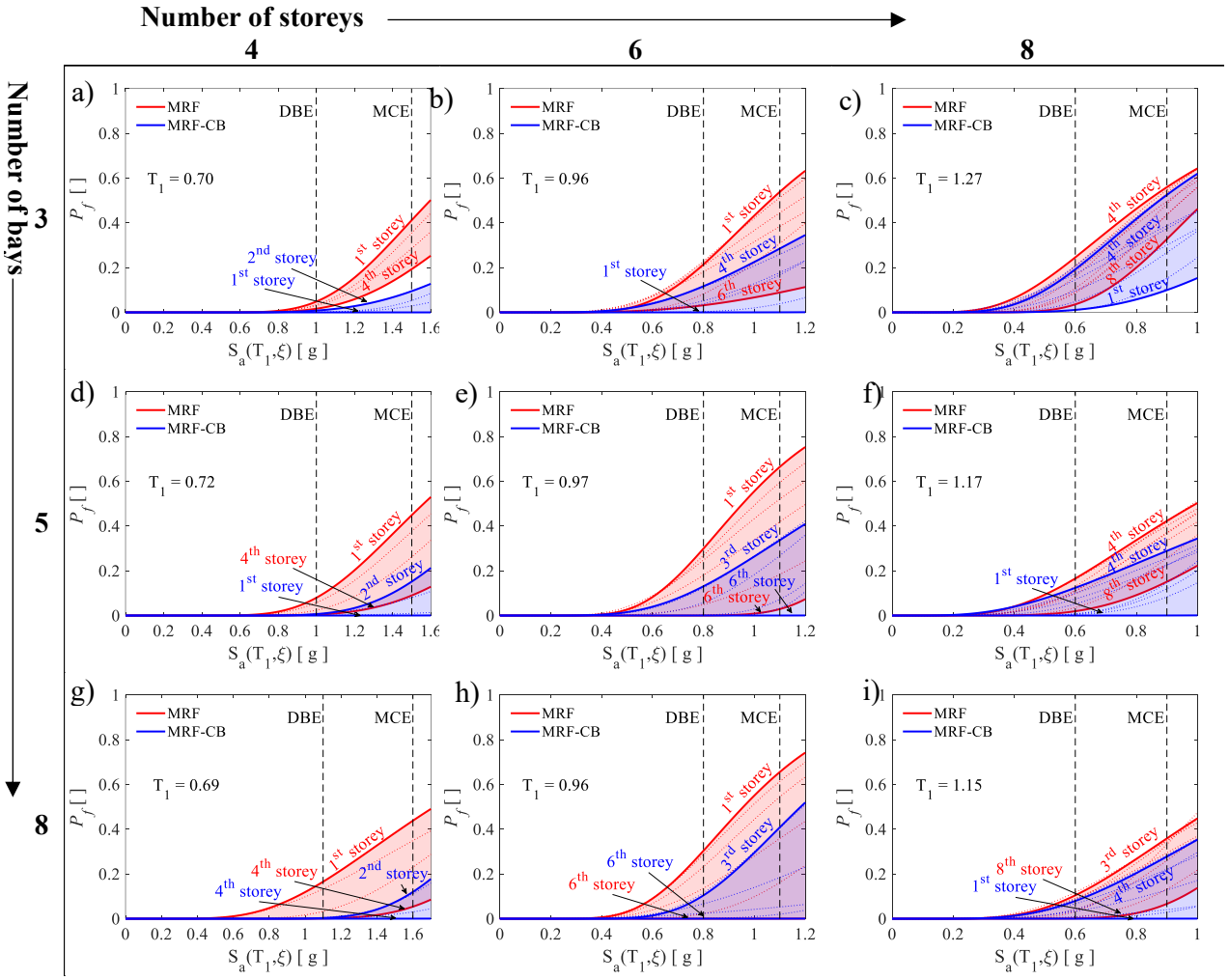

Figure 5.33: Comparison of the storey-level fragility curves for the residual interstorey drifts with respect to the threshold limit of 0.5% for the case study frames: (a) 3-4; (b) 3-6; (c) 3-8; (d) 5-4; (e) 5-6; (f) 5-8; (g) 8-4; (h) 8-6; (i) 8-8.

Regarding the structures equipped with the SC-CBs, the introduction of the proposed connections minimizes the probability of exceeding the 0.5% limit at the 1st storey (*i.e.,* $P_f \cong 0$). In some cases (*i.e.,* 8 bays 4 storey, 5 bays 6 storey and 8 bays 6 storey frames), due to the almost-elastic behaviour of the beams at the last storeys, the P_f of the last storeys assumes similar values to P_f at the 1st storey. Conversely, P_f is maximum at the intermediate storeys. These results demonstrate how the adoption of the SC-CBs provides a significant reduction of P_f at the lower storeys, while this effectiveness decreases along with the height, resulting in a reduction of the self-centring capability.

5.9 Influence of the seismic mass

The present section aims to extend the previous results by investigating the influence of an additional parameter (*i.e.,* the combination of the seismic mass and acceleration) on the self-centring behaviour of MRFs with SC-CBs. Three 5-bay steel MRFs with 4, 6 and 8 storeys are considered case-study structures, and two different values of the seismic mass (*i.e.,* M1 and M2) are used. Figure 5.34 shows the plan and the elevation views of the investigated case-study frames.

The seismic response of conventional MRF (*i.e.,* MRF) and the MRF with SC-CBs (*i.e.,* MRF-CB) are compared by adopting the same methodology already discussed in Section 5.8. Two different seismic masses (*i.e.,* M1 and M2) have been adopted considering different tributary areas due to a different number of bays in the *y*-direction, as represented by the hatching areas (*i.e.,* 3 bays in the *y*-direction for M1 and 5-bays in *y*-direction for M2). The seismic resisting system in the *x*-direction is composed of perimeter MRFs, while the interior part is composed of gravity frames. The geometrical dimensions are the same as in the case-study shown in Section 5.2. The MRFs are designed according to Eurocode 8 [1], considering the seismic input based on the product of the seismic mass (M1 or M2) and the corresponding spectral acceleration at the fundamental period of vibration. Notably, increasing the seismic mass or proportionally increasing the seismic input would generate equivalent results. Hence, despite the analysis being limited to the variation of the seismic mass, equivalent results are expected by varying the seismic input acceleration. Table 35 shows the fundamental periods of vibrations and the Spectral Accelerations corresponding to the DBE ($S_{a,\,DBE}$) and MCE ($S_{a,\,MCE}$) for all the case-study buildings.

Table 35. Fundamental periods of vibrations and S_a (T_1) corresponding to the DBE and MCE

Case-study	T_1 [sec]	$S_{a,\,DBE}$ [g]	$S_{a,\,MCE}$ [g]
MRF 5-4 (M1 / M2)	0.72 / 0.74	1.00 / 0.97	1.50 / 1.46
MRF 5-6 (M1 / M2)	0.97 / 1.04	0.74 / 0.70	1.12 / 1.05
MRF 5-8 (M1 / M2)	1.17 / 1.28	0.61 / 0.52	0.92 / 0.79

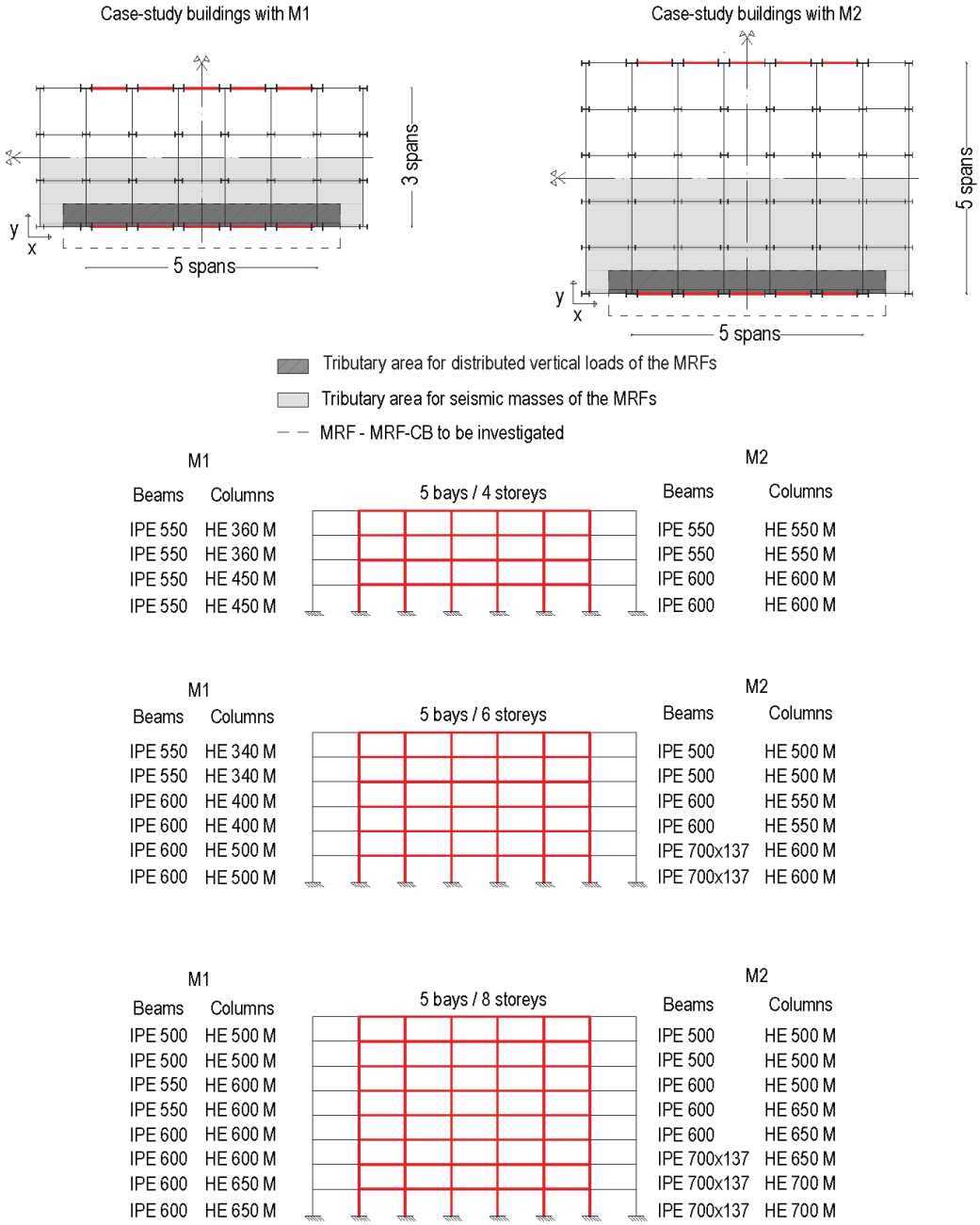

Figure 5.34: Case-study buildings: (a) Plan views; (b) Elevation views.

5.9.1 Incremental Dynamic Analysis

Peak and residual interstorey drifts are used to monitor the seismic performances of the case-studies investigated. The maximum values of these quantities among all the storeys are used as global EDPs (*i.e.,* $\theta_{\text{max-peak}}$ and $\theta_{\text{max-res}}$). The effectiveness of the SC-CBs in reducing the residual interstorey drifts is evaluated by comparing the seismic response of the MRF and the MRF-CB. Figure 5.35 (a) and (b) show the results of the IDAs for the maximum (among all the storeys) peak interstorey drifts ($\theta_{\text{max-peak}}$) for the 6-storeys case-study structures with mass M1 and M2, respectively. Similar results are observed for the other case-studies, which are not reported here for brevity. As expected from the design,

including the requirements for the Frequently Occurred Earthquake (*i.e.,* FOE, Damage Limit State - DLS - according to the European definition), the results for $\theta_{max\text{-}peak}$ for M1 and M2 are similar.

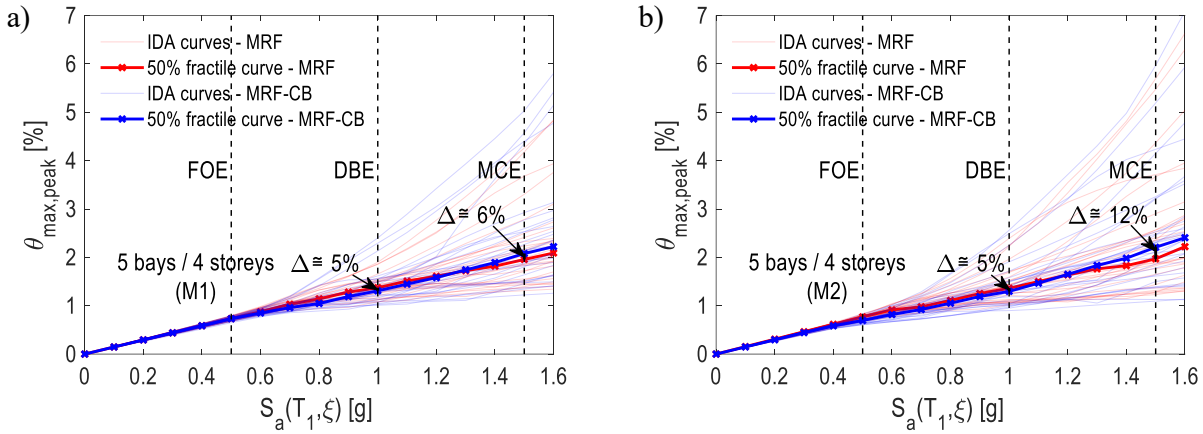

Figure 5.35: IDAs Results. Comparison of the maximum peak interstorey drifts for the case-study frames: (a) 5-4 (M1); (b) 5-4 (M2)

Figure 5.36 shows the results of the IDAs in terms of maximum (among all the storey) residual interstorey drift ($\theta_{max\text{-}res}$) for all the investigated structures. In Figure 5.36, each row refers to a case-study structure with the same number of stories for M1 (left) and M2 (right). Each figure shows IDA curves for all the ground motions for the MRFs (red lines) and the MRF-CBs (blue lines). Additionally, the median value of $\theta_{max\text{-}res}$ among all ground motions (*i.e.,* 50% percentile) is shown for both MRFs and MRF-CBs (bold red and blue lines). The results show that including SC-CBs produces beneficial effects in all cases, allowing a residual drift reduction for both M1 and M2 for all the IM values. Additionally, in all cases, the use of SC-CBs allows for reducing the median values of $\theta_{max\text{-}res}$ below the assumed repairability threshold (*i.e.,* 0.5%) for all the investigated IM values. Conversely, all the conventional MRFs with both M1 and M2 do not satisfy this limit for high IM values. Figure 5.36 shows minor differences in terms of residual drift reduction between the cases with M1 and M2.

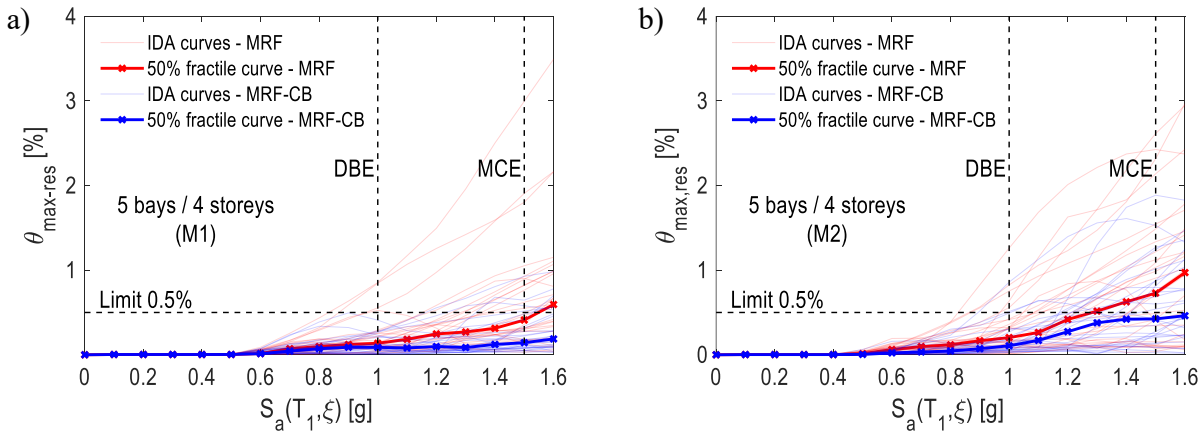

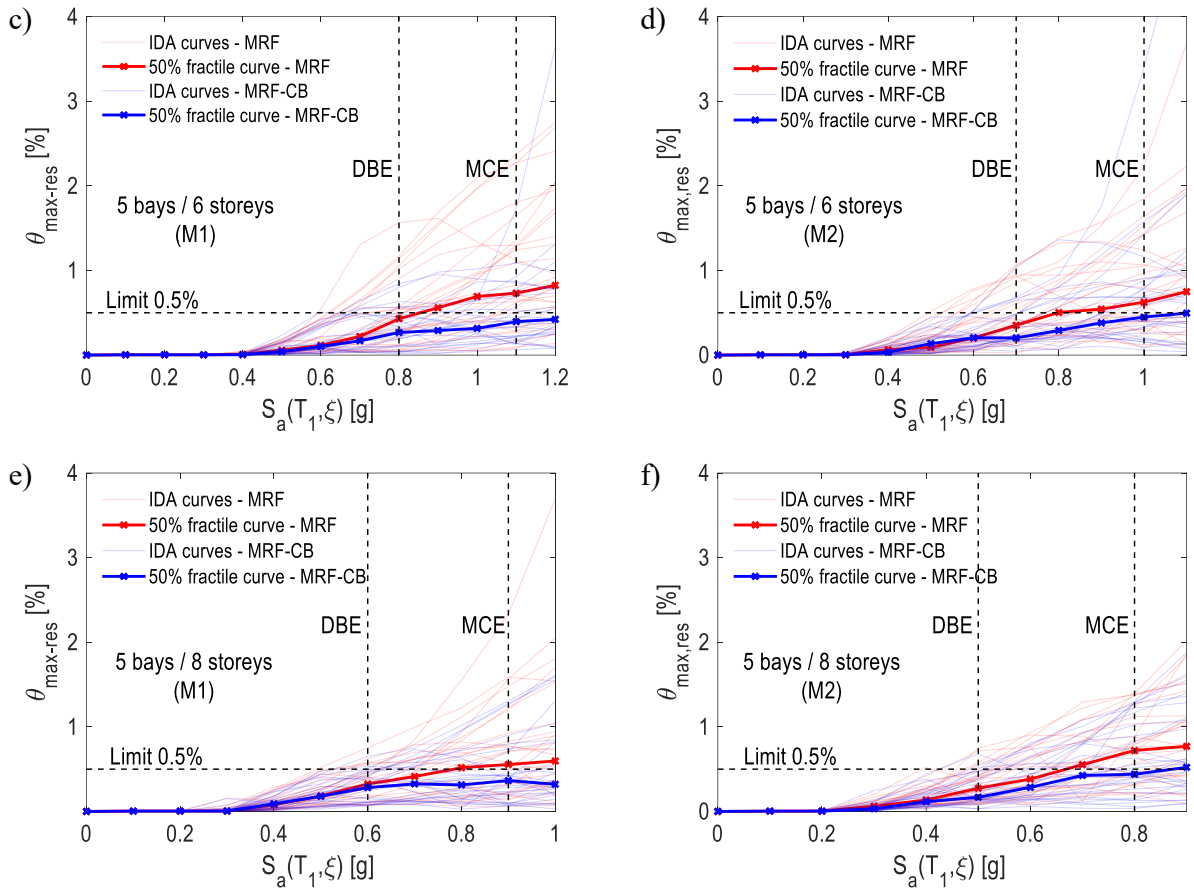

Figure 5.36: IDAs Results. Comparison of the maximum residual interstorey drifts for the case-study frames: (a) 5-4 (M1); (b) 5-4 (M2); (c) 5-6 (M1); (d) 5-6 (M2); (e) 5-8 (M1); (f) 5-8 (M2).

5.9.2 Fragility curves

Fragility curves quantify the probability of the maximum residual interstorey drifts (*i.e.,* $\theta_{max\text{-}res}$) exceeding the associated threshold equal to 0.5% for each IM value (*i.e.,* P_f). Numerical fragility curves are initially derived based on EDPs-IMs pairs obtained through IDAs and successively fitted by analytical lognormal curves through least-square minimisation. The comparison of the fragility curves is represented in Figure 5.37, where each row refers to a case-study structure with the same number of stories for M1 (left) and M2 (right), and the figures show the comparison between the MRFs (red line) and the MRF-CBs (blue line). Additionally, the percentage reduction of the probability of exceeding the limit value (*i.e.,* ΔP_f) is reported for the two seismic intensities of interest (*i.e.,* DBE and MCE). The fragility curves confirm the beneficial effect of the SC-CBs in reducing the residual interstorey drifts for the whole range of IM values of interest, *i.e.,* the MRF-CBs experience lower values of P_f with respect to the MRF for all IM values. It can be observed that the 4-storey case-study with M1 shows the highest beneficial effects (*i.e.,* the highest ΔP_f) of the use of SC-CBs in reducing the residual interstorey drifts.

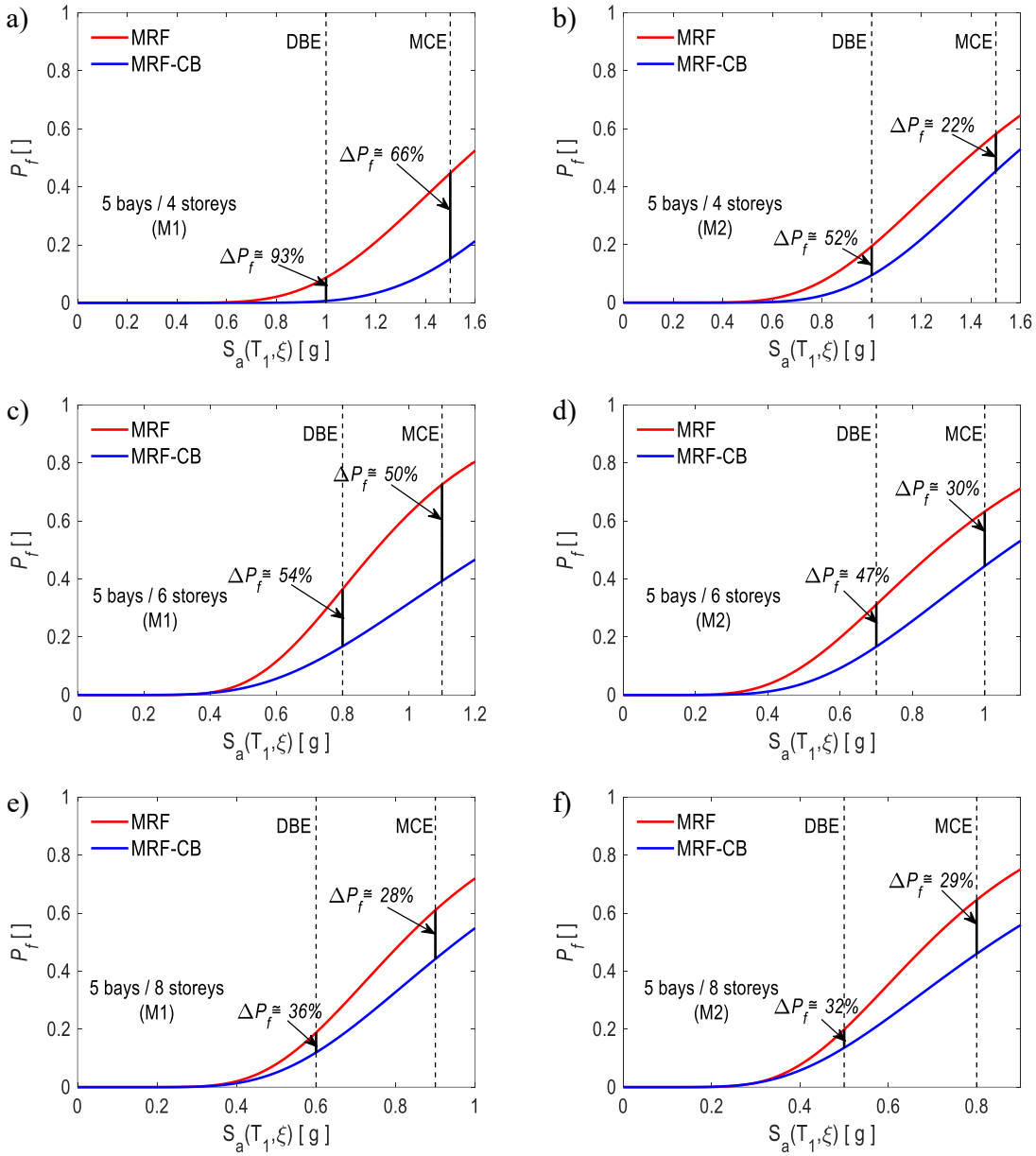

Figure 5.37: Fragility Curves: Comparison of the *Pf* for the case-study frames: (a) 5-4 (M1); (b) 5-4 (M2); (c) 5-6 (M1); (d) 5-6 (M2); (e) 5-8 (M1); (f) 5-8 (M2).

Results show that this difference progressively decreases in the 6- and 8-storey case-studies as observed in Section 5.8. Conversely, it can be observed that the higher mass value, M2, results in a lower, but more uniform and less sensitive from the number of stories, effectiveness of the SC-CBs in reducing the residual interstorey drifts.,

The results show the beneficial effect of the SC-CBs in reducing the residual interstorey drifts for all the investigated case study structures and the whole range of IM values of interest. For the lower mass M1, it can be observed that the effectiveness progressively decreases while increasing the number of stories, as observed in previous studies. Conversely, for the higher mass M2, the results show a lower sensitivity with respect to the number of stories and effectiveness of the SC-CBs in reducing the residual

interstorey drifts. The results herein presented refer to the investigated case-study frames. However, additional research studies are needed to provide a more general understanding of the influence of the investigated parameter on the self-centring capability of steel MRFs with SC-CBs.

5.10 Personal contribution

Chapter 5 represents one of the novelties of the present work and performs a numerical activity on several case-study SC-CBs with the objectives of investigating and comparing the seismic performance of several case-study perimeter steel MRFs equipped with the innovative SC-CB connections and the equivalent conventional, seismically designed, perimeter steel MRFs with full-strength CB connections. Successively, a parametric numerical analysis is performed to investigate two key aspects of the design of the MRFs equipped with the SC-CBs and their influence on the self-centring behaviour.

5.11 References

1 EN 1998-1, Eurocode 8: Design of structures for earthquake resistance – Part 1: General rules, seismic actions and rules for buildings, European Committee for Standardization, Brussels.
2 M. Latour, G. Rizzano, A. Santiago, L. Da Silva, Experimental response of a low-yielding, self-centring, rocking CB joint with friction dampers, Soil Dyn. Earthq. Eng. 116 (2019) 580–592
3 EN 1993-1-8, Eurocode 3: Design of steel structures, Part 1-8: Design of steel structure: General rules and rules for buildings, 2005, European Committee for Standardization, Brussels
4 S. Mazzoni, F. McKenna, M.H. Scott, G.L. Fenves OpenSEES: Open System for earthquake engineering simulation, Pacific Earthquake Engineering Research Centre (PEER), 2009, Univ. of California, Berkley, CA, Available at: http://opensees.berkeley.edu.
5 D. Vamvatsikos, C.A. Cornell, Incremental Dynamic Analysis, Earthq. Eng. Struct. Dyn. 31(3) (2002) 491–514.
6 D'Ayala, D., Meslem, A., Vamvatsikos, D., Porter, K., Rossetto, T., Silva, V. (2015) Guidelines for Analytical Vulnerability Assessment of Low/Mid-Rise Buildings, Vulnerability Global Component Project. DOI 10.13117/GEM.VULN-MOD.TR2014.12
7 O.S. Kwon, A. Elnashai, The effect of material and ground motion uncertainty on the seismic vulnerability curves of RC structure. Eng. Struct. 28(2) (2006) 289–303. DOI: 10.1016/j.engstruct.2005.07.010
8 M. Shinozuka, M.Q. Feng, H-K Kim, S-H Kim, Nonlinear static procedure for fragility curve development, J. Eng. Mech. 126 (12) (2000) 1287–95
9 J. McCormick, H. Aburano, M. Nakashima, Permissible residual deformation levels for building structures considering both safety and human elements, 14th World Conf. Earthq. Eng. 12-17 Oct 2008, Beijing, China.
10 Lignos D, Krawinkler H. Deterioration Modelling of Steel Components in Support of Collapse Prediction of Steel Moment Frames under Earthquake loading, J. Struct. Eng. 2011; **137**: 1291–1302.
11 Krawinkler H, Mohasseb S. Effect of PZ deformations on seismic response. J Constr Steel Res 1987;8:233–50.
12 Charney F, Downs W. Modelling procedures for PZ deformations in moment resisting frames. Connections in Steel Struct. V 2004. ESSC/AISC Workshop, Amsterdam.
13 Foutch DA, Yun S-Y. Modeling of steel moment frames for seismic loads, J. Constr. Steel Res. 2002; 58: 529–564.

14 Flores, F. Charney, D. Lopez-Garcia. The influence of gravity column continuity on the seismic performance of special steel moment frame structures, Journal of Constructional Steel Research, Volume 118, 2016, 217-230
15 Omid Ahmadi, James M. Ricles, Richard Sause, Modeling and seismic collapse resistance study of a steel SC-MRF, Soil Dynamics and Earthquake Engineering, Volume 113, 2018, Pages 324-338
16 Iervolino I, Galasso C, Cosenza E. REXEL: Computer aided record selection for code-based seismic structural analysis, B. Earthq. Eng. 2010; **8**: 339–362

Chapter 6 Pseudo-Dynamic Testing, Reparability and Resilience Assessment of a Large-Scale steel structure equipped with SC-CBs

6.1 Introduction

The previous chapters contributed to define design strategies for the proposed SC-CB, demonstrating the feasibility of the technology. However, further research is needed to assess the influence of the SC-CBs on the experimental response of a real- or large-scale case-study structure equipped with this CB joint typology. In addition, while many tests of isolated innovative CBs are currently available [*e.g.,* 1-5], the influence of the local behaviour of such connections on the overall response of MRFs under seismic loading conditions has rarely been experimentally analysed [*e.g.,* 6-7] leaving some uncertainties on the range of validity of the modelling approaches commonly adopted for numerical simulations, because of the limited availability of full- or large-scale experimental data. These considerations motivated the research activity illustrated in this Chapter, whose main objectives are: *i)* to experimentally assess the influence of the introduction of the SC-CBs on the overall structural performance of a large-scale steel structure; *ii)* to collect data for modelling validation.

In this framework, an experimental campaign was conducted at the STRENGTH (STRuctural ENGineering Test Hall) Laboratory of the University of Salerno as part of an ongoing experimental program. It consists of Pseudo-Dynamic (PsD) [8-9] on a large-scale one-bay two-storey steel structure equipped with the with Damage-Free Beam-to-Column Joints (DF-BCJs) (*i.e.,* FREEDAM BCJs) and the Damage-Free Self-Centring Column Bases (SC-CB) connections. The test specimen is first described, including a presentation of the preliminary characterisation tests. Then, the experimental program is shown, including the test matrix, the experimental setup and the instrumentations. Preliminary tests are conducted to obtain the modal properties of the test specimen. Then, a sequence of six ground motion records, scaled to several intensities, has been defined and applied. Global and local EDPs have been monitored to investigate the proposed SC-CBs' influence on the tested structure's seismic performance. Results demonstrate the effectiveness of the SC-CBs in limiting the residual drifts on the whole structure below the acceptable drift limits [10-11]. The experimental results are complemented with a detailed FE numerical model developed in OPENSEES [12], and comparisons between experimental and numerical results are presented for all the ground motions, discussing the accuracy and limitations of the modelling strategy.

6.2 Design of the tested structure

6.2.1 Design according to Eurocode 8

The test specimen is a large-scale (*i.e.,* 75%) representation of a prototype structure characterised by two storeys and three bays in both directions (Figure 6.1). The layout has interstorey heights of 4 m at both storeys, while the bays have a span length of 4 m. The seismic-resistant part comprises four MRFs in both directions (*i.e.,* red), while the internal part comprises gravity frames (*i.e.,* grey). Table 36 reports the indications of the loads and the masses of the prototype structure for each MRF. The design values of the loads are the following: *i)* the dead loads are equal to 3.90 kN/m^2 and 3.60 kN/m^2 at the first and at the roof levels, respectively; *ii)* the live loads are equal to 3.00 kN/m^2 and 0.5 kN/m^2 at the first and at the roof levels, respectively. The tributary area for the seismic mass on each MRF corresponds to 1/4 of the total floor area. The weight of the structural members and claddings has been accounted for by

increasing the masses by about 10%. In particular, the masses applied on each frame equal 19 tons and 14.2 tons at the first and second levels, respectively.

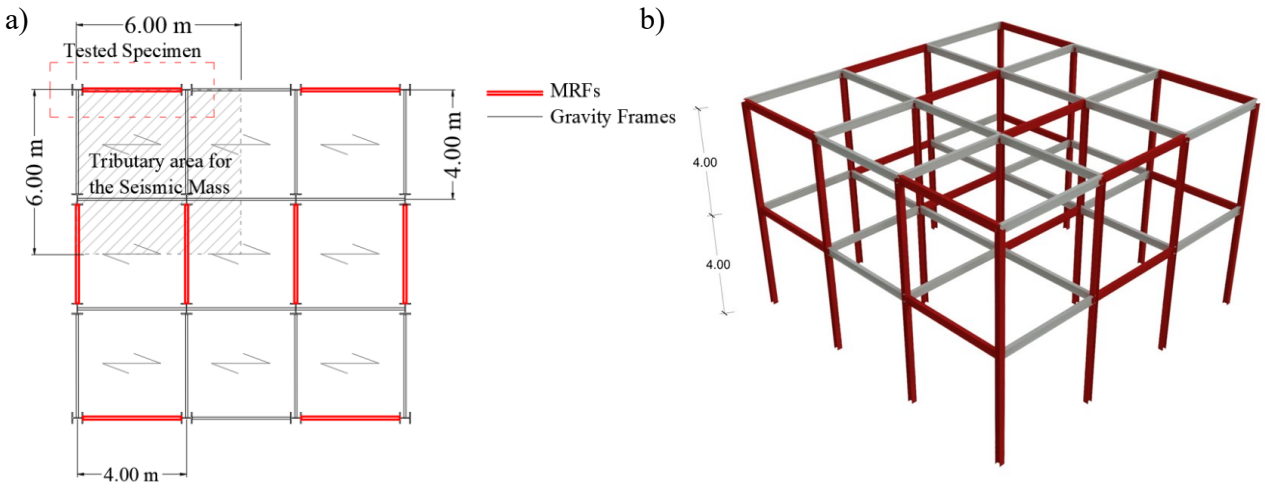

Figure 6.1. Reference prototype structure: a) Plan view and b) 3D view.

Table 36. Loads and masses of the reference structure.

Level [-]	*Gk* [kN/m^2]	*qk* [kN/m^2]	Mass [tons]
First Level	3.90	3.60	19.00
Second Level	3.00	0.50	14.20

***Note:** these values are referred to each MRF

The floor system (Figure 6.2) is formed by a HI BOND A55/P600 steel-concrete composite floor (*i.e.,* total height equal to 100 mm) and five equally spaced IPE 140 and HE 140B secondary beams, which are connected to the concrete slab with shear studs, while UPN 120 are used as in-plane bracings. Figure 6.3 shows the plan and the elevation views of the tested specimen. The seismic resisting system consists of two longitudinal MRFs (*i.e.,* the same MRFs belonging to the reference structure) and two transversal bracings to prevent undesired accidental torsional effects. The layout has interstorey heights of 2.40 m at both storeys, while the longitudinal and the transversal bays have span lengths equal to 4 m and 2 m.

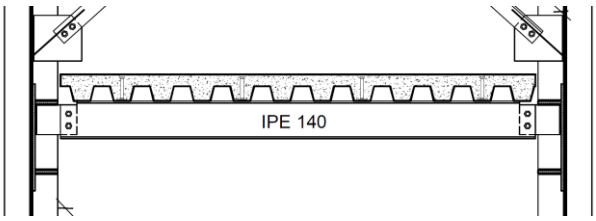

Figure 6.2. Tested structure: detail of the connection between the deck and the secondary beams

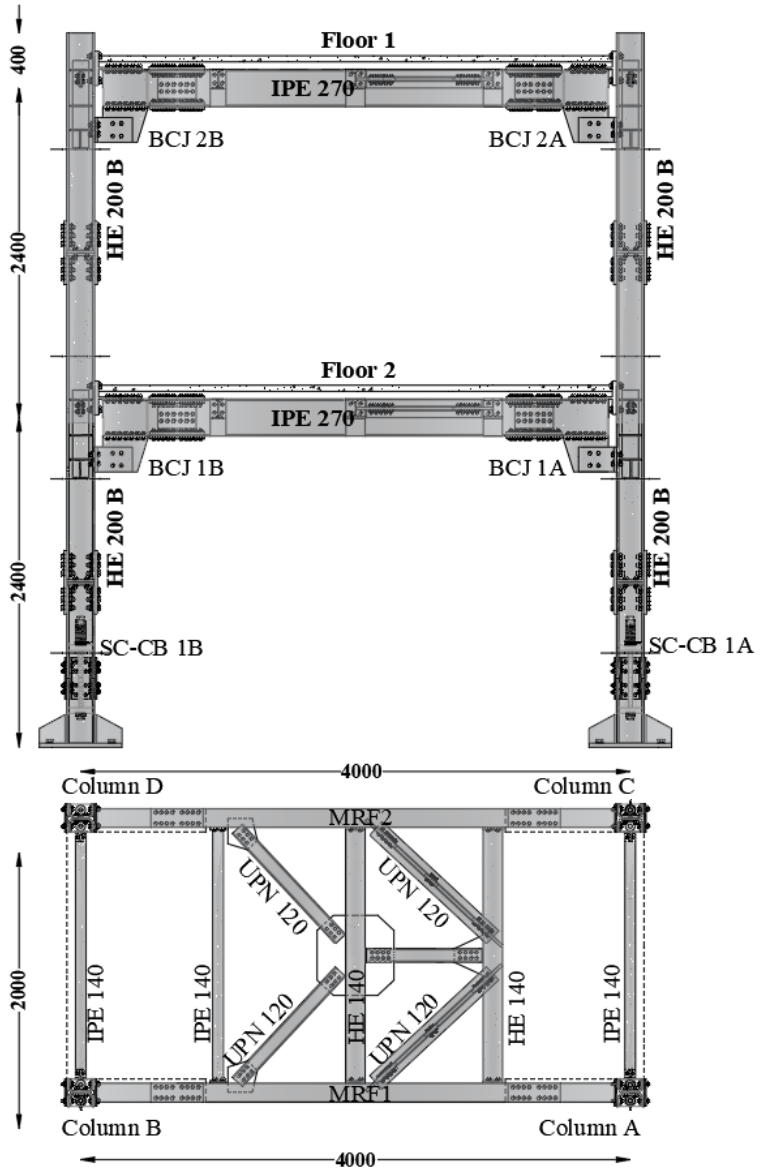

Figure 6.3. Tested structure: Plan and elevation view.

The design is carried out following Eurocode 8 [13] and the Theory of Plastic Mechanism Control (TPCM) [14]. The design earthquake at the Ultimate Limit State (*i.e.,* ULS: probability of exceedance of 10% in 50 years) is defined considering the Type 1 elastic response spectrum with a PGA equal to 0.35g and soil type B. The behaviour factor is evaluated according to Eurocode 8 [13] requirements for MRFs in DCH and hence assumed as q = 6. The interstorey drift limit for the Damage Limit State (*i.e.,* DLS: probability of exceedance of 10% in 10 years) is assumed to be 1% [13] for non-structural elements fixed in a way such as not to interfere with structural deformations. Figure 6.4 shows a picture of the tested specimen before testing.

Figure 6.4. Tested structure.

The two longitudinal MRFs are equipped with the FREEDAM BCJs and the SC-CB connections (Figure 6.5-Figure 6.6-Figure 6.7), whose main features and structural properties are detailed in the subsequent sections. It is worth highlighting that the design process has been performed on the hypothesis of full-strength BCJs without accounting for the characteristics of the joints with which the structure has been equipped for the pseudo-dynamic tests. The slab (Figure 6.8) is disconnected from the nodal region by leaving an appropriate gap between the concrete slab and the columns by adopting details consistent with the Eurocode 8 [13] provisions. However, it acts as a rigid diaphragm, distributing the forces to the frames equally.

a) b)

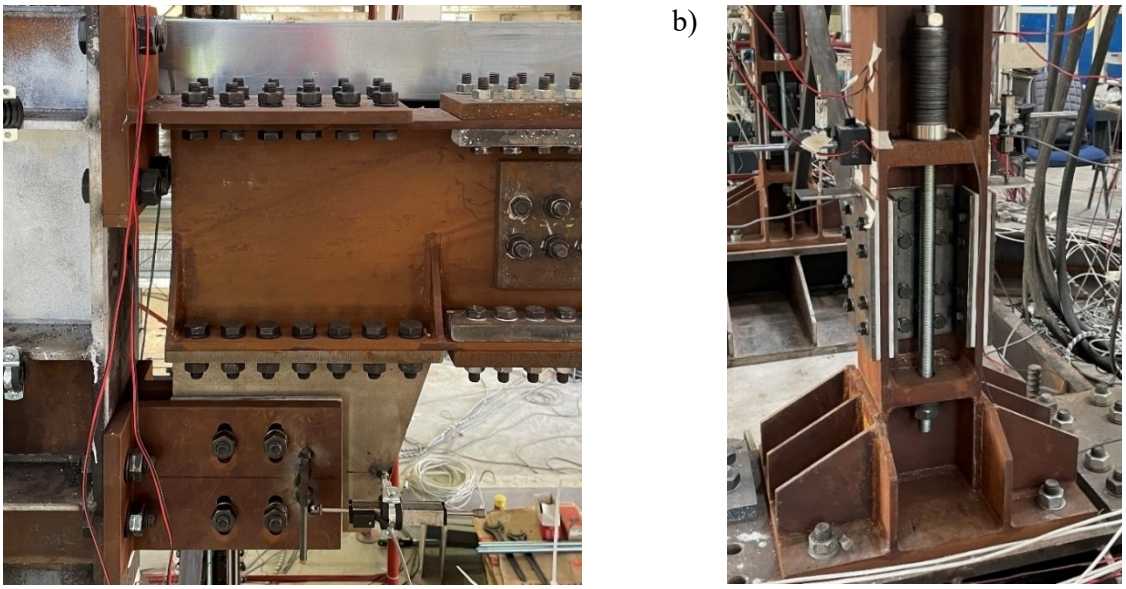

Figure 6.5. Tested structure: a) FREEDAM BCJ and b) SC-CB connection.

Figure 6.6. Assembly phases of the SC-CB connections

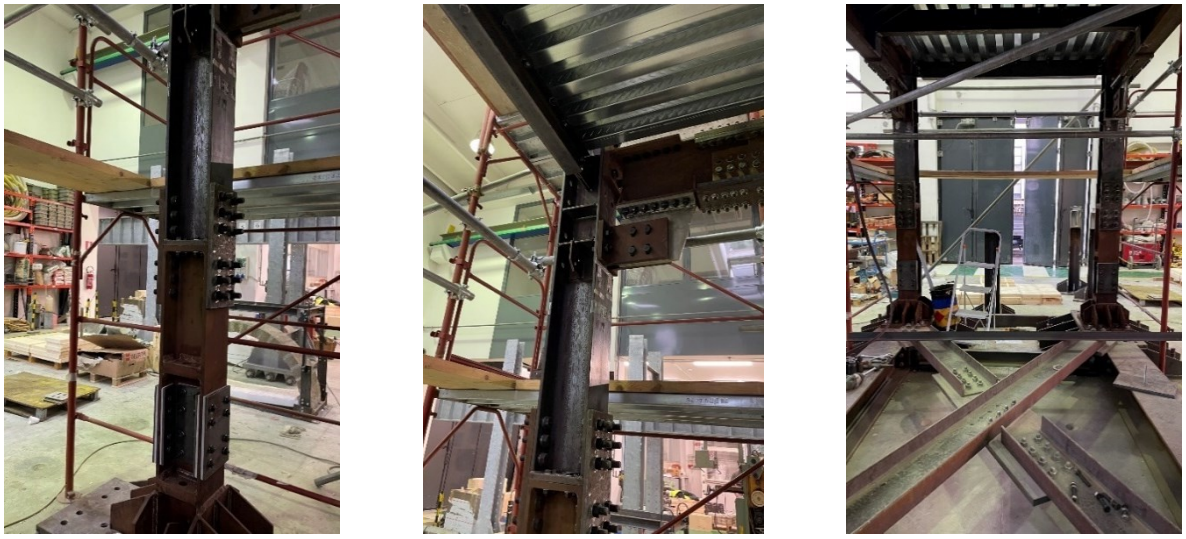

Figure 6.7. Assembly phases of the BCJs and of the structure

Figure 6.8. Details of the gap between the slab and the column

6.2.2 Design according to the TPMC

The Theory of Plastic Mechanism Control (TPMC) by Montuori *et al.* [14] has been developed to ensure the design of structures failing according to a collapse mechanism of global type. This theory aims to prevent undesired failure modes (*i.e.* partial mechanisms and soft-storey mechanisms) and, at the same time, to lead to the optimization of the energy dissipation capacity of the structures, which is achieved when a collapse mechanism of global type is developed since it is characterized by the activation of the dissipative fuses at the beam ends and the first-storey CBs, compatibly with the local ductility supply.

This approach is based on the kinematic theorem of plastic collapse extended to the mechanism equilibrium curve, considering the assumptions of a rigid-plastic structure behaviour and non-negligible consequences of the second-order effects. The design condition imposes that the mechanism equilibrium curve corresponding to the global mechanism must be located below those corresponding to all the undesired mechanisms up to a top sway displacement level compatible with the local ductility supply of dissipative zones. Structures can fail according to three possible mechanisms (Figure 6.9). As already reported, the global mechanism is the best solution; it can be considered a particular case of type-2 mechanism extended to all the storeys.

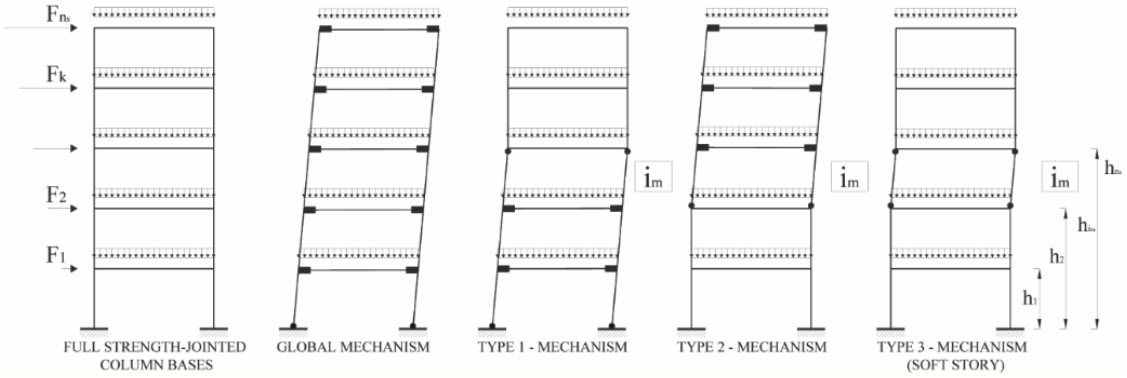

Figure 6.9. Collapse mechanism of full-strength-jointed MRFs.

For each collapse mechanism, the equilibrium curve can be derived by equating the external forces' work to the internal work due to the plastic hinges involved in the collapse mechanism, also evaluating the external second-order work due to the vertical loads. For the global mechanism, the work of external forces due to a virtual rotation $d\vartheta$ of the plastic hinges of the column, starting from a deformed configuration (Figure 6.10) characterized by a rotation ϑ is:

$$W_e = \alpha \sum_{k=1}^{n_s} F_k(h_k \cdot d\vartheta) + \frac{\delta}{h_{ns}} \sum_{k=1}^{n_s} V_k(h_k \cdot d\vartheta) \tag{6.1}$$

where α is the multiplier of horizontal forces; F_k and h_k are, respectively, the seismic force applied to the *k-th* storey height with respect to the foundation level; h_{ns} is the value of h_k at the top storey; δ is the maximum horizontal displacement at the top of the structure; V_k is the total vertical load acting on the *k-th* storey.

The first term of the equation represents the external work due to the seismic actions, while the second term is the work of the second-order effects. The vector of the vertical virtual displacement is:

$$dv_k = du_k \frac{\delta}{h_{ns}} = \frac{\delta}{h_{ns}} h_k \cdot d\vartheta \tag{6.2}$$

where dv_k represents the virtual vertical displacement at the *k-th* floor.

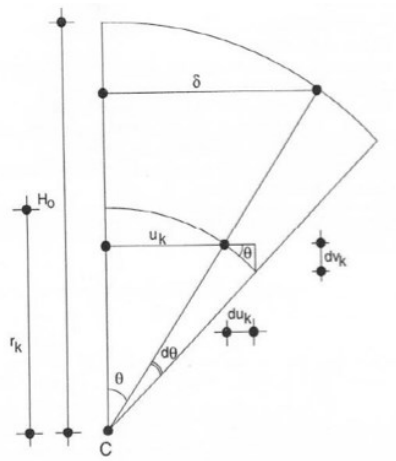

Figure 6.10. Rigid rotation

The internal work due to a virtual rotation $d\vartheta$ of column plastic hinges is:

$$W_i = \left(\sum_{i=1}^{n_s} M_{c,i1} + 2 \sum_{k=1}^{n_s} \sum_{j=1}^{n_b} M_{b,jk} \right) \cdot d\vartheta \tag{6.3}$$

where $M_{c,\,ik}$ is the reduced plastic moment of the *i-th* column of the *k-th* storey reduced due to the contemporary action of the axial force (in the case under examination k = 1), while n_c, n_b, n_s are, respectively, the number of columns, beams and storeys.

By equating the internal work to the external one, the following relation is obtained:

$$W_e = W_i \tag{6.4}$$

$$\alpha \sum_{k=1}^{n_s} F_k (h_k \cdot d\vartheta) + \frac{\delta}{h_{ns}} \sum_{k=1}^{n_s} V_k (h_k \cdot d\vartheta) = \left(\sum_{i=1}^{n_s} M_{c,i1} + 2 \sum_{k=1}^{n_s} \sum_{j=1}^{n_b} M_{b,jk} \right) \cdot d\vartheta \tag{6.5}$$

$$\alpha = \frac{\sum_{i=1}^{n_s} M_{c,i1} + 2 \sum_{k=1}^{n_s} \sum_{j=1}^{n_b} M_{b,jk}}{\sum_{k=1}^{n_s} F_k h_k} - \frac{1}{h_{ns}} \frac{\sum_{k=1}^{n_s} V_k h_k}{\sum_{k=1}^{n_s} F_k h_k} \delta \tag{6.6}$$

The equilibrium curve of the mechanism is a straight line, and it can be written as:

$$\alpha = \alpha_0 - \gamma\delta \tag{6.7}$$

Where α_0 is the kinematically admissible multiplier of horizontal forces according to first-order rigid-plastic analysis, and γ is the slope of the equilibrium curve of the mechanism. The formulations of α_0 and γ are reported for the different types of collapse mechanisms as follows.

Global mechanism:

$$\alpha_0^{(g)} = \frac{\sum_{i=1}^{n_c} M_{c,i1} + 2\sum_{k=1}^{n_s}\sum_{j=1}^{n_b} M_{b,jk}}{\sum_{k=1}^{n_s} F_k h_k} \tag{6.8}$$

$$\gamma^{(g)} = \frac{1}{h_{ns}} \frac{\sum_{k=1}^{n_s} V_k h_k}{\sum_{k=1}^{n_s} F_k h_k} \tag{6.9}$$

Type-1 mechanism:

$$\alpha_{im}^{(1)} = \frac{\sum_{i=1}^{n_c} M_{c,i1} + 2\sum_{k=1}^{i_m-1}\sum_{j=1}^{n_b} M_{b,jk} + \sum_{i=1}^{n_c} M_{c,i,im}}{\sum_{k=1}^{i_m} F_k h_k + h_{im}\sum_{k=i_m+1}^{n_s} F_k} \tag{6.10}$$

$$\gamma_{im}^{(1)} = \frac{1}{h_{im}} \frac{\sum_{k=1}^{i_m} V_k h_k + h_{im}\sum_{k=i_m+1}^{n_s} F_k}{\sum_{k=1}^{i_m} F_k h_k + h_{im}\sum_{k=i_m+1}^{n_s} F_k} \tag{6.11}$$

Type-2 mechanism:

$$\alpha_{im}^{(2)} = \frac{\sum_{i=1}^{n_c} M_{c,i,im} + 2\sum_{k=i_m}^{n_s}\sum_{j=1}^{n_b} M_{b,jk}}{\sum_{k=i_m}^{n_s} F_k\,(h_k - h_{im-1})} \tag{6.12}$$

$$\gamma_{im}^{(2)} = \frac{1}{h_{ns} - h_{im-1}} \frac{\sum_{k=i_m}^{n_s} V_k\,(h_k - h_{im-1})}{\sum_{k=i_m}^{n_s} F_k\,(h_k - h_{im-1})} \tag{6.13}$$

Type-3 mechanism:

$$\alpha_1^{(3)} = \frac{2\sum_{i=1}^{n_c} M_{c,i1}}{h_1 \sum_{k=1}^{n_s} F_k} \quad for\ i = 1 \tag{6.14}$$

$$\alpha_{im}^{(3)} = \frac{2\sum_{i=1}^{n_c} M_{c,i,im}}{(h_{im} - h_{im-1})\sum_{k=i_m}^{n_s} F_k} \quad for\ i > 1 \tag{6.15}$$

$$\gamma_{im}^{(3)} = \frac{1}{h_{im} - h_{im-1}} \frac{\sum_{k=i_m}^{n_s} V_k}{\sum_{k=i_m}^{n_s} F_k} \tag{6.16}$$

In the case of the global mechanism, the equilibrium curve attains its minimum slope. Therefore, according to the kinematic theorem of plastic collapse extended to the concept of the equilibrium curve of the mechanism, the design condition that must be satisfied to avoid undesired collapse mechanisms requires that the equilibrium curve corresponding to the global mechanism is located below those corresponding to the undesired mechanisms, up to a maximum top displacement δ_u compatible with the local ductility resources of the structure. The equilibrium curve of the global mechanism is:

$$\alpha_0^{(g)} - \gamma^{(g)}\delta_u \leq \alpha_{0.i_m}^{(t)} - \gamma_{i_m}^{(t)}\delta_u \qquad i_m = 1,2,3,\dots,n_s \quad t = 1,2,3 \tag{6.17}$$

$\alpha_{0.i_m}^{(t)}$ is the kinematically admissible multiplier of horizontal forces evaluated according to the first-order rigid-plastic analysis, $\gamma_{i_m}^{(t)}$ is the slope of the equilibrium curve of the mechanism (Figure 6.11), accounting for the second-order effects, i_m and t are respectively the mechanism index and the mechanism typology code. Similarly, $\alpha_0^{(g)}$ and $\gamma^{(g)}$ refer to the global mechanism.

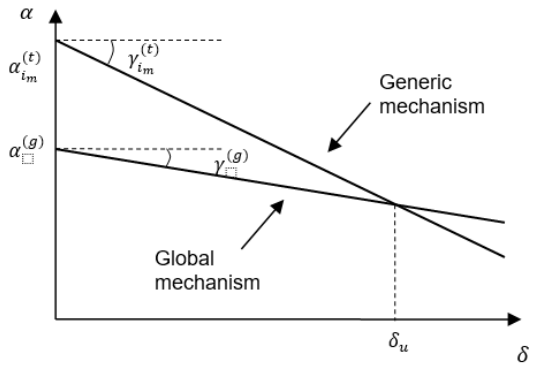

Figure 6.11. Design condition for the failure mode control

The design, according to the TPMC [14], is based on the following steps: *i)* selection of a design top sway displacement compatible with the ductility supply; *ii)* definition of the slopes of mechanism equilibrium curves with the equations previously shown and of the $\gamma_i^{(g)}$ provided as minimum among the $\gamma_{im}^{(t)}$ values; *iii)* design of the first storey columns. For the test structure, assuming $\vartheta = 0.045\,rad$, since $h_{ns} = 4.80\,m$, it results: $\delta_u = 0.216\,m$. The previous formulations have been applied to assess the slopes of the equilibrium curves both for a force distribution according to the first vibration mode (Table 37) and to the masses (Table 38):

Table 37. Slopes of the equilibrium curves (first vibration mode)

	γ_{im} *(1/cm)*		
i_m	Mechanism 1	Mechanism 2	Mechanism 3
2	0.122	0.195	0.195
1	0.275	**0.122**	0.275

Table 38. Slopes of the equilibrium curves (masses)

	γ_{im} *(1/cm)*		
i_m	Mechanism 1	Mechanism 2	Mechanism 3
2	0.137	0.273	0.273
1	0.275	**0.137**	0.275

Considering that the beams have been previously designed (*i.e.,* IPE270 beams), it is possible to design the first-storey columns. The sum of the columns' plastic bending moments reduced due to the simultaneous action of the axial stress required at the first-storey to prevent undesired collapse mechanisms is obtained with the following formulation:

$$\sum_{i=1}^{n_c} M_{c,i1} \geq \frac{2\sum_{k=1}^{n_s}\sum_{j=1}^{n_b} M_{b,jk} + \left(\gamma_1^{(3)} - \gamma^{(g)}\right)\delta_u \sum_{k=1}^{n_s} F_k h_k}{2\dfrac{\sum_{k=1}^{n_s} F_k h_k}{h_1 \sum_{k=1}^{n_s} F_k} - 1} \tag{6.18}$$

This relationship is obtained from the design condition with $i_m = 1$ and $t = 1$ or $t = 3$ because for $i_m = 1$ type 1 and type 3 mechanisms are equal.

$$\alpha_0^{(g)} - \gamma^{(g)}\delta_u \leq \alpha_{im}^{(t)} - \gamma^{(t)}\delta_u \tag{6.19}$$

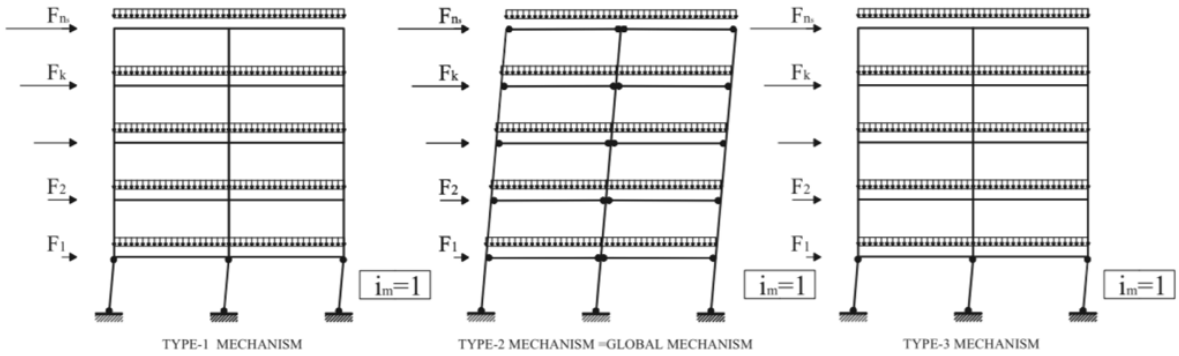

Figure 6.12. Collapse mechanism for im=1

$$\sum_{i=1}^{n_c} M_{c,i1,1st\ vibration\ mode} = 339.37\ kNm \tag{6.20}$$

$$\sum_{i=1}^{n_c} M_{c,i1,masses} = 396.01\ kNm \tag{6.21}$$

Consequently, it is possible to assess the axial acting in the columns at collapse state, *i.e.* when a collapse mechanism of global type is completely developed:

$$\sum_{i=1}^{n_c} N_{c,i,1st\ vibration\ mode} = 237.82\ kN \tag{6.22}$$

$$\sum_{i=1}^{n_c} N_{c,i,masses} = 237.82\ kN \tag{6.23}$$

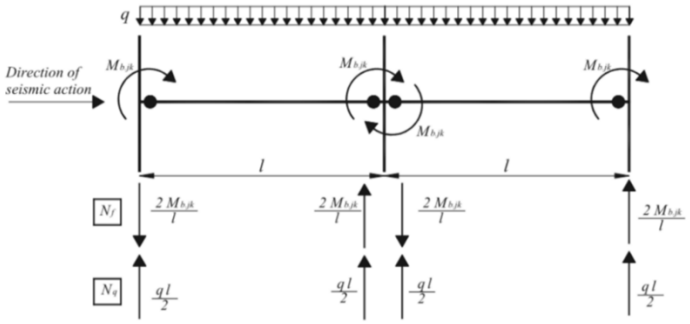

Figure 6.13. Loads transmitted by the beams to the columns at collapse state.

The sum of the plastic moments required on the first floor is distributed between the columns proportionally to the axial force. Therefore, it is possible to design the different sections of the columns (Table 39).

Table 39. Design of the columns' sections

N_{tot} (kN)	$M_{req,c,1st\ vibration\ mode}$ (kNm)	$W_{pl,eq}$ (cm^3)	Profile	$M_{pl,column}$ (kNm)
118.91	$\frac{N_{c,i}}{\sum_{i=1}^{n_c} N_{c,i}} \sum_{i=1}^{n_c} M_{c,i1} = 169.68$	$\frac{M}{f_{yk}}$	HE200B	228.10
N_{tot} (kN)	***$M_{req,c,masses}$ (kNm)***	***$W_{pl,eq}$ (cm^3)***	*Profile*	***$M_{pl,column}$ (kNm)***
118.91	$\frac{N_{c,i}}{\sum_{i=1}^{n_c} N_{c,i}} \sum_{i=1}^{n_c} M_{c,i1} = 198.00$	$\frac{M}{f_{yk}}$	HE200B	228.10

Considering that HE200B profiles have been chosen for the column, it is possible to assess the sum of the plastic bending moments at the column bases.

$$\sum_{i=1}^{n_c} M^*_{c,i1} = 2 \cdot 228.10\ kNm = 456.21\ kNm \tag{6.24}$$

The equilibrium curve of the mechanism can be calculated using this last value, which accounts for the right sections. Therefore, it is possible to calculate:

$$\alpha^{(g)}_{1st\ vibration\ mode} = 295.36 \tag{6.25}$$

$$\alpha^{(g)}_{masses} = 330.84 \tag{6.26}$$

Type-1 mechanism:

$$\sum_{i=1}^{n_c} M^{(1)}{}_{c,i,im} \geq \left(\alpha^{(g)} + \gamma^{(1)}_{im}\delta_u\right)\left(\sum_{k=1}^{i_m} F_k h_k + h_{im}\sum_{k=i_m+1}^{n_s} F_k\right) - \sum_{i=1}^{n_c} M^{*}{}_{c,i1} - 2\sum_{k=1}^{i_m-1}\sum_{j=1}^{n_b} M_{b,jk} \tag{6.27}$$

Type-2 mechanism:

$$\sum_{i=1}^{n_c} M^{(2)}{}_{c,i,im} \geq \left(\alpha^{(g)} + \gamma^{(2)}_{im}\delta_u\right)\sum_{k=i_m}^{n_s} F_k\,(h_{im} - h_{im-1}) - 2\sum_{k=i_m}^{n_s}\sum_{j=1}^{n_b} M_{b,jk} \tag{6.28}$$

Type-3 mechanism:

$$\sum_{i=1}^{n_c} M^{(3)}{}_{c,i,im} \geq \left(\alpha^{(g)} + \gamma^{(3)}_{im}\delta_u\right)\frac{h_{im} - h_{im-1}}{2}\sum_{k=i_m}^{n_s} F_k \tag{6.29}$$

The sum of the plastic bending moments required on each storey to avoid undesired collapse mechanisms can be assessed as the maximum values among the previous formulations, as follows:

$$\sum_{i=1}^{n_c} M_{\,c,i,im} = max\left\{\sum_{i=1}^{n_c} M^{(1)}{}_{c,i,im}\,;\sum_{i=1}^{n_c} M^{(2)}{}_{c,i,im}\,;\sum_{i=1}^{n_c} M^{(3)}{}_{c,i,im}\right\} \tag{6.30}$$

Table 40. Plastic Moment of the columns

	$\sum_{i=1}^{n_c} M_{\,c,i,im,1st\ vibration\ mode}$ (kNm)			
i_m	**Mechanism 1**	**Mechanism 2**	**Mechanism 3**	**Maximum**
2	343.64	86.88	215.26	343.64
1	266.91	456.21	361.56	456.21

	$\sum_{i=1}^{n_c} M_{\,c,i,im,masses}$ (kNm)			
i_m	**Mechanism 1**	**Mechanism 2**	**Mechanism 3**	**Maximum**
2	343.64	1.73	172.69	343.64
1	352.06	456.21	404.13	456.21

Hence, it is possible to check that the HEB200 with S355 steel grade can be selected as columns' profiles (Table 41).

Table 41. Check of the columns

Floor	N_{tot} (kN)	$M_{req,c}$ (kNm)	$W_{pl,eq}$ (cm^3)	Profile	$M_{pl,\,column}$ (kNm)
2	99.91	171.82	484.00	HEB200	228.10
1	118.91	228.10	642.55	HEB200	228.10

6.2.3 Check according to Eurocode 8

Once the structural elements have been designed, the fulfilment of the Eurocode 8 requirements has been checked. The design earthquake is expressed by the type 1 elastic response spectrum of Eurocode 8 with PGA equal to 0,35g and soil type B. (Figure 6.14).

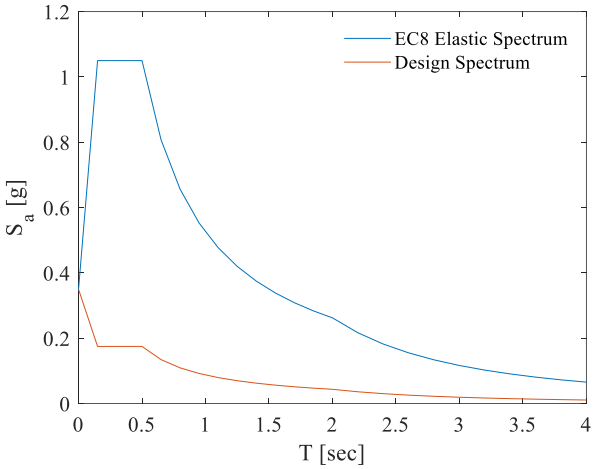

Figure 6.14. Eurocode 8 [13] spectrum

For the horizontal components of the seismic action, the elastic response spectrum $S_e(T)$ is defined by the following expressions:

$$0 \le T \le T_B : S_e(T) = a_g \cdot S \cdot \left[1 + \frac{T}{T_B} \cdot (\eta \cdot 2{,}5 - 1)\right] \tag{6.31}$$

$$T_B \le T \le T_C : S_e(T) = a_g \cdot S \cdot \eta \cdot 2{,}5 \tag{6.32}$$

$$T_C \le T \le T_D : S_e(T) = a_g \cdot S \cdot \eta \cdot 2{,}5 \cdot \left[\frac{T_c}{T}\right] \tag{6.33}$$

$$T_D \le T \le 4s : S_e(T) = a_g \cdot S \cdot \eta \cdot 2{,}5 \cdot \left[\frac{T_c T_D}{T^2}\right] \tag{6.34}$$

where the values of T_B, T_C , T_D and the S soil factor describing the shape of the elastic response spectrum depends upon the ground type. The value of η correction factor may be determined using the following expression:

$$\eta = \sqrt{\frac{10}{(5 + \xi)}} = 1.20 \ge 0{,}55 \tag{6.35}$$

Where ξ is the viscous damping ratio of the structure, expressed as a percentage, in this case, it is adopted the 2%. Furthermore, considering that the structure belongs to a DCH, [13] it is characterized by a behaviour factor equal to:

$$q = 5\frac{\alpha_u}{\alpha_1} = 6 \tag{6.36}$$

where α_1 is the multiplier of the seismic force for which the first element reaches its flexural strength; α_u is the multiplier of the seismic force for which several plastic hinges form to make the structure once labile.

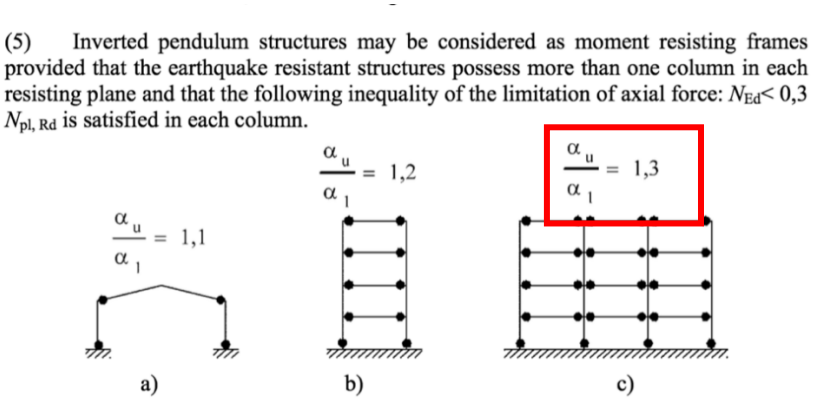

Figure 6.15. Schemes according to Eurocode 8 [13]

The base shear has been assessed through the following expression:

$$F_b = \frac{S_e \cdot m \cdot \lambda \cdot \delta}{q} \tag{6.37}$$

For the horizontal components of the seismic action, the design spectrum, $S_d(T)$, shall be defined by the following expressions:

$$0 \le T \le T_B : S_d(T) = a_g \cdot S \cdot \left[\frac{2}{3} + \frac{T}{T_B} \cdot \left(\frac{2,5}{q} - \frac{2}{3}\right)\right] \tag{6.38}$$

$$T_B \le T \le T_C : S_d(T) = a_g \cdot S \cdot \frac{2,5}{q} \tag{6.39}$$

$$T_C \le T \le T_D : S_d(T) = \begin{cases} a_g \cdot S \cdot \frac{2,5}{q} \cdot \left[\frac{T_c}{T}\right] \\ \ge \beta a_g \end{cases} \tag{6.40}$$

$$T_B \le T \le T_C : S_d(T) = a_g \cdot S \cdot \frac{2,5}{q} \tag{6.41}$$

Where β is the lower bound factor for the horizontal design spectrum. Regarding the accidental torsional effects, they may be accounted for by multiplying the action effects in the individual load-resisting elements resulting from the application of an eccentricity factor, the parameter δ (Figure 6.16):

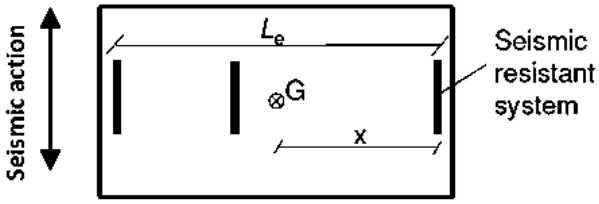

Figure 6.16. Accidental eccentricity [13]

$$\delta = 1 + 0.6\frac{x}{L_e} \tag{6.42}$$

In particular, x is the distance between the frame under examination and the centre of gravity of the masses, while L_e is the distance between the furthest seismic-resistant frames. According to this information, the design base shear F_b for the single MRF is equal to 63 kN. Therefore, it has been distributed along the height according to the first vibration mode and the masses. The distribution in elevation is determined by applying horizontal forces F_i to all storeys (the fundamental mode shape is approximated by horizontal displacements increasing linearly along the height):

$$F_i = F_b \frac{z_i m_i}{\sum z_j m_j} \tag{6.43}$$

where z_i, z_j are the heights of the masses m_i m_j above the level of application of the seismic action.

6.2.3.1 Beams

Once the structural elements have been designed, the fulfilment of the Eurocode 8 [13] checks must be verified. Firstly, the cross-sectional class of dissipative elements, depending on the ductility class, must be verified.

Ductility class	Reference value of behaviour factor q	Required cross-sectional class
DCM	$1{,}5 < q \leq 2$	class 1, 2 or 3
	$2 < q \leq 4$	class 1 or 2
DCH	$q > 4$	class 1

Figure 6.17. Check for cross-sectional class [13]

Considering the ductility class (DCH) and the behaviour factor q=6, the structural elements belong to class 1 (Figure 6.17). For the beams, it is necessary to check the following relationships:

$$\frac{M_{Ed}}{M_{pl,Rd}} \leq 1 \tag{6.44}$$

$$\frac{V_{Ed}}{V_{pl,Rd}} = \frac{V_{Ed,G} + V_{Ed,M}}{V_{pl,Rd}} \leq 0.5 \tag{6.45}$$

Where M_{Ed} and V_{Ed} are the design bending moment and the design shear. $M_{Pl,Rd}$ and V_{Pl} are the design resistances. The analysis is performed through SAP2000 software to define the bending moments and shear actions used for the checks.

6.2.3.2 Columns

The columns have been checked by computing the following relationships for N_{Ed}, M_{Ed} and V_{Ed} [13]:

$$N_{Ed} = N_{Ed,G} + 1{,}1\gamma_{ov}\Omega N_{Ed,E} \tag{6.46}$$
$$M_{Ed} = M_{Ed,G} + 1{,}1\gamma_{ov}\Omega M_{Ed,E} \tag{6.47}$$
$$V_{Ed} = V_{Ed,G} + 1{,}1\gamma_{ov}\Omega V_{Ed,E} \tag{6.48}$$

where the horizontal forces applied to the floors, have been amplified through the adoption of three coefficients: 1.10 to account for the hardening phenomenon; γ_{ov} , an overstrength factor and its value is 1.25 for this case; Ω, which is the minimum value of $\Omega_i = M_{pl,Rd,i}/M_{Ed,i}$ of all the beams in which the dissipative devices are positioned; $M_{Ed,i}$ is the design value of the bending moment of the beam in the seismic conditions, while $M_{pl,Rd,i}$ is the corresponding plastic moment. In this case, this value is 3.20.

Furthermore, the buckling check has been performed as follows:

$$\frac{N_{Ed}}{\frac{\chi_y N_{Rk}}{\gamma_{M1}}} + k_{yy}\frac{M_{y,Ed} + \Delta M_{y,Ed}}{\chi_{LT}\frac{M_{y,Rk}}{\gamma_{M1}}} + k_{yz}\frac{M_{z,Ed} + \Delta M_{z,Ed}}{\frac{M_{z,Rk}}{\gamma_{M1}}} \leq 1 \tag{6.49}$$

$$\frac{N_{Ed}}{\frac{\chi_z N_{Rk}}{\gamma_{M1}}} + k_{zy}\frac{M_{y,Ed} + \Delta M_{y,Ed}}{\chi_{LT}\frac{M_{y,Rk}}{\gamma_{M1}}} + k_{zz}\frac{M_{z,Ed} + \Delta M_{z,Ed}}{\frac{M_{z,Rk}}{\gamma_{M1}}} \leq 1 \tag{6.50}$$

The resistance and buckling checks for columns are performed thanks to previous inequalities, and they are satisfied. It is also verified that the columns are able to provide more than 30% of the flexural resistance of the connected beams.

6.2.3.3 (P- Δ) Effects

The second-order (P- Δ) effects must be checked by calculating the parameter ϑ, as indicated by Eurocode 8 [13]:

$$\vartheta = \frac{P_{tot} d_r}{V_{tot} h} \leq 0.10 \tag{6.51}$$

where P_{tot} is the total gravitational load above the plane under seismic conditions; V_{tot} is the horizontal seismic action; d_r is the design interstorey drift, and h is the interstorey height. The effects of the second order are negligible if $\vartheta \leq 0.10$, otherwise, they must be considered with a multiplicative coefficient of the horizontal forces equal to $1/(1-\vartheta)$ if $0.10 \leq \vartheta \leq 0.20$. In any case, ϑ cannot be greater than 0.30. It is

possible to observe that, in this case, the second-order effects are negligible (Table 42). In addition, it is worth mentioning that the second-order effects have been implicitly fulfilled through the TPMC [14].

Table 42. Check of the second-order effects [13]

i	z (m)	P_{tot} (kN)	d_r (m)	V_{tot} (kN)	h (m)	θ
1	2.40	66.00	0.035826	63.02	2.40	0.01563
2	4.80	28.00	0.036192	37.74	2.40	0.01118

6.2.3.4 Damage Limit State (DLS)

The DLS check must be satisfied by evaluating the interstorey drifts and comparing them with the limits reported by Eurocode 8 [13] to classify the non-structural elements that can be adopted for the structure under consideration. The drift limits are:

- $d_{rel} \cdot \nu \leq 0{,}005 \cdot h$ for buildings that have non-structural elements of fragile material connected to the structure;
- $d_{rel} \cdot \nu \leq 0{,}075 \cdot h$ for buildings having ductile non-structural elements;
- $d_{rel} \cdot \nu \leq 0{,}010 \cdot h$ for buildings without non-structural elements or fixed non-structural elements to not interfere with structural deformations.

Where d_{rel} is the interstorey drift, evaluated as the difference between the average lateral displacements d_s at the top and bottom of the storey under consideration, multiplied by q; $\nu = 0{,}5$ is the reduction factor, which considers the lower return period of the seismic action associated with the damage limitation requirements; and h is the interstorey height. In the last case, the limit interstorey displacement is 24 mm. Therefore, as it is possible to see in Table 43, the checks are satisfied.

Table 43. DLS check [13]

i	d (m)	d_{abs} (mm)	d_{rel} (mm)	ν d_{rel} (mm)	d_{lim} (mm)	Check
1	0.005971	35.83	35.83	17.91	24.00	OK
2	0.012003	72.02	36.19	18.10	24.00	OK

6.3 Design of the connections

6.3.1 FREE from DAMage connection (FREEDAM)

Figure 6.18 shows the FREEDAM BCJ adopted in this experimental campaign. This is the FREEDAM horizontal configuration where the FD is parallel to the beam's web. A steel haunch constitutes the FD bolted to the lower beam's flange, two steel L-stubs bolted to the column's flange and to the haunch, while the friction pads are symmetrically placed between the L-stub and the haunch. These elements are clamped together with high-strength pre-loadable bolts that are used to tune the friction force in the FD.

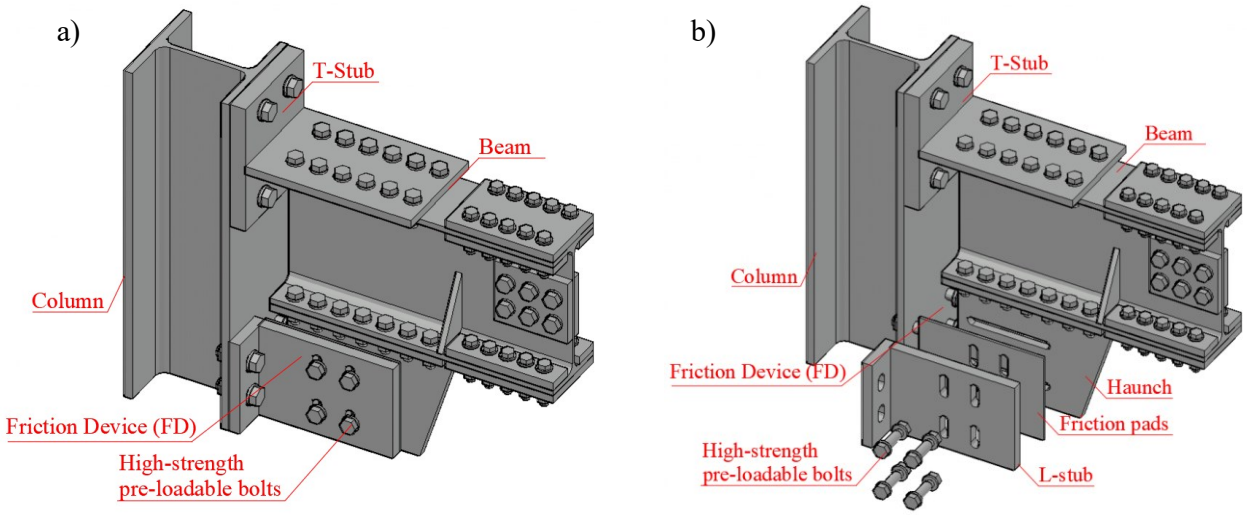

Figure 6.18. FREEDAM BCJ: Geometrical configuration. a) 3D view, b) exploded view

The friction pads are made of adequately coated steel plates with a friction material characterised by a nominal value of the dynamic friction coefficient (μ) equal to 0.53 [16-19]. The top beam's flange is bolted to the column's flange with a steel T-stub, fixing the COR. An IPE270 beam and a HEB200 column characterize the connection. It is worth mentioning that previous experimental works have already addressed essential aspects of the behaviour of this connection, such as the response of the FDs under cyclic loading histories or the behaviour of pre-loadable bolts at installation and over their service life [19-23].
Figure 6.19 shows the FREEDAM deformed configuration and design actions. The design methodology is based on a step-by-step procedure consisting of:

i) definition of the design input parameters;
ii) design of the dissipative components;
iii) design of the non-dissipative components;
iv) design of the structural details of the joint. Additional information regarding the design procedure can be found in Francavilla *et al.* [20].

Step 1. Evaluation of the design actions for the device and design of the tightening torque

The FD is the first element to be designed, representing the weakest component. Successively, all the other members will be designed to have an elastic response. In the following formulations, z is the distance between the centreline of the bolts and the upper T-stub (*i.e.,* the lever arm), where the COR is located. In the design phase, it is possible to assume z = 440 mm (Figure 6.19).

The design bending moment of the connection is equal to 100kNm. The design friction force can be assessed as:

$$F_{cf,Sd} = \frac{0.60 \cdot M_{Rd,IPE270}}{z} = 234\ kN \tag{6.52}$$

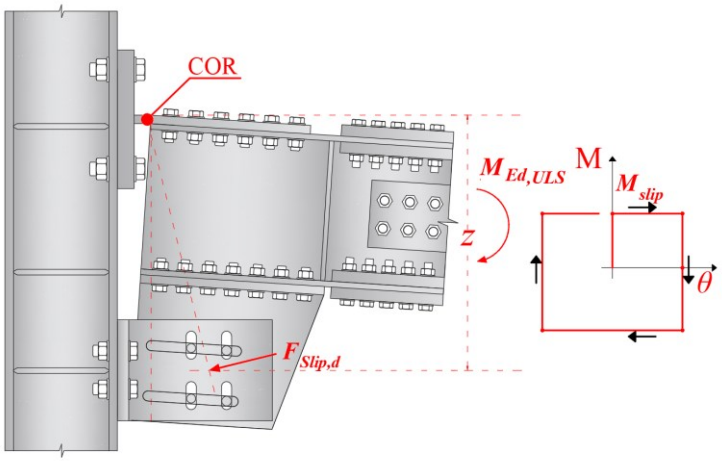

Figure 6.19. FREEDAM BCJ: Deformed configuration

Starting from the design slippage force (*i.e.,* defined as the target bending moment divided by the lever arm), the minimum number of bolts and their pre-load forces are defined, following the relationship:

$$n_{b,min} = \frac{F_{cf,d} \cdot \gamma_{M3} \cdot \gamma_{creep}}{\mu_{dyn,5\%} \cdot F_p \cdot n_s} = \frac{234 \cdot 1.10 \cdot 1.15}{0.53 \cdot 109.90 \cdot 2} = 2.54 \tag{6.53}$$

where $\mu_{dyn,5\%}$ is the dynamic friction coefficient of and F_p is the pre-load force of each bolt. According to this relationship, the number of bolts has been rounded to 4. In such a way, the bolts preload can be defined as equal to 55.6 kN, which is about 50% of the initial value:

$$F_{p,red} = \frac{234}{0.53 \cdot 4 \cdot 2} = 55.60\ kN \tag{6.54}$$

At this point, it is possible to recalculate the design friction resistance and the sliding bending moment of the FREEDAM BCJ.

$$F_{Slip,d} = \mu_{dyn,5\%} \cdot F_{p,red} \cdot n_b \cdot n_s = 234.30\ kN \tag{6.55}$$

$$M_{slip,d} = 234.30\ kN \cdot 0.44\ m = 103\ kNm \tag{6.56}$$

Step 2. Design of the slotted holes of the haunch

Subsequently, all the remaining non-dissipative components are designed to be sufficiently over-resistant by applying the design rules suggested by Eurocode 3 part 1.8 [24] and considering a proper value of the overstrength, which depends on the random variability of the bolt installation pre-load and the friction coefficient statistical variation, equal to 1.83, as demonstrated in previous experimental studies [16-19]. The geometry of the haunch is reported in Figure 6.20:

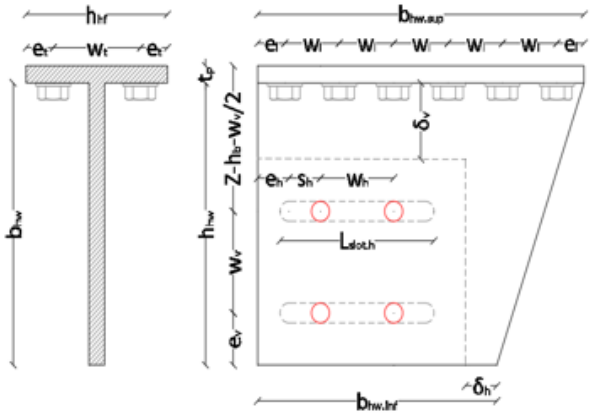

Figure 6.20. Geometrical properties of the haunch

Assuming $k_{wh} = 3.50$, $k_{eh} = 1.50$, $k_{wv} = 5.00$, $k_{ev} = 2.50$, the geometrical parameters can be assessed as:

$$w_h = k_{wh} \cdot d_0 \tag{6.57}$$
$$e_h = k_{eh} \cdot d_0 \tag{6.58}$$
$$w_v = k_{vh} \cdot d_0 \tag{6.59}$$
$$e_v = k_{ev} \cdot d_0 \tag{6.60}$$

Finally, the dimensions of the slotted holes are designed to accommodate the target rotation (*i.e.,* 40 mrad). The length of the horizontal slots is fixed equal to 170 mm to assure a rotation of 50 $mrad$, which is greater than the minimum required.

$$l_{slot,h} = 170\ mm\ > l_{slot,h,min} = \left(\frac{4}{2} - 1\right) \cdot 63 + 17 + 2 \cdot 0.05 \cdot \left(440 + \frac{90}{2}\right) = 140\ mm \tag{6.61}$$

Step 3. Assessment of the design actions for the non-dissipative components

According to the second principle of capacity design, the moment acting at the column flange is evaluated by considering a coefficient of over-resistance γ_{ov} = 1.78.

$$M_{cf,Rd} = M_{slip,d} \cdot \gamma_{ov} = 183\ kNm \tag{6.62}$$

The design resistance is:

$$F_{slip,d} = \frac{M_{cf,Rd}}{z} = \frac{183}{0.44} = 416.91\ kN \tag{6.63}$$

In the hypothesis of a distributed load applied on the beam equal to 9.50 kN/m, a beam length of 4.00m and the height of the column, 200mm, the design shear is:

$$V_{Ed} = \frac{2 \cdot 183}{4 - 0.10} + 9.5\frac{4 - 0.10}{2} = 114.60\ kNm \tag{6.64}$$

Step 4. Design of the T-stub

Both shear tension forces should be considered to design the diameter of the bolts connecting the T-stub (Figure 6.21) to the column flange:

$$F_{t,Ed} = \frac{F_{Slip,d}}{n_b} = \frac{416.91}{4} = 104.23\ kN - Tension \tag{6.65}$$

$$F_{v,Ed} = \frac{V_{Ed}}{2 \cdot n_b} = \frac{114.60}{8} = 14.32\ kN - Shear \tag{6.66}$$

According to Eurocode 3 [24], the resistant area of the bolts is:

$$A_{res,min} = max\left[\frac{\gamma_{M2}}{f_{ub}}\left(\frac{F_{v,Ed}}{\alpha_v} + \frac{F_{t,Ed}}{1.26}\right); \frac{\gamma_{M2} \cdot F_{t,Ed}}{0.9 \cdot f_{ub}}\right] = 144.76\ mm^2 \tag{6.67}$$

For this reason, M24 bolts with a resistant area equal to $353\ mm^2$ have been chosen. The horizontal distance between the bolts has been set equal to 81 mm. The width of the flange is:

$$b_T = 2e_{T,f} + w_{T,h} = 195\ mm \tag{6.68}$$

$$b_{eff} = min\{b_{eff,1}; b_{eff,2}; 0.5b_T\} = 97.5\ mm \tag{6.69}$$

The thickness of the T-stub has been set equal to 30 mm.

To avoid the interaction between the shear and bending moment at the base of the T-stub:

$$t_{T-stub,w} = \frac{V_{Ed} \cdot \sqrt{3} \cdot \gamma_{M0}}{0.5 \cdot b_t \cdot f_{y,T}} = 5.73\ mm \tag{6.70}$$

For this reason, it has been set $t_{T-stub,w}$ equal to $15\ mm$.

For simplicity, the width of the flange is assumed equal to the width of the web. Instead, the connection between the T-stub stem and the beam's upper flange is made through M16 bolts, with a minimum number equal to 8.37 and rounded to 12.

$$n_{b,min} = \frac{F_{friction,Rd} \cdot \gamma_{M2}}{\alpha_v \cdot A_{res} \cdot f_{ub}} = 8.37 \tag{6.71}$$

A proper gap must be left between the beam and the column in order to accommodate rotations up to 50 mrad:

$$gap_{min} = max\left\{t_{T,f} + 2 \cdot t_{T,w}; \Phi \cdot (m_T + n_T) + t_{T,f}; \Phi \cdot \left(e_v + \frac{w_v}{2} + z\right)\right\} =$$

$$= max\{60\ mm; 34.63\ mm; 29.28\ mm\} = 60\ mm \tag{6.72}$$

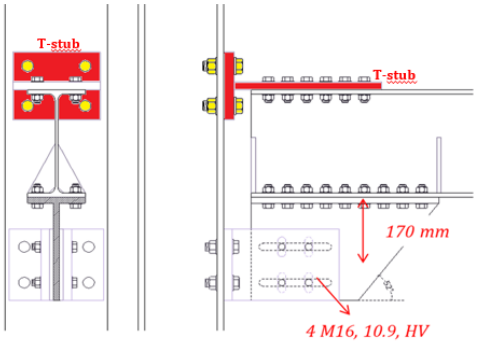

Figure 6.21. Design of the T-stub

Step 5. Design of the haunch

An iterative procedure is adopted to define the geometry of the haunch flange (Figure 6.20) according to a "trial and error" procedure by fixing the number of rows of bolts, the pitch, the diameter of the bolts and the distance of the terminal rows of the bolts from the edge. Two rows of M16 bolts are adopted, with a longitudinal pitch of $2.4d_0$=45 mm and a distance from the free edge of $1.5d_0$=22.5 mm.

$$F_{t,Ed} = \frac{F_{friction,Rd} \cdot h_h}{\sum_i d_i^2} \cdot d_{max} = 43.26\ kN \tag{6.73}$$

$$F_{v,Ed} = \frac{F_{friction,Rd}}{n_{b,h}} = 29.78\ kN \tag{6.74}$$

Where h_h is half-height of the haunch and d_i is the distance of the i-th bolt from the COR. The web thickness is assessed as:

$$t_{hw} \geq \frac{F_{friction,Rd} \cdot \gamma_{M0}}{(h_w - 2 \cdot d_0) \cdot f_y} = 9.50\ mm \tag{6.75}$$

It is assumed t_{hw} equal to 15 mm.

Step 6. Design of the L-stubs

The same approach adopted with the T-stub is used.

$$F_{t,Ed} = \frac{F_{friction,Rd}}{n_b} = 104.23\ kN - Tension \tag{6.76}$$

$$F_{v,Ed} = \frac{F_{friction,Rd}}{2 \cdot n_b} = 14.32\ kN - Shear \tag{6.77}$$

M20 bolts are chosen to connect the L-stubs to the column flange (Figure 6.22).

$$A_{res,min} = max\left[\frac{\gamma_{M2}}{f_{ub}}\left(\frac{F_{v,Ed}}{\alpha_v} + \frac{F_{t,Ed}}{1.26}\right); \frac{\gamma_{M2} \cdot F_{t,Ed}}{0.9 \cdot f_{ub}}\right] = 144.76\ mm^2 \tag{6.78}$$

The vertical slotted holes are designed as follows:

$$stroke_{v,D} = \varphi \cdot \left(gap + e_{L,f,h} + w_{L,f,h} + stroke_{h,A}\right) = 11.67\ mm$$
$$L_{slot,v,min} = 2 \cdot stroke_{v,D} + d_0 = 41.34\ mm \rightarrow 50\ mm$$
$$stroke_{v,D} = \varphi \cdot \left(gap + e_{L,f,h} + w_{L,f,h} + stroke_{h,A}\right) = 11.67\ mm$$
$$L_{slot,v,min} = 2 \cdot stroke_{v,D} + d_0 = 41.34\ mm \rightarrow 50\ mm$$

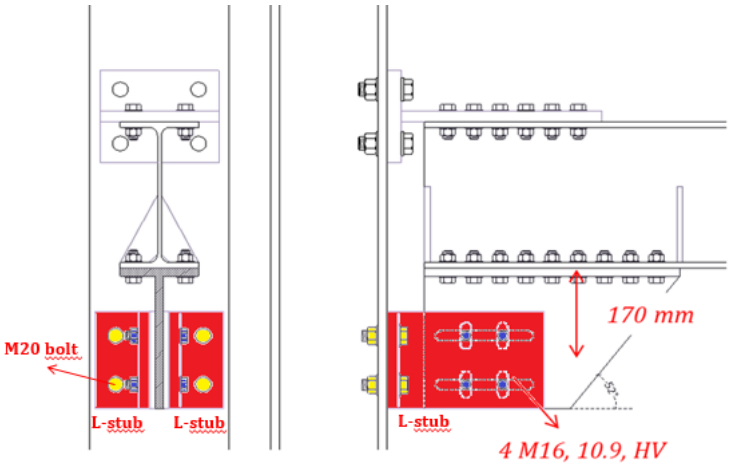

Figure 6.22. Geometry of the L-stubs

Step 7. Check of the beam resistance

The bending moment at the column flange should be higher than the plastic resistance of the beam. Therefore, it is essential to evaluate the bending moment at the presumed position of the plastic hinge $M_{b,Ed}$. The beam, in this case, is a non-dissipative zone and must be controlled by the following relation:

$$M_{b,Ed} = M_{cf,Rd}\frac{L_e - b}{L_e} = 183\frac{2.18 - 0.245}{2.18} = 162.43 \leq M_{b,Rd} \tag{6.79}$$

where b is the length of the haunch and L_e an equivalent length for shear:

$$L - 2a - \frac{M_{cf,Rd}}{V_{Ed}} = 2.18\ m \tag{6.80}$$

Table 44 summarises the design input and the FDs' main geometrical and structural properties.

Table 44: FREEDAM BCJ: Design input, geometry and structural properties

z	$M_{Ed,\ ULS}$	$F_{Slip,d}$	n_b	n_s	Class	d	Pre-load	Torque	slot
[m]	[kNm]	[kN]	[-]	[-]	[-]	[mm]	[kN]	[Nm]	[mm]
0.400	103	234	4	2	10.9	M16	55	145	170

6.3.2 Self-Centring Column Base (SC-CB)

The expected forces in each component have been developed by imposing static rotational equilibrium equations to derive, at first, the response to the action applied to the connection and then the moment rotation behaviour of the connection (Figure 6.23 (a)). The design of the SC-CB is based on a step-by-step procedure consisting of these steps: *i)* definition of the design input parameters; *ii)* design of the dissipative and self-centring components; *iii)* design of the structural details of the joint. The design methodology has already been presented and discussed in Chapter 3. However, in this section, the design procedure is reported to obtain the geometrical and structural properties of the SC-CB specimen used for the experimental tests.

Step 1. Design input parameters

The design procedure of the SC-CB requires as input parameters: *i)* the geometrical properties of the column (*i.e.,* cross-section properties and the splice position above the foundation (l_b)); *ii)* the design forces in the column (*i.e.,* the maximum/minimum expected axial forces ($N_{Ed,max}$;$N_{Ed,min}$) and the design bending moment (M_{Ed})) derived through the procedure suggested by Eurocode 8 [1], namely considering a proper overstrength of the dissipative zones.

The design shear force in the CB joint is estimated as follows:

$$V_{Ed} = \frac{M_{Ed}}{l_0} = \frac{127\ \text{kNm}}{1.10m} = 115\text{kN} \tag{6.81}$$

where $l_0 = l_s - l_b$ and l_s and l_b are respectively the column shear length and the distance between the splice and the base (Figure 6.23). Table 45 lists the geometrical configuration and the design input actions of the SC-CBs, defined by considering the proper location of the splices.

Table 45: Self-Centring Column Base (SC-CB) Design input

Profile	Splice (l_b)	z	M_{Ed}	N_{Ed}	V_{Ed}
[-]	[mm]	[mm]	[kNm]	[kN]	[kN]
HE 200B	500	185	127	+138, -119	115

Note: negative values are for tension; positive values are for compression

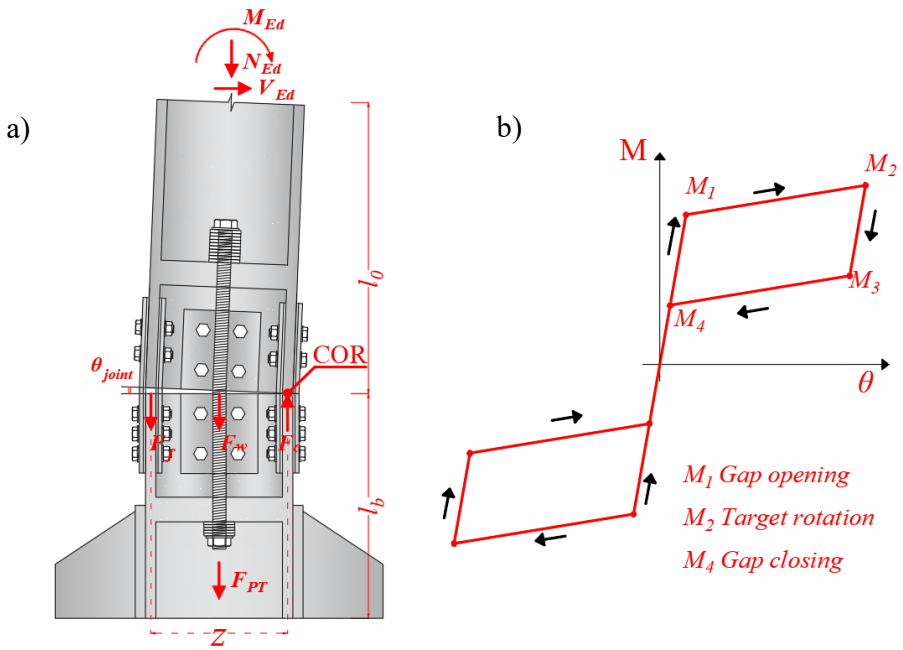

Figure 6.23. Self-Centring Column Base: (a) Schematic representation during the gap-opening; (b) Moment-Rotation behaviour

Once the input parameters are selected, the SC-CB connection design can be addressed by first designing the bolts of the web FD and, consequently, designing the PT bars and the bolts of the flange FDs. The objective of the design procedure is to satisfy at the same time three main conditions: *i)* no yielding of the column; *ii)* self-centring behaviour; *iii)* bending moment corresponding to the gap opening higher than the one defined by Eurocode 8 [13] for the seismic design combination according to the ULS. These conditions are summarised in the following system of inequalities:

$$\begin{cases} M_2 < M_{y,c} \\ M_D \geq M_{FD} \\ M_1 > M_{Ed} \end{cases} \tag{6.82}$$

where $M_{y,c}$ is the column's yielding bending moment.

Step 2: Design of the components

Web FD

The required pre-load force for each web bolt ($F_{p,w}$) is easily determined by imposing that the slippage force of the web FD (F_w) must be larger or equal to the required value of the design shear force (V_{Ed}), as follow:

$$F_w = \mu \cdot n_s \cdot n_{b,w} \cdot F_{p,w} \geq V_{Ed} \quad \rightarrow \quad F_{p,w} \geq \frac{V_{Ed}}{\mu \cdot n_s \cdot n_{b,w}} \geq \frac{115}{0.53 \cdot 2 \cdot 4} \geq 27.12 \qquad (6.83)$$

According to this relationship, 4 HV M14 Class 10.9 Bolts with a pre-load force of 28 each have been chosen for the web FD.

PT Bars

The post-tensioning force of the PT bars ($F_{PT,0}$) is defined by imposing the system of equations for the self-centring condition and the equilibrium between the internal and external bending moment in the SC-CB, as follows:

$$\begin{cases} F_{PT,0} \geq 2F_f + F_w - N_{Ed} \\ F_{PT,0} \cdot \left(\frac{z}{2}\right) + F_f\,(z) = M_{Ed} - (F_w + N_{Ed})\left(\frac{z}{2}\right) \end{cases} \quad \rightarrow \quad F_{PT,0} \geq \frac{127}{0.185} - 138 \geq 548.49 \qquad (6.84)$$

Conversely, in case of $N_{Ed,min}$ it is obtained:

$$\begin{cases} F_{PT,0} \geq 2F_f + F_w - N_{Ed} \\ F_{PT,0} \cdot \left(\frac{z}{2}\right) + F_f\,(z) = M_{Ed} - (F_w + N_{Ed})\left(\frac{z}{2}\right) \end{cases} \quad \rightarrow \quad F_{PT,0} \geq \frac{127}{0.185} + 119 \geq 753.80 \qquad (6.85)$$

According to this relationship, 2 PT Bars of Class 10.9 with a pre-load force of 400 kN each have been chosen for the web FD.

Flange FDs

In addition, the minimum pre-load force for each flange bolt ($F_{p,f}$) is provided by addressing the contribution of the force of the PT bars and the force of the web FD. The slippage force of the flange FDs (F_f) can be obtained as indicated by the following expressions:

$$F_f = \frac{M_{Ed}}{z} - \frac{1}{2}\left(F_w + N_{Ed} + F_{PT,0}\right) \rightarrow F_{p,f} = \frac{F_f}{\mu \cdot n_s \cdot n_{b,f}} = \frac{106.44}{0.53 \cdot 2 \cdot 8} = 25.10 \qquad (6.86)$$

According to this relationship, 4 HV M14 Class 10.9 Bolts with a pre-load force of 26 each have been chosen for the web FD.

Disk Spring system

The disk springs system is designed to be over-strength with respect to the PT bars by calculating the number of disk springs in parallel ($n_{ds,par}$) as follows:

$$F_{y,DS} \geq F_{y,PT} \qquad \rightarrow \quad n_{ds,par} = \frac{A_{s,res,PT} \cdot f_y}{F_{y,DS,1}} \qquad (6.87)$$

where $A_{s,res,PT}$ and f_y are the net area and the yield stress of the PT bar, respectively, and $F_{y,DS,1}$ is the yield strength of the single disk spring. 3 disk springs in parallel are selected.

The number of disk springs in series ($n_{ds,ser}$) controls the stiffness of the self-centring system (K_{eq}) by providing sufficient deformability to the system, and it is calculated assuming that:

$$\frac{(f_y \cdot A_{s,res,PT} - F_{p,PT})}{\delta_{PT}} = K_{eq,1} \geq K_{eq} \qquad \rightarrow n_{ds,ser} \geq n_{ds,par} K_{ds,1} \left(\frac{K_{PT} - K_{eq,1}}{K_{eq,1} K_{PT}} \right) \tag{6.88}$$

where $\delta_{PT} = \theta_t \cdot d_{PT}$ is the maximum elongation of the farther bar from the COR and d_{PT} is the distance of the PT bar with respect to the COR. It is worth noting that the previous equation provides the minimum number of disk springs in series ($n_{ds,ser}$) and it can be increased to reduce K_{eq}. A tensile resistance check of the PT bars is carried out, considering their elongation. This check ensures that both the PT bars and the disk springs remain elastic. 8 disk springs in series are selected. The selected disk springs are SCHNORR Din 6796 30, with the characteristics illustrated in Figure 6.24 and Table 46.

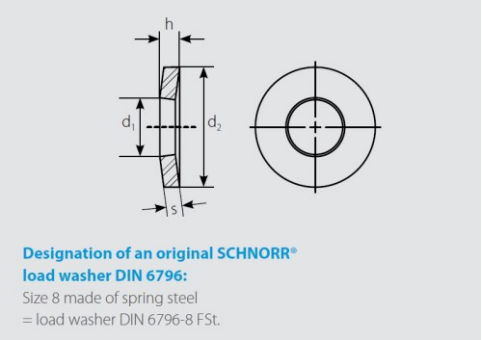

Figure 6.24. SCHNORR Disk Spring DIN 6796

Table 46: SCHNORR Disk Spring M30 DIN 6796

Article	Finish	Size	d_1	d_1	s	h_{min}	h_{max}	F	Min residual load
[-]	[-]	[mm]	[mm]	[kNm]		[kN]	[kN]	[N]	[N]
701800	blank, oiled	30	31	70	7	8	9.20	300000	196000

Table 47 summarises the web's main geometrical and structural properties, the flange FDs, and the SC system. The FDs comprise 8 mm coated friction pads of S355JR steel class for both web and flanges.

Table 47: SC-CB Geometry and structural properties

Element	Class	Number	Diameter	Pre-load	Torque
[-]	[-]	[-]	[-]	[kN]	[kNm]
Web FD	HV 10.9	4	M14	28	65
Flange FD	HV 10.9	4	M14	26	60
PT bars	10.9	2	M30	400	1000
Disk Springs	C60S	3 n_{par}, 8 n_{ser}	D30	-	-

The friction coefficient (μ) is assumed to be equal to 0.53, consistent with previous studies on friction interfaces [16-19]. The SC system includes high-strength PT bars 10.9 class and disk springs special washers DIN 6796 of C60S material installed after a pre-setting procedure using preliminary uniaxial compression tests.

Step 3: Design of the structural details

Anchorage plates

Anchorage plates for the PT bars are placed symmetrically along with the column's depth and welded to the column. The dimensions of the plates are known (*i.e.,* b_p and l_p), except for the thickness (t_p), which is designed and checked to resist the total force of the PT bars (F_{PT}). Anchorage plates of 40mm are designed.

Cover plates

The cover plates of the flange FDs are designed and verified to resist the tensile force provided by the design actions (*i.e.,* the contribution of M_{Ed}, N_{Ed}, F_w and F_{PT}). It is worth highlighting that the contribution of the friction shims to the tensile resistance of the FDs is neglected, as well as the flexural resistance of the flange cover plates and friction shims, as previously discussed. In addition, the flanges' plate thickness is checked to avoid local buckling. The FDs comprise 8 mm steel cover plates of S355JR steel for both web and flanges.

Web oversized holes and flange slots

Web oversized holes (d_h) and flange slots (l_{slot}) are designed to accommodate the design rotation (θ_t) during the gap opening phase. The holes' positions are designed to comply with the edge distances and spacing of bolts suggested by Eurocode 3 Part 1-8 [24]. Finally, the design resistance of the lower part of the connection is calculated and checked, considering the failure modes (*i.e.,* shear resistance, bearing resistance, punching shear resistance, combined shear and tension) as indicated in the Eurocode 3 Part 1-8 [24]. The geometry and the structural details of the web and flanges FDs and the self-centring system are reported in Table 48,

Table 49 and
Table 50, respectively. The symbology is consistent with that reported in the design formulations (see Chapter 3). The theoretical Moment-Rotation relationships of the SC-CB for N_{Max} and N_{Min} are respectively shown in Figure 6.25. Figure 6.26 illustrates the SC-CB adopted in this experimental campaign. In addition, the details of the SC-CB specimen with the geometrical dimensions are summarized in ANNEX B.

Table 48: Web cover plates geometry and structural properties

Specimen	b_{wp}	h_{wp}	t_{wp}	*e1*	*p1*	*e2*	*p2*	d_h	*z/2*
	[mm]	[mm]	[mm]	[mm]	[mm]	[mm]	[mm]	[mm]	[mm]
SC-CB	130	300	8	30	70	30	70	30	93

Table 49: Flange cover plates geometry and structural properties

Specimen	b_{fp}	h_{fp}	t_{fp}	*e1*	*p1*	*e2*	*p2*	l_{slot}	*z*
	[mm]	[mm]	[mm]	[mm]	[mm]	[mm]	[mm]	[mm]	[mm]
SC-CB	200	300	8	50	50	39	122	30	185

Table 50: Self-centring system geometry and structural properties

Specimen	t_p	K_{PT}	K_{DS}	K_{eq}	$\Delta l_{avg,PT}$	*z*
	[mm]	[kN/mm]	[kN/mm]	[kN/mm]	[mm]	[mm]
SC-CB	40	162	42	56	4	185

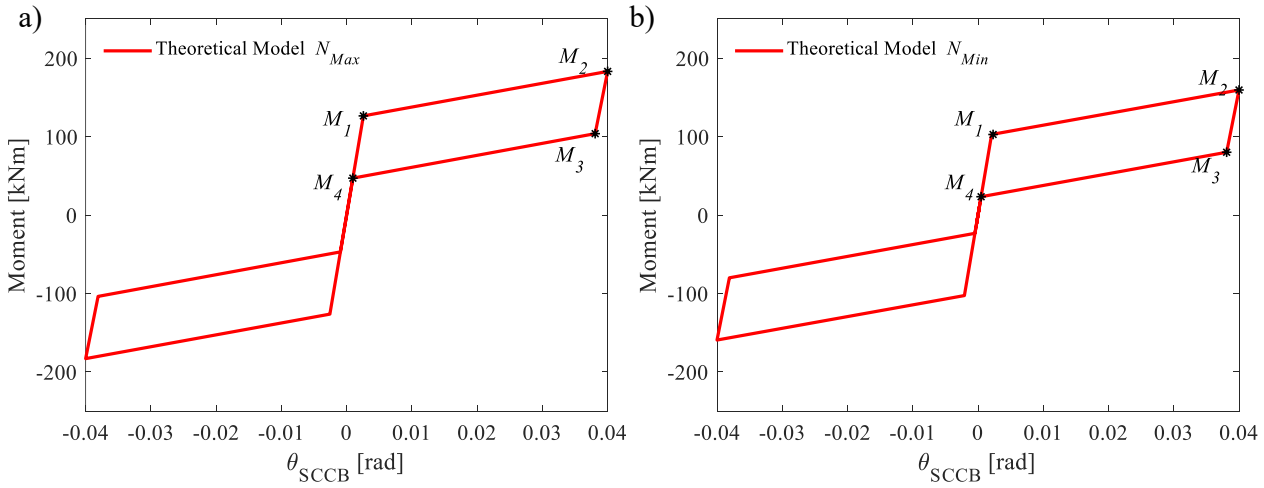

Figure 6.25. SC-CB: Theoretical Moment-Rotation relationship for a) N_{Max}; b) N_{Min}

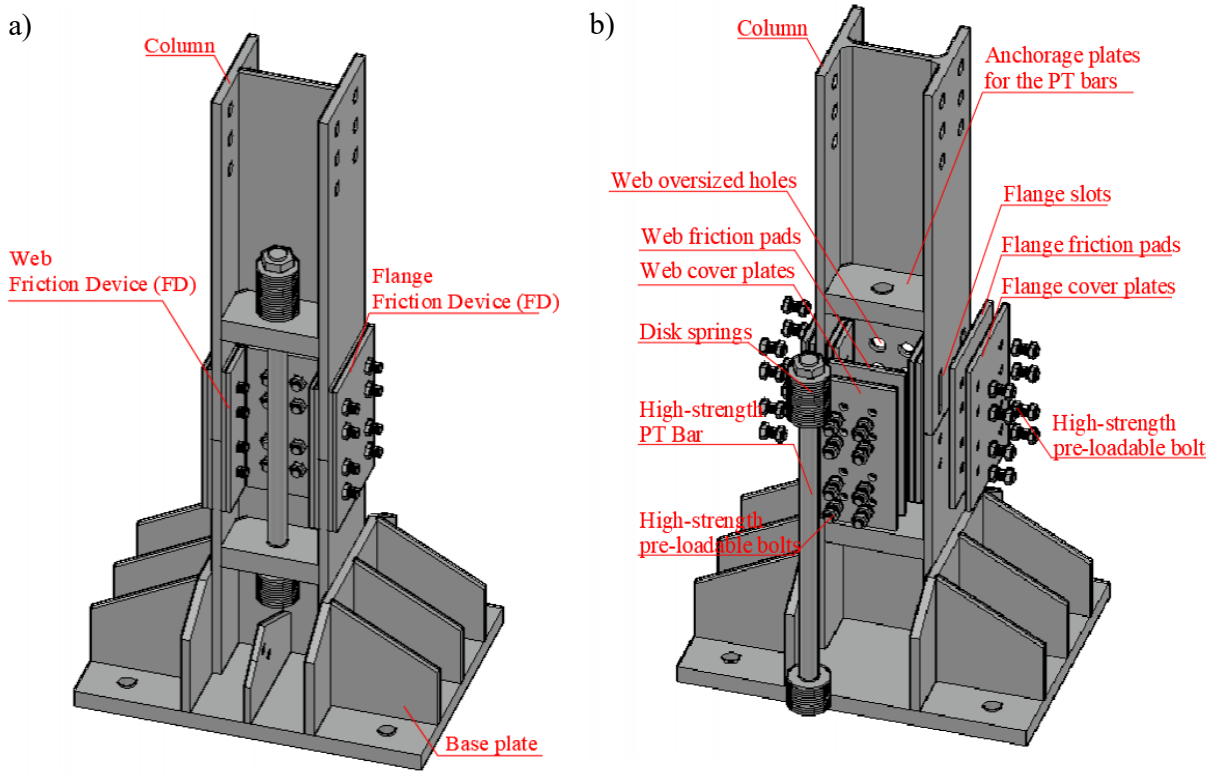

Figure 6.26. Self-Centring Column Base: Geometrical configuration. a) 3D view, b) exploded view.

6.4 Material Properties

6.4.1 Coupon Tests

Coupon tests have been carried out to determine the stress-strain curve of the adopted structural steel and characterise the modulus of elasticity (E), yield stress (σ_y), ultimate stress (σ_u) and the corresponding deformations. S355 steel classes were used for beams and columns of the structure, and three coupon specimens (*i.e.,* one web and two flanges for each element) were subjected to tensile tests according to EN ISO 6892-1 [25]. The results are listed in Table 51.

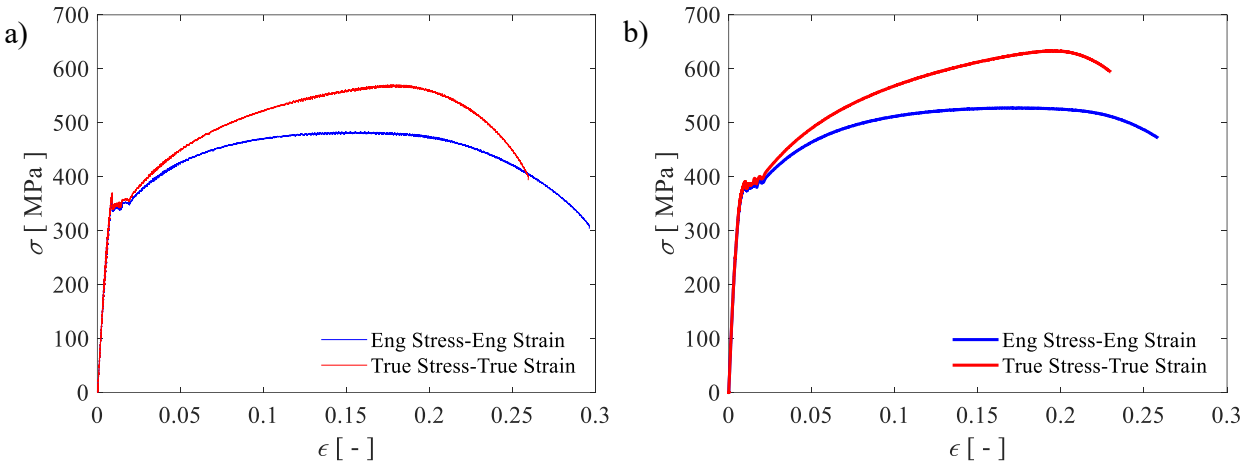

Figure 6.27. Coupon Test. Stress-strain curve for: a) Columns (Test 1); b) Beams (Test 1)

Table 51. Steel properties

Profile [-]	Test [-]	Element [-]	σ_y [MPa]	ε_y [%]	E [MPa]	σ_u [MPa]	ε_u [%]
Beam (IPE 200)	1	Flange	387	0.186	208064	527	38.0
	2	Flange	397	0.187	212299	520	39.4
	3	Web	451	0.210	214761	551	36.6
	-	Average	412	0.194	211708	532	38.0
Column (HE 200B)	1	Flange	354	0.168	210714	467	34.8
	2	Flange	355	0.167	212575	465	31.4
	3	Web	360	0.169	213018	462	31.0
	-	Average	356	0.168	212102	465	32.4

6.4.2 Characterization tests for the FDs

The friction force is affected by the bolt pre-loading force, F_b, and the friction coefficient of the shim-steel interface, μ. The preliminary tests described in this section allowed the characterization of the FD parameters to gain confidence in the following:

i) the definition of the friction coefficient, μ, for the interface materials;
ii) the definition of the bolts pre-loading force, F_b, used in the tests.

6.4.2.1 Tests for the Friction coefficient

The characterization tests for the friction coefficient have been performed on three sub-assemblages of S355JR steel plates and friction pads of S355JR steel plates coated with thermally sprayed material to test the uniaxial behaviour of friction interfaces. Figure 6.28 shows the geometry of the plates. The tests were performed using the universal testing machine SCHENCK HYDROPULS S56 LOADING CAPACITY +-630kN, maximum stroke equal to +-125mm and a self-balanced steel frame used to counteract the axial load (Figure 6.29).

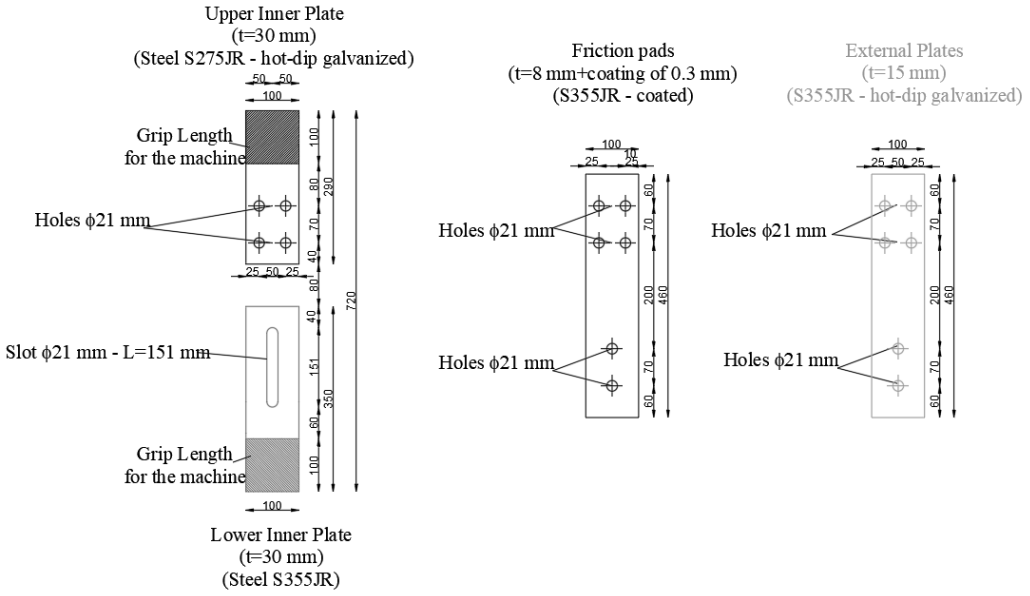

Figure 6.28. Characterization tests for the friction coefficient: geometry of the plates.

The layout has been defined as complying with the standardised sliding test suggested by EN1090-2 [26], while the loading protocol is consistent with EN 15129 [27] (*i.e.,* qualification of displacement-dependent dissipative devices). The loading protocol consists of 5 cycles at 25%, 50% and 40 cycles at 100% of the target displacement. In this case, the target displacement has been calculated considering the distance between the COR and the mid-centre of the friction damper of the SC-CB, equal to 7.4 mm = 0.04rad x 185mm (*i.e.,* z=185 mm is the internal lever arm of the connection) and it has been rounded in 10 mm. Therefore, the loading protocol consisted of 5 cycles at the amplitude of 2.5 mm +5 cycles at the amplitude of 5 mm +40 cycles at the amplitude of 10 mm. Increasing speed values were defined to remain in a quasi-static range due to the available equipment (*i.e.,* from 1mm/s for the first 10 cycles to 5mm/s for the cycles at the maximum amplitude).

Two HV M20 10.9 bolts with a maximum pre-load capacity of $F_{PC} = 0{,}7 \cdot A_{bolt} \cdot f_{ub}$ = 0.7 x 245 x 1000 = 171500 N = 171.5 kN have been used, with a pre-loading force set as the 50% (*i.e.,* 85.75 kN) of the maximum preload, corresponding to a tightening torque of 0.13x85.75x20=223Nm, where 0.13 is the k-factor. The pre-loading forces of the bolts have been applied with a calibrated torque wrench sensor FUTEK TAT460 (maximum capacity of 680Nm), while two FUTEK LTH500 load cells have been installed to monitor the forces before and during the test. The axial displacements of the devices will be

read directly from the transducer of the testing machine and, in the same way, the slippage force (*i.e.,* directly from the load cell of the machine). Three tests have been performed on one sub-assemblage having the same configuration and pre-loading values, and the average values between the three tests have been obtained.

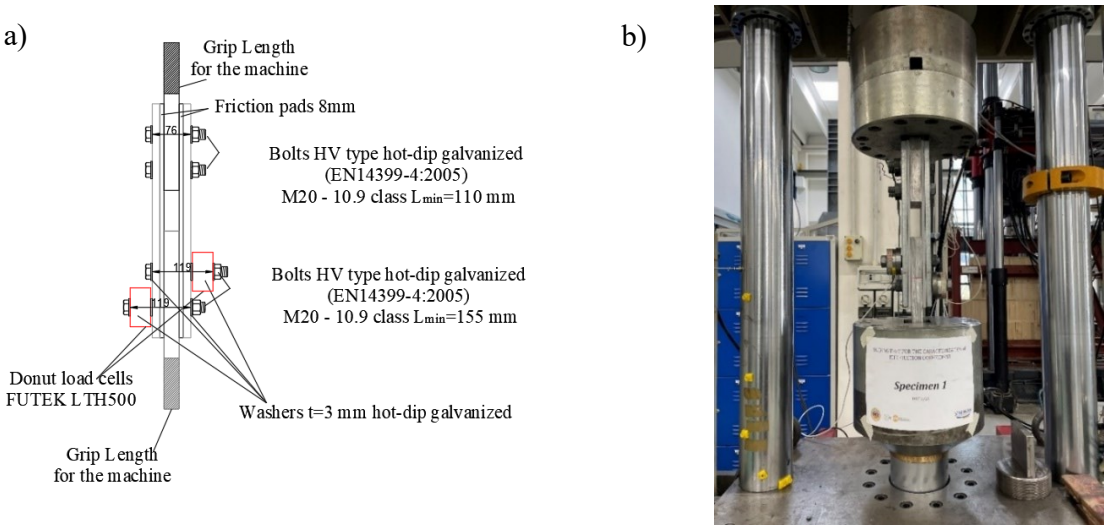

Figure 6.29. Characterization tests for the friction coefficient: a) Sub-assemblage; b) Test set-up.

There are two values of the friction coefficients: an effective value (μ_{eff}), calculated as the ratio between the slippage force and the sum of the nominal values of the pre-loading N_b. Conversely, the actual value (μ_{act}) has been determined as the ratio between the slippage force and the sum of the values of the bolts' forces directly read from the load cells during the test. Such an actual value provides the real measure of the friction coefficient, whose degradation is due only to the damage of the surfaces in contact, while the effects coming from bolt loosening are directly measured by means of the load cells.

$$\mu_{eff} = \frac{F}{n_s \, n_b \, N_b} \tag{6.89}$$

$$\mu_{act} = \frac{F}{n_s \, n_b \, N_{b,LC}} \tag{6.90}$$

where $N_{b,LC}$ is directly read from the load cells for each bolt during the test.

Figure 6.30 shows the force-displacement behaviour of Test 1, exhibiting a regular hysteretic behaviour with a slight kinematic hardening. It is worth noting that the hysteretic curve of one of the three tests is shown; however, a very small scatter of the response for the other tests was observed, evidencing a very low random variability of the friction coefficient for this material, consistently with previous tests [16-18]. This results in the possibility of predicting with a higher accuracy the value of the friction coefficient to be used in design from the practical point of view. Consistent results were obtained for the other tests, and the average value of the friction coefficient, μ, was equal to 0.53. In addition, Figure 6.31 shows the degradation of the friction interfaces after the tests.

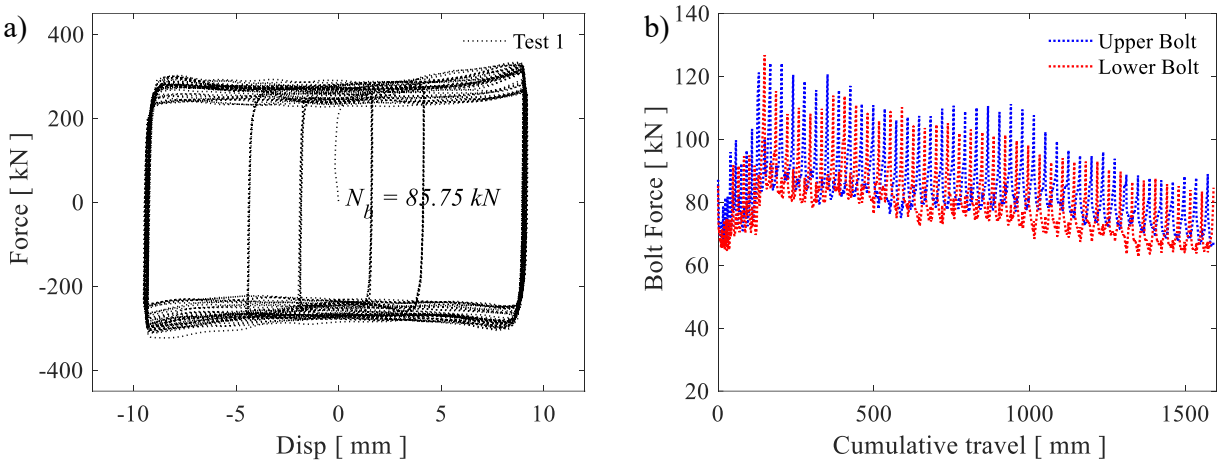

Figure 6.30. Characterization tests for the friction coefficient. a) Force-displacement behaviour; b) Bolt forces

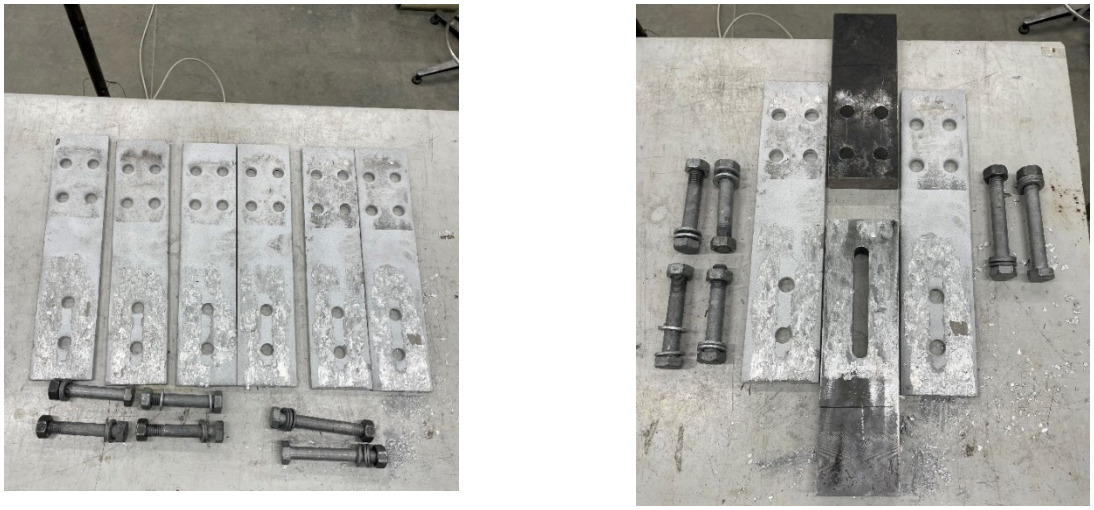

Figure 6.31. Degradation of the friction interfaces after the tests

6.4.2.2 Relationship between torque and the bolt pre-loading force

Figure 6.32 shows the test setup for the characterisation tests for the relationship between torque and bolt pre-load force. The bolts pre-loading force can be defined by the following equation:

$$N_b = \frac{T_b}{k \cdot d} \tag{6.91}$$

where T_b is the value of the tightening torque, d is the bolt diameter, and the recommended value of k is equal to 0.2, as suggested by Latour *et al.,* 2015 [15]. Previous studies showed that this relationship may under- or over-estimate the bolt pre-loading force, N_b, by 20% due to different bolt types and differences in temperature, humidity, thread conditions, lubrication, etc. Hence, the characterization tests aimed at deriving the k parameter that best described the relationship between T_b and N_b for the bolts used in the tests. The characterisation tests have been carried out considering three bolts of each type with different

torque values (*i.e.,* T_b from 60 to 100 Nm for the M14 and from 100 to 140 Nm for the M16). It is noteworthy that these values have been selected in a reasonable range of variation, considering the design torque of the bolts used in the experimental campaign. Regressions of 15 samples for each typology provided a value for k equal to 0.129, consistent with the recommendations provided by the manufacturer (Figure 6.33).

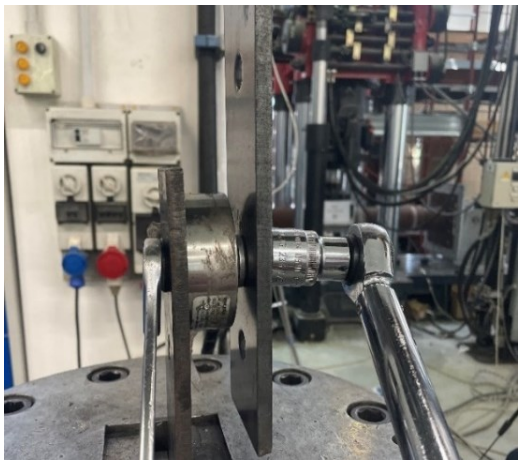

Figure 6.32. Relationship between the tightening torque T_b and the bolt pre-loading force N_b. Test set-up

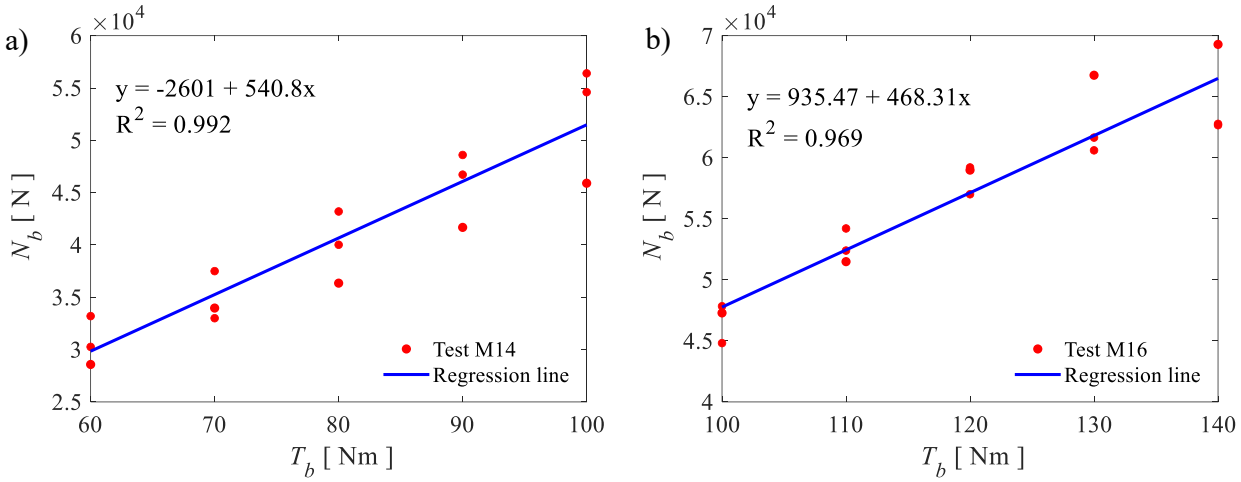

Figure 6.33. Results and interpolation curve for the: a) M14 bolts and: b) M16 bolts

6.4.2.3 Loading test on disk springs

A pre-setting procedure was performed on the disk springs to ensure their elastic response during the tests [28]. Figure 6.34 shows the test set-up and the force-displacement curves of three disk springs, highlighting the effect of the pre-setting procedure (*i.e.,* non-linear response) and the elastic response during the reloading and unloading phases. It is possible to observe that the disk springs show an elastic non-linear response for higher forces close to their complete flattening. This is further discussed in Section 6.8.2.

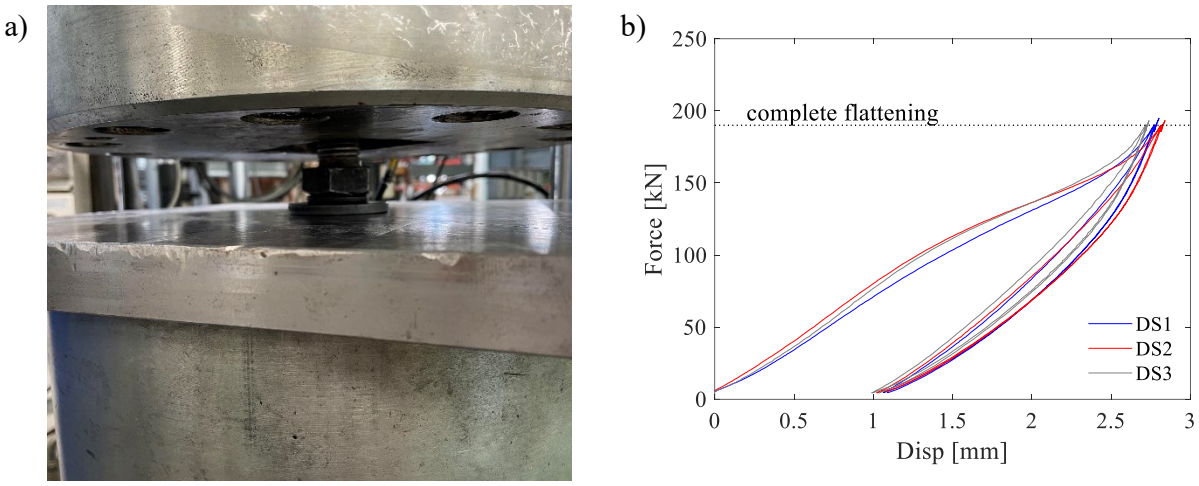

Figure 6.34. Disk Spring washers. a) Test set-up; b) Experimental behaviour of three single disk springs.

6.5 Experimental Program

6.5.1 Pseudo-dynamic Procedure

The PsD technique [8] was used to simulate the seismic response of the large-scale tested structure. This method was originally developed at the end of the 80s within the framework of the U.S. - Japan Cooperative Earthquake Research Program in Japan, at the Tsukuba Building Research, and in the United States, at Berkeley, University of California, and at Ann Arbor, University of Michigan. While the shaking table tests experimentally reproduce the seismic response of a structure through the application of the natural ground acceleration at its basement, the pseudo-dynamic method is a hybrid method characterized by the combination of experimental techniques and numerical simulations, making these two phases cyclically dependent. It imposes floor displacements on the structure by solving step-by-step equations of motion during the test. For this reason, the parameters used to set the numerical procedure can affect the experimental outcomes, and the more complex is the numerical modelling, the more time is required to solve step-by-step the equation of motion, inducing an increase in the test duration. The equipment is generally constituted by hydraulic actuators, fixed to rigid reaction walls or frames, which apply floor displacements to the analysed structure. In contrast, load cells and transducers monitor the information related to the reaction forces and the relative floor displacements. Figure 6.35 illustrates the conceptual scheme of the pseudo-dynamic testing method.

Among the main benefits of this test method is that it allows the adoption of the same experimental equipment that is used for quasi-static tests, and the inertia and viscous forces are simulated by preliminary defining the mass matrix and the damping matrix of the structure without the need for really applying the masses to the building. Furthermore, unlike the shaking-table tests, the quasi-static loading history application of the pseudo-dynamic method allows the continuous monitoring of the inspection of the behaviour exhibited by the structural elements (e.g. connections, members, devices), which results in complex and onerous in the case of real-time tests. Given the above-reported considerations, this experimental strategy can be fully exploited to check the reliability of the analytical models to predict the non-linear behaviour both at the local (materials) and global level (structures or their components).

This strategy represents an excellent solution to assess the seismic response of structures equipped with innovative devices. In fact, the rigid decks constituting buildings allow schematizing the structures as systems with n degrees of freedom in correspondence with which the masses are assigned and the imposed displacements evaluated with the implemented calculation routine. This aspect clarifies that the pseudo-dynamic approach is very effective in the case of systems characterized by discretized masses. In contrast, the complexity of adopting such an approach tends to increase in the case of structures characterized by uniformly distributed masses, such as pylons, monuments or towers.

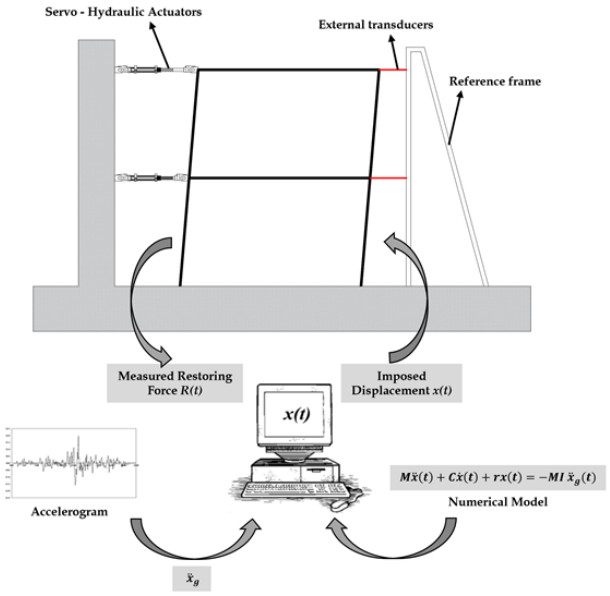

Figure 6.35. Conceptual scheme of the pseudo-dynamic testing method.

To perform a pseudo-dynamic test, it is necessary to define the viscous damping based on literature data, even though during the actual test, with the behaviour of the structure pushed in the plastic field, the hysteretic damping will tend to prevail over the viscous. The quasi-static nature of the test generates a low speed of structural deformation, inducing lower strength and stiffness than those expected during the earthquake. Such a phenomenon is known as relaxation, but it is worth highlighting that in the framework of this work, which is focused on steel structures, it can be considered insignificant. The classic pseudo-dynamic technique is characterized by the alternate execution of the experimental and numerical phases. No temporal requirements must be fulfilled; instead, the fast approach requires synchronization between the two phases, imposing a maximum time step period the jobs must end. These constraints can induce convergence problems in the case of complex tested structures; for this reason, mainly to ensure the stability of the numerical simulations, it is preferable to use the explicit central differences method for the experimental part and the implicit one for the analytical part. As already pointed out, the nature of the pseudo-dynamic method is based on a numeric-experimental approach based on solving step-by-step the dynamic equation of motion. Consequently, a model of the test sample is necessary; in the case of structures, it is possible to assume that the rigid decks to which the masses can be assigned allow defining a finite number of degrees of freedom whose main components are excited in the direction of the seismic loading. The equations of motion to be solved can be expressed as:

$$[M]\{a_i\} + [C]\{v_i\} + \{R_i\} + [K_g]\{d_i\} = -[M][B]\{a_{gi}\}$$

where:

- $[M]$ and $[C]$ are the mass and damping matrices, respectively;
- $\{R_i\}$ is the vector that includes the reaction forces;
- $[K_g]$ is the matrix of the geometric stiffness used to compensate the loads not present on the structure during the test;
- $\{a_i\}$, $\{v_i\}$ and $\{d_i\}$ are, respectively, the vectors of accelerations, velocities and displacements of the degrees of freedom of the structure at time i;
- $\{a_{gi}\}$ is the vector of ground accelerations at time i in each direction considered;
- $[B]$ is the transformation matrix of ground acceleration; the component B_{ij} corresponds to the acceleration in correspondence with the degree of freedom i when the structure acts as a rigid body due to a unitary acceleration to the ground of component j (in the case of a flat test with a single component of horizontal ground displacement $[B]$ is a unitary vector).

6.5.2 Test setup

The experimental setup is shown in Figure 6.36. It consists of two actuators (MTS 243.60–02 and MTS 243.45–01) employed respectively on the structure's first and second floor to apply horizontal loads. In particular, the actuator located on the first floor (MTS 243.60–02, Figure 6.37) has a load capacity equal to 648 kN in tension and 1000 kN in compression and a piston stroke equal to ±508 mm, while the actuator located on the second floor (MTS 243.45–01) has a load capacity equal to 649 kN in compression and 445 kN in tension and a piston stroke equal to ±1066 mm. The two actuators are connected to the deck of the tested building on one side, while on the other side, they are fastened to a reaction steel braced frame. Rigid braced steel footings fastened with high-strength Dywidag bars assure the specimen's connection to the laboratory's strong concrete floor and the base of the reaction-braced frame (Figure 6.38-Figure 6.39).

6.5.3 Instrumentation

Many measurement devices have been employed to monitor global and local displacements, rotations and deformations. The global response of the structure has been assessed using two wire transducers (WSs) per level, employed to measure the horizontal displacements of the floors, while two LVDT (Linear Vertical Displacement Transducers) (*i.e.,* max stroke 100 mm) per level have been used to check possible deck rotations (Figure 6.40-Figure 6.41). It is worth highlighting that, in the considered case, transversal movements and floor rotations can be due only to geometrical imperfections resulting in accidental eccentricities. Additionally, the local response of the structure and its components have been assessed using axial strain gauges (Figure 6.42) and LVDT (*i.e.,* max stroke 50 mm) (Figure 6.43). Axial strain gauges have been applied to the columns' top and bottom sections to check the bending moments

at the columns' ends. In this way, the bending moments at the connection level have been defined using the nodal equilibrium.

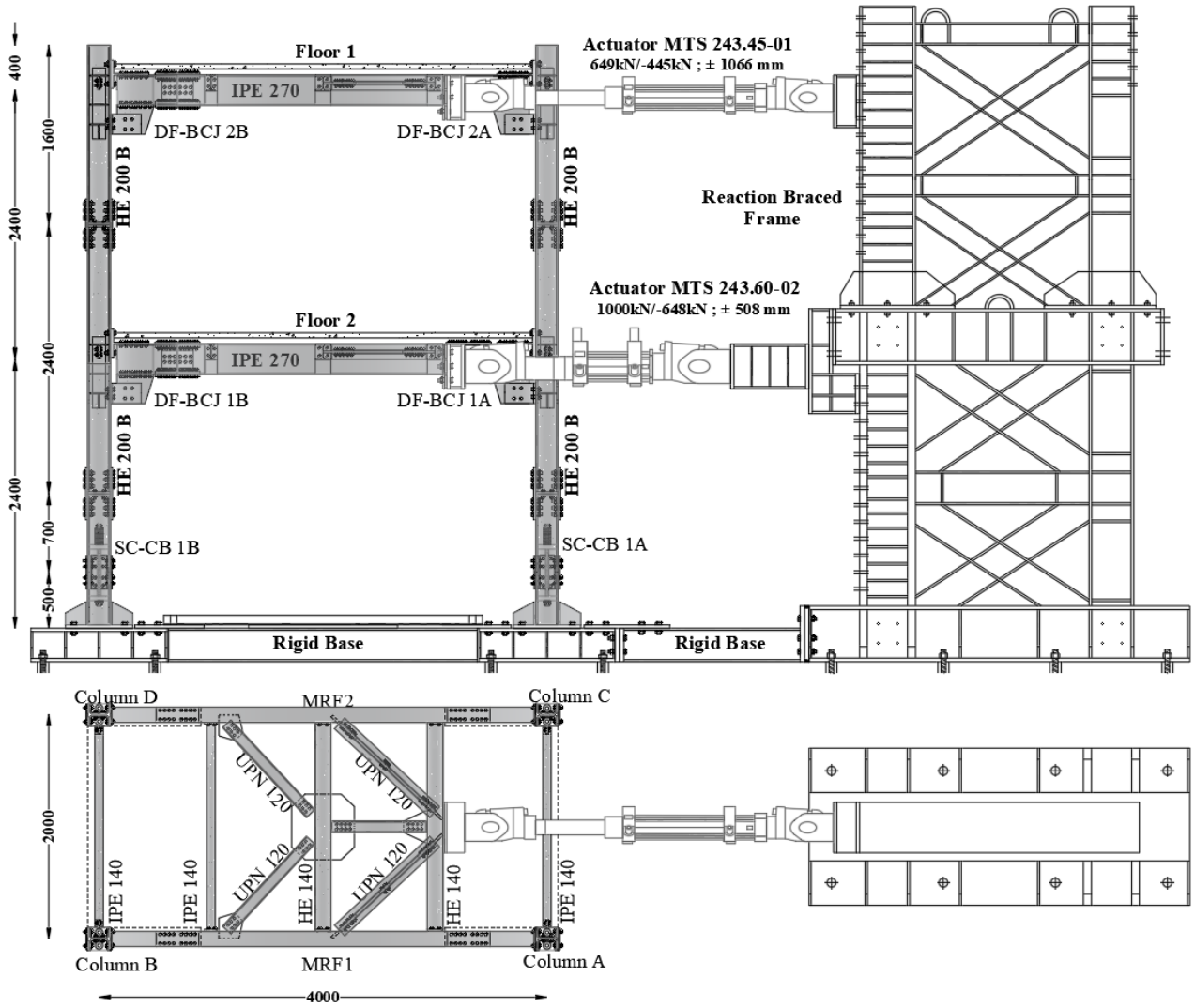

Figure 6.36. Experimental set-up.

Figure 6.37. Actuator at the first storey.

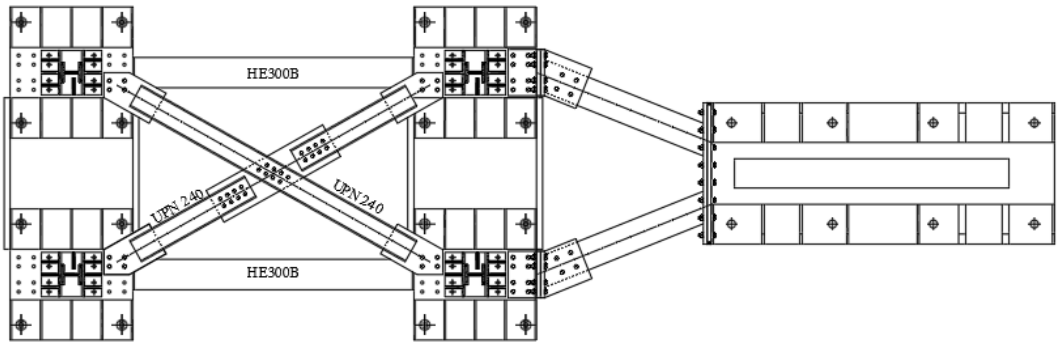

Figure 6.38. Rigid base (drawing).

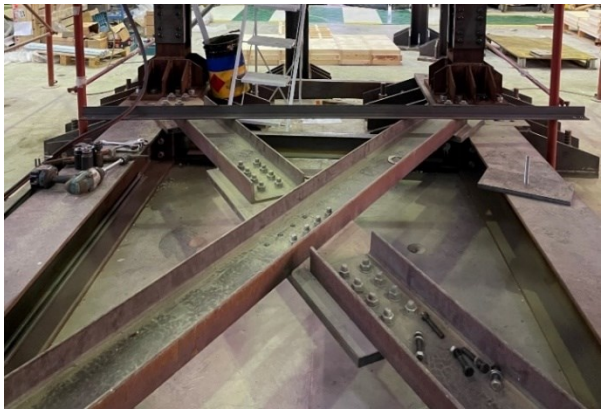

Figure 6.39. Rigid base.

The local response of the FREEDAM BCJs has been monitored using eight LVDTs (*i.e.,* max stroke 50 mm, one per joint) to measure the displacements. Starting from the knowledge of the horizontal displacements, the rotation of the FREEDAM BCJs has been evaluated, considering the distance from the COR. Regarding the bolt tightening procedure, the initial pre-load, according to EN 1090-2 [26] specifications, was increased by 10%, and the preload was added to the bolt loads to account for random variability of the bolt tightening and initial installation loss. Thus, a torque of 150 Nm for each bolt was applied in the FDs. Figure 6.45 and Figure 6.46 show the details of the instrumentation and the measurement devices used for the tests for the FREEDAM BCJ.

The local response of the SC-CB connections has been monitored using eight LVDT (*i.e.,* max stroke 50 mm, two per joint) to measure the vertical displacements in both column sides. Starting from the knowledge of the vertical displacements, the rotation of the SC-CBs has been evaluated considering the distance from the COR. A torque sensor, FUTEK TAT430, has been used to measure the initial torque applied to the bolts with the torque wrench. As for the FREEDAM BCJs, the initial pre-load, according to EN 1090-2 [26] specifications, was increased by 10% of the preload was added to the bolt loads to account for random variability of the bolt tightening and initial installation loss. Thus, a torque of 60 Nm was applied in the flanges and 65 Nm in the web FDs for each bolt. Four load cells IFF LWCF have been installed within the connection with different functions: i) to monitor the initial PT force in the PT bar by direct observation; ii) to monitor the tensile forces in the PT bars along each test duration. In

addition, the forces in the remaining four PT bars have been monitored by using four strain gauges located at the centre section of the PT bar. It is also worth highlighting that the load cell and the strain gauges have been installed on a single PT bar. Such a redundancy of the measurement devices has been crucial to find a correlation between the two measurements. Figure 6.47 and Figure 6.48 show the details of the instrumentation and the measurement devices used for the tests for the FREEDAM BCJ.

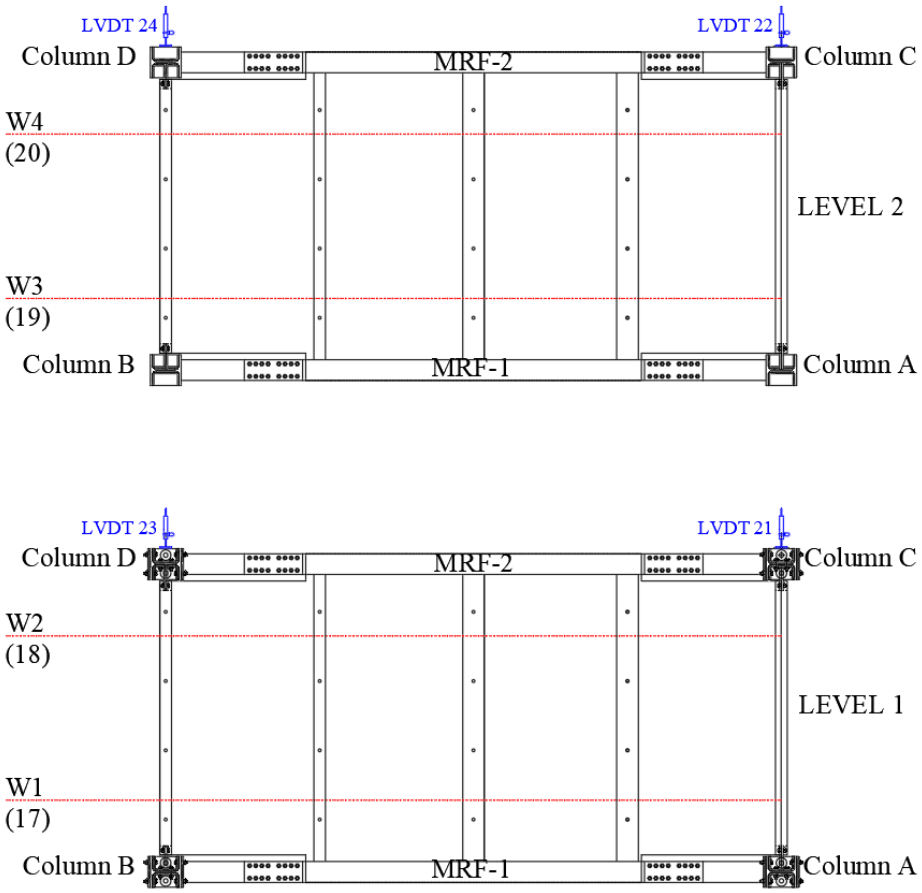

Figure 6.40. Location of the instrumentation in plan.

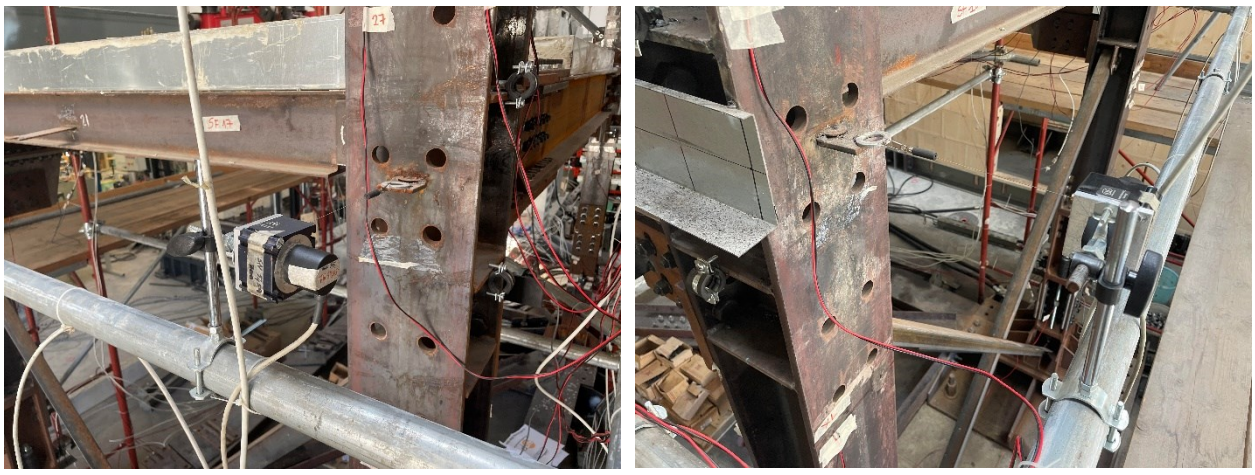

Figure 6.41. Wire sensors.

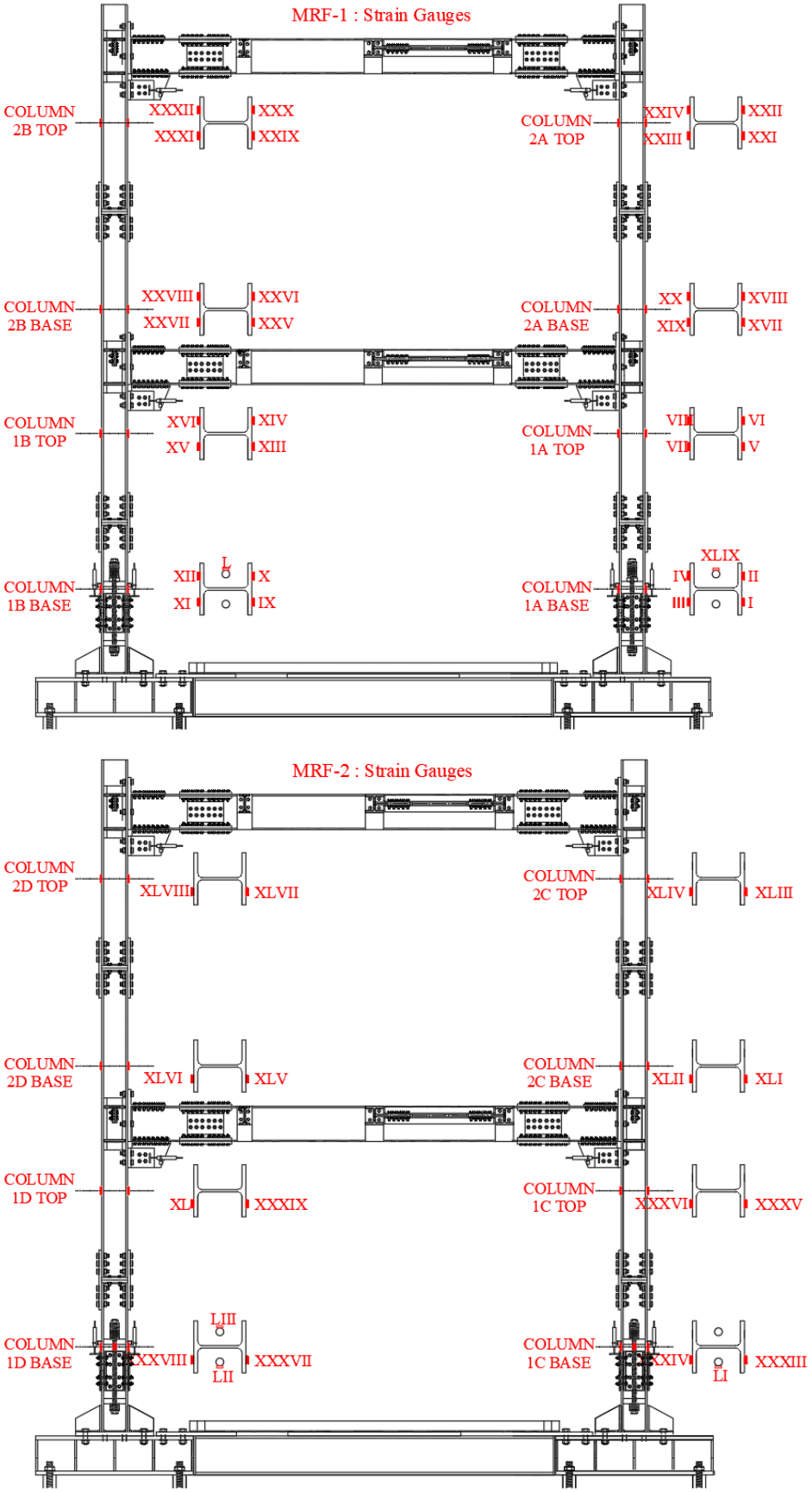

Figure 6.42. Location of the strain gauges.

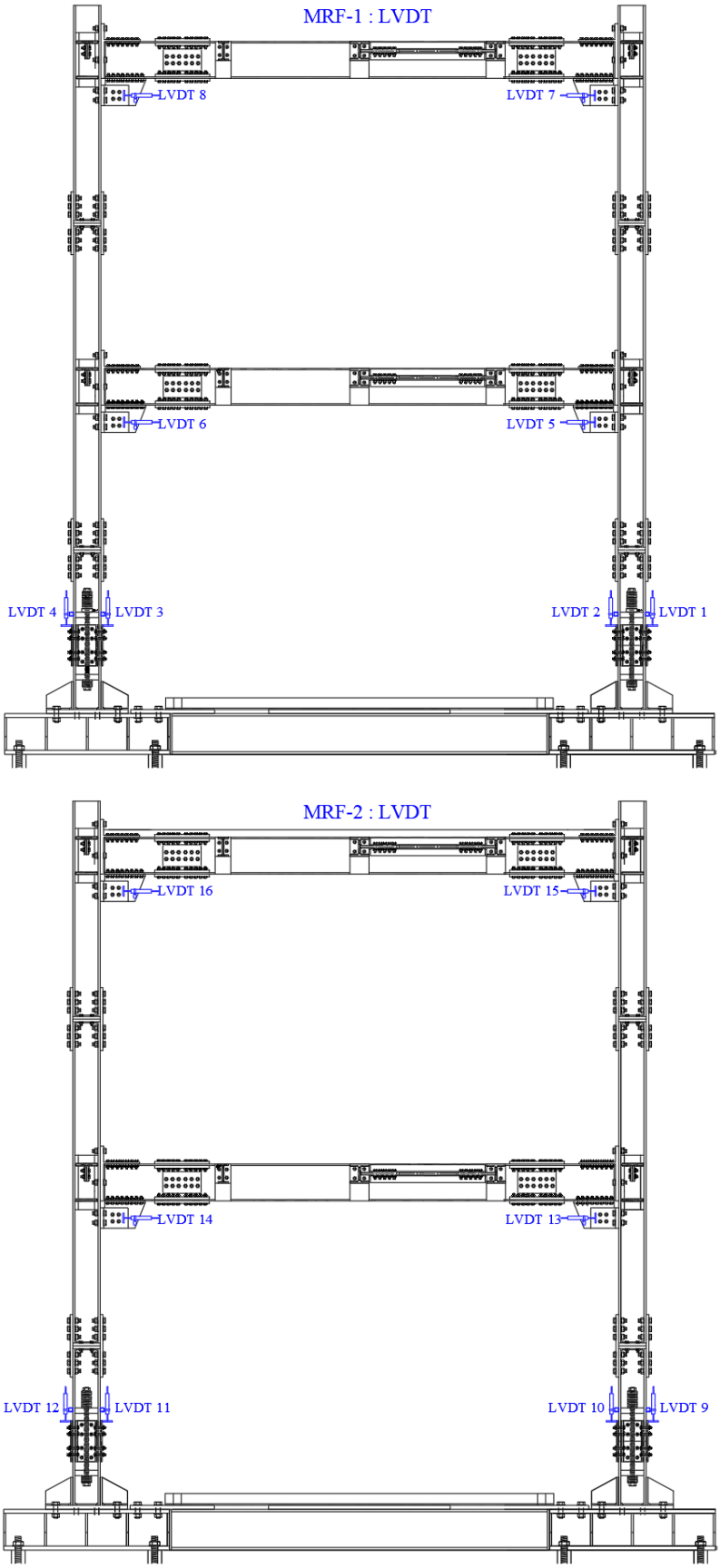

Figure 6.43. Location of the LVDT.

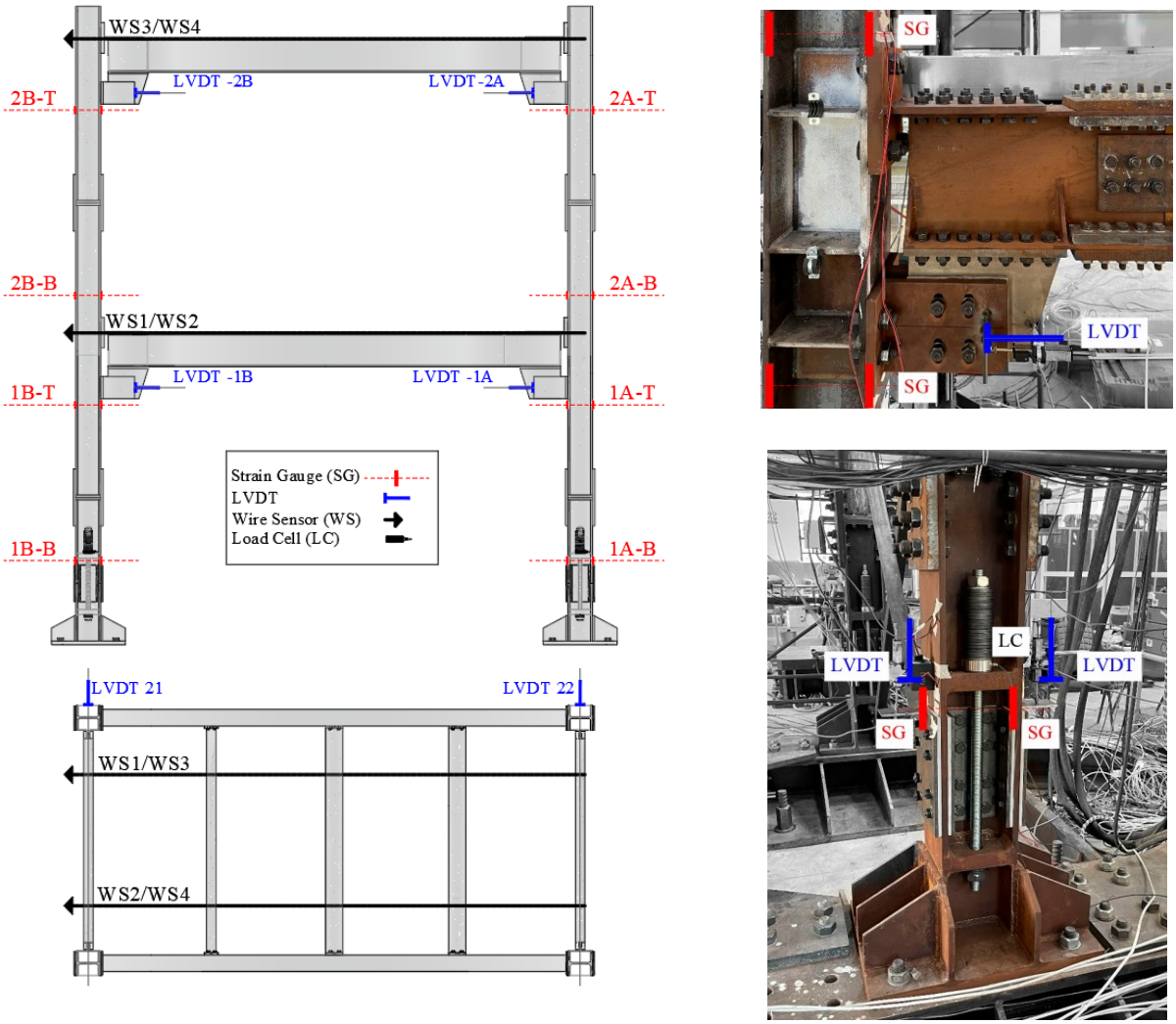

Figure 6.44. Scheme of the instrumentation.

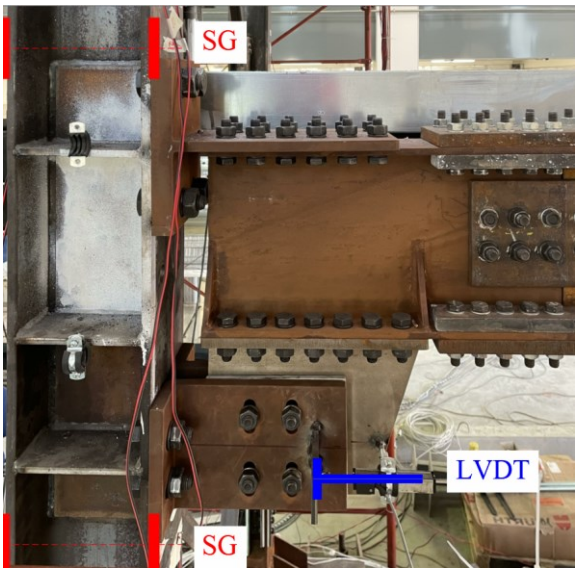

Figure 6.45. Location of the instrumentation for the FREEDAM BCJ.

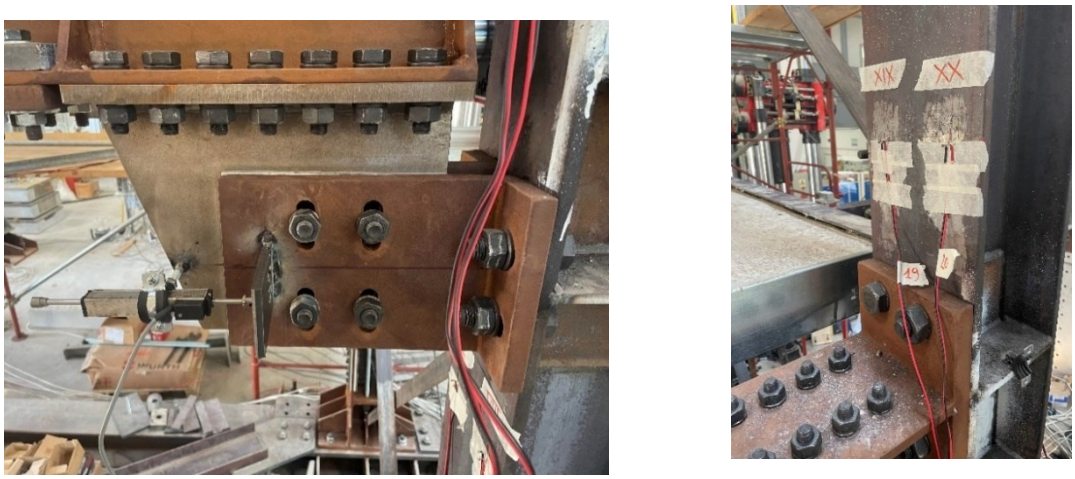

Figure 6.46. Details of the instrumentation for the FREEDAM BCJ.

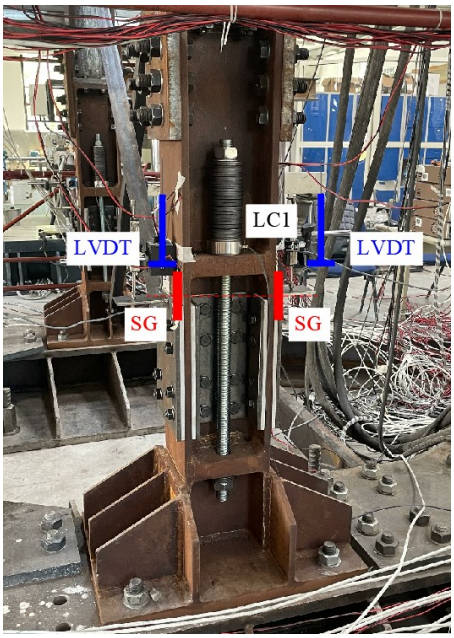

Figure 6.47. Location of the instrumentation for the SC-CB connection

Figure 6.48. Details of the instrumentation for the FREEDAM BCJ

6.5.4 Ground motions and test sequence

The Pseudo 2 software [9] provided by MTS Company has been used to perform the tests, adopting a time step of the algorithm equal to 0.01s. The algorithm is set to eventually reduce the time step if the equation of motion does not converge at a given time step. The mass matrix is defined starting from the loads previously introduced. Referring to the overall loads calculated for the couple of MRFs, the mass matrix can be written as:

$$\boldsymbol{M} = \begin{bmatrix} 38 & 0 \\ 0 & 28.4 \end{bmatrix} ton$$

The ground motion records have been chosen within a set of natural accelerograms, with a spectrum-compatibility selection with the Eurocode 8 [13] design spectrum (Figure 6.49) (*i.e.,* their mean spectrum is consistent with the type-1 spectrum for a PGA equal to 0.35g and a type-B soil).

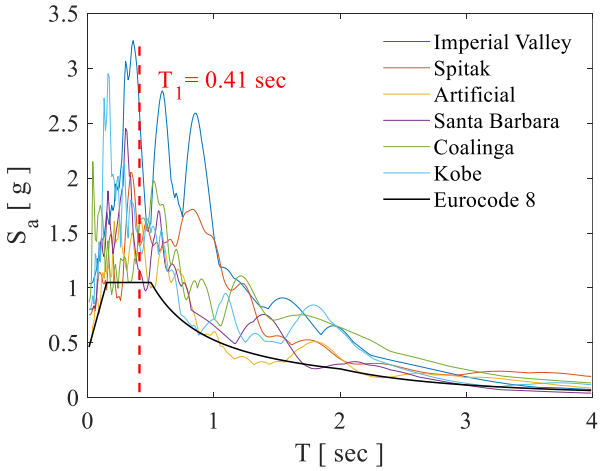

Figure 6.49. Spectra of the accelerograms (amplified PGAs)

The seismic inputs are shown in Figure 6.50. The Imperial Valley earthquake was applied to the building as the first seismic input. Instead, the second accelerogram, Spitak, was chosen because it is characterised by one main peak with significant amplitude. The third earthquake is an artificial seismic input obtained through the SIMQKE [31] tool by applying the same previous input parameters to investigate the effects of an earthquake characterized by a high number of peaks in terms of accelerations. Conversely, several peaks of moderate amplitudes characterised the other accelerograms. The high overstrength exhibited by the structure in previous experimental tests [6-7] required an increase in the values of the PGA for all the tests; therefore, the sequence of ground motion records has been applied using amplified PGAs. For example, the natural PGA of Test 1 (*i.e.,* Imperial Valley) was equal to 0.37g, but an amplified PGA equal to 1.10g, about three times the real one, has been employed. It is also highlighted that several zero acceleration points have been added to the end of each record to allow the free vibrations to stop and capture the residual deformations correctly and compatibly with the testing equipment.

Table 52 reports the matrix for the PsD [8] tests with the indications of the station, the magnitude, the fault mechanism, the direction, as well as the natural amplified PGAs used for the test. Firstly, preliminary tests have been carried out to obtain the modal properties of the structure. The fundamental period was estimated as T_1 = 0.41 sec. Subsequently, the sequence of eight scaled ground motions has been defined and applied. It is worth highlighting that Table 52 lists the spectral accelerations Sa(T_1) related to the ground motion spectra of the PsD tests (*i.e.,* with amplified PGAs), corresponding to the fundamental period of the structure (*i.e.,* T_1 =0.41sec). Figure 6.51(a) shows the test specimen in the configuration adopted for Tests 1 to 6. Two additional tests were successively carried out to investigate the influence of the axial force in the SC-CB for the self-centring behaviour. Test 7 was carried out by considering additional distributed gravity loads at both levels (*i.e.,* 3.50 kN/m^2), applied with flexible water tanks, as illustrated in Figure 6.51(b). Test 8 has been performed with the additional load but without the PT bars. This test aims to investigate the influence of the gravity load and the corresponding axial force in the column. Conversely, Test 8 was performed with the additional load but without the PT bars. For this case, the tightening of the bolts of the CBs' FDs was properly increased to cope with the reduction of the flexural resistance deriving from the decrease of the decompression moment. It is worth mentioning that, in all tests, the initial PT force was always equal to 400 kN for each bar, except for Tests 5 and 6, where it was approximately 350 kN.

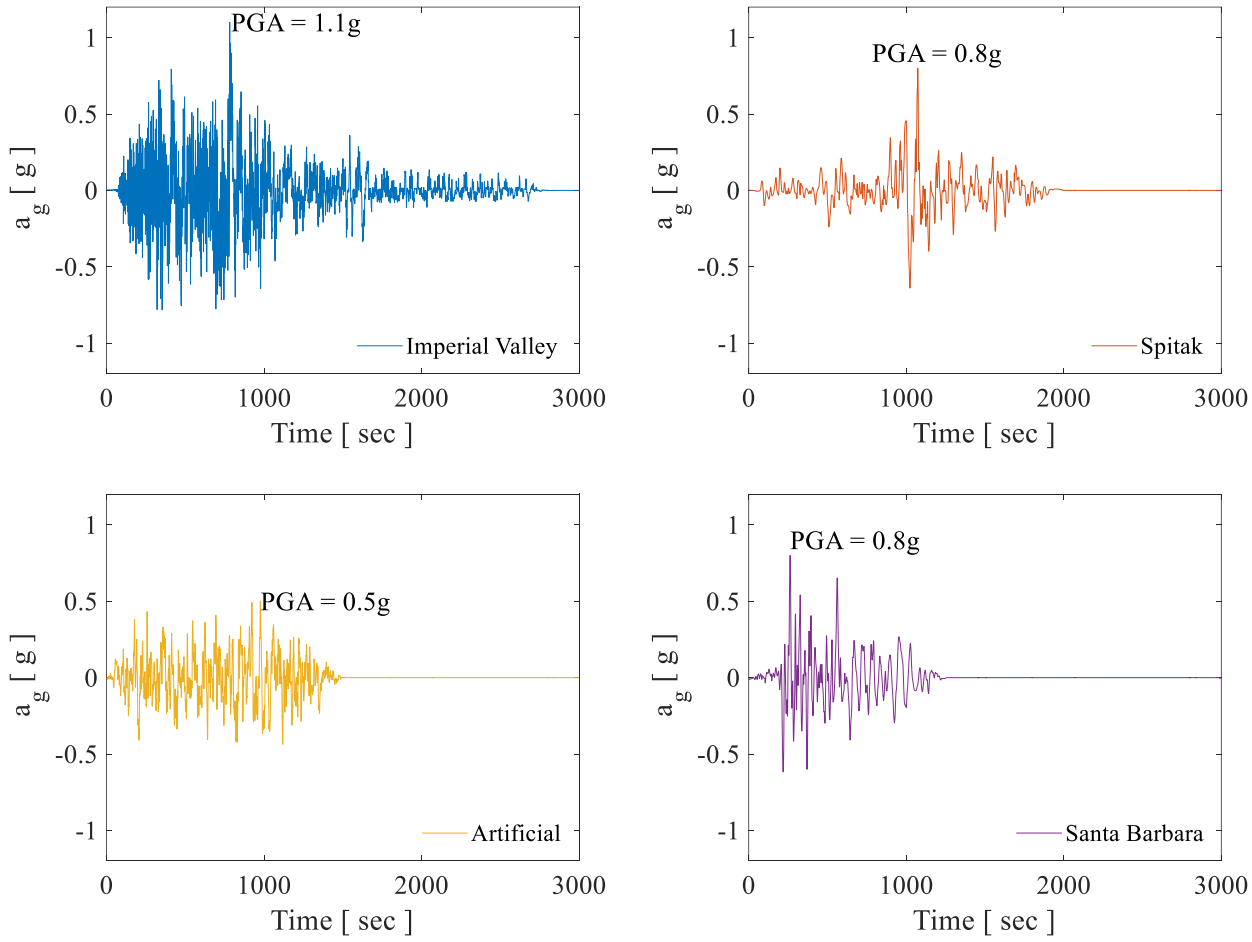

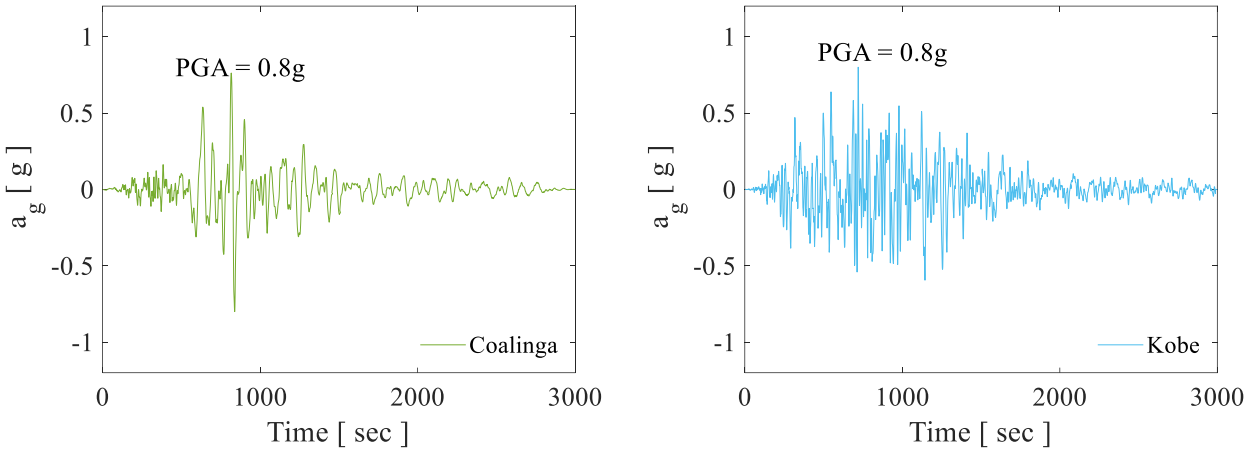

Figure 6.50. Accelerograms used for the test (amplified PGAs)

Table 52. Test Matrix

Test	Input	Station	Date	Direction	Natural PGA	PGA for the PsD	$S_a(T_1)$
[-]	[-]	[-]	[-]	[-]	[g]	[g]	[g]
1	Imperial Valley	Agrarias, USA	15/10/1979	N/S	0.37	1.10	2.01
2	Spitak	Gukasian, Armenia	07/12/1988	N/S	0.20	0.80	1.38
3	Artificial	SIMQKE_GR	-	-	0.35	0.50	1.56
4	Santa Barbara	Courth house, USA	13/08/1978	N-S	0.10	0.80	1.16
5	Coalinga	Slack Canyon, USA	02/05/1983	N/E-S/W	0.17	0.80	1.62
6	Kobe	Kakogawa, Japan	16/01/1995	N/S	0.25	0.80	1.40
7[1]	Imperial Valley	Agrarias, USA	15/10/1979	N/S	0.37	1.10	2.01
8[2]	Imperial Valley	Agrarias, USA	15/10/1979	N/S	0.37	1.10	2.01

[1] **Note**: additional distributed loads.

[2] **Note**: additional distributed loads and without the PT bars.

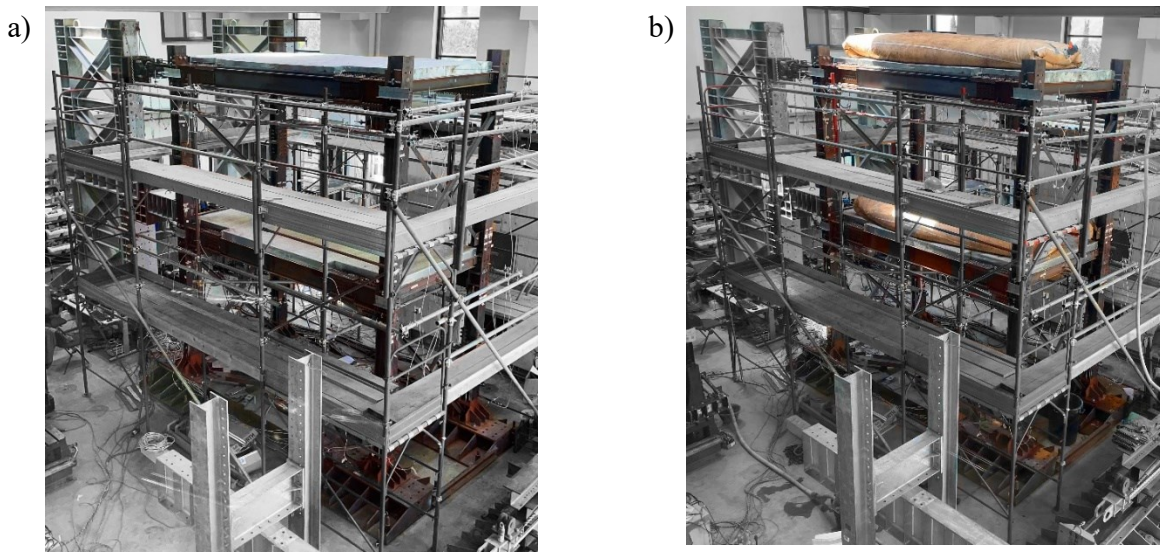

Figure 6.51. Tested specimen: a) Test 1 to 6; (b) Test 7-8

It is worth mentioning that the same friction pads were used in all the tests for the FDs of both the DF-BCJs and SC-CB connections. However, at the end of each test, the structure was repaired to perform the following tests. The repair process consisted of loosening the bolts of the FDs of the DF-BCJs and SC-CBs and re-tightening them to obtain the predefined preloading force. In addition, it is worth mentioning that, at the end of each test, the PT bars were re-tightened to obtain the predefined PT forces.

6.6 Results and Discussion

6.6.1 Modal properties

The stiffness and the modal properties of the tested structure were experimentally assessed through white-noise tests. Figure 6.52 reports the results of the tests performed with the sinusoidal input. The initial stiffness matrix was experimentally evaluated through preliminary elastic tests (*i.e.,* elastic test and sinusoidal input). The mass matrix considered for the numerical model of the PsD testing procedure was a diagonal matrix with values equal to 38 and 28.4 tons. The first and second natural periods of the MRFs in the tested direction were equal to 0.41 sec and 0.19 sec, respectively, and the participating mass of the first mode was equal to 88%. The viscous damping matrix was defined according to the Rayleigh approach, assuming a damping ratio for the two natural modes equal to 3% through the following damping constants: $\alpha M = 0.3607$ sec^{-1} and $\beta K = 0.000932$ sec.

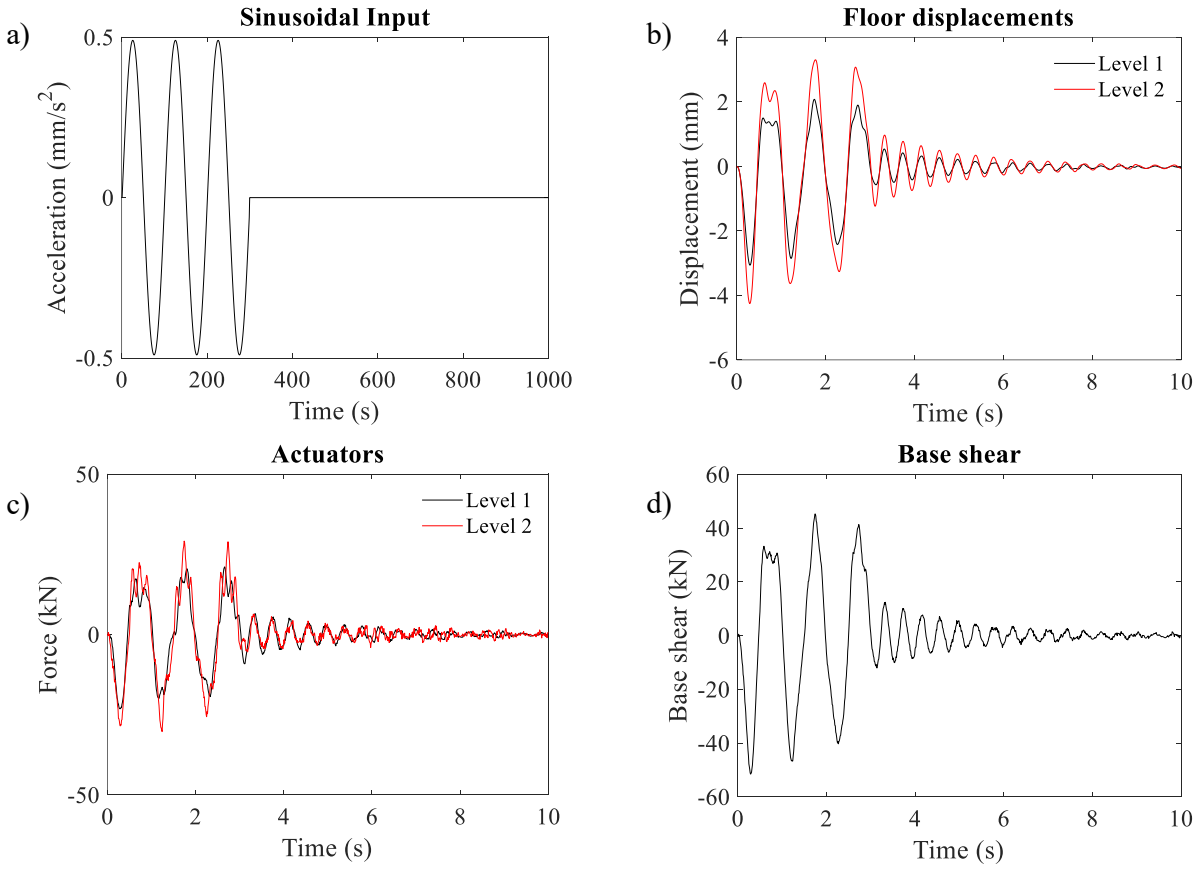

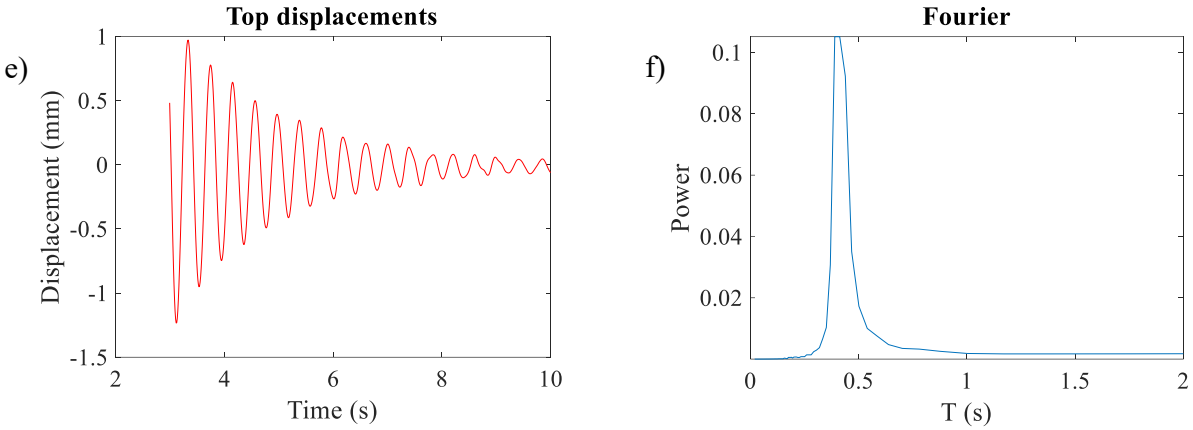

Figure 6.52. Sinusoidal input and results.

6.6.2 Imperial Valley (PGA = 1.10g)

6.6.2.1 Global Results

After the preliminary tests, the structure was subjected to the Tests Matrix discussed in the previous section. It is worth highlighting that the structure was subjected to the entire test sequence and ground motion intensities without any structural failure or significant residual drifts after testing. In addition, all the ground motions were successfully completed. The global results are shown in terms of displacement, Interstorey Drifts (IDRs), actuator forces and base shear (V_b) time histories for all the ground motion records (*i.e.,* Tests 1 to 8). The maximum values of these quantities (IDR_{Peak} and $V_{b,\,Max}$) are highlighted for both stories. In addition, the values of Residual IDR (IDR_{Res}) are compared with the repairability limit of 0.5% [10], which is conventionally assumed as a permissible residual drift to ensure buildings' repairability. For the sake of brevity, in this section, the global and local results are shown in detail for three records, while the other test results are shown in ANNEX B. Figure 6.53 shows the global results for Test 1 (*i.e.,* Imperial Valley PGA= 1.10g) in terms of displacement and interstorey drift histories, actuator forces and base shear.

The displacements at the first and second floors achieved peak values equal to 79.38 and 153.70 mm, corresponding to peak interstorey drifts of 3.31% and 3.10%, respectively. These values were well beyond the nominal elastic limit of the structure (equal to 1% according to the design), and the response was characterized by extensive slippage of the DF-BCJs and SC-CBs. The residual displacements experienced values of 7.28 and 19.59 mm at the first and second levels, corresponding to IDR_{Res} of 0.30% and 0.51%, respectively. It is possible to see that the first-storey IDR_{Res} was lower than the limit of 0.5% [10] due to the influence of the SC-CBs localised at the base. Conversely, the second-storey IDR_{Res} was closer to the limit due to the loss of the self-centring capability of the SC-CB along the height and the structure's high involvement in the plastic range. Figure 6.53 (c) and (d) show the actuator forces and the base shear, evidencing that the peak responses in terms of displacements and forces occur at the same instants for the regularity of the structure and the predominance of the first vibration mode. In addition, it is possible to highlight that, despite the different PGAs used for the tests, the maximum base shear experienced similar values for all the tests. The results are listed in Table 53.

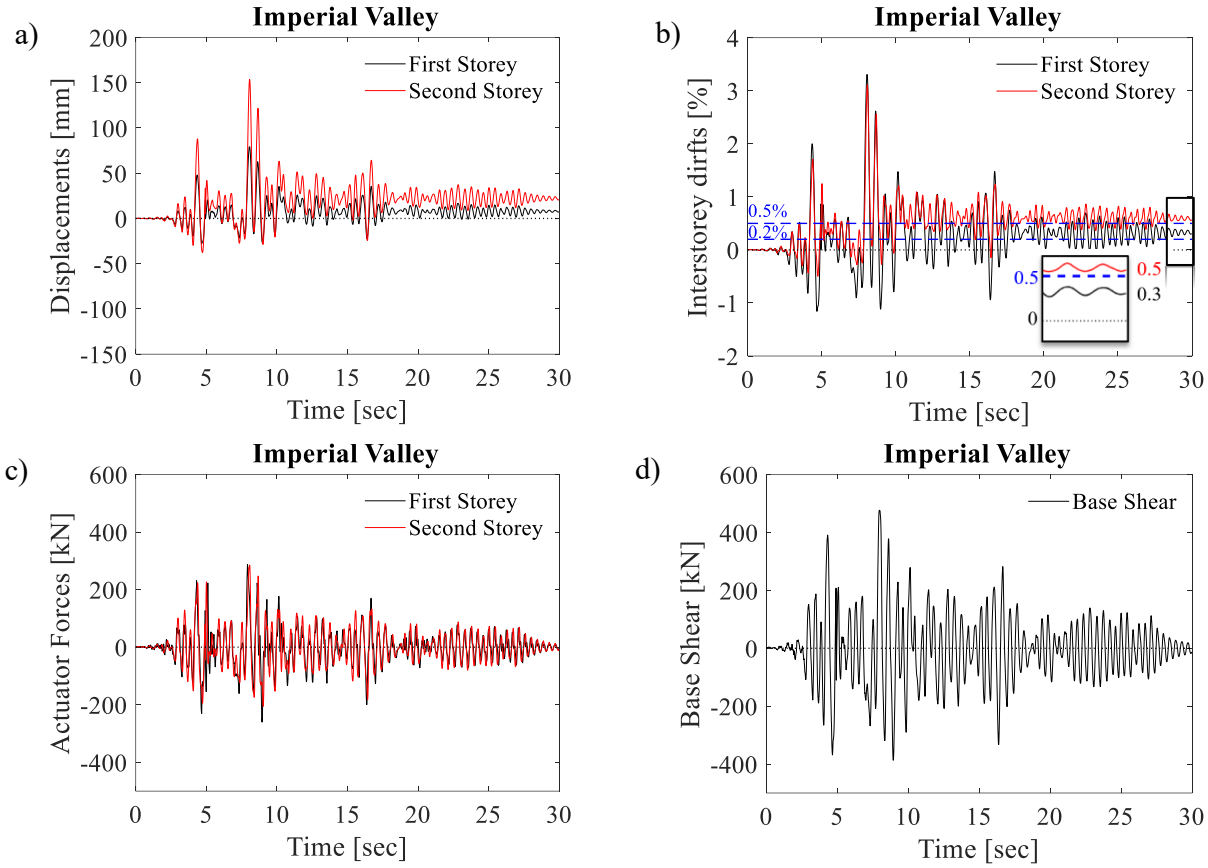

Figure 6.53. Global Results for Test 1.

Table 53. Global Results for Test 1.

Maximum Base Shear (kN)	Pull		-387
	Push		477
Peak displacement (mm)	Pull	Level 1	-27.79
		Level 2	-37.59
	Push	Level 1	79.30
		Level 2	153.58
Peak interstorey drift (%)	Pull	Level 1	-1.16
		Level 2	-0.50
	Push	Level 1	3.31
		Level 2	3.11
Residual displacement (mm)	-	Level 1	7.28
		Level 2	19.59
Residual interstorey drift (%)	-	Level 1	0.30
		Level 2	0.51

6.6.2.2 Local Results

Figure 6.54 shows the local results for Test 1 (*i.e.,* Imperial Valley – PGA = 1.10g) in terms of moment-rotation (θ_{BCJ}) of the BCJs. The hysteretic curves of the BCJs are reported only for the MRF1 (*i.e.,* BCJ 1A and 1B for the first storey and BCJ 2A and 2B for the second storey). However, consistent results

are observed for the other connections belonging to the MRF2, and they are not reported herein for brevity. The theoretical values of the maximum and minimum bending moments (M_{slip}) corresponding to the activation of the FDs of the BCJs are reported in dotted black lines. It is possible to observe that the BCJ connections experienced wide and stable hysteretic rectangular-shaped moment-rotation curves, as expected. In addition, it is possible to remark on the asymmetric behaviour of such connections, consistent with previous experimental tests on simple sub-assemblages [19]. The moments of the BCJs at the first storey achieved values of the maximum and minimum bending moments of 135 and 122 kNm, in absolute values consistent with the theoretical values (M_{slip}). The BCJs 1A and 2A experienced similar values of the maximum rotations (*i.e.,* about 0.02 rad), while the other joints reached slightly lower rotations.

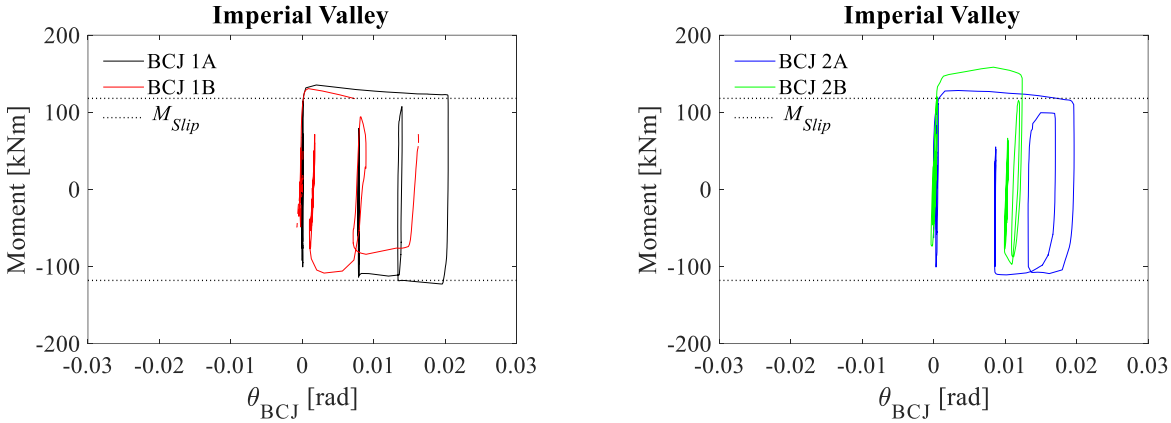

Figure 6.54. Moment-rotation curves of FREEDAM BCJs for Test 1.

Figure 6.55 shows the local results for Test 1 of the SC-CB connections. Figure 6.55 (a) shows the moment-rotation ($\theta_{SC\text{-}CB}$) behaviour of the SC-CB, which experienced a flag-shaped hysteretic curve with good self-centring behaviour and negligible residual rotations (*i.e.,* 0.001 rad). In addition, it is possible to observe that the SC-CB experienced only positive values of the rotation up to 0.02 rad, as peaks of higher amplitude characterised the accelerogram only in the positive direction. The moment corresponding to the gap opening (M_1) was consistent with the theoretical value. Conversely, the moment corresponding to the maximum rotation (M_2) obtained by the experimental results was lower than the theoretical value, as the maximum rotation achieved by the joint (*i.e.,* 0.02 rad) was lower than the target rotation. Figure 6.55 (b) shows the force fluctuation in the PT bars, which evidences a significant variability of the pre-loading forces in the PT bars during the loading history. The design initial PT force was equal to 400 kN for each bar, with very small differences from bar to bar. Then, both the PT bars were characterised by a loss of 10% of the initial PT force after the initial cycles of the loading history. Afterwards, they uniformly reached a relevant loss of the PT force of approximately 25% of the initial value. In addition, the tension force variation in the PT bars versus the joint rotation is illustrated in Figure 6.55 (c). The behaviour of the PT bars was mainly elastic, as evidenced in Figure 6.55 (d), which illustrates the stress-strain behaviour of one PT bar. It is highlighted that the strain measurement is directly read from the strain gauge applied on the PT bar. The measurements of the strain gauges applied on the PT bars are not reported for the sake of brevity, as their results are consistent with the measurements directly read from the load cells.

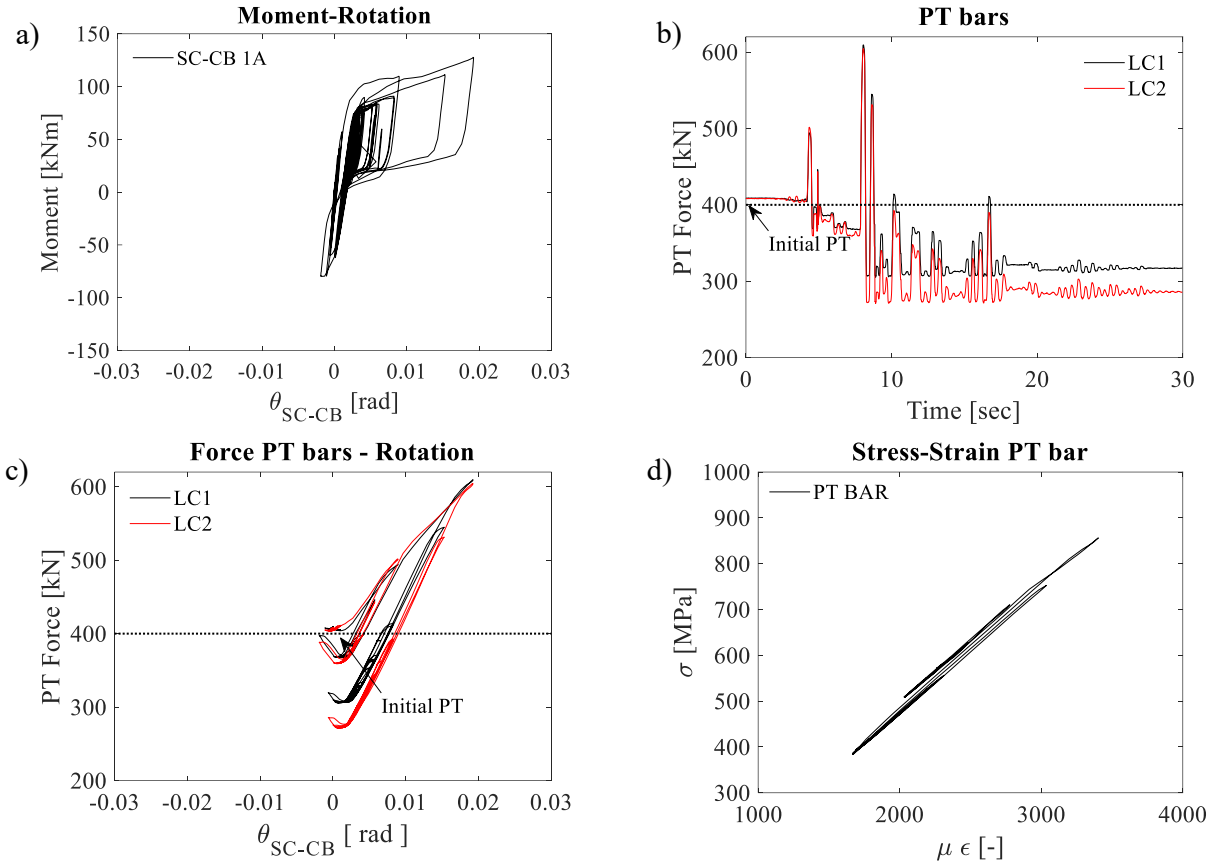

Figure 6.55. Results of SC-CB 1A for Test 1.

6.6.3 Spitak (PGA = 0.80g)

6.6.3.1 Global Results

Figure 6.56 shows the global results for Test 2 (*i.e.,* Spitak – PGA = 0.80 g). It is worth highlighting that the time history of this accelerogram was characterized by a single peak of modest amplitude leading to a single excursion of the structure beyond the elastic range. The residual displacements were equal to 1.52 and 5.73 mm at the first and second levels, corresponding to IDR_{Res} of 0.06% and 0.18%, respectively. In this case, the structure experienced IDR_{Res} lower than the 0.2% limit [11] at both storeys. The results are listed in Table 54.

6.6.3.2 Local Results

Figure 6.57 shows the local results for Test 2 (*i.e.,* Spitak – PGA = 0.80g). Similarly to Test 1, the hysteretic curves of the DF-BCJs at the first and second stories experienced similar responses, consistent with the theoretical values. It is worth mentioning that, considering that the Spitak accelerogram was characterized by one main large amplitude cycle, it was expected and experimentally confirmed that both the FDs of the DF-BCJs and the SC-CBs exhibited only one non-linear excursion for both directions, corresponding approximately to the instant of the loading history when the PGA was reached.

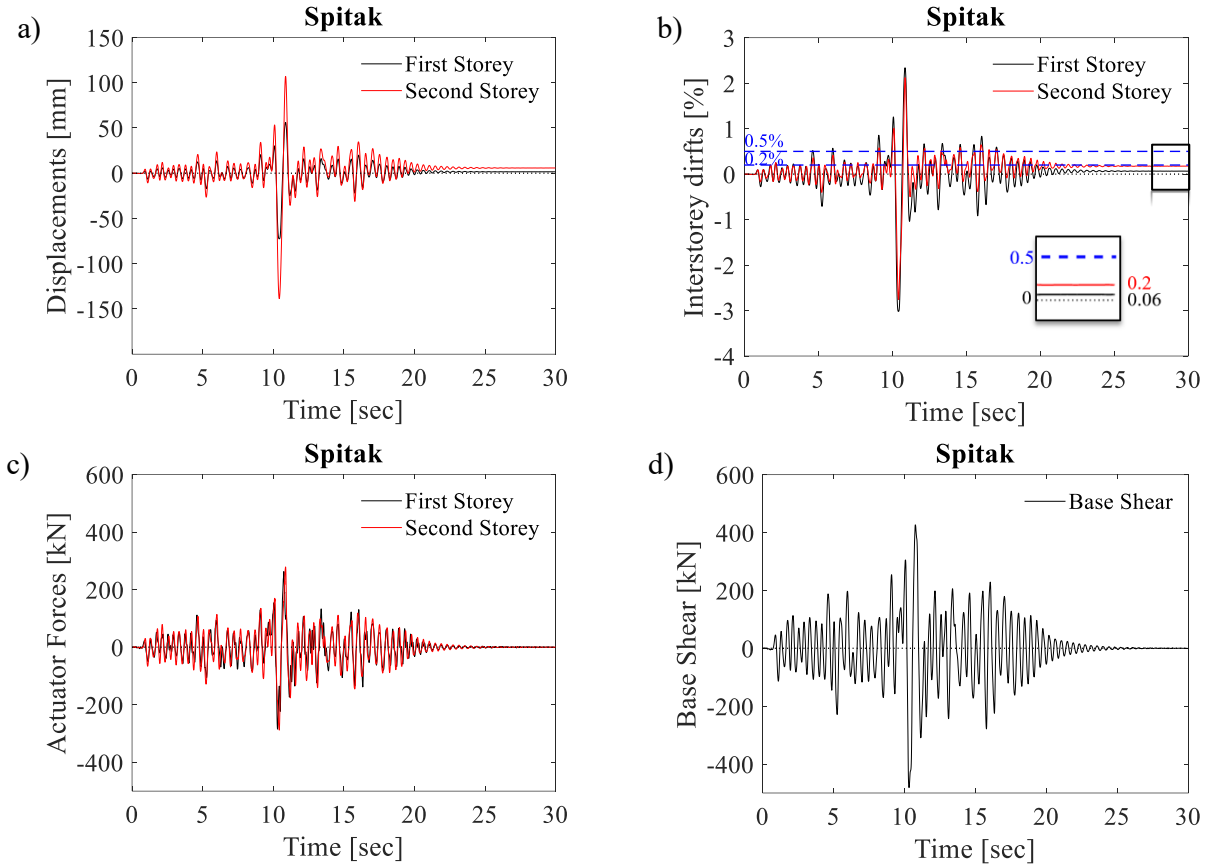

Figure 6.56. Global Results for Test 2.

Table 54. Global Results for Test 2.

Maximum Base Shear (kN)	Pull		-482
	Push		426
Peak displacement (mm)	Pull	Level 1	-72.47
		Level 2	-138.59
	Push	Level 1	56.15
		Level 2	106.91
Peak interstorey drift (%)	Pull	Level 1	-3.02
		Level 2	-2.75
	Push	Level 1	2.34
		Level 2	2.12
Residual displacement (mm)	-	Level 1	1.52
		Level 2	5.73
Residual interstorey drift (%)	-	Level 1	0.06
		Level 2	0.18

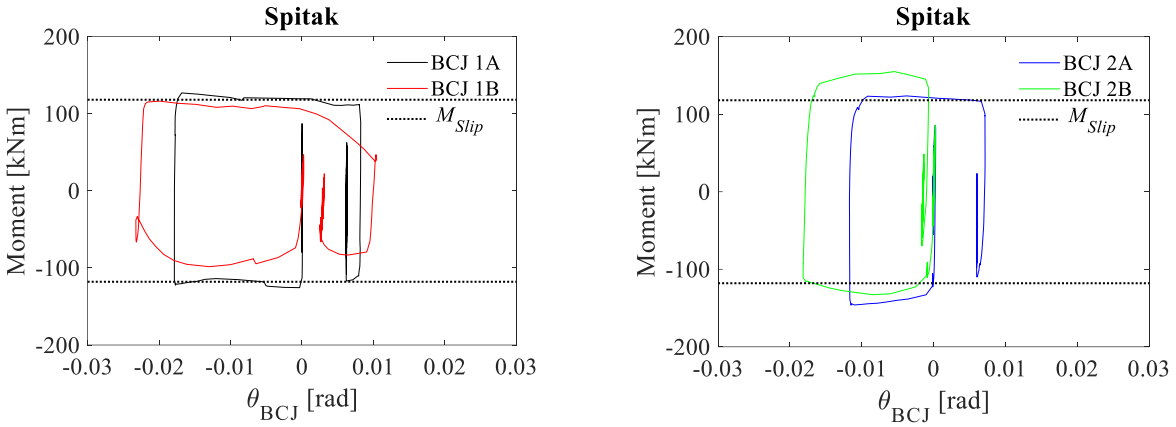

Figure 6.57. Moment-rotation curves of FREEDAM BCJs for Test 2.

Figure 6.58 shows the local results for Test 2 of the SC-CB connections.

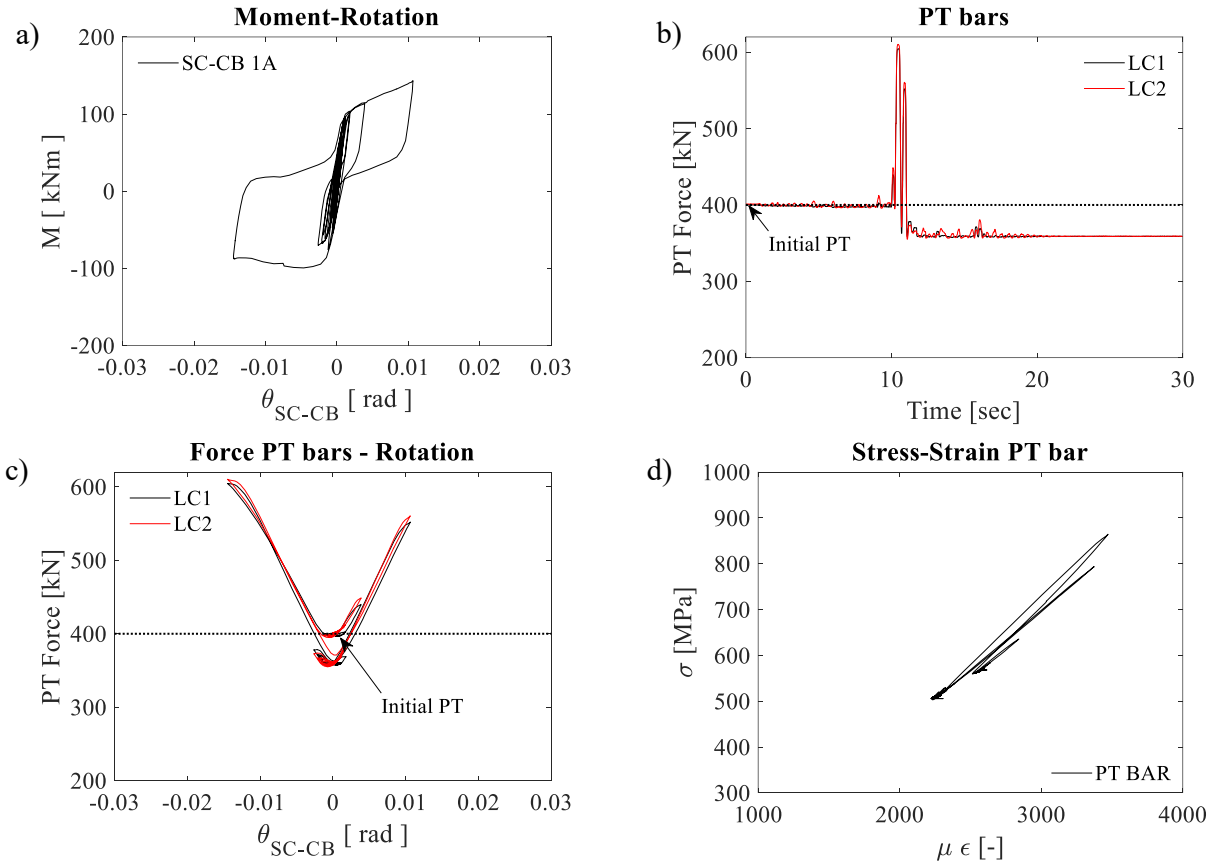

Figure 6.58. Results of SC-CB 1A for Test 2.

Figure 6.58 (a) shows that the SC-CB exhibited a flag-shaped hysteretic curve with a higher dissipative behaviour than the previous case, with rocking in both directions, characterised by positive and negative rotation values up to 0.02 rad. In addition, Figure 6.58 (b) shows a lower variability of the pre-loading forces in the bolts of the FDs and a lower force fluctuation of the PT bars during the loading history. Besides, it is observed that the two PT bars experience similar behaviour along the Test, with negligible

differences from bar to bar. Figure 6.58 (c) shows the tension force variation in the PT bars versus the joint rotation. Also, for this Test, the PT bars remained in the elastic range, as illustrated in Figure 6.58 (d).

6.6.4 Artificial record (PGA = 0.50g)

6.6.4.1 Global Results

Differently from the first and the second tests, the structure remained almost in the elastic range without relevant residual displacements in Test 3 (*i.e.,* Artificial – PGA = 0.5 g) and in Test 4 (*i.e.,* Santa Barbara – PGA = 0.8 g) tests. This is justified as peaks of relevant amplitude characterise both records; nevertheless, the adopted PGAs enabled only a moderate sliding of the DF-BCJs and the SC-CB joints. Results are illustrated in Figure 6.59 and in Table 55 for Test 3.

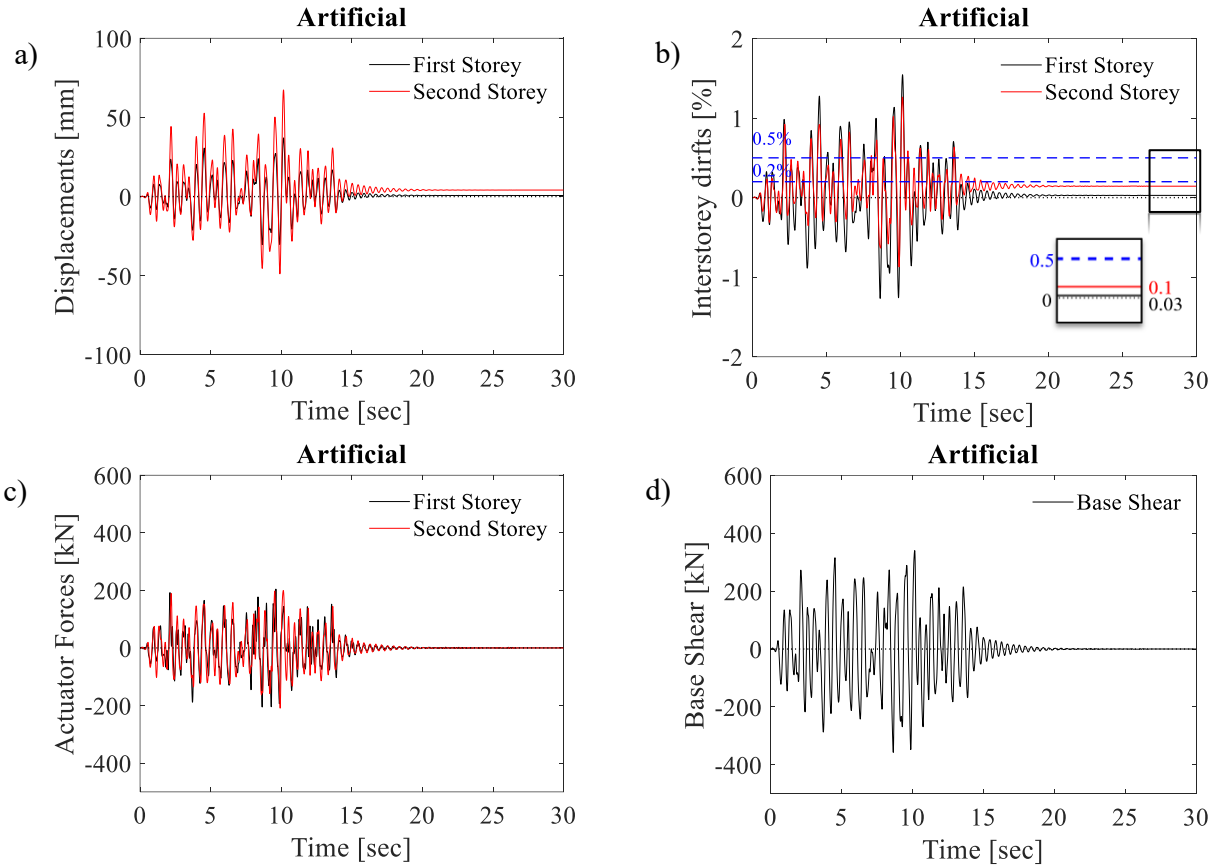

Figure 6.59. Global Results for Test 3.

6.6.4.2 Local Results

Differently from Tests 1 and 2, the DF-BCJs experienced no activation of the FDs and negligible rotations during Tests 3 (*i.e.,* Artificial – PGA = 0.50g) and 4 (*i.e.,* Santa Barbara, PGA=0.80g). A similar response was also observed in the SC-CBs, which experienced moderate sliding characterized by a maximum rotation of 0.005 rad in both tests. Results are illustrated in Figure 6.60 and Figure 6.61.

Table 55. Global Results for Test 3.

Maximum Base Shear (kN)	Pull		-358
	Push		340
Peak displacement (mm)	Pull	Level 1	-30.21
		Level 2	-48.78
	Push	Level 1	37.06
		Level 2	67.36
Peak interstorey drift (%)	Pull	Level 1	-1.25
		Level 2	-0.87
	Push	Level 1	1.54
		Level 2	1.26
Residual displacement (mm)	-	Level 1	0.65
		Level 2	4.09
Residual interstorey drift (%)	-	Level 1	0.04
		Level 2	0.23

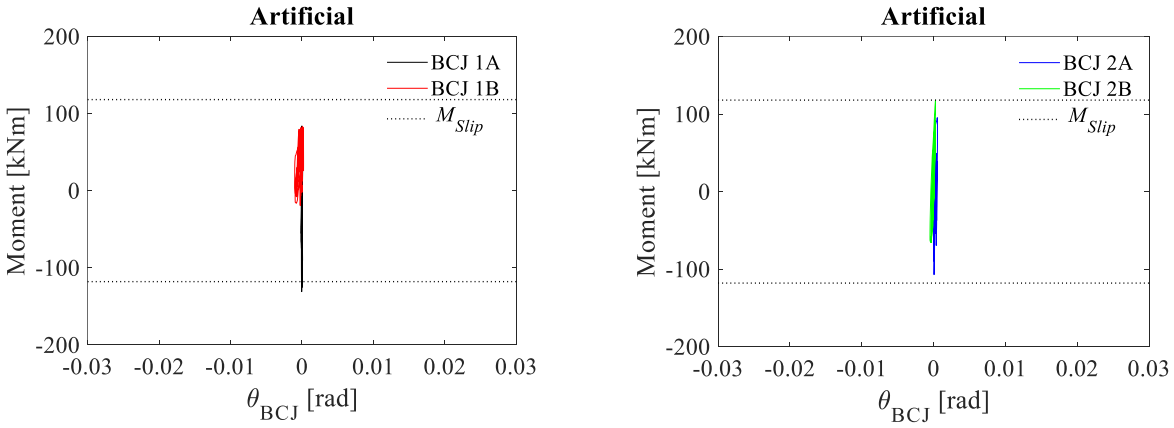

Figure 6.60. Moment-rotation curves of FREEDAM BCJs for Test 3.

Conversely, for Test 5 (i.e., Coalinga – PGA = 0.80 g) and 6 (i.e., Kobe – PGA = 0.80 g) shown in ANNEX B, the structure was highly involved in the inelastic range. In particular, for Test 5, the structure experienced the highest IDR_{Peak} among all tests. For Test 6, the IDR_{Res} experienced values of 0.34% and 0.55%, respectively, representing the highest residual drift response among all tests. Regarding the local results, for Test 5 (i.e., Coalinga – PGA = 0.80g), the DF-BCJs provided the highest energy dissipation with several hysteretic loops with rotations up to 0.02 rads in both directions. Similar behaviour was also observed in the SC-CBs. Similar results, but with lower rotations, were observed during Test 6 (i.e., Kobe – PGA = 0.80g). The main global and local results are summarised in Table 56 and in Table 57, while the extended results of the other tests are shown in the ANNEX B. Additional considerations about Tests 7 and 8 and the structure's repairability and resilience are further discussed in Section 6.10.

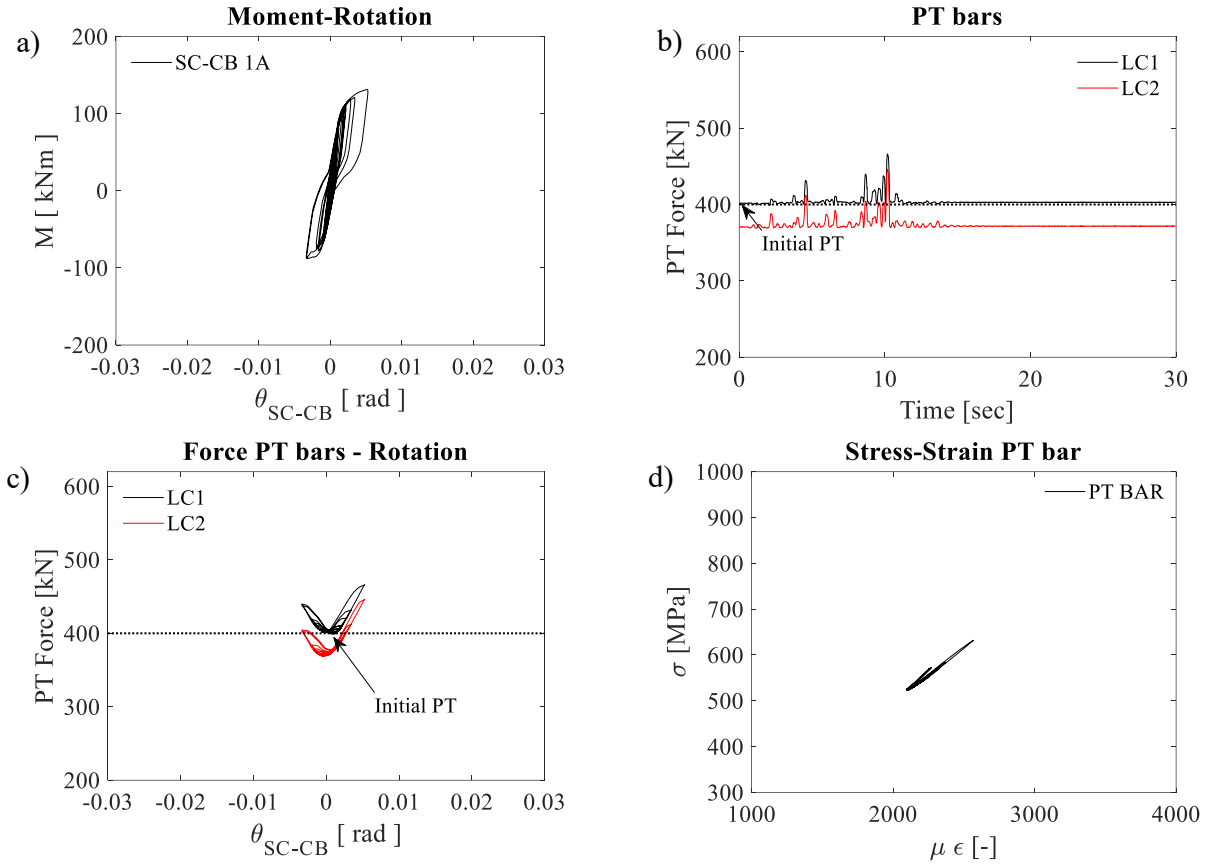

Figure 6.61. Results of SC-CB 1A for Test 3.

Table 56. Global results for all tests.

Test [-]	Input [-]	$d_{Max,1}$ [mm]	$d_{Max,2}$ [mm]	$d_{Res,1}$ [mm]	$d_{Res,1}$ [mm]	$IDR_{Max,1}$ [%]	$IDR_{Max,2}$ [%]	$IDR_{Res,1}$ [%]	$IDR_{Res,2}$ [%]	$F_{Max,1}$ [kN]	$F_{Max,2}$ [kN]	$V_{b,Max}$ [kN]
1	Imperial Valley	79.38	153.70	7.28	19.59	3.31	3.10	0.30	0.51	287	286	478
2	Spitak	72.47	138.59	1.52	5.73	3.02	2.75	0.06	0.18	285	288	482
3	Artificial	37.06	67.36	0.65	4.09	1.54	1.26	0.03	0.14	205	209	358
4	Santa Barbara	38.27	66.84	0.88	6.35	1.59	1.19	0.04	0.23	261	237	410
5	Coalinga	74.94	156.22	7.33	20.51	3.12	3.39	0.31	0.54	314	267	437
6	Kobe	51.17	93.86	8.11	21.10	2.13	1.78	0.34	0.55	258	276	405
7[1]	Imperial Valley	78.19	156.60	10.61	26.33	3.25	3.27	0.44	0.65	296	291	472
8[2]	Imperial Valley	86.75	172.74	35.30	74.21	3.58	3.61	1.47	1.62	291	281	449

Notes: [1]Additional distributed loads, [2]Additional distributed loads without the PT bars.

Table 57. Local results for all tests.

Test [-]	Input [-]	$M_{BCJ, Max,1}$ [kNm]	$M_{BCJ, Max,2}$ [kNm]	$\theta_{BCJ, Max,1}$ [mrad]	$\theta_{BCJ, Max2}$ [mrad]	M_1 [kNm]	M_2 [kNm]	$\theta_{SC-CB, Max}$ [mrad]
1	Imperial Valley	135, -122	128, -110	20.4	19.6	98.1	128	19.2, -1.9
2	Spitak	127, -126	124, -126	17.9	11.7	95.5	131	10.6, -14.5
3	Artificial	84, -131	96, -107	≅0	≅0	96.1	124	5.2, -3.3
4	Santa Barbara	75, -128	95, -124	≅0	≅0	90.1	111	5.3, -3.3
5	Coalinga	129, -133	118, -137	20.5	15.2	99.5	157	14.5, -10.8
6	Kobe	123, -125	108, -122	3.0	6.5	88.4	120	8.1, -9.3
7[1]	Imperial Valley	116, -117	111, -107	22.7	23.9	95.9	133	16.0, -5.0
8[2]	Imperial Valley	121, -104	129, -98	17.4	26.1	67	130	20.0, -2.1

Notes: [1]Additional distributed loads, [2]Additional distributed loads, without the PT bars.

6.7 Test observations

Figure 6.62 (a) and (b) show two SC-CB displacement configurations at the onset of rocking on the right and left edges for rotations of 0.02 rads. At the same instant, the structure exhibited the deformed configuration illustrated in Figure 6.63. Test observations at the end of the experimental campaign showed that the first-storey columns experienced no damage and were fully protected from yielding.

a) b)

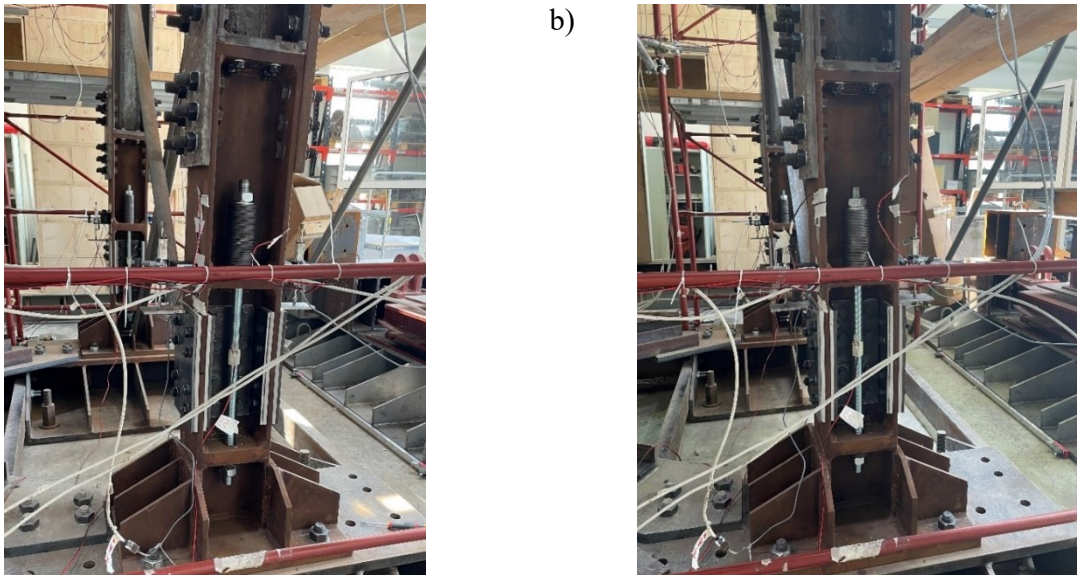

Figure 6.62. Test observations. Self-Centring Column Base (SC-CB) (a) rocking on the right edge with 0.02 rads; and (b) rocking on the left edge with 0.02 rads.

Figure 6.63. Test observations. Deformed configuration of the tested specimen.

Conversely, the energy dissipation was concentrated in the friction pads of the web and flange FDs of the SC-CBs, which resulted in scratches due to the sliding, as expected. In fact, the DF-BCJs practically exhibited no damage, except for the expected wearing of the friction pads belonging to the FDs, confirming the behaviour already exhibited in previous experimental tests [6]. Similarly, the SC-CBs exhibited no damage, except for the expected wearing of the friction pads belonging to the FDs (see Figure 6.64). On the contrary, it is worth highlighting that the same structure equipped with only the DF-BCJs and subjected to the same test sequence exhibited damage in the first-storey columns, which experienced yielding, physically recognised by the yield lines appearing on the surface of the column at the end of the experimental campaign [6].

Figure 6.64. Test observations. Damage in the friction pads of the SC-CBs at the end of the experimental campaign

6.8 Finite Element Modelling (FEM) and Validation

6.8.1 FE modelling

A 2D non-linear FE model of the MRF is developed in OPENSEES [12] to achieve different objectives: *i)* to perform blind predictions of the seismic performance of the structure; *ii)* to check the compatibility with the capacities of the test equipment (*i.e.,* with the actuators' limits in terms of displacements and forces); *iii)* to validate the modelling strategy. Figure 6.65 shows an overview of the OPENSEES [12] model with the details of the modelling strategy for the BCJs and the SC-CBs. The modelling strategy for the FE modelling is based on a mixed lumped and distributed plasticity approach. Beams and columns are modelled with inelastic displacement-based '*nonlinearBeamColumn elements*' [12] with four integration points. Each section is discretised into eight fibres along with the depth and four along each flange. Both beams and columns are defined by the 'Steel01' material [12] with 275 MPa and 355 MPa yield strength, respectively and 0.2% post-yield stiffness ratio. The 'section aggregator' function [12] accounts for the column's shear stiffness. Geometric nonlinearities are considered in the elements of the structure. The rigid-floor diaphragm is modelled by assigning a high value to the axial stiffness of the beams. Gravity loads are applied on the beams by considering the seismic combination of Eurocode 8 [13]. Lumped masses are concentrated below the centre of the spans to model the actuators' application points in the set-up. Damping sources other than the hysteretic energy dissipation are

modelled through the Rayleigh damping matrix, where the values of the mass-related and stiffness-related damping coefficients are considered for a damping factor of 3% for the first two vibration modes.

The BCJ strategy modelling is consistent with Di Benedetto *et al.* [6]. The rigid elements of the joints are modelled with *'elastic beam-column elements'* [12] with very high flexural stiffness. A hinge is used to model the physical location of the COR, located at the level of the T-stub, with a rotational spring represented by a '*zero-length element*' [12]. The FD is placed at the damper's centreline and modelled by a translational spring represented by a '*zero-length element*' [12] defined by '*uniaxial hysteretic material*' [12] with symmetric trilinear force-displacement law. This material adopts a yielding force equal to the sliding force of the FDs and negligible post-elastic hardening to simulate the FDs' behaviour. It is highlighted that the connection is conceived to concentrate the energy dissipation within the FDs; therefore, all the other nodal components have been modelled to have an elastic behaviour. Therefore, the PZ has not been explicitly modelled.

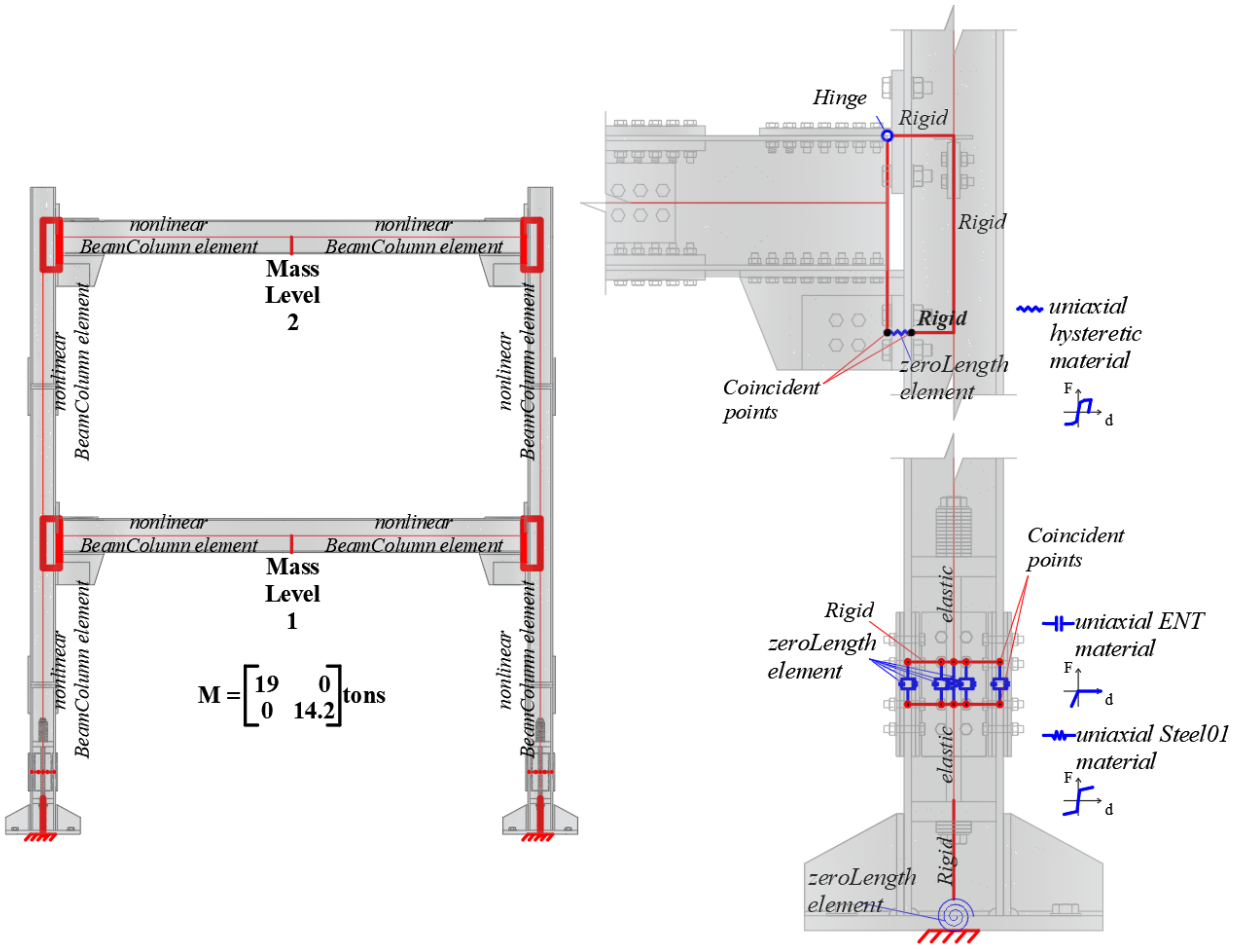

Figure 6.65: OPENSEES [12] model

The SC-CB strategy modelling is consistent with the validated strategy defined by Elettore *et al.* [29]. It consists of a 2D non-linear FE model where the rocking interface is modelled with 8 rigid *'elastic beam-column elements'* [12] with very high flexural stiffness. The web and flanges FDs are modelled with 4 translational springs represented by four' *zero-length elements*' [12]. They are defined by the

'*Steel01*' material [12], considering a rigid initial behaviour and a very low strain-hardening ratio to simulate the rigid plastic behaviour and a yield strength equal to the design slippage forces in the web and flanges FDs. The rocking behaviour is modelled with 4 translational springs' *zero length elements*' [12]) defined by the '*Compression-no-tension (ENT)*' material [12] with a very high value of the compression stiffness to capture the contact behaviour. The SC system is modelled with a single translational spring represented by a single '*zero-length element*' [12] with bilinear elastic-plastic behaviour. It is defined by the '*Steel01*' material [12], with an elastic stiffness equal to the equivalent stiffness and the yield strength of the SC system obtained from the design procedure. The initial PT force is modelled by imposing an initial strain using the '*Initial strain material*' [12]. The material properties for all the components are defined in Table 47. An additional rotational spring represented by a '*zero-length element*' [12] is included at the base plate level of each first-storey column to account for the deformability of the rigid base of the experimental set-up equipment.

6.8.2 Validation

The modelling strategy is validated by comparing the numerical FE model in OPENSEES [12] against the experimental results for all tests. The model was developed for a single MRF; however, the results of the validation process are shown for the whole structure. For validation purposes, quasi-static analyses have been performed by applying the horizontal displacement time histories obtained from the experimental results. The input displacements have been applied to two control points at the first and second stories corresponding to the actuators' application points. For the sake of brevity, the results for the modelling validation are shown only for Test 1 and Test 2. However, consistent results are obtained from the other comparisons, and the following considerations can be extended to all cases whose results are shown in ANNEX B. The validation process has been performed for global and local responses to gain confidence in the modelling assumptions and the numerical results, including the local behaviour of the DF-BCJs and SC-CBs. Figure 6.66 shows the displacements and the actuator forces (required to impose the displacements time history) at the first and second stories of the structure for Test 1 (Imperial Valley – PGA = 1.10g). Similarly, Figure 6.67 shows the same results for Test 2 (Spitak – PGA = 0.80g).

Obviously, there is a perfect match of the displacements as these were imposed in the numerical model based on the experimental results. The comparison in terms of forces shows a good agreement between the numerical and experimental results, demonstrating the OPENSEES [12] model's ability to simulate the seismic response of the structures. The results show that the OPENSEES [12] model slightly overestimates the first-storey forces by approximately 15%. Conversely, the second-storey forces are slightly underestimated. This effect is attributed to the contribution of the tests' setup flexibility at the column's base connections, which is simulated in the numerical model in a simplified way. Nevertheless, the comparison of the base shear shows an almost perfect match between the numerical and experimental results with very minor differences. For the same ground motion record (*i.e.,* Imperial Valley – PGA = 1.10g), Figure 6.68 shows the comparison between the numerical and the experimental results for the DF-BCJ and the SC-CB components (*i.e.,* hysteretic behaviour of the SC-CB, PT force fluctuations, force variation in the PT bars versus the joint rotation and stress-strain behaviour of the PT bars). The comparisons are carried out for the DF-BCJ 1A and SC-CB 1A; however, consistent results are observed for the other connections, and the same considerations can be extended.

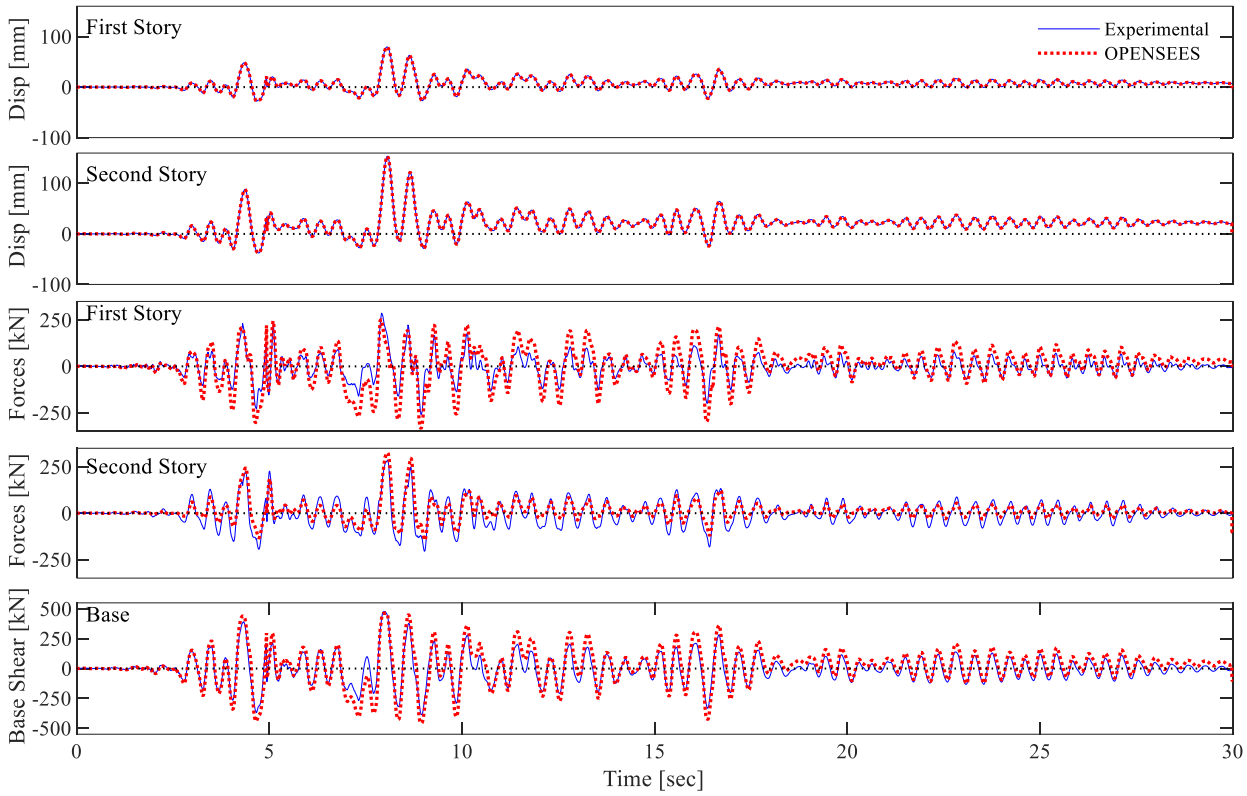

Figure 6.66. FEM validation. Displacements and actuator forces for Test 1

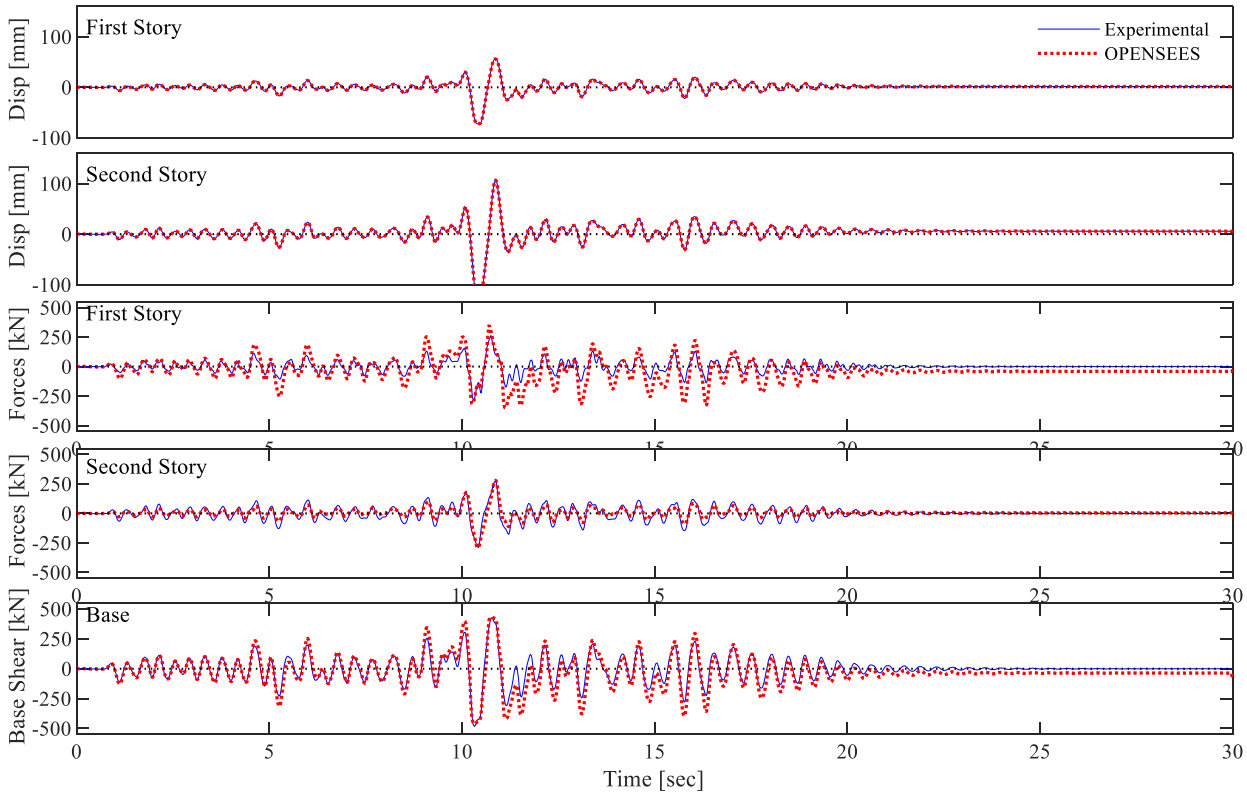

Figure 6.67. FEM validation. Displacements and actuator forces for Test 2

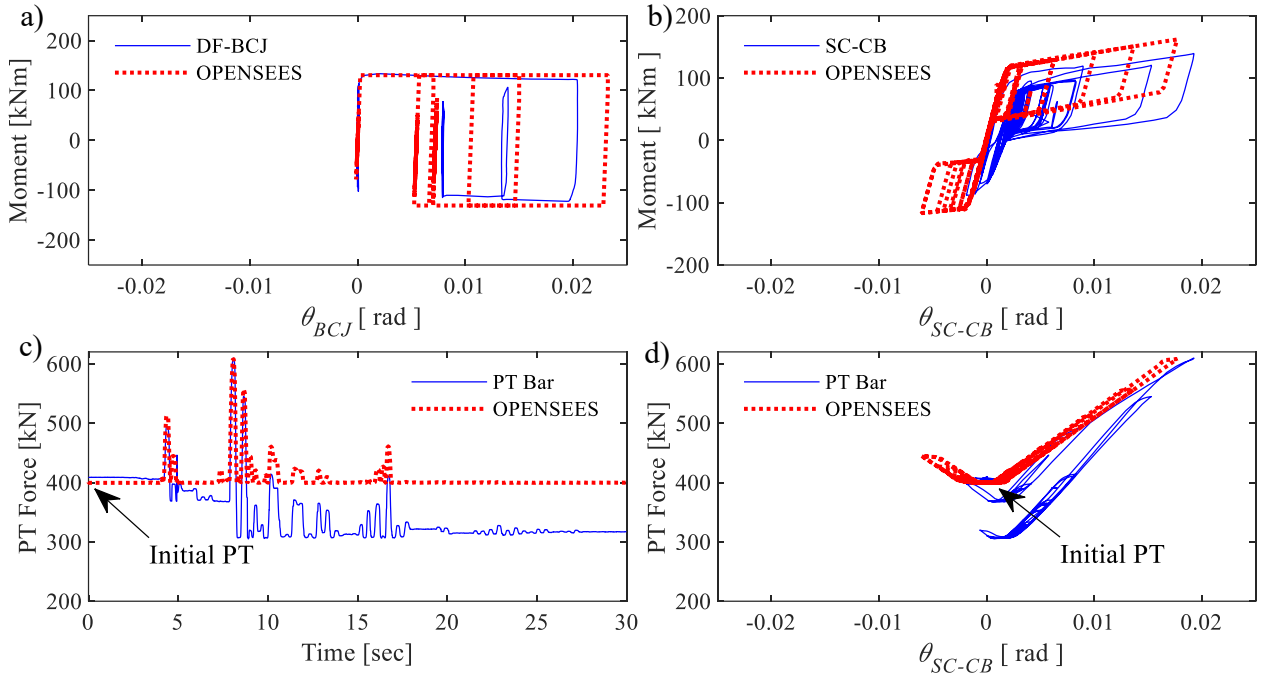

Figure 6.68. FEM validation. Local Results for Test 1

Figure 6.68 (a) shows the experimental and numerical moment-rotation curves of the DF-BCJ. The comparison highlights that the numerical model captures the moments corresponding to the activation of the FDs accurately, with a slight overestimation of the maximum rotation. Figure 6.68 (b) compares the experimental and numerical moment-rotation curves of the SC-CB. The analytical curve is not reported herein as it is based on the same assumptions and perfectly matches the numerical results. The comparison evidences that the numerical model captures the local response reasonably well. Nevertheless, some limitations can be highlighted. In particular, the numerical model shows a slightly higher strain-hardening behaviour with respect to the experimental results. This effect is mainly due to the loss of preloading forces in the FD's bolts and PT bars force experienced during the experimental tests and not simulated in the numerical model (see Figure 6.68 (c)). The initial PT force was equal to 400 kN for each bar, with minimal variations from bar to bar. Successively, the evolution of the PT force was consistent between the PT bars and reached a reduction of approximately 25%, after which it stabilized. This PT force loss occurred due to small non-linear mechanisms experienced by the SC system, including minor plastic deformations of the PT bars (*i.e.,* maximum measured PT force equal to 610 kN – nominal yielding strength of the PT bars corresponding to 522 kN) and limited non-linear response of the disk springs. The comparison of the results highlights that the numerical model successfully captures the increase in the PT force up to approximately 10 sec, while some differences can be observed for the following part of the test. Figure 6.68 (d) shows the tension force variation in the PT bars vs. the joint rotation. In addition to the PT force loss, these results showed that the face-to-face and face-to-edge friction effects of the disk springs generated some small hysteretic loops [28].

Similarly, Figure 6.69 compares the experimental and numerical local results for Test 2. Differently from Test 1, the hysteretic response of the connections experienced positive and negative rotation values

up to 0.02 rads, as the accelerogram was characterized by a large number of small amplitude cycles and a single peak of larger amplitude in both directions.

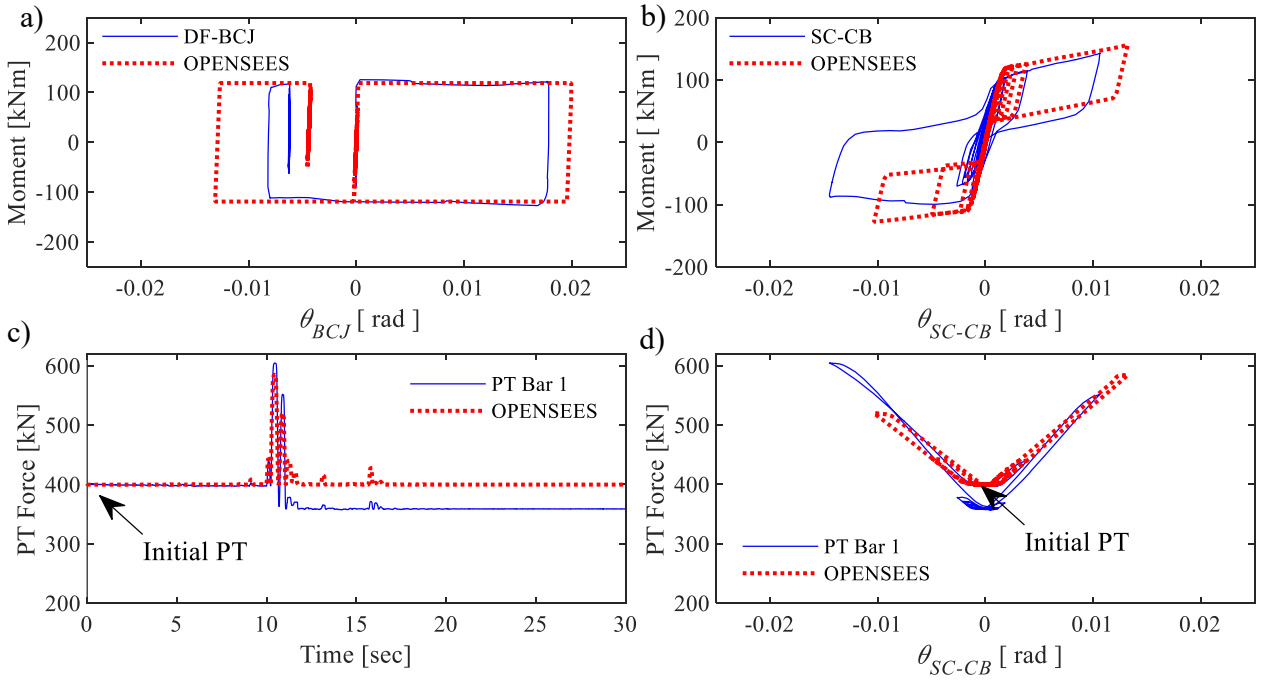

Figure 6.69. FEM validation. Local Results for Test 2

In particular, Figure 6.69 (a) compares the experimental and numerical hysteretic curves of the DF-BCJ, highlighting a satisfactory match of the results, with the numerical model only slightly overestimating the maximum rotations. Figure 6.69 (b) compares the numerical and experimental moment-rotation behaviour of the SC-CB. It is highlighted that there is no SC behaviour for one of the cycles, which may be related to the interaction of bending moments with tensile axial forces in the column. However, this did not affect the self-centering capability of the connection during the following cycles. Compared to Test 1, this test was characterized by a lower PT force loss during the loading history, illustrated in Figure 6.69 (b). Figure 6.69 (c) shows the tension force variation in the PT bars vs. the joint rotation, exhibiting the same stiffness for negative and positive rotations. Results for the other tests are shown in the ANNEX B. However, no significant force variability was observed in the PT bars for Tests 3, 4 and 6, and all the components remained in the elastic range. Conversely, in Test 5 (*i.e.,* Coalinga – PGA = 0.8g), the PT bars experienced small plastic deformations. However, this slight reduction of the axial force in the column did not significantly affect the behaviour of the SC-CB.

6.8.3 Non-linear time history analysis

In addition to the quasi-static analyses, Non-Linear Time History Analysis (NLTHA) has been performed by applying accelerations at the structure's base to assign the input ground motion. The adopted time-history analyses are characterized by a time step equal to 0.01 s. The equation of motion has been solved using the Newmark algorithm, setting a damping value equal to 3% in all the tests, with

a Rayleigh approach consistent with the pseudo-dynamic testing. For the sake of brevity, in this section, results are shown only for Test 1, while the results for the other tests are illustrated in ANNEX B. The NLTHA allowed the investigation of the modelling assumptions for predicting both the global and local responses of the DF-BCJs and the SC-CB connections with adequate accuracy. Figure 6.70 and Figure 6.71 compare the numerical and experimental results in terms of actuator forces and displacements at the first and second stories of the structure for Test 1 (Imperial Valley – PGA = 1.10g). The comparison shows a good agreement between the numerical and experimental results, demonstrating the OPENSEES [12] model's ability to simulate the dynamic response of the structure.

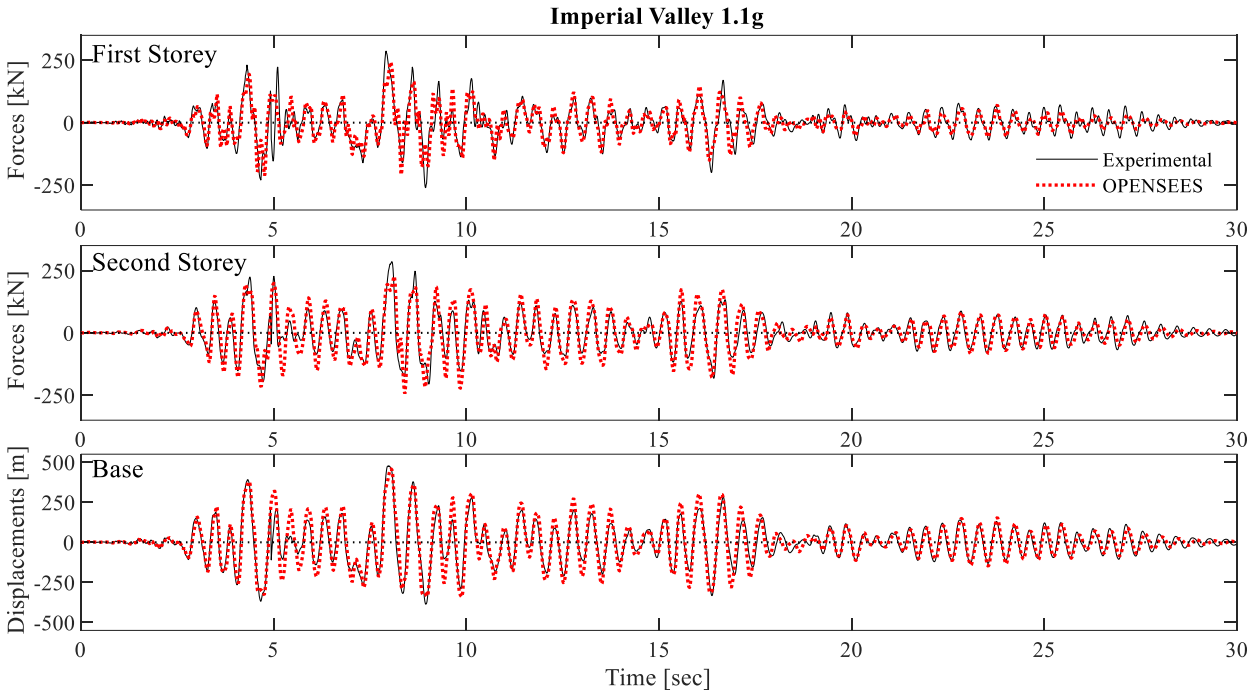

Figure 6.70. NLTH Analysis: Actuator forces for Test 1

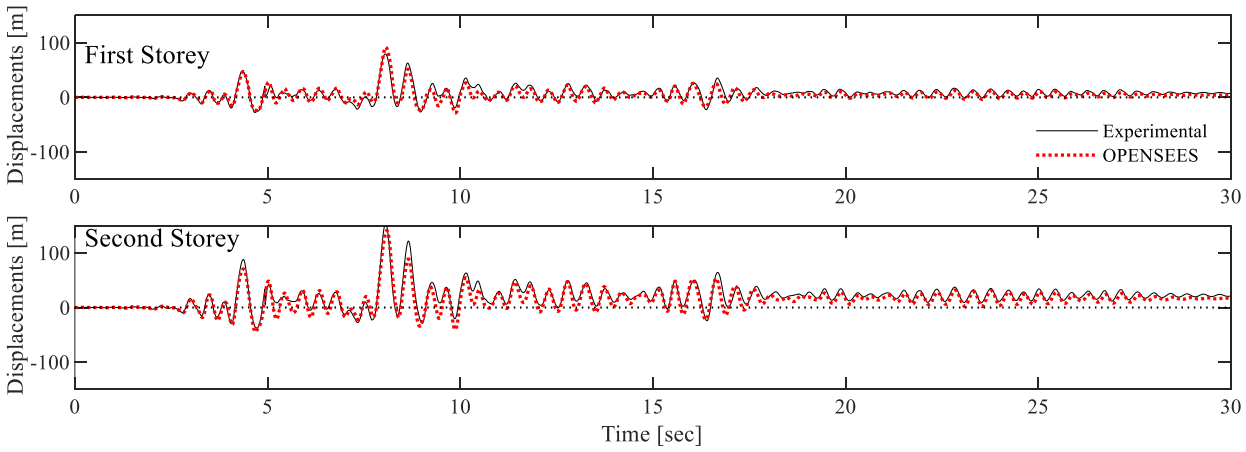

Figure 6.71. NLTH Analysis: Actuator forces for Test 1

Figure 6.72 compares the experimental and numerical local results for Test 1. Similar to the comparisons of the quasi-static analysis, a satisfactory match between numerical and experimental results is shown.

In particular, Figure 6.72 (a) compares the experimental and numerical hysteretic curves of the DF-BCJ, highlighting a satisfactory match of the results, with the numerical model capturing the maximum rotations with accuracy. Figure 6.72 (b) shows the experimental moment-rotation curve of the SC-CB compared to the numerical results, highlighting a slightly higher strain-hardening behaviour with respect to the experimental results. This effect is mainly due to the loss of the pre-loading forces in the bolts of the FDs and to the variability of the force in the PT bars during the loading history, illustrated in Figure 6.72 (c), which is not simulated in the numerical model, leading to some differences. In addition, Figure 6.72 (d) shows the tension force variation in the PT bars versus the joint rotation.

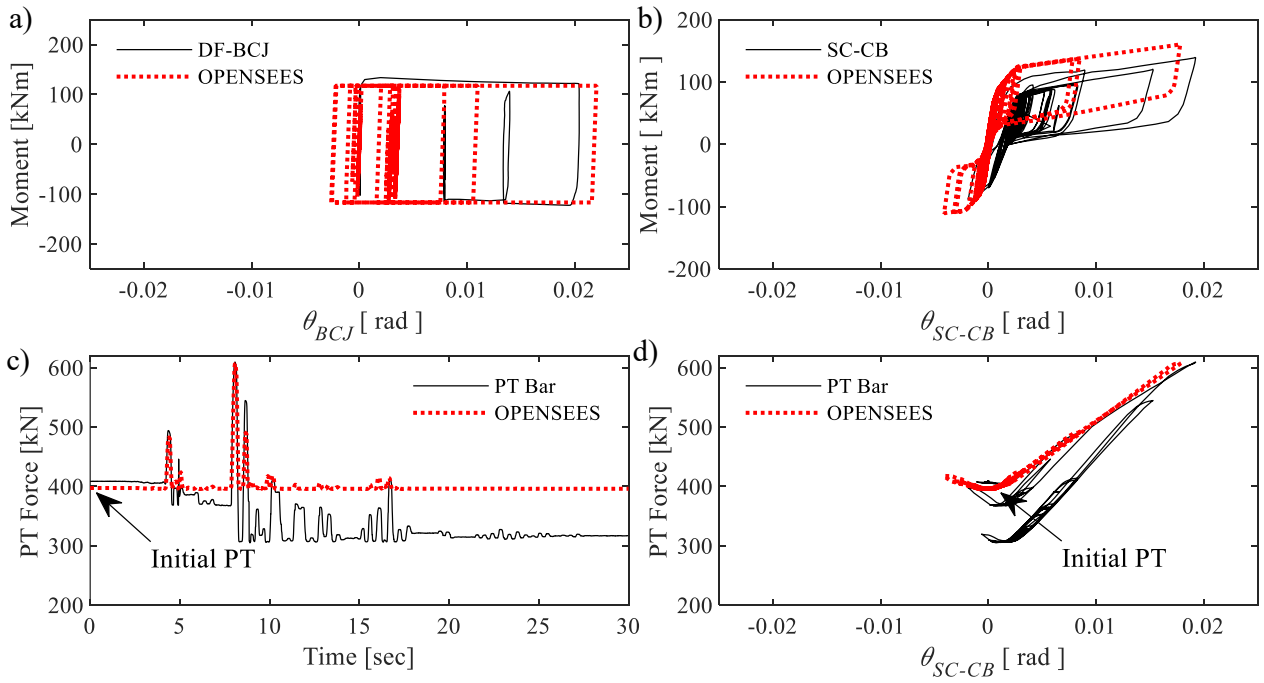

Figure 6.72. FEM validation. Local Results for Test 1

6.9 Comparison with the FREEDAM experimental campaign

In a previous experimental campaign [6], the structure was endowed only with the FREEDAM BCJs, and it was subjected to the same sequence of accelerograms. The comparison of the results is shown in Figure 6.73 in terms of interstorey drift histories and actuator forces for Test 2 (*i.e.,* Spitak PGA=0.8g). As it is possible to observe, in the structure equipped only with the FREEDAM BCJs, the residual drifts were 23.14 mm and 36.83 mm at the first and second storeys, corresponding to IDR_{Res} of 0.96% and 0.58%, respectively, both exceeding the reparability limit [10].

In addition, it is worth highlighting that the structure exhibited damage in the first-storey columns, physically recognised by the yield lines appearing on the surface of the column at the end of the experimental campaign [6]. This result confirms the beneficial effect of the SC-CB in reducing the residual interstorey drifts and protecting the first-storey columns from damage. In addition, Figure 6.74

shows the comparison in terms of actuator forces between the two structures. Results show no significant differences in terms of forces between the two structures.

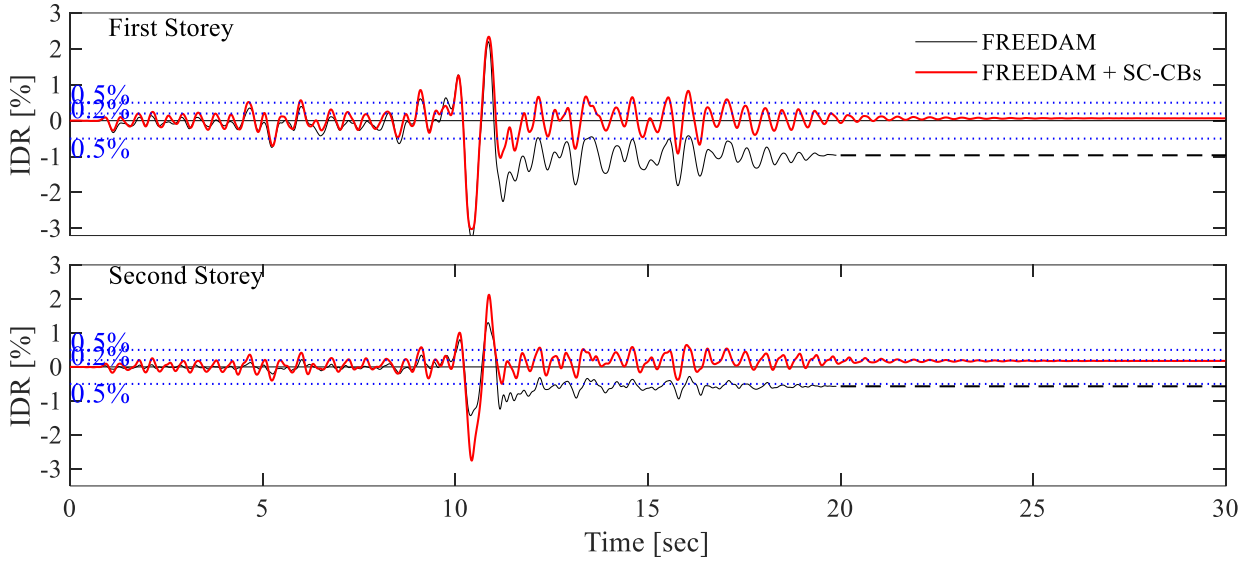

Figure 6.73. Comparison with the FREEDAM experimental campaign [6] IDR for Test 2

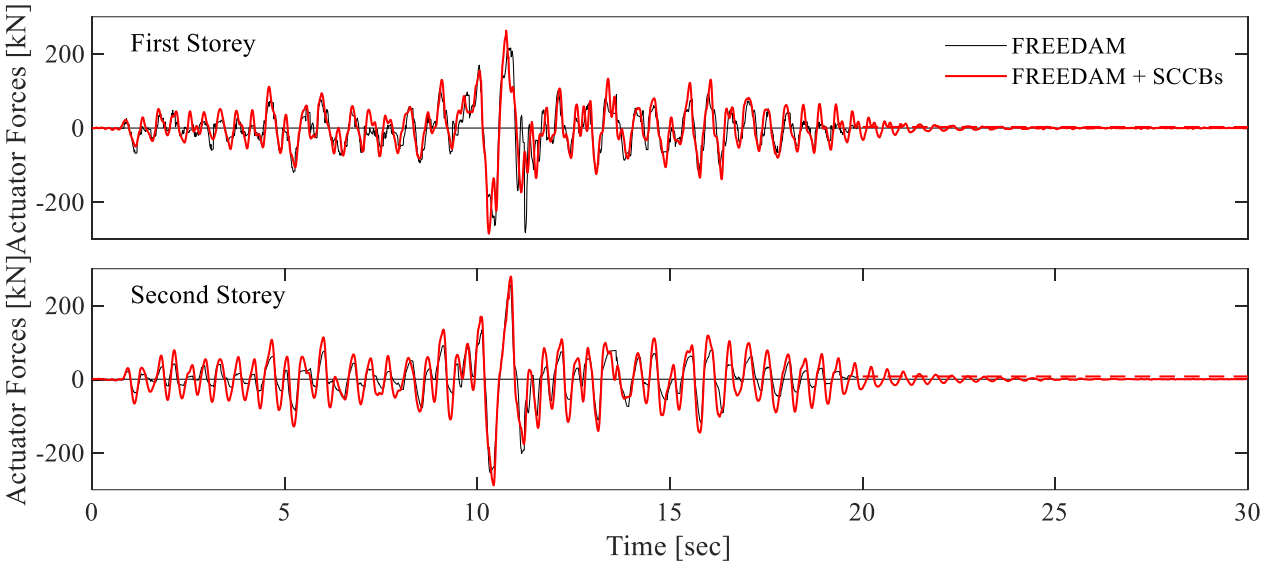

Figure 6.74. Comparison with the FREEDAM experimental campaign [6] Actuator Forces for Test 2

6.10 Reparability and Resilience Assessment

This part is dedicated to the investigation of simple repairing methodologies for the structural performance recovery of buildings to reinstate the original seismic performance in a short time. After the experimental campaign, all the high-strength pre-loadable bolts belonging to the FDs of both DF-BCJs and SC-CBs were loosened and re-tightened to investigate the effectiveness of the proposed repairing methodology on the residual drift reduction of the structure. In addition, the attention is

focused on the two of the tests performed with and without the contribution of the PT bars of the SC-CBs to assess their influence on the overall performance of the structure, including their contribution regarding the structure's resilience and reparability.

6.10.1 Influence of the PT Bars

The Tests Matrix also included Tests 7 and 8, which have not been extensively discussed so far. These tests were identical to Test 1 (*i.e.,* Imperial Valley – PGA = 1.10g) but included an additional load at both levels. Additionally, Test 8 was performed without the contribution of the PT bars. Figure 6.75 (a) and (b) show the comparison between these three tests in terms of IDR time histories for the first and second stories, respectively. The comparison among the three curves highlights three important aspects: *i)* the negligible influence of the considered additional distributed loads, *ii)* the ability of the repair process to restore the seismic performance of the undamaged structure, and *iii)* the crucial role of the PT bars in contributing to the residual drifts reduction. The comparison between Tests 1 and 7 shows no significant differences in terms of IDRs.

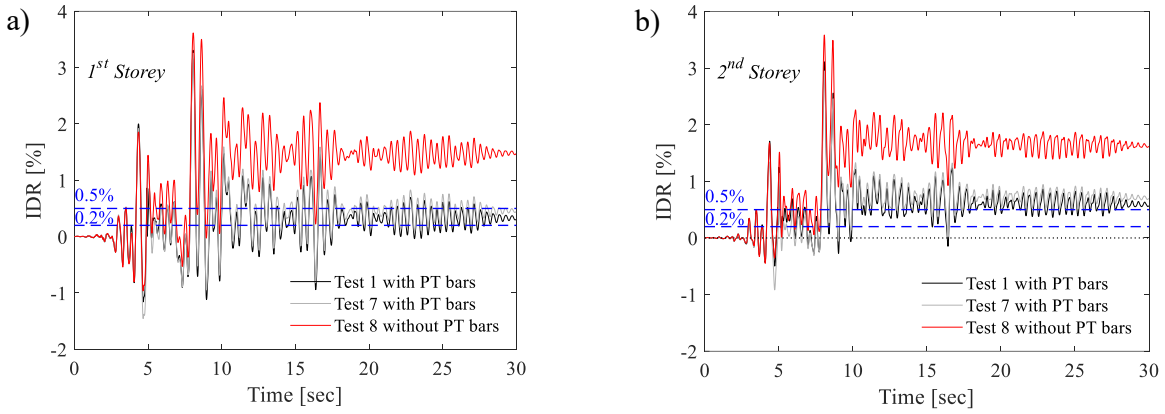

Figure 6.75. Comparison of interstorey drifts with and without the PT bars for the: a) First Storey; b) Second Storey

This was expected due to the limited contribution of the considered additional distributed loads with respect to the applied preload imposed by the PT bars (*i.e.,* 4% of the initial preload for each column). Therefore, in this case, the additional loads do not contribute to the self-centring behaviour nor alter the structural performance, as expected. Moreover, the match of the responses for Tests 1 and 7 confirms that the 'simple' repair process used in these tests allows for restoring the initial performance of the undamaged structure. On the other hand, the comparison of Tests 1 and 7 with Test 8 shows the crucial role of the PT bars. It can be observed that, in Tests 1 and 7, the introduction of the PT bars allows a significant reduction of the IDR_{Res} for both stories (*i.e.,* from 1.47% to 0.30% for the first storey and from 1.62% to 0.51% for the second storey). In addition, the structure with PT bars experiences IDR_{Res} lower than the 0.5% limit threshold [10] in the first storey, which is not satisfied for the structure without PT bars. Moreover, it is noteworthy that although the self-centring system is localized only at the base, it allows a residual drift reduction also at the higher stories, with a decreasing efficiency along the height. This beneficial effect was already pointed out in previous numerical studies [29-30].

6.10.2 Repairability

As previously mentioned, the structure was repaired at the end of each test. The repair process involved loosening all the high-strength pre-loadable bolts of the FDs of both DF-BCJs and SC-CBs (Figure 6.76) and re-tightening them to obtain the predefined preloading force. The entire loosening process consisted of two steps: *i)* loosening the bolts belonging to the FDs of the DF-BCJs starting from the second storey and *ii)* loosening the bolts belonging to the FDs of the SC-CBs, and it took approximately 15 minutes to complete the entire procedure. The aim was to investigate the system-level performance recovery in terms of restoration of the initial configuration (*i.e.,* before the Test). The measurements of the wire sensors were monitored for the first (*i.e.,* WS1, WS2) and the second stories (*i.e.,* WS3, WS4) during the loosening process. It is highlighted that, except for some slight differences, no significant variations were observed from the measurements of the WSs belonging to the same storey.

a) b)

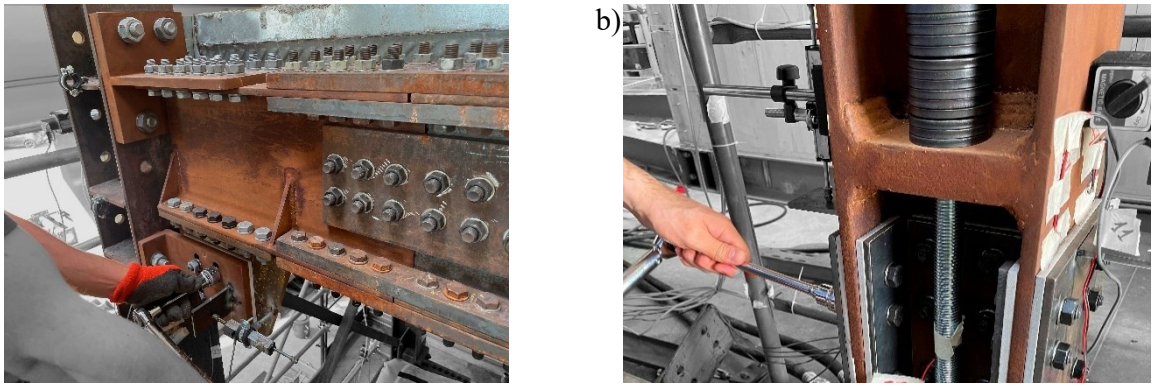

Figure 6.76. FDs bolts' loosening process at the end of each Test: a) DF-BCJs; b) SC-CBs

Figure 6.76 (a), (b) and (c) show the results of the loosening process performed after three tests, *i.e.,* Imperial Valley – Test 1, Coalinga – Test 5, and Kobe – Test 6, in terms of IDR *vs* time. These tests were selected as they resulted in the highest $IDR_{Res,}$ approximately equal to 0.3% at the first storey and close to the repairability limit of 0.5% [10] at the second storey. The repair process showed that the IDR reduced almost to zero by simply loosening the FD's bolts of the DF-BCJs and SC-CBs, hence demonstrating the repair method's effectiveness in terms of residual drift reduction. In other words, the structure can be recentred by simply loosening the FDs' bolts. The successive step of the repair process of re-tightening bolts and PT bars took approximately 20 min. Additionally, as discussed in the previous section, it was demonstrated that after each test, the structure behaved as a 'new' structure even after several tests (*i.e.,* comparison between Test 1 and 7), demonstrating that the repair process (*i.e.,* loosening and re-tightening the bolts and PT bars) can restore the seismic performance of the undamaged structure. This consideration, together with the observation of the easy and fast repair process, highlights the considerable benefits in terms of repairability, functional recovery, and resilience.

In addition, the results highlighted that the IDR_{Res} of 0.5%, typically considered as the repairability limit [10] and defined for conventional structures, may not apply to innovative structures like the one investigated. In fact, the experimental campaign highlighted the ability of the structural solution to drastically reduce the IDR_{Res} by simply applying easy and quick repair strategies. For comparison purposes, Figure 6.76 (d) shows the effects of the loosening process performed after Test 8 for the

specimen without PT bars. Differently from Tests 1, 5, and 6, the structure experienced IDR_{Res} (*i.e.,* 1.36% and 1.69% at the first and the second stories, respectively) well beyond the acceptable limits for structural repairability of 0.5% [10] and realignment of 0.2% [11]. In this case, even after applying the loosening process, the displacement did not decrease due to the absence of the PT bars. This result suggests that the repairing methodology applied to the structure without the PT bars is ineffective in reducing the residual displacements.

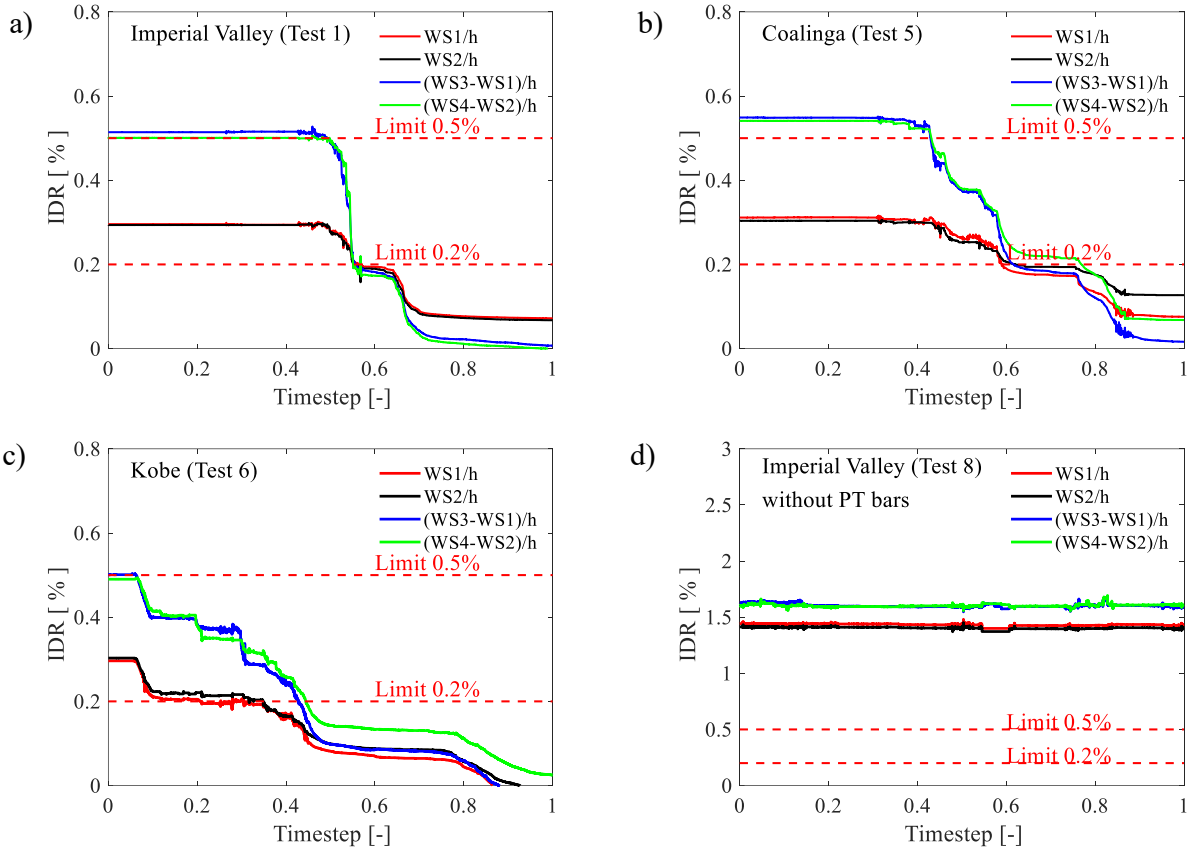

Figure 6.77. Interstorey drifts during the bolts' loosening process: a) Imperial Valley (Test 1); b) Coalinga (Test 5); c) Kobe (Test 6); Imperial Valley (Test 8)

6.10.3 Generalization of the results

In this section, IDAs [32] are performed in OPENSEES [12] to investigate the PT bars' influence on the frame's seismic response while also considering the influence of record-to-record variability. Two configurations are analyzed and compared: the MRF with the SC-CB and the equivalent MRF with the SC-CB without the PT bars. Non-linear time history analyses are performed by considering a suite of 30 ground motion records selected from the SIMBAD Database [33] with moment magnitude ranging from 6 to 7, the epicentral distance $R \leq 30$ km and spectrum-compatibility in the range of periods between 0.2 T_1 and 2 T_1. The mean elastic spectrum of the set is kept between 75% and 130% of the corresponding EC-based elastic response spectrum [13]. The spectral acceleration corresponding to the first vibration mode (*i.e.,* $Sa(T_1)$) is used as Intensity Measure (IM), where T_1= 0.41 sec for both structures. Sa(T1) is equal to 1.05g and 1.58g, respectively, for the ULS and CLS, representing the two

seismic intensities of interest. IDR_{Peak} and IDR_{Res} are recorded as global EDPs to analyse and compare the seismic performance of the two structural systems. Figure 6.78 and Figure 6.79 illustrate the comparison of IDR_{Peak} and IDR_{Res} vs. IM for the structure with and without PT bars in black and red lines, respectively. Bold lines represent the mean responses among all ground motions, while thin lines show the single IDA curves. Figure 6.78 shows that the introduction of PT bars does not significantly affect the peak values of the seismic demands in terms of global EDPs. Conversely, Figure 6.79 shows the contribution of the PT bars in significantly reducing the IDR_{Res} across the entire range of IM values investigated. In particular, the MRF with PT bars experiences IDR_{Res} lower than the 0.2% threshold [11] in terms of mean response, even for the CLS, at both stories. This effect represents a considerable benefit in terms of structure repairability, and this limit is never satisfied for the equivalent structure without PT bars.

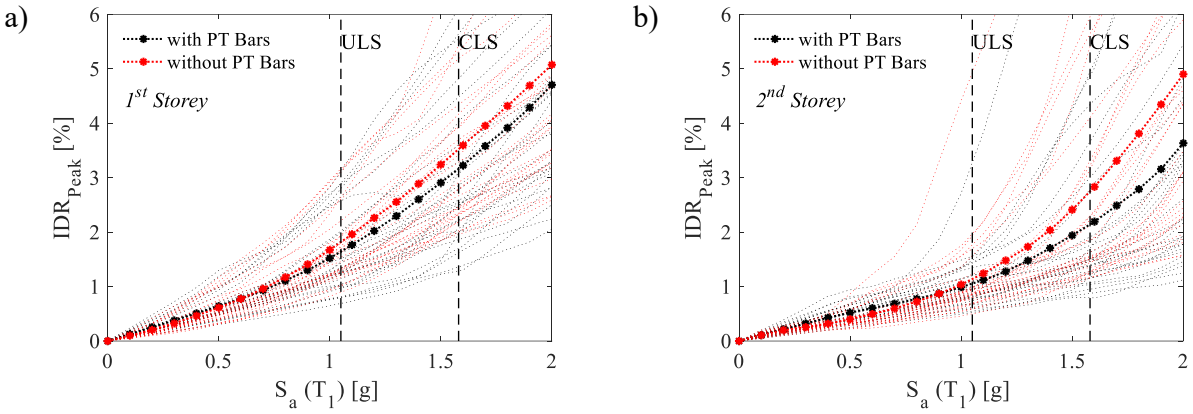

Figure 6.78. Peak interstorey drift (IDR_{Peak}) with and without the PT bars a) 1st storey; b) 2nd storey

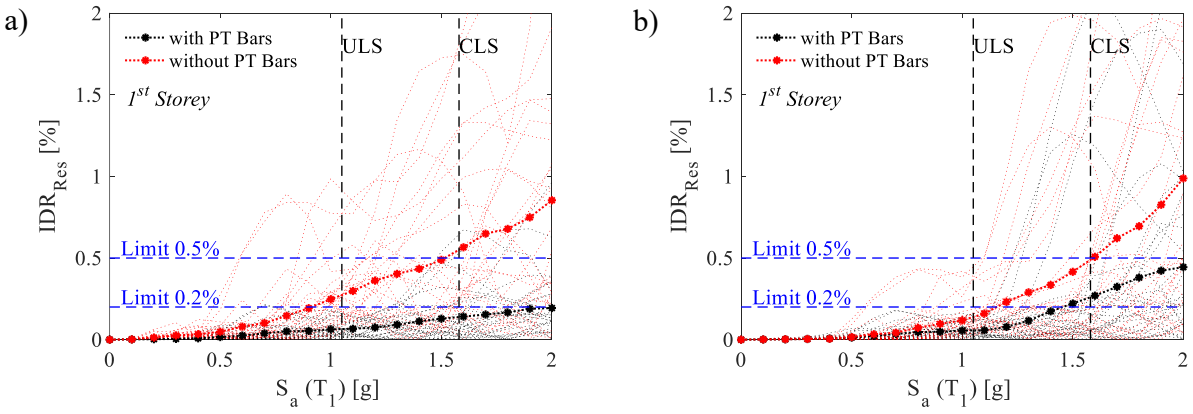

Figure 6.79. Residual interstorey drift (IDR_{Res}) with and without the PT bars: a) 1st storey; b) 2nd storey

6.11 Acknowledgements

The research activity presented in this Chapter was partially supported by the European Community by research grant RFSR-CT-2015-00022. In addition, this research was supported by the UCL Global Engagement Office under the 2020/21 Global Engagement Funded project "Full-scale pseudo-dynamic

experimental Test of a seismic-resilient steel moment resisting frame equipped with damage-free self-centring column bases." The Authors also acknowledge the support from the Royal Society - International Exchange programme under the grant agreement IES\R3\213175. Any opinions, findings, conclusions and/or recommendations expressed in this paper are those of the authors and do not necessarily reflect the views of the Funders. Lastly, thanks are extended to Dr. Eng. Francesco Perri and Eng. Ciro Esposito for the technical support during the experimental tests.

6.12 Personal contribution

Chapter 6 is the novelty of the present work since it deals with the pseudo-dynamic testing, reparability and resilience assessment of a large-scale steel structure equipped with SC-CB connections. The author contributed to define the experimental set-up, participating in the experimental campaign, post-processing the experimental data, providing numerical models of the tested structure through the software OPENSEES and validating the numerical models against the experimental results. In addition, this Chapter focuses on the investigation of simple repairing techniques for structural performance recovery.

6.13 References

1 Borzouie J, Macrae G, Chase JG, Rodgers GW, Clifton GC. Experimental studies on cyclic performance of CB strong axis–aligned asymmetric friction connections. J. Struct. Eng. (ASCE). 2016;142(1):1–10. https://doi.org/10.1061/(ASCE)ST.1943-541X.0001327

2 Freddi F, Dimopoulos CA, Karavasilis TL. Experimental Evaluation of a Rocking Damage-Free Steel CB with Friction Devices. J Struct Eng, 2020;146(10):1-20. 04020217 10.1061/(ASCE)ST.1943-541X.0002779

3 Wang XT, Xie CD, Lin LH, Li J, Seismic behaviour of self-centring concrete-filled square steel tubular (CFST) CB. J. Constr. Steel Res. 2019;156:75–85. 10.1016/j.jcsr.2019.01.025

4 Inamasu H, de Castro e Sousa A, Güell G, Lignos DG. Anchor-yield exposed column bases for minimising residual deformations in seismic-resistant steel moment frames. Earthquake Engng Struct Dyn. 2021;50:1083–1100. https://doi.org/10.1002/eqe.3392H.

5 Inamasu H, de Castro e Sousa A, Lignos DG. Development and Experimental Validation of Dissipative Embedded Column Base Connections for Enhanced Seismic Performance of Steel Moment-Resisting Frames, J Struct Eng. 2022; 148(3), https://doi.org/10.1061/(ASCE)ST.1943-541X.0003259

6 Di Benedetto S, Francavilla AB, Latour M, Piluso V, Rizzano G, Experimental response of a large-scale two-storey steel building equipped with low yielding friction joints, *Soil Dyn Earth Eng.* 2021; 152: 107022. https://doi.org/10.1016/j.soildyn.2021.107022

7 Di Benedetto S, Francavilla AB, Latour M, Piluso V, Rizzano G. Pseudo-dynamic testing of a full-scale two-storey steel building with RBS connections, *Eng. Struct.* 2020; 110494 https://doi.org/10.1016/j.engstruct.2020.110494

8 Mahin SA, Shing PB, Pseudo-dynamic method for seismic testing, *J Struct. Eng.* 1985; 111, 1482-1503. https://doi.org/10.1061/(ASCE)0733-9445(1985)111:7(1482)

9 Model 493.10/793.00 Controller Service. Minneapolis: MTS Systems Corp.; 2002.

10 McCormick J, Aburano H, Ikenaga M, Nakashima M. Permissible residual deformation levels for

building structures considering both safety and human elements. *14th World Conference of Earthquake Engineering*, 2008, Beijing, China.
11 FEMA P58-1. Seismic performance assessment of buildings. Volume 1-Methodology. Applied Technology Council, Redwood City, CA, 2012.
12 S. Mazzoni, F. McKenna, M.H. Scott, G.L. Fenves OpenSEES: Open System for earthquake engineering simulation, Pacific Earthquake Engineering Research Centre (PEER), 2009, Univ. of California, Berkley, CA, Available at: http://opensees.berkeley.edu.
13 EN 1998-1, Eurocode 8: Design of structures for earthquake resistance – Part 1: General rules, seismic actions and rules for buildings, European Committee for Standardization, Brussels.
14 R. Montuori, E. Nastri, V. Piluso, Advances in theory of plastic mechanism control: Closed form solution for MR-Frames. *Earthq. Eng. Struct. Dyn.*, **44**(7), 1035-1054, 2015
15 Latour, M., Piluso, V., Rizzano, G. (2015). "Free from damage beam-to-column joints: Testing and design of DST connections with friction pads." Eng. Struct.; 85, 219–233.
16 G.F. Cavallaro, A. Francavilla, M. Latour, V. Piluso, G. Rizzano, Experimental behaviour of innovative thermal spray coating materials for FREEDAM joint. Composites Part B 115 (2017) 289-299
17 G.F. Cavallaro, A. Francavilla, M. Latour, V. Piluso, G. Rizzano, Cyclic behaviour of friction materials for low yielding connections. Soil Dyn. Earthq. Eng. 114 (2018) 404–423.
18 M. Latour, V. Piluso, G. Rizzano, Experimental analysis of beam-to-column joints equipped with sprayed aluminium friction dampers, J. Constr. Steel Res. 146 (2018) 33–48.
19 Latour M, D'Aniello M, Zimbru M, Rizzano G, Piluso V, Landolfo R. Removable friction dampers for low-damage steel beam-to-column joints. *Soil Dyn Earthq Eng.* 2018;115:66-81.https://doi.org/10.1016/j.soildyn.2018.08.002
20 Francavilla AB, Latour M, Piluso V, Rizzano G. Design criteria for beam-to-column connections equipped with friction devices. *J Constr Steel Res.* 2020;172:106240. https://doi.org/10.1016/j.jcsr.2020.106240
21 A.F. Santos, A. Santiago, M. Latour, G. Rizzano, L.S. da Silva, Response of friction joints under different velocity rates. J. Const. Steel Res. 168 (2020) https://doi.org/10.1016/j.jcsr.2020.106004
22 D'Antimo M, Latour M, Cavallaro GF, Jaspart J-P, Ramhormozian S, Demonceau J-F, Short- and long-term loss of pre-loading in slotted bolted connections, *J. Constr. Steel Res*. 2020;167:105956 https://doi.org/10.1016/j.jcsr.2020.105956
23 Tartaglia R, D'Aniello M, Campiche A, Latour M, Symmetric friction dampers in beam-to-column joints for low-damage steel MRFs, *J. Constr. Steel Res*. 2021;184,106791.
24 EN 1993-1-8, Eurocode 3: Design of steel structures, Part 1-8: Design of steel structure: General rules and rules for buildings, 2005, *European Committee for Standardization*, Brussels.
25 EN ISO 6892-1. (2009) "Metallic materials - Tensile testing - Part 1: Method of test at room temperature." *European Committee for Standardization*, Brussels, Belgium.
26 EN 1090-2. Execution of steel structure and aluminium structure: technical requirements for steel structures.
27 EN 15129. Anti-seismic devices
28 Ramhormozian S, Clifton GC, MacRae GA, Davet GP, Stiffness-based approach for Belleville springs use in friction sliding structural connections, *J Constr Steel Res.* 2017;138:340-356. https://doi.org/10.1016/j.jcsr.2017.07.009.
29 E. Elettore, F. Freddi, M. Latour, G. Rizzano, Design and analysis of a seismic resilient steel moment-resisting frame equipped with damage-free self-centring column bases. J Constr Steel Res. 179 (2021)106543.
30 Elettore E, Lettieri A, Freddi F, Latour M, Rizzano G. Performance-based assessment of seismic-resilient steel moment resisting frames equipped with innovative column base connections.

Structures 2021; 32:1646-1664. https://doi.org/10.1016/j.istruc.2021.03.072

31 SIMQKE-1 (SIMulation of earthQuaKE ground motions) http://nisee.berkeley.edu/software/simqke1/

32 Vamvatsikos D, Cornell CA. Incremental dynamic analysis. Earthquake Engng Struct Dyn. 2002;31(3):491-514. DOI: 10.1002/eqe.141

33 I. Iervolino, C. Galasso, E. Cosenza, REXEL: Computer-aided record selection for code-based seismic structural analysis, B. Earthq. Eng. 8 (2010) 339–362.

Chapter 7 General conclusions and future work

7.1 Summary

The present thesis investigates the seismic behaviour of steel seismic-resilient steel MRFs equipped with innovative Damage-Free Self-Centring Column Bases (SC-CBs). The present work includes extensive analytical, numerical and experimental work to address the research questions. The results of this thesis highlight the effectiveness of the SC-CBs limiting the residual drifts of steel MRFs below the acceptable drift limits while not affecting their peak response, in protecting the first-storey columns from yielding, in providing a large set of validated simplified and advanced models and in giving insights on the use of the adopted SC-CB connections while defining the boundaries of the investigated parameters for their application. Overall, the main contributions provided by this thesis can be summarised in the following concepts:

- The concept and the design analytical formulations are described, highlighting the assumptions and limitations of the design methodology. Then, an experimental study of an isolated SC-CB prototype is reviewed, and two modelling strategies (*i.e.,* simplified and advanced) are developed and validated against the experimental results. The simplified modelling strategy is preliminarily used to investigate the main parameters affecting the moment-rotation hysteretic behaviour of the SC-CB connection. Conversely, the advanced modelling approach is developed to better investigate the influence of some design parameters. The results are compared and used to assess the validity of the analytical formulations.
- A parametric Finite Element (FE) analysis on the influence of the relevant design parameters is performed. This work is carried out by considering three case-study SC-CB connections with different structural properties. The SC-CBs' global and local performances are monitored and compared in all the configurations to investigate and identify the parameters that mainly affect the behaviour of SC-CBs in view of obtaining specific performance objectives (*i.e.,* minimal yielding of the joint components and self-centring capacity) while providing additional design recommendations for this joint typology.
- A Performance-Based Assessment of case-study steel MRFs equipped with SC-CBs is performed through extensive numerical simulations. Incremental Dynamic Analyses (IDAs) are carried out to evaluate the beneficial effects (*i.e.,* self-centring capabilities and damage-free behaviour) provided by the introduction of the innovative SC-CBs within the case study MRFs. Based on the results of the IDA, fragility curves are derived to evaluate the probability of exceedance of the value of residual interstorey drift limit of 0.5%, which is conventionally associated with the building's reparability. Additionally, a parametric numerical analysis is performed to investigate the frame layout's influence and the seismic mass on the self-centring capability of the considered case-study steel MRFs.
- An experimental program on a large-scale two-storey steel structure equipped with Damage-Free Beam-to-Column Joints (DF-BCJs) and SC-CB connections is carried out by applying the Pseudo-Dynamic (PsD) test procedure. Global and local Engineering Demand Parameters (EDPs) are monitored to investigate the influence of the proposed SC-CBs on the seismic performance of the tested structure. A sequence of eight ground motion records, scaled to several intensities, is applied considering different configurations of the tested structure. Additionally, at the end of each test, the specimen has been repaired by loosening and re-tightening all the

high-strength pre-loadable bolts belonging to the Friction Devices (FDs) of both DF-BCJs and SC-CBs. A detailed FE numerical model is developed, and comparisons between experimental and numerical results are presented for global and local results.

7.2 Design methodology for Damage-Free Self-Centring Column Bases (SC-CBs)

Chapter 3 of this thesis provides the design analytical formulations of the Damage-Free Self-Centring Column Bases (SC-CB), particularly focusing on the assumptions and limitations of the design methodology. In addition, an experimental study of an isolated SC-CB prototype is reviewed, and two modelling strategies are developed and validated against the experimental results. The main findings can be summarised as follows:

- The design of the SC-CB is based on a step-by-step procedure consisting of the definition of the design input parameters, the design of the components and the design of the structural details of the joint. The design procedure is based on some design assumptions and design choices, which are discussed and analysed in detail.
- The modelling strategies exhibit an accurate representation of the SC-CB behaviour. The simplified modelling strategy allows the investigation of the main parameters affecting the moment-rotation hysteretic behaviour of the column connection. Nevertheless, some limitations are highlighted in providing a more exhaustive view into the influence of some design parameters over the local behaviour of the connection. Conversely, the advanced modelling strategy correctly predicts the global hysteretic response observed during the experimental tests, providing useful insights into the characterisation of the local behaviour of the SC-CB connection. However, both modelling strategies are effective in assessing the validity of design assumptions and are consistent with the analytical formulations.

7.3 Parametric FE Analysis of SC-CBs with different structural properties

Chapter 4 of this thesis presents a parametric FE analysis performed on case-study SC-CBs to investigate the influence of three design parameters (*i.e.,* the thickness of the flanges' plates, the design shear load, and the design axial load). For each Configuration, global and local parameters are monitored to investigate the influence of these parameters on the global and local behaviour of the SC-CB connections. The results are compared for all the configurations to identify the best design solution in terms of improved self-centring capacity of the joint and minimal yielding of the components. Results from the FE parametric analysis provide a more comprehensive scenery of the assumptions and limitations of the design methodology, highlighting the crucial aspects of the design procedure and suggesting additional recommendations to improve the design requirements. Based on the obtained outcomes, the following remarks can be drawn:

- The moment-rotation behaviour of the connection is not affected by the considered design parameters, while the local behaviour is significantly influenced.

- The use of thinner flange plates represents a benefit in terms of reduction of the local plastic damage on the column while also allowing a reduction of the amount of the dissipated plastic energy. In addition, designing the web FD to carry a minor percentage (*i.e.,* 75%, 50% or 0%) of the design shear load represents an efficient design solution which reduces the strain concentrations on the column. Therefore, the optimal design configuration in terms of damage reduction is represented by the connection equipped with the thinner flanges' plates and designing the web FD to carry the 50% percentage of the design shear load.
- The moment-rotation behaviour of the SC-CB is strongly affected by the axial load. For the examined SC-CB subjected to the variable axial load history, the self-centring requirement is satisfied. This result suggests that it may be possible to consider the gravity axial force as design axial load for the SC-CB. Nevertheless, additional research is required to provide more general recommendations on this design aspect.

7.4 Performance-Based Assessment of case-study MRFs with SC-CBs

Chapter 5 of this thesis presents a Performance-Based Assessment of case-study steel MRFs equipped with SC-CBs, performed through extensive numerical simulations. Several case-study steel MRFs are extracted from prototype structures and designed following the Eurocode 8 provisions. Numerical models are developed for the MRFs with traditional full-strength CBs and for the equivalent MRFs equipped with the proposed SC-CB connections. Incremental Dynamic Analyses (IDA) are carried out on a set of 30 ground motion records to assess and compare the seismic performances of the two structures while accounting for the record-to-record variability. Fragility curves are derived based on the IDA results to evaluate the probability of exceedance of the value of residual interstorey drift limit of 0.5%, which, for building frames, is conventionally associated with building reparability. The following conclusions are drawn:

- The introduction of the SC-CBs significantly contributes to the reduction of the residual interstorey drifts for the seismic intensities of interests and to the protection of the first storey column from yielding, thus avoiding non-repairable damage of the columns under the seismic intensities of interest. These results provide significant advantages in terms of repairability and, hence, resilience of the structure.
- The introduction of the SC-CBs does not produce any detrimental effect on the peak values of the seismic demands in terms of global and components-based EDPs. Hence, the hierarchy of activation of the several mechanisms within the structure is the same for both the considered structures.
- Concerning the influence of the frame layout, the use of the SC-CBs is effective for re-centring low-rise buildings, while its effectiveness for medium- and high-rise buildings is significantly affected by the number of storeys of the frames. In fact, the self-centring effect tends to reduce for an increasing number of storeys. In particular, the efficiency is relevant for the 4- and 6-storey frames, while it decreases for the 8-storey frames. Conversely, no sensitivity to the variation in the number of bays of the structures is observed.

- Concerning the influence of the seismic mass, for the case-study with lower mass M1, it can be observed that the effectiveness progressively decreases while increasing the number of stories. Conversely, for the higher mass M2, the results show a lower sensitivity with respect to the number of stories.
- The use of a self-centring system localised only at the first storey allows a reduction of the residual drifts also at the higher storeys, with an efficiency that decreases along the height. This result demonstrates the potentiality of the proposed solutions, which are easy to implement from a technological point of view, and it is identified as a compromise that is easily applied in practice. Therefore, it is demonstrated that with a limited number of self-centring devices, it is possible to improve the self-centring behaviour of the whole system, reducing the complexity of the structural details with a negligible increase in the overall cost of the structure.

7.5 Pseudo-Dynamic Testing, Reparability and Resilience Assessment of a Large-Scale steel structure with SC-CBs

Chapter 6 of this thesis presents the experimental program on a large-scale two-storey steel structure equipped with DF-BCJs and SC-CB connections, carried out by applying the PsD test procedure. A sequence of eight ground motion records, scaled to several intensities, is applied. Global and local EDPs are monitored to investigate the influence of the proposed SC-CBs on the seismic performance of the tested structure. Additionally, at the end of each test, the specimen has been repaired by loosening and re-tightening all the high-strength pre-loadable bolts belonging to the FDs of both DF-BCJs and SC-CBs. Similar operations were performed on the PT bars. A detailed FE numerical model is developed and validated against experimental results. Finally, IDAs are performed to numerically investigate the PT bars' influence on the structure's seismic response while also considering the influence of record-to-record variability. The following conclusions can be drawn:

- The experimental results demonstrate the effectiveness of the SC-CBs in limiting the residual drifts on the whole structure below the acceptable drift limit, and the first-storey columns and the beams are protected from yielding, providing significant advantages in terms of repairability and, hence, resilience of the structure.
- The role of the PT bars is paramount in allowing a significant reduction of the residual interstorey drifts at both stories, and it does not produce any detrimental effect on the peak values of the seismic demands.
- The repair process (*i.e.,* loosening all the high-strength pre-loadable bolts of the FDs of both DF-BCJs and SC-CBs) and the re-tightening of the PT bars applied after each test is effective in the residual drift reduction and in restoring the seismic performance of the undamaged structure. This consideration, together with the observation of the easy and fast repair process, highlights the considerable benefits in terms of repairability, functional recovery, and resilience. Conversely, for the equivalent structure without the PT bars, the repairing methodology is ineffective in reducing the residual displacements.
- The numerical modelling approach allows the prediction of both global and local structural responses. The accuracy and limitations of the modelling strategy are highlighted and discussed.

In particular, for the global results, the comparison of the storey forces base shows an almost perfect match between the numerical and experimental results with very minor differences. Conversely, regarding the local results, some limitations can be highlighted as the numerical model does not simulate the loss of preloading forces in the FD's bolts and PT bars.

7.6 Future works

The present work provides a comprehensive perspective on steel seismic-resilient steel MRFs equipped with SC-CBs through different approaches. Nonetheless, some limitations and future challenges have been identified along the process, and some of them are enlisted in the following:

- The validity of the presented numerical model (Chapter 6) is limited to the characteristics of the materials and frame characteristics of the experiment. Although the model can be useful as a reference to assess other numerical models, further work may be necessary to generalise the model for other similar structures. In addition, advanced numerical models should be developed to simulate the repairing process consisting of loosening the FDs' bolts and successively retightening them to the design preload forces. A parametric analysis should be addressed while monitoring global and storey-level EDPs, including residual interstorey drifts and floor accelerations, to assess the reparability of the analysed case-study structures.

- As further development, a risk-based Life Cycle Cost Analysis (LCCA) approach should be addressed to quantify the cost/benefit ratio and, hence, to evaluate the effectiveness of the proposed solution in reducing seismic vulnerability and economic losses. The probabilistic approach should be applied to several case-study steel structures, and damage-to-loss ratios should be used to perform LCCA to evaluate and compare the loss savings for each of the analysed cases.

- The experimental results performed on the isolated SC-CB (Chapter 3) and on the large-scale steel structure (Chapter 6) are limited to the quasi-static structural response of the analysed specimens. In fact, additional studies are required to assess the response of such structures under 'real' dynamic load conditions (*i.e.,* shake-table tests).
  Unresolved issues include: *1)* to assess the influence of the impacts at the rocking interfaces, potentially inducing local damages in the connections and affecting the effective damping of the system, *e.g.,* PsD tests only numerically simulate the damping; *2)* to study the influence of the vertical component of the ground motion on the self-centring capacity of the CBs; *3)* to define quantitative measures for the repairability of the structures (*e.g.,* repair time) and seismic performance of the repaired structures. To this aim, it is also highlighted that the outcomes of this work have been also included in the project entitled **"SC-RESTEEL: Self-Centring seismic-RESilient sTEEL structures"**, recently funded within the framework of **ERIES: Engineering Research Infrastructures for European Synergies call**. The project will investigate the structural response, repairability, resilience, and performance recovery of steel MRFs with SC-CBs using shaking table tests. Figure 7.1 and Figure 7.2 show respectively the

prototype and the connections which will be tested via shake table test in the context of the project.

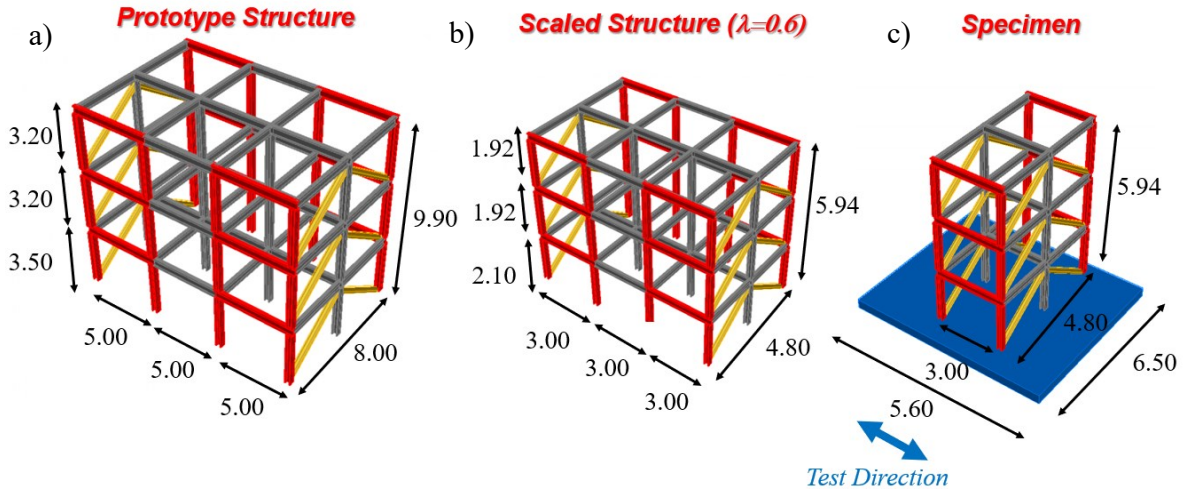

Figure 7.1 "SC-RESTEEL: Self-Centring seismic-RESilient sTEEL structures" ERIES - 3D view & geometries of: a) Prototype; b) Scaled Structure. c) Test Specimen. [Dimension in m].

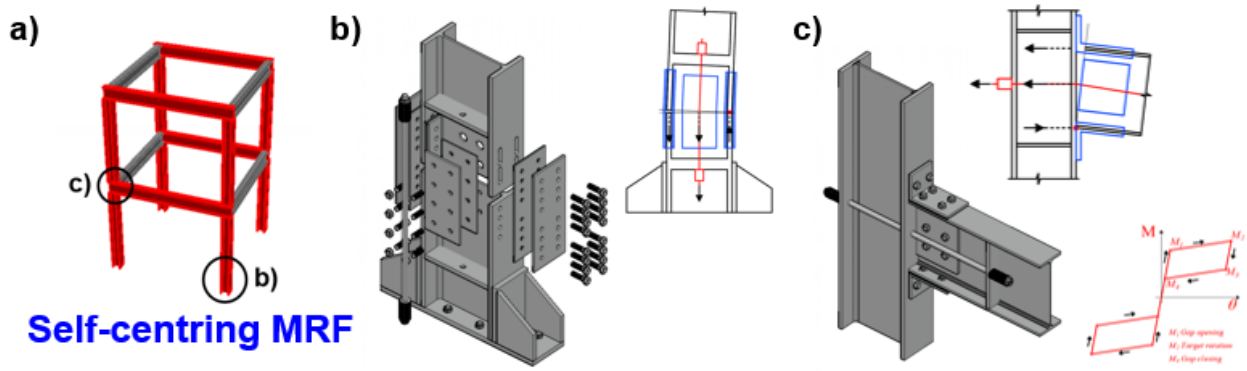

Figure 7.2 "SC-RESTEEL: Self-Centring seismic-RESilient sTEEL structures" ERIES Investigated Low-Damage Self-Centring Joints (combination of Friction Devices and Post-tensioned bars with disk springs) a) Self-Centring MRF; b) Self-Centring Column Base; c) Self-Centring Beam-Column Joint.

ANNEX A

ANNEX A

A1. Results of the Parametric Analysis (Chapter 5)

A1.1 IDA Results (Influence of the Frame Layout)

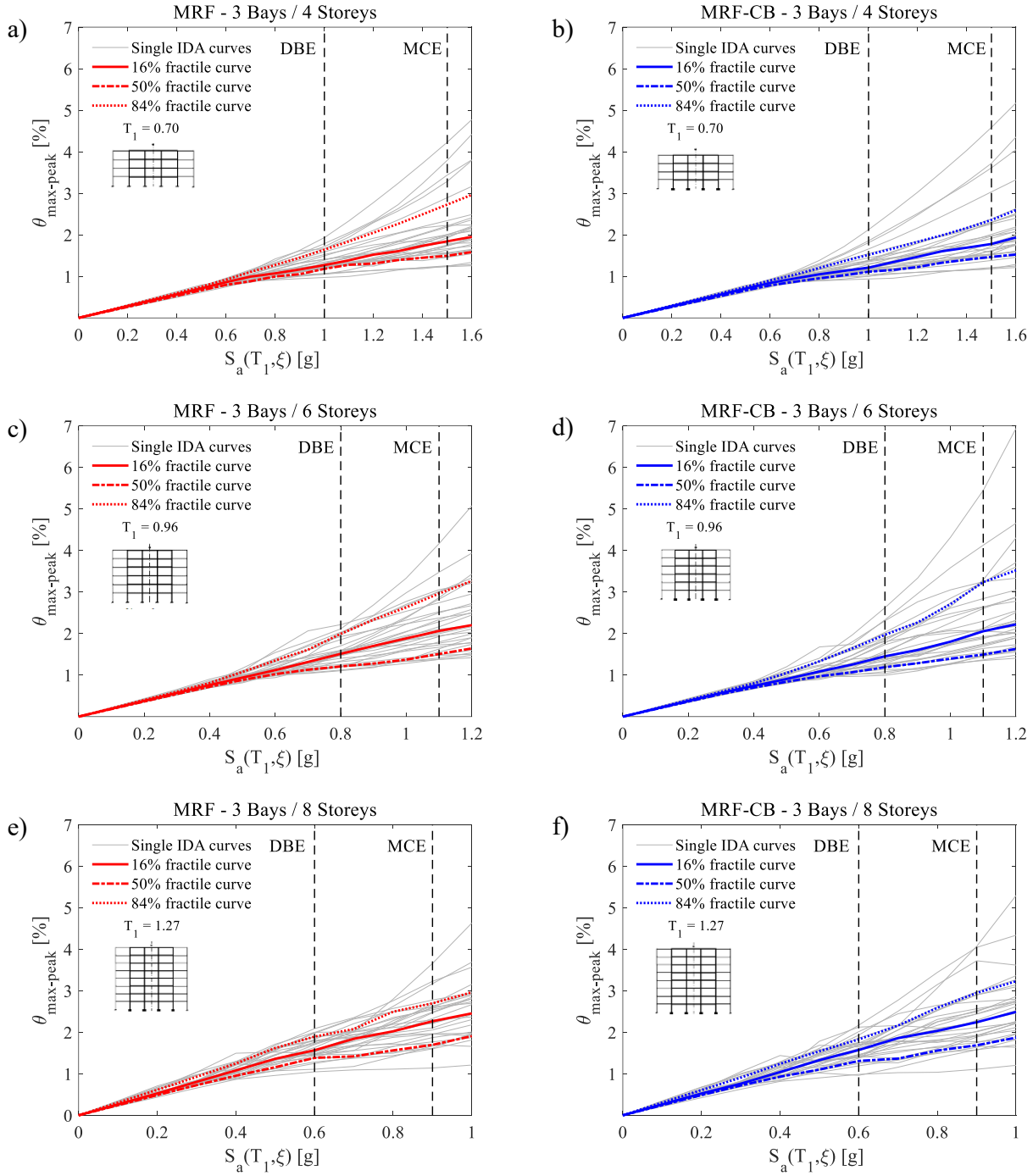

Figure A 1: IDA Results: Maximum peak interstorey drifts of the case-study MRFs: (a, b) 3-4; (c, d) 3-6; (e, f) 3-8.

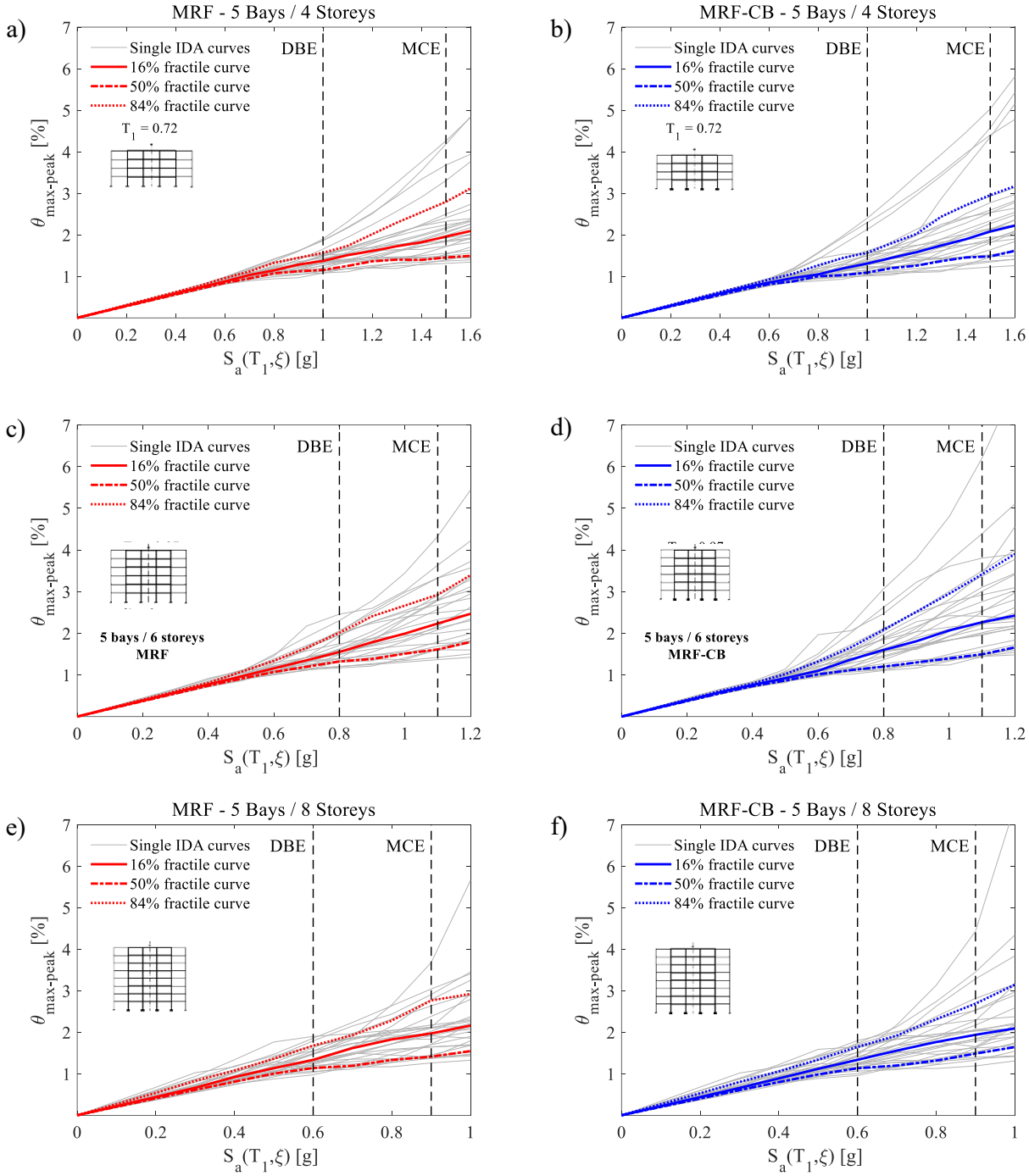

Figure A 2: IDA Results: Maximum peak interstorey drifts of the case-study MRFs: (a, b) 5-4; (c, d) 5-6; (e, f) 5-8.

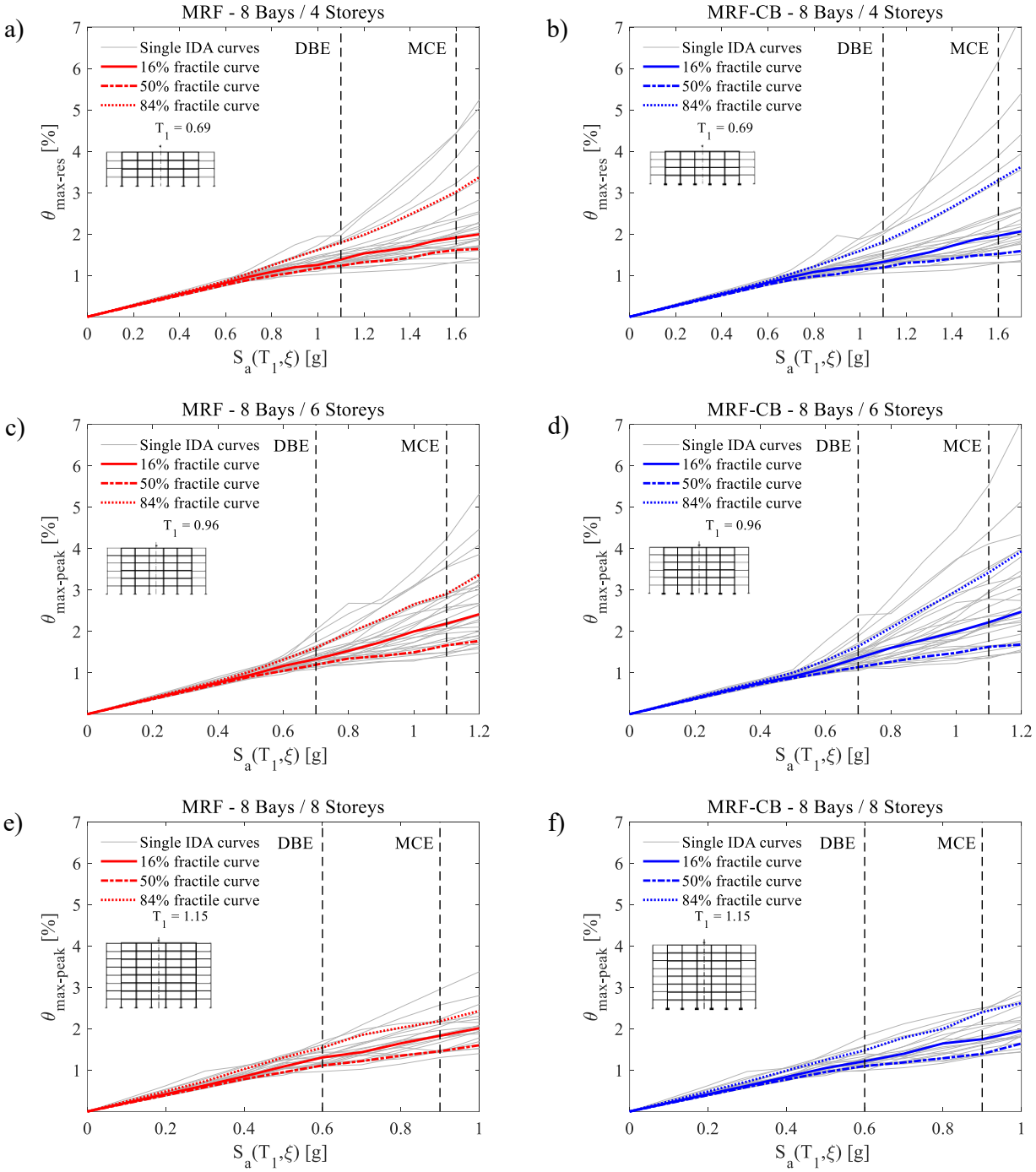

Figure A 3: IDA Results: Maximum peak interstorey drifts of the case-study MRFs: (a, b) 8-4; (c, d) 8-6; (e, f) 8-8.

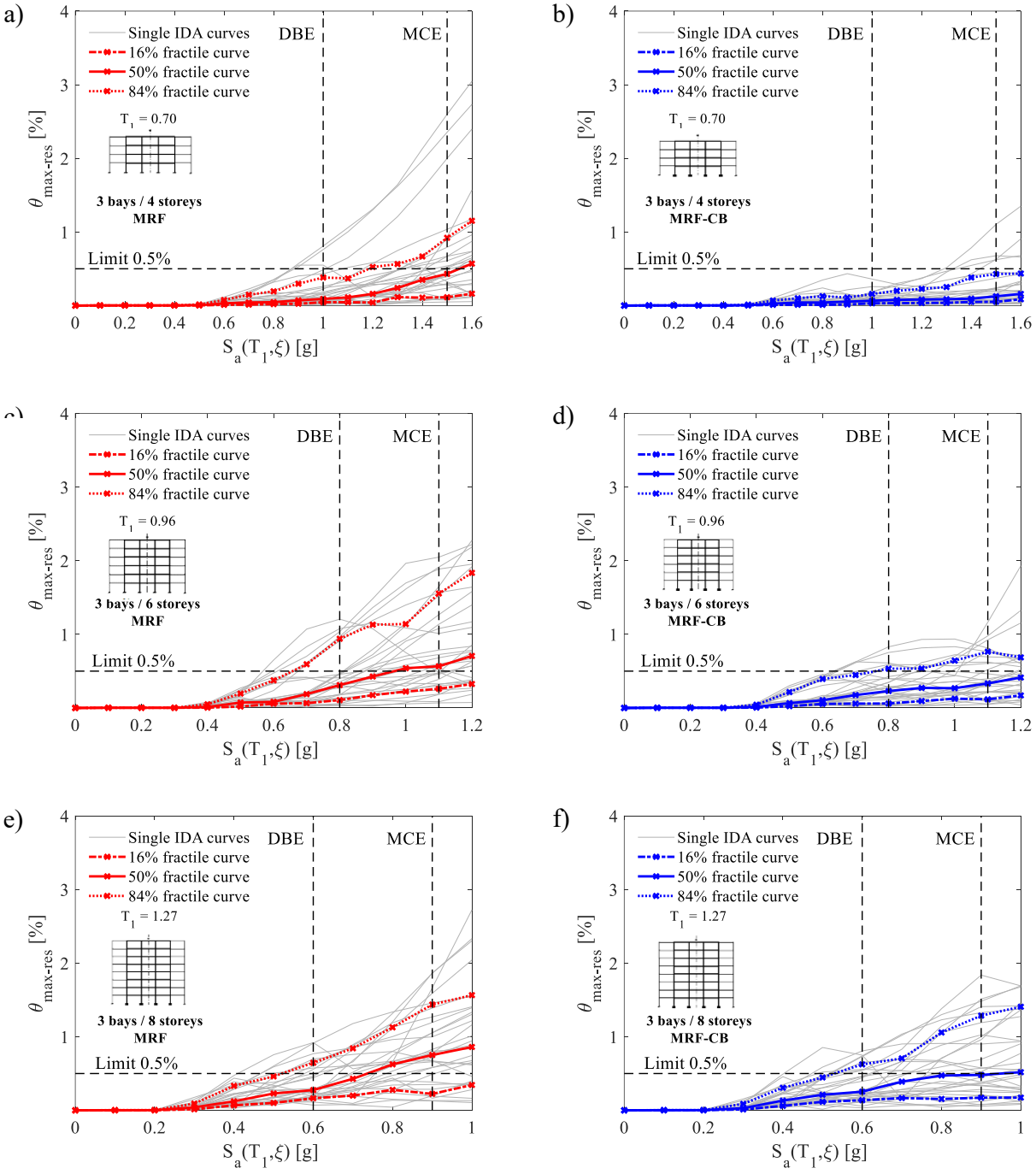

Figure A 4: IDA Results: Maximum residual interstorey drifts of the case-study MRFs: (a, b) 3-4; (c, d) 3-6; (e, f) 3-8.

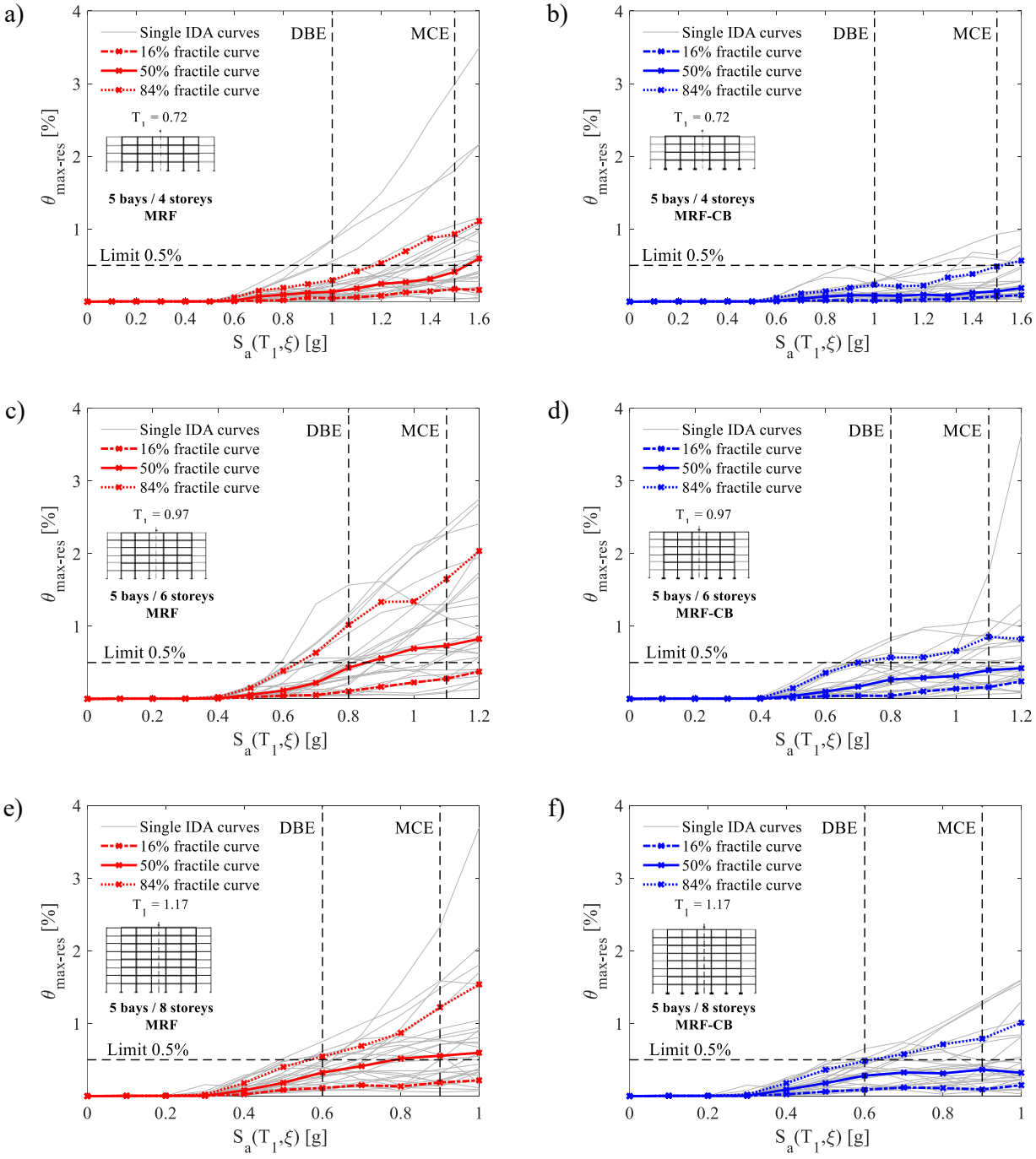

Figure A 5: IDA Results: Maximum residual interstorey drifts of the case-study MRFs: (a, b) 5-4; (c, d) 5-6; (e, f) 5-8.

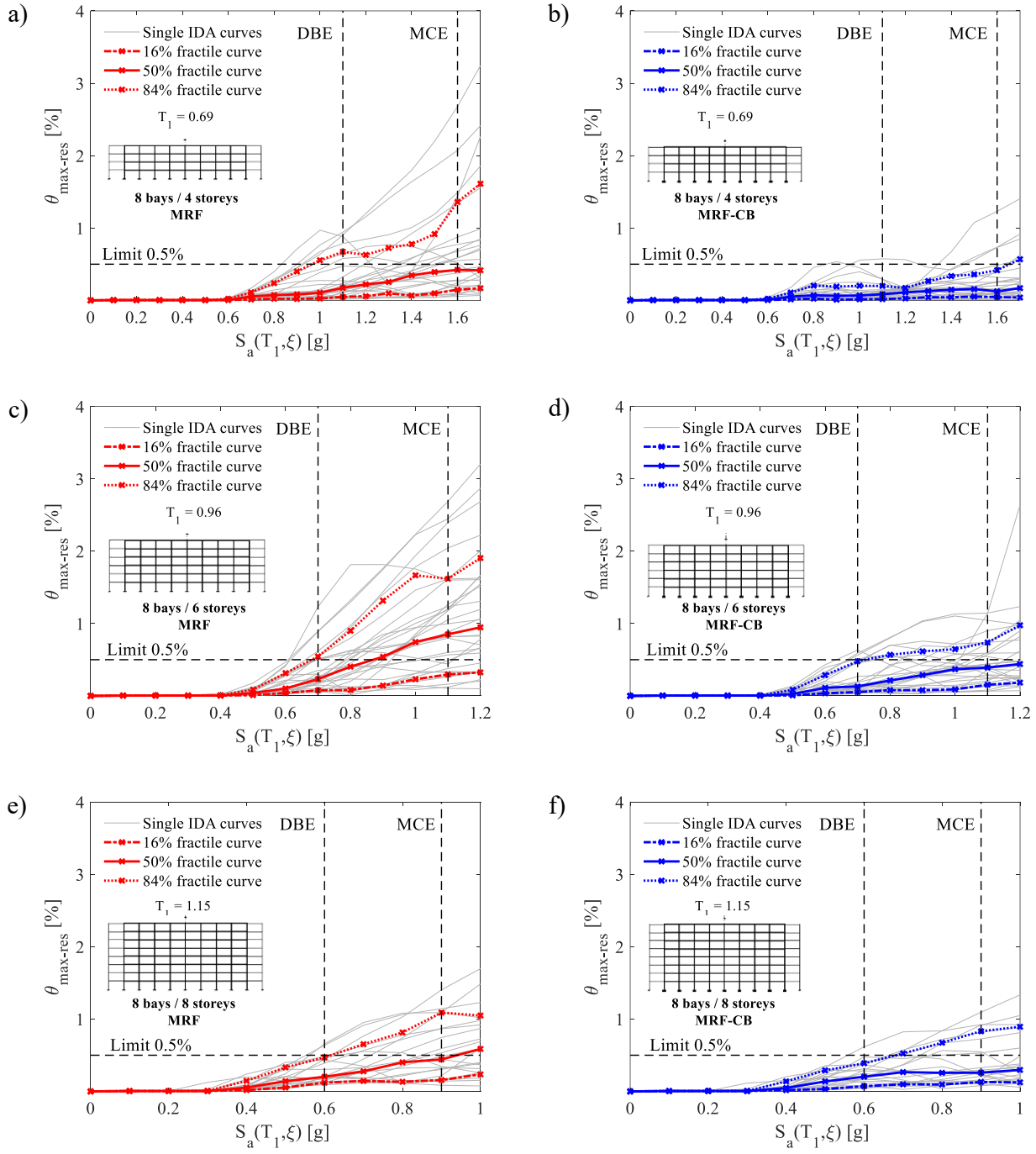

Figure A 6: IDA Results: Maximum residual interstorey drifts of the case-study MRFs: (a, b) 8-4; (c, d) 8-6; (e, f) 8-8.

A1.2 Fragility Curves (Influence of the Frame Layout)

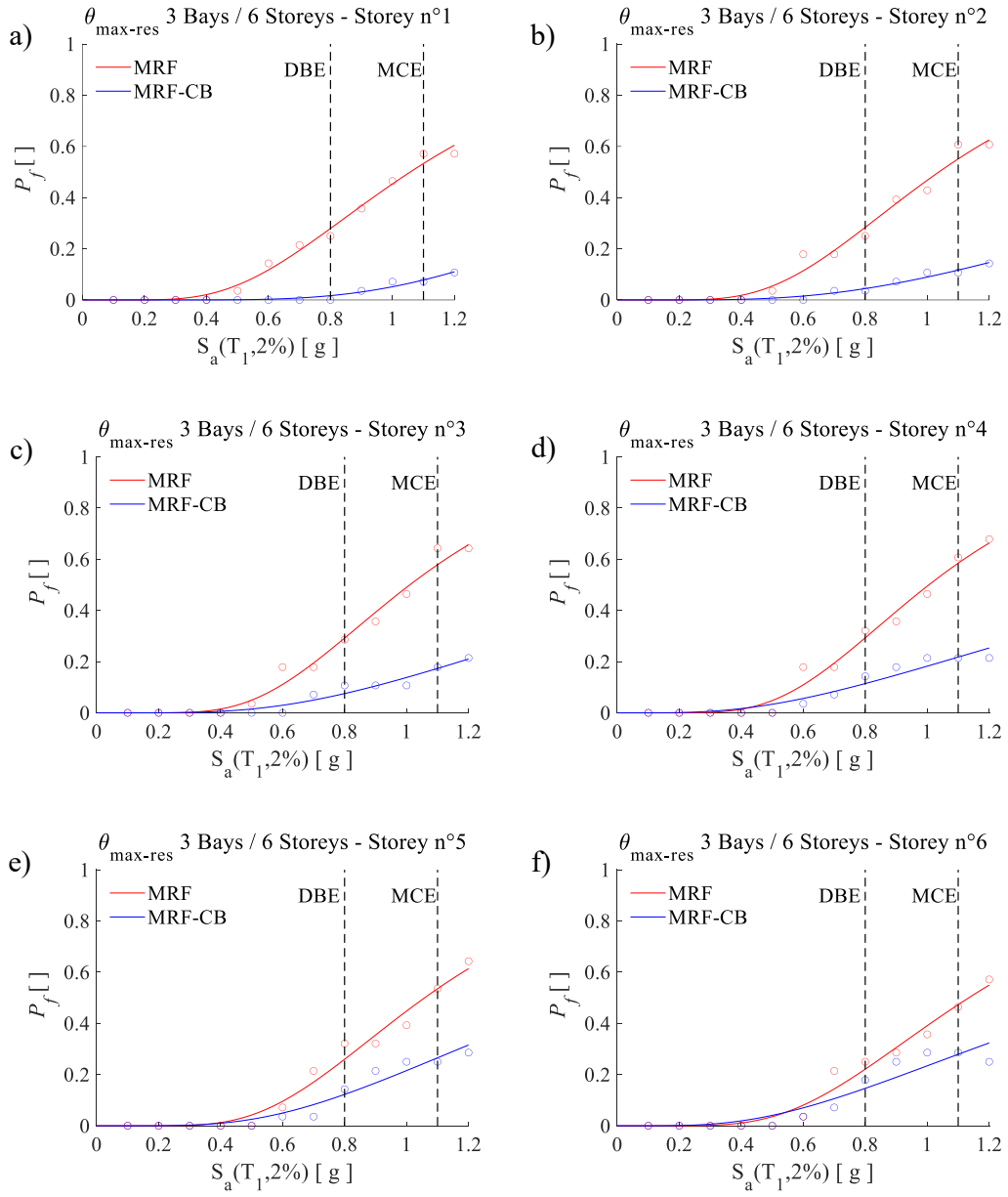

Figure A 7: Comparison of the storey-level fragility curves for the maximum residual interstorey drifts with respect to the threshold limit of 0.5%, for the MRF 3-6

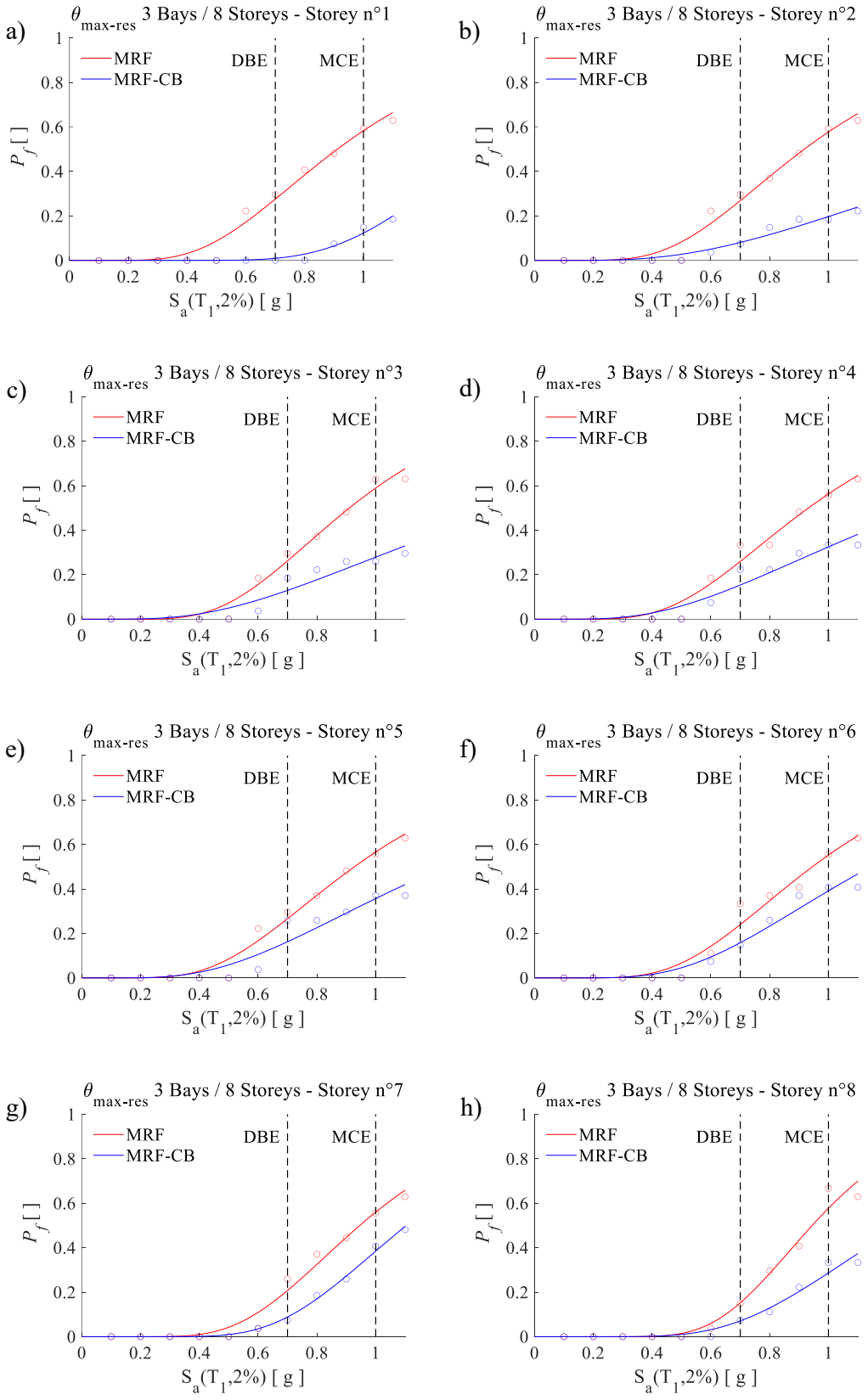

Figure A 8: Comparison of the storey-level fragility curves for the maximum residual interstorey drifts with respect to the threshold limit of 0.5%, for the MRF 3-8

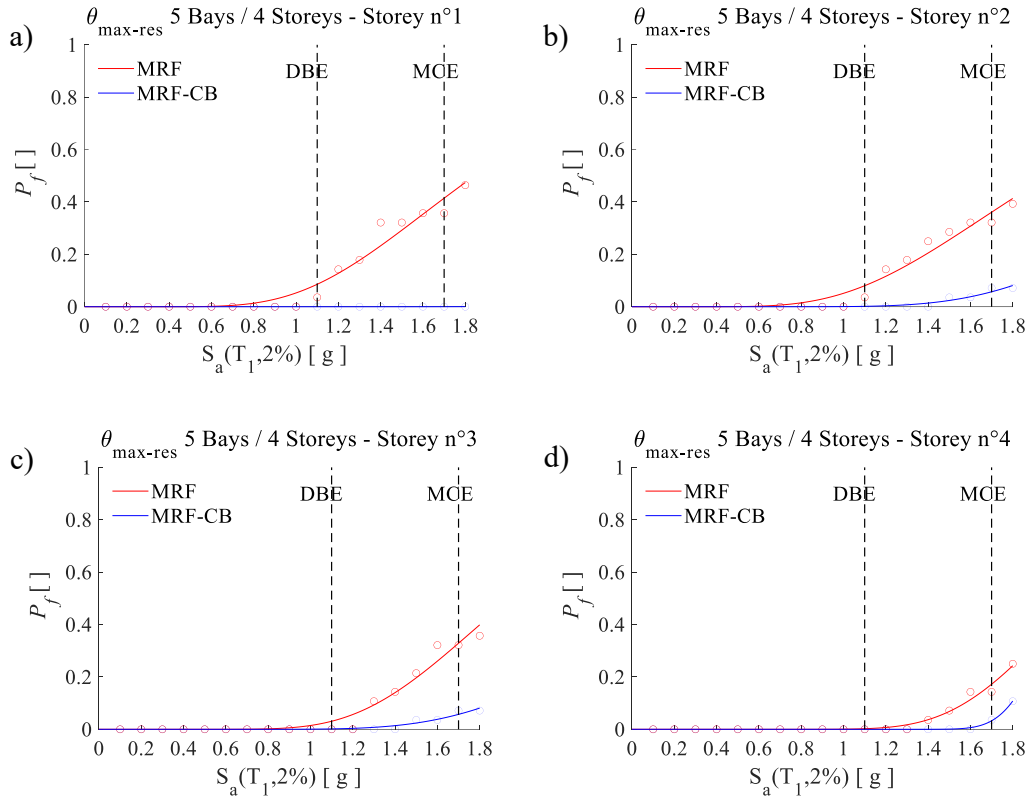

Figure A 9: Comparison of the storey-level fragility curves for the maximum residual interstorey drifts with respect to the threshold limit of 0.5%, for the MRF 5-4

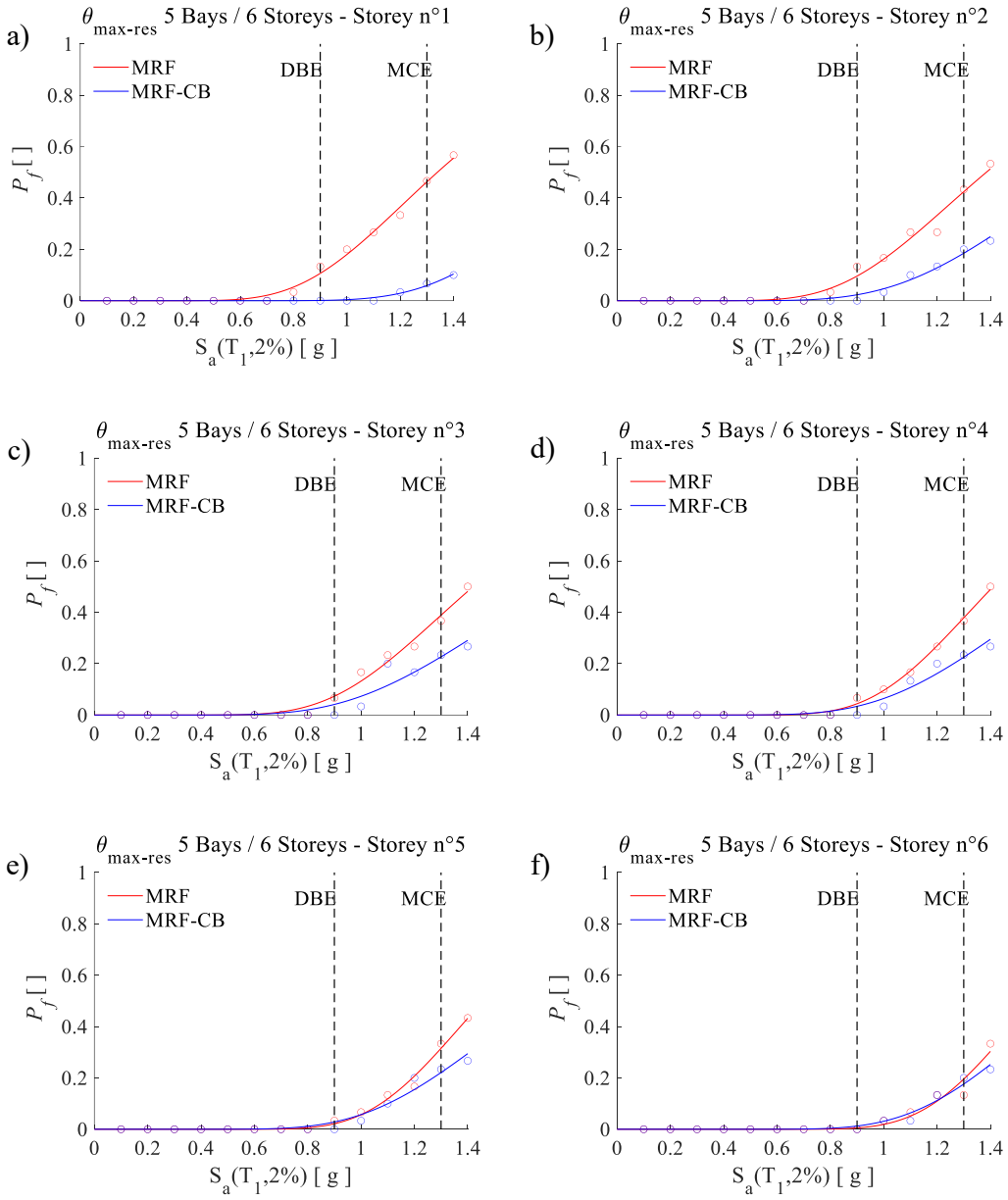

Figure A 10: Comparison of the storey-level fragility curves for the maximum residual interstorey drifts with respect to the threshold limit of 0.5%, for the MRF 5-6

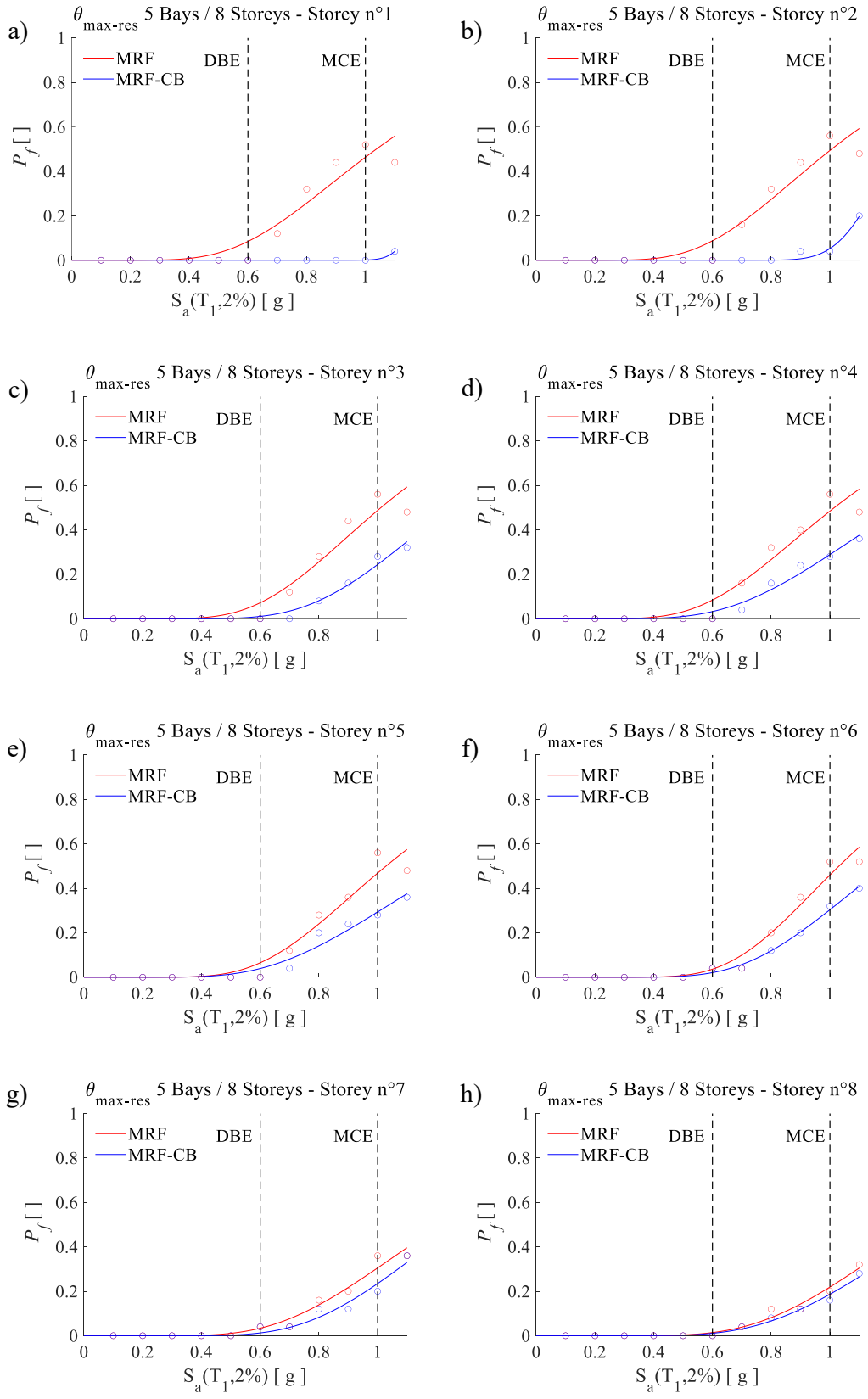

Figure A 11: Comparison of the storey-level fragility curves for the maximum residual interstorey drifts with respect to the threshold limit of 0.5%, for the MRF 5-8

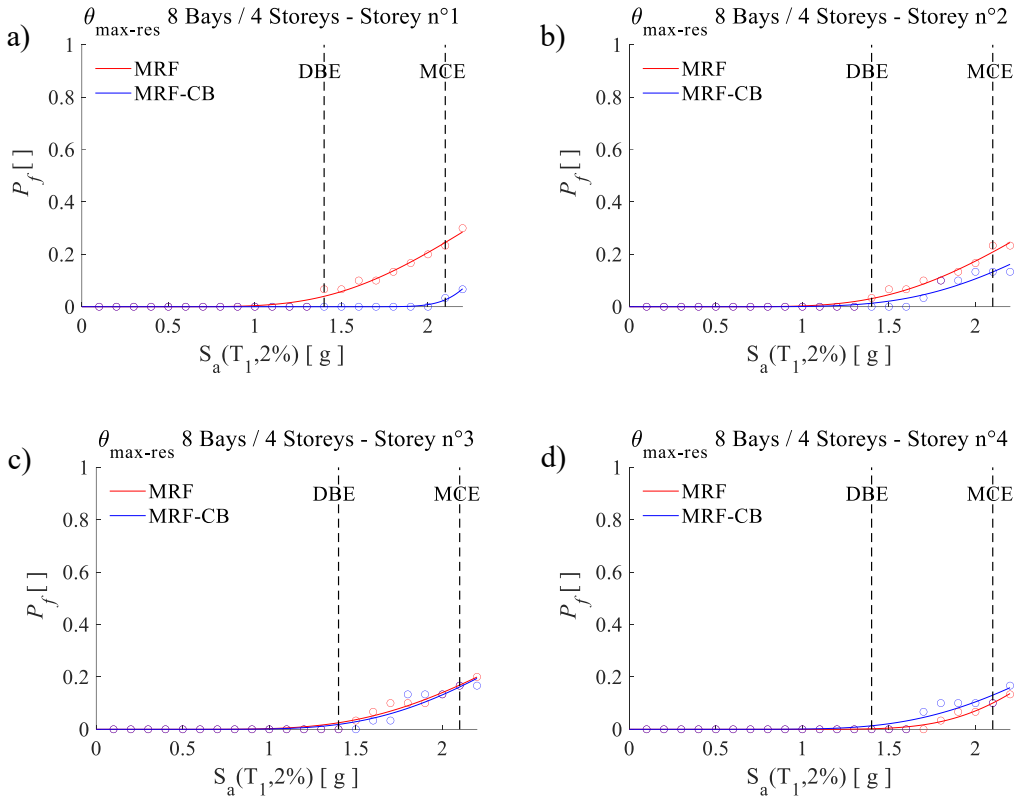

Figure A 12: Comparison of the storey-level fragility curves for the maximum residual interstorey drifts with respect to the threshold limit of 0.5%, for the MRF 8-4

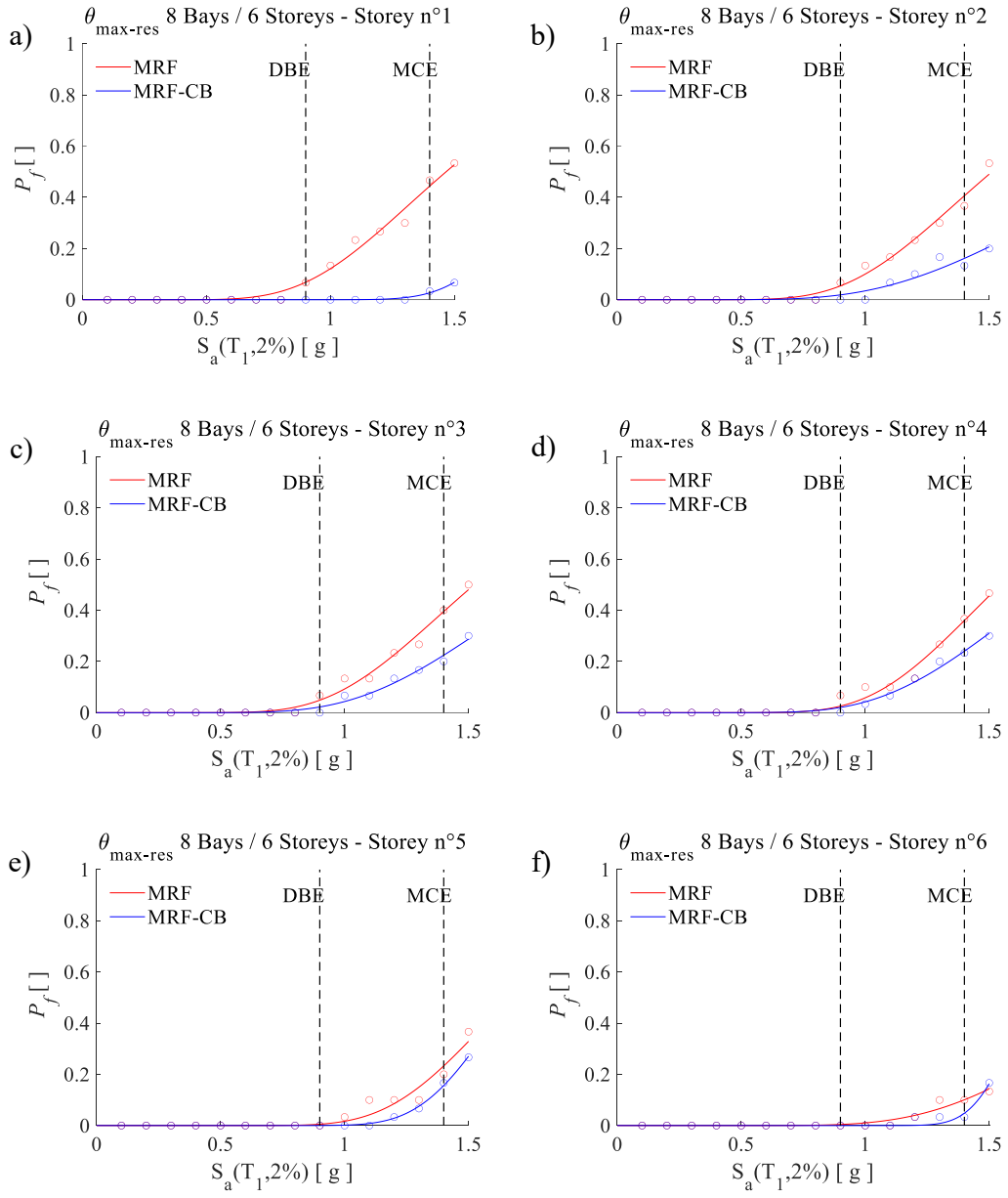

Figure A 13: Comparison of the storey-level fragility curves for the maximum residual interstorey drifts with respect to the threshold limit of 0.5%, for the MRF 8-6

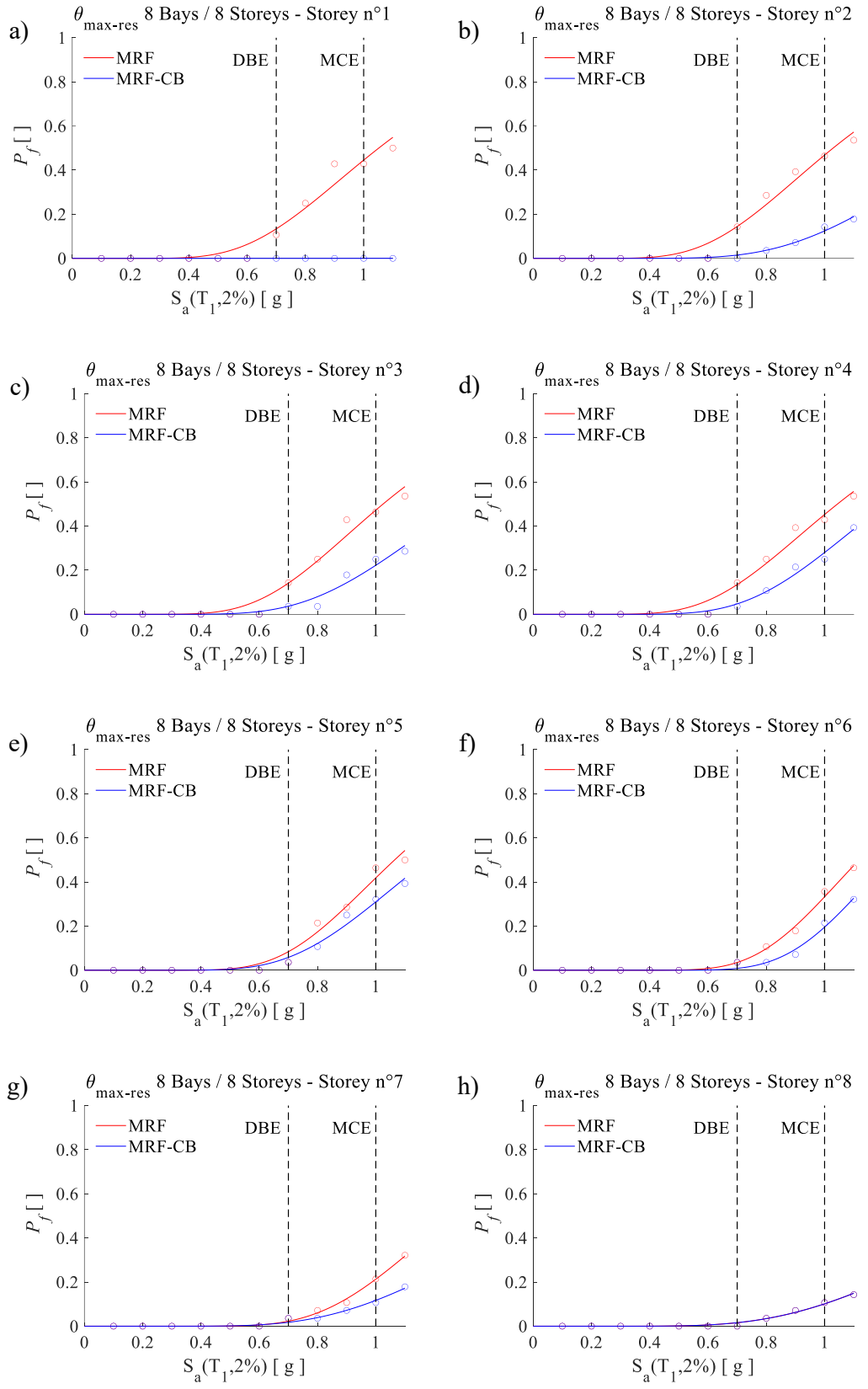

Figure A 14: Comparison of the storey-level fragility curves for the maximum residual interstorey drifts with respect to the threshold limit of 0.5%, for the MRF 8-8

ANNEX B

ANNEX B

B1. Details of the Large-Scale Structure (Chapter 6)

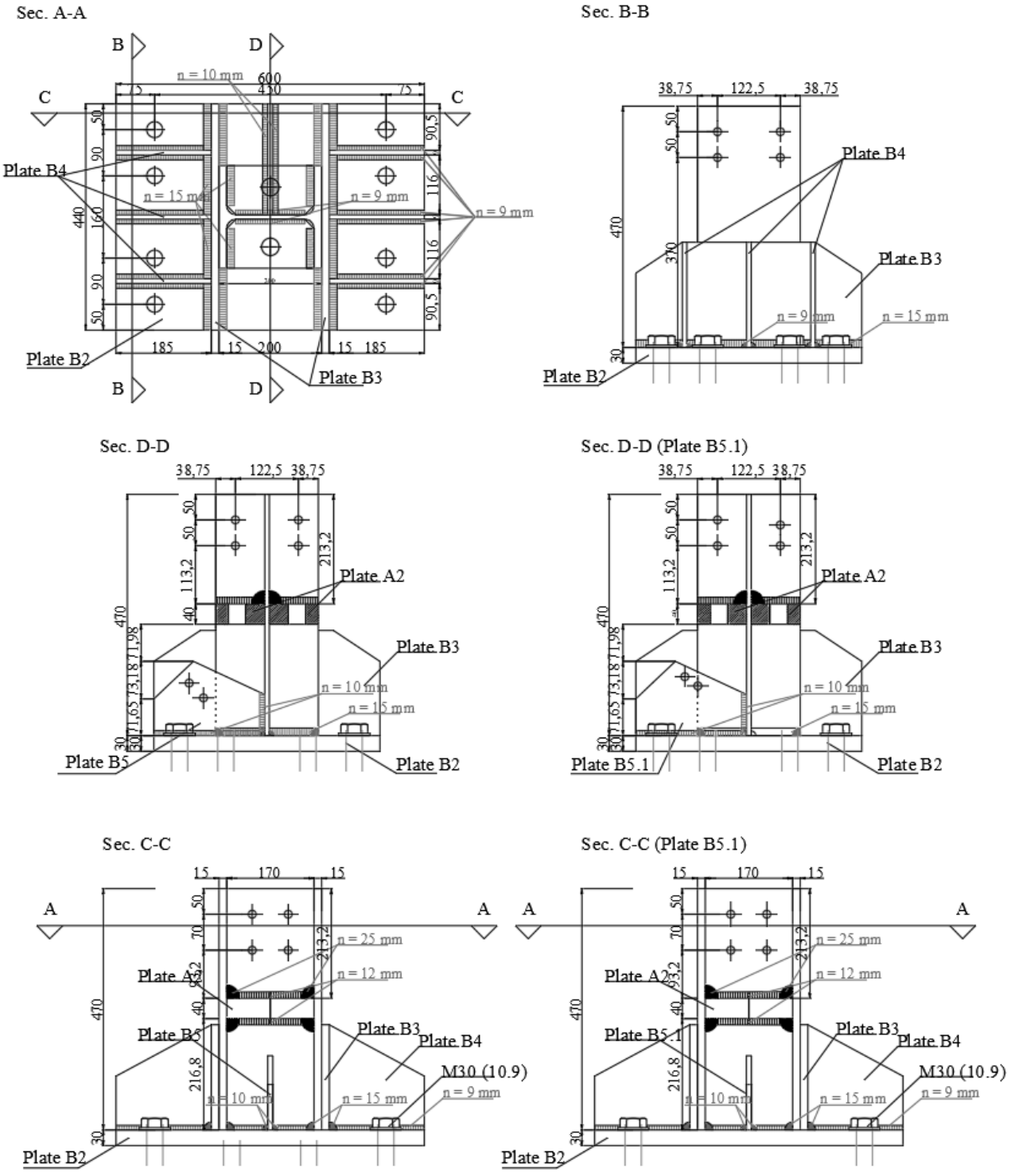

Figure B 1: Lower part of the SC-CB (dimensions in mm)

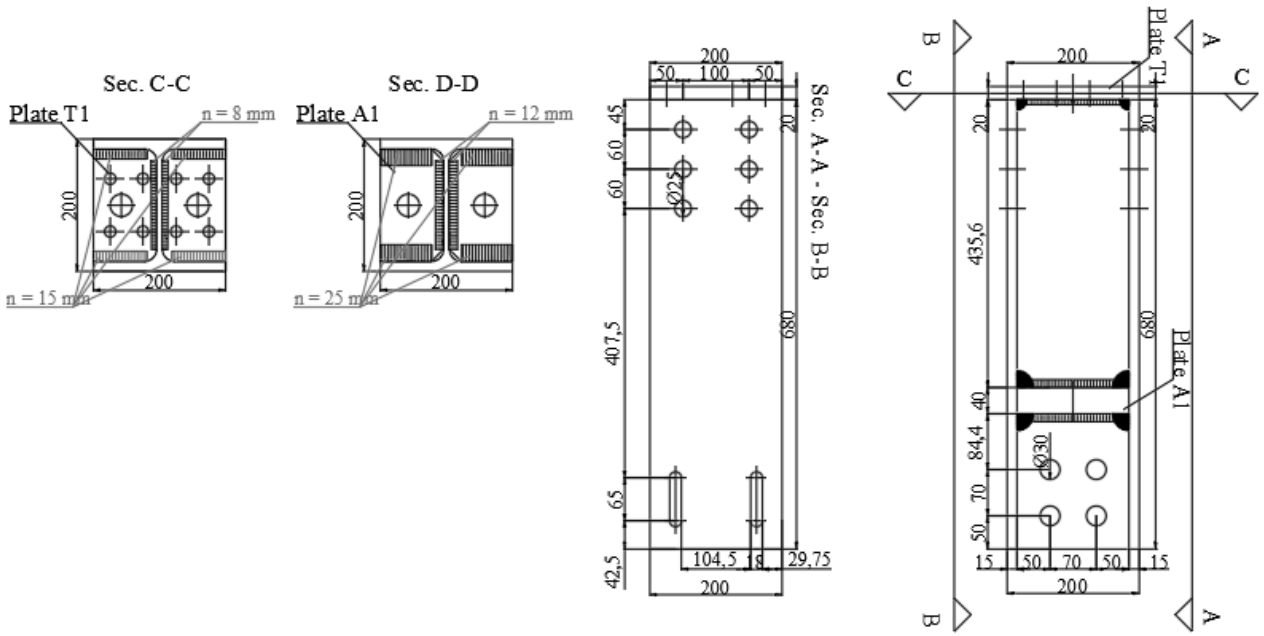

Figure B 2: Upper part of the SC-CB (dimensions in mm)

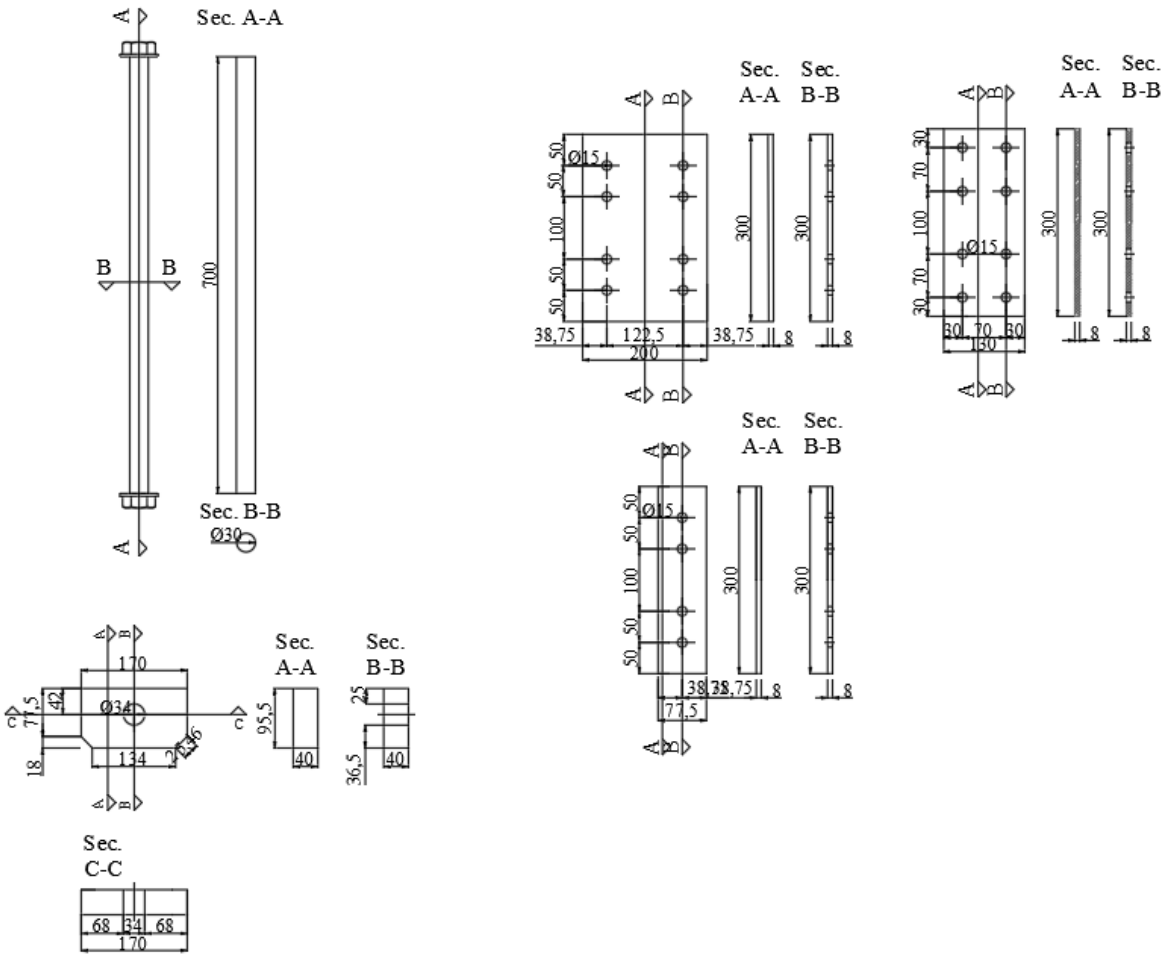

Figure B 3: Single components and plates of the SC-CB (dimensions in mm)

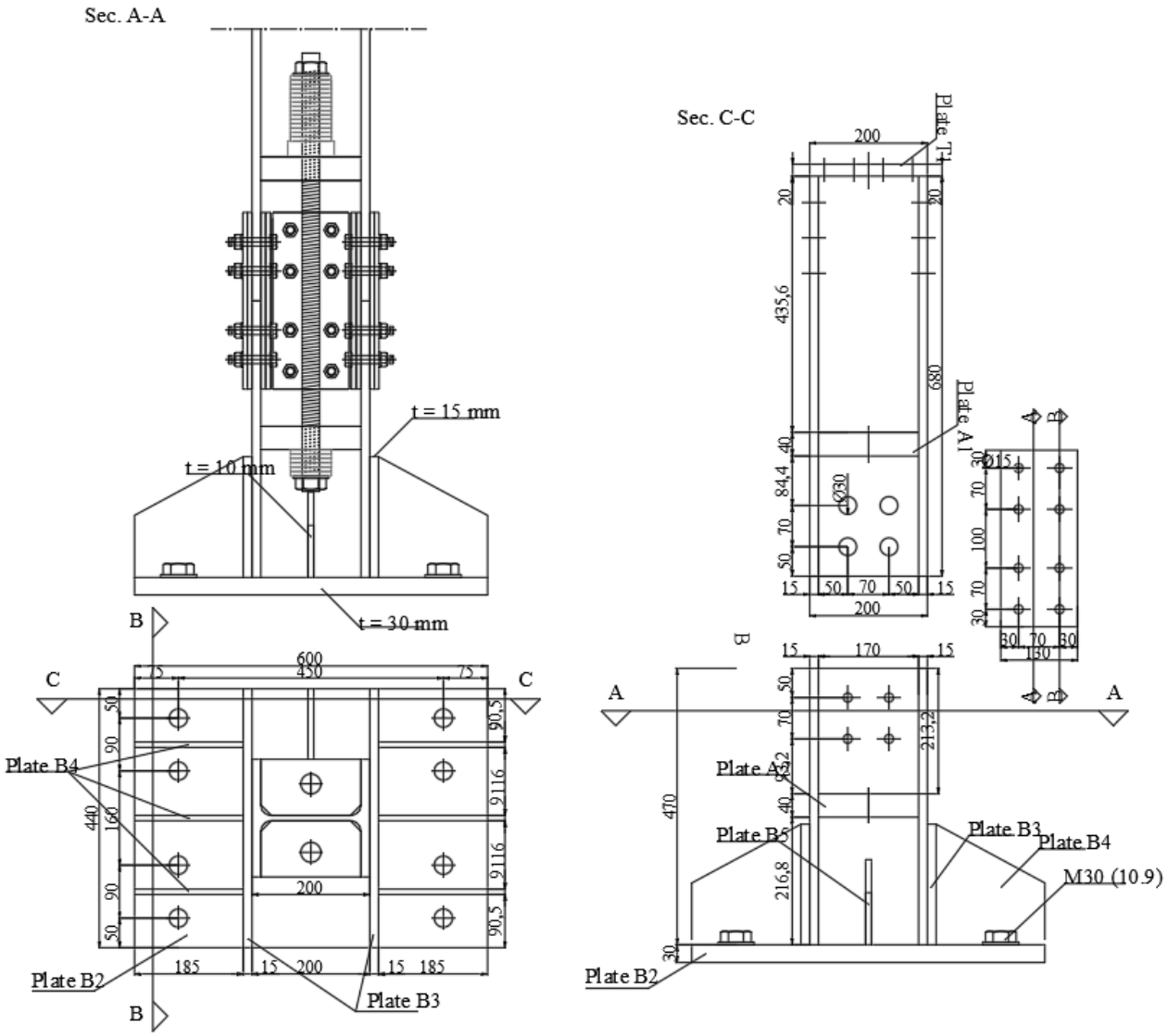

Figure B 4: Assembly of the SC-CB (dimensions in mm)

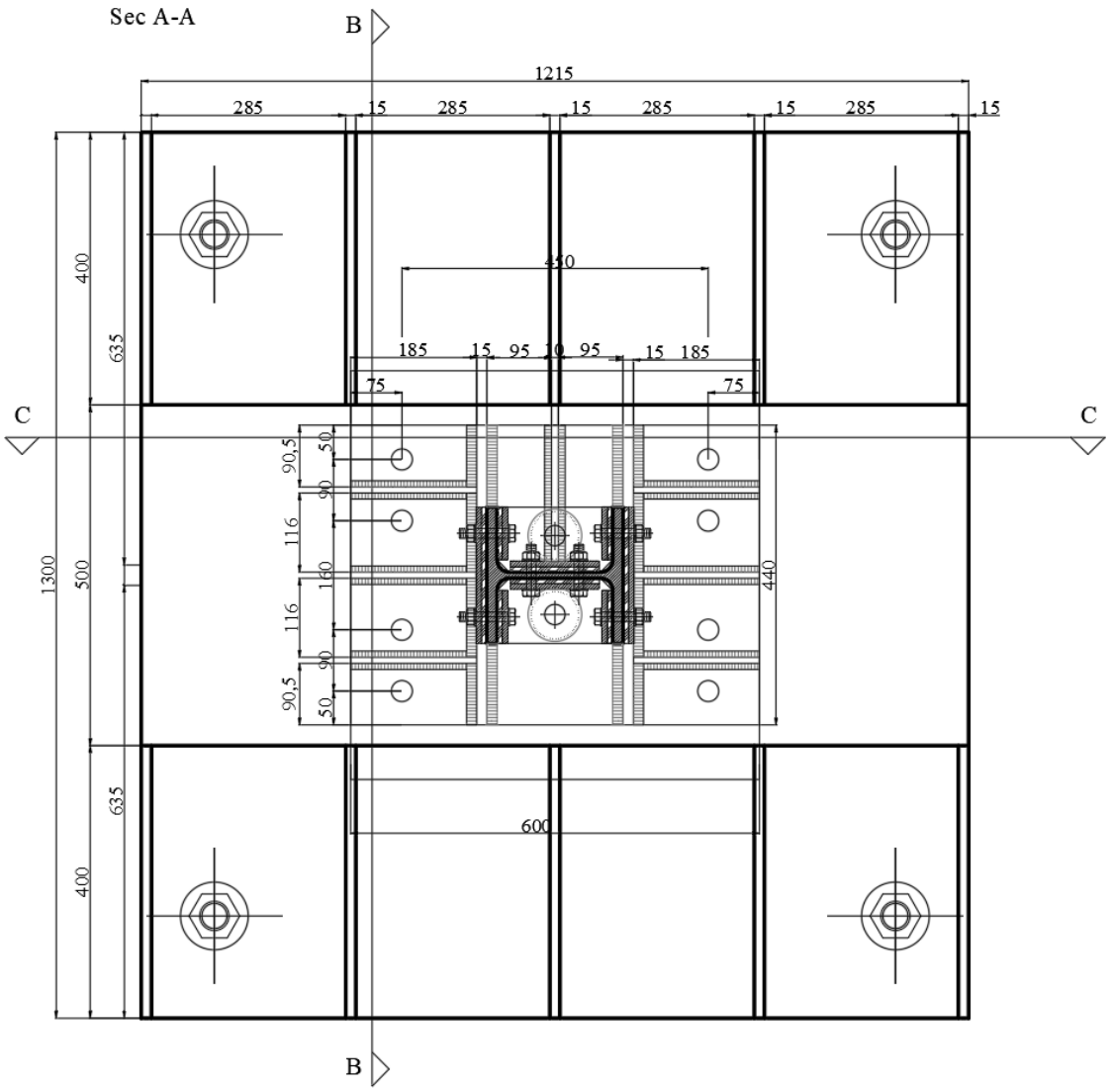

Figure B 5: Detail of the base plate in plan (dimensions in mm)

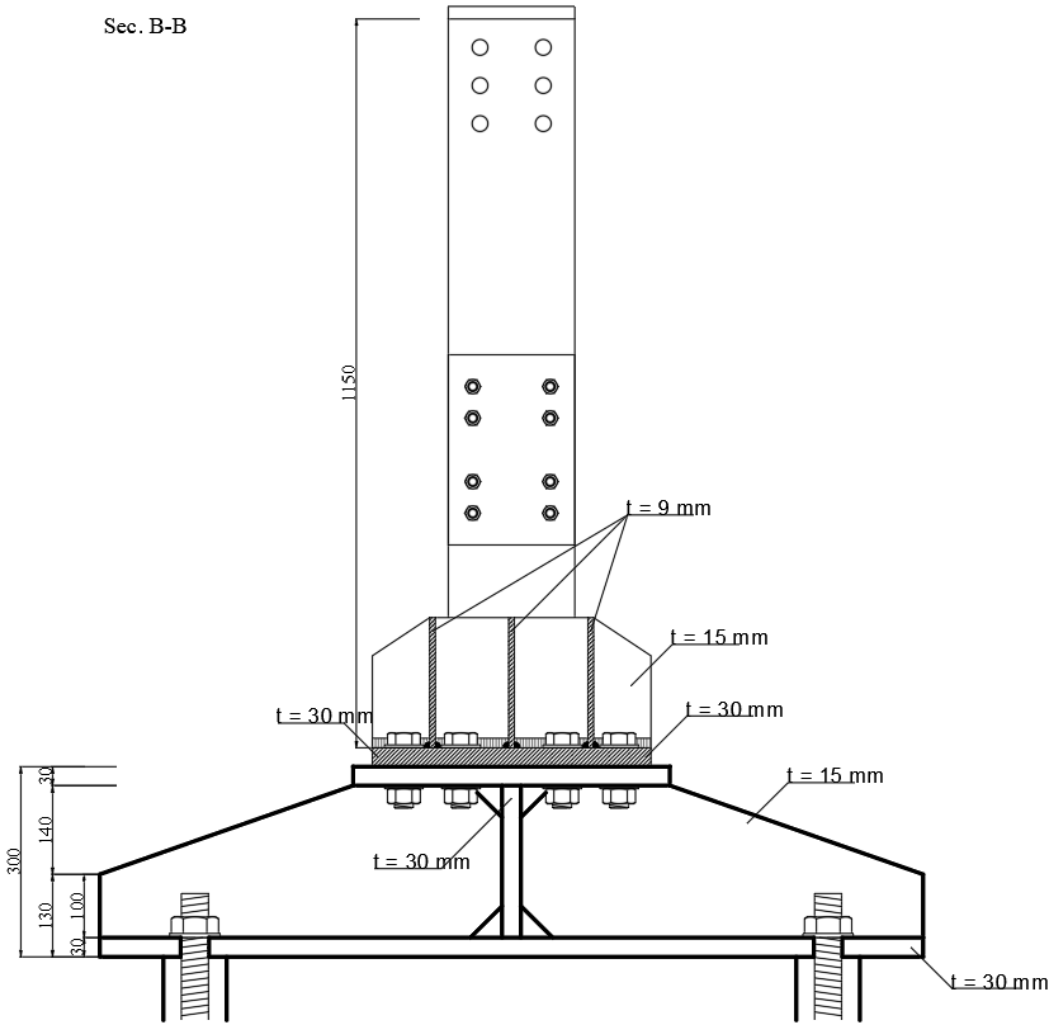

Figure B 6: Detail of the base plate in side view (dimensions in mm)

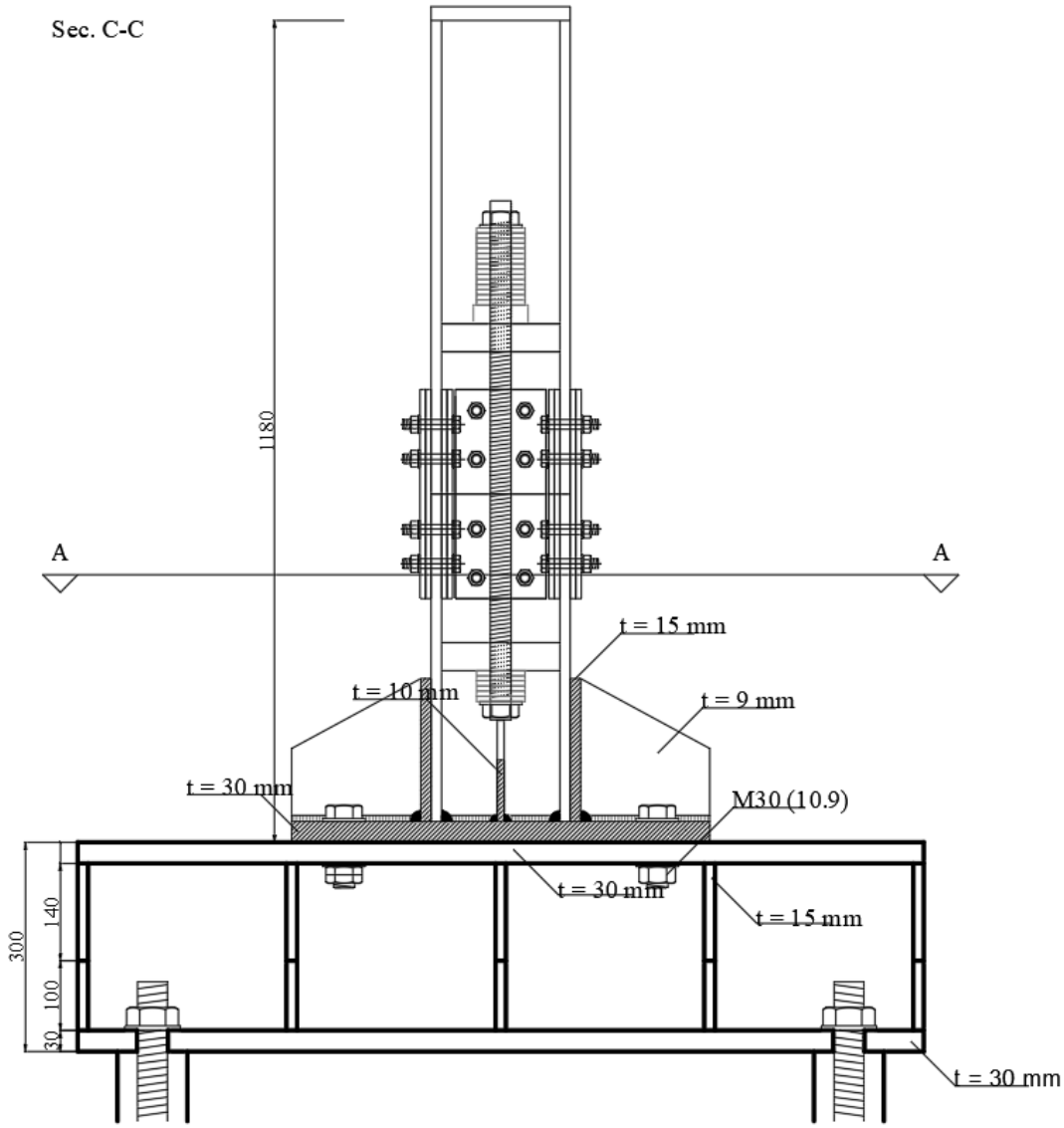

Figure B 7: Detail of the base plate side view (dimensions in mm)

B1. Results of the Experimental Campaign (Chapter 6)

B1.1 Santa Barbara (PGA=0.80g) Test 4

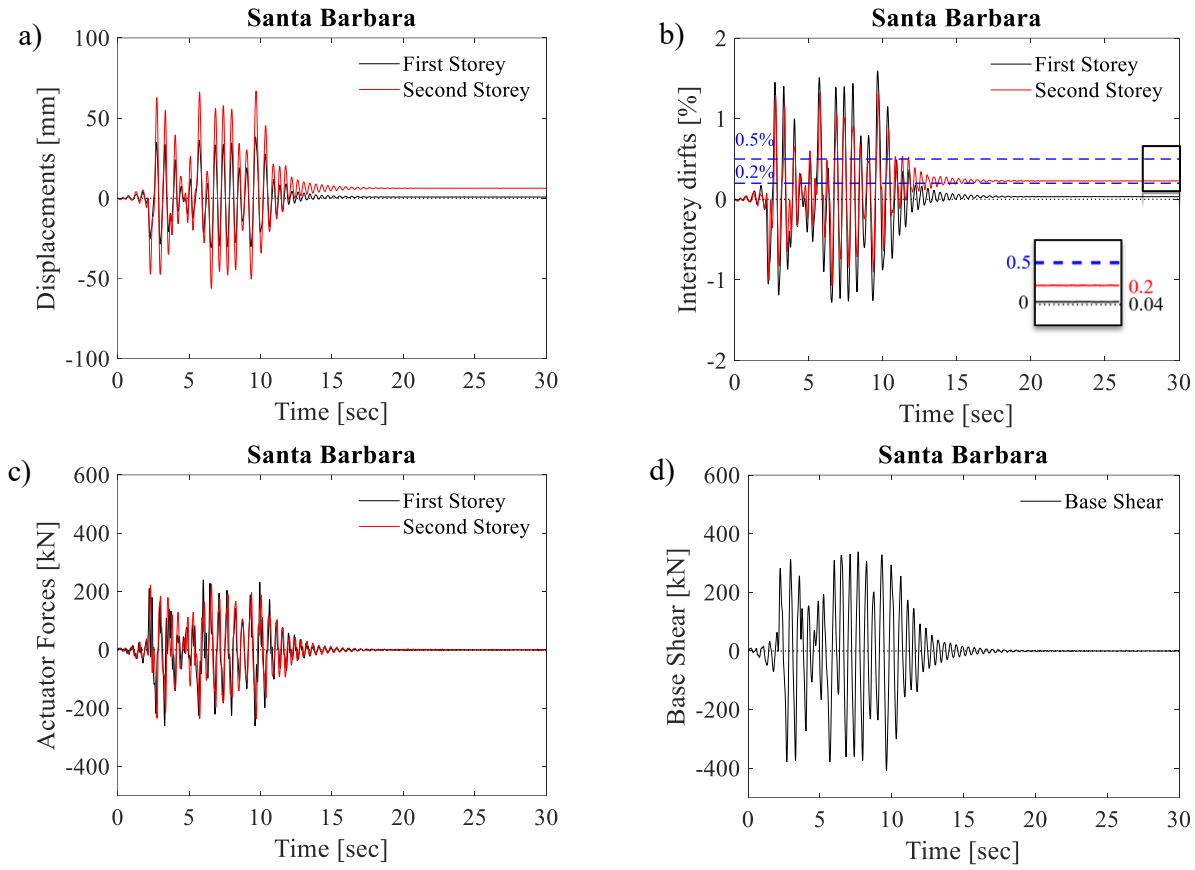

Figure B 8: Global Results for Test 4

Table 58. Global Results for Test 4

Maximum Base Shear (kN)	Pull		341
	Push		-357
Peak displacement (mm)	Pull	Level 1	-30.66
		Level 2	-56.15
	Push	Level 1	38.13
		Level 2	66.81
Peak interstorey drift (%)	Pull	Level 1	-1.07
		Level 2	-1.27
	Push	Level 1	1.32
		Level 2	1.59
Residual displacement (mm)	-	Level 1	0.88
		Level 2	6.35
Residual interstorey drift (%)	-	Level 1	0.04
		Level 2	0.23

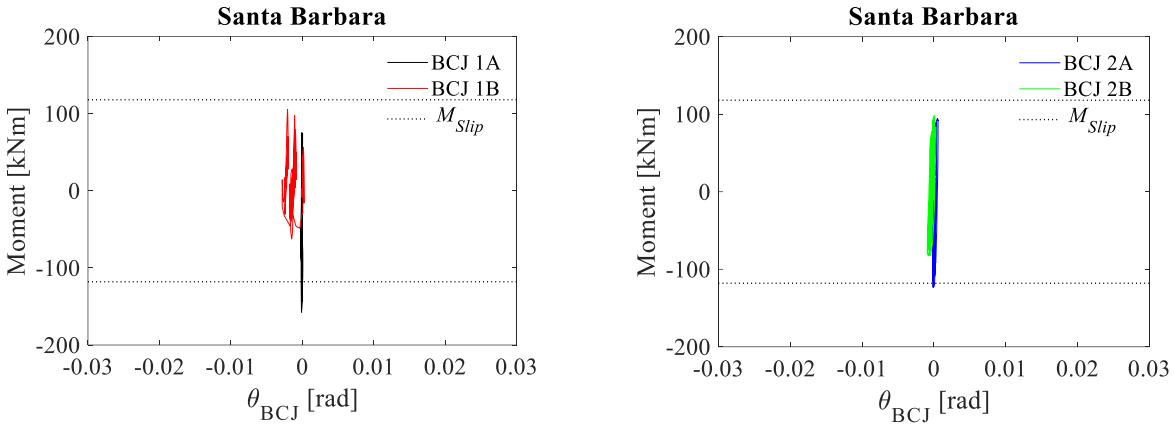

Figure B 9: Moment-rotation curves of FREEDAM BCJs for Test 4

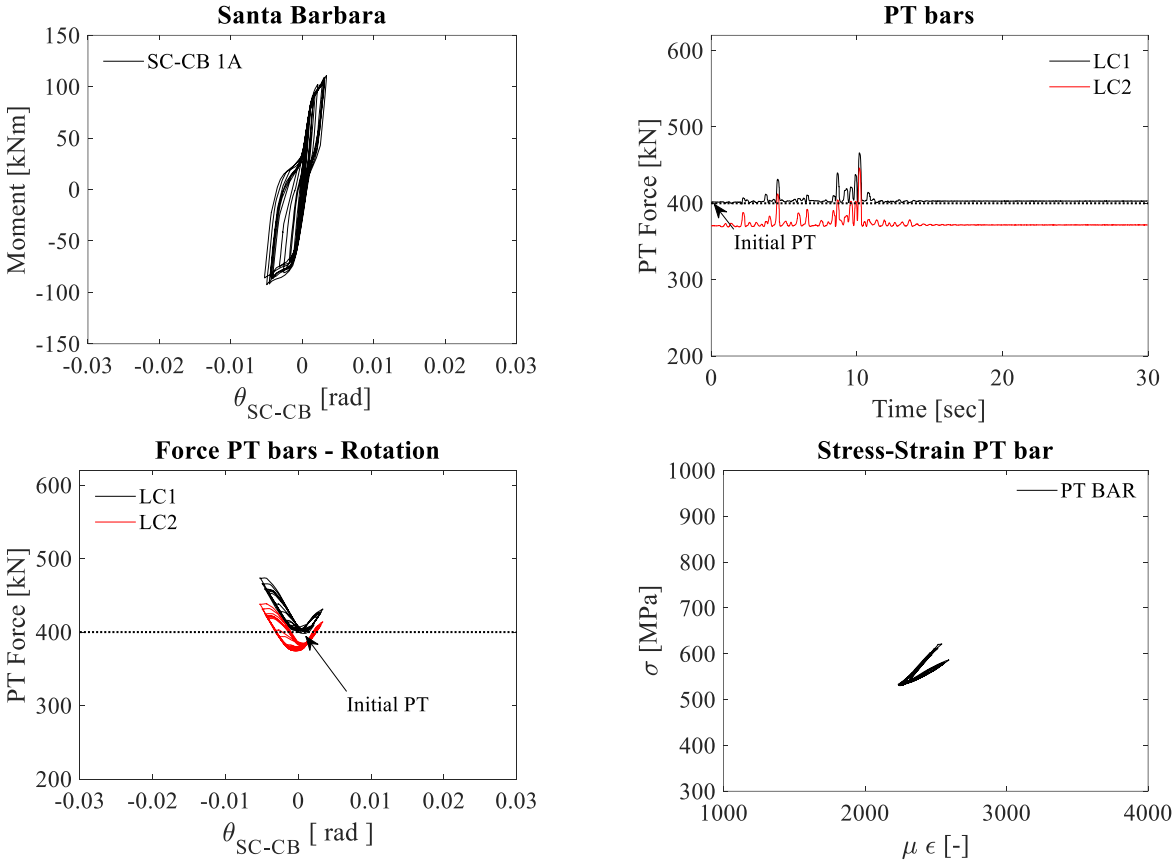

Figure B 10: Results of SC-CB 1A for Test 4

B1.2 Coalinga (PGA=0.80g) Test 5

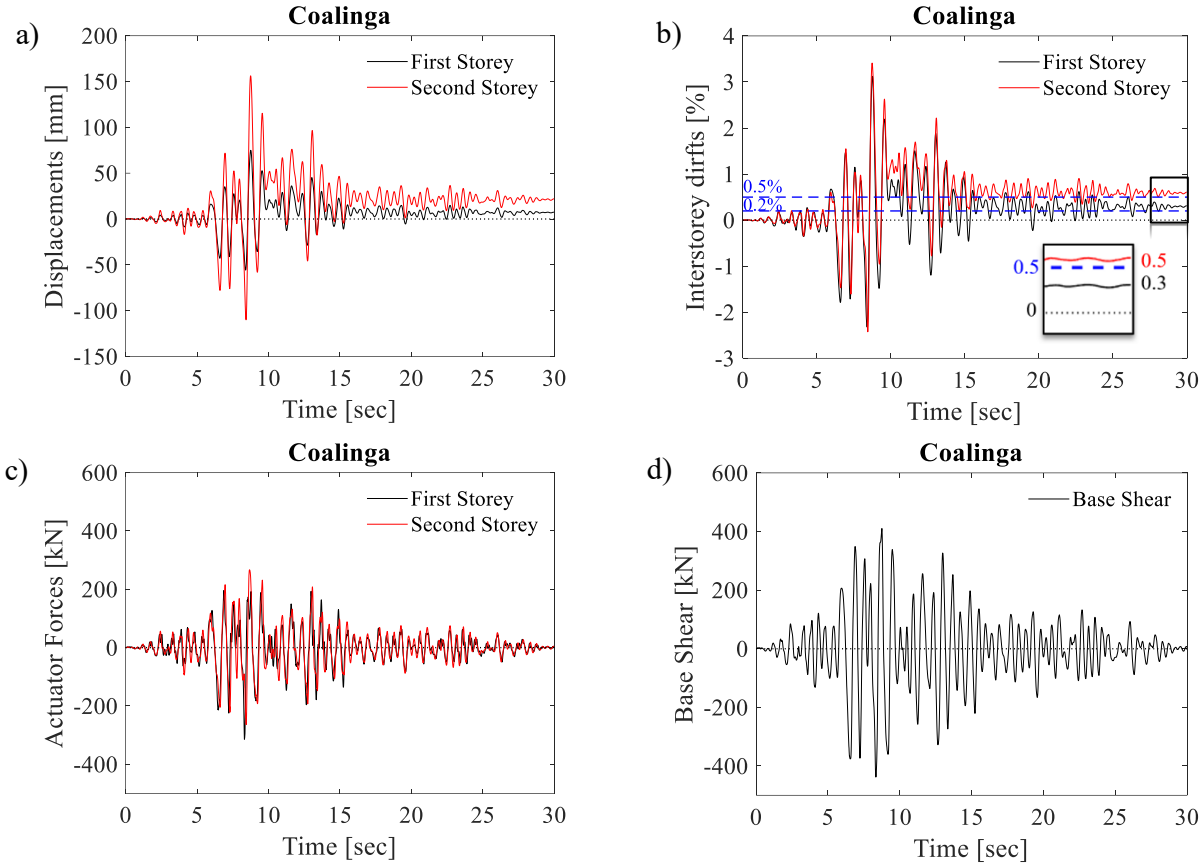

Figure B 11: Global Results for Test 5

Table 59. Global Results for Test 5

Maximum Base Shear (kN)	Pull		-438
	Push		411
Peak displacement (mm)	Pull	Level 1	-55.69
		Level 2	-109.99
	Push	Level 1	74.94
		Level 2	156.21
Peak interstorey drift (%)	Pull	Level 1	-2.32
		Level 2	-2.43
	Push	Level 1	3.12
		Level 2	3.41
Residual displacement (mm)	-	Level 1	7.32
		Level 2	20.51
Residual interstorey drift (%)	-	Level 1	0.31
		Level 2	0.54

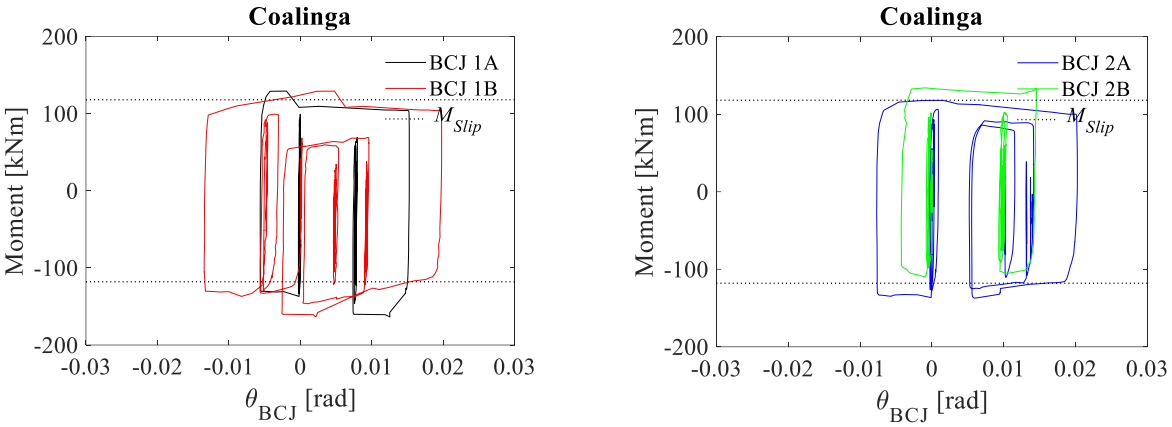

Figure B 12: Moment-rotation curves of FREEDAM BCJs for Test 5

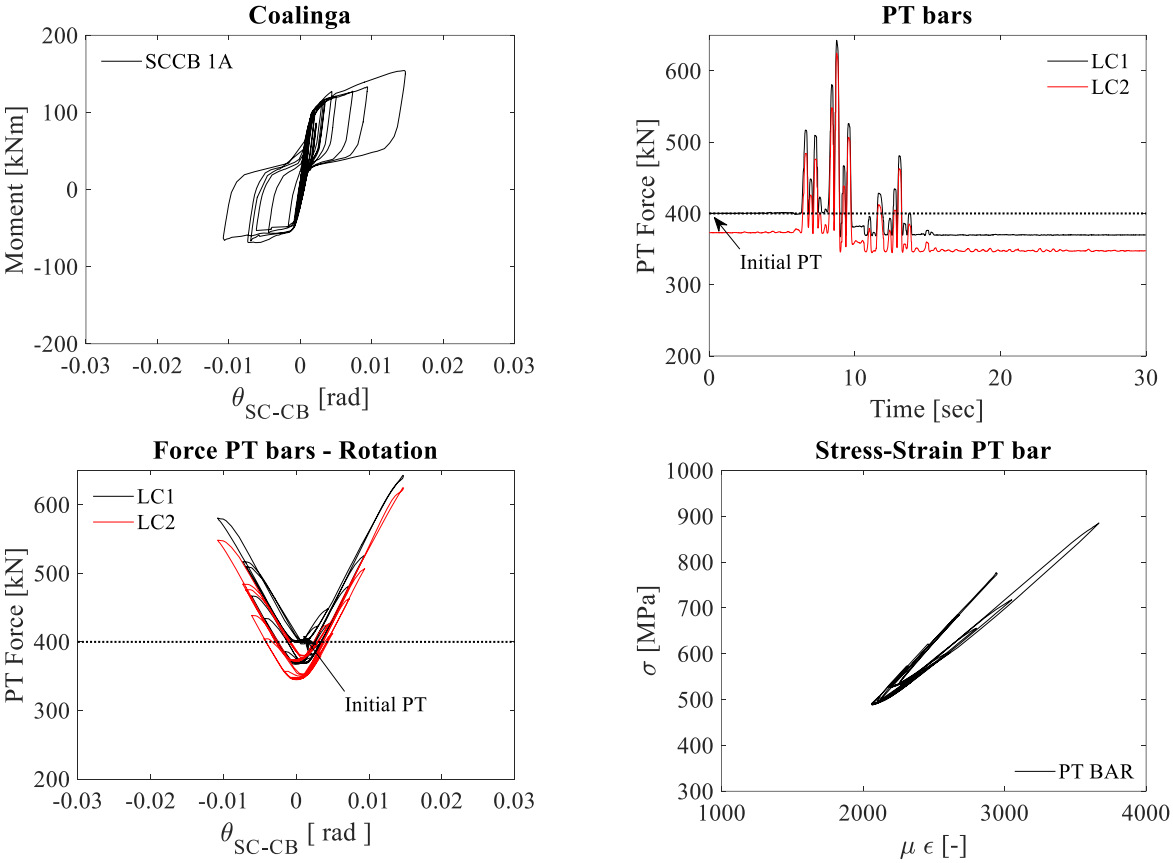

Figure B 13: Results of SC-CB 1A for Test 5

B1.3 Kobe (PGA=0.80g) Test 6

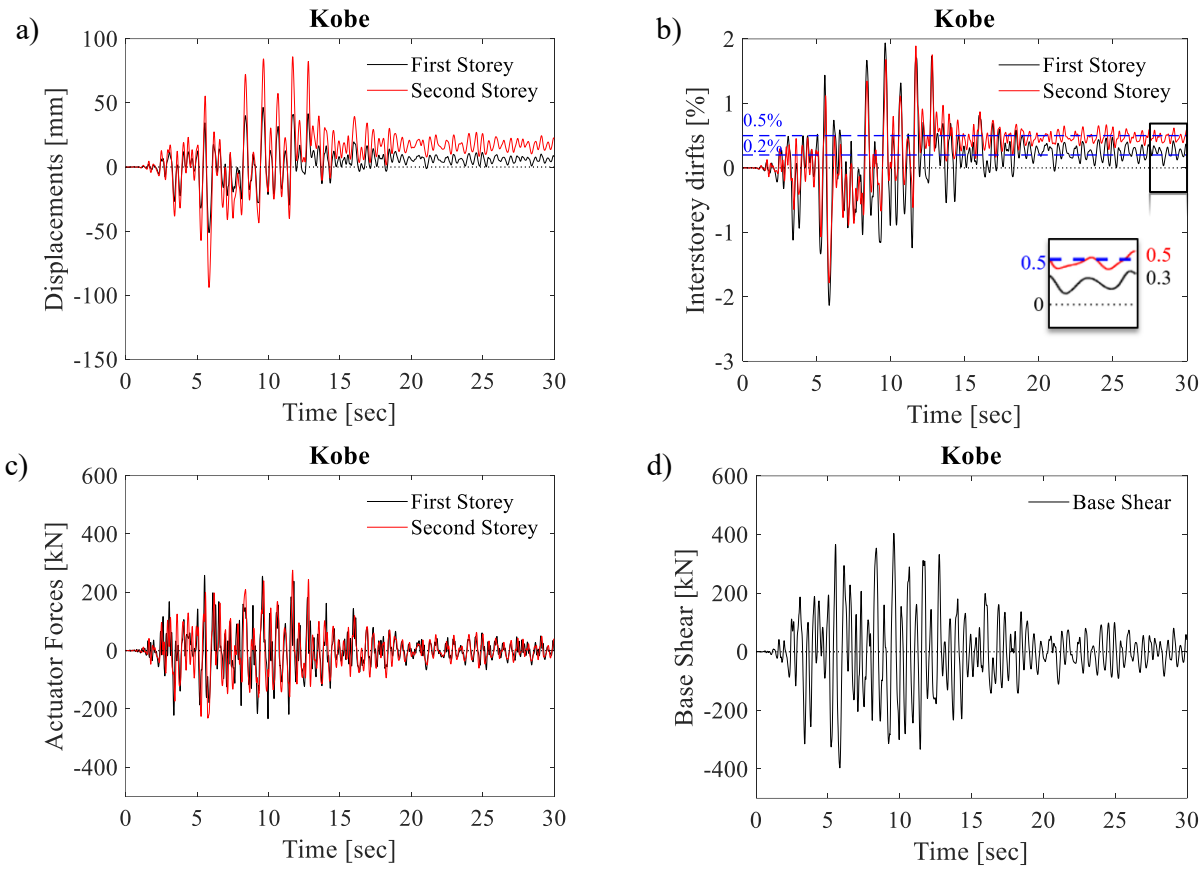

Figure B 14: Global Results for Test 6

Table 60. Global Results for Test 6

Maximum Base Shear (kN)	Pull		-395
	Push		404
Peak displacement (mm)	Pull	Level 1	-51.17
		Level 2	-93.86
	Push	Level 1	40.79
		Level 2	85.93
Peak interstorey drift (%)	Pull	Level 1	-2.12
		Level 2	-1.78
	Push	Level 1	1.70
		Level 2	1.89
Residual displacement (mm)	-	Level 1	8.11
		Level 2	21.10
Residual interstorey drift (%)	-	Level 1	0.34
		Level 2	0.55

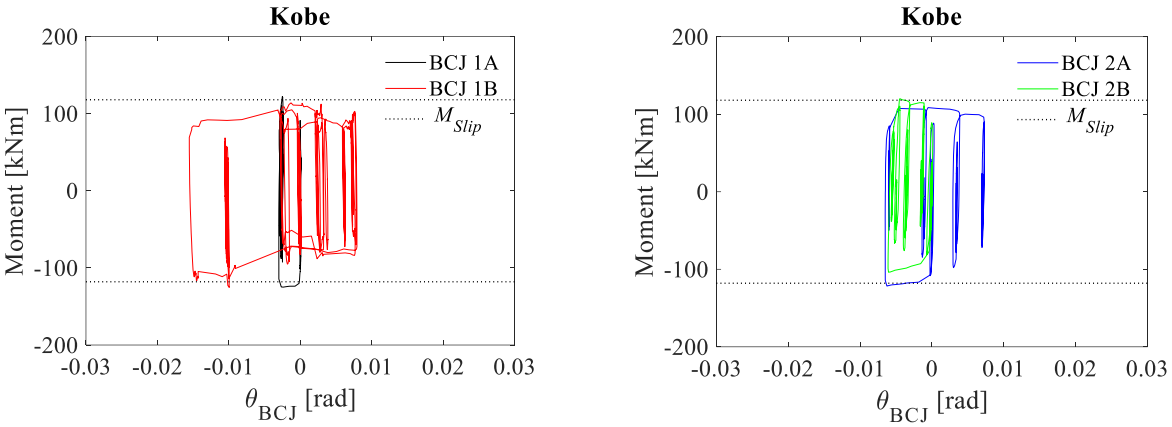

Figure B 15: Moment-rotation curves of FREEDAM BCJs for Test 6

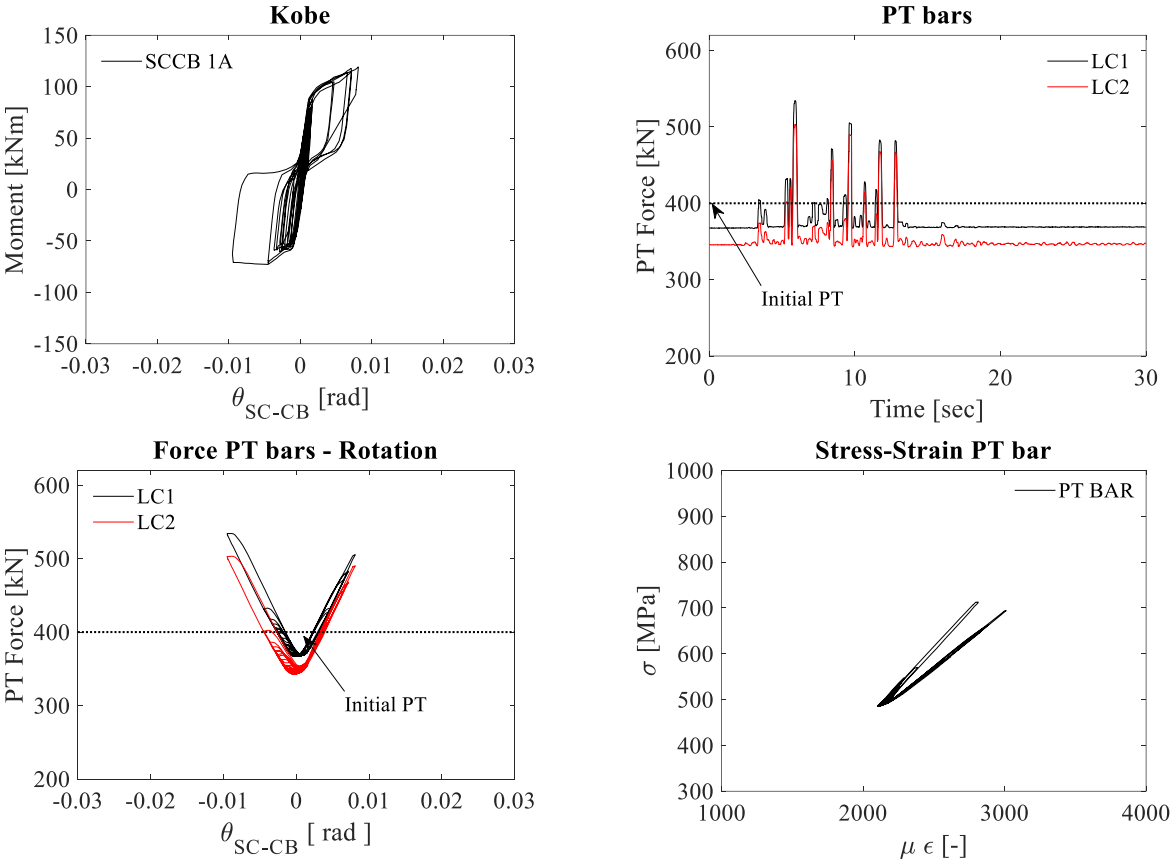

Figure B 16: Results of SC-CB 1A for Test 6

B1.4 Imperial Valley (PGA=1.10g) Test 7

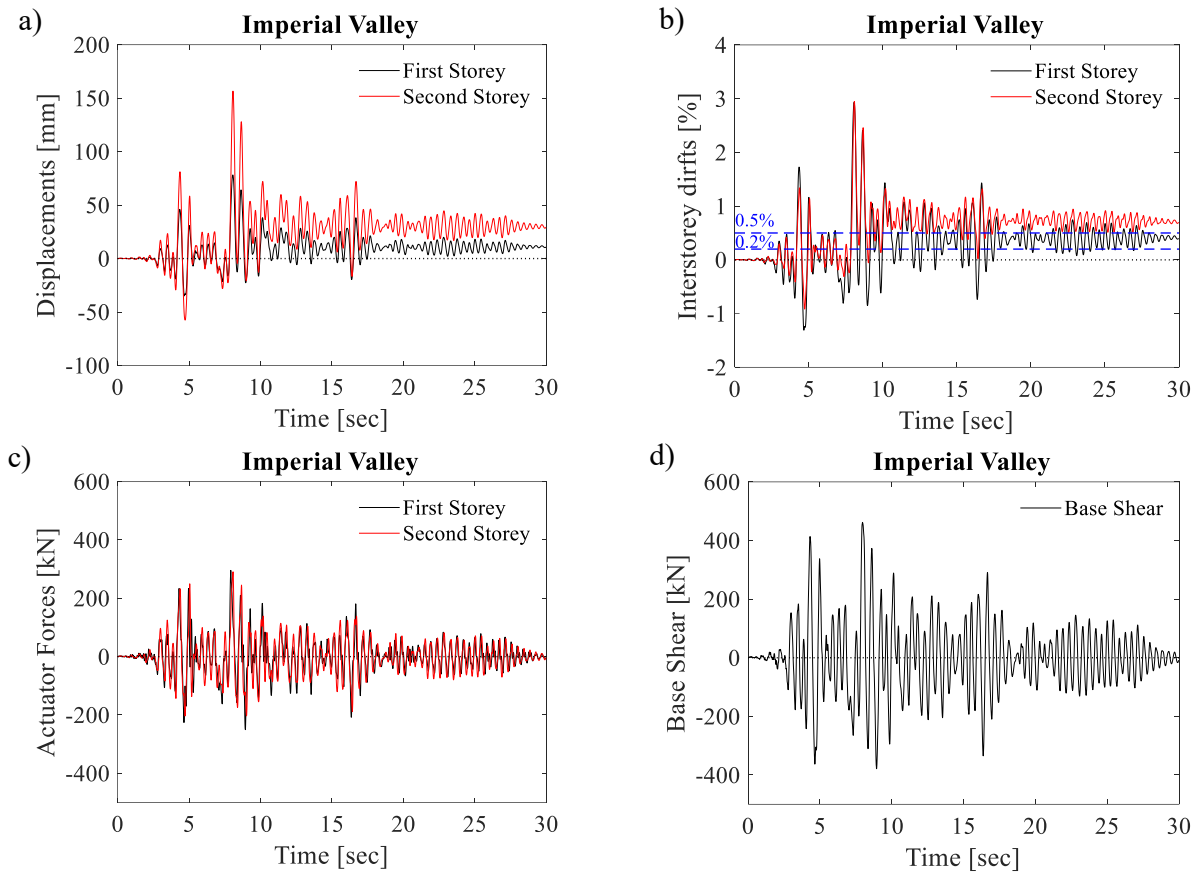

Figure B 17: Global Results for Test 7

Table 61. Global Results for Test 7

Maximum Base Shear (kN)	Pull		-379
	Push		462
Peak displacement (mm)	Pull	Level 1	-34.91
		Level 2	-57.50
	Push	Level 1	78.19
		Level 2	156.61
Peak interstorey drift (%)	Pull	Level 1	-1.31
		Level 2	-0.91
	Push	Level 1	2.93
		Level 2	2.94
Residual displacement (mm)	-	Level 1	10.61
		Level 2	29.26
Residual interstorey drift (%)	-	Level 1	0.39
		Level 2	0.69

B1.5 Imperial Valley (PGA=1.10g) Test 8

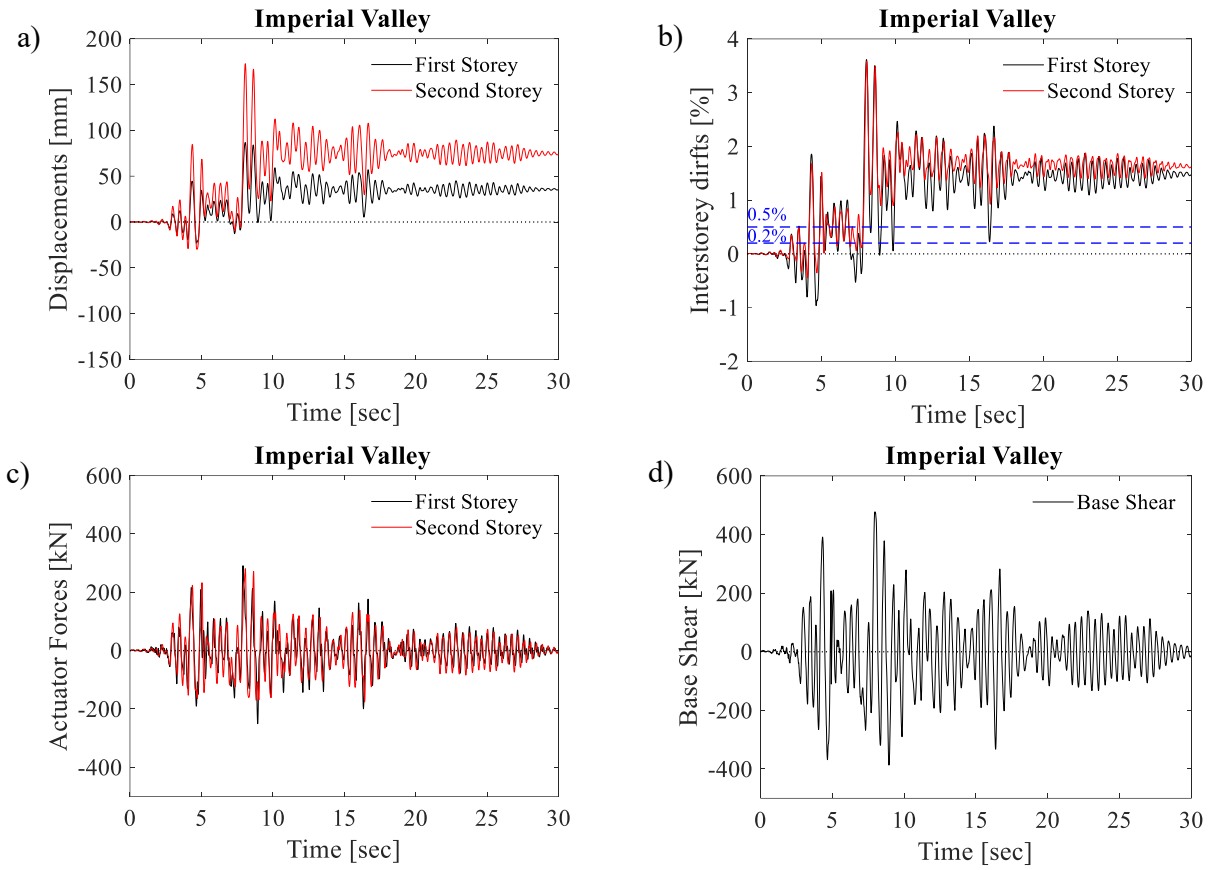

Figure B 18: Global Results for Test 8

Table 62. Global Results for Test 8

Maximum Base Shear (kN)	Pull		-359
	Push		449
Peak displacement (mm)	Pull	Level 1	-23.11
		Level 2	-29.77
	Push	Level 1	86.75
		Level 2	172.74
Peak interstorey drift (%)	Pull	Level 1	-0.96
		Level 2	-0.36
	Push	Level 1	3.62
		Level 2	3.58
Residual displacement (mm)	-	Level 1	35.29
		Level 2	74.21
Residual interstorey drift (%)	-	Level 1	1.48
		Level 2	1.62

B2. Validation of the numerical model (Chapter 6)

B2.1 Global Results

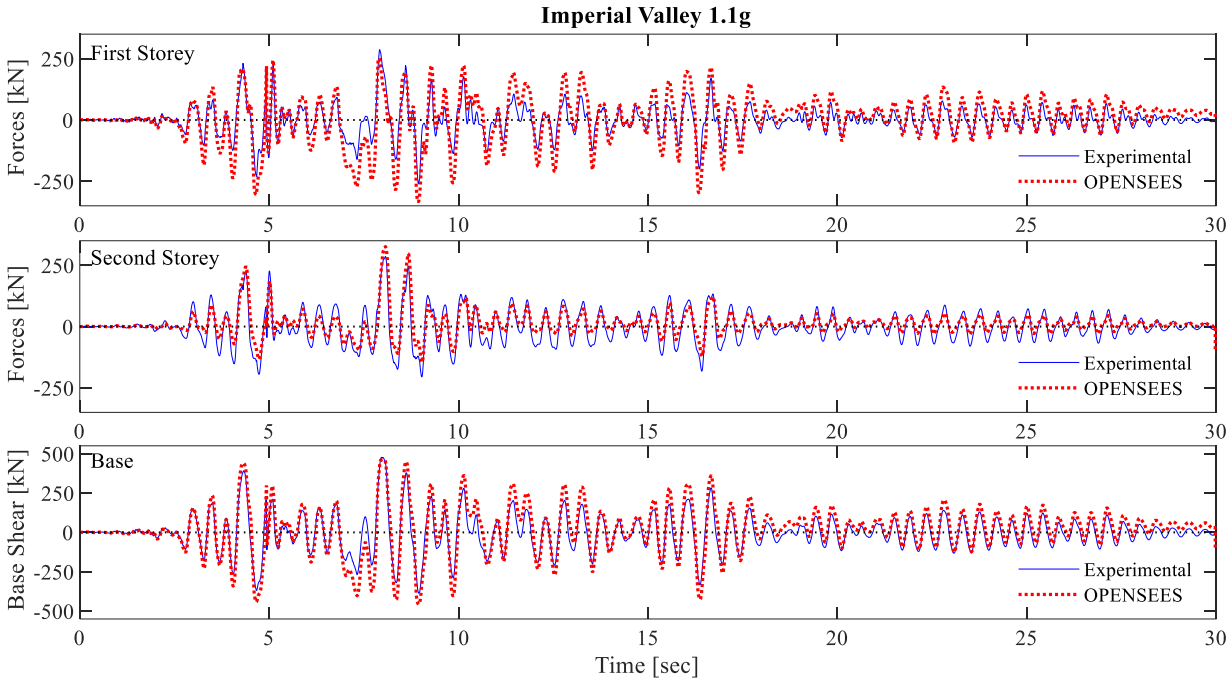

Figure B 19: FEM validation. Actuator forces and base shear for Test 1

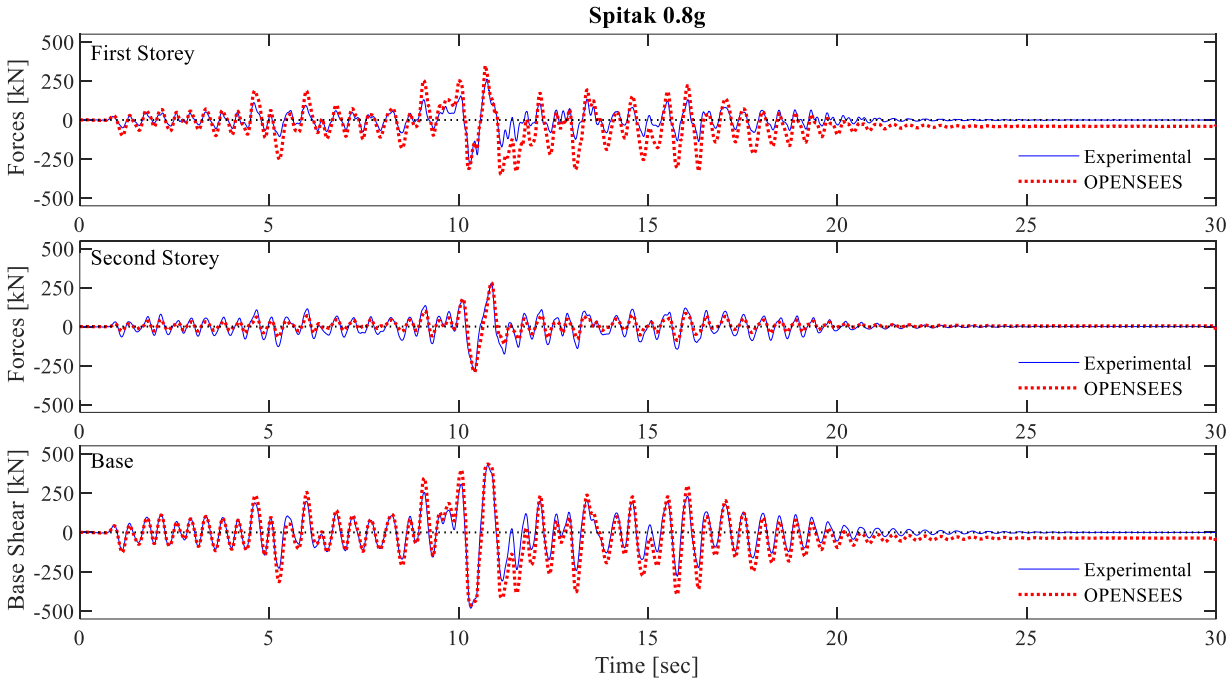

Figure B 20: FEM validation. Actuator forces and base shear for Test 2

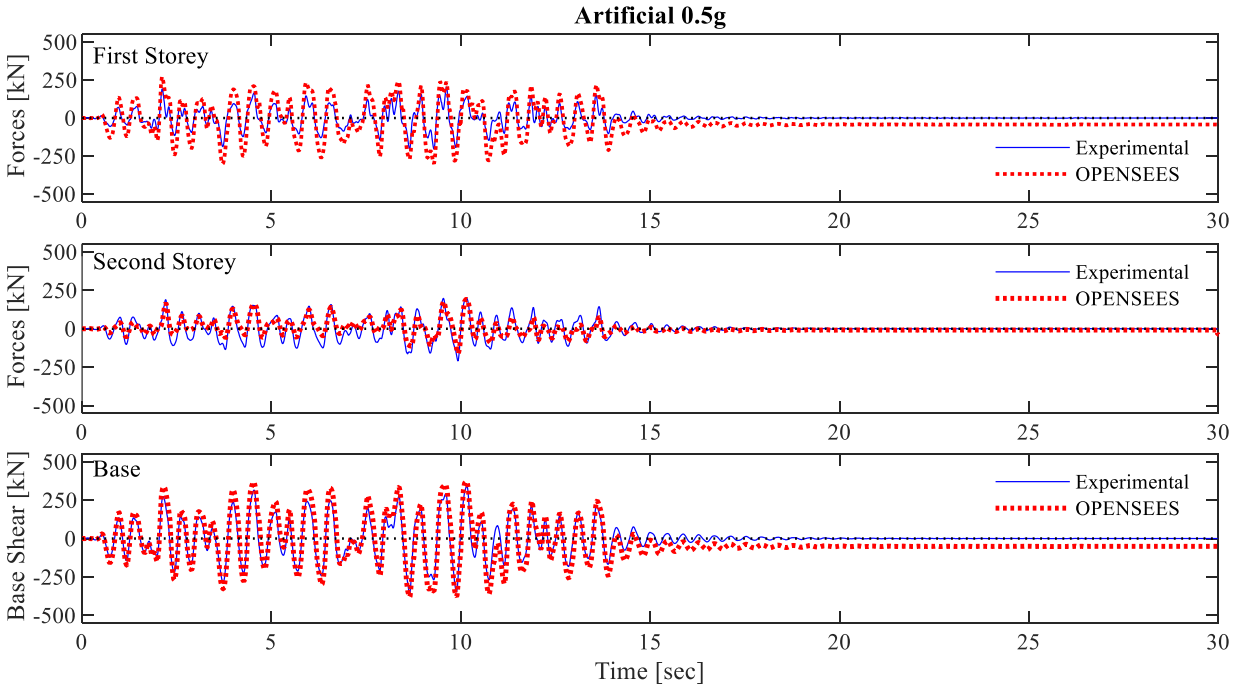

Figure B 21: FEM validation. Actuator forces and base shear for Test 3

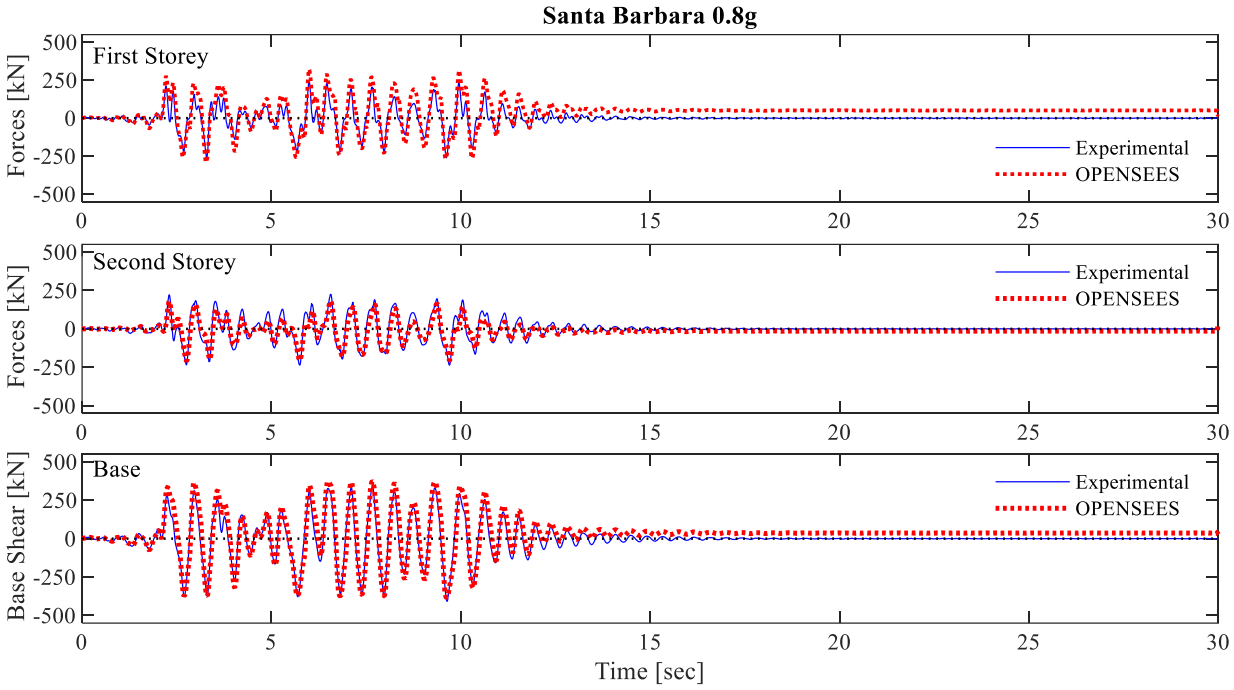

Figure B 22: FEM validation. Actuator forces and base shear for Test 4

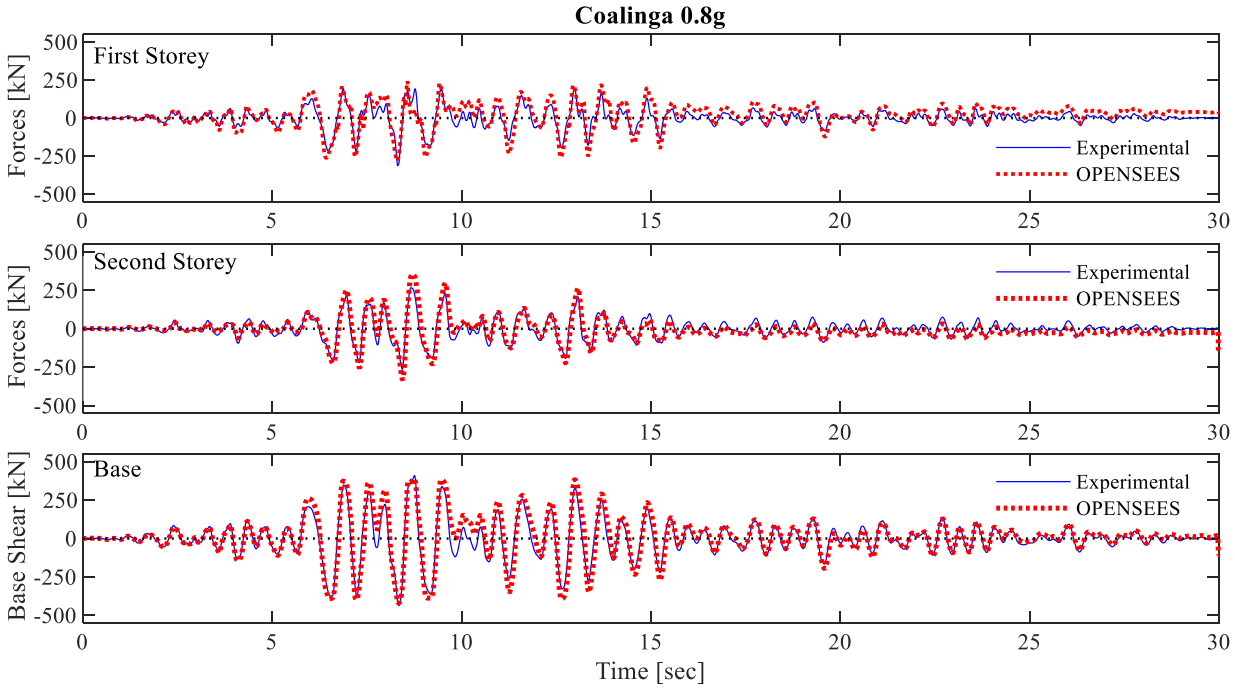

Figure B 23: FEM validation. Actuator forces and base shear for Test 5

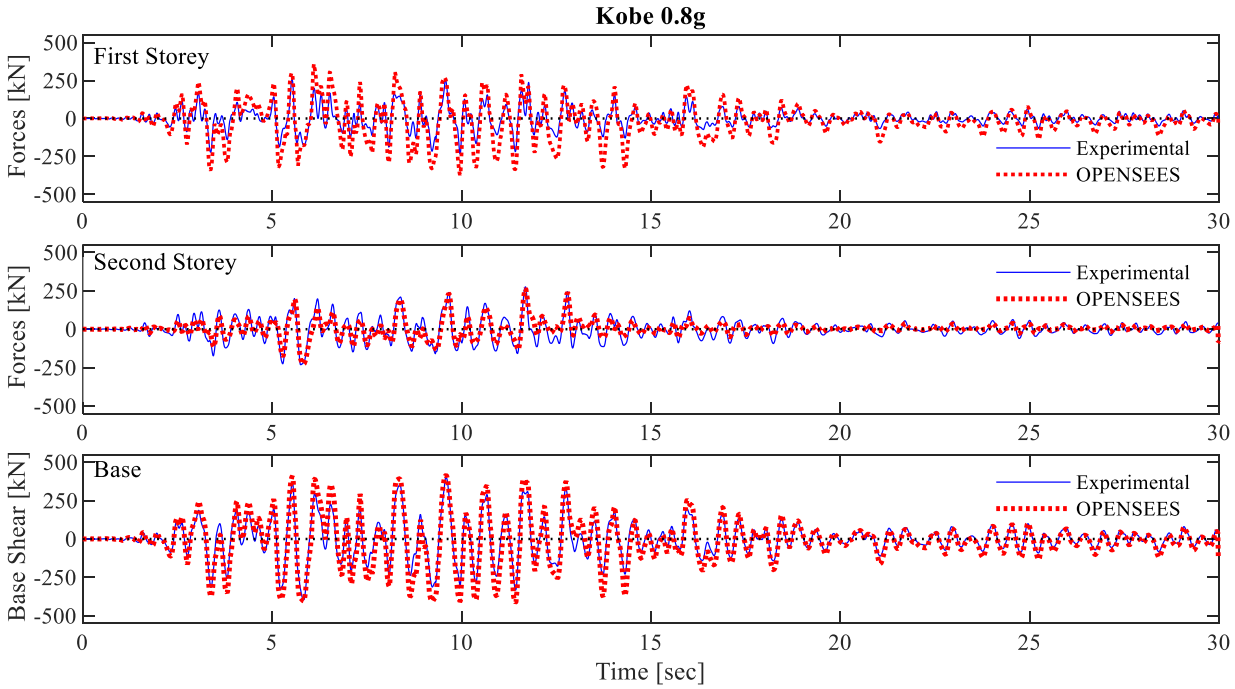

Figure B 24: FEM validation. Actuator forces and base shear for Test 6

B2.2 Local Results

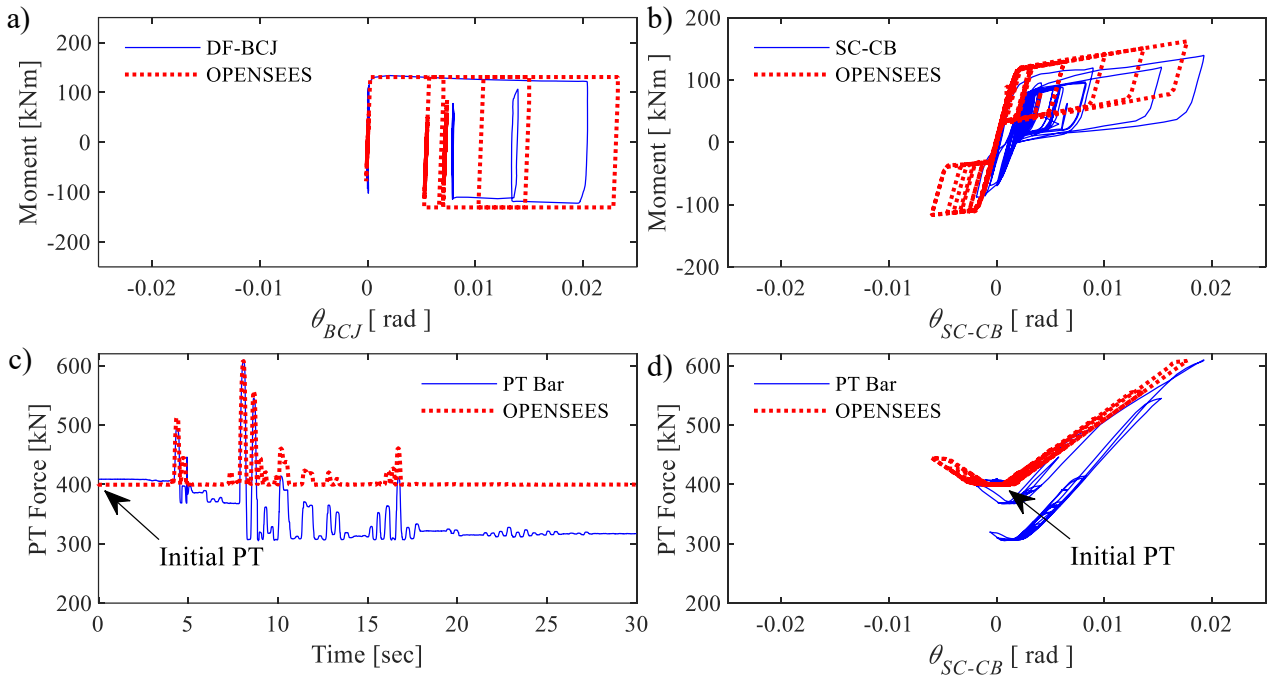

Figure B 25: FEM validation. Components of the SC-CB for Test 1

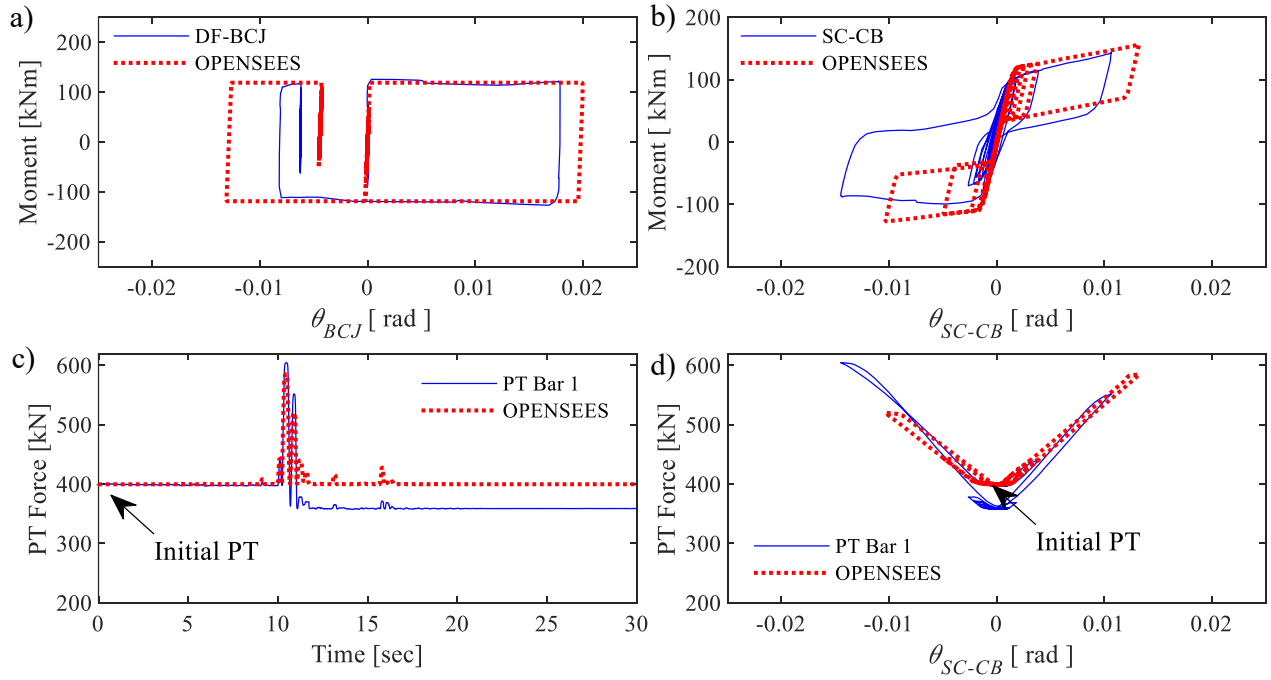

Figure B 26: FEM validation. Components of the SC-CB for Test 2

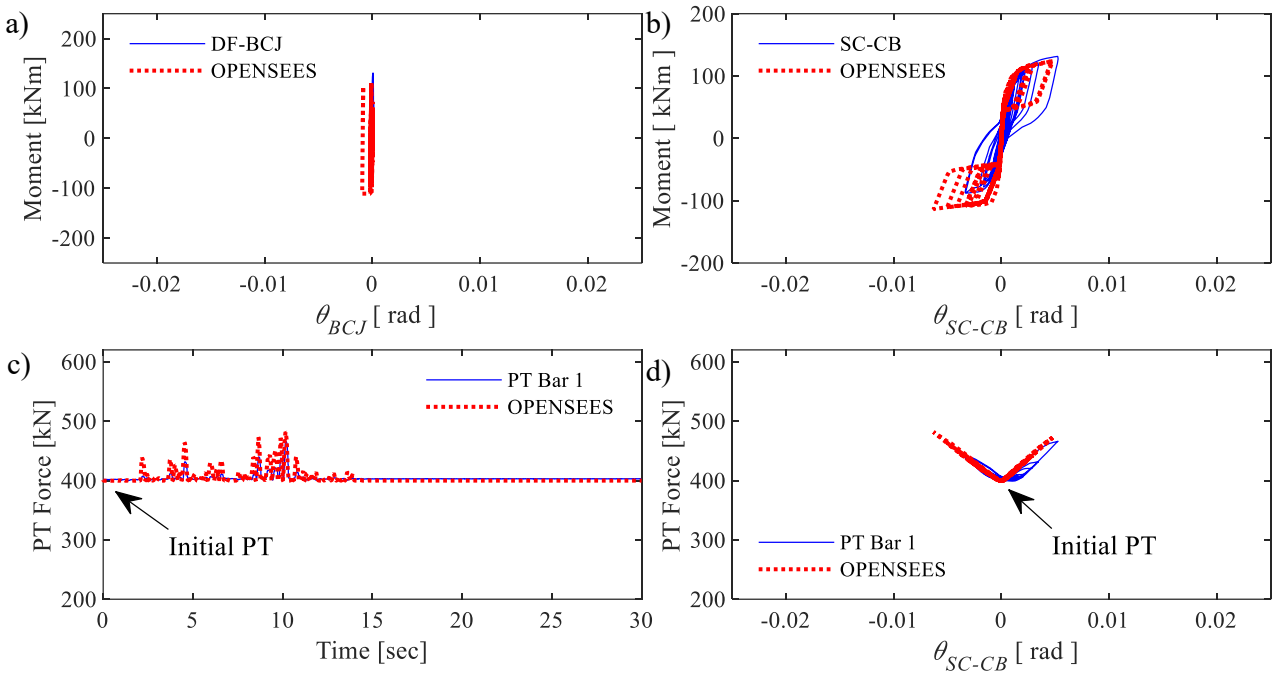

Figure B 27: FEM validation. Components of the SC-CB for Test 3

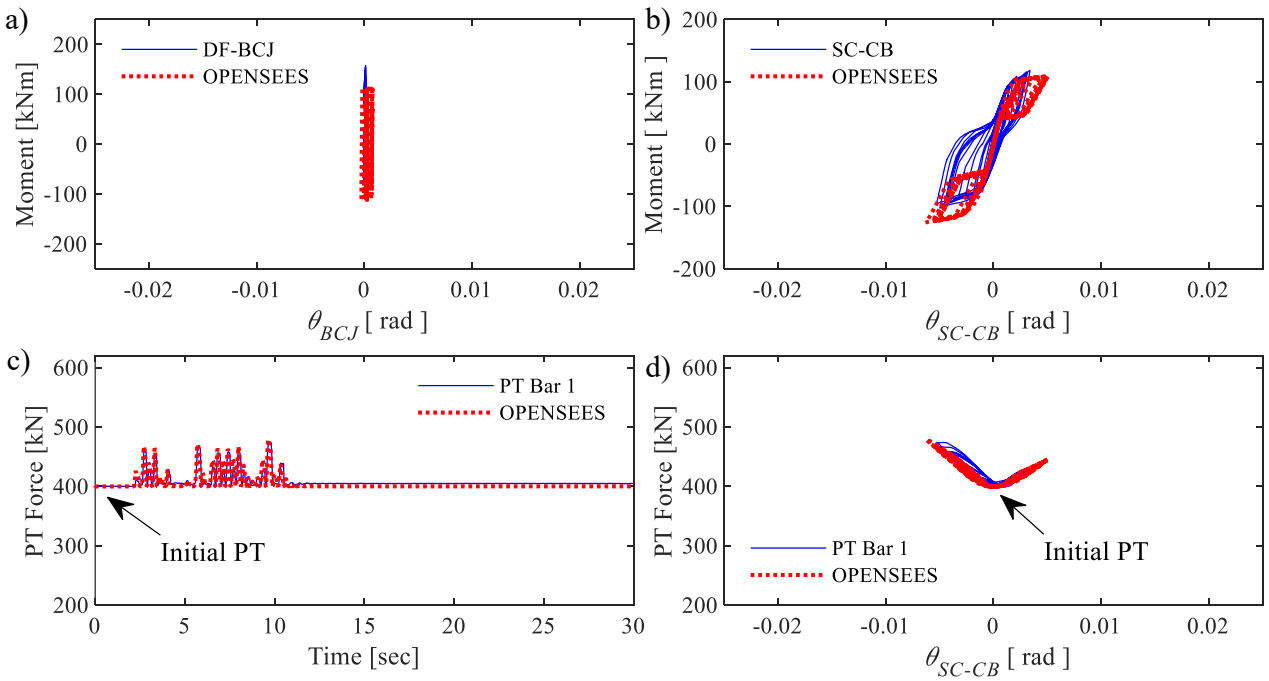

Figure B 28: FEM validation. Components of the SC-CB for Test 4

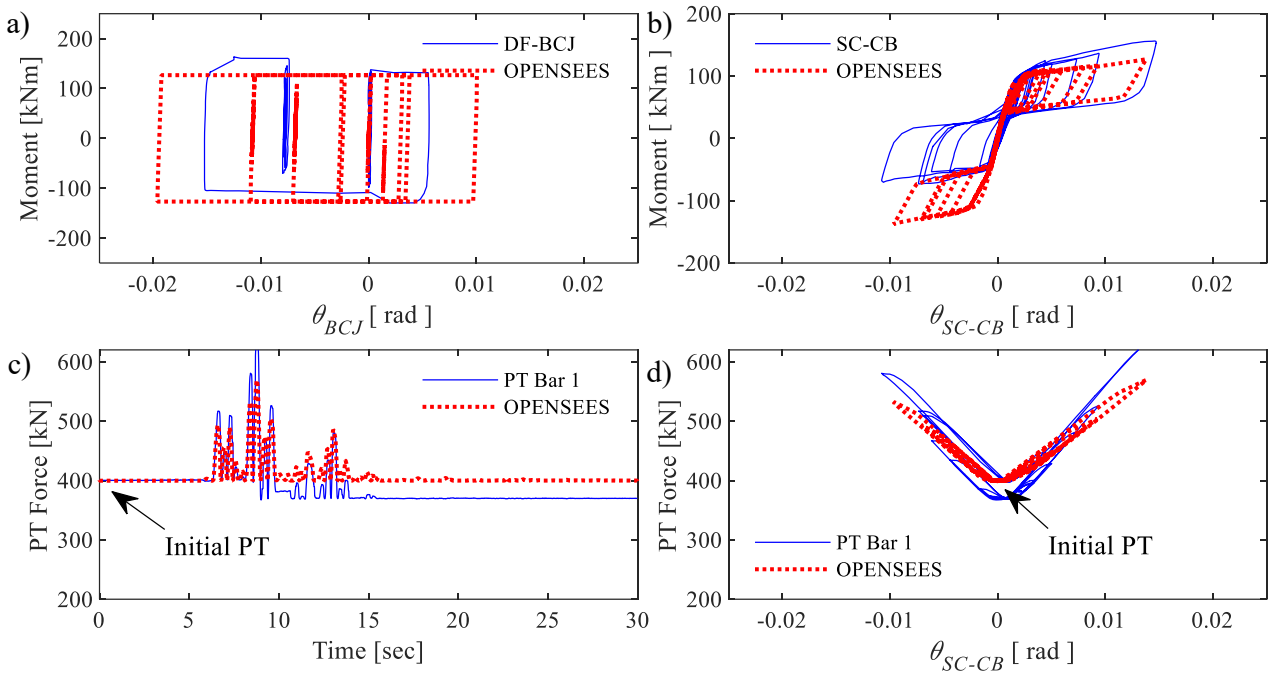

Figure B 29: FEM validation. Components of the SC-CB for Test 5

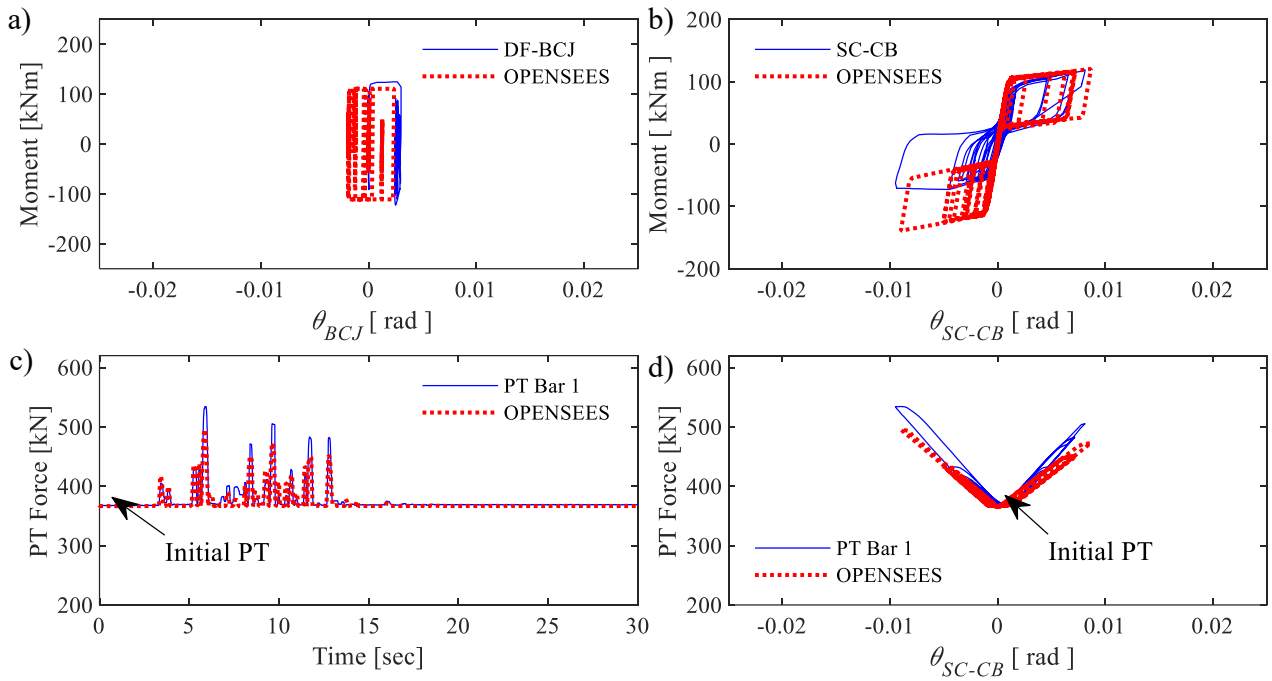

Figure B 30: FEM validation. Components of the SC-CB for Test 6

B2.3 Global Results (NLTHAs)

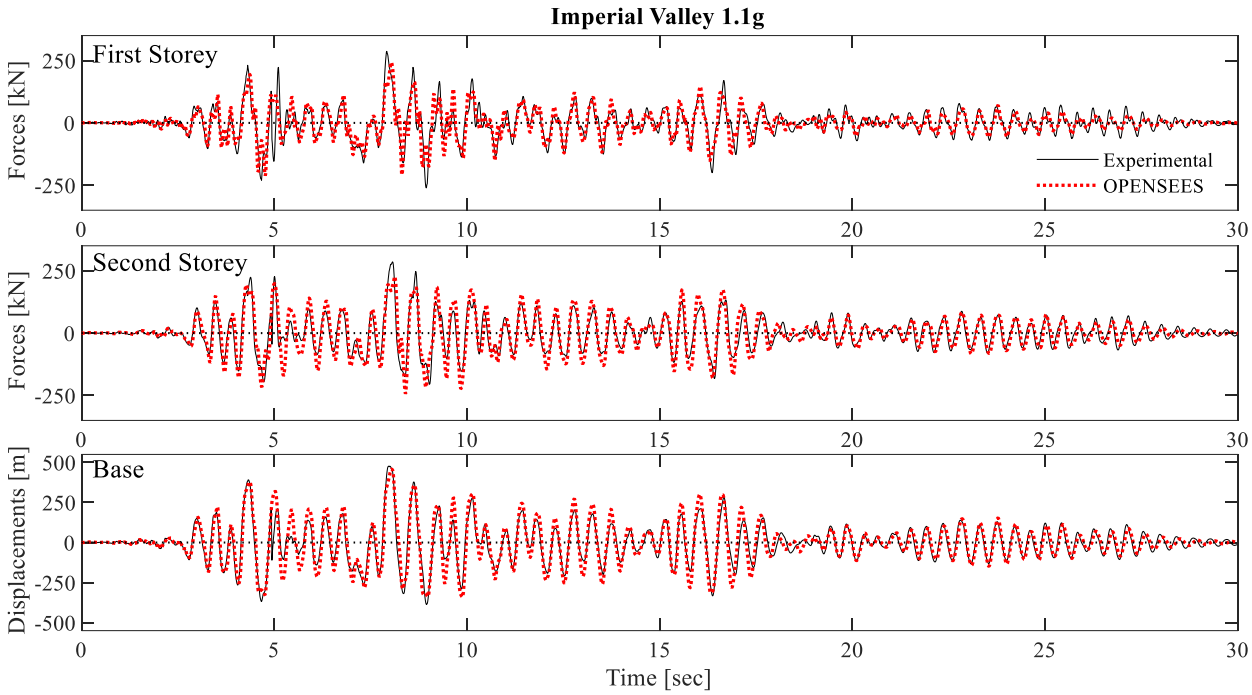

Figure B 31: NLTH Analysis: Actuator forces for Test 1

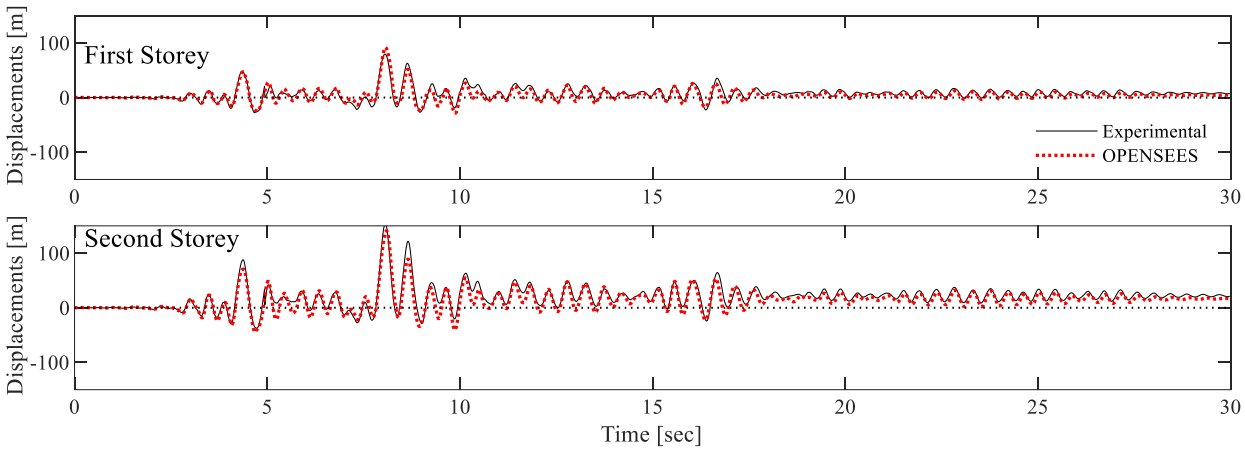

Figure B 32: NLTH Analysis: Displacements for Test 1

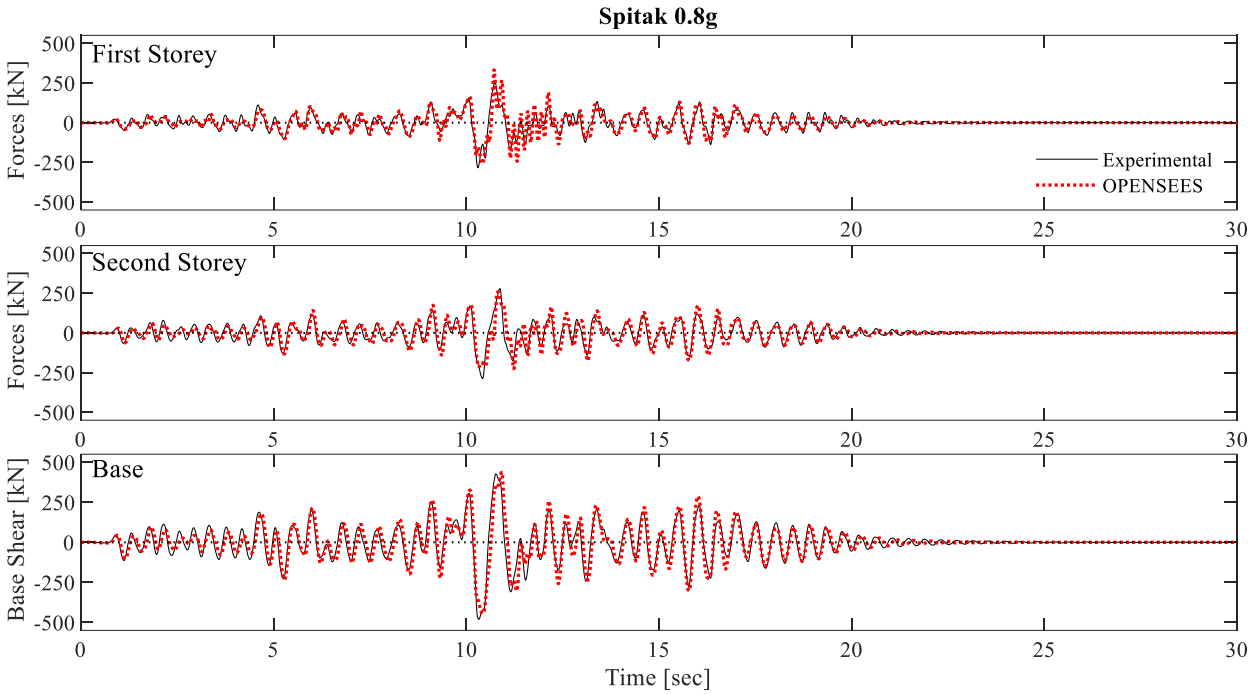

Figure B 33: NLTH Analysis: Actuator forces for Test 2

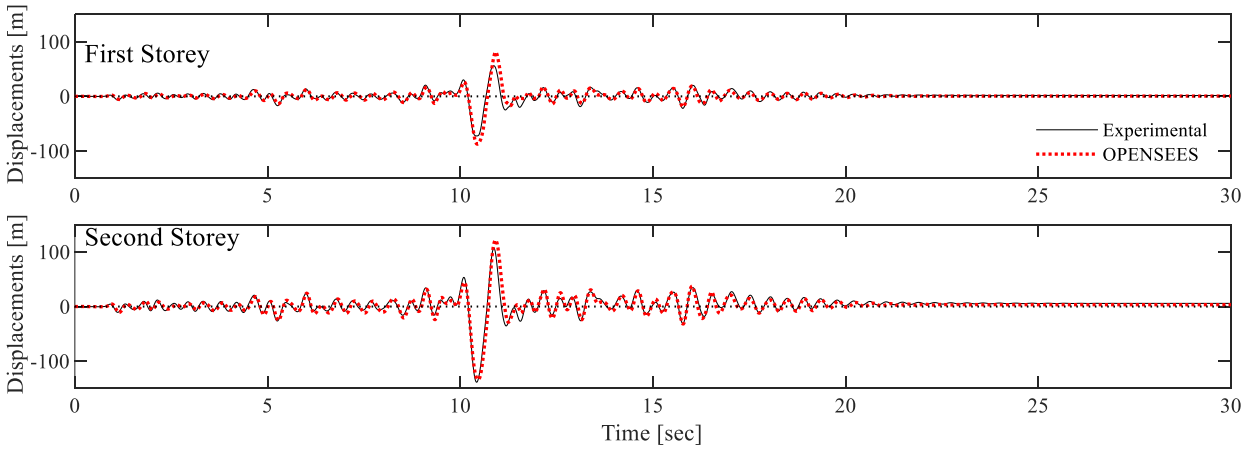

Figure B 34: NLTH Analysis: Displacements for Test 2

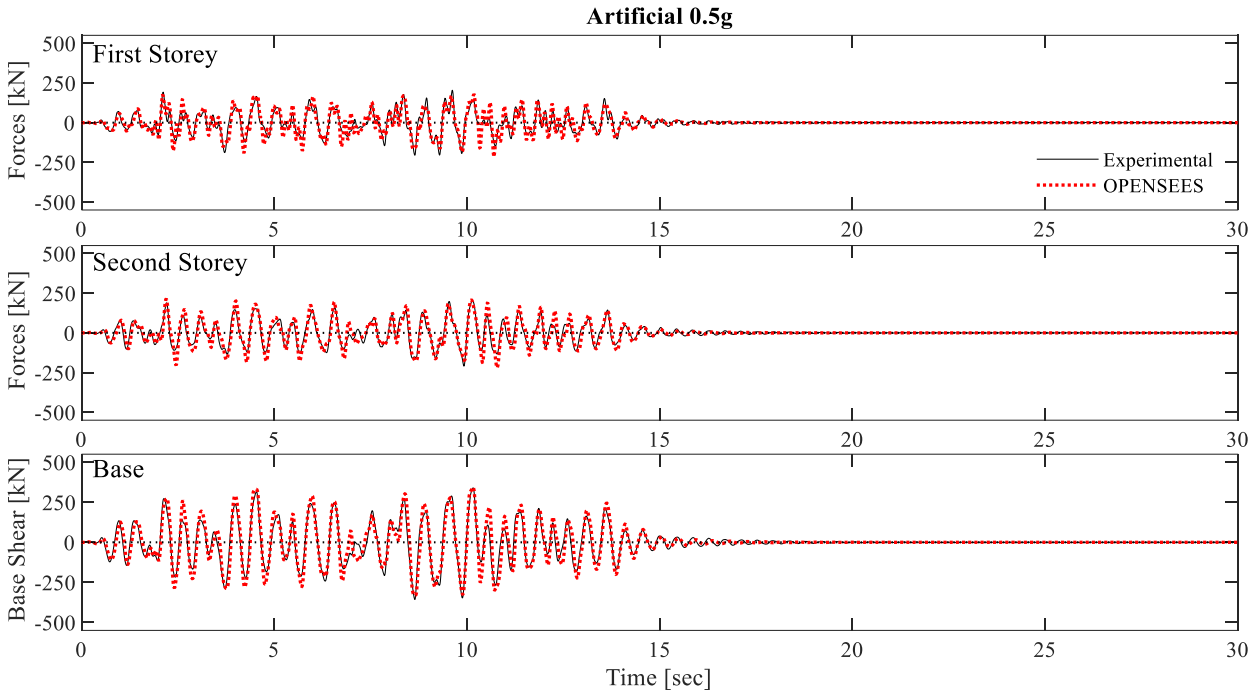

Figure B 35: NLTH Analysis: Actuator forces for Test 3

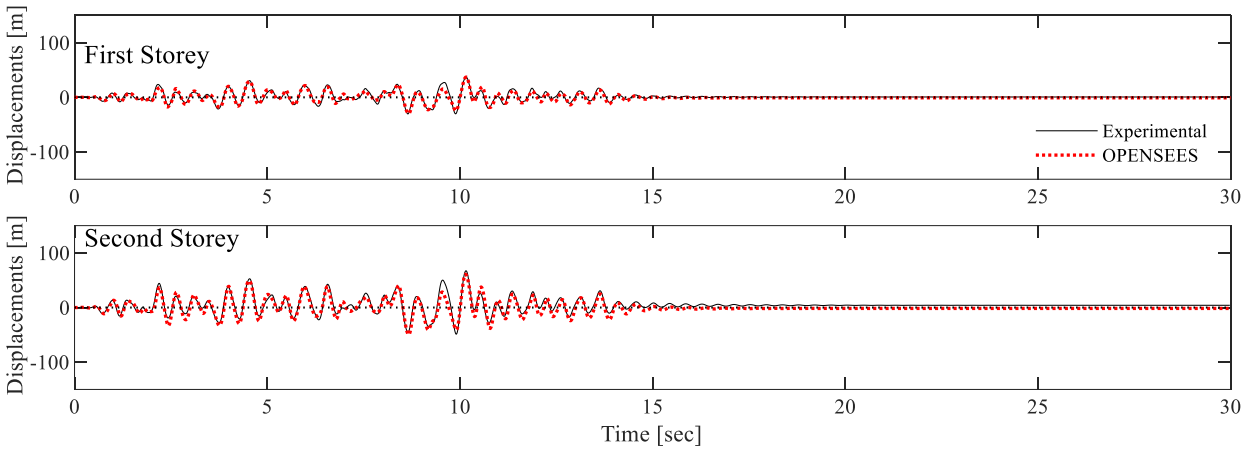

Figure B 36: NLTH Analysis: Displacements for Test 3

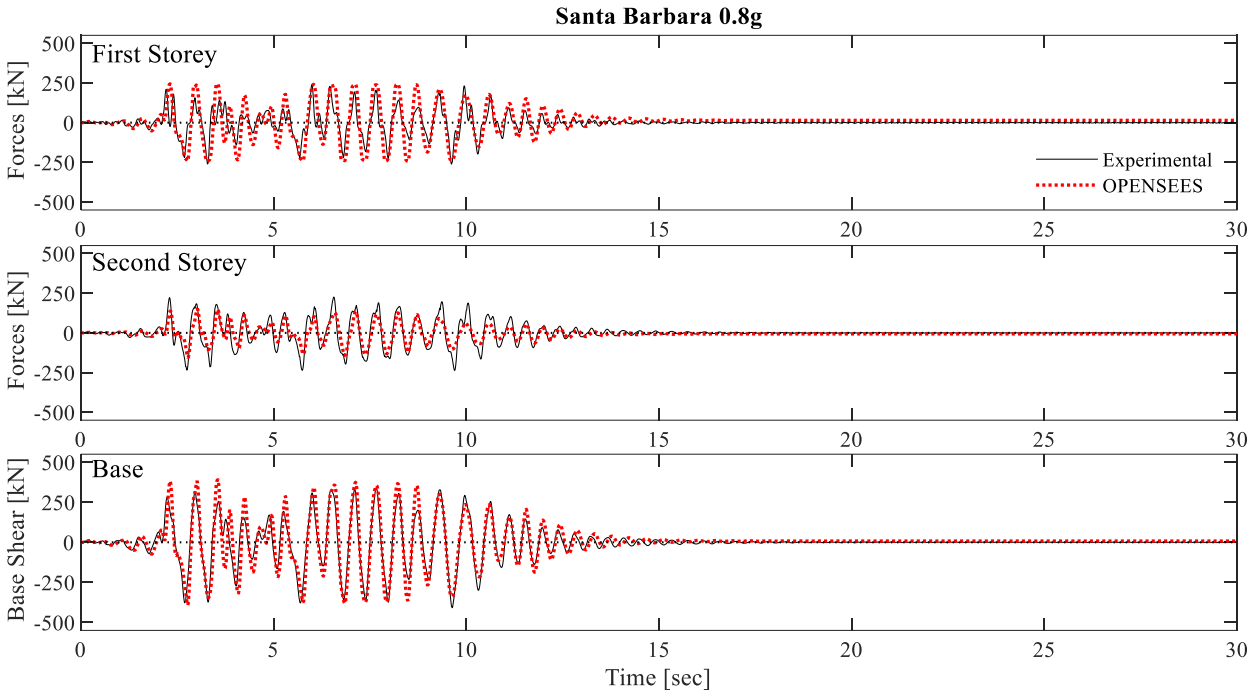

Figure B 37: NLTH Analysis: Actuator forces for Test 4

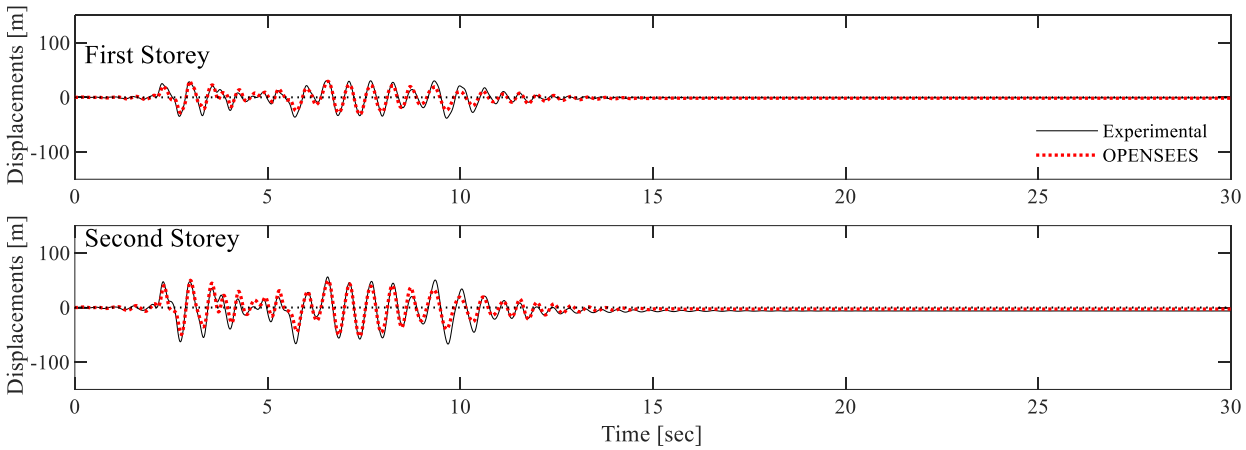

Figure B 38: NLTH Analysis: Displacements for Test 4

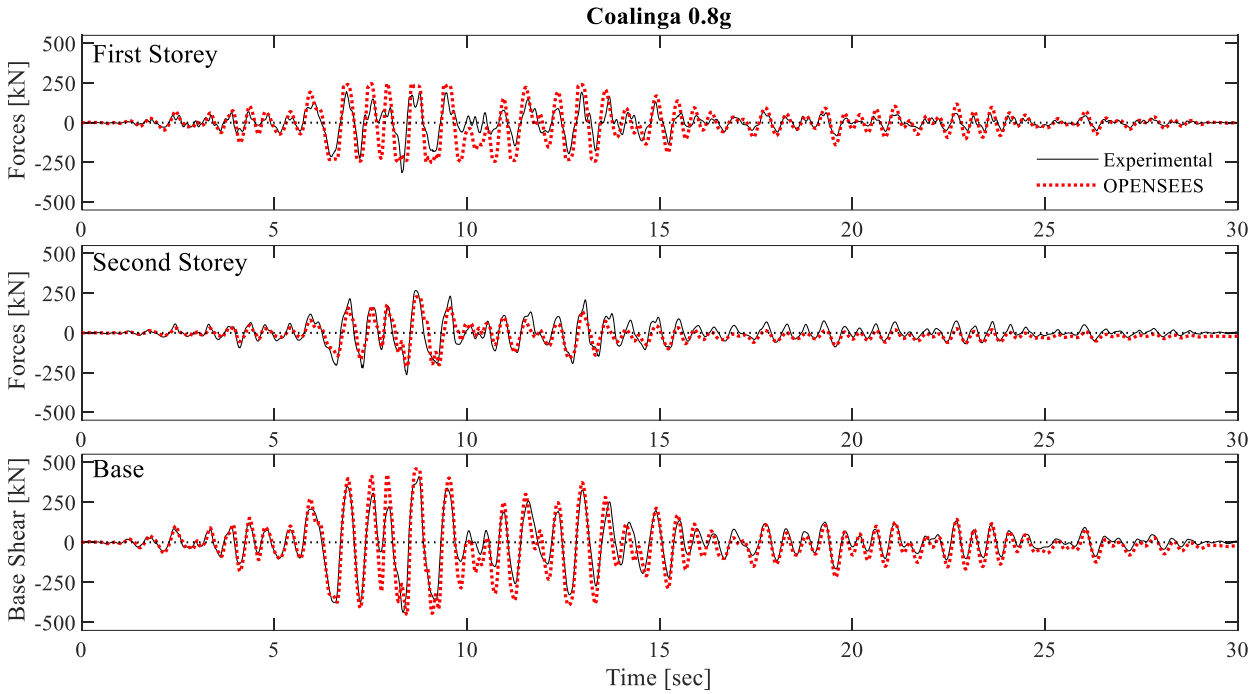

Figure B 39: NLTH Analysis: Actuator forces for Test 5

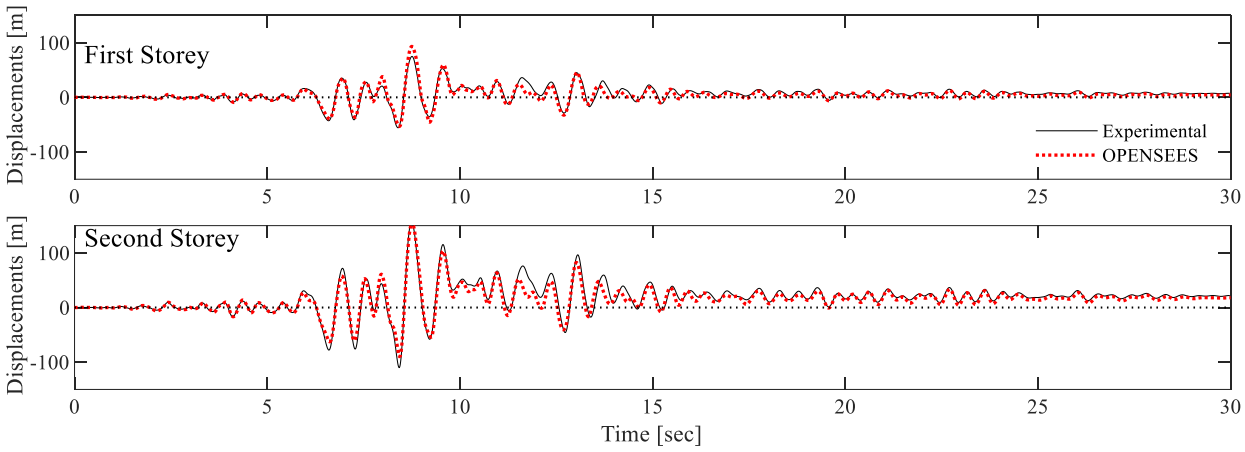

Figure B 40: NLTH Analysis: Displacements for Test 5

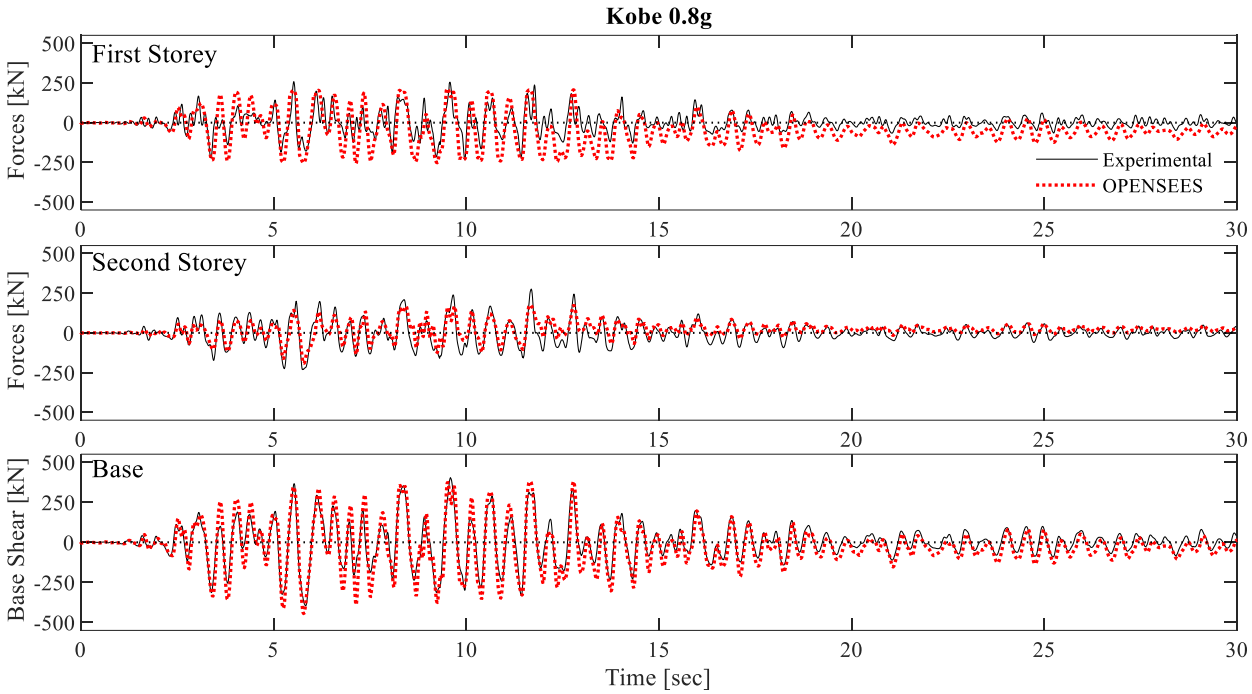

Figure B 41: NLTH Analysis: Actuator forces for Test 6

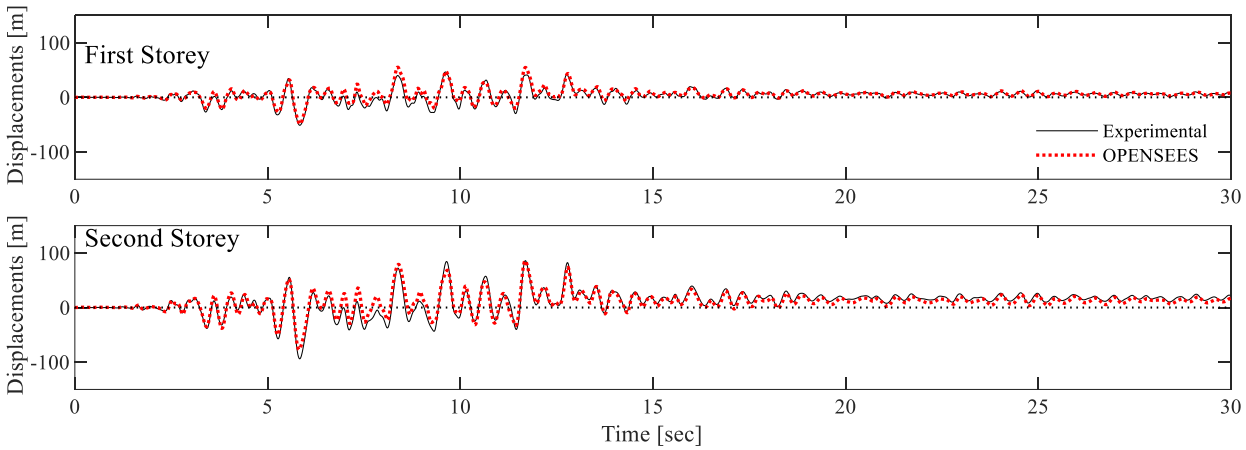

Figure B 42: NLTH Analysis: Displacements for Test 6

B2.4 Local Results (NLTHAs)

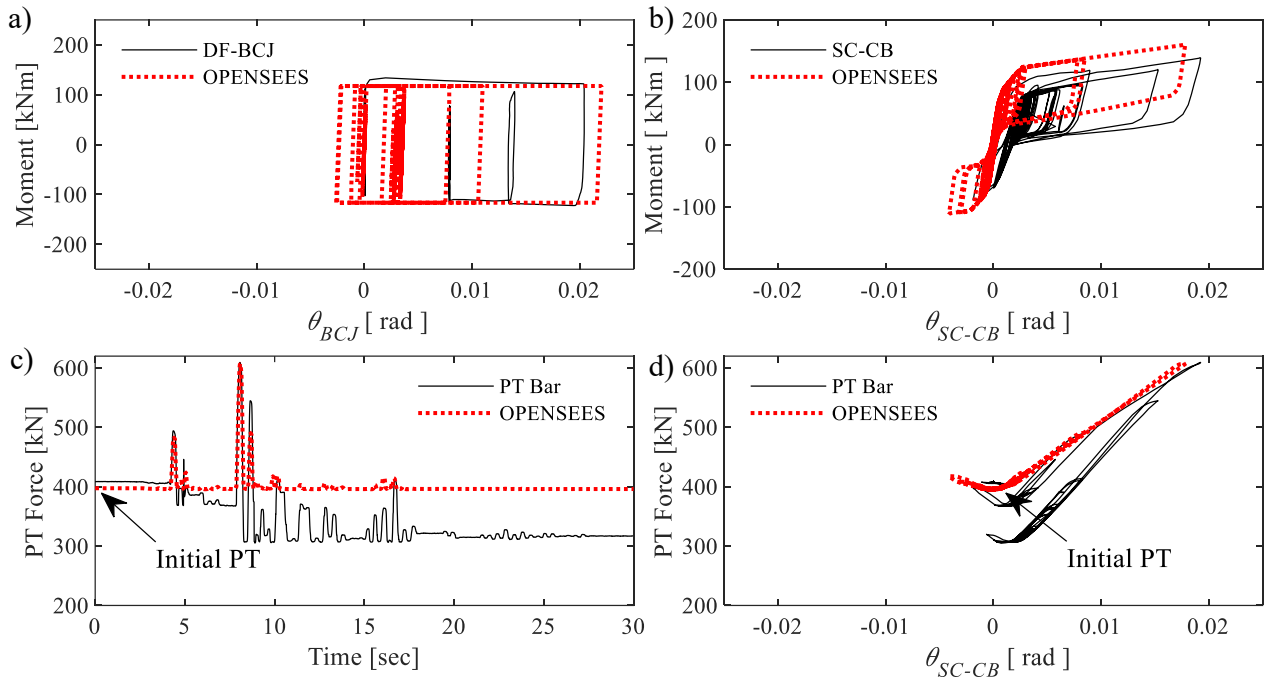

Figure B 43: NLTH Analysis: Local Results for Test 1

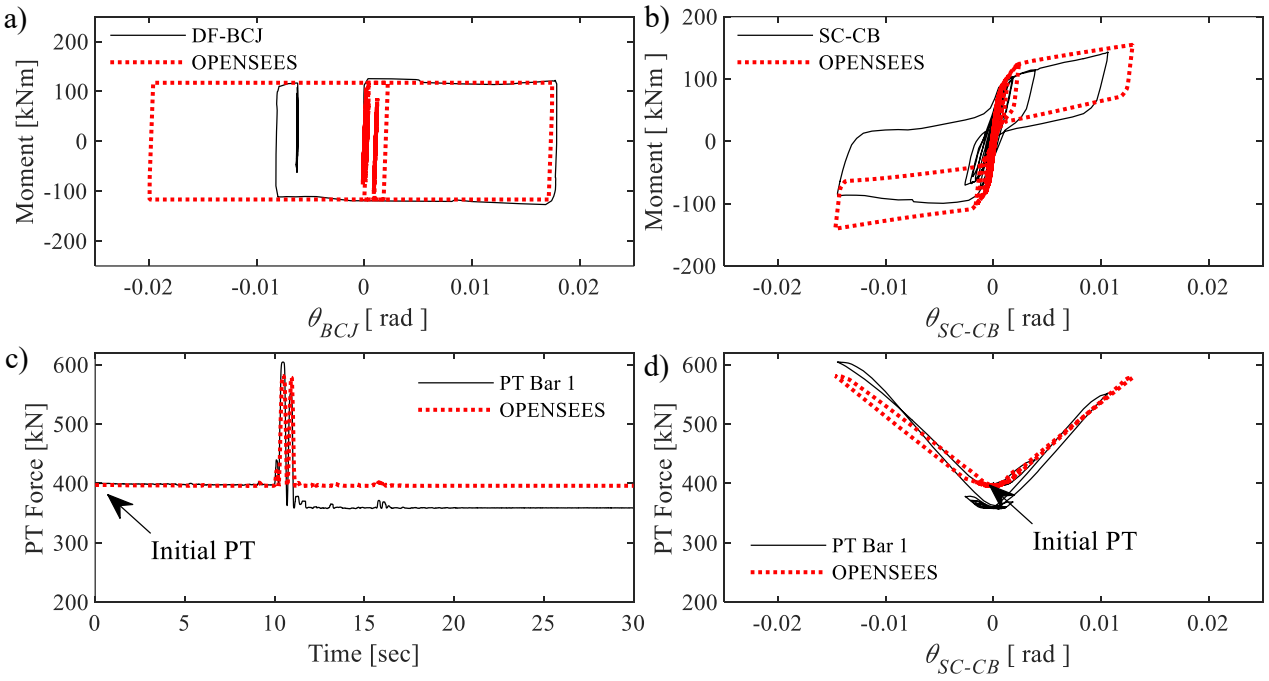

Figure B 44: NLTH Analysis: Local Results for Test 2

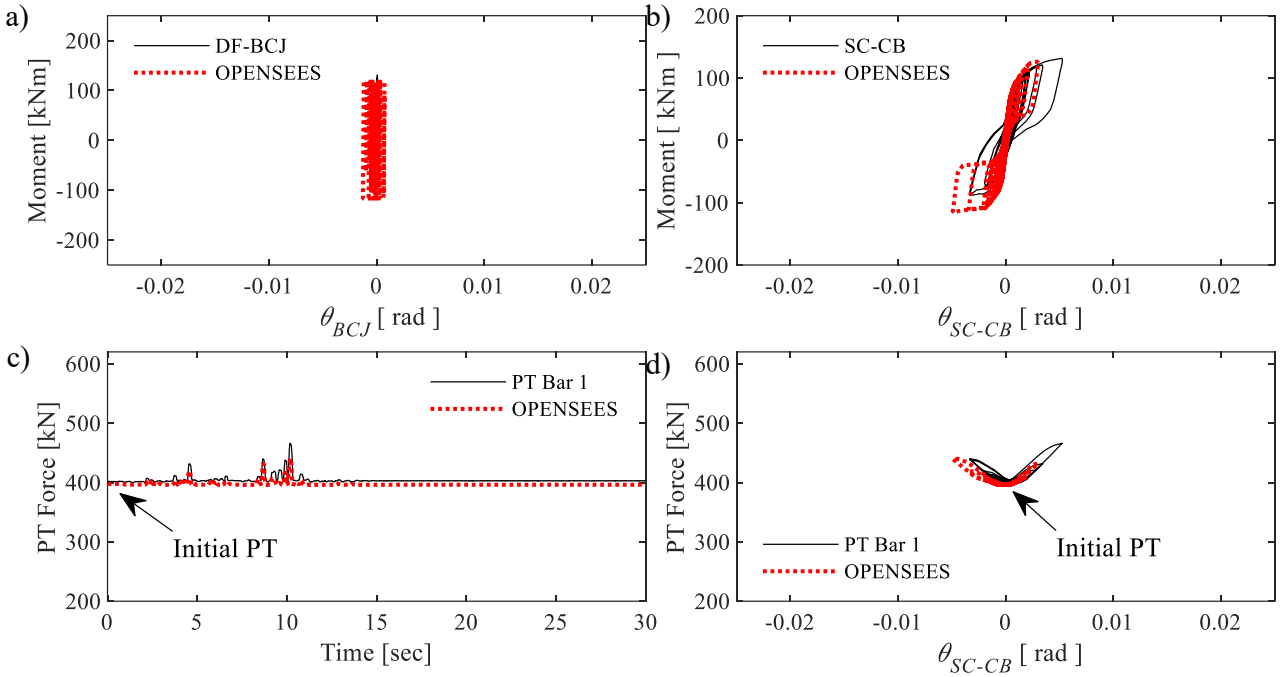

Figure B 45: NLTH Analysis: Local Results for Test 3

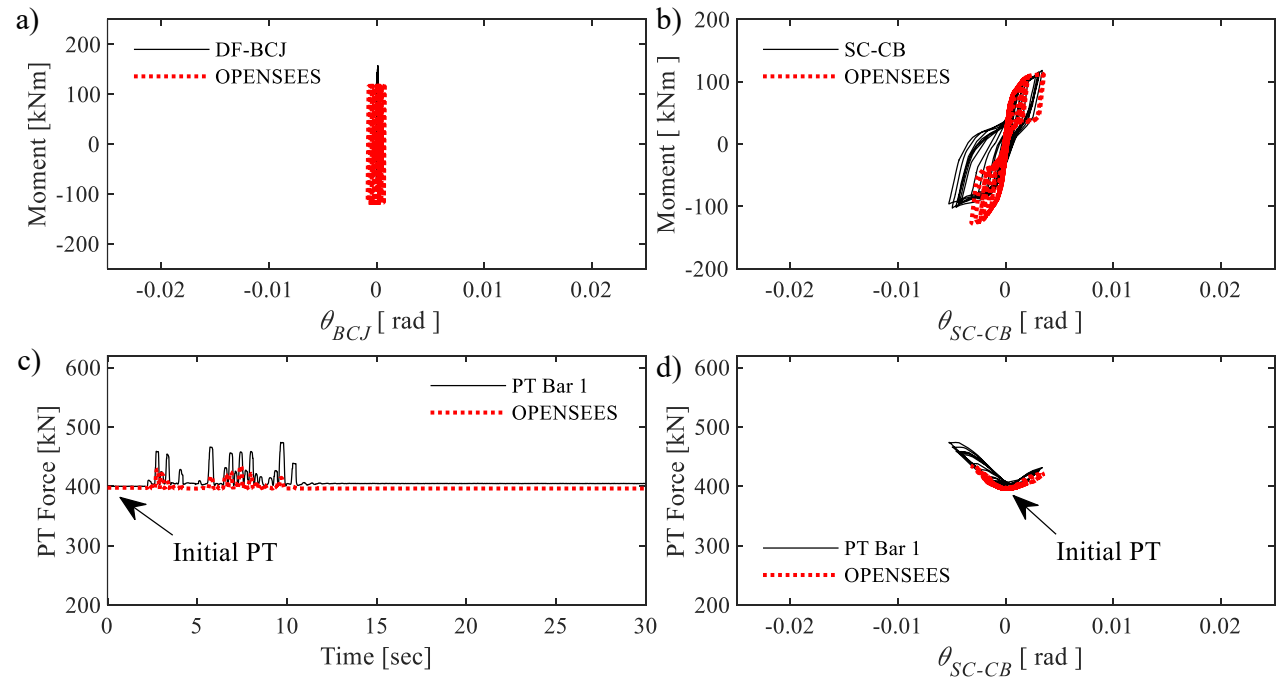

Figure B 46: NLTH Analysis: Local Results for Test 4

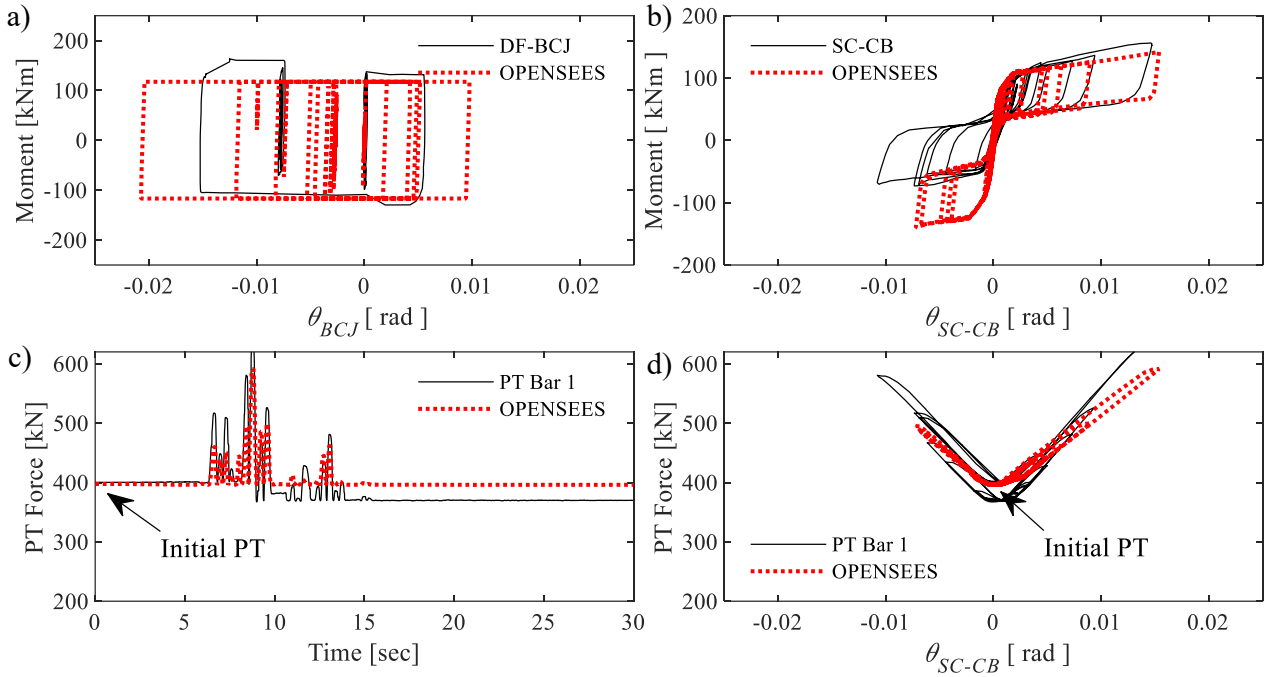

Figure B 47: NLTH Analysis: Local Results for Test 5

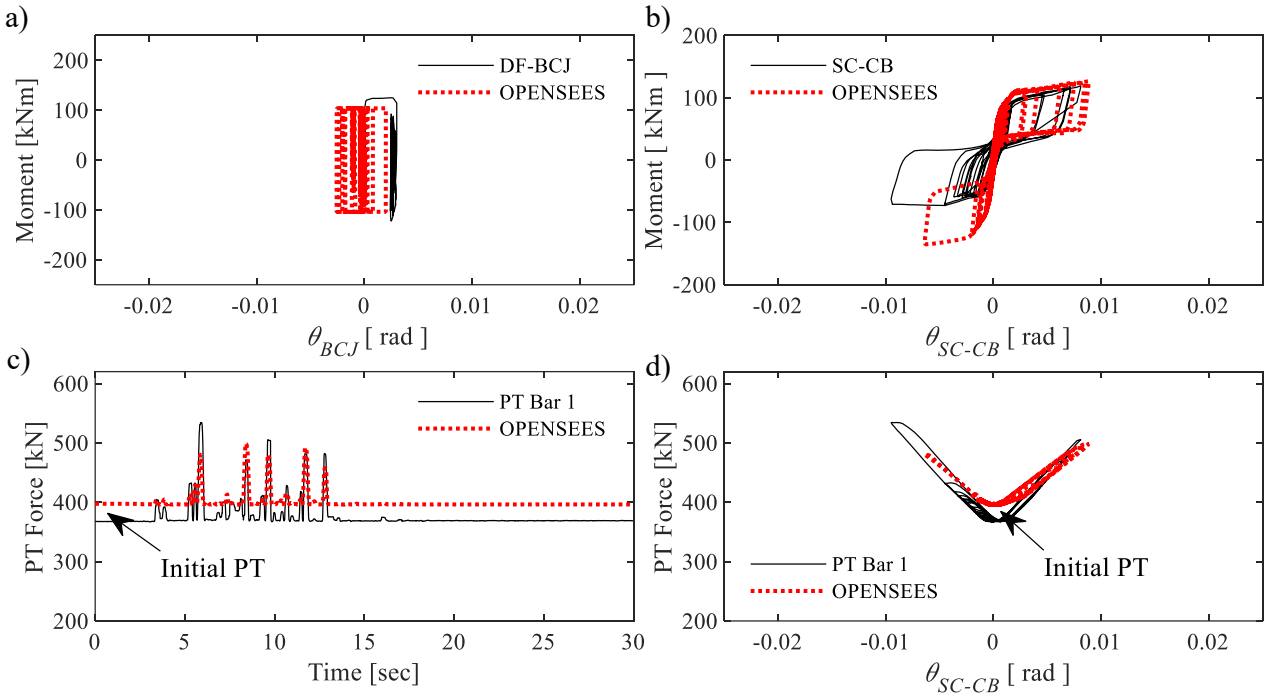

Figure B 48: NLTH Analysis: Local Results for Test 6